

銀河間空間における 非熱的エネルギーの観測的研究

(課題番号 11440074)

1999～2001 年度
文部科学省科学研究費補助金 基盤研究 (B)(2)

研究成果報告書

含む

中澤知洋 博士論文 “Hard X-ray Emission From Groups of Galaxies Detected with ASCA”
2000 年 12 月提出 東京大学

磯部直樹 博士論文 “X-ray Probing into Energetics Associated with Astrophysical Jets from
Active Galactic Nuclei”
2001 年 12 月提出 東京大学

2002 年 3 月

代表者：田代 信 (埼玉大学理学部 助教授)
分担者：深沢泰司 (広島大学大学院理学研究科 助教授)
分担者：牧島一夫 (東京大学大学院理学系研究科 教授)

目次

| | |
|---|-----------|
| 第 1 章 研究課題の概要 | 1 |
| 1.1 はしがき | 1 |
| 1.2 研究発表 | 3 |
| 第 2 章 研究内容の概観 | 11 |
| 2.1 はじめに—銀河間空間における電子冷却 | 11 |
| 2.2 電波ローブからの X 線 | 11 |
| 2.2.1 X 線放射のメカニズム | 11 |
| 2.2.2 「あすか」による電波ローブからの X 線の検出 | 12 |
| 2.2.3 AXAF/ Chandra による電波ローブからの X 線の検出 | 14 |
| 2.2.4 活動銀河核の活動度とジェット-ローブ系のエネルギー収支 | 16 |
| 2.2.5 磁場と電子の棲み分けの兆候 | 17 |
| 2.3 銀河団からの非熱的 X 線の観測 | 19 |
| 2.3.1 銀河団中心部の新描像と銀河間磁場 | 19 |
| 2.3.2 銀河団からの非熱的放射 | 20 |
| 2.3.3 銀河群からの硬 X 線の「あすか」による観測 | 20 |
| 2.3.4 HCG57/HCG16 のデータ解析 | 21 |
| 2.3.5 Chandra による観測 | 21 |
| 2.3.6 銀河団の X 線観測 | 22 |
| 2.3.7 銀河団中心部の電波銀河 | 22 |
| 2.3.8 銀河団ガスと電波ジェット | 23 |
| 第 3 章 参考論文 (投稿論文) | 27 |
| 3.1 M. Tashiro, et al., 2001, ApJ 546, L19 | 27 |
| 3.2 Y. Fukazawa, et al., 2001, ApJ 546, L87 | 33 |
| 第 4 章 参考論文 (博士論文) | 38 |
| 4.1 Isobe, Naoki: Ph. D. thesis | 38 |

4.2 Nakazawa, Kazuhiro: Ph. D. thesis 121

第1章 研究課題の概要

1.1 はしがき

本冊子は1999-2001年度の文部科学省科学研究費補助金—基盤研究(B)(2)「銀河間空間における非熱的エネルギーの観測的研究」(課題番号11440074)の研究成果報告書である。

宇宙空間からの宇宙X線観測によって、恒星、超新星残骸、コンパクト天体、銀河、銀河核、銀河団といったさまざまな階層での高エネルギー現象が解明されてきた。なかでも最近になって「非熱的放射」が注目されている。重力エネルギーなどが解放され最終的に平衡にいたった状態から熱的放射がなされるとすれば、非熱的放射は非平衡な系での、たとえば粒子加速による選択的なエネルギー解放過程を反映している。これは宇宙粒子線の起源として興味深いばかりでなく、これまであまり考慮されていなかったが、決して無視できない、エネルギー遷移の形態を明らかにすることにつながる。本研究は、我が国第4番目の宇宙X線観測衛星「あすか」によって我々が明らかにした、銀河間空間の非熱的放射過程に着目し、「あすか」を含む観測衛星による硬X線観測と次世代硬X線観測装置の開発を課題とした。

「あすか」を用いて我々は、ジェットの終端にひろがるローブ領域からのX線の検出に世界で初めて成功した。これによって銀河から100kpc以上はなれた銀河間空間の非熱的電子のエネルギーと銀河間空間磁場を測定することが可能となり、新しい観測領域と宇宙物理学の理解にいたる手法となった。また我々は、さらに大規模な天体である銀河群からも、広がった硬いX線放射を検出することにも成功した。これは銀河間空間に存在する非熱的エネルギーを示唆する結果であり、それらの粒子加速機構に手掛かりを与えるものと期待される。本研究課題では、1995年以降の「あすか」の切り開いたこれらの観測領域を、「あすか」のみならず米国のAXAF/Chandra衛星、欧州のXMM/Newton衛星を用いて系統的に発展させた。

なお本研究は、宇宙科学研究所の高橋忠幸教授、満田和久教授、スタンフォード大学のGreg Madejski博士、および東京大学理学系研究科牧島研究室、広島大学理学研究科深沢研究室、埼玉大学理学部田代研究室を含む各研究室の大学院生との密接な協力によって遂行された。また、全国の「あすか」チームの方々、およびアメリカ合衆国航空宇宙局ゴダード宇宙飛行センターのASCA Guest Observer Facilityのスタッフの方々によるたゆまぬ努力によって成果を挙げ続けている「あすか」衛星なしでは、本研究はその計画すら成り立たなかった。またこの研究に関わる装置開発実験は、ASTRO-E/HXD開発を共にした東京大学および宇宙研のHXD開発チームおよび「あ

すか」GIS 校正チームと一体となって行われている。

研究組織 —

研究代表者：田代 信 (埼玉大学理学部 助教授¹)

研究分担者：牧島一夫 (東京大学大学院理学系研究科 教授²)

研究分担者：深沢泰司 (広島大学大学院理学研究科 助教授³)

研究経費 —

1999 年度 7,800 千円

2000 年度 3,900 千円

2001 年度 1,800 千円

¹2000 年 9 月までは 東京大学大学院理学系研究科 助手

²2000 年 9 月まで

³2000 年 3 月までは 東京大学大学院理学系研究科 助手

1.2 研究発表

[1] 学術誌等

— 電波ローブの研究に関連して

1. Tashiro, M., Makishima, K., Iyomoto, N., Isobe, N., Kaneda, H., 2001, “X-Ray Measurements of the Field and Particle Energy Distributions in the West Lobe of the Radio Galaxy NGC 1316 (Fornax A)”, *The Astrophysical Journal*, Volume 546, Issue 1, pp. L19-L23.
2. Tashiro, M., Makishima, K., Kaneda, H., 2000, “ASCA Measurements of Field-Particle Energy Distribution in Radio Lobes”, *Advances in Space Research*, Volume 25, Issue 3-4, p. 751-756.
3. Kubo, H., Takahashi, T., Madejski, G., Tashiro, M., Makino, F., Inoue, S., Takahara, F., 2000, “ASCA Observations of Blazars and Multiband Analysis”, *Advances in Space Research*, Volume 25, Issue 3-4, p. 733-736.

— 活動銀河核の研究に関連して

4. Tanihata, C., Urry, C. M., Takahashi, T., Kataoka, J., Wagner, S. J., Madejski, G. M., Tashiro, M., Kouda, M., 2001, “Variability Timescales of TeV Blazars Observed in the ASCA Continuous Long-Look X-Ray Monitoring”, *The Astrophysical Journal*, Volume 563, Issue 2, pp. 569-581.
5. Iyomoto, N., Fukazawa, Y., Nakai, N., Ishihara, Y., “BeppoSAX Observation of NGC 3079”, *The Astrophysical Journal*, Volume 561, Issue 1, pp. L69-L72.
6. Sugiho, M., Kotoku, J., Makishima, K., Kubota, A., Mizuno, T., Fukazawa, Y., Tashiro, M., 2001, “A Possible X-Ray Periodicity at Several Tens of Hours of an Ultraluminous Compact X-Ray Source in IC 342”, *The Astrophysical Journal*, Volume 561, Issue 1, pp. L73-L76,
7. Matsumoto, Y., Fukazawa, Y., Nakazawa, K., Iyomoto, N., Makishima, K., 2001, “The FR-I Radio Galaxies NGC 315 and NGC 4261 Observed with ASCA”, *Publications of the Astronomical Society of Japan*, vol.53, no. 3, p. 475-481.
8. Isobe, N., Tashiro, M., Sugiho, M., Makishima, K., 2001, “ASCA Observations of the BL Lacertae Object OJ 287 in 1997 April and November”, 2001, *Publications of the Astronomical Society of Japan*, vol.53, no. 1, p. 79-84.

9. Takahashi, H., Okada, Y., Kokubun, M., Makishima, K., 2001, "ASCA Observations of the Central Regions of M 31", Publications of the Astronomical Society of Japan, Vol.53, No. 5, pp. 875-883.
 10. Watson, D., Smith, N., Hanlon, L., McBreen, B., Quilligan, F., Tashiro, M., Metcalfe, L., Doyle, P., Terasranta, H., Carraminana, A., Guichard, J., 2000, "ASCA and other contemporaneous observations of the blazar B2 1308+326", Astronomy and Astrophysics, v.364, p.43-52.
 11. Ezoe, Y., Iyomoto, N., Makishima, Kazuo, 2001, "Study of the Long-Term X-Ray Variability of a Possible Quasar RX J0957.9+6903 with ASCA", Publications of the Astronomical Society of Japan, vol.53, no. 1, p. 69-78.
 12. Takahashi, T., Kataoka, J., Madejski, G., Mattox, J., Urry, C. M., Wagner, S., Aharonian, F., Catanese, M., Chiappetti, L., Coppi, P., Degrange, B., Fossati, G., Kubo, H., Krawczynski, H., Makino, F., Marshall, H., Maraschi, L., Piron, F., Remillard, R., Takahara, F., Tashiro, M., Terasranta, H., Weekes, T., 2000, "Complex Spectral Variability from Intensive Multiwavelength Monitoring of Markarian 421 in 1998" The Astrophysical Journal, Volume 542, Issue 2, pp. L105-L109.
 13. Makishima, K., Kubota, A., Mizuno, T., Ohnishi, T., Tashiro, M., Aruga, Y., Asai, K., Dotani, T., Mitsuda, K., Ueda, Y., Uno, S., Yamaoka, K., Ebisawa, K., Kohmura, Y., Okada, K., 2000, "The Nature of Ultraluminous Compact X-Ray Sources in Nearby Spiral Galaxies", The Astrophysical Journal, Volume 535, Issue 2, pp. 632-643.
 14. Kataoka, J., Takahashi, T., Makino, F., Inoue, S., Madejski, G. M., Tashiro, M., Urry, C. M., Kubo, H., 2000, "Variability Pattern and the Spectral Evolution of the BL Lacertae Object PKS 2155-304", The Astrophysical Journal, Volume 528, Issue 1, pp. 243-253.
 15. Watson, D., Hanlon, L., McBreen, B., Smith, N., Tashiro, M., Foley, A. R., Metcalfe, L., Beckmann, V., Sanchez, S. F., Terasranta, H., 1999, "Simultaneous multifrequency observations of the BL Lac MS 0205.7+3509", Astronomy and Astrophysics, v.345, p.414-418.
- 系外ブラックホールおよびマイクロクエーサーの研究に関連して
18. Kubota, A., Makishima, K., Ebisawa, K., 2001, "Observational Evidence for Strong Disk Comptonization in GRO J1655-40", The Astrophysical Journal, Volume 560, Issue 2, pp. L147-L150.

19. Mizuno, T., Kubota, A., Makishima, K., 2001, "Spectral Variability of Ultraluminous Compact X-Ray Sources in Nearby Spiral Galaxies", *The Astrophysical Journal*, Volume 554, Issue 2, pp. 1282-1289.
20. Kubota, A., Mizuno, T., Makishima, K., Fukazawa, Y., Kotoku, J., Ohnishi, T., Tashiro, M., 2001, "Discovery of Spectral Transitions from Two Ultraluminous Compact X-Ray Sources in IC 342", *The Astrophysical Journal*, Volume 547, Issue 2, pp. L119-L122.
21. Kubota, A., Tanaka, Y., Makishima, K., Ueda, Y., Inoue, H., Yamaoka, K., Dotani, T., 2000, "ASCA observation of the X-ray transient GRS 1009-45", *Advances in Space Research*, Volume 25, Issue 3-4, p. 449-452.
22. Kotoku, J., Mizuno, T., Kubota, A., Makishima, K., 2000, "ASCA Observation of Ultra-Luminous X-Ray Sources in the Nearby Spiral Galaxy NGC 2403", *Publ. of the Astronomical Society of Japan*, v.52, p.1081-L1085.
23. Mizuno, T., Ohnishi, T., Kubota, A., Makishima, K., Tashiro, M., 1999, "ASCA Observations of Two Ultra-Luminous Compact X-Ray Sources in the Edge-On Spiral Galaxy NGC 4565", *Publ. of the Astronomical Society of Japan*, v.51, p.663.

— 銀河団の研究に関連して

24. Fukazawa, Y., Iyomoto, N., Kubota, A., Matsumoto, Y., Makishima, K., 2001, "Excess hard X-ray emission from the obscured low luminosity AGN in the nearby galaxy M 51 (NGC 5194)", *Astronomy and Astrophysics*, v.374, p.73-82.
25. Fukazawa, Y., Nakazawa, K., Isobe, N., Makishima, K., Matsushita, K., Ohashi, T., Kamae, T., 2001, "Detection of Excess Hard X-Ray Emission from the Group of Galaxies HCG 62", *The Astrophysical Journal*, Volume 546, Issue 2, pp. L87-L90.
26. Ezawa, H., Yamasaki, N. Y., Ohashi, T., Fukazawa, Y., Hirayama, M., Honda, H., Kamae, T., Kikuchi, K., Shibata, R., 2001, "ASCA Observations of the Temperature Structure and Metal Distribution in the Perseus Cluster of Galaxies", *Publications of the Astronomical Society of Japan*, Vol.53, No. 4, p. 595-604.
27. Makishima, K., Ezawa, H., Fukuzawa, Y., Honda, H., Ikebe, Y., Kamae, T., Kikuchi, K., Matsushita, K., Nakazawa, K., Ohashi, T., Takahashi, T., Tamura, T., Xu, H., 2001, "X-Ray Probing of the Central Regions of Clusters of Galaxies", *Publications of the Astronomical Society of Japan*, vol.53, no. 3, p. 401-420.

28. Ishihara, Y., Nakai, N., Iyomoto, N., Makishima, K., Diamond, P., Hall, P., 2001, "Water-Vapor Maser Emission from the Seyfert 2 Galaxy IC 2560: Evidence for a Super-Massive Black Hole", Publications of the Astronomical Society of Japan, vol.53, no. 1, p. 215-225.
29. Takahashi, I., Fukazawa, Y., Kodaira, K., Makishima, K., Nakazawa, K., Xu, H., 2000, "ASCA Observations of Three Shakhbazyan's Compact Groups of Galaxies", Publ. of the Astronomical Society of Japan, v.52, p.769-774.
30. Nakazawa, K., Makishima, K., Fukazawa, Y., Tamura, T., 2000, "ASCA Observations of a Near-by Cluster in Antlia", Publ. of the Astronomical Society of Japan, v.52, p.623-630.
31. Tamura, T., Makishima, K., Fukazawa, Y., Ikebe, Y., Xu, H., 2000, "X-Ray Measurements of the Gravitational Potential Profile in the Central Region of the Abell 1060 Cluster of Galaxies", The Astrophysical Journal, Volume 535, Issue 2, pp. 602-614.
32. Kikuchi, K., Itoh, C., Kushino, A., Furusho, T., Matsushita, K., Yamasaki, N. Y., Ohashi, T., Fukazawa, Y., Ikebe, Y., Bohringer, H., Matsumoto, H., 2000, "Detection of an X-Ray Hot Region in the Virgo Cluster of Galaxies with ASCA", The Astrophysical Journal, Volume 531, Issue 2, pp. L95-L98.
33. Fukazawa, Y., Makishima, K., Tamura, T., Nakazawa, K., Ezawa, H., Ikebe, Y., Kikuchi, K., Ohashi, T., 2000, "Statistical properties of metal abundances of the intracluster medium in the central region of clusters", Monthly Notices of the Royal Astronomical Society, Volume 313, Issue 1, pp. 21-31.
34. Matsumoto, H., Tsuru, T. G., Fukazawa, Y., Hattori, M., Davis, D. S., 2000, "Gas, Iron, and Gravitational Mass in Galaxy Clusters: The General Lack of Cluster Evolution at $z \leq 1.0$ ", Publ. of the Astronomical Society of Japan, v.52, p.153.
35. Nakazawa, K., Makishima, K., Fukazawa, Y., Tamura, T., 2000, "ASCA Observation of a Near-by Cluster, Antlia", Advances in Space Research, Volume 25, Issue 3-4, p. 607-610.
36. Ohashi, T., Kikuchi, K., Matsushita, K., Yamasaki, N., Ezawa, H., Fukazawa, Y., Makishima, K., Kamae, T., Hirayama, M., Honda, H., Shibata, R., Matsumoto, H., Ikebe, Y., 2000, "Metallicity and Temperature Distributions in Clusters of Galaxies", Advances in Space Research, Volume 25, Issue 3-4, p. 593-598.
37. Osone, S., Makishima, K., Matsuzaki, K., Ishisaki, Y., Fukazawa, Y., 2000, "Search for Hot Gas in the Local Group with ASCA", Advances in Space Research, Volume 25, Issue

3-4, p. 589-592.

38. Obayashi, H., Makishima, K., Tamura, T., 2000, "ASCA observations of the Sculptor Supercluster", *Advances in Space Research*, Volume 25, Issue 3-4, p. 625-628.
39. Matsumoto, R., Valinia, A., Tajima, T., Makishima, K., Shibata, K., 2000, "Formation of Localized Strongly Magnetized Regions in Galaxies and Clusters of Galaxies", *Advances in Space Research*, Volume 25, Issue 3-4, p. 499-504.
40. Ikebe, Y., Makishima, K., Fukazawa, Y., Tamura, T., Xu, H., Ohashi, T., Matsushita, K., 1999, "Two-Phase Intracluster Medium in the Centaurus Cluster of Galaxies", *The Astrophysical Journal*, Volume 525, Issue 1, pp. 58-79.
41. Hwang, U., Mushotzky, R. F., Burns, J. O., Fukazawa, Y., White, R. A., 1999, "Mass and Metallicity of Five X-Ray-bright Galaxy Groups", *The Astrophysical Journal*, Volume 516, Issue 2, pp. 604-618.
42. Kikuchi, K., Furusho, T., Ezawa, H., Yamasaki, N. Y., Ohashi, T., Fukazawa, Y., Ikebe, Y., 1999, "ASCA Measurements of Metallicity and Temperature Distributions in Three Clusters: A4059, MKW 3s, and 2A 0335+096", *Publ. of the Astronomical Society of Japan*, v.51, p.301-315.

— 観測装置の開発に関して

38. Tashiro, M., et al., "Performance of the ASTRO-E Hard X-ray Detector", *IEEE Trans. Nucl. Sci.*, submitted.
39. Sugiho, M., Kamae, T., Makishima, K., Takahashi, T., Murakami, T., Tashiro, M., Fukazawa, Y., et al., 2001, "Spatially dependent response of thick and large area p-i-n diode for ASTRO-E hard X-ray detector" *IEEE Trans. Nucl. Sci.*, vol. 48, pp.426-429.
40. Kokubun, M., Fukazawa, Y., Idesawa, E., Kataoka, J., Kamae, T., Matsuzaki, K., et al., 1999 "Activation of the ASTRO-E hard X-ray detector in low Earth orbit" *IEEE Trans. Nucl. Sci.*, vol. 46, pp.371-376.
41. Ota, N., Murakami, T., Sugizaki, M., Kaneda, M., Tamura, T., Ozawa, H., et al., 1999, "Thick and large area PIN diodes for hard X-ray astronomy," *Nucl. Instr. Meth.*, vol. A436, pp. 291-296.

[2] 研究会収録等

— “Broad Band X-ray Spectra of Cosmic Sources”, Proceedings of the E1.1 Symposium of COSPAR Scientific Commission E, held during the 32nd COSPAR Scientific Assembly, 12-19 July, 1998 in Nagoya, Japan.

47. Tashiro, M.; Makishima, K.; Kaneda, H., 2000, “ASCA Measurements of Field-Particle Energy Distribution in Radio Lobes”, Edited by K. Makishima, L. Piro, and T. Takahashi. Published for the Committee on Space Research by Pergamon Press, 2000., p.751.
48. Kubo, H.; Takahashi, T.; Madejski, G.; Tashiro, M.; Makino, F.; Inoue, S.; Takahara, F., 2000, “ASCA Observations of Blazars and Multiband Analysis”, Broad Band X-ray Spectra of Cosmic Sources, Proceedings of the E1.1 Symposium of COSPAR Scientific Commission E, held during the 32nd COSPAR Scientific Assembly, 12-19 July, 1998 in Nagoya, Japan. Edited by K. Makishima, L. Piro, and T. Takahashi. Published for the Committee on Space Research by Pergamon Press, 2000., p.733.
49. Nakazawa, K., Makishima, K., Fukazawa, Y., Tamura, T., 2000, “ASCA Observation of a Near-By Cluster, Antlia”, Broad Band X-ray Spectra of Cosmic Sources, Proceedings of the E1.1 Symposium of COSPAR Scientific Commission E, held during the 32nd COSPAR Scientific Assembly, 12-19 July, 1998 in Nagoya, Japan. Edited by K. Makishima, L. Piro, and T. Takahashi. Published for the Committee on Space Research by Pergamon Press, 2000., p.607.
50. Ohashi, T., Kikuchi, K., Matsushita, K., Yamasaki, N., Ezawa, H., Fukazawa, Y., Makishima, K., Kamae, T., Hirayama, M., Honda, H., Shibata, R., Matsumoto, H., Ikebe, Y. “Metallicity and Temperature Distributions in Clusters of Galaxies”, Broad Band X-ray Spectra of Cosmic Sources, Proceedings of the E1.1 Symposium of COSPAR Scientific Commission E, held during the 32nd COSPAR Scientific Assembly, 12-19 July, 1998 in Nagoya, Japan. Edited by K. Makishima, L. Piro, and T. Takahashi. Published for the Committee on Space Research by Pergamon Press, 2000., p.593.
51. Osone, S., Makishima, K., Matsuzaki, K., Ishisaki, Y., Fukazawa, Y., “Search for Hot Gas in the Local Group With ASCA”, Broad Band X-ray Spectra of Cosmic Sources, Proceedings of the E1.1 Symposium of COSPAR Scientific Commission E, held during the 32nd COSPAR Scientific Assembly, 12-19 July, 1998 in Nagoya, Japan. Edited by K.

Makishima, L. Piro, and T. Takahashi. Published for the Committee on Space Research by Pergamon Press, 2000., p.589.

52. Obayashi, H.; Makishima, K.; Tamura, T., "ASCA Observations of the Sculptor Supercluster", Broad Band X-ray Spectra of Cosmic Sources, Proceedings of the E1.1 Symposium of COSPAR Scientific Commission E, held during the 32nd COSPAR Scientific Assembly, 12-19 July, 1998 in Nagoya, Japan. Edited by K. Makishima, L. Piro, and T. Takahashi. Published for the Committee on Space Research by Pergamon Press, 2000., p.625.

— 「あすか」 GIS の較正と ASTRO-E HXD の開発

53. Nakazawa, K., Kamae, T., Makishima, K., Takahashi, T., Murakami, T., Tashiro, M., Fukazawa, Y., Tamura, T., Iyomoto, N., Ebisawa, K., Ezoe, Y., Hamaya, M., Horii, M., Isobe, N., Kokubun, M., 1999, "Fabrication of the ASTRO-E hard-x-ray detector", Proc. SPIE Vol. 3765, p. 148-159, EUV, X-Ray, and Gamma-Ray Instrumentation for Astronomy X, Oswald H. Siegmund; Kathryn A. Flanagan; Eds.

54. Terada, Y., Yamaoka, K., Kokubun, M., Kotoku, J., Mizuno, T., Kataoka, J., Takahashi, T., Murakami, T., Makishima, K., Kamae, T., The Hxd Team, 2000, "Capability of the ASTRO-E Hard X-Ray Detector for High-Energy Transients and γ -Ray Bursts", The Fifth Compton Symposium, Proceedings of the fifth Compton Symposium, held in Portsmouth, NH, USA, September 1999. Melville, NY: American Institute of Physics (AIP), 2000. Edited by Mark L. McConnell and James M. Ryan AIP Conference Proceedings, Vol. 510., p.667.

Tanihata, C., Kataoka, J., Murakami, T., Ota, N., Ozawa, H., Takahashi, T., Tamura, T., Uchiyama, Y., Watanabe, S., Yamaoka, K., Yonetoku, D., Ezoe, Y., Fukazawa, Y., Isobe, N., Iyomoto, N., 1999, "Preflight performance of the ASTRO-E hard-x-ray detector", Proc. SPIE Vol. 3765, p. 645-663, EUV, X-Ray, and Gamma-Ray Instrumentation for Astronomy X, Oswald H. Siegmund; Kathryn A. Flanagan; Eds.

第2章 研究内容の概観

2.1 はじめに—銀河間空間における電子冷却

活動銀河核は、しばしば「ジェット」とよばれる光速に近い速度で吹き出す双極子流と、ジェット末端に「電波ローブ」と呼ばれる風船状に広がった電波源をもっている。これらは、差し渡しで 100kpc ($\sim 3 \times 10^{21}$ m) を超える系をなすものもおおく、銀河をサイズにおいて遙かに超え、銀河間空間に延びる壮大な粒子加速器をなしている。

相対論的電子が銀河間空間で冷却される経路には、主に、磁場との散乱によるシンクロトロン放射と光子との散乱による逆コンプトン散乱がある。冷却経路の分岐比は、散乱する相手の散乱断面積に比例するので、両方の経路からの放射を比較すれば、放射場の光子と磁場のエネルギー密度の比を正確に測定することができる。さらに逆コンプトン散乱される光子のエネルギー密度を別の方法で推定すれば、そこから電子と磁場のエネルギー密度を決定することができる。この単純で美しい物理法則を、活動銀河核のジェット—ローブ系、および銀河団中にあると予測される非熱的電子に当てはめ、磁場と電子のエネルギーを求めるのが、本研究を特徴づける手法である。

2.2 電波ローブからの X 線

2.2.1 X 線放射のメカニズム

ジェットはそもそもどのようにして駆動されるのか、ジェット中の正電荷は陽子かそれとも陽電子かなど、ジェットに関してはさまざま事柄が、現代宇宙物理学の未解決問題のままである。

一般的にはジェットの形成には磁場が重要であると考えられることが多いが、どの程度の役割を果たしているかについては、いまだに決定的な観測事実があるわけではない。たがって、ジェットの場所で粒子と磁場のエネルギー密度(以後、それぞれ u_e と u_m とする)を測定し、ジェットのエネルギー収支を調査することが、ジェットの謎を解くための大きな手がかりとなるはずである。IC X 線の検出には、広い X 線帯域において、高い感度、広い視野、低バックグラウンド、適度なエネルギー分解能と角分解能を備えた検出器が必要である。昨年まで稼働していた「あすか」衛星に搭載されていた GIS 検出器はこの条件をほぼ全て満たす理想的な検出器の一つである。

電波の分光および偏光観測から、電波ローブはシンクロトロン放射で輝いていることが明らか

となっており、放射源となる相対論的速度をもった高エネルギー電子は、中心核からのジェットによって供給されていると考えられる。

先に述べたように、電波ローブ中の相対論的電子はシンクロトロン過程と逆コンプトン過程によって冷却されるが、このスケールで支配的な光子は、マイクロ波背景放射 (CMB) になる。CMB のエネルギー密度は、天体のある系の赤方偏移で決まるので、観測からシンクロトロン放射強度と逆コンプトン放射強度を測定できれば、ローブ中の電子と磁場のエネルギー密度を正確に決定することができるようになる。

仮に磁場と電子のエネルギー平衡を仮定すると、シンクロトロン電波強度から、これらはほぼ $10^{-14} \text{ J m}^{-3}$ ($= 10^{-13} \text{ erg cm}^{-3}$) 程度とみつめられる。このとき磁場の強度は 0.1 nT ($= 1$ マイクロガウス程度)、シンクロトロン放射の周波数から電子のエネルギーは $\gamma \sim 10^3\text{--}5$ の間に分布していることが予想される。この電子が CMB を逆コンプトン散乱すると、光子のエネルギーは X 線からガンマ線領域にまで高められることになる。ただし、実際にこれを X 線で検出するためには、電波ローブを空間分解しつつ、エネルギーフラックスにして $10^{-14}\text{--}15 \text{ W m}^{-2}$ ($= 10^{-12}\text{--}13 \text{ erg s}^{-1} \text{ cm}^{-2}$) ほどの微弱な信号を検出しなければならない (Harris & Grindrey 1979)。これが撮像能力と高い感度を誇る「あすか」衛星の登場によってようやく現実の観測対象となった。

2.2.2 「あすか」による電波ローブからの X 線の検出

電波銀河 Fornax A (NGC 1316) が最初の逆コンプトン X 線の検出例となった。我々は、この天体の電波ローブから、広がった硬 X 線を検出し、その光度とスペクトルから、シンクロトロン電子による CMB の逆コンプトン X 線であることを証明した (Kaneda et al. 1995)。これはほぼ同時期に独立に発表された Feigelson らによる ROSAT 衛星の観測結果と一致するものであった。

しかし 1994 年の観測は、中心銀河を「あすか」GIS の視野中央においたため、ローブでの相対的な感度が低い観測になっていた。そこで我々は、1997 年に西のローブの長時間観測を提案、実行し、高い S/N でのスペクトルおよび精密な画像を得ることに成功した (図 2.1)。

1994 年の観測結果と 1997 年の 2 回にわたる結果、合わせて 14 万秒の露出を行ない非常によい統計のスペクトルを得たので、電波ローブからの X 線の強度を精度良く見積もることができた。

電波銀河 PKS 1343-601 (Centaurus B) は、差し渡し 12 分角ほどの電波ローブをもつ。われわれは第二の観測対象としてこの天体を選んだ。

この天体は中心核の活動性が高く、X 線で観測すると中心核からの AGN 成分が卓越してしまう。このため X 線反射鏡に由来する中心核からの散乱成分が、ローブ領域を覆い観測しにくくしてしまう。そこで我々は、中心核からの X 線スペクトルを 1.5 分角の狭い領域で評価し、これをもとにエネルギー帯域ごとに X 線反射鏡と観測装置の応答をシミュレート、AGN からの予想される画像を合成した。これを実際に観測された画像から差し引くことによって、中心核成分を取り

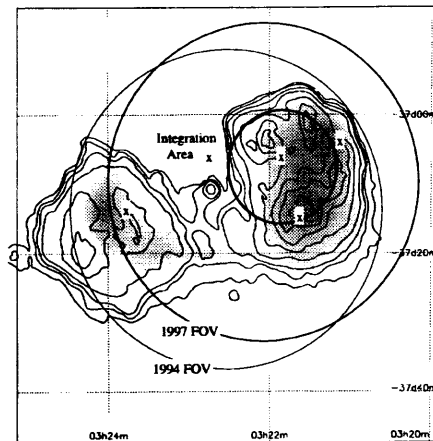


図 2.1: Fornax A の X 線と電波による画像。「あすか」による X 線 (1.7–7 keV) 画像を濃淡で、1.5GHz 帯の電波干渉系による画像を等高線で表している。X 線画像は、X 線の強いところを濃く表現しており、また、中心銀河の成分は図から除かれている。X 線画像は Kaneda et al. 1995 より、電波の画像は、Ekers et al. 1983 による。1994 年と 1997 年の「あすか」による観測の視野と、1997 年の観測でスペクトルを積分した領域をそれぞれ円で示してある。図中の「x」は ROSAT 衛星によってわかっている点源の位置を示す (Tashiro et al. 2001 より)。

除いた。このようにして得られた画像を図 2.2 に示す。

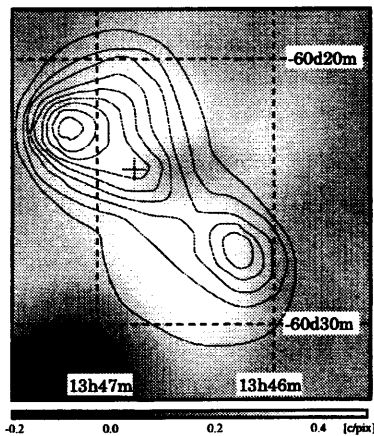


図 2.2: 「あすか」GIS によって得られた 1.5–3.0 keV X 線の画像を濃淡で示した。色の薄いところが X 線で明るいところである。同じ領域の McAdam(1991) による電波干渉計 (843 MHz) の画像を等高線で表した (Tashiro et al. 1998 より)。

ローブ全体を含む、中心核から 5 分角以内のスペクトルを図 2.3 右に示した。視野中の天体を含まない領域でバックグラウンドスペクトルを積分し、これをデータから差し引いてある。1.5 分角以

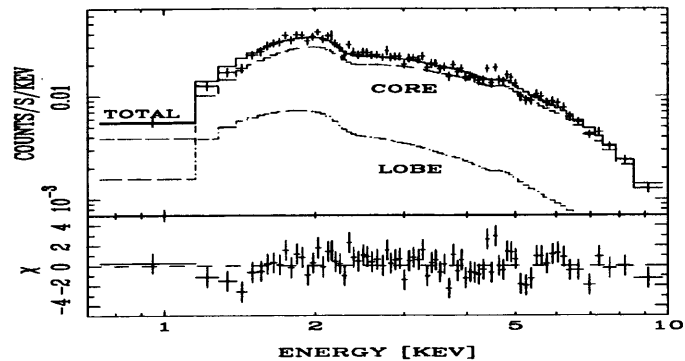


図 2.3: GIS で得られた中心核から 5 分角以内の X 線スペクトル。バックグラウンド成分は差し引いてある。中心核成分を破線で、ローブ成分を一点鎖線で、さらにモデル全体の合計を実線、データを十字で表している。中心核成分は、1.5 分角以内から得られたスペクトルで別に評価し、ここでは固定モデルとして導入している (Tashiro et al. 1998 より)。

内で見積もった中心核成分（スペクトル図中の一点鎖線）だけでは、全体のスペクトルを表すことはできず、別の成分が必要であった。この成分は、画像解析で見つかったローブに付随して広がった成分と考えられる。そのスペクトルは、power-law 型の関数で表現でき、そのべきはシンクロナン電波のものと一致した。これは、電波ローブ中の相対論的電子による逆コンプトン X 線であることを示す。（詳細は Tashiro et al. 1998 を参照）。物理量の評価については、他の天体とまとめて表 1 で示す。

三番目の検出例となったのが、NGC 612 ($z = 0.0290$; Spinrad et al. 1985) である。この天体は電波で明るく (~ 11 Jy at 843 MHz) 比較的大きなスケール (500 kpc \times 130 kpc) のローブをもつ (Jones & McAdam 1992)。我々は、「あすか」による観測を 1996 年 7 月に行った。硬 X 線に比較して軟 X 線画像は非等方的な広がりを示している。この広がりの断面をローブ方向とそれと垂直な方向に分けて評価すると、垂直方向には点源と矛盾しない広がりしか見られないが、ローブ方向にはローブのスケールに見合った広がりがあることが明らかになった。またこの広がりは、200 kpc にも達し中心の楕円銀河に付随するプラズマにしては明らかに大きすぎる。

我々はさらに広がった成分のスペクトル解析を行い、シンクロナン電波と矛盾しないべきをもつ power-law 型のスペクトルを示すことを確認した。また硬 X 線で強い点源は、非常に強く光電吸収をうけた power-law 型のスペクトルで表され、これは低エネルギー域では隠されていた中心核が見えていると考えられる。

2.2.3 AXAF/ Chandra による電波ローブからの X 線の検出

「あすか」GIS では空間分解できないような、より小さなローブを持つ電波銀河に対しては、0.5 秒角というかつてない高い角度分解能を持つ Chandra 衛星搭載の ACIS 検出器が理想的である。しかし、「あすか」に比べて有効面積が小さいわりに、バックグラウンドが高く広がった X 線の検出には不向きな可能性がある。そこで、我々は注意深く様々な電波銀河を調査し、我々の目的に最適な観測天体として電波銀河 3C 452 を選択し、Chandra 衛星で 80 ksec にわたる観測を行った¹。

¹XMM/ Newton でも Centaurus B の再観測を行い、現在、解析中である。

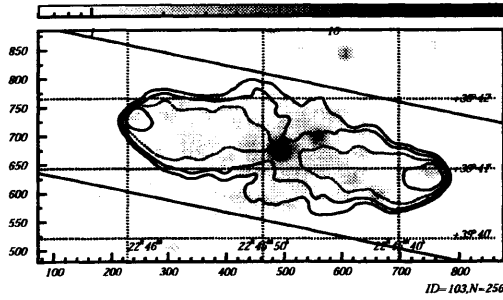


図 2.4: *Chandra* ACIS によって得られた電波銀河 3C 452 の 0.3 – 7 keV の X 線カラーイメージ。比較のために、1.4GHz の電波のイメージを等高線で重ねてある (Isobe Ph. D. thesis より)。

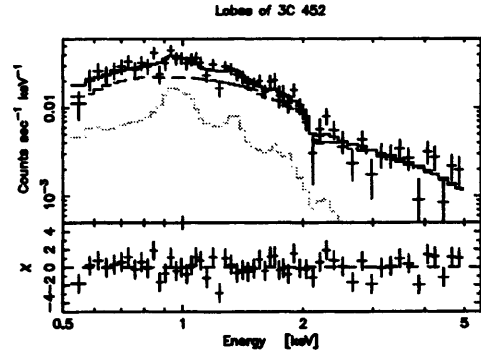


図 2.5: *Chandra* ACIS による、3C 452 の広がった X 線源のスペクトル。破線、スペクトルのフィットに用いたモデルを示す (Isobe Ph. D. thesis より)。

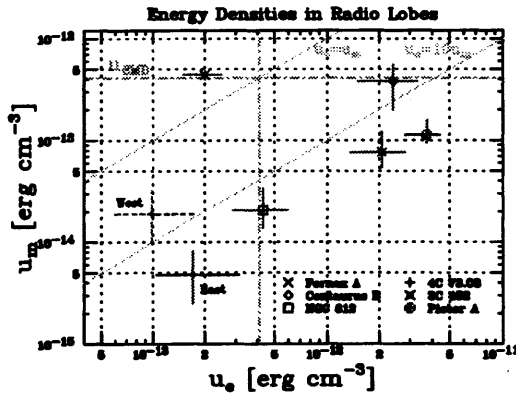


図 2.6: ローブにおける u_e と u_m の関係。Fornax A (Kaneda et al. 1995) と Centaurus B (Tashiro et al. 1998) も同時に示した。水平のグレーの線は、 u_{CMB} を表している (Isobe Ph. D. thesis より)。

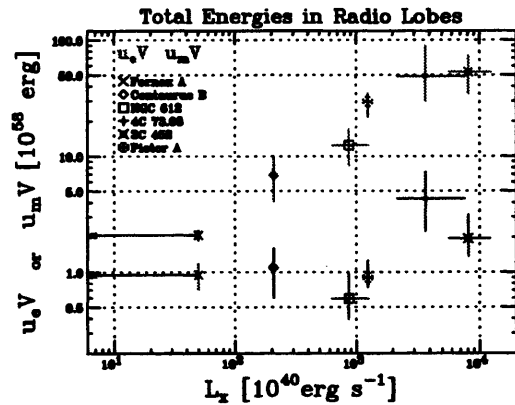


図 2.7: ローブにおける磁場と電子の全エネルギー、 $u_e V$ と $u_m V$ 、を中心核の X 線ミノシテイ L_x に対して図示した (Isobe Ph. D. thesis より)。

Chandra で得られた結果の一例として 3C 452 の解析結果を示す。図 2.4 は *Chandra* ACIS で得られた 3C 452 の X 線イメージである。3C 452 の中心核を含むいくつかの明るい X 線点源に加えて、ローブを埋め尽くすように広がった暗い X 線が検出されているのがわかる。そこで、点源を正しく取り除いて求めた広がった成分の X 線スペクトルを図 2.5 に示す。我々は、さまざまなモデルでスペクトルのフィッティングを行なったところ、5 keV 以上までのびるハード成分 (図中の破線) と熱的なプラズマによるソフト成分 (図中のグレー一点鎖線) の和で、観測されたスペクトルを良く説明できることがわかった。特に、ハード成分のスペクトル指数が SR 電波のスペクトル指数と非常に良く一致していることから、このハードが IC X 線であると結論した。

2.2.4 活動銀河核の活動度とジェット-ローブ系のエネルギー収支

ここまでみてきたローブについて、シンクロトン放射 (SR) 電波と逆コンプトン (IC) X線の強度の比較から u_e と u_m を計算した。その結果を図 2.6 にまとめた。明らかに、エネルギー当分配はまったく成立しておらず、多くのローブで u_e は u_m の 10 倍以上にもなっている。これは従来の電波観測だけを用いた方法では、 u_e を少なくとも数倍は過小評価しており、X線を用いなければ正しいエネルギー評価は行なえないことを示唆している。またほとんどすべてのローブで $u_m \lesssim u_{\text{CMB}}$ となっており、ローブ中の電子は主に IC 散乱でエネルギーを放出していることがわかる。

ローブに存在する電子や磁場はもともとジェットによって中心核から供給されたと考えられる。そこで我々は、中心核の X線ルミノシティ L_X とローブの u_e, u_m の関係を調査した。 u_e, u_m 自身は L_X とはっきりした相関を示さないものの、ローブ全体の体積 V で積分した電子と磁場の全エネルギー $u_e V, u_m V$ は L_X ときれいに相関していることを発見した。これを示したのが図 2.7 である。明らかに、 $u_e V$ は L_X にほぼ比例するように増加しているが、 $u_m V$ はほぼ一定である。このうち、 $u_e V$ の振舞いについては、次のように理解することができる。すでに述べたように、ローブ中の電子は主に IC 散乱でエネルギーを放出し続けている。したがって、IC 散乱による冷却時間を T_{IC} とすると、 $L_{\text{kin}} \simeq u_e V (1 + \kappa) / T_{\text{IC}}$ で表されるようなパワーがジェットからローブに常に供給されていなければならない。ここで、 κ はジェット中の陽子がジェットの終端衝撃波で得るエネルギーを電子の得るエネルギーで規格化したパラメタであり、通常は $\kappa = 1$ と考えられている。我々はそれぞれのローブの対して実際に L_{kin} を求めたところ、図 2.9 のようになった。つまり、 $L_{\text{kin}} \sim 10^{42-44} \text{ erg s}^{-1}$ であり、 L_{kin} は L_X にきれいに比例している。この比例関係は、中心核が質量降着によって輝いていると考えれば、ジェットのエネルギー源も中心核への質量降着であることを示した重要な観測事実であると考えられる。

ローブの電子のエネルギーから推定した L_{kin} を、実際にジェットが持ち出していると考えられるパワー L_{jet} と比較することは、非常に重要である。電波銀河をジェットの正面から観測したような天体であると考えられているブレイザーは、この目的に非常に有効な天体である。ブレイザーの時間変動は非常にはやいことから、比較的ジェットの根本に近い領域が観測されているものと考えられる。特に、最近の X線や γ 線の観測で IC 放射のスペクトルが得られているブレイザーについては、SR 放射のスペクトルとの比較から、 L_{jet} を見積もることができる。我々は、窪 (1999) による結果をもとにブレイザーの L_{jet} を推定したところ、約 $L_{\text{jet}} \sim 10^{42-44} (1 + \eta) \text{ erg s}^{-1}$ であった。ここで、 η は陽子の質量の効果を表すパラメタであり、ジェットが陽子を含んでいれば $\eta \sim 2000$ 、含まなければ $\eta \sim 0$ である。もし、 $\eta = 2000$ とすると、 L_{jet} は L_{kin} より、はるかに大きな値になってしまうが、 $\eta = 0$ であれば L_{jet} と L_{kin} はほぼ一致する。このことは、ローブが電波銀河やブレイザー、つまりジェットを持つ活動銀河中心核に共通に見られるものであれば、ジェットにはあまり多くの陽子が含まれない方が好ましい、ということを示唆していると考えられる。

2.2.5 磁場と電子の棲み分けの兆候

ローブ中で粒子のエネルギーが卓越する傾向は、すくなくともジェット終端で、粒子がジェットを主導して、銀河間空間に磁場を供給していることを示唆する。すなわち、前項までは、個々のローブで平均した u_e と u_m をもとに議論してきたが、 u_e と u_m の空間分布を調査することも重要になる。 u_{CMB} は空間的に極めて一様であるため、ローブからの IC X 線の空間分布から電子の空間分布を求めることができる。また SR 電波と IC X 線の分布の比から、磁場の空間分布を求めることができる。

実際に我々は Centaurus B の「あすか」による観測から磁場がローブの端にむかって相対的に強くなっていることを示した (Tashiro et al. 1998)。すなわちこれは、先端に向かって磁場は圧縮され、電子は冷却されていくことを示唆している。これは、超新星残骸であるかに星雲とよく似た状況であり、共通の物理を示唆している。かに星雲では相対論的パルサー風の post-shock 領域で、磁場と電子のエネルギー密度の比が外側に行くに従って 0.1 - 2 と変化していると計算されている (Kennel & Coroniti 1984)。

また Fornax A の西ローブ X 線強度分布も、電波強度と強度の高い位置がずれていることがわかった (Tashiro et al. 2001)。電波が強い領域はローブの周縁に分布しているのにくらべ、X 線の強い領域はコンパクトにまとまっており、強度のもっとも高い領域は、電波のものとはずれている。X 線強度のもっともつよい場所を中心に、X 線と電波の半径輝度分布をとったものが図 2.8 である。X 線は中心集中型なのに対して、電波がシェル状の分布を示していることがよくわかる。これからも、磁場の電子に対するエネルギー密度比がローブの周縁に向かって増加していることが示唆されている。

さらに *Chandra* 観測結果から、もっとも質の良い IC X 線のデータが得られた 3C 452 のローブについて、その軸に沿った電子と磁場の分布の推定を行った。その結果、電子はローブを比較的に満たしているのに対して磁場はローブの周辺に向かって強まっていることがわかった。これを分かりやすく示したのが図 2.10 である。ローブの中心付近では $u_e \gg u_m$ であるのに対して、ローブの端の近くでは $u_e \simeq u_m$ であることがわかった。なぜこのようないわば電子と磁場の棲み分けが生じるのかは、今後の課題である。

「あすか」を含む最新の結果については、第 4 章に収録した磯部の博士論文に詳しい。

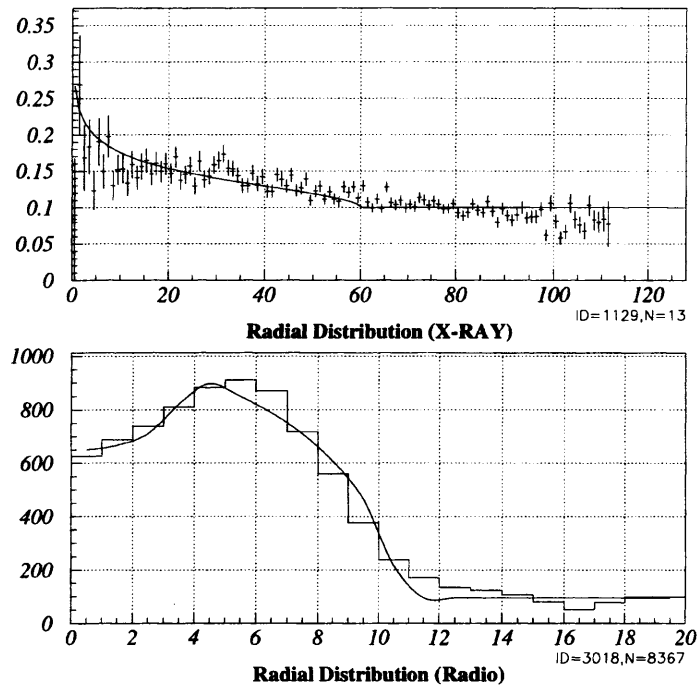


図 2.8: Fornax A 西ローブの X 線 (上) と電波 (下) の半径輝度分布。X 線は、「あすか」GIS によってえられた 1994 年と 1997 年の観測結果を合成したもの。電波の半径輝度分布は Ekers et al. (1978) による干渉計のマップをもと作成した。実線はモデルを表す。X 線では輝度分布が三次元半径に対して反比例の分布を持つ場合、コンスタントなバックグラウンド成分とあわせたときのモデルフィットの例。電波では、二つの半径の間にだけ放射源が存在する厚みのある「球殻」モデルでフィットした例を示している。二つの図の横軸は、X 線が GIS のピクセル、電波が分角をあらわし、両者のスケールは合わせてある。

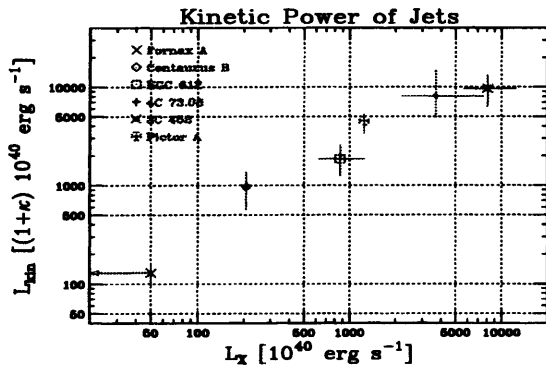


図 2.9: ジェットがローブに供給するパワー L_{kin} と中心核の X 線ルミノシティ L_X との関係。(Isobe Ph. D. thesis より)

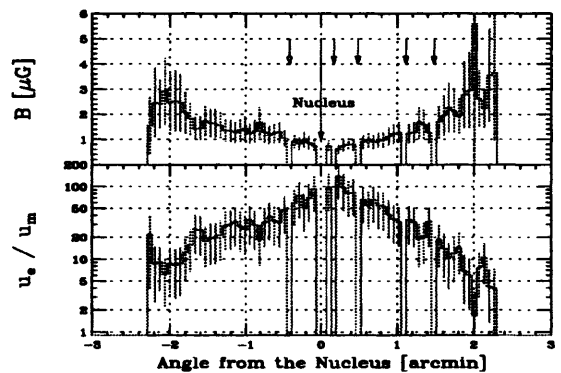


図 2.10: 電波銀河 3C 452 のローブの軸に沿った磁場 B と u_e / u_m 比の分布。(Isobe Ph. D. thesis より)

(田代 信)

2.3 銀河団からの非熱的 X 線の観測

銀河団は、重力的に閉じた宇宙で最も大きな系であり、狭い空間の中に数 100–数 1000 の銀河が集まっている。銀河団には銀河だけでなく、銀河団を包み込むように $10^7\text{--}10^8$ K もの高温ガスが存在しており、その質量は銀河の質量の和よりも大きいくらいである。この高温ガスは X 線で明るく光っており、X 線による観測で高温ガスの性質を詳しく調べることができる。例えば、高温ガスの温度分布と密度分布から、高温ガスを閉じ込めるために必要な重力質量を計算できるので、暗黒物質の研究を行なうことができる。また、銀河団を用いて、宇宙構造形成や宇宙パラメータに制限をつける研究や、高温ガスに含まれる重元素を調べることによって、重元素を放出したと思われる個々の銀河の進化についての研究も行われている。

銀河団では、銀河以外にも高温ガスという成分が銀河間空間を満たしていることが知られているが、他にも非熱的な構成要素の存在も考えられる。例えば、高温プラズマには磁場と一緒に存在していてもおかしくないし、高温ガスよりもさらに高エネルギーの非熱的粒子の存在も期待される。また、銀河団の中心に電波銀河および電波ジェットがしばしば存在しており、磁場や高エネルギー粒子があることはまちがいない。我々は、日本の X 線天文衛星「あすか」により、X 線による銀河団の観測を通して、銀河団空間を満たす磁場や非熱的粒子の探査を行なった。

2.3.1 銀河団中心部の新描像と銀河間磁場

銀河団の中心部は、高温ガスの密度が 10^{-8}m^{-3} (10^{-2}cm^{-3}) 近くもあり、放射冷却時間が宇宙年齢よりも短い場合もしばしばである。Einstein 衛星による軟 X 線の観測から、銀河団中心では X 線源の強い集中がみられ、それは高温ガスが等温静水圧平衡モデルから予想される輝度分布を超過していた。これに対し、周辺の高エネルギーガスが放射冷却して中心にむかって落ち込んでいる、という cooling flow 説が唱えられ (review Fabian 1994)、10 年来のパラダイムとなっていた。この説を支持する結果が多少あるとはいえ、この説には落ち込んだガスがどうなるかという大きな問題をはらんでいる。落ち込む率は多いもので数 $100M_{\odot}$ (太陽質量)/yr にもなり、宇宙年齢で積算すると $10^{12}M_{\odot}$ オーダーにもなり、1つの銀河に匹敵する重量になってしまうが、電波などの観測でそのような冷たいガスは見つかっていない。

このような状況の中、「あすか」によって銀河団中心部について新しい観測結果が得られた。それは、(1) 中心部にしばしば周囲の温度よりも低い温度の 10^7 K くらいの成分が存在するが、その質量は $10^{10}M_{\odot}$ ほどしかない、しかも、低温成分は高温成分と共存しているように見える (2) 中心部ではしばしばガス中の重元素アバundanceが増加しており、その空間スケールは中心の巨大楕円銀河の勢力圏と一致する。(3) 軟 X 線で見られた銀河団中心での X 線集中は硬 X 線でも見られるため、中心集中した分布をもつ重力ポテンシャルの形を反映したものである、という三つの重要な結果である (Fukazawa et al. 1994; Ikebe 1995; Ikebe et al. 1996; Ikebe et al. 1997; Xu

et al. 1997; Xu et al 1998)。これらの現象は、(1) 低温成分は、フィールドの楕円銀河に見られるハローの類推として、銀河団中心の巨大楕円銀河に付随するハロー、(2) 重元素超過は巨大楕円銀河から放出されたもの、(3) 中心で集中した重力ポテンシャルは、巨大楕円銀河の重力ポテンシャルが見えている、とすることで説明でき、銀河団中心部では銀河団の高温成分と巨大楕円銀河の低温成分が熱伝導を妨げる磁場で分けられて共存している、という説が提案され (Makishima 1995)、cooling flow 説に対し異なった見方を示した。高温ガスを閉じ込めるには、数 $\times 10^{-11}$ T (数 μ Gauss) 磁場が必要であるが、この強さは渦巻き銀河内部の磁場に匹敵するため、もし存在しているとするとその起原なども含めて非常に興味深い。さらに、もしこの説が正しいとすると、放射冷却を妨げるような熱源も必要となり、銀河間磁場のリコネクションなどの高エネルギー現象が隠れているかもしれない。

2.3.2 銀河団からの非熱的放射

銀河団は、重力的に閉じた宇宙で最も大きな系であるので、形成時に莫大なエネルギーが解放されたと思われ、以前から理論的に高エネルギー粒子などによる銀河団からの非熱的放射が予測されていた。また前項で述べたような傍証が集まりつつあったものの、最近まで直接の検出例がなかった。これは、観測感度の良い 10keV 以下では高温ガスの熱的成分が卓越していることと、10keV 以上で感度の良い検出器が今までなかったことによる。しかし、最近になっていろいろな観測例から、高エネルギー粒子の存在が浮き彫りになってきた。

EUVE 衛星の 5 つの銀河団観測で、0.1–0.4keV での放射強度が高エネルギー側の高温ガスの熱的成分を延長したときよりも有意に大きい soft excess が見つかった。(e.g. Bowyer and Berghofer 1998; Mittaz et al. 1997)。Sarazin and Lieu (1998) は、この放射は電子のローレンツ因子にして $\gamma \sim 300$ くらいの高エネルギー電子による CMB の逆コンプトン散乱であるとすれば空間分布なども説明できる、と指摘している。この場合、高エネルギー電子のエネルギー密度は高温ガスの 10% ほどになる。次に、BeppoSAX 衛星の硬 X 線検出器 PDS により、いくつかの銀河団から数 10keV 以上で、高温成分の熱的放射よりも超過した hard tail が検出された (Fusco-Femiano et al. 1999)。

2.3.3 銀河群からの硬 X 線の「あすか」による観測

「あすか」を用いて観測を行った 18 の銀河群のおよそ半数から硬 X 線超過成分を検出した。これらの成分はメンバー銀河中の活動銀河核や低質量連星系などの点源からの放射、あるいは背景 X 線放射のゆらぎとしては説明できない。また HCG 62 を筆頭とするいくつかの銀河群においては、この硬 X 線が有意に広がっていること、その広がり is intra-group medium の輝度分布のプロファイルと似ているかより広がっていることがわかった。硬 X 線成分のスペクトルは、光子指数

～2のべき型を示す。これは熱的な起源をもつとしても矛盾しないが、その場合スペクトルから要求される温度は $kT \sim 10$ keV に達する。ただし硬 X 線成分が微弱な場合は、より低い温度となる。

観測された硬 X 線成分は、銀河群ごとにばらついていた。もっとも確実な検出例では、その光度は $1 - 18 \times 10^{34} h_{75}^{-2}$ W、あるいは IGM の 10～20% 程度である。もっとも弱い場合では、IGM の～5% 程度が上限となった。また、有意な硬 X 線超過のあった銀河群では、硬 X 線光度と IGM の光度比が、すでに報告されている 3 つの銀河団における硬 X 線超過のものに類似していた。

硬 X 線超過の放射機構として、非熱的制動放射は、クーロン損失が大きすぎるため非現実的と考えられる。逆コンプトン散乱で説明するためには、非常に弱い磁場 (~ 0.01 nT) が要求されるので、非一様な磁場が必要になる。また、少なくともいくつかの銀河群とすべての銀河団については、圧力平衡を前提とする限り熱的放射を起源とする説は適応できない。さらに磁場による閉じこめを実現するためには ~ 2 nT もの磁場が必要になる。

現状の観測結果からは、加速あるいは加熱機構については制限がつけられない。しかしながら、我々は、有意な硬 X 線超過をしめす銀河群のほとんどについて、それらの中央部にいくつかの明るい銀河を含んでいることを見いだした。銀河群内部のプラズマ中を運動するメンバー銀河が、その運動エネルギーを硬 X 線放射へと供給している可能性がある。これらの銀河群の「あすか」による観測結果は、中澤の博士論文にまとめられている (第 4 章参照)。

2.3.4 HCG57/HCG16 のデータ解析

渦巻銀河が支配的な HCG57/HCG16 の ASCA のデータを解析した。HCG57 からは少ないながらも高温ガスの成分とハード成分が検出された。ハード成分の空間分布は広がっているどうか区別できなかったが、少なくとも 1 つの点源では説明できない。HCG16 からは、4 つの渦巻銀河から低光度 AGN からのハード X 線を検出し、そのうち 3 つは強く吸収されていた。広がったハード X 線の兆候は見られなかった。

2.3.5 Chandra による観測

ASCA でハード X 線が有意に検出された銀河群 HCG62/RGH80 を Chandra で観測し、ハードな点源を調べた結果、点源のフラックスをすべてたし合わせても、ASCA で検出されたハード X 線を説明することはできなかった。よって、ASCA のハード成分は確かに広がったものである可能性が高まった。2 つのクーリングフロー銀河団 2A0335/A2199 の中心部を詳細に温度構造を調べた結果、1keV 以下の低温成分や超過吸収は見られず、温度が下げ止まっていることがわかった。これは放射冷却が何らかの機構で抑制されていることを示唆するが、その 1 つの可能性として銀河間磁場の影響が考えられる。

2.3.6 銀河団の X 線観測

そして、我々も「あすか」を用いてそうした放射を検出した。「あすか」は 10keV 以下にしか感度がないので、普通の銀河団では高温ガスの成分しか見えないが、温度の低い銀河群だと高温ガスの成分は 5keV 以下に限られるので、このような hard tail 探しを行うことができる。その結果、23 個中 18 個くらいから有意に hard tail が見つかった (図 1)。その光度は $10^{41} \sim 35$ W に分布しており、明るい数個については広がっていることもわかった。hard tail をプラズマの熱制動放射モデルでフィットすると温度が 20keV 以上になり、かなりハードであることがわかる。

この放射の起源として、 $\gamma \sim 10^3 \sim 4$ くらいの高エネルギー電子による CMB の逆コンプトン散乱、あるいは ~ 100 keV のエネルギーを持つ非熱的電子と高温ガスの非熱的制動放射が考えられる。もし、逆コンプトン放射とすると、Coma cluster の場合はシンクロトロン電波強度がわかっているなので、磁場は ~ 0.015 nT (0.15 μ G) という非常に低い値となり、高エネルギー電子のエネルギー密度も高温ガスの 10% 以下にしかならないので、銀河団における非熱的圧力の寄与が小さいことになるが、このような高エネルギー粒子が存在していること自体が興味深いし、EUV の観測と関連がある可能性がある。一方、非熱的制動放射の場合は高エネルギー電子のエネルギー密度は高温ガスの数 10% にもなる可能性があり、銀河団における非熱的圧力が無視できないことになる。いずれにせよ、どちらも銀河団の新しい描像を与えることには間違いない。

2.3.7 銀河団中心部の電波銀河

電波銀河には、ジェットがくねくね曲がっていて電波の弱い FR-I 型とジェットが発達していて電波の強い FR-II 型が存在する。銀河団の中心付近にはしばしば電波銀河が存在し、近傍銀河団では FR-I 型の弱めの電波銀河が多く存在する。有名な Virgo cluster の中心の M87 や、Perseus cluster の NGC1275 などともそうである。こうした電波銀河からのジェットなどは、銀河団中の非熱的現象 (磁場、高エネルギー粒子) を作り出していることは理論的にも予測されており (e.g. Ensslin et al. 1997)、電波銀河の AGN を調べることは、そうしたことを考える材料を得ることにつながる。

銀河団中心の電波銀河の AGN 成分の X 線検出は、これまでほとんどなかった。M87 については、「ぎんが」衛星で 10^{35} W (10–20keV) のものが検出されたという報告があるが (Takano and Koyama 1991)、それ以外の衛星では RXTE (Reynolds et al. 1998) も含めて検出されていないので、よくわからない。我々は、「あすか」衛星を用いて低光度低温銀河団中の電波銀河の AGN 成分を 2 つの銀河団 (A194, NGC4261 group) について検出した。NGC4261 は、HST で回転しているガスのイメージが撮影されている有名な天体で (Jaffe et al. 1996)、ROSAT により電波銀河の場所に点源が見つかったが、「あすか」により初めて hard な AGN 成分が検出された (図 7)。X 線光度は、 10^{34} W (10^{34} W と FR-II に比べて 3 桁くらい弱く、特に強い吸収もないので、intrinsic に暗い AGN であるようだ。我々が「あすか」で観測した他の FR-I もほぼ同じ傾向を示す。今後

こうした観測例が増えれば、銀河団中の非熱的成分（磁場、高エネルギー粒子）に対する情報となるだろう。

2.3.8 銀河団ガスと電波ジェット

銀河団中心の電波銀河からは当然ながら、電波ジェットが観測されている。そのジェットが銀河団ガスと相互作用することによって、磁場が供給されたり、高エネルギー粒子が生成される。

ROSAT 衛星による近傍の FR-I 電波銀河を含む銀河団銀河群の軟 X 線観測では、ジェット中で粒子と磁場のエネルギー等分配を仮定した場合に、ジェットの圧力は銀河団ガスの熱的圧力の数分の 1 にしかならないことが指摘されており (Feretti et al. 1995, Massaglia et al. 1996, Trussoni et al. 1997)、ここでも粒子優勢のジェットが指摘されている。

こうした観測例の他にもジェットに関する情報が得られる可能性がある。我々は、電波銀河を含む銀河団 B2 1615+35 を観測し、ジェットの辺りで hard な成分がある兆候を見つけた (図 3)。このハードな成分の起源としては、ジェットによるショックで暖められたガスからの放射、あるいは高エネルギー電子による CMB の逆コンプトン散乱が考えられる。ジェットからの逆コンプトン散乱は、先に述べたように、「あすか」と ROSAT によって Fornax-A から検出された例がある (Kaneda et al. 1995; Feigelson et al. 1995)。もし、逆コンプトン散乱だとすると、その X 線 flux は粒子と磁場のエネルギー等分配を仮定して得られるものよりも 1 桁ほど明るいことになり、粒子優勢のジェットということが示唆される。しかし、「あすか」のデータでは逆コンプトン散乱なのかどうか識別できないので、今後のさらなる観測例の増加が待たれるところである。

(深沢 泰司)

参考文献

- Blandford, & Konigl, 1979, ApJ 232, 34
Blandford, & Levinson, 1995, ApJ 441, 79
Bowyer, & Berghofer, 1998, ApJ 506, 502
Dermer, Schlickeiser, & Mastichiadis, 1992, A&A 256, L27
Ekers, Goss, Kotanyi, & Skellern, 1978, A&A 69, L2
Ensslin et al. 1997, ApJ 477, 560
Fabian 1994, ARA&A 32, 277
Fomalont, Ebner, Breugel, & Ekers, 1989, ApJ 346, L17
Feigelson et al. 1995, ApJ 449, 149
Feretti et al. 1995, A&A 298, 699
Fukazawa et al. 1994, PASJ 46, L55
Fusco-Femiano et al. 1999, astro-ph/9901018
Ghisellini & Maraschi, 1989, ApJ 340, 181
Harris & Grindlay, 1979, MNRAS 188, 25
Hattori et al. 1998, ApJ 503, 593
Ikebe, 1994, Ph. D. thesis, Univ. of Tokyo (RIKEN IPCR CR-87 (1996))
Ikebe, et al. 1996, Nature 379, 427
Ikebe, et al. 1997, ApJ 481, 660
Inoue, & Takahara, 1996, ApJ 438, 555
Jaffe et al. 1996, ApJ 460, 214
Jones, & McAdam, 1992, ApJS 80, 137
Kaneda, et al., 1995, ApJ 453, L13
Kataoka, et al., 1999, ApJ, in press
Kubo, et al., 1998, ApJ 504, 693
Kubo, Ph. D. thesis, 1997, University of Tokyo
Makishima K. 1995, in *Elementary Processes in Dense Plasmas*, ed. S. Ichimaru and S. Ogata
(Addison Wesley: New York) p.47
McAdam, 1991, Proc. ASA 9(2), 255
Mittaz, et al. 1997, ApJ 498, L17
Massaglia, et al. 1996, A&A 309, 75
Ota, et al. 1998, ApJ 495, 170
Rees, 1967, MNRAS 137, 429

- Reynolds, et al. 1998, astro-ph/9812031
Roettiger, et al. 1997, ApJS 109, 307
Sarazin & Lieu, 1998, ApJ 494, 177
Sikora, Begelman, & Rees, 1994, ApJ 421, 153
Spinrad, Djorgovski, Marr, & Aguilar, 1985, PASP 97, 932
Takahashi, et al., 1996, ApJ 470, L89
Takano, & Koyama, 1991, PASJ 43, 1
Tashiro, et al., 1998, ApJ 499, 713
Trussoni, et al. 1997, A&A 327, 27
Westerlund & Smith, 1966, Australian J. Phys 19, 181
Wu, & Fang, 1996, ApJ 467, L45
Xu, et al. 1997, PASJ 49, 9
Xu, et al. 1998, ApJ 500, 738

第3章 参考論文(投稿論文)

3.1 M. Tashiro, et al., 2001, ApJ 546, L19

X-RAY MEASUREMENTS OF THE FIELD AND PARTICLE ENERGY DISTRIBUTIONS IN THE WEST LOBE OF THE RADIO GALAXY NGC 1316 (FORNAX A)

M. TASHIRO,¹ K. MAKISHIMA,² N. IYOMOTO,³ N. ISOBE,² AND H. KANEDA³

Received 2000 May 10; accepted 2000 October 24; published 2000 December 29

ABSTRACT

A follow-up X-ray study was made of the west lobe of the radio galaxy Fornax A (NGC 1316) that was based on new *ASCA* observations made in 1997 for 98 ks and that incorporated the previous observation in 1994 for 39 ks. The 0.7–10 keV spectrum of the emission can be described by a power law with an energy index of 0.74 ± 0.10 , which agrees with the synchrotron radio index of 0.9 ± 0.2 . Therefore, the X-rays are reconfirmed to arise via the inverse Compton scattering of the cosmic microwave photons, as Kaneda et al. and Feigelson et al. concluded. The surface brightness of the inverse Compton X-rays exhibits a relatively flat distribution over the west lobe, indicative of an approximately spherical emissivity distribution with a radius of $\sim 11'$ (75 kpc). In contrast, the 1.4 GHz radio image by Ekers et al. exhibits a rim-brightened surface brightness, consistent with a shell-like emissivity distribution whose inner and outer boundaries are $4'$ and $11'$, respectively. These morphological differences between radio and X-rays suggest that the relativistic electrons are distributed homogeneously over the lobe volume, whereas the magnetic field is amplified toward the lobe rim region.

Subject headings: galaxies: individual (NGC 1316) — magnetic fields — radiation mechanisms: nonthermal — radio continuum: galaxies — X-rays: galaxies

1. INTRODUCTION

The jet terminal lobes of radio galaxies are gigantic intergalactic structures consisting of magnetic fields and relativistic particles, both of which are supposed to be supplied by the active galactic nuclei (AGNs) through the jets. Nevertheless, we do not yet know the relative importance of the magnetic fields and the relativistic particles in the mechanism of jet formation. To find this out, we need to measure the spatial distributions of the field and particle energy densities along various locations of the AGN-jet-lobe system.

The relativistic electrons in the radio lobes interact with the magnetic fields and soft photons to produce synchrotron radiation and inverse Compton (IC) emission, respectively. Feigelson et al. (1995, hereafter F95) and Kaneda et al. (1995, hereafter K95) discovered the IC X-ray emission with *ROSAT* (Trümper 1982) and *ASCA* (Tanaka, Inoue, & Holt 1994), respectively, from the lobes of the radio galaxy Fornax A (NGC 1316, redshift $z = 0.00587$; Longhetti et al. 1998), followed by authors reporting the lobe IC X-rays from Centaurus B (PKS 1343–601; Tashiro et al. 1998), 3C 219 (Brunetti et al. 1999) and NGC 612 (Tashiro, Makishima, & Kaneda 2000). These authors estimated the energy density of soft photons and succeeded in determining the magnetic field intensity and the energy densities of electrons in the lobes. Among these pioneering results, Tashiro et al. (1998) and Brunetti et al. (1999), respectively, show that the lobes of Centaurus B and 3C 219 exhibit a clear dominance of particle energy in their inner regions. Notably, Tashiro et al. (1998) found relative enhancements of the magnetic fields toward the periphery in the Centaurus B lobes.

Our next task is to resolve spatial distributions of the IC X-ray emission in order to trace the dynamics of the jet-lobe system. The lobes of Centaurus B, however, are not in fact the

best target for this investigation with *ASCA* because of the bright nucleus and the relatively small angular separation of its lobes. In this Letter, we present results from *ASCA* follow-up observations of the west lobe of Fornax A. This prototypical IC source is ideal for our purpose because of its nearly dormant nucleus (Iyomoto et al. 1998), the large ($\sim 10'$ in radius) angular size of its lobes, and the high integrated IC flux.

2. OBSERVATION

In the first *ASCA* observation of Fornax A carried out on 1994 January 11, K95 placed the nucleus at the center of the field of view (FOV). This was less efficient for observing the lobes because of the vignetting effect of the X-Ray Telescope (XRT; Serlemitsos et al. 1993), and, furthermore, some portion of the lobes fell outside the FOV. Aiming at a detailed study of the lobe, we conducted follow-up observations of Fornax A by placing the west lobe, which is less contaminated by point sources (F95; K95; see also Kim, Fabbiano, & Mackie 1998) than the other lobe, in the center of the Gas Imaging Spectrometer (GIS; Ohashi et al. 1996; Makishima et al. 1996) FOV. We concentrate on the GIS data because a fair amount of the lobe emission remained outside the $22' \times 11'$ FOV of the Solid-State Imaging Spectrometer (SIS; Burke et al. 1991; Yamashita et al. 1997) at the 2-CCD mode. The observations were carried out on 1997 August 17–18 and December 26–27. The good time exposure after standard data screening is 35 and 62 ks for the August and December observations, respectively. Including the observation in 1994, the total exposure time amounts to 137 ks, which is more than 4 times as long as that obtained by K95.

3. RESULTS

3.1. Imaging Analysis

In Figure 1, we show 0.7–10 keV GIS images obtained in the two observations in 1997. We smoothed the raw images with a two-dimensional Gaussian function of $\sigma = 0.5$ but left the cosmic and intrinsic backgrounds in these images (Fig. 1). Both images show the diffuse IC emission over the west lobe

¹ Department of Physics, Saitama University, Shimo-Okubo, Urawa, 338-8570, Japan; tashiro@phy.saitama-u.ac.jp.

² Department of Physics, University of Tokyo, Hongo, Bunkyo, 113-0033, Japan.

³ Institute of Space and Astronautical Science, Yoshinodai, Sagami-hara, 229-8510, Japan.

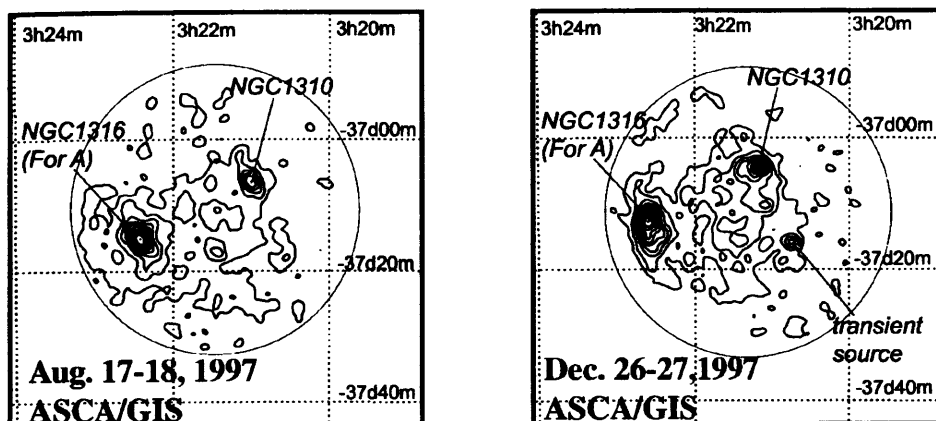


FIG. 1.—Background-inclusive GIS images obtained on 1997 August 15–16 (*left*) and December 26–27 (*right*), excluding the rim region beyond $20'$ from the center of the FOV. The images are smoothed with a two-dimensional Gaussian function of $\sigma = 0.5$ but are not corrected for exposure or vignetting. Ten linear contour levels, including backgrounds, are in the ranges of $(1.7\text{--}11) \times 10^{-5}$ and $(1.7\text{--}8.9) \times 10^{-5}$ counts s^{-1} for the August and December data, respectively.

region, as first revealed by F95 and K95. The brightest and second brightest discrete sources are, respectively, the host galaxy NGC 1316 and the SB galaxy NGC 1310. Besides a new transient source that appeared on the second occasion to the southwest of the lobe, we see no significant variation of the sources in the FOV. We therefore co-add the GIS (GIS2 + GIS3) data from the present observations with those from the

first one made in 1994 in order to study the IC X-ray emission with the best signal-to-noise ratio. For that purpose, we subtracted the intrinsic non-X-ray background (NXB) utilizing nighttime Earth exposures close in time to each observation, corrected the image (containing the cosmic X-ray background [CXB] and the sources) for the exposure and vignetting effect, and smoothed it with a two-dimensional Gaussian function of $\sigma = 0.4$.

The synthesized X-ray map is shown in Figure 2 with gray scales, where the 1.4 GHz radio contours by Ekers et al. (1983) are overlaid. We detected four additional pointlike source candidates (labeled 1–4) with a threshold of 4σ deviation above the average flux over the lobe region. Apart from these small-scale features, we see the diffuse IC emission exhibiting a good coincidence with the radio lobe. We analyzed the ROSAT-PSPC (Pfeffermann & Bruehl 1986) archival data of these regions and found that all the sources but the transient source were identified with the ROSAT data as point sources. The extrapolated 2–10 keV flux is higher than $2 \times 10^{-17} \text{ W m}^{-2}$ from their spectrum fitting results, and the derived energy indices range from 1.5 to 3.2. These soft X-ray spectra imply that the discrete sources do not originate from the possible local enhancements of the diffuse IC emission. We examined ASCA data for NGC 1310 and sources 1–4 and confirmed that their intensities stayed constant within the errors found in these observations with ASCA and ROSAT. Although sources 1 and 2 are included in the region employed by K95 for their spectral analysis, the sum flux of these sources is not more than 1/10 of the flux reported by K95. These sources do not affect their conclusion very much; in fact, we assume that these sources are fairly stable.

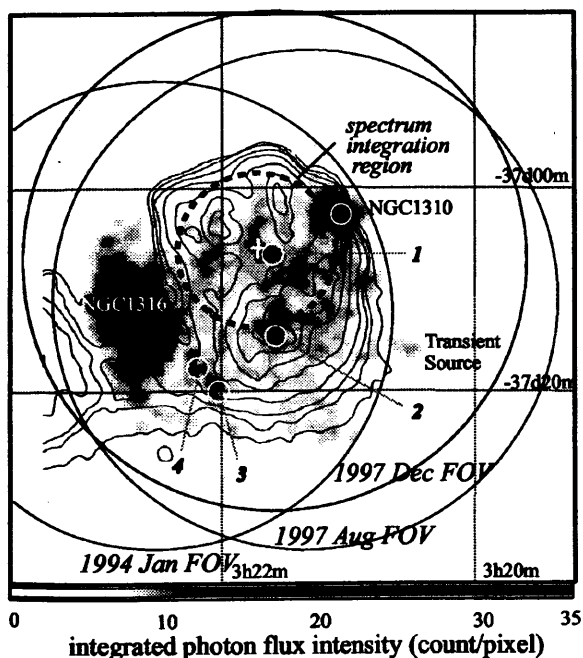


FIG. 2.—Gray scale showing Fornax A in a synthesized image (0.7–10 keV) obtained by co-adding GIS2 and GIS3 data from the three pointings, normalized to the exposure and corrected for vignetting after subtracting the intrinsic background. The FOVs of individual pointings (see § 2) are indicated with circles. The 1.4 GHz radio image from Ekers et al. (1983) is overlaid with contours. The dash-lined circle within the west lobe indicates the region that is used to accumulate the GIS spectrum (see § 3.2 and Fig. 3). The white circles represent discrete sources detected in the west lobe with ROSAT, whose extrapolated 2–10 keV fluxes exceed $2 \times 10^{-17} \text{ W m}^{-2}$ (§ 3.1).

3.2. Spectrum of the Diffuse Emission

We accumulate the GIS events over a circular region (the dash-lined circle in Fig. 2) around the X-ray brightness peak (marked with a cross in Fig. 2). We limited the area within $7.25'$ to avoid source contamination from the host galaxy NGC 1310 and source 2, although source 1 is inevitably contained in the integration region. Since there is essentially no source-free region in the on-source FOV, we estimated the background (NXB + CXB) utilizing archival blank-sky observations accumulated for 1653 ks. Furthermore, we decomposed the back-

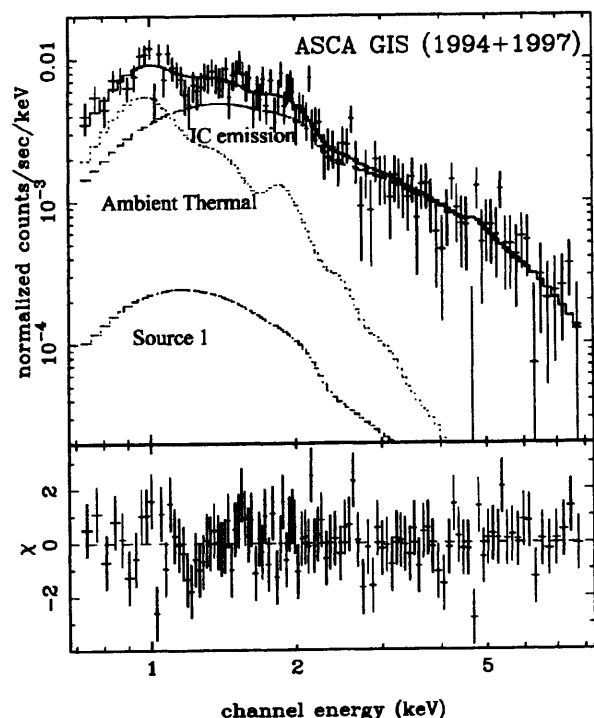


Fig. 3.—ASCA-GIS spectrum (0.7–10 keV) accumulated from the integration region shown in Fig. 1. Three spectra from the three pointings were co-added. The cosmic and intrinsic backgrounds were subtracted from each spectrum, taking into account the secular change of the NXB (see text). The best-fit model and its constituent components are shown, and the best-fit parameters are given in Table 1.

ground spectrum into the NXB and CXB components by referring to the nighttime Earth data, and we rescaled the NXB normalization to take into account the secular change in the NXB by comparing the nighttime Earth spectrum between the epoch of the on-source observation (in 1994 or 1997) and that of the blank-sky archival data (mostly obtained in 1993). We thus generated an appropriate background spectrum (CXB + rescaled NXB) for each on-source observation and subtracted it from the raw spectrum of each GIS instrument. Then we summed the GIS spectra from the observations into a single spectrum.

In Figure 3, we show the obtained background-subtracted GIS2 + GIS3 spectrum of the west lobe region. It is relatively hard and significantly detected up to ~ 8 keV, implying a considerable improvement over the results in K95. We fitted the spectrum with a model consisting of three components: (1) a power law with a free energy index and free normalization, representing the IC emission; (2) a thin thermal emission (Raymond & Smith 1977) with free temperature and free normalization, but with the metallicity fixed at 0.4 solar abundance, which represents the soft thermal emission surrounding the radio galaxy as detected by K95; and (3) the contaminating source 1. We analyzed the *ROSAT*-PSPC spectrum of source 1 and found that it can be described with a power law with an energy index of 3.2 ± 0.7 and a flux density of $0.008 \pm 0.001 \mu\text{Jy} [= (8 \pm 1) \times 10^{-35} \text{ W m}^{-2} \text{ Hz}^{-1}]$ at 1 keV, absorbed by a column density of $(8.0 \pm 0.2) \times 10^{24} \text{ H atoms m}^{-2}$ with $\chi^2/\text{degree of freedom (dof)} = 12.1/17$. In the fit to the GIS data, we constrained the third component to take these best-fit

TABLE 1
RESULTS OF THE MODEL FIT TO THE 0.7–10 keV GIS SPECTRUM
FROM THE LOBE REGION^a

| Component | N_{H}^b | Energy Index | kT (keV) | $F_{1 \text{ keV}}^c$ |
|-----------------|------------------|-----------------|-----------------|-----------------------|
| Source 1 | 8.0^d | 3.2^d | ... | 0.008^d |
| IC emission | 2.06^e | 0.74 ± 0.26 | ... | 0.10 ± 0.01 |
| Ambient thermal | 2.06^e | ... | 0.85 ± 0.15 | 0.11 ± 0.05 |

^a The χ^2 fit is 94.7 for 103 dof. All the errors refer to single-parameter 90% confidence limits.

^b Photoelectric absorption column density in units of $10^{24} \text{ H atoms m}^{-2}$.

^c Flux density at 1 keV in units of $1 \mu\text{Jy} = 1 \times 10^{-32} \text{ W m}^{-2} \text{ Hz}^{-1}$.

^d Fixed at the best-fit values of the *ROSAT*-PSPC data.

^e Fixed at the Galactic line-of-sight value.

ROSAT parameters. We calculated the ASCA response function for the three observations individually, and then we took their weighted average. With this three-component model, we have successfully described the spectrum with $\chi^2/\text{dof} = 94.7/103$. The best-fit parameters are shown in Table 1. The 2–10 keV flux obtained from the lobe region is $4.8 \times 10^{-16} \text{ W m}^{-2}$, which is consistent with that evaluated by K95. The derived energy index of the IC component (0.74 ± 0.26) agrees with that obtained by K95 (1.4 ± 0.7), and the accuracy is much improved. A similar good fit was obtained by replacing the power-law component with a second thin thermal plasma emission model of temperature $kT = 8.4^{+3.2}_{-3.2} \text{ keV}$, with an emission measure of $\int n_e n_H dV = (6.6 \pm 1.2) \times 10^{56} \text{ m}^{-3}$ and an abundance fixed at 0.4 solar.

3.3. X-Ray Brightness Distribution

We saw in Figure 2 that the IC X-ray emission is relatively concentrated on the center of the lobe. To quantify the surface brightness distributions, we masked the contaminant discrete sources (§ 3.1) and made a 1.0–10 keV radial brightness profile around the X-ray brightness peak (the cross in Fig. 2). The X-ray surface brightness distribution is so flat within a few arcminutes that the radial profile is less sensitive to the position of the center (Fig. 2). To compare this with the X-ray radial profile around the same center, we made a radial brightness profile in radio utilizing the 1.4 GHz image by Ekers et al. (1983); we show these profiles in Figure 4. Thus, the two profiles resemble each other but differ in two points: the rim-brightened feature seen in the radio profile is absent in X-rays, and the X-ray distribution appears to have a larger radius than the radio distribution.

To examine possible instrumental artifacts, we simulated an expected X-ray image with the XRT and GIS response simulator to fit the observed radial brightness profile. The position resolution and vignetting effect were calculated based on calibration data from Cygnus X-1 (Ikebe 1995; Takahashi et al. 1995). We assume an isotropic distribution of the emissivity through the simulation. This analysis revealed that a homogeneously filled spherical emissivity model with an outer boundary of $12' \pm 1'$ reproduces the observed X-ray radial profile very well (Fig. 4, *solid line*).

On the other hand, a shell-shaped emissivity model reproduced the rim-brightened radio profile very well, as represented by the dashed line in Figure 4. The outer boundary of the shell is constrained to be $11' \pm 0.5'$, while the inner boundary is $4' \pm 0.5'$. The shell-shaped model, however, could not describe the obtained X-ray profile with a finite inner boundary. Therefore, unlike the case of X-ray emissivity, the radio profile requires a reduced emissivity at the lobe center, although we see

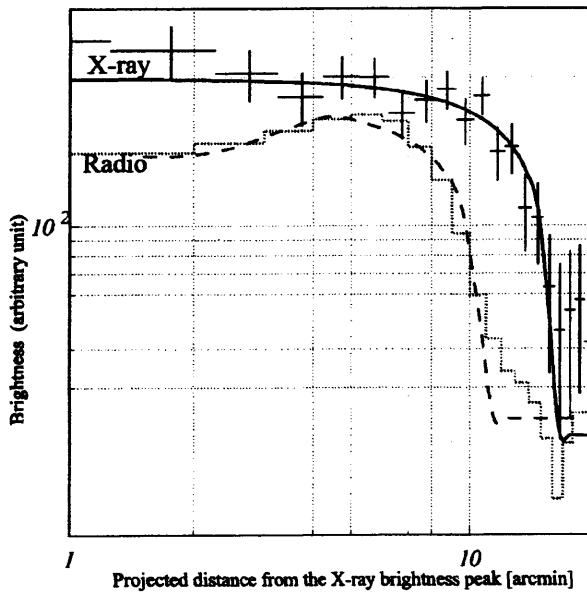


FIG. 4.—Radial X-ray (0.7–10 keV) and radio surface brightness distributions measured from the west radio lobe of Fornax A. The abscissa is the projected distance from the X-ray peak in units of arcminutes, while the ordinate is the relative brightness in an arbitrary unit. The X-ray data (crosses) are obtained from the ASCA observations of 1994 and 1997 after subtracting the background, while the radio distribution (dotted histogram) is compiled from the map presented by Ekers et al. (1983). The fitted model distributions are also indicated. The filled-sphere model (solid line) and the shell model (dashed line) are fitted to the X-ray profile and the radio profile, respectively (see text).

no significant discrepancy between the derived outer boundaries of the X-ray and radio profiles. Since the radio data provided better accuracy, we regard the value of $\sim 11'$ derived from radio data as the common outer boundary of radio and X-rays (see § 4).

4. DISCUSSION

We measured the diffuse X-rays of the Fornax A west lobe with an improved accuracy employing the ASCA follow-up observations. The diffuse emission spatially coincides with the radio synchrotron lobe on a large scale. The derived 0.7–10 keV spectrum of the lobe X-rays is well described with a power-law model whose energy index of 0.74 ± 0.26 agrees with the synchrotron radio emission energy index of 0.9 ± 0.2 derived from published radio fluxes observed at 408 MHz, 1.4 GHz, and 2.7 GHz (see Cameron 1971, Ekers et al. 1983, and Shimmins 1971, respectively). Although the spectrum that we obtained formally includes a thin thermal plasma model, the spectrum's high temperature ($kT = 8.4_{-3.2}^{+∞}$ keV) precludes us from using either the gravitational confinement or the cooling flow to explain the emission. The derived emission measure requires a thermal pressure of $\sim 3 \times 10^{-13} \text{ J m}^{-3}$. If we assume a magnetic field of ~ 1 nT to confine the possible thermal plasma, that field will reduce the synchrotron cooling time down to $\sim 10^6$ yr (Iyomoto

et al. 1998). This is too short for the relativistic electrons to diffuse in all of the lobes, considering the estimated growth speeds of the lobes (Scheuer 1995). Therefore, we reconfirm, with a higher accuracy, that the diffuse X-ray emission is produced via the IC process in which the cosmic microwave background photons are boosted by the synchrotron electrons, as F95 and K95 concluded.

With the follow-up observations pointing at the west lobe, we examined the brightness distribution of the IC X-ray emission and revealed that it indicates a center-filled emissivity distribution in contrast to the rim-brightening radio shape. This indicates that the relativistic electrons are homogeneous in the sphere of radius $\sim 75 h_{75}^{-1} \text{ kpc}$ ($= 11'$), where h_{75} is the Hubble constant normalized to $75 \text{ km s}^{-1} \text{ Mpc}^{-1}$. We therefore regard the rim-brightened radio emission as a direct indicator of the magnetic pressure distribution, represented by a shell of inner and outer boundaries of $\sim 27 h_{75}^{-1} \text{ kpc}$ ($= 4'$) and $\sim 75 h_{75}^{-1} \text{ kpc}$ ($= 11'$), respectively. On the basis of the spectral and spatial analysis, we evaluate the energy densities of the magnetic field (u_B) and the electrons (u_e) according to Harris & Grindlay (1979). Since u_B is determined by the ratio of the synchrotron radio flux to the IC X-ray flux emitted from the same volume, u_B is in inverse proportion to the volume ratio of the shell to the electron-filled sphere, which is ~ 0.95 . We estimate that the 1.4 GHz flux falling inside the X-ray integration region is 50 Jy ($= 5 \times 10^{-25} \text{ W s}^{-1} \text{ m}^{-2}$), based on the radio map by Ekers et al. (1983). We then calculate u_B after Harris & Grindlay (1979), considering the filling factor (f) to the shell region and assuming that the magnetic fields have random directions to the line of sight. The result is $u_B = (4.6 \pm 0.4)f^{-1} \times 10^{-14} \text{ J m}^{-3}$.

The derived u_B corresponds to a magnetic field strength of $0.34 \pm 0.02 \text{ nT}$ at $f = 1$. Note here that we adopted an IC scattering electron density, at a Lorentz factor of $\gamma \sim 1000$, estimated using an extrapolation from the observed synchrotron spectrum at $\gamma \sim 5000$ – $13,000$. Utilizing equation (10) of Harris & Grindlay (1979), we also derive u_e in the sphere. We assume that the electron Lorentz factor ranges from $\gamma = 10^3$ to 10^5 in the calculation below, as K95 adopted. Thus, we obtained u_e from the estimated IC X-ray flux (Table 1) as $u_e = (2.0 \pm 0.5)(r_{\text{out}}/11')^{-3} h_{75} \times 10^{-14} \text{ J m}^{-3}$. Although the derived u_B is nominally larger than the u_e by a factor of 2.3 in the shell, we cannot immediately reject an electron–magnetic field equipartition ($u_B = u_e$) there without first determining the electron energy spectrum below $\gamma \sim 5000$. If the spectrum is turned down just below $\gamma = 5000$, the estimated $u_B/u_e \approx 8.3$. On the contrary, assuming that the spectrum extends down to $\gamma \sim 350$ (~ 2 MHz in synchrotron emission), the integrated u_e becomes equivalent to u_B in the shell region.

The results obtained here suggest a picture in which the lobe interior is dominated by the particle pressure, whereas the magnetic field pressure becomes significant in the shell region defined by the lobe boundary. Interestingly, we see a similar situation in the lobes of Centaurus B (PKS 1343–601), as Tashiro et al. (1998) show. The similarity is thought to reflect the energetics and evolutions of radio lobes (e.g., Blundell & Rawlings 2000) and the intergalactic environments of particle and magnetic fields. Further investigations with the recent advanced X-ray observatories are expected.

REFERENCES

- Blundell, K. M., & Rawlings, S. 2000, *AJ*, 119, 1111
 Brunetti, G., Comastri, A., Setti, G., & Feretti, L. 1999, *A&A*, 342, 57
 Burke, B. E., Mountain, R. W., Harrison, D. C., Bautz, M. W., Doty, J. P., Ricker, G. R., & Daniels, P. J. 1991, *IEEE Trans. Electron Devices*, 38, 1069
 Cameron, M. J. 1971, *MNRAS*, 152, 439
 Ekers, R. D., Goss, W. M., Wellington, K. J., Bosma, A., Smith, R. M., & Schwaizer, F. 1983, *A&A*, 127, 361
 Feigelson, E. D., Laurent-Muehleisen, S. A., Kollgaard, R. I., & Fomalont, E. B. 1995, *ApJ*, 449, L149 (F95)

- Harris, D. E., & Grindlay, J. E. 1979, *MNRAS*, 188, 25
Ikebe, Y. 1995, Ph.D. thesis, Univ. Tokyo
Iyomoto, N., Makishima, K., Tashiro, M., Inoue, S., Kaneda, H., Matsumoto, Y., & Mizuno, T. 1998, *ApJ*, 503, L31
Kaneda, H., et al. 1995, *ApJ*, 453, L13 (K95)
Kim, D.-W., Fabbiano, G., & Mackie, G. 1998, *ApJ*, 497, 699
Longhetti, M., Rampazzo, R., Bressom, A., & Chiosi, C. 1998, *A&AS*, 130, 267
Makishima, K., et al. 1996, *PASJ*, 48, 171
Ohashi, T., et al. 1996, *PASJ*, 48, 157
Pfeffermann, E., & Bruel, U. G. 1986, *Proc. SPIE*, 733, 519
Raymond, J. C., & Smith, B. W. 1977, *ApJS*, 35, 419
Scheuer, P. A. G. 1995, *MNRAS*, 277, 331
Serlemitsos, P., Loewenstein, M., Mushotzky, R. F., Marshall, F. E., & Petre, R. 1993, *ApJ*, 413, 518
Shimmins, A. J. 1971, *Australian J. Phys. Astrophys. Suppl.*, 21, 1
Takahashi, T., et al. 1995, *ASCA Newsl.*, 3, 34
Tanaka, Y., Inoue, H., & Holt, S. S. 1994, *PASJ*, 46, L37
Tashiro, M., et al. 1998, *ApJ*, 499, 713
Tashiro, M., Makishima, K., & Kaneda, H. 2000, *Adv. Space Res.*, 25, 751
Trümper, J. 1982, *Adv. Space Res.*, 2(4), 241
Yamashita, A., et al. 1997, *IEEE Trans. Nucl. Sci.*, 44, 847

3.2. Y. Fukazawa, et al., 2001, ApJ 546, L87

33

3.2 Y. Fukazawa, et al., 2001, ApJ 546, L87

DETECTION OF EXCESS HARD X-RAY EMISSION FROM THE GROUP OF GALAXIES HCG 62

YASUSHI FUKAZAWA,^{1,2} KAZUHIRO NAKAZAWA,² NAOKI ISOBE,² KAZUO MAKISHIMA,² KYOKO MATSUSHITA,^{2,3}
TAKAYA OHASHI,⁴ AND TSUNEYOSHI KAMAE^{1,2}

Received 2000 May 26; accepted 2000 October 25; published 2001 January 9

ABSTRACT

We detected an excess of hard X-ray emission at energies above ~ 4 keV from the group of galaxies HCG 62 using data from the *ASCA* satellite. The excess emission is spatially extended up to $\sim 10'$ from the group center and somewhat enhanced toward the north. Its spectrum can be represented by either a power law of photon index 0.8–2.7 or a bremsstrahlung of temperature greater than 6.3 keV. In the 2–10 keV range, the observed hard X-ray flux, $(1.0 \pm 0.3) \times 10^{-12}$ ergs cm⁻² s⁻¹, implies a luminosity of $(8.0 \pm 2.0) \times 10^{41}$ ergs s⁻¹ for a Hubble constant of 50 km s⁻¹ Mpc⁻¹. The emission is thus too luminous to be attributed to X-ray binaries in the member galaxies. We discuss possible origins of the hard X-ray emission.

Subject headings: galaxies: clusters: individual (HCG 62) — galaxies: evolution — X-rays: galaxies

1. INTRODUCTION

Clusters of galaxies are thought to have released a large amount of dynamical energy in their initial collapse phase. During their subsequent evolution, starburst-driven winds, cluster mergers, radio galaxies, and random galaxy motions may have supplied additional heating energy to the intracluster space. Presumably, these processes have generated energetic particles (e.g., Kang, Ryu, & Jones 1996; Takizawa 2000), as evidenced by diffuse synchrotron radio emission from some clusters.

Such energetic particles are expected to produce nonthermal X-rays as well, by Compton-boosting cosmic microwave background (CMB) photons. Long searches for such effects among galaxy clusters have recently revealed two candidates: the excess soft X-ray emission detected with the *Extreme Ultraviolet Explorer* (Lieu et al. 1996; Mittaz, Lieu, & Lockman 1998; Bowyer & Berghofer 1998) and the spectral hard X-ray tail observed with *BeppoSAX* (Fusco-Femiano et al. 1999; Kaastra et al. 1999). However, the exact nature of these emission components remains unclear.

Groups of galaxies are the poorest class of galaxy clusters. Their thermal emission is limited to energies below ~ 5 keV, because the temperature of their hot intragroup medium is about 1 keV (e.g., Mulchaey et al. 1996; Fukazawa et al. 1996). Therefore, they allow us to search for nonthermal X-ray emission, even with instruments operating below an energy of ~ 10 keV. Here we report the detection of excess hard X-ray emission from the group of galaxies HCG 62 with the *ASCA* Gas Imaging Spectrometer (GIS; Ohashi et al. 1996; Makishima et al. 1996). We employ 90% confidence limits throughout this Letter and use the Hubble constant of 50 km s⁻¹ Mpc⁻¹. Solar abundances refer to Anders & Grevesse (1989).

2. OBSERVATIONS AND DATA REDUCTION

With a redshift of 0.0137 (Hickson, Kindl, & Huchra 1988), HCG 62 is one of the nearest Hickson compact galaxy groups. It was observed twice with *ASCA*: on 1994 January 14–15 in a single pointing and on 1998 January 13–17 in four pointings to cover the whole group region. The GIS was operated in PH mode, and the Solid-State Imaging Spectrometer (SIS) in 2-CCD FAINT mode in 1994. We do not use the SIS data taken in 1998 because of the insufficient field of view of 1-CCD mode employed at that time. After an appropriate gain correction, we co-added all the available data from different sensors, chips, and pointings, separately for the GIS and the SIS. The live time is ~ 30 ks for the 1994 observation and ~ 20 ks for each of the four pointings of the 1998 observation. The total GIS live time thus amounts to 110 ks.

For our purpose, it is important to accurately subtract the GIS background, which consists of cosmic X-ray background (CXB) and intrinsic detector background (IDB). We first summed data of the *ASCA* Large Sky Survey (Ueda et al. 1999), conducted in 1993 December and 1994 June over blank sky fields, with a total exposure time of 233 ks. Then, after Ikebe (1995), we excluded regions in the GIS images where the count rate exceeds those from surrounding regions by $\geq 2.5 \sigma$. This eliminates faint sources with 2–10 keV flux greater than 8×10^{-14} ergs s⁻¹ cm⁻².

We next corrected the IDB level of each pointing individually for its gradual increase by 2%–3% yr⁻¹ and for its random day-by-day fluctuation by 6%–8% (Ishisaki et al. 1997). For this purpose, we derived three GIS spectra, denoted $S(E)$, $B(E)$, and $N(E)$, from the on-source data, the blank sky data prepared as above, and night Earth data, respectively. They were accumulated over an annulus of radius 13'–25' from the GIS field center and in the 6–10 keV energy range, to ensure that $S(E)$ is free from the HCG 62 emission and that the CXB is relatively minor compared to the IDB in $S(E)$ and $B(E)$. Then, assuming that the IDB spectrum and its radial profile are both constant, we fitted $S(E)$ with a linear combination $B(E) + fN(E)$; here f is a free parameter and $fN(E)$ represents the secular IDB change between the two epochs when $S(E)$ and $B(E)$ were acquired. We have obtained $f = 0.00$ and $f = 0.08$ –0.12 for the 1994 and 1998 data, respectively, in agreement with the IDB long-term increase (Ishisaki et al. 1997). By analyzing various *ASCA* data, we also confirmed

¹ Department of Physical Sciences, Graduate School of Science, Hiroshima University, 1-3-1 Kagamiyama, Higashi-Hiroshima, Hiroshima 739-8526, Japan; fukazawa@hirax6.hepl.hiroshima-u.ac.jp.

² Department of Physics, Graduate School of Science, University of Tokyo, 7-3-1 Hongo, Bunkyo-ku, Tokyo 113-0033, Japan.

³ Max-Planck-Institut für Extraterrestrische Physik, Giessenbachstrasse, D-85748 Garching, Germany.

⁴ Department of Physics, Faculty of Science, Tokyo Metropolitan University, Minami-Ohsawa, Hachioji, Tokyo 192-0397, Japan.

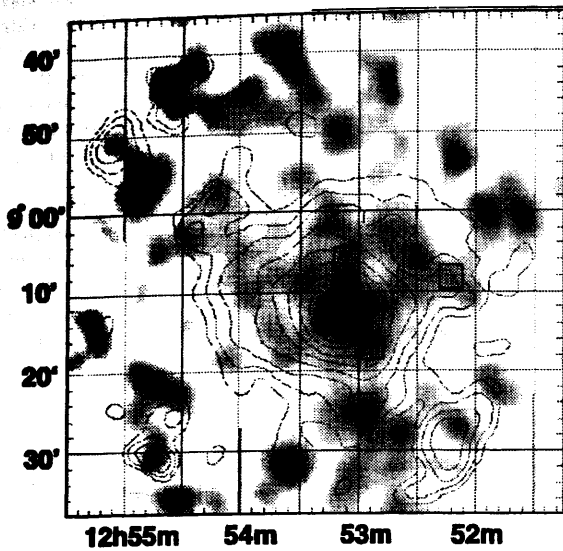


FIG. 1.—Background-subtracted GIS image of HCG 62 in 4.5–8 keV (gray scale) and 1.0–2.4 keV (contours). Both images have been smoothed with a Gaussian filter of $\sigma = 1'$, and their scales are logarithmic. The four squares are positions of the *ROSAT* point sources that would also be detected with the GIS.

that this method can reproduce, to within 5%, the GIS background spectra and its radial profiles acquired at any epoch over 1993–1999.

The SIS has a lower efficiency in the hard X-ray band, a shorter exposure time, and a smaller field of view than the GIS. We therefore utilize the SIS spectrum only to determine the soft thermal emission from the intragroup medium. We subtract the SIS background in a conventional way, utilizing the archival SIS background set.

3. RESULTS

To avoid the diffuse thermal emission with a typical plasma temperature of $kT \sim 1.0$ keV (Ponman et al. 1993; Fukazawa et al. 1998; Davis, Mulchaey, & Mushotzky 1999), we produced the GIS image of HCG 62 in the hard 4.5–8 keV band, as shown in Figure 1. There we overlaid the 1.0–2.4 keV image as a measure of the thermal emission, of which the brightness peak coincides in position with the group center to within $1'$. The image reveals a hard X-ray emission, which apparently extends up to $\sim 10'$ from the group center.

Figure 2 shows the radial GIS count rate profile in the energy band of 4.5–8 keV, centered on the soft X-ray brightness peak. Also shown are the instrumental point-spread function (PSF) and the profile of the estimated background. Thus, the background level is well reproduced at larger radii within 5%, and the hard X-ray emission is more extended than the PSF, detectable up to $10'$ from the group center. As shown in the inset to Figure 2, the hard X-ray surface brightness is higher in the north region than in the south region. Such a feature cannot be explained as a spillover from the 1 keV thermal emission. The hard X-ray brightness is not correlated with the galaxy distribution, either, including emission-line galaxies (de Carvalho et al. 1997).

The observed hard X-ray emission, although apparently extended, could simply be a result of several hard point sources,

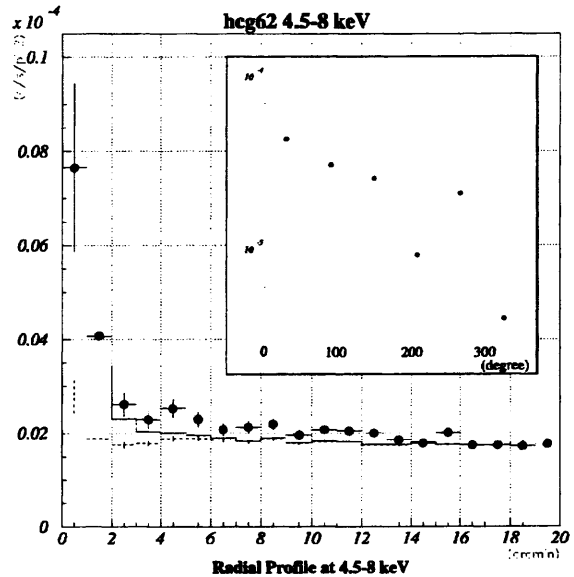


FIG. 2.—GIS radial count rate profile of HCG 62 (crossed circles) centered on the soft X-ray peak position, including the background. The dashed crosses represent the estimated background, and the solid line shows the *ASCA* X-Ray Telescope + GIS PSF plus the estimated background. The inset shows the background-subtracted azimuthal count rate profile in 4.5–8 keV (crossed circles) and 1.0–2.4 keV (dotted histogram). The angle is defined counter-clockwise, with east being the origin.

such as active galaxies, either related or unrelated to HCG 62. To answer this issue, we examined the archival *ROSAT* image of HCG 62 and found four point sources with $0.1\text{--}2$ keV fluxes of $(4\text{--}8) \times 10^{-14}$ ergs s^{-1} cm^{-2} (Fig. 1, open squares) at the locations where the hard-band GIS image actually exhibits possible enhancements with the implied 2–10 keV fluxes of $\sim 10^{-13}$ ergs s^{-1} cm^{-2} . The flux ratio between *ASCA* and *ROSAT* indicates that the source spectra have a power-law shape of photon index ~ 1.5 . We have accordingly excluded photons falling within $2.5'$ of these four sources. In addition, in order to remove possible pointlike sources at the central region of HCG 62, we excluded photons within $3'$ of the group center. Then, the 4.5–8 keV GIS2 + GIS3 flux from the on-source data has become 3772 ± 61 photons over the radius of $3'\text{--}15'$, compared to 3351 ± 20 expected from the background count rate. The excess, 421 ± 65 counts, well exceeds the ~ 60 counts expected for the 1 keV thermal emission. Thus, the presence of the extended excess hard X-ray emission is significant from the GIS imagery even after excluding possible point-source contamination.

In order to examine the excess hard X-ray emission through spectroscopy, we have produced spectra over the radius of $3'\text{--}15'$ by utilizing all the available data from the GIS and only the first pointing data from the SIS. The regions within $2.5'$ of the four pointlike sources were again excluded. We discarded the SIS data above 4 keV for the reason described before. The obtained spectra are presented in Figure 3. We fitted them simultaneously by a single-temperature plasma emission model (Raymond & Smith 1977; R-S model) with solar abundance ratios (Fukazawa et al. 1996, 1998), modified by photoelectric absorption. As shown in Table 1 and Figure 3, the model successfully reproduced the data in lower energies, and the derived temperature and metallicity are consistent with those of Fu-

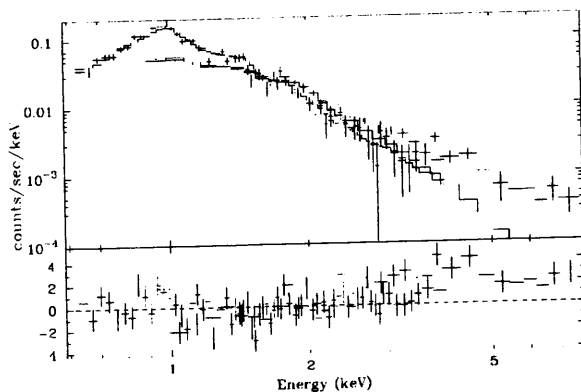


FIG. 3.—GIS + SIS simultaneous spectral fitting of HCG 62 with the single-temperature R-S model. The crosses and solid lines represent the data and model, respectively. The SIS data above 4 keV are discarded.

kazawa et al. (1998). However, the model is not acceptable due to significant residuals seen in the GIS fit over energies of greater than 3 keV. When we limit the energy band to less than 2.4 keV, the fit becomes acceptable with a reduced χ^2 of 1.29 and the best-fit temperature of 0.95 ± 0.05 keV. In contrast, when we use only the hard energy band above 2 keV, the best-fit temperature increases to 2.1 ± 0.3 keV; this is inconsistent with that indicated by the soft-band data and is much higher than the prediction from the galaxy velocity dispersion of ~ 300 km s $^{-1}$ (Mulchaey et al. 1996). These results reconfirm the presence of excess hard X-ray emission above the prediction of the thermal emission of temperature ~ 1 keV. The results of Finoguenov & Ponman (1999), who reported a high temperature of greater than 1.5 keV around 5' of the group center, are also consistent with ours.

We refitted the whole-band spectra by adding a bremsstrahlung or a power-law component to represent the excess hard X-ray emission. As summarized in Table 1, either modeling has given an acceptable joint fit to the ASCA spectra. The bremsstrahlung temperature has been constrained as greater than 6.3 keV, while the power-law photon index α_{ph} was found at $1.5^{+1.2}_{-0.7}$. Although α_{ph} can be as high as 2.7, such a steep power law forces the R-S component to have an extremely high metallicity. When we fix the metallicity of the R-S component at 0.30 solar, which is typically found from clusters of galaxies, the upper limit on α_{ph} becomes 2.2. Below, we utilize this limit instead of the original one. The normalization of the hard component does not change by more than 20% if we use plasma emission codes other than the R-S code.

The upper limit on narrow Fe K line features at ~ 6.6 keV is uninteresting, several keV in equivalent width. The absorp-

tion column density cannot be constrained in any case and is consistent with the Galactic value of 2.9×10^{20} cm $^{-2}$ (Stark et al. 1992). The 2–10 keV X-ray flux and luminosity of the hard X-ray component are $(1.0 \pm 0.3) \times 10^{-12}$ ergs cm $^{-2}$ s $^{-1}$ and $(8.0 \pm 2.0) \times 10^{41}$ ergs s $^{-1}$, respectively, regardless of the choice between the two modelings. This amounts to about 20% of the 0.5–10 keV thermal component luminosity of 4.9×10^{42} ergs s $^{-1}$ (Fukazawa 1997).

Although we have carefully estimated the background, it is still important to examine to what extent our results are affected by possible background uncertainties. To see this, we intentionally increased the IDB background level by 5% and found that the 2–10 keV flux and luminosity of the hard component become $(5.5\text{--}8.4) \times 10^{-13}$ ergs s $^{-1}$ cm $^{-2}$ and $(4.3\text{--}6.5) \times 10^{41}$ ergs s $^{-1}$, respectively. Thus, the hard emission remains statistically significant.

4. DISCUSSION

From the galaxy group HCG 62, we have detected the excess X-ray emission with a very hard spectrum, which extends up to more than 10' from the group center and is somewhat enhanced at the north region. Although its surface brightness is only $\sim 20\%$ of that of the GIS background, we have confirmed its reality through careful analysis. Below, we discuss the origin and nature of this phenomenon.

An immediate possibility is a collection of binary X-ray sources in the member galaxies of HCG 62. However, based on the total optical luminosity of HCG 62 ($\sim 1 \times 10^{11} L_{\odot}$; de Carvalho et al. 1997) and the optical versus X-ray luminosity correlation among elliptical galaxies (Matsushita 1997), this contribution is estimated to be at most 4×10^{40} ergs s $^{-1}$, which is an order of magnitude short of the observed luminosity. A second possibility is an assembly of faint active galactic nuclei (AGNs) in HCG 62. However, the optical evidence for AGNs in HCG 62 is moderate (de Carvalho et al. 1997), and we have already subtracted such candidates based on the ROSAT image. Any remaining AGNs are estimated to contribute no more than 30%–40% of the total hard X-ray emission. Yet another possibility is the fluctuation of background faint sources. Utilizing the log N –log S relation in the 2–10 keV band (Ueda et al. 1999), this contribution is estimated to be at most $\sim 2 \times 10^{-13}$ ergs cm $^{-2}$ s $^{-1}$ over the radius of 3'–15', which is again too low to explain the data. From these considerations, we conclude that the excess hard X-ray emission cannot be explained by the assembly of discrete hard X-ray sources, whatever their nature be.

Considering the loose constraint on the Fe K line, the excess emission might be of thermal origin from very hot plasmas. Actually, Buote (2000) described the ASCA spectra of HCG 62, integrated over a radius of 0'–3', by a two-temperature

TABLE 1
RESULTS OF JOINT FITTING OF THE GIS AND SIS SPECTRA OF HCG 62 WITH VARIOUS MODELS

| Model | $\chi^2/\text{Degrees of Freedom}$ | N_{H}^a ($\times 10^{20}$ cm $^{-2}$) | kT^b (keV) | Solar Abundance ^b | Normalization ^b ($\times 10^{17}$ cm $^{-5}$) | Normalization of Hard Component ^c |
|---|------------------------------------|---|----------------------|------------------------------|---|--|
| R-S | 2.24 | <3.7 | 1.02 ± 0.03 | 0.15 ± 0.02 | 7.2 ± 0.6 | $1.2^{+0.7}_{-0.2} \times 10^{17}$ |
| R-S + bremsstrahlung ^d | 0.99 | <3.5 | 0.95 ± 0.05 | 0.18 ± 0.05 | 5.9 ± 1.0 | $1.7^{+5.7}_{-1.0} \times 10^{14}$ |
| R-S + power law ^e | 0.99 | <3.4 | $0.96^{+0.3}_{-0.6}$ | >0.14 | $5.6^{+1.3}_{-3.5}$ | |

^a Column density of photoelectric absorption.

^b Parameters of R-S model.

^c Normalization of bremsstrahlung model or power-law model in units of cm $^{-5}$ or counts s $^{-1}$ cm $^{-2}$ keV $^{-1}$, respectively.

^d Temperature of bremsstrahlung model kT_{brems} > 6.3.

^e Power-law photon index $\alpha_{\text{ph}} = 1.5^{+1.2}_{-0.7}$.

plasma model of $kT = 0.7$ and $kT = 1.5$ keV. We have independently reconfirmed their results. However, our spectra (Fig. 3) that are accumulated over the 3'–15' range require a temperature of greater than 6.3 keV; the original two-temperature model found by Buote (2000) gives a very poor fit ($\chi^2/\nu = 1.66$). Thus, thermal emission with an "ordinary" temperature cannot explain the data. Insignificant detection of excess hard X-rays over a radius of 0'–3' might be due to poor photon statistics and complex spectra of thermal components (Fukazawa et al. 1998) at the center region, spectral change of hard components, and so on. There might still be plasmas much hotter than the escape temperature, as is actually found in starburst galaxies (e.g., Ptak et al. 1997). However, within 15' of HCG 62, there are no bright *IRAS* sources with the 60 μm flux exceeding 2 Jy (SkyView at the High Energy Astrophysics Science Archive Research Center). We therefore conclude that the thermal interpretation of the excess hard X-ray emission is unrealistic.

Given the difficulties with the discrete source and thermal interpretations of the diffuse hard X-ray emission, we regard the nonthermal interpretation as the most promising. One popular scenario of nonthermal X-ray production is inverse Compton scattering of the CMB photons by relativistic electrons with Lorentz factor $\gamma \sim 10^3$ – 10^4 , as has been invoked to explain the excess hard X-ray emission from rich clusters (e.g., Fusco-Femiano et al. 1999). However, we cannot constrain the intragroup magnetic field in HCG 62 because of a lack of information on the diffuse radio flux. If we assume a representative magnetic field intensity of 1 μG , we would observe synchrotron radio emission with a flux density of ~ 0.3 Jy. Since such a strong radio emission is not seen from HCG 62 (SkyView; NRAO Very Large Array Sky Survey image), the inverse Compton interpretation holds for HCG 62 only if its magnetic field is much weaker than 1 μG . The reality of such a weak magnetic field is an open question and in an apparent contradiction to the generally accepted intergalactic field strengths of

$\sim 1 \mu\text{G}$ (Kronberg 1994), even though such a condition is suggested by the *BeppoSAX* and *RXTE* observations of some rich clusters of galaxies (Valinia et al. 1999; Fusco-Femiano et al. 1999).

An alternative interpretation is nonthermal bremsstrahlung between the thermal gas and subrelativistic particles, as proposed for the hard X-ray emission from Abell 2199, of which diffuse radio flux is quite weak (Kempner & Sarazin 2000), as in the case of HCG 62. Let us assume for simplicity that the nonthermal electrons have typical energies of 10–100 keV and their spatial density distribution is similar to that of the thermal intragroup gas. Then, the nonthermal to thermal luminosity ratio in the 0.5–10 keV band becomes $\sqrt{10}\alpha$, where α is the density ratio of the nonthermal electrons to the thermal ones. The observed luminosity ratio of ~ 0.2 implies $\alpha \sim 0.06$, indicating that the energy density of nonthermal electrons is 0.6–6 times as high as that of thermal electrons (depending on the spectrum). If this is the case, the mechanism of such particle acceleration becomes an important issue. In addition, the nonthermal pressure associated with such a particle population would considerably increase the total mass of HCG 62, and hence its dark matter content, estimated from the X-ray data.

The diffuse hard X-ray emission has been observed with *ASCA* from some other galaxy groups as well (Fukazawa 1999). However, its prominence relative to the thermal X-ray emission appears to scatter from object to object, similar to that seen in rich clusters (Molendi et al. 1999), with HCG 62 being one of the strongest cases. Although what makes such variety is yet to be studied, the hard X-ray emission might be related with transient phenomena such as mergers.

The authors are grateful to M. Takizawa for helpful discussions and to an anonymous referee for helpful comments. This research was supported in part by the Grants-in-Aid for the Center-of-Excellence (COE) Research of the Ministry of Education, Science, and Culture in Japan (07CE2002).

REFERENCES

- Anders, E., & Grevesse, N. 1989, *Geochim. Cosmochim. Acta*, 53, 197
 Bowyer, S., & Berghofer, T. W. 1998, *ApJ*, 506, 502
 Buote, D. A. 2000, *MNRAS*, 311, 176
 Davis, D. S., Mulchaey, J. S., & Mushotzky, R. F. 1999, *ApJ*, 511, 34
 de Carvalho, R. R., Ribeiro, A. L. B., Capelato, H. V., & Zepf, S. E. 1997, *ApJS*, 110, 1
 Finoguenov, A., & Ponman, T. J. 1999, *MNRAS*, 305, 325
 Fukazawa, Y. 1997, Ph.D. thesis, Univ. Tokyo
 ———. 1999, *Astron. Nachr.*, 320, 377
 Fukazawa, Y., et al. 1996, *PASJ*, 48, 395
 Fukazawa, Y., Makishima, K., Tamura, T., Ezawa, H., Xu, H., Ikebe, Y., Kikuchi, K., & Ohashi, T. 1998, *PASJ*, 50, 187
 Fusco-Femiano, R., Fiume, D. D., Feretti, L., Giovannini, G., Grandi, P., Matt, G., Molendi, S., & Santangelo, A. 1999, *ApJ*, 513, L21
 Hickson, P., Kindl, E., & Huchra, J. P. 1988, *ApJ*, 331, 64
 Ikebe, Y. 1995, Ph.D. thesis, Univ. Tokyo
 Ishisaki, Y., et al. 1997, *ASCA Newsl.*, 5, 25
 Kaastra, J. S., Lieu, R., Mittaz, J. P. D., Bleeker, J. A. M., Mewe, R., Colafrancesco, S., & Lockman, F. J. 1999, *ApJ*, 519, L119
 Kang, H., Ryu, D., & Jones, T. W. 1996, *ApJ*, 456, 422
 Kempner, J. C., & Sarazin, C. L. 2000, *ApJ*, 530, 282
 Kronberg, P. P. 1994, *Nature*, 370, 179
 Lieu, R., Mittaz, J. P. D., Bowyer, S., Lockman, F. J., Hwang, C.-Y., & Schmitt, J. H. M. M. 1996, *ApJ*, 458, L5
 Makishima, K., et al. 1996, *PASJ*, 48, 171
 Matsushita, K. 1997, Ph.D. thesis, Univ. Tokyo
 Mittaz, J. P. D., Lieu, R., & Lockman, F. J. 1998, *ApJ*, 498, L17
 Molendi, S., de Grandi, S., Fusco-Femiano, R., Colafrancesco, S., Fiore, F., Nesci, R., & Tamburelli, F. 1999, *ApJ*, 525, L73
 Mulchaey, J. S., Davis, S. S., Mushotzky, R. F., & Burstein, D. 1996, *ApJ*, 456, 80
 Ohashi, T., et al. 1996, *PASJ*, 48, 157
 Ponman, T. J., & Bertram, D. 1993, *Nature*, 363, 51
 Ptak, A., Serlemitsos, P., Yaqoob, T., Mushotzky, R., & Tsuru, T. 1997, *AJ*, 113, 1286
 Raymond, J. C., & Smith, B. W. 1977, *ApJS*, 35, 419
 Stark, A. A., Gammie, C. F., Wilson, R. W., Bally, J., & Linke, R. A. 1992, *ApJS*, 79, 77
 Takizawa, M. 2000, *ApJ*, 532, 183
 Ueda, Y., et al. 1999, *ApJ*, 518, 656
 Valinia, A., Henriksen, M. J., Loewenstein, M., Roettiger, K., Mushotzky, R. F., & Madejski, G. 1999, *ApJ*, 515, 42

第4章 参考論文(博士論文)

4.1 Isobe, Naoki: Ph. D. thesis

X-ray Probing into Energetics Associated with
Astrophysical Jets from Active Galactic Nuclei

活動銀河核から噴出する宇宙ジェットにおける
エネルギー分配のX線観測による診断

Naoki Isobe

Department of Physics, Faculty of Science, University of Tokyo
isobe@amalthea.phys.s.u-tokyo.ac.jp

Contents

| | | |
|----------|--|-----------|
| 1 | Introduction | 1 |
| 2 | Review | 5 |
| 2.1 | Astrophysical Jets | 5 |
| 2.1.1 | What is the nature of the astrophysical jets ? | 5 |
| 2.1.2 | Issues on the astrophysical jets | 7 |
| 2.2 | Radio Galaxies | 8 |
| 2.2.1 | Classification of the active galactic nuclei | 8 |
| 2.2.2 | Properties of the radio galaxies | 8 |
| 2.3 | Radiation from Radio Lobes and Hot Spots | 12 |
| 2.3.1 | Synchrotron radiation | 12 |
| 2.3.2 | Inverse Compton scattering | 14 |
| 2.3.3 | Parameters determined from observations | 17 |
| 2.4 | Previous and Recent X-ray Observations | 23 |
| 2.4.1 | The CMB boosted X-rays from radio lobes | 23 |
| 2.4.2 | The AIC X-rays from radio lobes | 26 |
| 2.4.3 | Hot spots | 28 |
| 2.4.4 | Jets | 29 |
| 2.4.5 | Blazars | 30 |
| 3 | Instruments | 33 |
| 3.1 | The <i>ASCA</i> Satellite | 33 |
| 3.1.1 | X-ray Telescope (XRT) | 35 |
| 3.1.2 | Solid-State Imaging Spectrometer (SIS) | 38 |
| 3.1.3 | Gas Imaging Spectrometer (GIS) | 41 |
| 3.2 | <i>Chandra</i> X-ray Observatory | 46 |
| 3.2.1 | High Resolution Mirror Assembly (HRMA) | 47 |
| 3.2.2 | Advanced CCD Imaging Spectrometer (ACIS) | 50 |

| | | |
|----------|--|-----------|
| 4 | CONTENTS | |
| 3.2.3 | The ACIS performance | 53 |
| 3.2.4 | The ACIS data | 54 |
| 4 | Observations | 59 |
| 4.1 | <i>ASCA</i> Observations | 59 |
| 4.2 | <i>Chandra</i> Observations | 62 |
| 4.2.1 | Radio lobes | 62 |
| 4.2.2 | Hot spots | 64 |
| 4.2.3 | Log of <i>Chandra</i> observations | 66 |
| 5 | Analysis and Results of <i>ASCA</i> Observations | 69 |
| 5.1 | Data Reduction | 69 |
| 5.2 | NGC 612 | 70 |
| 5.2.1 | The X-ray image | 70 |
| 5.2.2 | The X-ray spectrum of the host galaxy | 73 |
| 5.2.3 | The X-ray spectrum of the lobes | 75 |
| 5.3 | 4C 73.08 | 77 |
| 5.3.1 | The X-ray image | 77 |
| 5.3.2 | The X-ray spectrum of the east lobe | 80 |
| 5.3.3 | The X-ray spectrum around the host galaxy | 81 |
| 6 | Analysis and Results of <i>Chandra</i> Observations | 85 |
| 6.1 | Data Reduction | 85 |
| 6.1.1 | Data reduction | 85 |
| 6.1.2 | Background rejection | 85 |
| 6.2 | 3C 452 | 86 |
| 6.2.1 | The X-ray image | 86 |
| 6.2.2 | The X-ray spectrum of the lobes | 91 |
| 6.2.3 | The X-ray spectrum of the nucleus | 94 |
| 6.3 | Pictor A | 96 |
| 6.3.1 | The X-ray image | 96 |
| 6.3.2 | The X-ray spectrum of the west lobe | 98 |
| 6.3.3 | The X-ray spectrum of the nucleus | 100 |
| 6.4 | Hot Spots | 102 |
| 6.4.1 | The west hot spot of Pictor A | 102 |
| 6.4.2 | Cygnus A | 102 |
| 6.4.3 | 3C 123 | 104 |

CONTENTS

5

7 Discussion

107

7.1 Energetics in Radio Lobes 107

7.1.1 Multi frequency spectra 107

7.1.2 Candidates for seed photons 107

7.1.3 Energy densities of electrons and magnetic fields 110

7.1.4 Uncertainties in the calculation 115

7.2 Kinetic Power of the Jets 119

7.2.1 Relation between the lobe energetics and the activities of the nuclei 119

7.2.2 Kinetic power of the jets 119

7.2.3 Comparison with the blazar jets 122

7.2.4 Electron dominance in the lobes 124

7.3 Spatial Distributions of Electrons and Magnetic Fields 125

7.4 Energetics in Radio Hot Spots 128

7.4.1 Multi frequency spectra 128

7.4.2 Energy densities of electrons and magnetic fields 129

7.4.3 Comparison with the blazar jets 132

8 Conclusion

135

42

List of Figures

- 43
- 2.1 The radio images of astrophysical jets. The left panel shows the radio structure of the jets of NGC 6251 on various scales (Bridle and Perler 1984). At a redshift $z = 0.025$ of NGC 6251, 1 arcmin corresponds to ~ 28 kpc. The total length of the jet exceeds 200 kpc. The right panel shows the 22 GHz radio image of the jet of 3C 345 (Zensus et al. 1995) on a scale very close to the nucleus. In this panel, 1 milliarcsec correspond to 5 pc ($\sim 1.5 \times 10^{19}$ cm). The transverse motion of the blob C4 is “superluminal”, or $3 \sim 10$ times the light speed. 6
- 2.2 The unified picture of the AGNs. 8
- 2.3 A schematic drawing which shows the typical radio structure of radio galaxies. 9
- 2.4 The radio spectrum of the radio galaxy 3C 452. The data are from Laing and Peacock (1980), Kuhr et al. (1979), and Jägers (1987). 10
- 2.5 The 10.6 GHz VLA image of the radio galaxy 4C 73.08 (Klein et al. 1994). (left) The total intensity map. The vectors represent the orientation of magnetic fields, and their length are proportional to the polarized intensity. (right) The linearly polarized intensity map. The vectors again represent the orientation of magnetic fields, but their length are proportional to the fractional polarization. 11
- 2.6 The archetype of FR I and FR II subclasses. The left and right panel shows the 5 GHz radio images obtained with the VLA of the FR I radio galaxy Hydra A (3C 218, Taylor et al. 1990) and the FR II radio galaxy Cygnus A (3C 405, Perlay et al. 1984), respectively. 11
- 2.7 The dimensionless function $F(x)$, describing the synchrotron power spectrum. 13
- 2.8 The geometry of scattering in the observer’s frame K and in the electron rest frame K' . The electron moves toward x axis in the K frame, which corresponds to x' axis in the K' frame. 15
- 2.9 The function $G(\alpha)$ 19
- 2.10 A comparison between u_{IR} and u_{CMB} . The IR luminosity of the nucleus and the redshift are assumed to be $L_{\text{IR}} = 10^{46}$ erg s^{-1} and $z \sim 0$, respectively. 20
- 2.11 SR and SSC spectra in various parameters calculated from the SSC code provided by Dr. Kataoka (Kataoka et al. 1999). The solid lines in each panel show the SR and SSC spectra, with $B = 100 \mu\text{G}$, $N_0 = 0.1$, $\gamma_1 = 10^2$, $\gamma_2 = 10^5$, $p = 2.5$, and $R = 10^{21}$ cm. The panels (a), (b), and (c) show their dependences on B , N_0 , and R , respectively. 22
- 2.12 The 0.7-10 keV X-ray image of Fornax A obtained with the *ASCA* GIS (color; Kaneda et al. 1995). The X-rays from the host galaxy NGC 1316 are masked. The larger circles indicate the GIS field of view of individual observations, and the smaller circle indicates the integration region of the X-ray spectra. The 1.4 GHz radio contours from Ekers et al. (1983) are overlaid. 24
- 2.13 The X-ray spectrum of the west lobe of Fornax A, integrated over a circular region with a radius of 7.25 arcmin centered on the X-ray brightness peak shown in Figure ?? (Tashiro et al. 2001). The intrinsic and cosmic backgrounds were subtracted. 24
- 2.14 Radial X-ray (0.7-10 keV) and radio (1.4 GHz) surface brightness distributions around the X-ray centroid in the west lobe of Fornax A (Tashiro et al. 2001). The larger radius of X-ray profile is thought to be instrumental, and the radius of the radio profile is regarded as the lobe radius. 25
- 2.15 (left) The 1.5–3.0 keV IC X-ray image of lobes of Centaurus B (color). The contribution from its nucleus is subtracted. The 843 MHz radio contour from McAdam et al. (1991) is overlaid. (right) The map u_m/u_e in the lobes of Centaurus B. The dotted region is masked in analysis due to low statistics. From Tashiro et al. (1998) 26
- 2.16 The 0.1–2 keV X-ray image of 3C 295 obtained with the *Chandra* ACIS in which the AGN component is negligible (Brunetti et al. 2001). Contribution from a cluster of galaxies surrounding 3C 295 is subtracted, although the X-rays from the hot spot are included. The 8.4 GHz VLA map is overlaid with contours. At the redshift of $z = 0.461$ for 3C 295, the plate scale is ~ 4.6 kpc/arcsec. 27
- 2.17 X-ray images of Cygnus A. The left panel shows X-ray contours obtained with the *ROSAT* HRI, overlaid on the 327 MHz VLA color image (Harris et al. 1994). The right panel shows the gray-scale X-ray image obtained with the *Chandra* ACIS (Wilson et al. 2000). 28

| | | |
|------|---|----|
| 2.18 | The multi frequency features of the jet in 3C 273 (Marshall et al. 2001). (left) The first panel shows a 1.647 GHz radio image, the second one shows a optical image obtained with Hubble Space Telescope, and the third one shows the <i>Chandra</i> X-ray image. The optical contours are overlaid on the X-ray image. The nucleus of 3C 273 locates ~ 12 arcsec toward the upper direction in this figure. (right) The optical and X-ray brightness profiles projected onto the axis of 3C 273 jet. At a redshift $z = 0.158$ of 3C 273, 1 arcsec corresponds to 2.4 kpc. | 30 |
| 2.19 | The multifrequency spectrum of the γ -ray blazar Mkn 421 (Inoue and Takahara 1996). The solid lines represent the model predictions. The best fit parameters are also shown. | 31 |
| 2.20 | Distributions of magnetic fields and Lorentz factors of electrons in blazars, plotted against the peak frequencies of the SR components (Kubo 1996). | 31 |
| 3.1 | Schematic drawing of the <i>ASCA</i> satellite. | 34 |
| 3.2 | Configuration of the XRT and focal-plane instruments onboard <i>ASCA</i> | 34 |
| 3.3 | configuration of the Walter type I optics. | 35 |
| 3.4 | The effective area of the <i>ASCA</i> XRT (four units summed up). The left panel shows the energy dependence of the XRT effective area, compared with those of <i>Einstein</i> and <i>ROSAT</i> . The right panel show its dependence on the incident angle. | 37 |
| 3.5 | The XRT + GIS image of a representative X-ray point source, Cygnus X-1. Contours are drawn to logarithmic scales with levels shown at the top of this figure. The circle indicate the field of view of the GIS. | 37 |
| 3.6 | The cross section of one SIS sensor. | 38 |
| 3.7 | The definition and examples of event grade. | 40 |
| 3.8 | A cross sectional view of the GIS sensor. | 42 |
| 3.9 | A schematic view showing the X-ray detection principle of the GIS. | 43 |
| 3.10 | Integrated spectrum of night-earth observations which characterize the NXB of the GIS, together with those of cosmic X-ray background and of the day-earth observations. The Ar-K line is due to atmospheric fluorescence, Cu-K line is instrumental, while O-, Ne-, Mg-, and Si-K lines originate in solar coronae. | 44 |
| 3.11 | A schematic drawing of the <i>Chandra</i> X-ray Observatory. The grating systems inside the optical bench are also shown. | 46 |
| 3.12 | Schematic drawing which shows the structure of the <i>Chandra</i> HRMA. | 48 |

| | | |
|------|---|----|
| 3.13 | The effective area of <i>Chandra</i> HRMA. (left) The energy dependence of the effective area of the HRMA, compared with that of the <i>ASCA</i> XRT. The contributions of individual shells are also shown. (right) The angular dependence of the HRMA effective area, in 1.49, 4.51, 6.40 and 8.63 keV. Effective areas are normalized to the on-axis values for each energy. | 48 |
| 3.14 | The simulated HRMA plus HRC images of a point source in representative energies. Contours are logarithmically spaced and the innermost one in each panel is at 90 % of the peak brightness. | 49 |
| 3.15 | A picture which shows the structure of the ACIS. | 51 |
| 3.16 | Schematic drawing of the ACIS focal plane which is seen from the HRMA. Definitions of the terminology and the coordinate systems are shown in the bottom. The nominal aimpoints on I3 and S3 are denoted with 'x' and '+', respectively. Various ways to refer to a particular CCD are indicated; array plus number, chip serial number, and ACIS chip number. | 52 |
| 3.17 | The energy resolution of ACIS S2 (FI chip) and S3 (BI chip) as a function of row number for particular energies. These data are taken in orbit at an operating temperature of -120°C | 53 |
| 3.18 | The encircled power of the HRMA plus ACIS at 1 keV, as a function of a radius. These data were obtained in the ACIS observation of a point source PG 1643-706, during in-flight calibrations. | 53 |
| 3.19 | (left) The quantum efficiency of the ACIS, convolved with the transmission of the optical blocking filter. (right) The ACIS/HRMA effective area . The dashed or dotted lines are for the BI CCDs, and the solid lines for the FI CCDs. The data for the FI CCDs are taken from the rows nearest the frame store region. | 54 |
| 3.20 | Examples of various ACIS subarrays. Only the data in the shaded regions are read out. The cross ('+') in each panel indicates the nominal aimpoint. | 55 |
| 3.21 | The schematic drawing for the definition of the event grade. The grade is determined by the sum of the numbers for pixels above the threshold. A single pixel event is grade 0 | 56 |
| 3.22 | The trailed image for a bright X-ray source. | 58 |

| | | |
|------|--|----|
| 3.23 | The effect of pileup for the 1.49 KeV Al-K α line as a function of a source intensity. These spectra are taken during the pre-flight HRMA/ACIS calibration, and shown as a function of pulse-height. Single-photon events corresponding to the Al-K α line are concentrated near a pulse height of \sim 380 channel, and events with 2 photons have a pulse height twice that of the single-photon events. | 58 |
| 4.1 | The radio images of our targets for <i>ASCA</i> observations. The left panel shows the 843 MHz VLA contours of NGC 612 (Jones and McAdam 1992). The right panel shows the 608 MHz VLA color image of 4C 73.08 (Leahy, Bridle, and Strom 1996). The 'x' and star in each panel represent the positions of their host galaxies. | 61 |
| 4.2 | The radio images of the targets for our <i>Chandra</i> observations. (<i>left</i>) The 1.4 GHz VLA image of 3C 452 (Leahy, Bridle, and Strom 1996). (<i>right</i>) The 1.4 GHz VLA contours of 3C 427.1 (Neff et al. 1995). | 63 |
| 4.3 | The 1.4 GHz VLA image of Pictor A (Perley et al. 1997). | 64 |
| 4.4 | The VLA images of radio galaxies which we have selected for the analysis of hot spots. The right panel shows the 4.5 GHz image of Cygnus A (Perley et al. 1984) and the left panel shows the 1.4 GHz image of 3C 123 (Leahy, Bridle, and Strom 1996). | 65 |
| 5.1 | The 0.7 – 10 keV raw X-ray image of NGC 612, shown to the entire field of view of the GIS. The smaller circle indicates the region in which the spectrum of the lobes (including the nucleus) is accumulated, and the larger one indicates the background integration region. | 70 |
| 5.2 | The X-ray images around NGC 612 in 0.7 – 3 keV (<i>left</i>) and 3 – 10 keV (<i>right</i>), smoothed with a Gaussian kernel of $\sigma = 1$ arcmin. The 843 MHz radio contours (Jones and McAdam 1992) are overlaid on both images. The red crosses represent the optical position of the host galaxy of NGC 612. The regions, where the linear surface brightness profiles were extracted, are indicated as X and Y | 71 |

| | | |
|-----|--|----|
| 5.3 | The background subtracted linear profiles around the X-ray peak in 0.7 – 3 keV (upper) and 3 – 10 keV (lower). (<i>left</i>) The profiles accumulated along a band parallel to the lobe axis (i.e. the X direction), with the left corresponding to east in the sky (toward left in Figure ??). (<i>right</i>) The profiles perpendicular to the lobe axis (i.e. the Y direction), with the left in these two panels corresponding to south in the sky (toward bottom in Figure ??). The histograms in individual panels represent the projected PSF of the XRT plus the GIS. The observed profiles and the PSF are normalized to each other by their peak counts. | 72 |
| 5.4 | (<i>left</i>) The background subtracted GIS spectrum of the host galaxy of NGC 612. The histogram shows the best-fit RS (green) plus PL (red) model. (<i>right</i>) The confidence contours of the absorption column density and the spectral index for the hard component determined by the RS plus PL (red) model. Contours represent 68% (black), 90% (red), and 99% (green) confidence levels. | 73 |
| 5.5 | The background subtracted GIS spectrum, derived from a circular region with a radius of 5 arcmin, centered on NGC 612. The histograms in the left panel represent the the best-fit RS (green) plus PL (red) model for the host galaxy of NGC 612. The histograms in the right panel represent the best-fit spectrum, after introducing an additional power law component (blue). | 76 |
| 5.6 | The 0.7 – 10 keV X-ray image of 4C 73.08, shown to the entire GIS field of view. The circles indicated as N , L , and B are the regions over which the spectra of the host galaxy, the east lobe, and the background are integrated, respectively. | 77 |
| 5.7 | The X-ray images around 4C 73.08 in (<i>left</i>) 0.7 – 3 keV and (<i>right</i>) 4 – 10 keV, smoothed with a Gaussian of $\sigma = 1$ arcmin. The 608 MHz VLA contours (Jones and McAdam 1992) are overlaid on both images. The star represents the position of the host galaxy of 4C 73.08. | 78 |
| 5.8 | The linear profiles around 4C 73.08 in (a) 608 MHz, (b) 0.7 – 3 keV, and (c) 4 – 10 keV, with the right and left corresponding to the direction indicated as "E" and "W" in Figure ??, respectively. The histogram in the panel (c) represents the projected PSF of the GIS in 4 – 10 keV. The observed profile and the PSF are normalized to each other by their peak counts. | 79 |

- 5.9 (*left*) The background subtracted GIS spectrum of the east lobe of 4C 73.08. The histogram shows the best-fit PL model modified with a free absorption. (*right*) The confidence contours of the absorption column density and the spectral index. 81
- 5.10 The background subtracted GIS spectrum accumulated around the host galaxy of 4C 73.08. The histograms in the left panel shows the best-fit double PL model determined with all the spectral parameters left free. The histograms in the right panel shows the best-fit RS (green) plus PL (red) model, with the parameters for the hard component fixed at the values determined above 4 keV. 82
- 5.11 (*left*) The X-ray spectrum around the host galaxy of 4C 73.08 above 4 keV. The histogram shows the best-fit heavily absorbed PL model. (*right*) The confidence contours for the absorption column density and the spectral index. 83
- 6.1 The raw 0.3 – 7 keV ACIS image of 3C 452. Only the data obtained with ACIS-S3 are displayed. The image is binned into 4×4 pixels, and hence the angular resolution of the image is 2 arcsec. The rectangular region is expanded to Figure ?? 86
- 6.2 The 0.3 – 7 keV image around 3C 452, smoothed with a two dimensional Gaussian kernel of $\sigma = 4$ arcsec (8 ACIS pixels). The 1.4 GHz VLA contours are overlaid (Leahy, Bridle, and Strom 1996). The red cross represents the optical position of the host galaxy of 3C 452. The linear surface brightness profiles are extracted between the two solid lines for the directions parallel to the radio structure and between the two dashed lines for the perpendicular direction. 87
- 6.3 The linear profiles of the ACIS background in 0.3 – 7 keV, which are extracted from the point source removed black sky data base (Markevitch 2001). The data shown by black points are integrated over the same detector area as for the profile along the radio axis. The total exposure of this background data is ~ 136 ksec. 88
- 6.4 The linear profile along the major radio axis of 3C 452, in (a) 1.4 GHz , (b) 0.3 – 1.5 keV, and (c) 1.5 – 7.0 keV. The projected positions of some apparent X-ray point sources are indicated as blue arrows in panel (b). The data points for the nucleus at position 0 are too high to be included in this figure. 89

- 6.5 The linear profile in the direction perpendicular to the major radio axis of 3C 452, in (a) 1.4 GHz , (b) 0.3 – 1.5 keV, and (c) 1.5 – 7.0 keV. The projected positions of some apparent X-ray point sources are indicated as blue arrows in panel (b). 90
- 6.6 The linear profiles of the hardness ratio parallel (*left*) and perpendicular (*right*) to the radio structure. Arrows are written in the same way as in Figures ?? and ??. 90
- 6.7 The integration region for the data (red) and the background (black) spectra. 91
- 6.8 A comparison between the raw (red) and the background (black) spectra, normalized to their integration areas. 91
- 6.9 The background subtracted ACIS spectrum of the lobes of 3C 452. The histogram in the left panel shows the single PL model and those in the left panel represents the best-fit PL (blue) plus RS (green) model. 92
- 6.10 The confidence contours of the absorption column density N_{H} and the spectral index α for the PL plus RS model. 93
- 6.11 The background subtracted ACIS spectrum of the nucleus of 3C 452 in 0.5 – 10 keV energy range. 94
- 6.12 The background subtracted ACIS spectrum of the nucleus of 3C 452, above 4 keV. The histogram in the left panel shows a prediction by the single PL model, and that in the right panel a prediction by the best-fit PL plus Gaussian model 95
- 6.13 The confidence contours of the absorption column density and the spectral index α 96
- 6.14 The 0.3 – 7 keV raw ACIS image of Pictor A. Only the data obtained with ACIS 6 and 7 in the observation of ID = 346 are displayed. The image is binned into 4×4 pixels, and hence the angular resolution of the image is 2 arcsec. The straight line running from north-east to south-west is the trailed image of the nucleus. 97
- 6.15 The 0.3 – 7 keV ACIS image around Pictor A, smoothed with a 2-dimensional Gaussian function of $\sigma = 4$ arcsec. (*left*) The X-ray color image. (*right*) The X-ray contours overlaid on the VLA 1.465 GHz gray scale image (Perlay et al, 1997). 97
- 6.16 The integration region for the spectrum (red circle). The data inside black boxes or circles are rejected. 98
- 6.17 A comparison between the raw (red) and the background (black) spectra, normalized to their exposure. 98

| | | |
|------|--|-----|
| 6.18 | The background subtracted ACIS spectrum of the west lobe of Pictor A. The histograms in the left panel show the best-fit PL plus RS model. The right panel shows the confidence contours of the absorption column density N_{H} and the spectral index α | 99 |
| 6.19 | (left) The background subtracted ACIS spectrum of the nucleus of Pictor A. The histogram shows the best-fit PL model. (right) The confidence contours of the absorption column density and the spectral index α | 101 |
| 6.20 | The background subtracted ACIS spectrum of the west hot spot of Pictor A. The histogram shows the best-fit PL model. | 102 |
| 6.21 | The 0.3 – 7 keV raw ACIS image of Cygnus A, binned by 2×2 ACIS pixels. Only the data obtained in the observation of ID = 360 are displayed. | 103 |
| 6.22 | The background subtracted ACIS spectra of the hot spots A (left) and D (right). The histograms in both panels show the best-fit PL model to the individual spectra. | 104 |
| 6.23 | The 0.3 – 7 keV raw ACIS image of 3C 123. | 104 |
| 6.24 | The background subtracted ACIS spectrum of the east hot spot of 3C 123. The histogram shows the best-fit PL model. | 104 |
| 7.1 | The spectral energy distributions of radio lobes. (a) NGC 612. The radio data are taken from Ekers et al. (1978). (b) 4C 73.08. The radio data are from Mayer (1979), Kuhr et al. (1979), and Saripalli et al. (1996). (c) 3C 452. The radio data are from Laing and Peacock (1980), Kuhr et al. (1979), and Jägers (1987). (d) Pictor A. The radio data are from Perley et al. (1997). As the IC X-ray spectra of the lobes of 3C 452 and Pictor A, only their PL components are shown. | 108 |
| 7.2 | Schematic drawings which show how to estimate the volume of the lobes. | 111 |
| 7.3 | The relation between u_e and u_m in each lobe. The data for the lobes of Fornax A and Centaurus B are from Tashiro et al. (2001) and Tashiro et al. (1998), respectively. Two green dashed lines show u_{CMB} , neglecting the redshift dependence. | 112 |
| 7.4 | The relation between $u_e V$ and $u_m V$ in each lobe. | 114 |
| 7.5 | The polarization structure of Pictor A at 4.9 GHz (Perley et al. 1997) and 3C 452 (Black et al. 1992) as representatives of our targets. The directions of lines show those of the observed electric field vector, and their length are proportional to the degree of polarization. The projected directions of the magnetic fields are normal to the lines. | 116 |
| 7.6 | A simple modeling of a magnetic field localization in the lobes. | 118 |

| | | |
|------|--|-----|
| 7.7 | The ratio $(u_e V)_{\text{true}} / (u_m V)_{\text{true}}$ in the lobes as a function of the volume filling factor, f , of magnetic fields. The two curves specify two representative values for the observed electron-to-field energy density ratio, u_e / u_m | 118 |
| 7.8 | The relation between u_e (red) or u_m (blue) in the radio lobes and the X-ray luminosities, L_X , of their nuclei. The green dashed line shows u_{CMB} , neglecting the redshift dependence. | 120 |
| 7.9 | The total energy of electrons (red) and magnetic fields (blue) in the lobes, plotted as a functions of their nuclear X-ray luminosities. | 120 |
| 7.10 | Kinetic powers of the jets, L_{kin} , as a function of the X-ray luminosity of the nucleus, L_X | 122 |
| 7.11 | The ratio u_e / u_m as a function of the X-ray luminosity of the nucleus. | 125 |
| 7.12 | A simple modeling of a homogeneous distribution of electrons in an ellipsoid, and the corresponding IC X-ray profile projected onto the major axis. | 126 |
| 7.13 | The IC X-ray brightness profile of the lobes of 3C 452 in 0.3 – 7 keV, projected on the major axis. The data are the same as Figure ?? . The histograms represent the model prediction. The blue arrows show the projected positions of the X-ray point sources. | 127 |
| 7.14 | A rough estimation of the magnetic field distribution in 3C 452 along its radio axis. The blue arrows show the projected positions of the X-ray point sources. | 127 |
| 7.15 | The spectral energy distribution of hot spots. (a) The hot spot A of Cygnus A. (b) The hot spot D of Cygnus A. (c) The east hot spot of 3C 123. The red points represent the data of the whole hot spot, and the blue ones represent the data of its secondary component. (d) The west hot spot of Pictor A. The radio data for the two hot spots of Cygnus A are from Carilli et al. (1991), Meisenheimer et al. (1997), and Alexander, Brown & Scott (1984). Those for the east hot spot of 3C 123 are from Looney & Hardcastle (2000), Okayasu et al. (1992), Riley & Pooley (1978), Readhead & Hewish (1974), and Meisenheimer et al. (1997). Those for the west hot spot of Pictor A are from Meisenheimer et al. (1997). The dashed and solid lines in panel (a), (b), and (c) represent the model predictions for the SR and SSC components, respectively, calculated by the numerical code of Kataoka et al. (1999). | 130 |
| 7.16 | A simple picture of the jet and the hot spot. | 133 |

List of Tables

| | | |
|-----|--|-----|
| 2.1 | Parameters of astrophysical jets on various scales (Fukue 1993). | 5 |
| 3.1 | Design parameters of the <i>ASCA</i> XRT | 36 |
| 3.2 | Design parameters and performance of the SIS. | 39 |
| 3.3 | Design parameters and performance of the GIS. | 41 |
| 3.4 | Characteristics of the <i>Chandra</i> HRMA | 47 |
| 3.5 | Characteristics of the ACIS. | 51 |
| 3.6 | The nominal (optimal) frame time in second for standard subarrays of ACIS-S. | 55 |
| 3.7 | The comparison between the ACIS grade and the SIS grade. See Figures ?? and ??. | 56 |
| 4.1 | Radio galaxies observed with <i>ASCA</i> . | 60 |
| 4.2 | Parameters of the radio lobes selected from the <i>ASCA</i> public data. | 61 |
| 4.3 | The <i>ASCA</i> observation log of radio galaxies for our analysis. | 62 |
| 4.4 | Parameters of the radio lobes observed with <i>Chandra</i> . | 64 |
| 4.5 | Parameters of radio hot spots. | 66 |
| 4.6 | Observational log of our <i>Chandra</i> targets. | 68 |
| 5.1 | Good exposures remained after the standard screening. | 69 |
| 5.2 | The best-fit spectral parameters of the host galaxy of NGC 612, determined from the double-component models. | 74 |
| 5.3 | The best-fit spectral parameters for the excess diffuse component. | 75 |
| 5.4 | The best-fit spectral parameters of the east lobe of 4C 73.08. | 80 |
| 5.5 | The best-fit parameters for the spectrum around the host galaxy of 4C 73.08 | 83 |
| 6.1 | A summary of the data and the background in representative energy bands. | 91 |
| 6.2 | The best-fit spectral parameters of the lobes of 3C 452. | 93 |
| 6.3 | The best-fit spectral parameters of the nucleus of 3C 452, determined by the spectrum above 4 keV. | 95 |
| 6.4 | A summary of the data and background in representative energy bands. | 99 |
| 6.5 | The best-fit spectral parameters of the west lobe of Pictor A. | 99 |
| 6.6 | The best-fit spectral parameters of the nucleus of Pictor A. | 101 |
| 6.7 | A summary of the spectral parameters of the hot spots. | 105 |
| 7.1 | A summary of spectral parameters of the SR radio emission and the IC X-rays from individual lobes. | 109 |
| 7.2 | A comparison of energy densities of possible seed photon sources in radio lobes. | 110 |
| 7.3 | A summary of the physical parameters, spatially averaged over each lobe. | 113 |
| 7.4 | Total electron and magnetic field energy in the lobes. | 114 |
| 7.5 | Kinetic power of the jets, required to maintain the energies in the lobes. | 121 |
| 7.6 | Kinetic power of jets of representative blazars. | 123 |
| 7.7 | A summary of radio and X-ray spectral parameters of individual hot spots. | 129 |
| 7.8 | A summary of the physical parameters in hot spots | 131 |
| 7.9 | Typical parameters in the hot spots and blazars. | 132 |

Chapter 1

Introduction

Astrophysical jets are a pair of highly collimated plasma flows which are ejected from a central source with relativistic velocities in the opposite directions to each other. The jet phenomena are found all over the universe on various scales, such as in active galactic nuclei, Galactic binaries involving collapsed stars, young stellar objects, and so forth. However, the mechanism of jets formation is still one of the unsolved important issues in astrophysics. In particular, many pieces of evidence indicate that the jet phenomena generally involve magnetic fields, but it is still unclear how essential they are in the formation of astrophysical jets. In order to better understand the jet phenomena, it is vitally needed to quantitatively measure the relative dominance of particle energy and magnetic-field energy, associated with the jets.

Lobes of radio galaxies provide one of the ideal laboratories to investigate the issue, because their radio emission is of no doubt produced via synchrotron process, i.e., an interplay between the relativistic particles and magnetic fields. The former carries over the bulk kinetic energy of the jets, presumably randomized by jet-terminal shocks, while the latter is also thought to be supplied by the jets. However, what can be measured by the radio observations is only the product $u_e u_m$, where u_e and u_m are energy densities of relativistic particles and magnetic field, respectively. In order to individually evaluate them, it is conventional to assume an equipartition between particle and magnetic energies, or a minimum energy condition.

Relativistic particles in radio lobes can produce X-rays or γ -rays by inverse-Compton (IC) scattering off some soft seed photons. The IC X-ray observations yield the product $u_e u_{\text{soft}}$, where u_{soft} is the energy density of the soft seed photons. Therefore, if u_{soft} is already known, a comparison of the synchrotron radio flux and the IC X-ray flux allows us to independently determine u_e and u_m , without invoking the minimum energy or equipartition assumptions. Especially, soft photons in the lobes of radio galaxies are

usually dominated by the cosmic microwave background (CMB), of which the energy density $u_{\text{CMB}} = 4.1 \times 10^{-13} (1+z)^4 \text{ erg cm}^{-3}$ (where z is the cosmological redshift of the objects) is accurately known. Therefore in such cases, the determination of u_e and u_m is possible with a high precision, as has long been anticipated (Haris and Grindlay 1979).

The IC X-ray emission had received increasing attention from astrophysicists in 1960s. The CMB-boosted X-rays were once thought to be a possible origin of extended hard X-rays from a number of clusters of galaxies detected by *Uhuru* survey (Gursky et al., 1972), which are now recognized as thermal emission from hot cluster gas (Serlemitsos et al., 1977). Fetlen & Morrison (1966) attempted to explain the cosmic X-ray background radiation (CXB) as IC X-rays of electrons in the Galactic halo scattering off the CMB or the starlight in the Galaxy, although the predicted X-ray flux was more than an order of magnitude lower than the observed CXB flux. Because u_{CMB} is proportional to $(1+z)^4$, and hence the IC X-rays from lobes of distant radio galaxies or quasars may partially contribute to the observed CXB.

Although the search for the IC X-rays from the lobes of radio galaxies has long been unsuccessful due to their faintness, at least Feigelson et al. (1995) and Kaneda et al. (1995) have independently succeeded in detecting the diffuse IC X-rays from the lobes of the radio galaxy Fornax A (NGC 1316), using *ROSAT* and *ASCA* respectively. This has motivated us to observe other radio lobes, and to achieve subsequent detections of the IC X-rays from Centaurus B (Tashiro et al. 1998) and NGC 612 (Tashiro et al. 1999). In lobes of Fornax A of which the nucleus has already become inactive (Iyomoto et al. 1997), an equipartition between electrons and magnetic field is almost realized (Kaneda et al. 1995, Tashiro et al. 2001). On the other hand, a particle dominance is found in Centaurus B hosting an active nucleus. These results suggest that u_e tend to dominate u_m , particularly when the nucleus is active.

Recently, using the *Chandra* X-ray Observatory which has an unprecedented angular resolution, non-thermal X-rays has been detected from hot spots which is thought to be a shock front at the jet terminal, in a number of radio galaxies. These X-rays are interpreted to arise via synchrotron-self-Compton (SSC) process, where synchrotron radio emission itself provides seed soft photons. In 3C 295 (Harris et al. 2000), 3C 123 (Hardcastle et al. 2001), and Cygnus A (Wilson et al. 2000), an equipartition between u_e and u_m is almost achieved, while in Pictor A (Wilson et al. 2001) the magnetic field strength is by an order-of-magnitude lower than the equipartition field. However, these results is thought to be subject to uncertainties in u_{soft} associated with unresolved structures of the hot spots, especially their volumes.

In this thesis, we intend to develop our knowledge on the jet/lobe energetics, by

studying the IC X-rays from a number of radio lobes. We put a particular emphasis on the relations between the activity of the nucleus and u_e or u_m in the radio lobes. The IC X-rays from radio lobes are intrinsically diffuse and faint emission, and can be identified by its spatial association with the radio lobes, and by a featureless hard power-law spectrum with the same slope as the synchrotron radio spectrum. The Gas Imaging Spectrometer (GIS) onboard *ASCA* is one of the ideal instruments for lobes with the size larger than ~ 5 arcmin, because it can perform an imaging spectroscopy with a high-sensitivity, utilizing its low and stable background level, a reasonable field of view, and a reasonable angular resolution (~ 3 arcmin) over a wide energy band. However, the angular resolution of the GIS is not high enough to resolve smaller and hence more distant lobes, from their nucleus. The *Chandra* X-ray Observatory, with an angular resolution of ~ 0.5 arcsec, is the best instrument to detect the IC X-rays from such compact lobes.

In Chapter 2, we briefly review the X-ray emission mechanism in radio lobes and previous observations of them. The instruments onboard *ASCA* and *Chandra* are described in Chapter 3. The log of observations is presented in Chapter 4. The results of *ASCA* and *Chandra* data analysis are shown in Chapter 5 and 6, respectively. We summarize and discuss the obtained results in Chapter 7, using multi frequency spectral information, and conclude in Chapter 8.

Throughout this thesis, we assume the Hubble constant and the deceleration parameter to be $H_0 = 75 \text{ km s}^{-1} \text{ Mpc}^{-1}$ and $q_0 = 0.5$, respectively.

Chapter 2

Review

2.1 Astrophysical Jets

2.1.1 What is the nature of the astrophysical jets ?

From gravitational centers of various kinds of celestial objects, highly collimated twin flows of plasma, which are thought to consist of relativistic particles and magnetic fields, are often ejected in the opposite directions with relativistic velocities. This phenomenon is usually called "astrophysical jets". The astrophysical jets are observed all over the universe on a variety of scales, such as in active galactic nuclei (AGN) which are thought to be super massive black holes locate in the centers of external galaxies, in Galactic black hole, neutron star or white dwarf binaries, and in young stellar objects. We show the characteristic parameters of various astrophysical jets in Table 2.1.

The concept of astrophysical jets has originally been developed through observations of active galaxies, including in particular radio galaxies and quasars. For the first time in

Table 2.1: Parameters of astrophysical jets on various scales (Fukue 1993).

| | AGN jets | | Galactic jets | |
|----------------|---------------------------|------------------------------|-------------------------------|------------------------------|
| | Size | pc - Mpc | 100 AU - 100 pc | 0.1 - 1 pc |
| Velocity | $\lesssim c$ | $0.26c - 0.92c$ | $\sim 5000 \text{ km s}^{-1}$ | $10 - 150 \text{ km s}^{-1}$ |
| Age | $\sim 10^6 \text{ year}$ | $\sim 10^3 \text{ year}$ | | $\sim 10^4 \text{ year}$ |
| Collimation | $\sim 1^\circ$ | $\sim 1^\circ$ | | $\sim 10^\circ$ |
| Central Source | super massive black holes | black holes neutron stars | white dwarfs | young stellar objects |

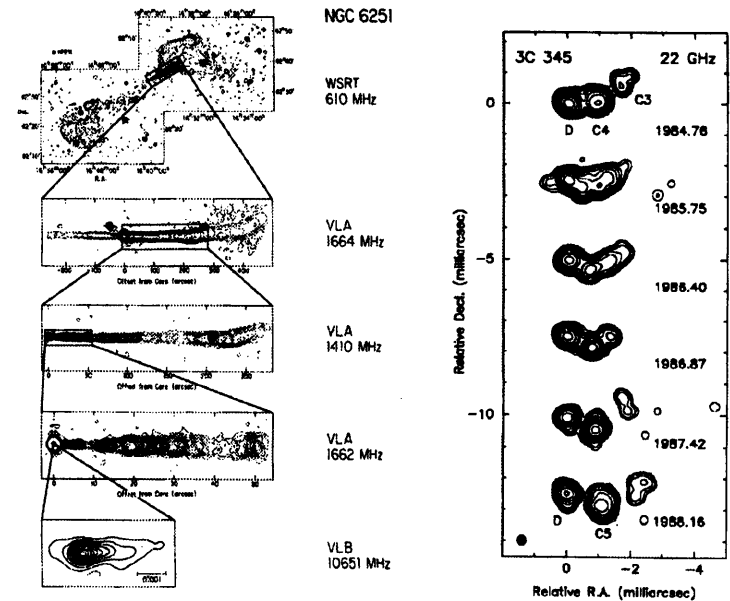


Figure 2.1: The radio images of astrophysical jets. The left panel shows the radio structure of the jets of NGC 6251 on various scales (Bridle and Perler 1984). At a redshift $z = 0.025$ of NGC 6251, 1 arcmin corresponds to ~ 28 kpc. The total length of the jet exceeds 200 kpc. The right panel shows the 22 GHz radio image of the jet of 3C 345 (Zensus et al. 1995) on a scale very close to the nucleus. In this panel, 1 milliarcsec correspond to 5 pc ($\sim 1.5 \times 10^{19}$ cm). The transverse motion of the blob C4 is "superluminal", or 3 \sim 10 times the light speed.

1918, Curtis (1918) optically discovered the jet structure emanating from the nucleus of M 87. In the 1950s, the advent of radio interferometers has allowed detections of largely extended radio structure, called "lobes", from a number of external galaxies. These galaxies have hence been named "radio galaxies". In the late 1970s, with the development of large scale interferometers such as the Very Large Array (VLA), narrow bridge structures (i.e. radio jets) have been discovered between the radio lobes and the nuclei of the host galaxies.

As an example, we show in the left panel of Figure 2.1 the jet in a radio galaxy NGC 6251 observed with radio interferometers with various angular resolutions. Apparently, the jet is still highly collimated and almost keeps its initial direction after traveling

over ~ 200 kpc. In 1980s, “superluminal motion”, in which the transverse speed of the jet blobs apparently exceeds the speed of light, has successively been detected with the Very Long Base Line Interferometry (VLBI). We show one such example in the right panel of Figure 2.1. The superluminal motion can be explained by a model in which the jet blob move toward the line of sight with a relativistic velocity (Blandford and Kognil 1979).

2.1.2 Issues on the astrophysical jets

It is generally agreed that a considerable fraction of astrophysical jets are produced by mass accretion onto the central source. However, there are yet no clear answers to the question about how to effectively convert the released gravitational energies into the bulk kinetic energies of the jets, and how to highly collimate them over the long distance. Actually, various kinds of models are proposed where the jets are assumed to be driven by gas pressure (e.g. Begelman et al. 1983; Takahara et al. 1989), by radiation pressure (e.g. Icke 1980) or by magnetohydrodynamical forces (e.g. Blandford 1976; Uchida and Shibata 1985; Kudoh et al 1998), but no general consensus has been achieved among them.

We may naturally imagine that the jets are produced, collimated and guided by the magnetic filed lines. However, recently some X-ray observations suggest that the energy density of the relativistic electrons, u_e , dominates that of the magnetic field, u_m (e.g. Inoue and Takahara 1996; Tashiro et al. 1998). Therefore, in order to shed light on the jet formation mechanism, it is of vital importance to measure the relative dominance of u_e and u_m in various parts along the jets.

Independently, whether the jets are composed of electron-proton plasma or electron-positron plasma is another important unsolved issue on the jets. The energy required to drive electron-proton jets into a relativistic velocity is more than three order of magnitude larger than to produce electron-positron jets. In order to investigate the plasma composition of the jets, it is vitally important to probe into energetics associated with them.

2.2 Radio Galaxies

2.2.1 Classification of the active galactic nuclei

Radio Galaxies are a class of AGNs, characterized by their strong radio emission. Then, we make a brief classification of AGNs. The unified picture of AGNs, which are visualized in Figure 2.2, are discussed by Antonucci and Miller (1985), or Antonucci (1993).

The AGNs are usually divided into “radio loud” and “radio quiet” objects, from the point of view of their radio luminosities. About one tenth of the AGNs, including radio galaxies, radio loud quasars and blazars, are radio loud. The radio loud AGNs frequently exhibit the active jet structures emanating from their nuclei. The radio quiet AGNs consist of Seyfert galaxies and radio quiet quasars.

Independently, the AGNs are frequently classified into type I and type II AGNs by their viewing angle from our line of sight. The nuclei of the type I AGNs (i.e. super massive black holes) are observable almost directly from us, although those of the type II objects are usually obscured by the molecular torus from our line of sight.

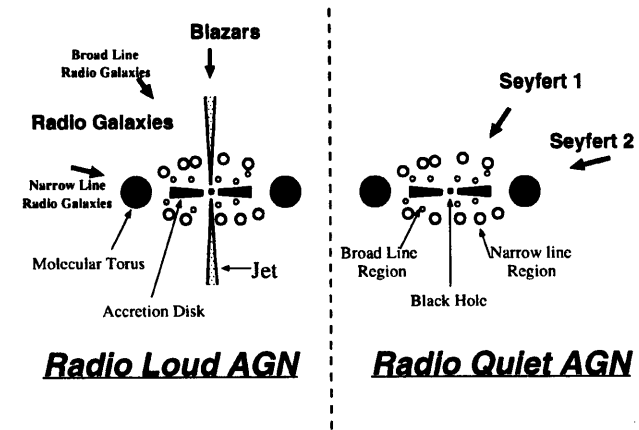


Figure 2.2: The unified picture of the AGNs.

2.2.2 Properties of the radio galaxies

As shown in Figure 2.2, radio galaxies are thought to be observed at a rather large angle relative to their jet axes. Therefore, they are thought to provide one of the best laboratories for studying the jet phenomena.

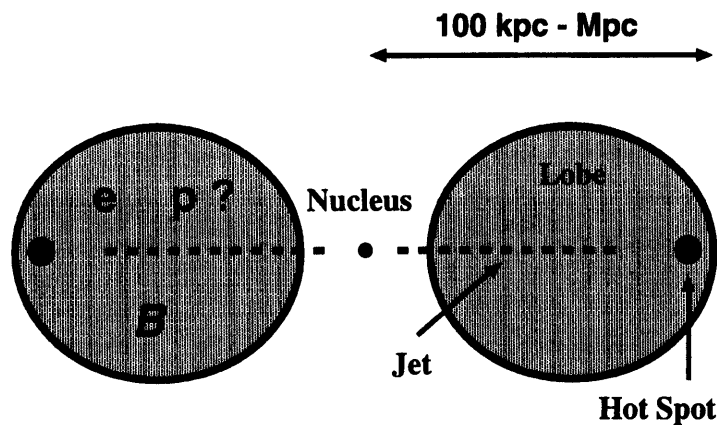


Figure 2.3: A schematic drawing which shows the typical radio structure of radio galaxies.

We show in Figure 2.3 the simplified structure of radio galaxies, observed in the radio frequency. From a nucleus which locates near the center of the radio structure and of which the position coincide with the center of the optical galaxy, a pair of jets are ejected toward opposite directions. The emission from the jets themselves is not necessarily observed, because they move with relativistic velocities, and hence their emissions are strongly beamed toward their direction. Near the end point or on the way of the jets, there exist fairly compact regions of high radio brightness which are called “hot spots”. The hot spots are thought to be working surfaces of the jet-terminal shocks (e.g. Meisenheimer, et al. 1989). Through these shock fronts, the bulk kinetic energy of the jets is randomized, and redistributed among particles which are scattered into radio lobes. The radio lobes are diffuse and low surface brightness radio structure extending in sparse intergalactic space, which is thought to contain time-integrated information of the jet activities.

We show in Figure 2.4 the representative of radio spectra of the radio galaxies. Figure 2.5 represents the map of the total and polarized intensities of the typical radio galaxy. Because of a nonthermal power-law spectral shape and a strong linear polarization, the radio emission from radio galaxies is thought to be of no doubt produced via synchrotron radiation, in which relativistic electrons interact with a magnetic field. Assuming that an equipartition condition is established between electrons and magnetic field in radio lobes, we can estimate that there exist a magnetic field of $B =$ a few $\sim 10\mu\text{G}$ and relativistic electrons with Lorentz factors of at least $\gamma_e = 10^{3-5}$. These relativistic electrons inevitably produce X-ray or γ -ray photons via inverse Compton (IC) scattering off soft seed photons.

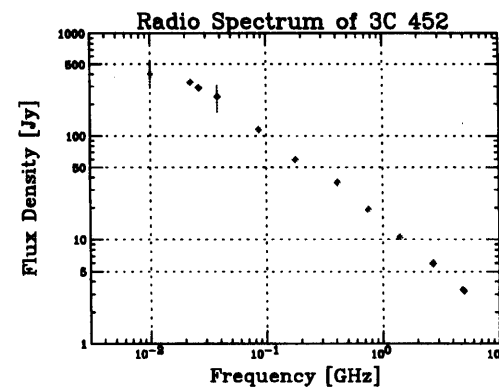


Figure 2.4: The radio spectrum of the radio galaxy 3C 452. The data are from Laing and Peacock (1980), Kuhr et al. (1979), and Jägers (1987).

We discuss these radiation process and the parameters determined by observing them in the next section.

The radio galaxies are usually divided into two sub-classes from the relative positions of hot spots and radio lobes to the central AGN; so-called FR I and FR II (Fanaroff and Riley, 1974) classes. The FR I class is defined as those of which the ratio of the distance between the hot spots (originally the brightest region) on opposite sides to the total extent is lower than 0.5, and the FR II class is defined as the reverse. We show the archetypes of each class in Figure 2.6. As a whole in radio observations, the FR II sources are more lobe dominant and more luminous than the FR I radio galaxies (Fanaroff and Riley 1974; Urry and Padovani 1995). In the X-ray band, the nuclei of the FR II is more active than the FR I nuclei (Hardcastle and Worrall 1999, Matusmoto et al. 2001).

As shown in Figure 2.2, when the jet direction is close to our line of sight, an AGN is observed as blazars. Because of the relativistic beaming effect, electromagnetic radiation from blazars is dominated by nonthermal emission from relativistic electrons in the jet. Their intensities are rapidly and highly variable in every observable frequencies, and then, the radiation sites of blazars are thought to be located relatively near the base of the jets ($\sim 10^{17-18}$ cm from their nuclei; e.g. Kataoka 2000). In the unified picture of blazars, their multi-frequency spectra exhibit two pronounced components; the low frequency synchrotron radiation and the high frequency inverse Compton component.

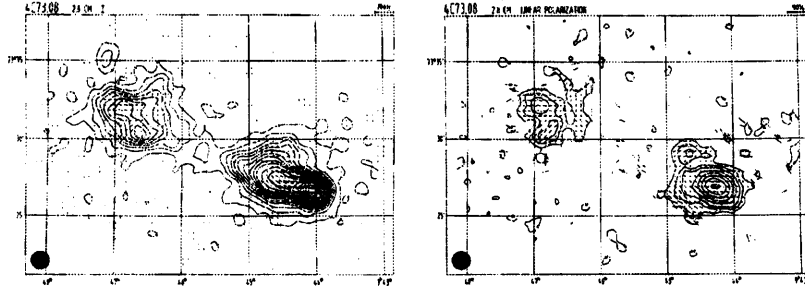


Figure 2.5: The 10.6 GHz VLA image of the radio galaxy 4C 73.08 (Klein et al. 1994). (left) The total intensity map. The vectors represent the orientation of magnetic fields, and their length are proportional to the polarized intensity. (right) The linearly polarized intensity map. The vectors again represent the orientation of magnetic fields, but their length are proportional to the fractional polarization.

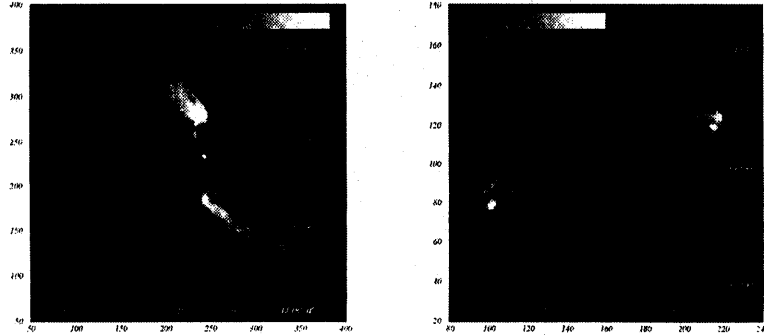


Figure 2.6: The archetype of FR I and FR II subclasses. The left and right panel shows the 5 GHz radio images obtained with the VLA of the FR I radio galaxy Hydra A (3C 218, Taylor et al. 1990) and the FR II radio galaxy Cygnus A (3C 405, Perlay et al. 1984), respectively.

2.3 Radiation from Radio Lobes and Hot Spots

In this section, we discuss two important emission mechanisms from relativistic particles; the synchrotron radiation and the inverse Compton scattering. The detection of both emissions from radio lobes or hot spots provide important tools for probing into the energetics there. Basic properties of each radiation mechanism are discussed in detail, e.g. by Blumenthal and Gould (1970) and by Rybicki and Lightman (1974). We first follow their results. Next, we discuss practical methods to evaluate the energetics in radio galaxies. In the following, we consider the emission only from relativistic electrons.

2.3.1 Synchrotron radiation

Relativistic electrons gyrating in a magnetic field B will radiate. This radiation, forming a continuum spectrum, is known as *synchrotron radiation* (SR). The SR power per unit frequency radiated from a single electron with a Lorentz factor of γ is given as

$$P_{SR}(\nu, \gamma) = \frac{\sqrt{3}e^3\beta^2 B \sin\phi}{mc^2} F\left(\frac{\nu}{\nu_c}\right) \quad (2.1)$$

where c is the speed of light, β is the speed of the electron normalized by c , m and e are the mass and charge of an electron, respectively, and ϕ is the angle between the magnetic field and electron velocity (pitch angle). The dimensionless function $F(x)$, which is shown in Figure 2.7, is defined as

$$F(x) \equiv x \int_x^\infty K_{\frac{5}{3}}(\xi) d\xi \quad (2.2)$$

where $K_{\frac{5}{3}}(\xi)$ is the modified Bessel function of $\frac{5}{3}$ order, and ν_c is given as

$$\nu_c = \frac{3\gamma^2 e B \sin\phi}{4\pi mc} \simeq 4.2 \times 10^6 \gamma^2 B \sin\phi \quad (2.3)$$

is the critical frequency. Since the peak of $F(x)$ is around $x = 0.29$, the SR spectrum peaks at

$$\nu_p = 0.29 \nu_c = 120 \left(\frac{\gamma}{10^4}\right)^2 \left(\frac{B}{1 \mu\text{G}}\right) \sin\phi \text{ MHz} \quad (2.4)$$

By integrating equation (2.1) over all frequencies, we obtain the total SR power from one electron as

$$P_{SR} = 2 \sigma_T c \gamma^2 \beta^2 \sin^2\phi u_m, \quad (2.5)$$

where $\sigma_T = 8\pi e^4/3m^2c^4$ is the Thomson cross section, and $u_m = B^2/8\pi$ is the energy density of the magnetic field. For an isotropically distributed electrons with γ , it is necessary to average equation (2.5) over the pitch angle. Using the relation $\langle \sin^2\phi \rangle = \frac{1}{4\pi} \int \sin^2\phi d\Omega = \frac{2}{3}$, we obtain the averaged SR power as

$$P_{SR} = \frac{4}{3} \sigma_T c \gamma^2 \beta^2 u_m. \quad (2.6)$$

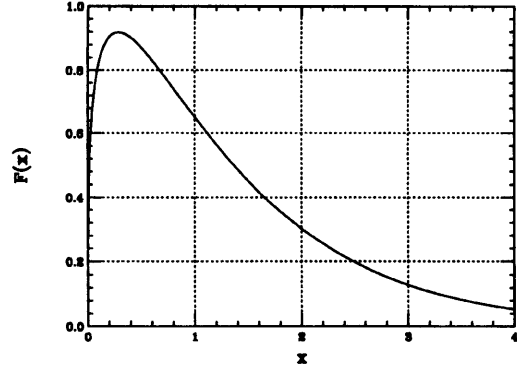


Figure 2.7: The dimensionless function $F(x)$, describing the synchrotron power spectrum.

Thus, P_{SR} is proportional to u_m . The electron loses half of its energy by the SR emission in a characteristic time scale as

$$T_{\text{SR}} = \frac{3mc}{4\sigma_T u_m} \gamma^{-1}. \quad (2.7)$$

Practically, we want to obtain the SR spectrum from a population of relativistic electrons which have a power-law energy distribution in $\gamma \gg 1$. We describe the number density of electrons with Lorentz factors between γ and $\gamma + d\gamma$ as

$$N(\gamma)d\gamma = N_0\gamma^{-p}d\gamma, \quad (2.8)$$

where N_0 is a normalization, and p is a positive constant called spectral index. Usually, this spectrum is valid only in a limited energy range, $\gamma_1 < \gamma < \gamma_2$. Using equations (2.1) and (2.8), we can obtain the SR power spectrum per unit volume $P_{\text{SR}}(\nu)$ as

$$\begin{aligned} P_{\text{SR}}(\nu) &= \int_{\gamma_1}^{\gamma_2} P_{\text{SR}}(\nu, \gamma) N(\gamma) d\gamma \\ &= \frac{\sqrt{3}e^3 B N_0 \sin \phi}{2mc^2} \left(\frac{4\pi mc}{3eB \sin \phi} \nu \right)^{-\frac{p-1}{2}} \int_{x_2}^{x_1} F(x) x^{\frac{p-3}{2}} dx, \end{aligned} \quad (2.9)$$

where we change the variable of integration to $x \equiv \nu/\nu_c$, with x_1 and x_2 corresponding to γ_1 and γ_2 , respectively. We here approximate $\beta \simeq 1$ because $\gamma \gg 1$. Assuming the electron power-law spectrum is valid over a sufficiently wide energy band, we can approximate $x_2 \simeq 0$ and $x_1 \simeq \infty$, and obtain

$$P_{\text{SR}}(\nu) = \frac{\sqrt{3}e^3 B N_0 \sin \phi}{mc^2(p+1)} \Gamma\left(\frac{p}{4} + \frac{19}{12}\right) \Gamma\left(\frac{p}{4} - \frac{1}{12}\right) \left(\frac{2\pi mc}{3eB \sin \phi} \nu \right)^{-\frac{p-1}{2}} \quad (2.10)$$

where we use the formula

$$\int_0^\infty x^s F(x) dx = \frac{2^{s+1}}{s+2} \Gamma\left(\frac{s}{2} + \frac{7}{3}\right) \Gamma\left(\frac{s}{2} + \frac{2}{3}\right). \quad (2.11)$$

Thus, we find that the SR spectrum from power-law electrons also has a power-law shape, and its spectral energy index α_{SR} is related to the electron index as

$$\alpha_{\text{SR}} = \frac{p-1}{2}. \quad (2.12)$$

2.3.2 Inverse Compton scattering

Free electrons at rest can scatter off incoming photons. This is known as *Compton scattering*. Using the conservation of energy and momentum, we can relate the energy of the incident photon, ϵ , to that of the scatter photon, ϵ_1 , as

$$\epsilon_1 = \frac{\epsilon}{1 + \frac{\epsilon}{mc^2}(1 - \cos \theta)} \quad (2.13)$$

where θ is the angle between the directions of the incident and scattered photons. For low energy photons, $\epsilon \ll mc^2$, the scattering becomes approximately elastic ($\epsilon \approx \epsilon_1$). This is known as *Thomson scattering*. In the Thomson limit, the differential and total cross sections are written as

$$\begin{aligned} \frac{d\sigma_T}{d\Omega} &= \frac{1}{2} r_0^2 (1 + \cos^2 \theta) \\ \sigma_T &= \frac{8\pi}{3} r_0^2 \end{aligned} \quad (2.14)$$

where $r_0 \equiv e^2/mc^2$ is the classical electron radius. For high energy photons, $\epsilon \gg mc^2$, because of a quantum effect, the scattering becomes less efficient and the scattering cross section is described by the Klein-Nishina formula,

$$\frac{d\sigma}{d\Omega} = \frac{r_0^2}{2} \frac{\epsilon_1^2}{\epsilon^2} \left(\frac{\epsilon}{\epsilon_1} + \frac{\epsilon_1}{\epsilon} - \sin^2 \theta \right). \quad (2.15)$$

In the limit of $\epsilon_1 \approx \epsilon$, equation (2.15) reduces to the Thomson cross section.

When the electron moves with a sufficient kinetic energy compared to that of the photon, net energy may be transferred from the electron to the photon in contrast to equation (2.13). This process is usually called *inverse Compton (IC) scattering*. We show in Figure 2.8 a scattering event seen from the observer's frame K and from the electron rest frame K'. Quantities observed in the K' frame are denoted with prime ('), and those in the K frame are without prime. In the following, we show basic properties of the IC process, assuming $\epsilon' \ll mc^2$ in the K' frame (i.e. $\gamma\epsilon \ll mc^2$ in the K frame), and hence that the scattering takes place in the Thomson limit. This assumption is almost valid

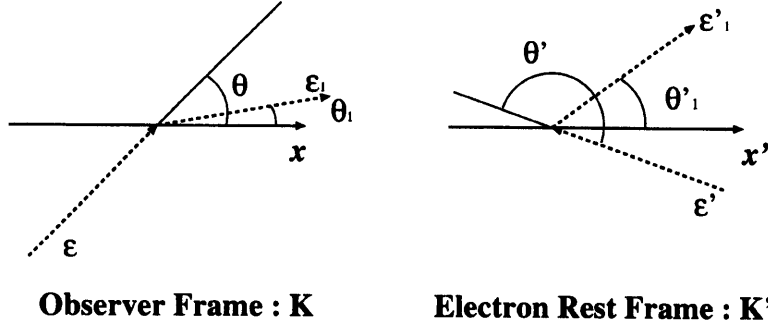


Figure 2.8: The geometry of scattering in the observer's frame K and in the electron rest frame K'. The electron moves toward x axis in the K frame, which corresponds to x' axis in the K' frame.

in various kinds of astrophysical phenomena. From the Lorentz transformation (or the Doppler shift), we obtain

$$\begin{aligned}\epsilon' &= \epsilon\gamma(1 - \beta \cos \theta) \\ \epsilon_1 &= \epsilon'_1\gamma(1 + \beta \cos \theta'_1)\end{aligned}\quad (2.16)$$

where θ and θ'_1 are the angle between the direction of motion of the electron and that of the photon before and after scattering, respectively. Equation (2.13) holds in the K' frame, and we obtain

$$\begin{aligned}\epsilon'_1 &\approx \epsilon' \left[1 - \frac{\epsilon'}{mc^2} (1 - \cos \Theta) \right] \\ \cos \Theta &= \cos \theta'_1 \cos \theta' + \sin \theta' \sin \theta'_1 \cos(\phi' - \phi'_1)\end{aligned}\quad (2.17)$$

where ϕ' and ϕ'_1 are the azimuthal angles of the incident and scattered photon, respectively in the K' frame. For relativistic electrons with $\gamma^2 \gg \epsilon/mc^2$, we can approximate

$$\epsilon : \epsilon' : \epsilon'_1 = 1 : \gamma : \gamma^2 \quad (2.18)$$

since θ and θ'_1 become typically order of $\pi/2$. Thus, the energy of incident soft photon is boosted by a factor of γ^2 in the IC scattering.

We next want to derive average IC power from an isotropic distribution of relativistic electrons ($\gamma \gg 1$) scattering off isotropically distributed incident seed photons. We let $n(\epsilon)$ and $n'(\epsilon')$ be the number densities of seed photons per unit photon energy in the K and K' frame, respectively. The scattered power per electron in the K' frame is given by

$$\frac{dE'}{dt'} = c\sigma_T \int \epsilon'_1 n'(\epsilon') d\epsilon' \quad (2.19)$$

We need to note that $nd\epsilon/\epsilon$ and dE/dt are both Lorentz invariant. Using equation (2.16) and neglecting the energy change in the K' frame (i.e. $\epsilon' \approx \epsilon'_1$) we obtain the total scattered power in the K frame as

$$\begin{aligned}\frac{dE}{dt} &= c\sigma_T \int \epsilon'_1 n'(\epsilon') d\epsilon' \\ &= c\sigma_T \gamma^2 \int (1 - \beta \cos \theta)^2 \epsilon n(\epsilon) d\epsilon\end{aligned}\quad (2.20)$$

Averaging this over the scattering angle, we obtain

$$\frac{dE}{dt} = c\sigma_T \gamma^2 \left(1 + \frac{1}{3}\beta^2\right) u_{\text{soft}} \quad (2.21)$$

in which

$$u_{\text{soft}} = \int \epsilon n(\epsilon) d\epsilon \quad (2.22)$$

is the energy density of the incident seed photons. Thus, the net power transferred from electrons into photons in the IC scattering is calculated as

$$P_{\text{IC}} = \frac{dE}{dt} - c\sigma_T u_{\text{soft}} = \frac{4}{3} \sigma_T c \gamma^2 \beta^2 u_{\text{soft}} \quad (2.23)$$

where $c\sigma_T u_{\text{soft}}$ is the power of incident photon. The individual electron loses half of its energy by the IC radiation in a characteristic time scale as

$$T_{\text{IC}} = \frac{3mc}{4\sigma_T u_{\text{soft}}} \gamma^{-1} \quad (2.24)$$

Comparing equation (2.23) with equation (2.6), we have a general relation of basic importance,

$$\frac{P_{\text{SR}}}{P_{\text{IC}}} = \frac{u_m}{u_{\text{soft}}} \quad (2.25)$$

Equation (2.23) also means that the representative energy ϵ_{IC} of an IC photon scattered by a relativistic electron of Lorentz factor γ is given as

$$\epsilon_{\text{IC}} = \frac{4}{3} \gamma^2 \epsilon, \quad (2.26)$$

where we approximate $\beta \approx 1$.

We want also to derive the IC spectrum. We again assume that electrons and photons have isotropic distributions and that the Thomson limit holds in the K' frame. Let N be the number density of electrons moving with γ , and F_0 be the incident photon number of energy ϵ per unit area, per unit solid angle, per unit time. In this case, we can write the emission function of IC scattering as

$$j_{\text{IC}}(\epsilon_1) = \frac{3N\sigma_T F_0}{4\gamma^2 \epsilon} f(x) \quad (2.27)$$

$$x \equiv \frac{\epsilon_1}{4\gamma^2\epsilon} , \quad (2.28)$$

where $f(x)$ is approximately described, for relativistic electrons of $\gamma \gg 1$, as

$$f(x) = 2x \ln x + x + 1 - 2x^2 . \quad (2.29)$$

We can finally calculate the IC power spectrum from a power-law distribution of electrons [equation (2.8)] scattering off an arbitrary initial photon spectrum. This can be done by expressing F_0 with the number density $n(\epsilon)$ of incident photons and replacing N with the electron distribution $N(\gamma)d\gamma$. Integrating over the incident photon spectrum and over the electron energy in the same way for the SR spectrum, we obtain the IC spectrum,

$$\begin{aligned} P_{IC}(\epsilon_1) &= 4\pi\epsilon_1 j_{IC}(\epsilon_1) \\ &= \frac{3}{4} c\sigma_T N_0 \int d\epsilon \frac{\epsilon_1}{\epsilon} n(\epsilon) \int_{\gamma_1}^{\gamma_2} d\gamma \gamma^{-p-2} f(x) \\ &= 3c\sigma_T N_0 2^{p-2} \epsilon_1^{-\frac{p-1}{2}} \int d\epsilon n(\epsilon) \epsilon^{\frac{p-1}{2}} \int_{x_2}^{x_1} dx x^{\frac{p-1}{2}} f(x) \end{aligned} \quad (2.30)$$

and the IC spectral index,

$$\alpha_{IC} = \frac{p-1}{2} . \quad (2.31)$$

Thus, the IC index is identical to the SR index described in equation (2.12).

2.3.3 Parameters determined from observations

As easily recognized from equation (2.10), what can be measured from observing the synchrotron radio spectrum alone is α_{SR} and the product $N_0 B^{1+\alpha_{SR}}$. In order to evaluate the magnetic field strength B , it has therefore been traditional to assume a minimum energy condition in which the product $u_e u_m$ is minimized, or an equipartition between u_e and u_m , where u_e is the energy density of the electrons given as

$$u_e = mc^2 \int_{\gamma_1}^{\gamma_2} \gamma N(\gamma) d\gamma . \quad (2.32)$$

For example, in the minimum energy condition, we can estimate B from observed quantities as (Miley et al. 1980),

$$B_{ME} = 5.69 \times 10^{-5} \left[\frac{1+k}{f} (1+z)^{3+\alpha} \frac{1}{\theta_x \theta_y s \sin^{\frac{1}{2}} \psi} \frac{S_{SR}}{\nu_{SR}^{\alpha_{SR}}} \frac{\nu_2^{-\alpha_{SR}+\frac{1}{2}} - \nu_1^{-\alpha_{SR}+\frac{1}{2}}}{-\alpha_{SR} + \frac{1}{2}} \right]^{\frac{2}{3}} \quad (2.33)$$

where z is a redshift of the object, θ_x and θ_y are angular diameters in orthogonal directions in arcsec, f is a filling factor, k is a ratio of energy of heavily particles to those of electrons,

s is a path length through the object in kpc, ν_1 and ν_2 are the lower and upper limits of the observed frequency in GHz, S_{SR} is a flux density at ν_{SR} (GHz) in Jy ($= 10^{-23}$ erg s^{-1} cm^{-2} Hz^{-1}), and ψ is an angle between the averaged magnetic field and the line of sight.

It is apparent from equation (2.25) that, if we can observe both the SR radio emission and IC X-ray emission from a single object, we can separately determine B and u_e , on condition that we can evaluate u_{soft} accurately. In lobes or hot spots of radio galaxies, several different sources may provide some radiation fields are possible to furnish the seed photons; the cosmic microwave background (CMB) radiation, the SR radio emissions themselves, and infra-red (IR) radiation from the nucleus of the radio galaxy. In the following, we discuss each of these possibilities. As shown in equations (2.12) and (2.31), the indices of the IC X-ray and the radio spectra from the same population of electrons are identical, and hence we simply describe both indices as α .

IC scattering of the cosmic microwave background (CMB)

In radio lobes which are extended on sufficiently large scales, the soft seed photons are usually dominated by the CMB photons of which the energy density is precisely known as

$$u_{CMB} = 4.1 \times 10^{-13} (1+z)^4 \text{ erg } s^{-1} . \quad (2.34)$$

The basic calculation of this process is discussed in Harris & Romanishin (1974), and the redshift dependence of u_{CMB} is properly introduced first by Harris & Grindlay (1979). The characteristic frequency of the CMB is $\nu_{CMB} = 1.6 \times 10^{11} (1+z)$ Hz. Then, using equation (2.26), the characteristic frequency ν_{IC} and energy ϵ_{IC} of the CMB-boosted IC X-ray photon are written as

$$\nu_{IC} = 2.11 \times 10^{17} \left(\frac{\gamma}{10^3} \right)^2 \text{ Hz} \quad (2.35)$$

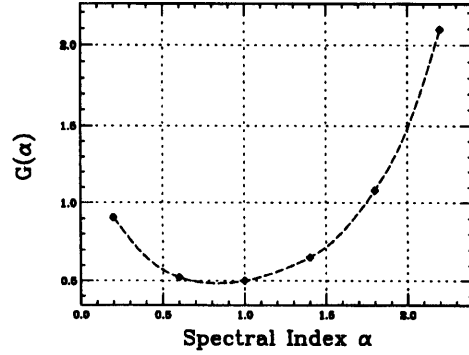
$$\epsilon_{IC} = 8.73 \times 10^{-1} \left(\frac{\gamma}{10^3} \right)^2 \text{ keV} . \quad (2.36)$$

Thus, IC X-ray photons of 1 keV ($= 2.42 \times 10^{17}$ Hz) are typically scattered from electrons of $\gamma \sim 1000$.

The electron spectrum can be related to the SR radio spectrum as

$$N(\gamma_{SR}) = \frac{4\pi D^2 mc^2 C(\alpha) (1+z)^{\frac{1}{2}}}{V} \frac{S_{SR}}{(\nu_{SR} B)^{\frac{1}{2}}} \quad (2.37)$$

where V is the volume of the lobe, D is the luminosity distance at a redshift z , S_{SR} is the flux density in Jy observed at ν_{SR} which are typically radiated from electrons with γ_{SR} . We must relate γ_{SR} to ν_{SR} , by introducing the effect of the cosmological redshift into equation (2.3). Although $C(\alpha)$ is a function of spectral index α , we can approximate

Figure 2.9: The function $G(\alpha)$.

$C(\alpha) \sim 1.15 \times 10^{31}$ in $0.5 < \alpha < 2.0$ with an error of at most 17%. The electron spectrum is also determined by the IC X-ray spectrum as

$$N(\gamma_{IC}) = 2.25 \times 10^{49} \frac{4\pi D^2 mc^2}{G(\alpha)V(1+z)^2} \frac{S_{IC}}{\nu_{IC}^{\frac{1}{2}}} \quad (2.38)$$

where S_{IC} is the IC flux density in Jy at an observed frequency ν_{IC} which correspond to electrons with γ_{IC} by equation (2.36), and $G(\alpha)$ is a function of α as shown in Figure 2.9.

Comparing equations (2.37) and (2.38) and using equation (2.8), we can directly determine the magnetic field B from only observed quantities as

$$B^{\alpha+1} = \frac{(5.05 \times 10^4)^\alpha C(\alpha) G(\alpha) (1+z)^{\alpha+3} S_{SR} \nu_{SR}^\alpha}{1.00 \times 10^{47} S_{IC} \nu_{IC}^\alpha} \quad (2.39)$$

Using equation (2.38), we can also calculate u_e as

$$\begin{aligned} u_e &= mc^2 \int_{\gamma_1}^{\gamma_2} \gamma N(\gamma) d\gamma \\ &= 3.06 \times 10^5 \frac{4\pi D^2 (1.07 \times 10^3)^{2\alpha+1}}{G(\alpha)V(1+z)^2} \frac{1}{1-2\alpha} S_{IC} \left(\frac{\epsilon_{IC}}{1 \text{ keV}} \right)^\alpha (\gamma_2^{1-2\alpha} - \gamma_1^{1-2\alpha}) \\ &\quad \text{erg s}^{-1} \quad (2.40) \end{aligned}$$

IC scattering of infra-red (IR) photons from AGN

As discussed in detail in Brunetti et al. (1997) and Brunetti (2000), radiation from the nucleus may serve as a dominant source of the seed photons, in radio lobes of a small scale, or in an innermost region of radio lobes. The typical quasar spectrum, which is thought

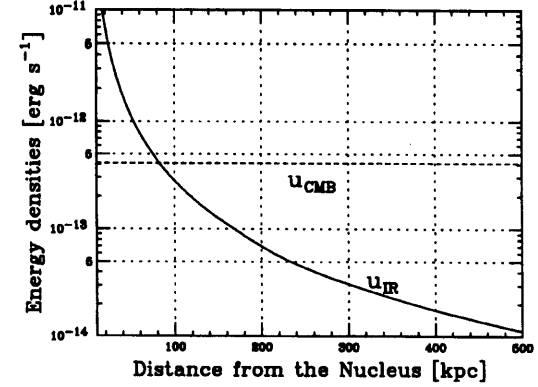


Figure 2.10: A comparison between u_{IR} and u_{CMB} . The IR luminosity of the nucleus and the redshift are assumed to be $L_{IR} = 10^{46}$ erg s $^{-1}$ and $z \sim 0$, respectively.

to apply also to the spectrum of the nucleus of radio galaxies, peaks around the infra-red (IR) band ($\sim 10^{14}$ Hz; Sanders et al. 1989), and hence, these IC X-rays are thought to be boosted by mildly energetic electrons with $\gamma \sim 100$. The synchrotron radiation from these electrons typically falls in a kHz range. Because the observations in this frequency band are very difficult or impossible, measurements of these IC X-rays may be the unique tools to study the energy distribution of low energy electron populations with $\gamma < 1000$.

Figure 2.10 compares u_{CMB} with the energy density of the IR radiation from the nucleus, u_{IR} , as a function of the radius from the nucleus. Assuming the typical spectrum of quasars (Sanders et al. 1989), the IR luminosity of the nucleus is ~ 10 times higher than the X-ray luminosity. Hence, we here adopt an IR luminosity of the nucleus $L_{IR} = 10^{46}$ erg s $^{-1}$, corresponding to the X-ray luminosity of $L_X \sim 10^{45}$ erg s $^{-1}$ which is near the highest end of those of radio galaxies (Sambruna et al. 1999). Since the energy density of the nuclear photons decreases as r^{-2} where r is the distance from the nucleus, u_{IR} increases toward the inner regions of the lobes. Thus the nuclear IR photons become dominant for $r \lesssim 100$ kpc.

When this mechanism works, we expect the far-side lobe to appear more luminous than the near-side one, if the radio galaxy is inclined to the sky plane; Brunetti (2000) called this effect *anisotropic inverse Compton (AIC) scattering*. This is qualitatively recognized as follows. While the IR photons have a bulk momentum from the nucleus toward the lobe, the electrons in radio lobes are thought to be isotropically distributed. This means that there will be many more scattering events when the electrons move toward the nucleus.

As shown in the previous section, a relativistic electron with $\gamma^2 \gg 1$ will scatter off the incoming photon toward a narrow cone about its instantaneous direction. As a result, the IC emission is enhanced toward the nucleus. There is yet another effect enhancing the far-side/near-side anisotropy. In order to produce an IC X-ray photon of a given energy, an electron of a given Lorentz factor γ requires higher-energy seed photons when the electron is moving in the same direction as the incoming photon (i.e., situation in the near-side lobe) than when they make a head-on collision (i.e., situation in the far-side lobe).

Calculation of the AIC X-ray flux, however, is very much subject to uncertainties in evaluating L_{TR} and the geometry of its radiation pattern. In this thesis, we therefore select radio galaxies of which the lobe size is sufficiently large ($\gtrsim 100$ kpc), so that the seed photons are dominated by the CMB and hence the AIC contribution can be neglected.

Synchrotron-self-Compton process

In fairly compact emission regions with a high brightness, such as hot spots of radio galaxies or blazars, the synchrotron photons themselves can be effectively scattered by the same electron population that produces the synchrotron radiation. This process is known as *synchrotron-self-Compton (SSC)* radiation, and is discussed in detail, e.g., by Band & Grindlay (1985).

Practically, we use in this thesis a numerical code kindly provided by Dr. Kataoka (Kataoka et al. 1999). In this code, the relativistic electrons and the magnetic fields are homogeneously distributed in one-zone sphere of radius R . Then, the SR and SSC spectra can be calculated for any given energy distribution of electron. Thus, this code has six input parameters; R , B , N_0 , p , γ_1 , and γ_2 . The scattering is treated in the exact Klein-Nishina limit in this code.

In Figure 2.11, we show typical SSC spectra calculated by the Kataoka's code. In this figure, panel (a) shows dependences on B (i.e., u_m) of the SSC X-ray spectrum together with the SR radio spectrum. As is obvious from equation (2.10), the SR flux F_{SR} is proportional to B^2 (i.e., $\propto u_m$). Because the SR photons serve as the seed photons, the SSC flux F_{SSC} is expected to vary as B^2 . The maximum and minimum frequencies of the SR spectrum increase as $\propto B$, as is expected from equation (2.3). We also show their dependence on N_0 (i.e., u_e) in Figure 2.11 (b). Because F_{SR} is proportional to N_0 , F_{SSC} is proportional to N_0^2 (i.e., u_e^2).

Figure 2.11 (c) shows the dependences of F_{SSC} and F_{SR} on the radius of the emission region R . It is clear from this figure that they scale as $\sim R^3$ (i.e. volume V). This means that an evaluation of the volume can introduce a large uncertainty when we attempt to

determine u_m and u_e from the observed F_{SR} and F_{SSC} . In order to avoid this problem, we must carefully examine radio images obtained with a sufficient angular resolution.

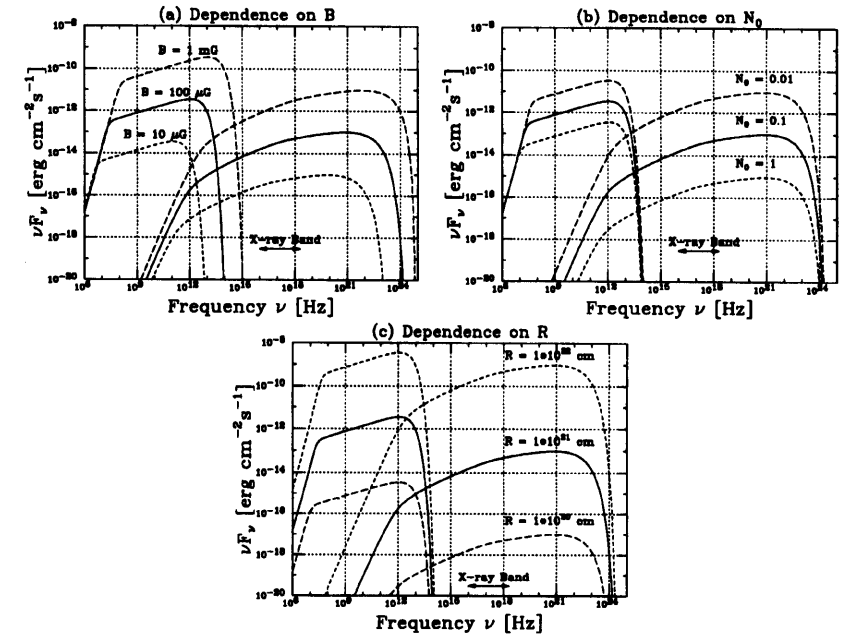


Figure 2.11: SR and SSC spectra in various parameters calculated from the SSC code provided by Dr. Kataoka (Kataoka et al. 1999). The solid lines in each panel show the SR and SSC spectra, with $B = 100 \mu\text{G}$, $N_0 = 0.1$, $\gamma_1 = 10^2$, $\gamma_2 = 10^5$, $p = 2.5$, and $R = 10^{21}$ cm. The panels (a), (b), and (c) show their dependences on B , N_0 , and R , respectively.

2.4 Previous and Recent X-ray Observations

2.4.1 The CMB boosted X-rays from radio lobes

The search for IC X-rays from lobes of radio galaxies have been conducted, but unsuccessful for a long time. This is because the intensities of IC X-rays were under the sensitivities of previous X-ray instrument. Pioneering results were obtained in 1995, independently by Fiegelson et al. and Kaneda et al. They have detected non-thermal X-rays associated with the lobes of a bright southern radio galaxy Fornax A, using *ROSAT* and *ASCA*, respectively. The X-ray image obtained with *ASCA* is shown in Figure 2.12.

In the follow-up *ASCA* observations pointing to the west lobe of Fornax A, which was conducted in 1997, we have confirmed this X-ray emission with a better statistics (Tashiro et al. 2001; N. Isobe being a co-author). We show the X-ray spectrum of the west lobe accumulated from these observations in Figure 2.13. It is well described with a model which consists of three components; a hard power law component, a soft thermal component, and a power law component representing a contaminating faint point source. The derived energy index of the hard component, $\alpha_X = 0.74 \pm 0.26$, is consistent with that of the synchrotron radio emission, $\alpha_R = 0.9 \pm 0.2$, which is determined radio from published radio fluxes over a frequency range of 408 MHz to 2.7 GHz (Cameron 1971; Ekers et al. 1983; Shimmins et al. 1971). Therefore, we have concluded that the hard X-rays are the CMB-boosted IC emission by the synchrotron electrons in the lobes. Comparing the flux of the hard X-ray component and the radio flux, we have obtained spatially averaged values of $u_e = 2.0 \pm 0.5 \text{ erg cm}^{-3}$ and $u_m = 4.3 \pm 0.4 \text{ erg cm}^{-3}$, the latter yielding a magnetic field strength of $B \sim 3 \mu\text{G}$. Thus, the equipartition (or a slightly magnetic dominant) condition is almost achieved.

In order to roughly investigate the spatial distributions of u_e and u_m , we have extracted the X-ray and radio radial brightness profiles centered on the X-ray brightness peak in the west lobe of Fornax A. As shown in Figure 2.14, the X-rays show a center-filled morphology, while a rim-brightened feature is seen in the radio profile. The X-ray profile indicates that the relativistic electrons in the lobe are nearly homogeneously distributed in a sphere-like region of a radius $\sim 75 \text{ kpc}$ (corresponding to 11 arcmin). Therefore, we regard the radio profile as the direct indicator of the distribution of u_m , which has an inner radius of $\sim 27 \text{ kpc}$ (corresponding to 4 arcmin) and an outer radius of 75 kpc. Thus, we find a condition of $u_e > u_m$ in the lobe interior, whereas $u_e < u_m$ in the lobe periphery.

Iyomoto et al. (1997) have examined the X-ray spectrum of NGC 1316, the host galaxy of Fornax A. The spectrum is well described by a sum of a soft thermal emission

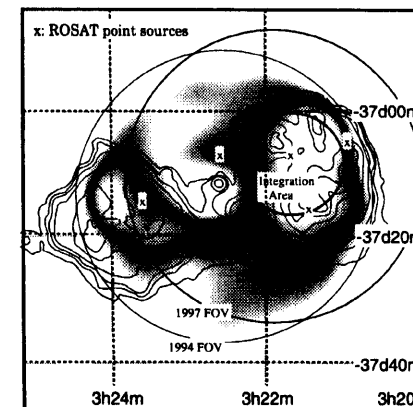


Figure 2.12: The 0.7-10 keV X-ray image of Fornax A obtained with the *ASCA* GIS (color; Kaneda et al. 1995). The X-rays from the host galaxy NGC 1316 are masked. The larger circles indicate the GIS field of view of individual observations, and the smaller circle indicates the integration region of the X-ray spectra. The 1.4 GHz radio contours from Ekers et al. (1983) are overlaid.

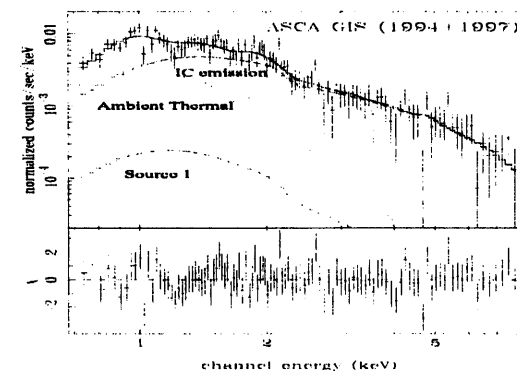


Figure 2.13: The X-ray spectrum of the west lobe of Fornax A, integrated over a circular region with a radius of 7.25 arcmin centered on the X-ray brightness peak shown in Figure 2.12 (Tashiro et al. 2001). The intrinsic and cosmic backgrounds were subtracted.

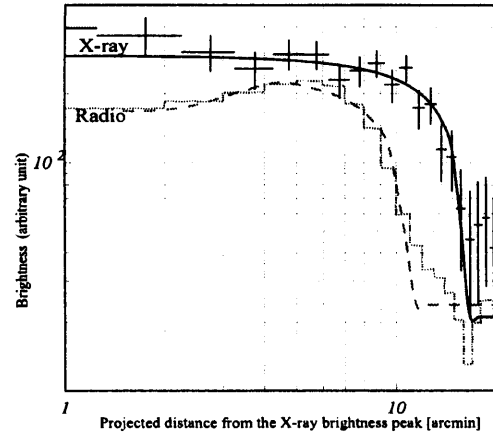


Figure 2.14: Radial X-ray (0.7-10 keV) and radio (1.4 GHz) surface brightness distributions around the X-ray centroid in the west lobe of Fornax A (Tashiro et al. 2001). The larger radius of X-ray profile is thought to be instrumental, and the radius of the radio profile is regarded as the lobe radius.

with $kT \sim 0.8$ keV from the hot interstellar medium, and a hard continuum interpreted as integrated hard X-rays from neutron star binaries in the galaxy; contribution from its AGN is undetectable. This means that the AGN of Fornax A has become already inactive, and its powerful synchrotron lobes are a relic of the past AGN activity. The life time of the synchrotron electrons in the lobes is estimated to be $\sim 10^8$ year using the magnetic field $B \sim 3 \mu\text{G}$. The AGN is thought to have been fading off over this time scale.

Tashiro et al. (1998) have made a subsequent detection of non-thermal diffuse X-rays from the lobes of Centaurus B (PKS 1343-601). We show in Figure 2.15 the X-ray image of Centaurus B obtained with the *ASCA* GIS. The X-ray spectrum integrated over the lobes is well described with power law of $\alpha_X = 0.88 \pm 0.19$, which is consistent with the radio slope $\alpha_R = 0.78$ (Christensen et al. 1997; McAdam 1991). Thus, this became the second case in which the CMB-boosted IC X-ray from radio lobes are detected. From a comparison between the synchrotron flux and the IC flux, Tashiro et al. (1998) have obtained $u_e = 3.8 \pm 1.8 \text{ erg cm}^{-3}$ and $u_m = 24 \pm 9 \text{ erg cm}^{-3}$, and found that u_e dominates u_m ($u_e/u_m = 6.3 \pm 3.8$) in the lobes of Centaurus B. Its nucleus is active, of which the 2–10 keV X-ray luminosity is $L_X = 2.1 \times 10^{42} \text{ erg s}^{-1}$. In the right panel of Figure 2.15, we show the map of the ratio of the radio brightness to the squared X-ray brightness, which

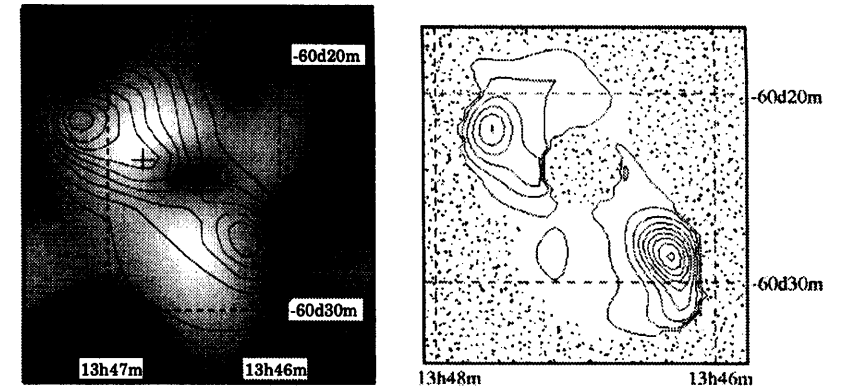


Figure 2.15: (left) The 1.5–3.0 keV IC X-ray image of lobes of Centaurus B (color). The contribution from its nucleus is subtracted. The 843 MHz radio contour from McAdam et al. (1991) is overlaid. (right) The map u_m/u_e in the lobes of Centaurus B. The dotted region is masked in analysis due to low statistics. From Tashiro et al. (1998)

characterizes the map of u_m/u_e . Thus, like the west lobe of Fornax A, the radio lobes of Centaurus B also show the tendency of outward increase in the u_m/u_e ratio.

These results suggest two important features which are thought to be realized in radio lobes. One is that when spatially averaged over radio lobes, the equipartition between particles and magnetic field are not always achieved, and u_e tend to dominate u_m particularly in lobes with an active nucleus. The other is that the u_m/u_e ratio increases from the lobe interior toward the lobe exterior; in other word, that magnetic field is thought to be compressed by particles toward the edge of the lobes.

2.4.2 The AIC X-rays from radio lobes

Through detailed analysis of the X-ray image obtained with the *ROSAT* HRI and the X-ray spectra obtained with the *ASCA* GIS and the *ROSAT* PSPC, Brunetti et al. (1999), have detected diffuse hard X-ray emissions associated with the inner lobes of 3C 219. Its nucleus is very active with the measured 2–10 keV X-ray luminosity is $L_X = 2 \times 10^{44} \text{ erg s}^{-1}$ and the expected 6–100 μm IR luminosity of $L_{\text{IR}} \sim 5 \times 10^{45} \text{ erg s}^{-1}$. They argue that the X-ray morphology and the X-ray spectrum are well reproduced by the AIC process where the IR photon from the nucleus provides seed soft photons. They claim that this is the first direct observational evidence of electrons with $\gamma_e \sim 100$ in radio lobes. They

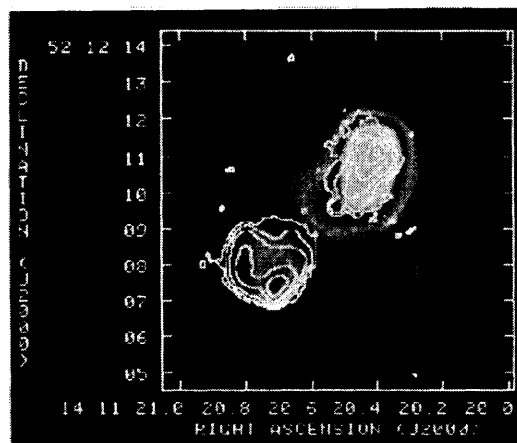


Figure 2.16: The 0.1–2 keV X-ray image of 3C 295 obtained with the *Chandra* ACIS in which the AGN component is negligible (Brunetti et al. 2001). Contribution from a cluster of galaxies surrounding 3C 295 is subtracted, although the X-rays from the hot spot are included. The 8.4 GHz VLA map is overlaid with contours. At the redshift of $z = 0.461$ for 3C 295, the plate scale is ~ 4.6 kpc/arcsec.

also found that the magnetic field strength is $B \sim 3 \mu\text{G}$ and u_e is two order of magnitude higher than u_m . However, the obtained u_m and u_e may be local values specific to the innermost region, rather than representing overall properties of the lobes of 3C 219.

Recently using *Chandra*, Brunetti et al. (2001) have also detected a strong evidence of extended X-rays from the lobes of 3C 295. The X-ray image of 3C 295 obtained with *Chandra* is shown in Figure 2.16. The X-ray morphology is very asymmetrical in which the northern lobe is brighter than the southern one, whereas the radio fluxes of the two lobes are similar. From 3C 295, they also detected a strongly absorbed X-ray nucleus with the 0.1–10 keV luminosity of $L_X \sim 6 \times 10^{44} \text{erg s}^{-1}$, from which the IR luminosity is estimated to be $L_{\text{IR}} \sim 10^{46} \text{erg s}^{-1}$, assuming the typical spectrum of radio loud quasar (Sanders et al. 1989). They argue that this X-ray lobe asymmetry can be best accounted for by the AIC scattering of a photons from its hidden nucleus. Indeed, using $L_{\text{IR}} \sim 10^{46} \text{erg s}^{-1}$, the energy density of the nuclear photons is almost an order of magnitude higher than that of the CMB in its lobes (see Figure 2.10), because the size of 3C 295 is very small (~ 30 kpc). They have evaluated that the magnetic field in the lobes is $B = 35 \sim 100 \mu\text{G}$, which is slightly lower than the equipartition value of $B_{\text{eq}} = 120 \mu\text{G}$. They also found that the power law electron spectrum defined by the radio spectrum

can be extrapolated down to $\gamma_e < 100$ (The radio frequency 8.4GHz correspond to the electrons with $\gamma_e \sim 4000$, assuming $B_{\text{eq}} = 120 \mu\text{G}$). However, the derived magnetic field strength is obviously quite subject to the uncertainties in the modeling of L_{IR} and the radiation pattern of the nucleus.

2.4.3 Hot spots

X-ray emission from radio hot spots of radio galaxies is first detected by Harris et al. (1994), using the *ROSAT* HRI. As shown in the left panel of Figure 2.17, they have detected diffuse X-rays from the two bright radio hot spots in the powerful radio galaxy Cygnus A, together with its nucleus and a diffuse component surrounding them; the latter apparently contaminates to hot spots. The obtained X-ray fluxes of individual hot spots are both almost consistent with those predicted by the SSC model with minimum energy magnetic fields, $B_{\text{me}} \sim 250 \mu\text{G}$, determined from the radio spectra. Harris et al. (1998) have also detected X-rays associated with a northern radio/optical hot spot of the radio galaxy 3C 390.3, also using the *ROSAT* HRI. Its X-ray flux can be almost explained by an extrapolation from the radio-to-optical synchrotron spectrum. Assuming $B_{\text{me}} \sim 44 \mu\text{G}$ of the hot spot, these X-rays are thought to be radiated from relativistic electrons of $\gamma \sim 10^8$. However, no spectral capability and an insufficient spatial resolution of the *ROSAT* HRI have left the true features of these hot spot uncertain.

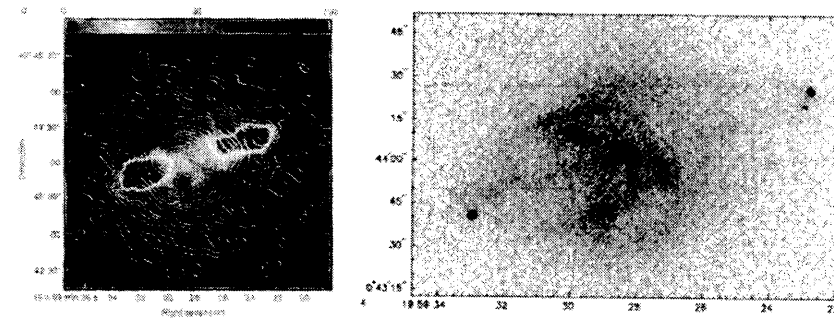


Figure 2.17: X-ray images of Cygnus A. The left panel shows X-ray contours obtained with the *ROSAT* HRI, overlaid on the 327 MHz VLA color image (Harris et al. 1994). The right panel shows the gray-scale X-ray image obtained with the *Chandra* ACIS (Wilson et al. 2000).

Recently, one of these results is confirmed with the advent of the *Chandra* X-ray Observatory which is characterized by an excellent angular resolution and a good spectral resolution. The X-ray image of Cygnus A obtained by Wilson et al. (2000) using the *Chandra* ACIS is shown in the right panel of Figure 2.17. Two radio hot spots are clearly resolved from the nucleus and the diffuse emission. Their X-ray spectra are well described by a single power-law model with the spectral index of $\alpha_X = 0.8 \pm 0.2$, modified by an absorption with our Galaxy. Moreover, their overall multi-frequency spectra are well reproduced by the SSC model. The derived magnetic fields, $B \sim 150 \mu\text{G}$, are slightly lower than B_{me} .

Using the *Chandra* ACIS, X-ray emission from hot spots of a number of radio galaxies have successively detected; these include 3C 295 (Harris et al. 1999), 3C 123 (Hardcastle et al. 2000) and Pictor A (Wilson et al. 2001). The X-ray spectra of 3C 295 and 3C 123 are well described by the SSC model together with the radio synchrotron spectra. The derived magnetic field B of these hot spots are slightly lower than B_{me} . On the other hand, the observed X-ray spectrum of the west hot spot of Pictor A, of which the index $\alpha_X \sim 1.1$ is slightly different from the radio one $\alpha_{\text{SR}} \sim 0.74$, can not be explained solely by SR emission nor by SSC component.

2.4.4 Jets

The left panel of Figure 2.18 shows the X-ray image of a kpc-scale jet in a powerful quasar 3C 273 obtained with the *Chandra*, together with its radio and optical ones (Marshall et al. 2001). The overall shape of the jet is similar in the optical and X-ray bands, and some optically bright regions called “knots” are clearly detected in X-ray image. However, as shown in the right panel of Figure 2.18, the X-ray emission seems to fade out along the jet, while the optical knots have similar brightness. The X-ray spectra of these knots can be naturally explained by a simple SR emission. Especially for the brightest X-ray knot (A1 in 2.18), the radio-to-optical SR power-law spectrum can be extrapolated up to the *Chandra* bandpass, without no break over nearly nine orders of magnitude in frequency. Assuming $B_{\text{me}} = 80 \mu\text{G}$, the electron spectrum extends up to at least $\gamma \sim 4 \times 10^7$.

Recently, *Chandra* has successively uncover the X-ray features of kpc-scale jets, in a number of radio galaxies and quasars; such as Centaurus A (Kraft et al. 2000), PKS 0637-752 (e.g., Schwartz et al. 2000, Chartas et al. 2000), Pictor A (Wilson et al. 2001), 3C 371 (Pesce et al. 2001), M 87 (Marshall et al. 2001), and 3C 66B (Hardcastle et al. 2001). The X-ray spectra of these jets, except for PKS 0637-752, can be as a whole explained by the SR emission. Thus, electrons are thought to be accelerated typically to $\gamma \sim 10^7$ in these jets. However, their true magnetic fields can not be determined from these X-ray

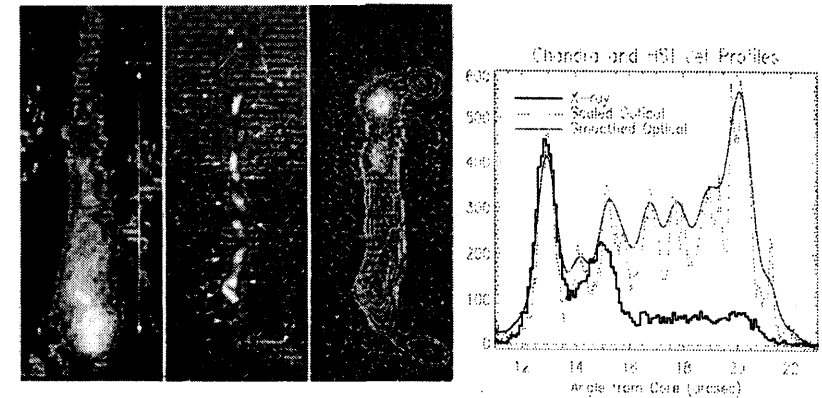


Figure 2.18: The multi frequency features of the jet in 3C 273 (Marshall et al. 2001). (left) The first panel shows a 1.647 GHz radio image, the second one shows a optical image obtained with Hubble Space Telescope, and the third one shows the *Chandra* X-ray image. The optical contours are overlaid on the X-ray image. The nucleus of 3C 273 locates ~ 12 arcsec toward the upper direction in this figure. (right) The optical and X-ray brightness profiles projected onto the axis of 3C 273 jet. At a redshift $z = 0.158$ of 3C 273, 1 arcsec corresponds to 2.4 kpc.

observations.

The X-ray spectrum of the brightest knot in the 100 kpc-scale jet of PKS 0637-752 is difficult to explain by the SR emission from the same electron population which is responsible for the radio-to-optical continuum. Although it may be reproduced by the SSC model, the required magnetic field becomes $B \sim 6 \mu\text{G}$ which is about 50 times lower than $B_{\text{me}} \sim 320 \mu\text{G}$ (Schwartz et al. 2000). Tavecchio et al. (2000) have proposed that if the knot moves with a relativistic velocity, these X-rays are produced through IC scattering off the CMB photons. Because of relativistic beaming, u_{CMB} seen is enhanced by a factor of Γ^2 in the co-moving frame of the knot, where Γ is a bulk Lorents factor of the knot (e.g. Dermer & Schlickeiser 1994). In this model, the X-ray spectrum can be almost explained, assuming B_{me} and $\Gamma \sim 10$.

2.4.5 Blazars

As already mentioned, the overall spectra of blazars are dominated by nonthermal radiations from electrons which exist in the inner parts of relativistic jet pointing close to our line of sight. This makes blazars one of ideal targets for the the jet study. Various

kinds of observations in every observable frequency, including X-rays and γ -rays have so far been conducted. Among them, we review here two results which are closely related to energetics in the blazar jet.

Inoue & Takahara (1996) have theoretically calculated the SR and IC spectra of blazars, in a simple SSC framework. They also considered various kinds of seed photons for IC scattering, such as internal SR radiations and thermal radiation external to the jet. By fitting the model to the observed spectra of two γ -ray blazars, 3C 279 and Mkn 421, they have determined the physical parameters such as B and the maximum Lorentz factors of electrons in the jets of these blazars. Figure 2.19 shows one of their results, the multi frequency spectra of Mkn 421. Their results strongly indicates particle-dominant condition in these blazars ($u_e/u_m \sim 3$ for 3C 279 and ~ 14 for Mkn 421, η in Figure 2.19).

Kubo et al. (1998) have analyzed in detail the multi frequency spectra of 18 blazars which were observed by *ASCA*. Comparing the *ASCA* spectra with γ -ray spectra, they have precisely evaluated the SSC components, and successfully determined physical parameters in these blazars. Figure 2.20 plots the magnetic field and the maximum Lorentz factor, γ_b , of relativistic electrons, against the observed peak frequency of the SR component. They found that the derived magnetic fields, $B = 0.1 \sim 1$ G, are relatively constant among all kinds of blazars, although maximum electron Lorentz factors increase with the observed peak frequencies of their SR components.

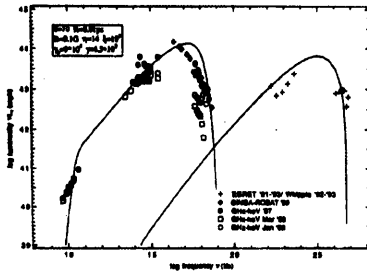


Figure 2.19: The multifrequency spectrum of the γ -ray blazar Mkn 421 (Inoue and Takahara 1996). The solid lines represent the model predictions. The best fit parameters are also shown.

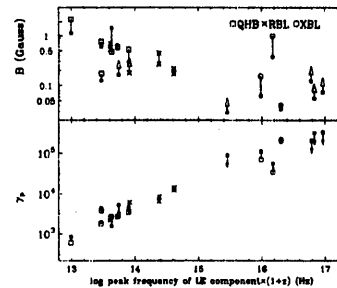


Figure 2.20: Distributions of magnetic fields and Lorentz factors of electrons in blazars, plotted against the peak frequencies of the SR components (Kubo 1996).

Chapter 3

Instruments

3.1 The ASCA Satellite

ASCA (Advanced Satellite for Cosmology and Astrophysics), which was developed under a collaboration between Japan and the USA, is the fourth Japanese X-ray astronomical satellite (Tanaka et al. 1994), following *Hakucho*, *Tenma*, and *Ginga*. It was successfully launched by the M-3SII-7 rocket from Kagoshima Space Center of the Institute of Space and Astronautical Science (ISAS) on February 20, 1993. It has achieved a near-circular orbit with a perigee of 520 km, an apogee of 620 km, and an inclination angle of $31^\circ.1$. Its orbital period is approximately 96 minute. It weights about 420 kg, and its length amounts to 4.7 m after its extensible optical bench (EOB) has been fully extended. We show the in-orbit configuration of *ASCA* in Figure 3.1

ASCA carries four identical X-ray telescopes (XRT) at the top of the EOB, with their optical axes all aligned with the z-axis of the satellite. Two kinds of imaging spectrometers are used at the focal lane of the XRTs; one is two X-ray CCD cameras (Solid-state Imaging Spectrometer, or SIS), and the other is two gas scintillation proportional counters (Gas Imaging Spectrometer, or GIS). The configuration of these instruments are illustrated in Figure. 3.2. These enable X-ray imaging spectroscopy over a wide energy band from ~ 0.6 keV up to 10 keV.

Unfortunately, *ASCA* lost its attitude control during a geomagnetic storm induced by a strong solar flare on July 14, 2000, after which no scientific observation was conducted. It has reentered the Earth's atmosphere on March 3, 2001, after spending 8 years in orbit as one of the most successful missions of X-ray astrophysics.

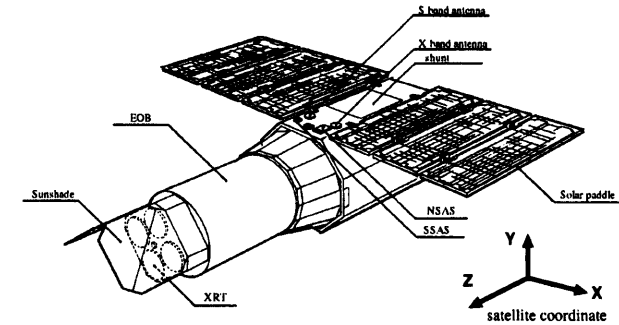


Figure 3.1: Schematic drawing of the *ASCA* satellite.

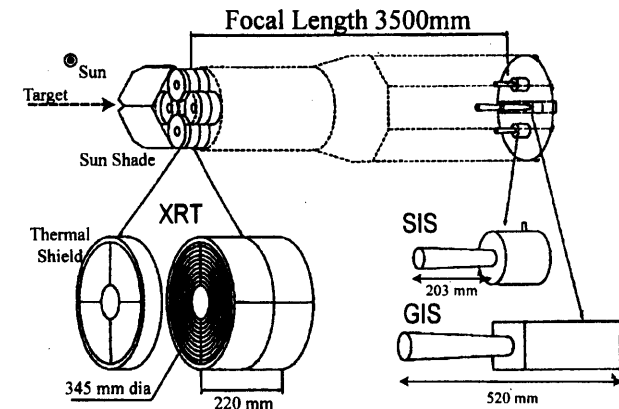


Figure 3.2: Configuration of the XRT and focal-plane instruments onboard *ASCA*.

3.1.1 X-ray Telescope (XRT)

The *ASCA* XRT was jointly developed by NASA Goddard Space Flight Center (GSFC), Nagoya University, and ISAS. It is designed to achieve a large effective area and a moderate angular resolution in a wide energy band (Serlemitsos et al. 1995; Tsusaka et al. 1995). It has for the first time enabled hard X-ray imaging studies up to 10 keV.

Soft X-rays are totally reflected by a smooth surface, only when their incident angle is smaller than a certain critical value. This is known as grazing-incidence reflection. The critical angle, typically $\sim 1^\circ$, is inverse proportional to the X-ray energy and rapidly increases with increasing number density of free electrons in reflecting material. X-ray telescope mirrors use this mechanism generally in so-called Wolter type I configuration, which is shown in Figure 3.3. These optics employ paraboloid and hyperboloid surfaces as the primary and secondary mirrors, respectively, so as to remove the first-order aberration. The effective area is usually increased by nesting multiple mirrors with a common focus. In order to obtain a large effective area up to 10 keV, it is essential to make the grazing angle as small as possible, and to increase the number of nested mirrors by making each

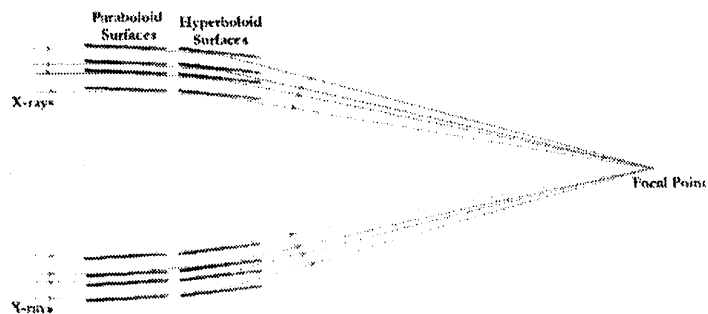


Figure 3.3: configuration of the Wolter type I optics.

The mirrors of *ASCA* XRT are all made of thin ($127 \mu\text{m}$) aluminum foil. These foils are coated with $\sim 10 \mu\text{m}$ thick acrylic lacquer to improve its surface smoothness, over which 50 nm of gold is vacuum-deposited for increasing the reflectivity for harder X-rays. They are bent into a conical surface to approximate paraboloid or hyperboloid, and 120 of them are nested together. Thus, the aperture of the *ASCA* XRT has inner and outer diameters of 120 mm and 345 mm, respectively, and its focal length is 3.5 m. We briefly summarize the design parameters and basic performance of the *ASCA* XRT in Table 3.1.

Table 3.1: Design parameters of the *ASCA* XRT

| | |
|----------------------------------|---|
| Mirror substrate | 127 μm aluminum foil |
| Mirror surface | 10 μm acrylic lacquer + 50 nm Au |
| Mirror length | 100 mm |
| Number of nested foils | 120 foils |
| Inner and outer diameter | 120 mm and 345 mm |
| Focal length | 3500 mm |
| Incident angle | $0^\circ.24 - 0^\circ.70$ |
| Total weight of four XRTs | ~ 40 kg |
| Geometrical area of one XRT unit | 558 cm^2 |
| Energy range | ≤ 10 keV |
| Field of View (FWHM) | $\sim 24'$ at 1 keV and $\sim 16'$ at 7 keV |
| Half power diameter | $\sim 3'$ |

We shown in the left panel of Figure 3.4 the effective area of the *ASCA* XRT as a function of X-ray energy. It reached $\sim 1300 \text{ cm}^2$ below ~ 2 keV, which is almost a factor of 6 and 2 larger than those of *Einstein* and *ROSAT*, respectively. Moreover, it retains a very large effective area even towards higher energies, with the energy upper limit as high as ~ 10 keV. Its effective area is also dependent on the incident angle of X-rays. The effective area gradually decreases as the off-axis angle of the incident X-ray increases. This phenomenon is called vignetting. As shown in the right panel of Figure 3.4, the vignetting effect of the *ASCA* XRT is more prominent in higher energies.

The *ASCA* XRT has moderate angular resolution. The X-ray image of Cygnus X-1 obtained with the GIS, which characterizes the point spread function (PSF) of the *ASCA* XRT, is shown in Figure 3.5. The half power diameter of the PSF, within which half the X-ray flux from a point source is contained, is about 3 arcmin on axis. If statistics allow, the *ASCA* XRT can resolve two point source as close as 30 arcsec. The shape of the PSF has only a slight dependence on the X-ray energy, although it is strongly dependent on the incident angle of X-rays.

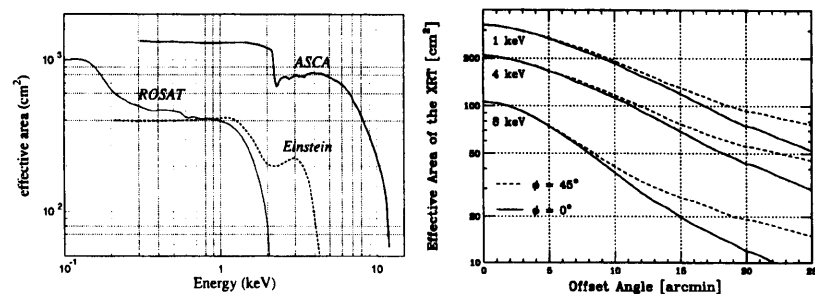


Figure 3.4: The effective area of the ASCA XRT (four units summed up). The left panel shows the energy dependence of the XRT effective area, compared with those of *Einstein* and *ROSAT*. The right panel show its dependence on the incident angle.

67

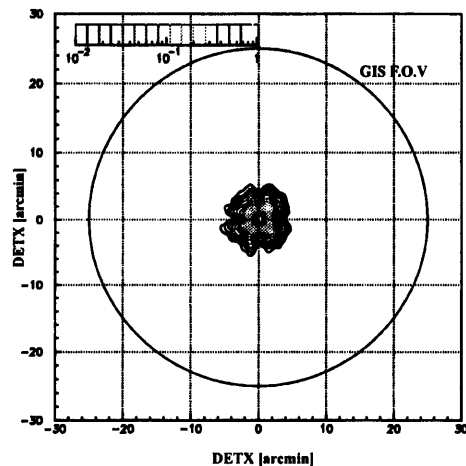


Figure 3.5: The XRT + GIS image of a representative X-ray point source, Cygnus X-1. Contours are drawn to logarithmic scales with levels shown at the top of this figure. The circle indicate the field of view of the GIS.

3.1.2 Solid-State Imaging Spectrometer (SIS)

The Solid-State Imaging Spectrometer (SIS) was developed by the Massachusetts Institute of Technology (MIT), the Pennsylvania State University, ISAS and the Osaka University. The SIS is equipped with X-ray CCD cameras which is used for the first time in a photon counting mode in a space environment. It is characterized by a high energy resolution over a wide energy band (0.4 ~ 10 keV). Detailed design and in-orbit performances are described in Burke et al. (1991) and Yamashita et al. (1997).

The SIS consists of two identical sensors, called SIS0 and SIS1. We show the configuration of each SIS sensor in Figure 3.6, summarize their design parameters in Table 3.2. Each sensor has four CCD chips which are aligned in a 2×2 square format with narrow gaps between them. Each CCD chip has a size of 11 mm square, made up of 420×422 pixels, and covers a 11 arcmin square region in the sky. The thickness of depletion layers reaches $40\mu\text{m}$ under the operating bias condition, which enables detection of hard X-rays up to 10 keV. These CCDs are cooled down to -62°C by thermo-electric cooler (TEC), in order to reduce thermal noises. In front of the CCD chips, an optical blocking filter is placed for preventing optical lights from coming into them.

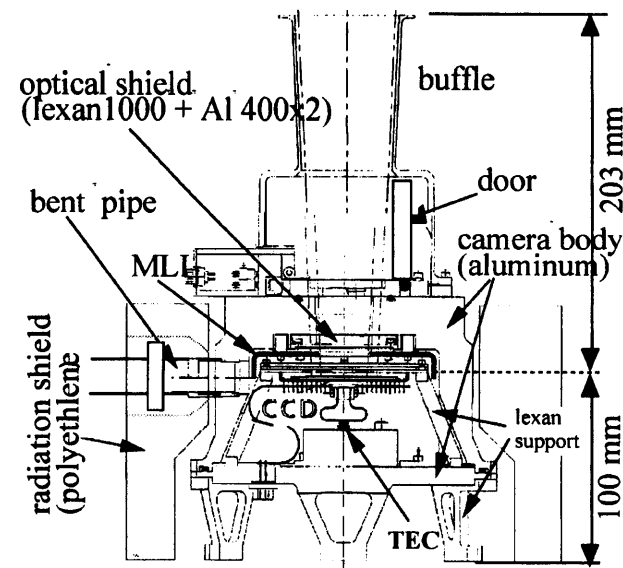


Figure 3.6: The cross section of one SIS sensor.

Table 3.2: Design parameters and performance of the SIS.

| | |
|-------------------------------|--------------------------------|
| Irradiation Method | Front irradiation |
| Charge Transfer Method | Frame Transfer |
| Clock | 3-phase drive |
| Number of Pixels in each chip | 420 pixels \times 422 lines |
| Pixel Size | 27 μm |
| Area of one chip | 11 \times 11 mm ² |
| Field of View of one chip | 11' \times 11' |
| Thickness of Depletion Layer | \sim 40 μm |
| Drive Temperature | \sim -62 $^{\circ}\text{C}$ |
| Energy Band | 0.4 - 12 keV |
| Quantum Efficiency | \sim 80% at 5.9 keV |
| Energy Resolution | 2% (FWHM) at 5.9 keV |

In order to observe various objects with different X-ray intensities and angular sizes, the SIS has three different clocking modes; i.e. 1CCD, 2CCD and 4CCD modes. In the n CCD mode, data from n chips in each SIS are read out. The observable field of view is the largest in the 4CCD mode (22 \times 22 arcmin² in the sky), although the time resolution is the slowest and the effect of event pile-ups may become severe.

The SIS has three different telemetry data formats. The *faint* mode is used for faint objects, the *bright* for bright objects, and the *fast* mode for timing analysis. In the *faint* mode, pulse-heights of 3 \times 3 pixels centered on a pixel with an event detection are recorded and transferred to ground, together with its position and its time. This pulse-height pattern is called "event grade", and its definition is shown in Figure 3.7. An X-ray event does not extend no more than four pixels, because the pixel size is larger than a typical size of an electron cloud (\sim 5 μm) produced by an X-ray photon. Therefore, examining the event grade on ground, abnormal events, such as those due to charged particles, can be rejected. Normally, events with grade 0,2,3,4 are selected for analysis. In the *bright* mode, the event grade are judged on board, and the summed pulse-height with specified grades are recorded, together with its position and time. In the *fast* mode, events are recorded with the high time resolution, although without imaging informations.

There are several properties with the SIS as stated below, which make it unsuitable for the present thesis. Its field of view is relatively narrower and its efficiency for hard X-ray is lower than those of the GIS. The optical light leakages are found in two chips of SIS0.

So called "hot" and "flickering" pixels, which occasionally report false event detection, are found, and its number is increasing with time due to accumulation of radiation damages. The radiation damage has also degraded the charge transfer efficiency of the CCDs, and this significantly affects energy response of the SIS. Moreover, the SIS background varies in a complicated way. These features of the SIS make it difficult to study diffuse and faint X-ray emission with a hard spectrum, such as inverse Compton X-rays from the lobes of radio galaxies. Therefore, we do not analyze data from the SIS extensively in this thesis.

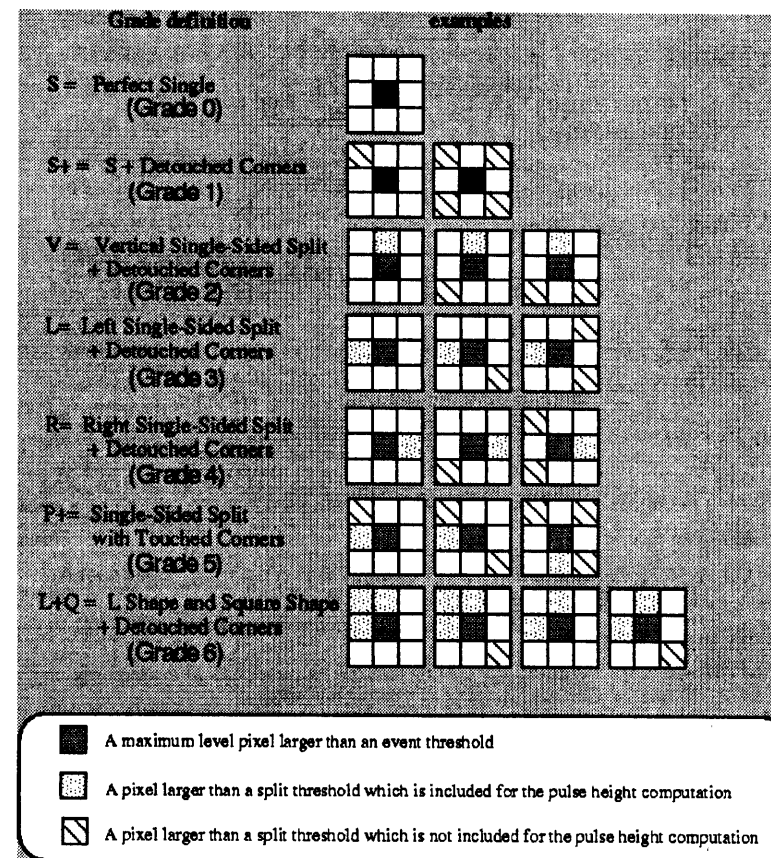


Figure 3.7: The definition and examples of event grade.

3.1.3 Gas Imaging Spectrometer (GIS)

The Gas Imaging Spectrometer (GIS) was mainly developed by the University of Tokyo, the Tokyo Metropolitan University, the ISAS, Meisei Electric Co. Ltd., and Japan Radio Corporation Co. Ltd. The GIS is two set of gas scintillation imaging proportional counters. Its design is based on the GSPC experiment on board *Tenma* (Koyama et al. 1984). It is characterized by a wide field of view ($\sim 50^\circ$ in diameter), a low and stable detector background level, a moderate energy and spatial resolution over a wide energy band, and a high detection efficiency for hard X-rays. The key parameters of the GIS are summarized in Table 3.3. Details about its design and in-flight performance are described in Ohashi et al. (1996) and Makishima et al. (1996), respectively.

Structure

The GIS has two sensor assemblies, named GIS2 and GIS3, and one main electronics package called GIS-E. GIS2 and GIS3 are almost identical except that a Radiation Belt Monitor (RBM), a small PIN-diode detector to monitor a radiation environment, is attached only at the bottom of GIS2. We show the structure of GIS2 in Figure 3.8. It consists of a gas cell, an imaging photo-multiplier tube (IPMT), front end electronics, and a high voltage supply unit.

The gas cell is made of a ceramic cylinder, with a $10 \mu\text{m}$ thick beryllium entrance window at the top and a quartz exit window at the bottom. It is filled with a mixture of 96 % xenon and 4 % helium to a pressure of 1.2 atm at 0°C . The gas cell is divided into two regions by a mesh electrode; a drift region in the top 10 mm and a scintillation region in the bottom 15 mm. The electric potentials of the entrance window and the mesh electrode are held at -6 kV and -5.3 kV, respectively. X-rays are absorbed in the drift

Table 3.3: Design parameters and performance of the GIS.

| | |
|---------------------|---|
| Energy Band | 0.7 - 15 keV |
| Energy Resolution | 8% (FWHM) at 5.9 keV |
| Effective Diameter | 50 mm |
| Entrance Window | $10 \mu\text{m}$ beryllium |
| Absorption Material | Xe (96%) + He (4%), 10 mm depth, 1.2 atm at 0°C |
| Position Resolution | 0.5 mm (FWHM) |
| Time Resolution | $\sim 61 \mu\text{sec}$ (highest value in PH Mode) |
| | 1.95 msec (highest value in MPC Mode) |

region, and generate primary electrons through photo-ionization and subsequent impact ionization, at the rate of one electron per 21.5 eV. These electrons slowly drifts to the mesh electrode, and then accelerated in the scintillation region due to a strong electric field ($\sim 5 \text{ V}$). The xenon gas is excited by the accelerated electrons and creates a large numbers of ultra-violet (UV) photons. Through the quartz window these UV photons are collected by the IPMT, and their distribution and intensity are measured. We illustrate the overall detection principles in Figure 3.9.

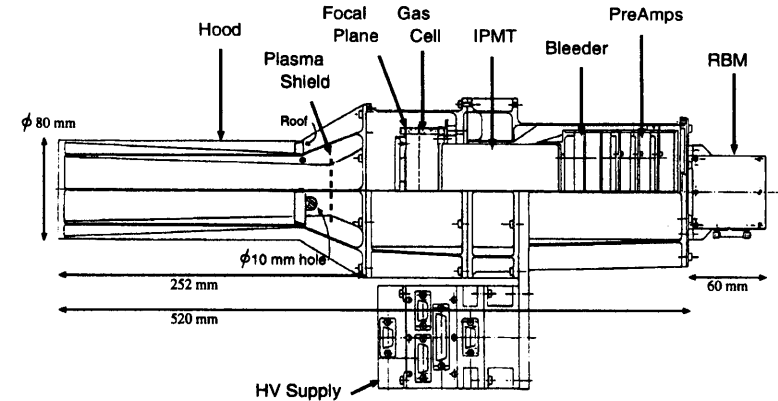


Figure 3.8: A cross sectional view of the GIS sensor.

Signal Processing

Signals from the GIS are first processed by the front-end electronics, and then handled in detail by GIS-E. Those from the last dynode of each GIS sensor go through a charge sensitive amplifier in the front-end electronics, of which the outputs are transferred to GIS-E. Then, signals go through lower and upper discriminatory (**LD** and **UD**, respectively), and then to pulse-height and rise-time analogue-to-digital converters (ADCs). The pulse-height ADC converts the pulse height of each event into a 12 bit value, denoted *PH* and the rise time ADC converts the rise-time of each signal into an 8 bit value, denoted *RT*. The lower and upper rise-time discriminatory (**RTL**D and **RTUD**, respectively) operate on this *RT*. Signals from 32 anode wires (16 of which are for x-axis and the reminder for y-axis) are multiplexed in the front-end electronics into four channels, and then transferred to 4 flash ADCs in GIS-E, which convert them into 32 8-bit values of *X0-Xf* and *Y0-Yf*. The arrival time of the event is measured by a clock, and converted into 10 bit value, denoted

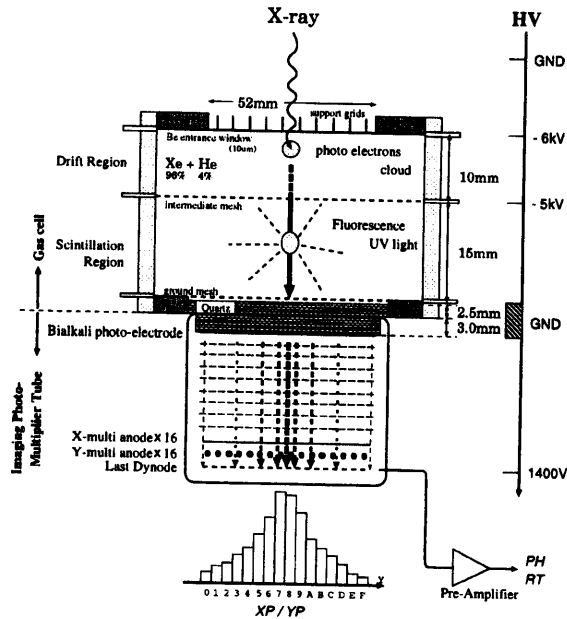


Figure 3.9: A schematic view showing the X-ray detection principle of the GIS.

TIM. Only when the event satisfies the condition of $LD \leq PH \leq UD$ and $RTLD \leq RT \leq RTUD$, all the values (PH , RT , $X0-Xf$, $Y0-Yf$ and TIM) are transferred to the onboard CPU.

Using $X0-Xf$, $Y0-Yf$, the onboard CPU calculates two dimensional positions of an X-ray event ($RAWX$, $RAWY$), with an algorithm which employs a linearized fitting to one-dimensional Lorentzian distribution. The CPU also calculates a spread (SP) of the distribution. The quantities ($RAWX$, $RAWY$) and SP are used for background rejection.

Raw GIS images are somewhat distorted toward the edge of the detector, due to non-linearity of the position response. Therefore, for imaging analyses of celestial objects, $RAWX$ and $RAWY$ should be linearized into $DETX$ and $DETY$ in ground analyses. The relation between ($RAWX$, $RAWY$) and ($DETX$, $DETY$) was precisely established in pre-flight calibration, and confirmed in orbit.

In spectral analyses, the PH value of each event is usually converted into a PI (Pulse Invariant) value, which is directly proportional to the energy of the incident X-ray photons. PI is approximately proportional to PH , and the overall conversion factor from PH to

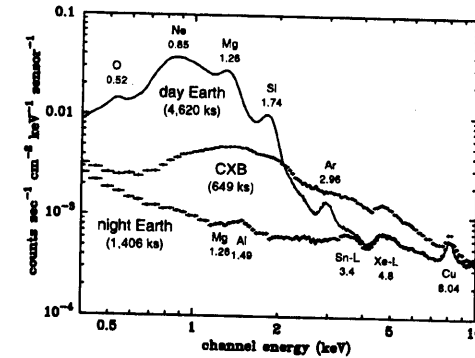


Figure 3.10: Integrated spectrum of night-earth observations which characterize the NXB of the GIS, together with those of cosmic X-ray background and of the day-earth observations. The Ar-K line is due to atmospheric fluorescence, Cu-K line is instrumental, while O-, Ne-, Mg-, and Si-K lines originate in solar coronae.

PI is called "gain". In addition, the PH to PI conversion function has structures across M- and L-edges of Xe, as has been calibrated through extensive ground tests incorporating available information from atomic physics. The gain of the GIS depends on the detected position of the events, and the temperature of the GIS. The position dependence of the GIS gain is mainly caused by non-uniformity of the IPMT. This is corrected using "gain map" files which summarize relative gains as a function of the event position. The GIS gain and its dependence on the temperature are continuously monitored in orbit, using the ^{55}Fe isotopes, which is mounted near the rim of each GIS and emits fluorescent X-rays with the energy of 5.898 keV. These are summarized as "gain history" files and distributed world wide, by which the observers can determine absolute gain of particular observations they wish to analyze.

Background Properties

One of the major design goals of the GIS is to achieve a low and stable non-X-ray background (NXB) level. This provides an important advantage to the analysis of diffuse emission such as the IC X-rays from radio lobes (i.e. the theme of this thesis). This is achieved with both hard-wired and software-based background rejection techniques. The hard-wired rejections are the already mentioned PH and RT discriminations. The PH of most of charged particles are larger than those of normal X-ray events because they deposit large energy in the gas cell. Therefore, the PH discrimination can effectively

exclude particle events. Unlike X-rays, a charged particle produces a long ionization track up the gas cell. Therefore, the *RT* of charged particles are longer than those of normal X-ray events which has a narrow distribution around $3\mu\text{sec}$, and hence the *RT* discrimination can very efficiently reduce NXB. One of the software-based rejections is a more strict “*RT* mask”, which takes into account of broadening of the *RT* distribution toward lower energies because of the worse signal to noise ratio, and position dependence of the *RT* distribution. However, the *RT* selection does not work effectively for particles of which trajectories are perpendicular to the electric field in the gas cell, i.e. parallel to the window plane. Because these events have much larger *SP* than normal X-ray events, they can be effectively rejected by the *SP* discrimination (SPD).

We show the in-orbit NXB spectrum of the GIS which is thus achieved in Figure 3.10. The NXB level is about 1×10^{-3} cts $\text{sec}^{-1} \text{cm}^{-2} \text{keV}^{-1}$ below 1 keV, and $(4-7) \times 10^{-4}$ cts $\text{sec}^{-1} \text{cm}^{-2} \text{keV}^{-1}$ above 1.5 keV, which is about twice as low as that of *ROSAT* PSPC. The variation of the NXB level is within $\sim 5\%$ in each observation, after removing secular changes in orbit. The properties of the GIS background are described in detail by Ishisaki (1997).

3.2 Chandra X-ray Observatory

The *Chandra* X-ray Observatory (CXO), previously known as the Advanced X-ray Astronomical Facility (AXAF), is one of the four “Great Observatories” of NASA, together with the Hubble Space Telescope (HST), the Compton Gamma-Ray Observatory (CGRO) and the forth-coming Space Infra-Red Telescope Facility. It is named after Chandrasekhar, a great Indian-American astrophysicist who had demonstrated that there is an upper limit (now called the Chandrasekhar limit) to the mass of white dwarfs. It is designed to provide an unprecedented angular resolution of ~ 0.5 arcsec, an excellent energy resolving power of $E/\Delta E \sim 500$, and a wide energy coverage from 0.1 to 10 keV.

Chandra was successfully launched by the Space Shuttle Columbia on July 23, 1999. It has achieved a highly elliptical orbit with an apogee of $\sim 138,800$ km, a perigee of $\sim 10,100$ km and a period of 63.5 hours. Because a large portion of its orbit is well above the radiation belts, and free from Earth occultation, *Chandra* has achieved a high observing efficiency; hence long continuous observations are made possible.

We show the in-orbit configuration of *Chandra* in Figure 3.11. It is equipped with one X-ray telescope called the High Resolution Mirror Assembly (HRMA). It carries two kinds of focal plane instruments; the Advanced CCD Imaging Spectrometer (ACIS) which consists of two CCD arrays, and the High Resolution Camera (HRC) which is comprised of two microchannel plate imaging detectors. One of these instruments is selected in every observation. For high resolution spectroscopy, it carries two kinds of grating systems; the High-Energy Transmission Grating (HETG) and the Low-Energy transmission Grating (LETG). One (or none) of these gratings can selectively operate with the HRMA, and disperses the spectrum of a nearly point source on one of the focal plane instruments.

In the subsequent sections, properties of the HRMA and the ACIS, which are mainly used in this thesis, are briefly summarized.

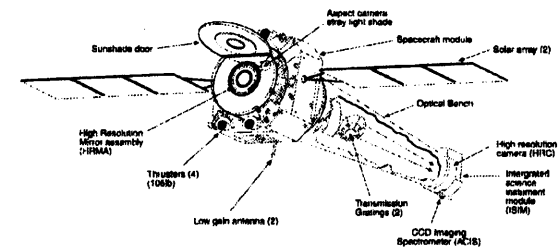


Figure 3.11: A schematic drawing of the *Chandra* X-ray Observatory. The grating systems inside the optical bench are also shown.

3.2.1 High Resolution Mirror Assembly (HRMA)

The *Chandra* HRMA mainly consists of four pairs of Wolter type I mirrors (Figure 3.3). The mirrors were made of Zerodur glass by Scott Glasswerke, polished by Hughes Danbury Optical Systems, coated with Iridium by Optical Coating Laboratory. Their alignment and mounting were completed by Eastman-Kodak Co. Ltd.

We show in Figure 3.12, the configuration of the HRMA. The outermost mirror pair is number 1, processing inwards 3, 4 and 6, and their diameters range from 1.23 m to 0.65 m. The HRMA is originally designed to contain six mirror pairs, but numbers 2 and 5 were eliminated. Basic parameters of the HRMA are summarized in Table 3.4. Its focal length and unobscured geometric area are 10.066 m and 1145 cm², respectively. It weighs 1484 kg, which is about 40 times heavier than the *ASCA* XRT.

Table 3.4: Characteristics of the *Chandra* HRMA

| | |
|------------------------------------|--------------------------|
| Mirror substrate | polished glass |
| Mirror surface | 33 nm Iridium |
| Mirror length | 84 cm |
| Total length | 276 cm |
| Mirror diameter (shell 1, 3, 4, 6) | 1.23, 0.99, 0.87, 0.65 m |
| Focal length | 10.066 ± 0.002 m |
| Total weight | 1484 kg |
| Unobscured aperture | 1145 cm ² |
| Angular resolution (FWHM) | 0.5 arcsec |
| Ghost free field of view | 30 arcmin diameter |

The left panel of Figure 3.13 shows the effective area of the HRMA as a function of incident X-ray energy. As is clear from this figure, the outer shell is efficient for hard X-rays, and the inner one for soft X-rays. The total effective area of the HRMA is about 2 times smaller than that of the *ASCA* XRT below 4 keV, and decreases rapidly toward harder energies. The right panel of Figure 3.13 visualizes the vignetting effect of the HRMA. Below ~ 4 keV, its effective area has only slight dependence on the off-axis angle; it retains about 90% of the on-axis value at ~ 8 arcmin (corresponding to the size of 1 CCD chip, see next section). However, its angular dependence becomes more prominent in higher energies.

The *Chandra* HRMA has an unprecedented angular resolution. We show in Figure 3.14 the simulated X-ray images of an on-axis point source in some representative ener-

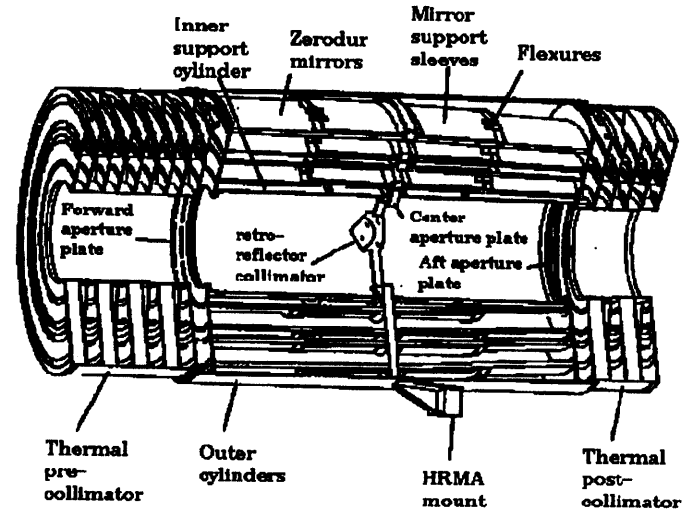


Figure 3.12: Schematic drawing which shows the structure of the *Chandra* HRMA.

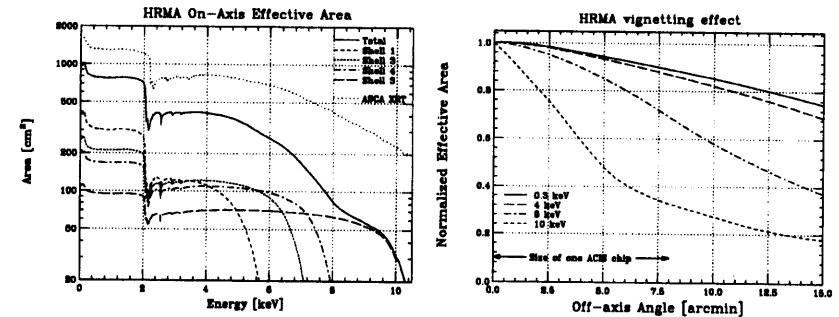


Figure 3.13: The effective area of *Chandra* HRMA. (left) The energy dependence of the effective area of the HRMA, compared with that of the *ASCA* XRT. The contributions of individual shells are also shown. (right) The angular dependence of the HRMA effective area, in 1.49, 4.51, 6.40 and 8.63 keV. Effective areas are normalized to the on-axis values for each energy.

gies, which characterize the point spread function (PSF) of the HRMA. The half power diameter of the PSF is ~ 0.3 arcsec over the 0.3 – 6 keV range. However, as is clearly seen in 3.14, the core of the PSF is off-center by 0.2 arcsec above ~ 8 keV, because the shell 6 is slightly misaligned with respect to the other shells. The effect is not important compared with uncertainties in the aspect solution of the spacecraft.

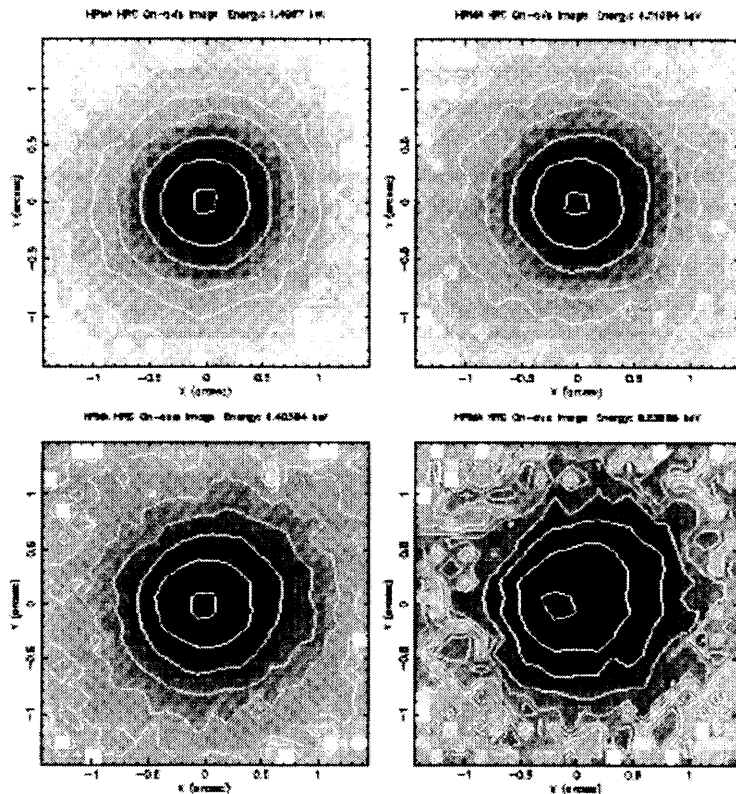


Figure 3.14: The simulated HRMA plus HRC images of a point source in representative energies. Contours are logarithmically spaced and the innermost one in each panel is at 90 % of the peak brightness.

3.2.2 Advanced CCD Imaging Spectrometer (ACIS)

The ACIS is designed to simultaneously offer a high-spatial-resolution X-ray image and a moderate-energy-resolution X-ray spectrum, over a sufficiently wide energy band (0.3 – 10 keV). It can be also used as a readout for the HETG, in order to obtain unprecedentedly high spectral resolution. The ACIS was developed by a collaboration between the Pennsylvania State University, the MIT Center for Space Research and the Jet Propulsion Laboratory. The CCDs of the ACIS were developed by the Lincoln Laboratory of the MIT.

We show the configuration of the ACIS in Figure 3.15, and summarize its basic parameters in Table 3.5. The ACIS mainly consists of 10 planar CCD chips; two of them are back-side illuminated (BI) whereas others are all front-side illuminated (FI). The CCDs have an "active" region which is exposed to the incident radiation and in which the X-ray absorption takes place, and a shielded frame store region, where the obtained data are passed to a local processor. The active region of individual CCDs has a size of ~ 24 mm square which is almost twice as large as those of the *ASCA* SIS, is made up of 1024×1024 pixels, and covers a 8.3 arcmin square region in the sky. Each active region is also divided into 4 parallel signal channels called "nodes". These CCDs can be operated in $-90 \sim -120^\circ\text{C}$. Just over the CCDs, optical blocking filters composed of a polyimide sandwiched between two thin aluminum layers, are placed.

Figure 3.16 illustrates the focal-plane configuration of the ACIS as seen from the HRMA. Four CCDs (the chip number = 0 – 3) are arranged in a 2×2 square array (ACIS-I; I0 – I3) which is used for imaging spectroscopy, and six (the chip number = 4 – 9) are in a 1×6 linear array (ACIS-S; S0 – S5) used either for imaging spectroscopy or as a grating readout. The CCDs in each array are tilted to approximate the relevant focal plane. Two BI CCD chips are both in the ACIS-S array. Any combination of up to 6 CCDs may be used simultaneously. There are narrow gaps between the CCDs in each array; the spacecraft is dithered in a Lissajous pattern, spanning 16 arcsec peak to peak, in order to provide some exposure to sky regions corresponding to the gaps. The dither also effectively smoothes out pixel-to-pixel variations in the energy response. Although the ACIS assembly can be moved on the focal plane, there are two nominal positions called "aimpoints". In one of them, the optical axis of the HRMA falls on the corner of I3 of ACIS-I, and in the other case, it falls near the boundary between the node 0 and node 1 on S3 of ACIS-S. In ACIS-S observations, it has now been standard to place the target (point) source 20 arcsec offset toward S4 ($\Delta Y = -20$ arcsec in Figure 3.16) from the original aim point, in order to assure that the dithered flux is placed entirely on the node 1 of S3.

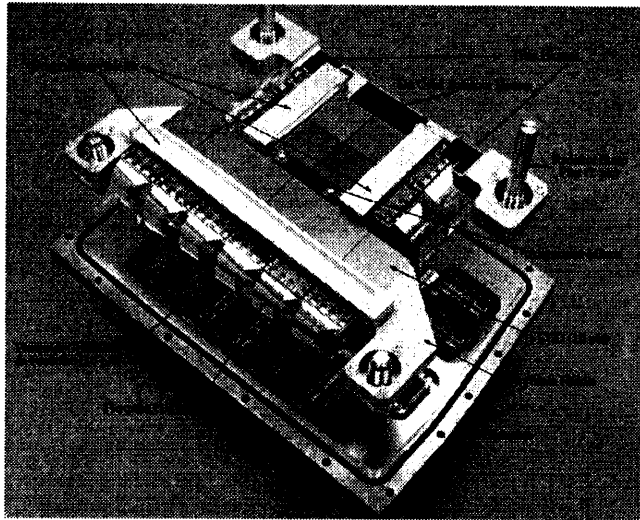


Figure 3.15: A picture which shows the structure of the ACIS.

Table 3.5: Characteristics of the ACIS.

| | |
|-------------------------------|---|
| Illumination Method | 2 CCDs are back-side illumination (BI) |
| | 8 CCDs are front-side illumination (FI) |
| Charge Transfer Method | Frame Transfer |
| Number of pixels in each chip | 1024 by 1024 pixels |
| Pixel Size | 24 μm (corresponding to 0.492 ± 0.0001 arcsec) |
| Frame transfer time | 41 μsec |
| Frame time | 0.2 to 10.0 sec (nominally 3.2 sec) |
| Operating temperature | -90 to -120 $^{\circ}\text{C}$ (nominally -120 $^{\circ}\text{C}$) |
| Quantum Efficiency | FI chip $\gtrsim 80\%$ (3.0 - 5.0 keV) |
| | $\gtrsim 30\%$ (0.8 - 8.0 keV) |
| | BI chip $\gtrsim 80\%$ (0.8 - 6.5 keV) |
| | $\gtrsim 30\%$ (0.3 - 8.0 keV) |
| Arrays | ACIS-I 4 CCDs in a square configuration |
| | ACIS-S 6 CCDs in a linear configuration |
| Field of view | ACIS-I 16.9 by 16.9 arcmin ² |
| | ACIS-S 8.3 by 50.3 arcmin ² |

ACIS FLIGHT FOCAL PLANE

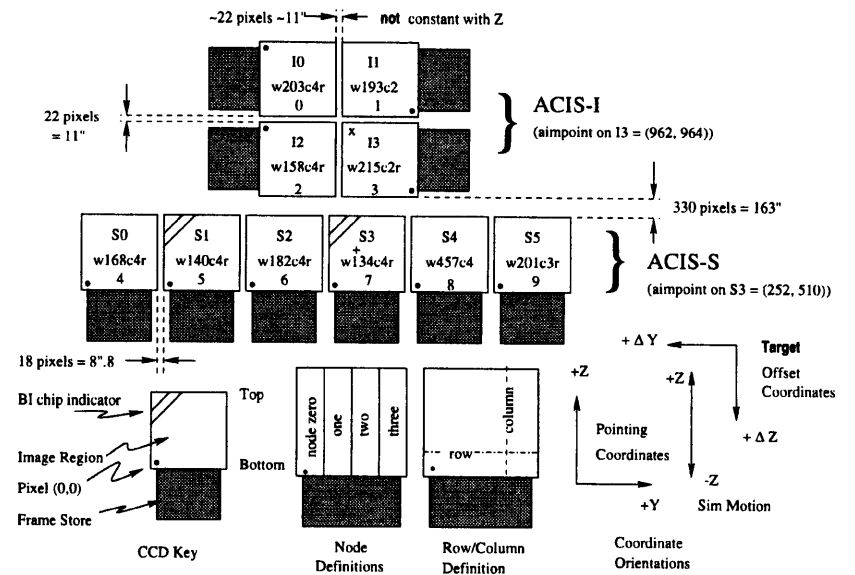


Figure 3.16: Schematic drawing of the ACIS focal plane which is seen from the HRMA. Definitions of the terminology and the coordinate systems are shown in the bottom. The nominal aimpoints on I3 and S3 are denoted with 'x' and '+', respectively. Various ways to refer to a particular CCD are indicated; array plus number, chip serial number, and ACIS chip number.

3.2.3 The ACIS performance

In Figure 3.17, we show the dependence of the ACIS energy resolution on the row number. Before launch, the energy resolution of the FI CCDs originally approached the theoretical limit at almost all energies, while the BI chips exhibited a little poorer resolution. However, because of in-orbit radiation damage, the energy resolution of the FI CCDs has been substantially degraded, and has become a function of the row number of the CCD; the energy resolution is near the pre-launch value close to the frame store region, while it becomes gradually worse toward the farthest row. The damage was mainly caused by low energy protons, encountered during the spacecraft passage through the radiation belt early in the mission life. Since the protons are thought to be "reflected" by the HRMA and "focused" on the CCDs, it soon became practice to displace the ACIS from the focal position, during the radiation belt; by introducing this operation, the CCD degradation has stopped. Because the position dependent energy resolution of the FI CCDs depends strongly on the ACIS temperature, it is now set at -120°C , the lowest temperature safely achievable. The two BI CCDs were not affected and their energy resolution have remained at the pre-launch values.

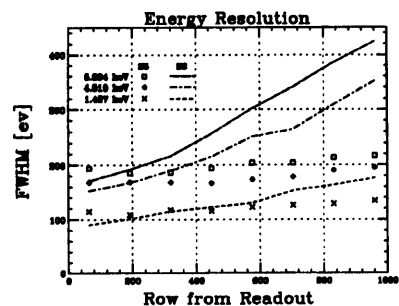


Figure 3.17: The energy resolution of ACIS S2 (FI chip) and S3 (BI chip) as a function of row number for particular energies. These data are taken in orbit at an operating temperature of -120°C .

The spatial resolution of the ACIS for an on-axis point source is limited by the physical size of the CCD pixel, rather than by the HRMA. Figure 3.18 shows the encircled fractional energy for an on-axis point source as a function of radius. Approximately 90% of the X-

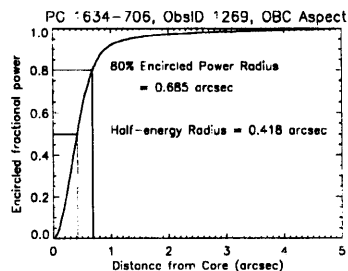


Figure 3.18: The encircled power of the HRMA plus ACIS at 1 keV, as a function of a radius. These data were obtained in the ACIS observation of a point source PG 1643-706, during in-flight calibrations.

ray flux from a point source is contained within a diameter of ~ 2 arcsec at 1.49 keV and ~ 2.5 arcsec at 6.4 keV.

In Figure 3.19, we show the quantum efficiency of the ACIS CCDs and the convolved HRMA/ACIS effective area. These data include the transmission efficiency of the optical blocking filters. The BI CCDs are more efficient than the FI ones in the soft energy band below ~ 1 keV, although the FI CCDs are more efficient in the hard band above ~ 5 keV. The quantum efficiency of the FI CCDs depends on the row number, and decreases by 5 \sim 15% farthest from the frame store region above 4 keV.

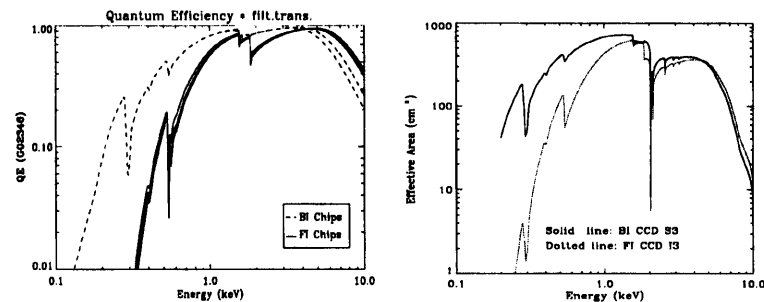


Figure 3.19: (left) The quantum efficiency of the ACIS, convolved with the transmission of the optical blocking filter. (right) The ACIS/HRMA effective area. The dashed or dotted lines are for the BI CCDs, and the solid lines for the FI CCDs. The data for the FI CCDs are taken from the rows nearest the frame store region.

3.2.4 The ACIS data

Operating modes

The ACIS has two operating modes; the Timed Exposure (TE) mode and the Continuous Clocking (CC) mode. The mode selection applies simultaneously to all the selected CCDs. In the TE mode, each CCD collects data for a preselected amount of time (nominally 3.2 sec), called the frame time. Once this interval has passed, the charges of all pixels in the active region are quickly transferred to the frame store region with a frame transfer time of 41 μsec , and subsequently read out through 1024 serial registers. The CC mode allows us to obtain 3 msec timing information at the expense of one dimensional spatial resolution. Details as to the spatial distribution in the column are lost.

The frame time in the TE mode is selectable within a range from 0.2 to 10 sec. The nominal and optimal frame time is 3.2 sec, if the data from the entire region in the each CCD are utilized. A shorter frame time decreases the probability of event pileups, although it will introduce a time during which no data are acquired. This is because it takes 3.2 sec to read out the data regardless of the frame time.

It is also possible to restrict the region on the CCD in which the data are taken. This region is called "subarray". The standard subarrays are shown in Figure 3.20. The optimal frame time T for individual subarrays is determined by

$$T = 41 \times m + 2.84 \times n + 5.2 + 0.040 \times m \times q \text{ msec}$$

where m is the total number of the CCDs which are turned on, and n and q are shown in Figure 3.20. The optimal frame times for the standard subarrays are summarized in Table 3.6.

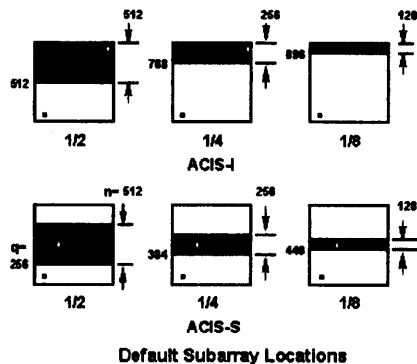


Table 3.6: The nominal (optimal) frame time in second for standard subarrays of ACIS-S.

| Subarray | 1 | 1/2 | 1/4 | 1/8 |
|----------|-----|-----|-----|-----|
| 1 Chip | 3.0 | 1.5 | 0.8 | 0.4 |
| 6 Chips | 3.2 | 1.8 | 1.1 | 0.7 |

Figure 3.20: Examples of various ACIS subarrays. Only the data in the shaded regions are read out. The cross ('+') in each panel indicates the nominal aimpoint.

Telemetry format

The ACIS has three different telemetry formats; **Faint**, **Graded** and **Very Faint** format. In the **Faint** format, which corresponds to the *faint* format in the ASCA SIS, the telemetry data for each event consist of its event position on the CCDs, its arrival time, the pulse-height, and the contents of 3 x 3 pixels centered on the pixel where it is detected; the last information characterizes the event grade. In the **Graded** format, which corresponds to

the **bright** format in the ASCA SIS, the telemetry sends out the event position, together with the time and pulse-height of the specified grade. The **Very Faint** format are almost same as the **Faint** mode except that this mode provides the contents of the 5 x 5 pixels centered on the pixel of event detection.

The **Faint** and **Graded** formats are available for both the TE and CC modes, although **Very Faint** is only for the TE mode. Thus, every events are assigned a specific grade even in the CC mode.

Event grade

Each event detected with the ACIS is assigned a grade on the basis of the patterns of the 3 x 3 pixels centered on the local charge maximum, regardless of the operating mode. Although the grading method is quite similar to that adopted in the ASCA SIS, the grade definition which is illustrated in Figure 3.21 is more complex. The relationship between the ACIS grade and the ASCA grade is briefly summarized in Table 3.7. Depending on the grade, the data are transferred to the telemetry. Certain grades are suppressed onboard in order to limit the telemetry bandwidth devoted to the background events.

In spite of the complicated definition of the event grade, most of the calibration of the ACIS are based on a specific set of the grade, equivalent to the ASCA grade of 0, 2, 3, 4 and 6. In the absence of the event pileup, this particular grade selection appears to optimize the signal-to-background ratio.

| | | |
|-----------|-----------|------------|
| 32 | 64 | 128 |
| 8 | 0 | 16 |
| 1 | 2 | 4 |

Table 3.7: The comparison between the ACIS grade and the SIS grade. See Figures 3.7 and 3.21.

| ACIS | ASCA | Comments |
|-------------------|-------|------------------------|
| 0 | 0 | Single pixel event |
| 64 65 68 69 | 2 | Vertical split up |
| 2 34 130 162 | 2 | Vertical split down |
| 16 17 48 49 | 4/3 | Horizontal split right |
| 8 12 136 140 | 3/4 | Horizontal split left |
| 72 76 104 108 | 6 | |
| 10 11 138 139 | 6 | |
| 18 22 50 54 | 6 | |
| 80 81 208 209 | 6 | |
| 24 66 107 214 255 | 7 | Discarded onboard |
| others | 1/5/7 | |

Figure 3.21: The schematic drawing for the definition of the event grade. The grade is determined by the sum of the numbers for pixels above the threshold. A single pixel event is grade 0

Trailed image and pileup

It takes 41 μsec to transfer the charge from one pixel to another. As a consequence, each pixel is exposed not only to the region in the sky at which the pixel is pointing during the frame time, but also to every other region in the sky along the column for 41 μsec each. Thus, any single pixel always contains the data corresponding to other pixels in the column, which may produce a "trailed" image for a bright X-ray source. An example of trailed images is shown in Figure 3.22.

When two or more X-ray photons are absorbed in one pixel during a single frame time, pileup results. Because almost all of the flux from a point source falls within only a few pixels (see Figure 3.18), the ACIS is affected by the pileup much more easily than the *ASCA* SIS. The fundamental impact of the pileup is that the obtained energy spectrum becomes harder than the true one because multiple events add together in pulse height, and that the photon flux is underestimated because two or more photons are counted as one event. Figure 3.23 visualizes the effect of pileup. The pileup introduce a change of grades, called "grade mitigation", because the charge clouds from two or more photons merge. Thus, some of the events may be no more included in the standard grade set, and be rejected because of bad grade. The core of the image in Figure 3.22 is faint due to the grade mitigation. The pileup also introduce a pulse saturation and distort the shape of the PSF.

Unfortunately, there are no clear methods yet to remove all or some of the effect of pileup from the obtained ACIS data. Thus, for observations of bright point sources, observers should employ some strategy to avoid pileups, such as a shorter frame time or an offset pointing. In general, the pileup should not be a severe problem in observations of diffuse objects, such as the IC X-rays associated with lobes of radio galaxies.

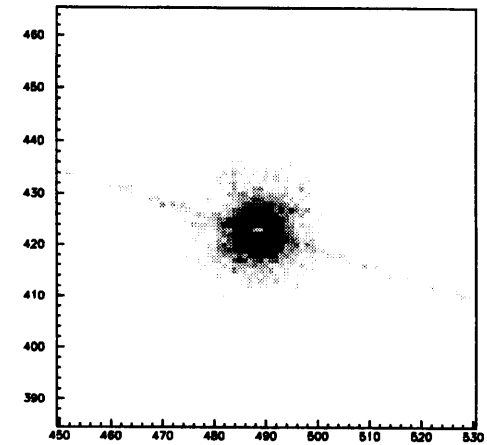


Figure 3.22: The trailed image for a bright X-ray source.

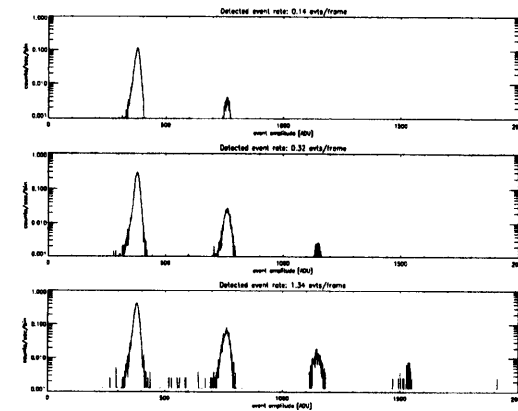


Figure 3.23: The effect of pileup for the 1.49 KeV Al-K α line as a function of a source intensity. These spectra are taken during the pre-flight HRMA/ACIS calibration, and shown as a function of pulse-height. Single-photon events corresponding to the Al-K α line are concentrated near a pulse height of ~ 380 channel, and events with 2 photons have a pulse height twice that of the single-photon events.

Chapter 4

Observations

4.1 ASCA Observations

Our objective is to detect IC X-rays with the *ASCA* GIS from the lobes of radio galaxies other than Fornax A and Centaurus B. However, this is very difficult, since these IC X-rays are intrinsically very faint and diffuse emission. Moreover, they are thought to be severely contaminated by the X-rays from the nuclei, which can potentially be much brighter in X-rays. Therefore, we have searched the public *ASCA* data on radio galaxies for good candidates, under the following criteria.

1. Radio morphology and radio spectrum should be well known.
2. In order to resolve the lobes from the nucleus with the angular resolution of the *ASCA* GIS, the lobes should be larger than ~ 5 arcmin in angular size.
3. The lobes should have a high integrated radio flux density S_{SR} , e.g. a few Jy at 1.4 GHz, in order to secure the detection of the IC X-rays. By assuming the equipartition condition and simply scaling the *ASCA* results on Fornax A, $S_{\text{SR}} = 5$ Jy at 1.4 GHz corresponds to the 2 – 10 keV IC X-ray flux of $F_{\text{IC}} \gtrsim 1 \times 10^{-13}(1+z)^4$ erg cm $^{-2}$ s $^{-1}$.
4. The lobes should have a relatively uniform radio surface brightness distribution, without being dominated by radio hot spots or jets. This ensures the soft seed photons to be dominated by the CMB.
5. The object should have a lobe-dominant morphology, and the nucleus should be relatively inactive or rather obscured, like narrow line radio galaxies, in order to prevent the lobes from being severely contaminated by strong X-rays from the nucleus.
6. The object should not be in a rich cluster environment, for avoiding the contamination from cluster thermal emission.

Table 4.1: Radio galaxies observed with *ASCA*.

| Target | z | S_{SR}^{\dagger} | Size * | Comments |
|-------------------|----------|---------------------------|------------------|---|
| 3C 109 | 0.3056 | 4.0 | 2" \times 2' | |
| 3C 111 | 0.0485 | 13.5 | 1' \times 3' | |
| 3C 120 | 0.0330 | 10.2 | | core-dominated |
| 3C 129 | 0.0208 | 5.3 | 2' | wide-angle tailed source |
| 3C 215 | 0.4121 | 1.4 | 1' \times 1' | in a cluster |
| 3C 218 (Hydra A) | 0.0538 | 43.5 | 10" \times 1' | in a cluster |
| 3C 219 | 0.1744 | 8.5 | 30" \times 3' | |
| 3C 220.1 | 0.6100 | 2.3 | 20" \times 30" | possibly in a cluster |
| 3C 223 | 0.1368 | 3.6 | 1' \times 5' | in a group of galaxies |
| 3C 234 | 0.1848 | 5.6 | 30" \times 2' | hot spot |
| 3C 249.1 | 0.3115 | 2.3 | 10" \times 30" | |
| 3C 254 | 0.7340 | 3.1 | | |
| 3C 270 (NGC 4261) | 0.007465 | 18.6 | 2' \times 5' | in a group of galaxies |
| 3C 275 | 0.4800 | 3.8 | 2" \times 5" | |
| 3C 293 | 0.0450 | 4.6 | 1' \times 3' | core-dominated |
| 3C 295 | 0.4599 | 22.8 | 2" \times 5" | in a cluster |
| 3C 303 | 1.570 | 2.7 | 20" \times 40" | |
| 3C 313 | 0.4610 | 3.6 | 4' | |
| 3C 321 | 0.0961 | 3.6 | 1' \times 6' | hot spot dominated |
| 3C 330 | 0.5500 | 7.1 | 30" \times 2' | possibly in a cluster |
| 3C 346 | 0.1620 | 3.8 | 10" \times 20" | bright hot spot |
| 3C 351 | 0.3721 | 3.1 | 20" \times 1' | hot spot |
| 3C 353 | 0.0304 | 56.5 | 1' | |
| 3C 368 | 1.1310 | 1.1 | 10" | |
| 3C 382 | 0.05787 | 5.8 | 2' \times 3' | hot spot |
| 3C 390.3 | 0.0561 | 11.3 | 1' \times 3' | hot spot |
| 3C 405 (Cygnus A) | 0.056075 | 1500 | 1' \times 2' | in a cluster |
| 3C 411 | 0.467 | 3.5 | 1' | core-dominated |
| 3C 433 | 0.1016 | 12 | 1' \times 1' | tailed source |
| 3C 445 | 0.0562 | 5.5 | 2' \times 10' | hot spot |
| 4C 55.16 | 0.2420 | 8.53 | | |
| 4C 73.08 | 0.0581 | 2.47 | 5' \times 15' | |
| 4C 06.41 | 1.270 | 1.4 | | |
| 4C 73.18 | 0.3021 | 3.9 | | |
| 4C 74.26 | 0.1040 | 1.6 | | |
| Centaurus A | 0.001825 | 1330 | 5" \times 10" | significantly larger than the GIS F.O.V |
| Pictor A | 0.035058 | 66 | 2' \times 4' | hot spot |
| Hercules A | 0.154 | 45 | | core-dominated |
| NGC 612 | 0.023016 | 10.9 | 5' \times 15' | |
| NGC 6251 | 0.023016 | 2.6 | \times | hot spot |
| IC 4296 | 0.012465 | 8 | 5' \times 10' | in a group of galaxy |

\dagger flux density at 1.4 GHz.

* total angular size in arcmin.

only the radio galaxies, with $S_{\text{SR}} > 1$ Jy, are listed.

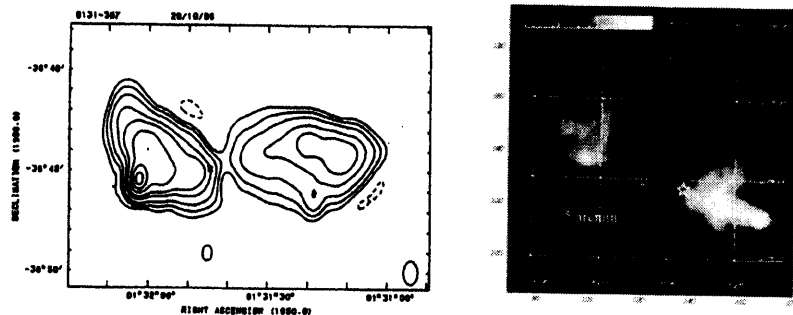


Figure 4.1: The radio images of our targets for *ASCA* observations. The left panel shows the 843 MHz VLA contours of NGC 612 (Jones and McAdam 1992). The right panel shows the 608 MHz VLA color image of 4C 73.08 (Leahy, Bridle, and Strom 1996). The 'x' and star in each panel represent the positions of their host galaxies.

Table 4.2: Parameters of the radio lobes selected from the *ASCA* public data.

| Target | $(\alpha^{2000}, \delta^{2000})$ | z | 1 arcmin | S_{SR}^{\dagger} | $\alpha_{SR}(\text{Jy})$ | B_{me}^{\ddagger} | Size * |
|----------|----------------------------------|--------|----------|--------------------|--------------------------|---------------------|-----------|
| NGC 612 | (01:33:57.7, +36:29:36) | 0.0298 | 32.9 kpc | 10.9 | 0.6 | 1.3 | $\sim 7'$ |
| 4C 73.08 | (09:49:45.9, +73:14:23) | 0.0581 | 61.2 kpc | 2.47 | 0.85 | 0.5 | $\sim 6'$ |

\dagger evaluated at 1.4 GHz

* diameter of the single lobe

\ddagger minimum energy magnetic field in μJy

The radio data of NGC 612 are from Ekers et al. (1978).

The radio data of 4C 73.08 are from Mayer (1979).

Table 4.1 summarizes the radio properties of radio galaxies observed with *ASCA*. Among them, only two objects, NGC 612 and 4C 73.08, satisfy all of our selection criteria. Because of a little poor angular resolution of *ASCA*, the angular sizes of the lobes which are thought to be resolved with *ASCA* are exceptionally large among radio galaxies. Consequently, our sample is still very small in number, and limited to relatively nearby radio galaxies at redshifts of $z \lesssim 0.06$.

The *ASCA* observations of NGC 612 and 4C 73.08 were originally proposed by Kaneda et al., in order to search the IC X-rays from their lobes. The result on NGC 612 have been already reported briefly by Tashiro et al. (1999; N. Isobe being a co-author), and that on 4C 73.08 by Isobe et al. (2001). In the present thesis, we re-analyze these data in

detail. Prior to *ASCA*, no X-ray observations of these radio galaxies have been reported.

We show in detail the radio properties of NGC 612 and 4C73.08 in Table 4.2, and show their radio images obtained with VLA in Figure 4.1. The lobes in both radio galaxies are sufficiently large (> 5 arcmin) in size, and show relatively uniform brightness distributions, while their nuclei are both faint in the radio images. They have moderately high radio flux densities, which predict sufficient IC X-ray fluxes.

The log of *ASCA* observations of NGC 612 and 4C 73.08 is shown in Table 4.3. In these observations, the SIS was operated in 1-CCD mode, and most of these lobes are outside the field of view of the SIS. Thus, we use mainly the GIS data.

Table 4.3: The *ASCA* observation log of radio galaxies for our analysis.

| Target | Observation Date | Exposure [s] | | SIS mode | |
|----------|------------------|--------------|-------|----------|--------------|
| | | SIS | GIS | clock | telemetry |
| NGC 612 | 1996.07.12 | 70944 | 79584 | 1CCD | <i>faint</i> |
| 4C 73.08 | 1998.10.23 | 40000 | 44416 | 1CCD | <i>faint</i> |

4.2 Chandra Observations

4.2.1 Radio lobes

For smaller and hence more distant lobes which cannot be resolved with *ASCA*, the *Chandra* ACIS, which features an unprecedented angular resolution of ~ 0.5 , is apparently one of the ideal instruments. Therefore, we have searched the VLA results on 3CR radio galaxies (e.g., Jones and McAdam 1992; Leahy and Perley 1991; Black et al. 1992; Leahy et al. 1997; Neff et al. 1995) for new targets suited to *Chandra* observations, under the same criteria for *ASCA*, but excluding the second one. The fifth criterion is not necessary, considering the angular resolution of the ACIS, but is still important to avoid event pile-ups of the ACIS. Then, we have picked up three lobe-dominant radio galaxies, and proposed them for the *Chandra* Cycle-2 observations. Two of them, 3C 452 and 3C 427.1, have been actually approved.

We summarize the radio parameters of 3C 452 and 3C 427.1 in Table 4.6, and show their radio images in Figure 4.2. Each target shows relatively symmetrical double-lobe morphology with rather uniform brightness distributions. The radio nuclei of the both radio galaxies are not so bright. The total angular extent of 3C 452 is $\sim 1 \times 4$ arcmin², or $\sim 82 \times 330$ arcmin². From its lobes, weak X-ray emission ($\sim 5 \times 10^{-13}$ erg cm⁻² s⁻¹) had

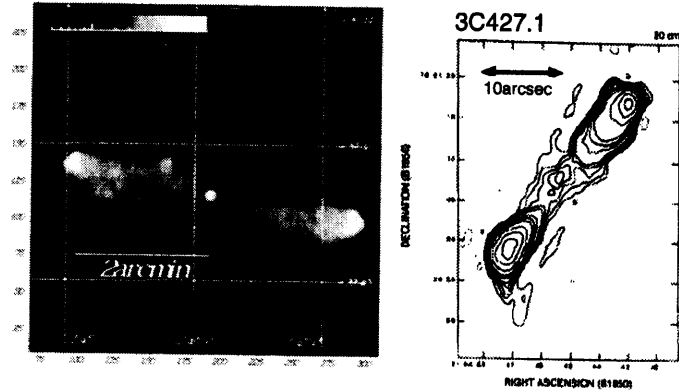


Figure 4.2: The radio images of the targets for our *Chandra* observations. (left) The 1.4 GHz VLA image of 3C 452 (Leahy, Bridle, and Strom 1996). (right) The 1.4 GHz VLA contours of 3C 427.1 (Neff et al. 1995).

already been detected with *Einstein* (Fabbiano et al. 1984), but its X-ray structure and spectrum is not yet well understood. The size of individual lobes of 3C 427.1 is $\sim 5 \times 10$ arcsec², which is the smallest in our sample, but is still larger compared with the angular resolution of *Chandra*. Moreover, it locates at a relatively high redshift of $z = 0.572$, so that a high S_{IC}/S_{SR} ratio is expected, because u_{CMB} is proportional to $(1+z)^4$. Any X-ray observation of 3C 427.1 with previous instrument is not reported.

In order to further enlarge the sample of X-ray lobes, we have checked the public archival data of *Chandra* observations on radio galaxies, under the same criteria but now excluding the fifth one. We have limited ourselves to the data obtained by the ACIS-S with no grating system, because the energy response of the ACIS-I is not well understood and the grating system may distort the quality of obtained images. For a practical reason, we have also limited to the archival data which became already public as of August 31, 2001.

The only one radio galaxy, Pictor A, has satisfied the criteria among the *Chandra* archival targets. The radio parameters of Pictor A are shown also in Table 4.6. As shown in Figure 4.3, it has symmetrical double lobes with nearly circular morphologies. The individual lobes have large radio flux densities, which ensure the sufficient IC X-ray fluxes. The total angular extent of Pictor A is $\sim 4 \times 8$ arcmin², which is comparable to the size of the one ACIS chip. Although it has two bright hot spots near the end of its

each lobe, they do not severely contaminate the lobes, because the lobes is much larger than the angular resolution of the ACIS.

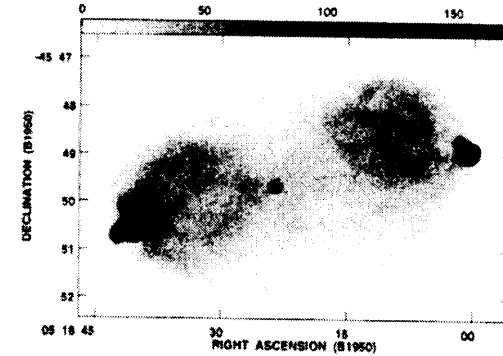


Figure 4.3: The 1.4 GHz VLA image of Pictor A (Perley et al. 1997).

Table 4.4: Parameters of the radio lobes observed with *Chandra*.

| Target | $(\alpha^{2000}, \delta^{2000})$ | z | 1 arcmin | S_{SR}^{\dagger} | α_{SR} | B_{me}^{\ddagger} | Size * |
|----------|----------------------------------|--------|----------|--------------------|-------------------|---------------------|-------------------|
| 3C 452 | (22:45:48.8, +39:41:16) | 0.0811 | 82.3 kpc | 10.9 | 0.78 | 2.7 | 1' \times 4' |
| 3C 427.1 | (21:04:06.4, +76:33:12) | 0.5720 | 299 kpc | 4.0 | 1.08 | 24 | 6'' \times 30'' |
| Pictor A | (05:19:49.7, -45:46:44) | 0.0350 | 38.3 kpc | 32.9 [‡] | 0.72 [‡] | 3.0 | 4' \times 8' |

[†] evaluated at 1.4 GHz in the unit of Jy

* diameter of the whole target

[‡] evaluated for the west lobe.

[‡] minimum energy magnetic field in μ G

The radio data of 3C 452 are taken from Black et al. (1992), those of 3C 427.1 are from Black et al. (1992) and Herbig and Readhead (1992), and those of Pictor A are from Perley et al. (1997).

4.2.2 Hot spots

In order to probe into the energetics also in hot spots of radio galaxies, we have selected three radio galaxies which have bright radio hot spots, Pictor A, Cygnus A, and 3C 123 from the public data of *Chandra*. These hot spots are already detected by some observers, using the *Chandra* ACIS (Wilson et al. 2000, Wilson et al. 2001, and Hardcastle et al. 2001). We systematically re-analyze their ACIS data in the present thesis. We show

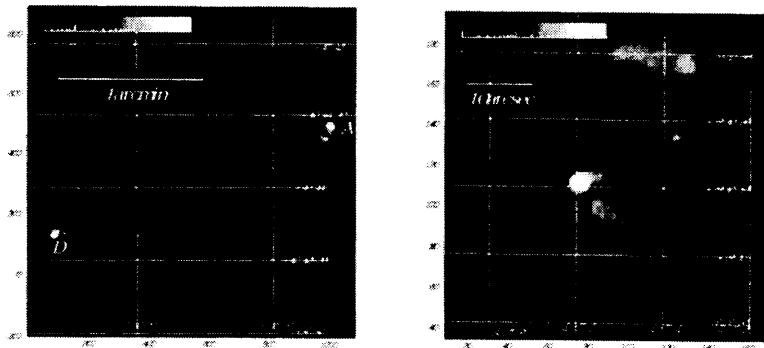


Figure 4.4: The VLA images of radio galaxies which we have selected for the analysis of hot spots. The right panel shows the 4.5 GHz image of Cygnus A (Perley et al. 1984) and the left panel shows the 1.4 GHz image of 3C 123 (Leahy, Bridle, and Strom 1996).

the radio parameters of these targets in Table 4.5. Figure 4.4 shows their radio images, excluding that of Pictor A which is already shown in 4.3.

Pictor A has two bright radio spot spots in the periphery of each lobe. Especially, the western hot spot is optically detected, and its radio SR spectrum is smoothly extrapolated to the optical band (Meisenheimer et al. 1997). Wilson et al. (2001) have already reported the detection of X-rays from this hot spot, although its X-ray spectrum is difficult to be explained by a simple SR or a SSC model.

The powerful radio galaxy Cygnus A contains two bright radio hot spots. The western and eastern hot spots are usually called hot spot A and B, respectively. These are the brightest among all radio hot spots which have so far been detected. The detailed knowledge on radio structures and spectra of these hot spots (e.g Carilli et al. 1991) make them ideal targets for our study. Actually, X-rays from these hot spots have been already detected with the *ROSAT* HRI (Harris et al. 1994). Recently, using the *Chandra* ACIS, Wilson et al. (2000) have confirmed this result (see §2.4.3). Although the radio fluxes of individual lobes of Cygnus A are sufficiently high, Cygnus lies in a dense cluster environment. We therefore analyze only the X-rays from the hot spots.

3C 123 exhibits an unusual radio structure, which may be induced by a precession of the jet axis (Cox et al. 1991), with two compact hot spots well aligned across the nucleus. Although the western hot spot is relatively weak, the eastern one is the second brightest

hot spot known after Cygnus A. The spectrum and structure of the western hot spot is well known (e.g. Hardcastle et al. 1997; Meisenheimer et al. 1997). The X-ray emission of from the western hot spot has been already detected with the *Chandra* ACIS (Hardcastle et al. 2001). 3C 123 is located in a cluster environment (Spinrad et al. 1985), and then, we do not analyze the X-rays from its lobes.

Beside these hot spots, Harris et al. (2000) have reported the X-ray detection of the northern hot spot of radio galaxy 3C 295. However, the structure of this hot spot is thought to be still unresolved well in radio images. Actually, Harris et al. (2000) have assumed some possible geometry in determining the physical parameters in this hot spot. Therefore, we exclude the northern hot spot of 3C 295 from our sample.

Table 4.5: Parameters of radio hot spots.

| Target | $(\alpha^{2000}, \delta^{2000})$ † | z † | 1 arcmin | Hot Spot | S_{SR} † | α_{SR} ‡ |
|----------|------------------------------------|--------|----------|----------|------------|-----------------|
| Pictor A | (05:19:49.7, -45:46:44) | 0.0350 | 38.3 kpc | West | 3.99 | 0.74 |
| Cygnus A | (19:59:28.3, +40:44:02) | 0.0560 | 59.2kpc | West (A) | 93 | 0.88 |
| | | | | East (D) | 104 | 0.79 |
| 3C 123 | (04:37:04.6, +29:40:15) | 0.2177 | 179 kpc | East | 15.8 | 0.75 |
| | | | | West | 0.867 | 0.74 |

† for host galaxies † evaluated at 1.4 GHz in Jy ‡ evaluated in GHz band

The radio data of Pictor A, Cygnus A, and 3C 123 are taken from Meisenheimer et al. (1997), Carilli et al. (1991), and Looney & Hardcastle (2000), respectively.

4.2.3 Log of *Chandra* observations

Table 4.6 shows the log of *Chandra* observations of all the radio galaxies which we have selected for the analysis of the X-rays from their lobes and hot spots. These include both the targets which we have proposed and have approved, and the archival ones.

We have planned to observe 3C 452 with 2 arcmin offset toward ACIS-8 from the aimpoint of ACIS-S ($\Delta Y = -2$ arcmin in Figure 3.16), in order to observe the whole lobes in the ACIS-7. We have also planned to observe 3C 427.1 with $\Delta = -30$ arcsec, in order to observe the whole lobes in the single node of ACIS-7. The estimated X-ray fluxes of their nuclei should not cause notable event pile-ups of the ACIS. Then, we have decided to observe both targets with a nominal frame time (3.2 sec) of the ACIS (not employing any subarrays), because the narrower field of view in the shorter frame time is not suitable for the detection of diffuse X-rays associated with their lobes. Although the observation

of 3C 427.1 was originally scheduled to be performed at October 15, 2001, it has been postponed three times, and has not yet been performed.

The targets, which we have picked up from the *Chandra* archival data, are observed in various observing modes. Among them, the observations of Pictor A are performed twice with a nominal frame time (i.e. a nominal field of view), once with a short frame time (0.4 sec). We use the data obtained with a nominal frame time (ID = 346) for the analysis of its lobes, and those obtained with a sorter frame time (ID = 443) for its nucleus, in order to avoid the effect of severe event pile-ups. Similarly, the observations of Cygnus A are conducted once with a nominal frame time, twice with a short frame time. We analyze data obtained in the observation of ID = 360, for examining the X-rays from its hot spots.

Table 4.6: Observational log of our *Chandra* targets.

| Target | PI | ID | Date | Exp. [†] | Chip* | ($\Delta Y, \Delta Z$) [†] | Frame ^o | Subarray | Comments |
|----------|-----------|------|------------|-------------------|--------|---------------------------------------|--------------------|----------|-----------------------------------|
| 3C 452 | Isobe | 2195 | 2001.08.21 | 80947 | 235678 | (-2', 0) | 3.2 | | |
| 3C 427.1 | Isobe | 2194 | 2001.12.05 | 40000 | 235678 | (-30'', 0) | 3.2 | | not yet observed |
| Pictor A | Wilson | 345 | 1999.11.02 | 3910 | 23678 | (-20'', 0) | 3.2 | | not analyzed |
| | Wilson | 346 | 2000.01.18 | 28595 | 23678 | (-1', 0) | 3.2 | | pile up for the nucleus, |
| | Wilson | 443 | 2000.06.20 | 5577 | 7 | (-5', 3'.5) | 0.4 | 1/8 | analysis for the nucleus |
| 3C 123 | Hadcastle | 829 | 2000.03.21 | 47254 | 235678 | (-20'', 0) | 3.2 | | |
| Cygnus A | Wilson | 359 | 2000.03.08 | 2350 | 7 | (-20'', 0) | 0.4 | 1/8 | |
| | Wilson | 360 | 2000.05.21 | 35168 | 235678 | (-20'', 0) | 3.2 | | pile up for nucleus, not analyzed |
| | Wilson | 1707 | 2000.05.26 | 10174 | 7 | (-20'', 0) | 0.4 | 1/8 | not analyzed |

[†] the total exposures in the unit of s.

* the ACIS chip number which is turned on.

[†] the offset angle from the aimpoint. (-20'', 0) is the default value. (Figure 3.16)

^o the frame time of the ACIS.

Chapter 5

Analysis and Results of *ASCA* Observations

5.1 Data Reduction

As already mentioned in §4.1, we mainly analyze the GIS data. We reduce the data, using the analysis software package, **HAESOFT** version 5.0, which is provided and supported by the *ASCA* Guest Observer Facility at the NASA GSFC and the ISAS. According to the standard manner, we screen the data as follows. We employ the criteria for a geomagnetic cut-off rigidity (*COR*) at ≥ 4 GV and for an elevation angle from the Earth's limb at $\geq 5^\circ$. The data obtained during the spacecraft passage through the South Atlantic Anomaly (*SAA*) are rejected. We selected the data obtained when the an attitude jittering of the spacecraft from the mean pointing directions is smaller than 0.6 arcmin. Thus, we obtain good exposures for individual targets as shown in Table 5.1.

Table 5.1: Good exposures remained after the standard screening.

| | NGC 612 | 4C 73.08 |
|-------------------|---------|----------|
| GIS Exposure (ks) | 62.3 | 41.1 |

5.2 NGC 612

5.2.1 The X-ray image

We show the 0.7 – 10 keV raw GIS image of NGC 612 in Figure 5.1. We have combined the data obtained with the two GIS sensors (GIS2+3), but have not subtracted the background events from this image. X-ray emission from NGC 612 is clearly detected, with no other confusing bright point sources in the field.

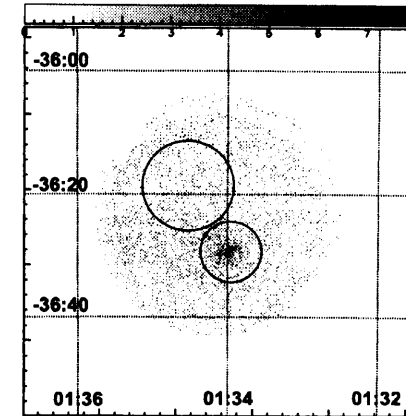


Figure 5.1: The 0.7 – 10 keV raw X-ray image of NGC 612, shown to the entire field of view of the GIS. The smaller circle indicates the region in which the spectrum of the lobes (including the nucleus) is accumulated, and the larger one indicates the background integration region.

Figure 5.2 shows the X-ray images around NGC 612 smoothed with a two dimensional Gaussian function of $\sigma = 1$ arcmin, in the soft (0.7 – 3 keV) and the hard (3 – 10 keV) energy bands. The backgrounds are not subtracted either. The 843 MHz VLA contour image is overlaid (Jones and McAdam 1992). The X-ray peak is rather clear, especially in the hard band image, and coincides in position with the optical galaxy within the positional uncertainty of the GIS, although the radio nucleus of NGC 612 is very faint. The soft band image reveals apparently diffuse emission, which extends up to ~ 5 arcmin (~ 160 kpc) from the host galaxy. This size well exceeds typical spatial extent of the diffuse X-ray emission associated with nearby elliptical galaxies (Matsushita 1997). Moreover,

this diffuse emission appears anisotropically distributed around the host galaxy, elongated in the direction toward the radio lobes. On the contrary, the hard band image is roughly point-like, suggesting the dominance of the host galaxy or its nucleus.

In order to more clearly visualize these extended X-ray features, we have projected the unsmoothed images in the hard and soft energy bands, onto the two directions; one parallel and the other orthogonal to the radio lobe structure. The projection regions have a width of 3 arcmin, corresponding to the core of the PSF of the XRT plus the GIS, and shown in the right panel of Figure 5.2 with 'X' and 'Y'. We have subtracted the background events using the point-source removed black sky observations (Ikebe 1995; Ishizaki 1997). Figure 5.3 shows these profiles in comparison with the PSF. As the appropriate PSF, we here use the GIS image of Cygnus X-1 observed at a similar detector position (see Figure 3.5). As is clear from these profiles, the angular extent of the X-ray peak in the hard energy band, is almost consistent with that of a point source. On the other hand, the soft band profiles are significantly extended beyond the PSF, particularly along the lobe axis nearly up to the periphery of the radio lobes. Thus, we think that the GIS images reveal a diffuse X-ray source associated with the radio lobes of NGC 612.

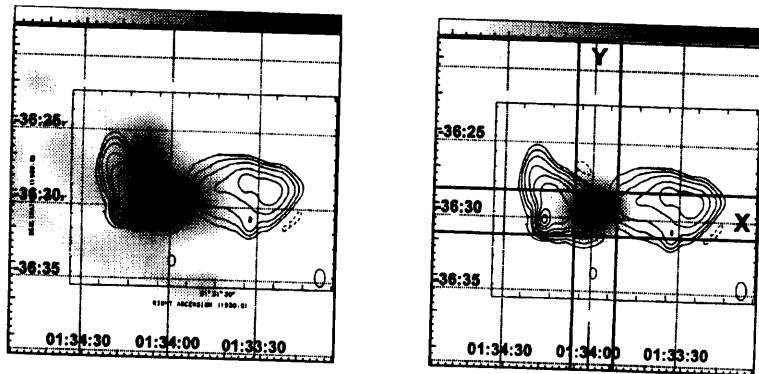


Figure 5.2: The X-ray images around NGC 612 in 0.7 - 3 keV (*left*) and 3 - 10 keV (*right*), smoothed with a Gaussian kernel of $\sigma = 1$ arcmin. The 843 MHz radio contours (Jones and McAdam 1992) are overlaid on both images. The red crosses represent the optical position of the host galaxy of NGC 612. The regions, where the linear surface brightness profiles were extracted, are indicated as X and Y.

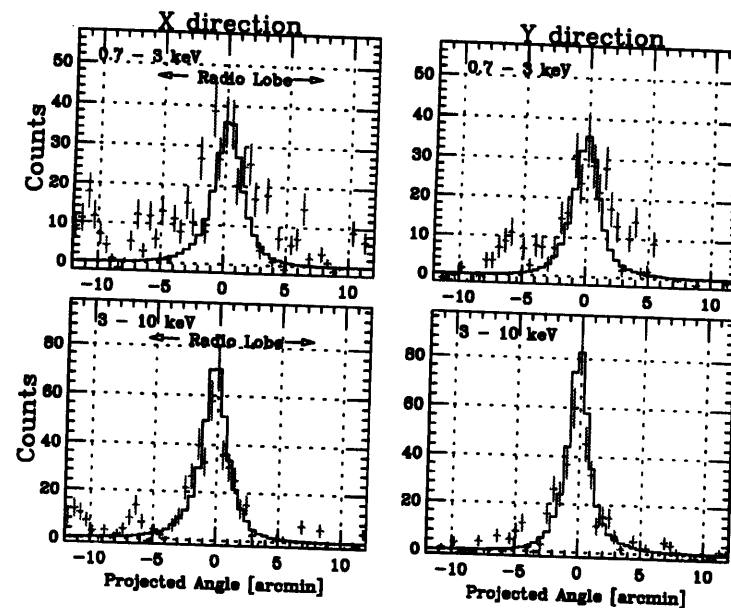


Figure 5.3: The background subtracted linear profiles around the X-ray peak in 0.7 - 3 keV (upper) and 3 - 10 keV (lower). (*left*) The profiles accumulated along a band parallel to the lobe axis (i.e. the X direction), with the left corresponding to east in the sky (toward left in Figure 5.2). (*right*) The profiles perpendicular to the lobe axis (i.e. the Y direction), with the left in these two panels corresponding to south in the sky (toward bottom in Figure 5.2). The histograms in individual panels represent the projected PSF of the XRT plus the GIS. The observed profiles and the PSF are normalized to each other by their peak counts.

5.2.2 The X-ray spectrum of the host galaxy

Our objective is to determine the spectral parameters of the possible excess diffuse emission associated with the lobes of NGC 612. However, the X-rays from the lobes are apparently contaminated by the emission from the host galaxy or its nucleus, because the separation between the lobes and the host galaxy is near the angular resolution of the GIS (Figure 5.3). Then, we have to precisely evaluate the nuclear X-ray spectrum. Moreover, we relate the nuclear luminosity to the lobe properties, later in Chapter 7. Therefore, we first analyze the X-ray spectrum of the host galaxy.

In order to study the X-ray emission from the host galaxy including its nucleus, we have extracted the GIS spectrum within a circular region of a radius 1.5 arcmin (~ 50 kpc), centered on NGC 612. This radius corresponds to the core of the GIS PSF, so that this spectrum is thought to be dominated by the X-ray emission from the host galaxy of NGC 612. The background spectrum was accumulated over a neighboring source free-region with a radius of ~ 7.5 arcmin, which is indicated by the larger circle in Figure 5.1. The left panel of Figure 5.4 shows the background subtracted GIS (GIS2+GIS3) spectrum thus obtained, without removing the instrumental response. Errors of this spectrum represent photon statistics. The signal X-rays have been clearly detected over the 0.7 – 10 keV range.

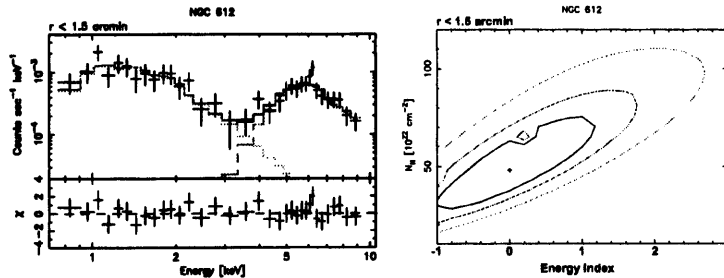


Figure 5.4: (*left*) The background subtracted GIS spectrum of the host galaxy of NGC 612. The histogram shows the best-fit RS (green) plus PL (red) model. (*right*) The confidence contours of the absorption column density and the spectral index for the hard component determined by the RS plus PL (red) model. Contours represent 68% (black), 90% (red), and 99% (green) confidence levels.

The spectrum has too complex a shape to be reproduced by any single component models modified by absorption; it requires at least two (hard and soft) spectral components. Moreover, the hard component seems to be heavily absorbed. Spectra of this shape

Table 5.2: The best-fit spectral parameters of the host galaxy of NGC 612, determined from the double-component models.

| | Soft Component | | Hard Component | | $\chi^2/d.o.f$ |
|---|----------------------------------|---------------------|--|---------------------|----------------|
| | N_H (cm^{-2}) | α / kT (keV) | N_H (cm^{-2}) | α | |
| Double PL | $1.86 \times 10^{20\dagger}$ | 1.6 ± 0.5 | $5.5^{+3.3}_{-2.5} \times 10^{23}$ | $0.1^{+1.4}_{-1.2}$ | 21.1/29 |
| RS + PL | $1.86 \times 10^{20\dagger}$ | $1.7^{+1.3}_{-0.5}$ | $4.8^{+3.0}_{-2.2} \times 10^{23}$ | $0.0^{+1.3}_{-1.1}$ | 22.2/29 |
| F_X ($\text{erg cm}^{-2} \text{s}^{-1}$) [†] | $(1.7 \pm 0.3) \times 10^{-13*}$ | | $5.1^{+2.3}_{-1.7} \times 10^{-12\circ}$ | | |
| L_X (erg s^{-1}) [†] | $(3.1 \pm 0.5) \times 10^{41*}$ | | $8.7^{+3.9}_{-2.4} \times 10^{42\circ}$ | | |

[†] fixed at the Galactic value. * in 0.5 – 10 keV \circ in 2 – 10 keV

[‡] absorption-corrected value, assuming the hard component index is $\alpha = 0.7$

have been observed frequently from a so-called type II AGNs (e.g, Makishima et al. 1994; Iwasawa et al. 1997).

We accordingly tried to fit the spectrum with double-component models, which consist of a soft and a hard one. For the soft component, we have adopted either a power law (PL) model or a Raymond-Smith (RS) thin thermal model, and fixed the absorption column density to the Galactic value, $N_H = 1.86 \times 10^{20} \text{ cm}^{-2}$ (Stark et al. 1992). We also fixed the abundance of heavy elements in the RS model at 0.4 solar abundance, a typical value for elliptical galaxies (Awaki et al. 1994; Matsushita et al. 2000). For the hard component, we adopted a PL model modified by a free absorption. Regardless of the soft component, the double-component models have successfully described the observed spectrum, with the parameters of the hard component unchanged. The derived spectral parameters are shown in Table 5.4. Thus, the implied column density for the hard component is very high, $N_H \sim 5 \times 10^{23} \text{ cm}^{-2}$. In the following, we use the RS model for the soft component.

Since the spectral index α and the column density N_H for the hard component are often coupled strongly with each other, we show the confidence contours of these two parameters in the right panel of Figure 5.4. Thus, the derived index, though with large errors, is consistent with a typical index of active galactic nuclei, $\alpha = 0.7 \sim 0.9$. Assuming the index to be $\alpha = 0.7$, the absorption-corrected 2–10 keV X-ray flux becomes $F_X \sim 5 \times 10^{-12} \text{ erg cm}^{-2} \text{ s}^{-1}$. The corresponding intrinsic 2–10 keV X-ray luminosity becomes $L_X \sim 9 \times 10^{42} \text{ erg s}^{-1}$, which is near the lowest end of the nucleus luminosity of radio galaxies (Sambruna et al. 1999). Thus, the hard component is naturally interpreted as an emission from the active nucleus of NGC 612, which is thought to be highly obscured by the molecular torus from our line of sight (see Figure 2.2).

The best-fit temperature and 0.5–10 keV luminosity of the soft component are $kT \sim$

1.7 keV and $L_X \sim 3 \times 10^{41}$ erg s $^{-1}$, respectively. These values are almost consistent with those of thermal emission from the interstellar medium (ISM) of nearby normal elliptical galaxies (Matsushita et al. 2000). We, therefore, ascribe the soft component to be the thermal emission from the soft component of the host galaxy of NGC 612.

5.2.3 The X-ray spectrum of the lobes

In order to examine X-ray spectrum of the possible excess diffuse component associated with the lobes of NGC 612 (see Figure 5.3), we have derived another GIS spectrum within a radius of 5 arcmin (~ 160 kpc) centered on NGC 612. The integration region is shown with the smaller circle in Figure 5.1. Although there is a possible contaminating source to the south of NGC 612 in Figure 5.2, it is outside the integration region and its contamination is negligible. We employed the same background spectrum as used for examining the spectrum of the host galaxy.

Figure 5.5 shows the background subtracted GIS spectrum thus obtained from the larger integration region. This spectrum is thought to include both the emission from the host galaxy and the diffuse component. The histogram in the left panel of Figure 5.5 represents the X-ray spectrum of the host galaxy, which is reproduced by the best-fit RS plus PL model determined from the spectrum with the smaller integration region in the previous section. Here, we precisely took into account the difference in the integration region for the spectrum. As is clear from this figure, the observed spectrum can not be explained by the emission from the host galaxy alone (the reduced chi-square of $\chi^2/d.o.f. = 3.05$); the data leaves significant residuals in lower energies, although the two spectra agree with each other above 4 keV. This is quite reasonable from the results of imaging analysis, shown in Figure 5.3, where the excess diffuse emission is prominent only below 3 keV, and the hard X-ray image above 3 keV is point like. The excess photons can be identified with the diffuse emission seen in Figure 5.3.

Table 5.3: The best-fit spectral parameters for the excess diffuse component.

| | α or kT | S_X^\dagger | $\chi^2/d.o.f$ |
|--------|---------------------|------------------|----------------|
| PL | 1.0 ± 0.5 | 37^{+14}_{-12} | 33.7/32 |
| | 0.6^\ddagger | 28 ± 6 | 35.5/33 |
| Bremss | $3.9^{+9.9}_{-2.1}$ | | 34.3/32 |

† absorption corrected value at 1 keV in nJy

‡ fixed at the radio SR index

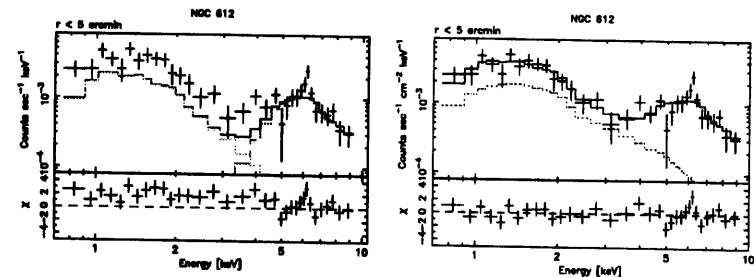


Figure 5.5: The background subtracted GIS spectrum, derived from a circular region with a radius of 5 arcmin, centered on NGC 612. The histograms in the left panel represent the the best-fit RS (green) plus PL (red) model for the host galaxy of NGC 612. The histograms in the right panel represent the best-fit spectrum, after introducing an additional power law component (blue).

In order to evaluate the excess diffuse component, we have introduced an additional PL component absorbed by the Galactic column density of $N_H = 1.86 \times 10^{20}$ cm $^{-2}$, with all the spectral parameters describing the host galaxy fixed. The resulting best-fit spectrum ($\chi^2/d.o.f. = 1.05$) is shown in the right panel of Figure 5.5 with the histograms, and derived spectral parameters of the excess component are summarized in Table 5.3. The estimated absorption-corrected 2 – 10 keV flux of the excess component is $F_X = 1.5 \pm 0.7 \times 10^{-13}$ erg cm $^{-2}$ s $^{-1}$. The obtained spectral index, $\alpha = 1.0 \pm 0.5$, is consistent with the SR radio index $\alpha_{SR} = 0.6$ observed from the lobes of NGC 612. Then, we also fitted the spectrum with the spectral index fixed at 0.6, and obtained parameters are shown in in Table 5.3.

For examining the possibility of the thermal origin of the excess emission, we replaced the PL with a thermal bremsstrahlung (hereafter Bremss) model. This model is statistically satisfactory with $\chi^2/d.o.f. = 1.07$. However, the derived temperature, $kT = 3.9^{+9.9}_{-2.1}$ keV, is too high compared with the virial temperature of the host galaxy, ~ 1 keV. Moreover, the corresponding thermal pressure becomes $p_e \sim 3 \times 10^{-12}$ dyne cm $^{-2}$. To confine such thermal plasma, a magnetic field at least $B \sim 10$ μ G is required, which is significantly larger than $B_{me} \sim 1.3$ μ G. We consider that this situation is unrealistic.

Thus, we conclude that the diffuse X-rays are produced by the IC scattering from the SR electrons in the lobes. In Chapter 7, we further discuss the physical parameters in the lobe determined utilizing the multi frequency spectra.

5.3 4C 73.08

5.3.1 The X-ray image

We show the 0.7 – 10 keV raw GIS (GIS2+3) image of 4C 73.08 in Figure 5.6. We have not subtracted the background events from this image. X-ray emission from 4C 73.08 is clearly detected and seems somewhat elongated toward the northeast direction in this image. No other confusing bright point sources are detected in the GIS field of view.

Figure 5.7 shows the X-ray images around 4C 73.08 smoothed with a two dimensional Gaussian function of $\sigma = 1$ arcmin, in the soft (0.7 – 3 keV) and the hard (4 – 10 keV) energy bands. The backgrounds are not subtracted either. The 608 MHz VLA contours are superposed (Leahy, Bridle, and Strom 1996). In the hard band image, the X-ray peak is rather clear, appears point like, and coincides in position with the optical host galaxy, although the radio nucleus is very faint. The soft band image reveals apparently diffuse emission associated with its lobes, especially its east one.

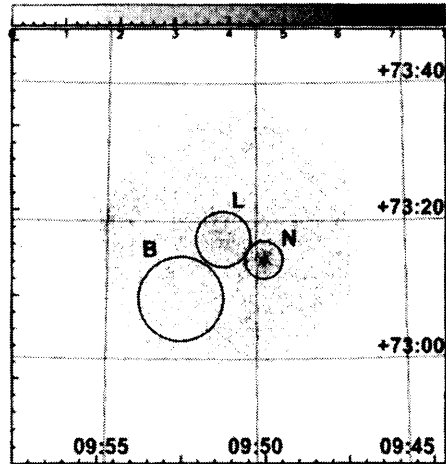


Figure 5.6: The 0.7 – 10 keV X-ray image of 4C 73.08, shown to the entire GIS field of view. The circles indicated as N, L, and B are the regions over which the spectra of the host galaxy, the east lobe, and the background are integrated, respectively.

In order to more clearly visualize these X-ray features, we have projected unsmoothed image in the soft and hard energy band, onto to the direction parallel to the radio lobe axis. The projection region, which is shown in the right panel of Figure 5.7 with "E – W", has a width of ~ 6 arcmin, and hence it contains almost the whole radio lobes. We have subtracted the background events using the point-source removed black sky observations (Ikebe 1995; Ishizaki 1997). We show these profiles in Figure 5.8, together with the 608 MHz radio profile. We also shows the appropriate PSF (i.e. the profile for Cygnus X-1) in the hard band profile. As is clear from these profiles, the angular extent of the X-ray peak in the hard energy band is almost consistent with that of a point source. We have also found some excess counts associated with the east lobe in the hard band profile. On the other hand, the soft band profile is quite different from that of a point source, and is dominated by the diffuse emission extending over the radio lobes. Moreover, the east lobe is brighter in the soft X-ray band, although the radio profile reveals the opposite tendency. The X-ray brightness in each lobe seems relatively uniform. Thus, we think that the GIS image clearly reveals the diffuse X-ray source associated with the lobes of 4C73.08.

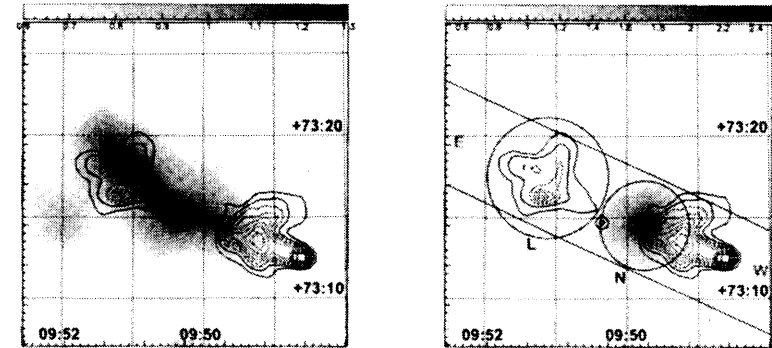


Figure 5.7: The X-ray images around 4C 73.08 in (left) 0.7 – 3 keV and (right) 4 – 10 keV, smoothed with a Gaussian of $\sigma = 1$ arcmin. The 608 MHz VLA contours (Jones and McAdam 1992) are overlaid on both images. The star represents the position of the host galaxy of 4C 73.08.

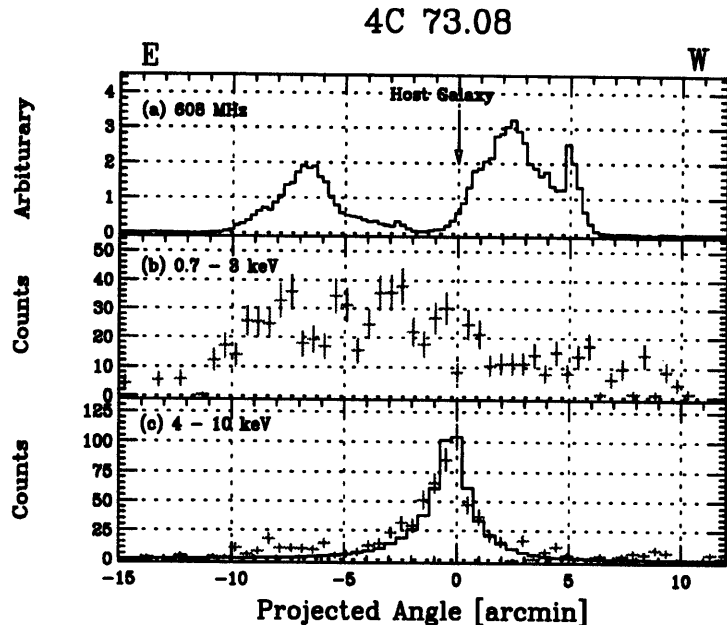


Figure 5.8: The linear profiles around 4C 73.08 in (a) 608 MHz, (b) 0.7 – 3 keV, and (c) 4 – 10 keV, with the right and left corresponding to the direction indicated as “E” and “W” in Figure 5.7, respectively. The histogram in the panel (c) represents the projected PSF of the GIS in 4 – 10 keV. The observed profile and the PSF are normalized to each other by their peak counts.

5.3.2 The X-ray spectrum of the east lobe

For examining the emission mechanism of the diffuse X-ray sources associated with the lobes of 4C 73.08, we have extracted the X-ray spectrum of its east lobe within a circular region of a radius 4 arcmin (~ 250 kpc). This region is indicated as “L” both in Figures 5.6 and 5.7. The background spectrum was accumulated over a neighbouring source free region with a radius of 6 arcmin, which is indicated as “B” in Figures 5.6 and 5.7. The left panel of Figure 5.9 shows the background subtracted GIS (GIS2+3) spectrum of the east lobe of 4C 73.08, thus obtained. The signal X-rays have been clearly detected over the 0.8 – 10 keV range.

The spectrum seems relatively featureless. We fitted the spectrum, and have successfully described the observed spectrum with a single PL model modified by an absorption with the column density left free. The best-fit model prediction is shown by the histograms in Figure 5.9, and the obtained parameters are summarized in Table 5.4. The data leaves some residuals around ~ 1.6 keV, which may look like an emission line. We introduced a Gaussian in order to evaluate this feature, but we could not reproduce it with any meaningful parameters. Therefore, we do not think that the feature is real.

The right panel of Figure 5.9 shows the confidence contours between the spectral index α and the column density N_H . The derived index $\alpha \sim 0.65$, though with a large errors, is consistent with the SR radio index $\alpha_{SR} = 0.85$ observed from the lobes of 4C 73.08 (Ekers et al. 1978). Then, we fitted the spectrum with α fixed at 0.85 and obtained the parameters as shown in Table 5.4. The derived column density, $N \sim 4 \times 10^{21} \text{ cm}^{-2}$, is slightly higher, but consistent with the Galactic value, $N_H = 2.52 \times 10^{20} \text{ cm}^{-2}$, at the 3 sigma level (see the right panel of Figure 5.4).

Table 5.4: The best-fit spectral parameters of the east lobe of 4C 73.08.

| | N_H^\dagger | α or $kT(\text{keV})$ | S_X^\ddagger | $\chi^2/d.o.f.$ |
|--------|-------------------------|------------------------------|------------------|-----------------|
| PL | 2.3 ($\lesssim 7.2$) | $0.65^{+0.51}_{-0.38}$ | 55^{+45}_{-21} | 20.5/30 |
| | $3.8^{+2.7}_{-2.3}$ | 0.85* | 70 ± 12 | 21.0/31 |
| Bremss | 0.82 ($\lesssim 4.3$) | $13.8^{+\infty}_{-8}$ | | 20.9/30 |

\dagger in 10^{21} cm^{-2} \ddagger evaluated at 1 keV in nJy

* fixed at the radio SR index

In order to examine the possibility of the thermal origin for the diffuse emission, we also fitted the spectrum with a Bremss model. Although this model is statistically acceptable, an exceptionally high temperature, $kT \gtrsim 6$ keV, is obtained. Moreover, the corresponding

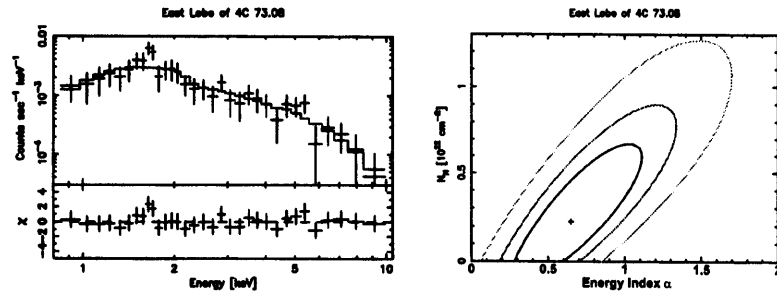


Figure 5.9: (*left*) The background subtracted GIS spectrum of the east lobe of 4C 73.08. The histogram shows the best-fit PL model modified with a free absorption. (*right*) The confidence contours of the absorption column density and the spectral index.

thermal pressure becomes $p_e \sim 7 \times 10^{-12}$ dyne cm^{-2} . To confine such thermal plasma, a magnetic field at least $B \gtrsim 10 \mu\text{G}$ is required, which is more than an order of magnitude higher than $B_{\text{me}} \sim 0.5 \mu\text{G}$. We consider that this situation is unrealistic, like in the lobes of NGC 612.

Thus, we conclude that the diffuse X-ray emission arise via the IC scattering from the SR electrons in the lobe. In Chapter 7, we further discuss the physical parameters in the lobe determined utilizing the multi frequency spectra.

5.3.3 The X-ray spectrum around the host galaxy

In order to study the X-ray emission from the host galaxy including its nucleus, we have extracted another spectrum with a region of a radius 3 arcmin centered on 4C 73.08. The integration region is shown with the smallest circles indicated as "N" in Figures 5.6 and 5.7, and dose not intersect with the region "L". We employed the same background spectrum as for the east lobe. Figure 5.10 shows the background subtracted X-ray spectrum around 4C 73.08. Like in the case of NGC 612, the spectrum has a complex shape and requires at least two spectral components, soft and hard ones. Moreover, the hard components seems to be heavily absorbed.

We first tried to fit the spectrum by a double PL model both modified by a free absorption. The best-fit model spectrum is shown with the histograms in the left panel of Figure 5.10, and its parameters are shown in Table 5.5 (Double PL 1). Although a good fit was obtained with this model, the soft component becomes unusually hard ($\alpha \sim -0.4$), even increasing toward higher energies. Since X-ray emission with such a reversed power law spectrum has never been observed from any celestial object, we considered the fit

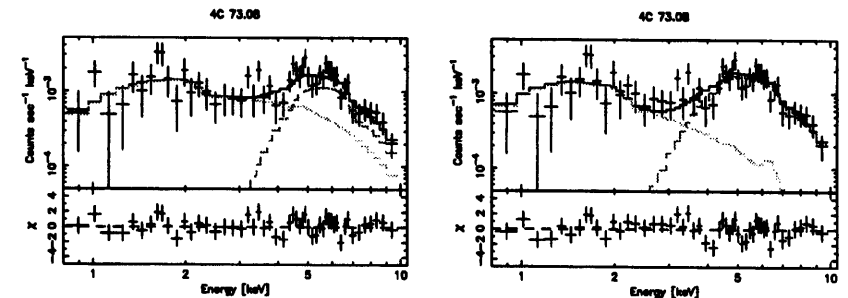


Figure 5.10: The background subtracted GIS spectrum accumulated around the host galaxy of 4C 73.08. The histograms in the left panel shows the best-fit double PL model determined with all the spectral parameters left free. The histograms in the right panel shows the best-fit RS (green) plus PL (red) model, with the parameters for the hard component fixed at the values determined above 4 keV.

unphysical.

In order to avoid the above problem, we may first evaluate the hard component that is dominant above ~ 4 keV, supposing it originates from the obscured nucleus. We have fitted the X-ray spectrum above 4 keV with a single PL model modified by an absorption. The best-fit spectrum is shown in the left panel of Figure 5.11, and its parameters are shown in Table 5.5 (PL). We show the confidence contours of N_{H} and the spectral index α in the right panel of Figure 5.11. The fit is successful, and the obtained index $\alpha \sim 0.8$ and the absorption-corrected 2 – 10 keV X-ray luminosity, $L_{\text{X}} \sim 4 \times 10^{43}$ erg s^{-1} , are both reasonable as those of active galactic nuclei, in particular those of radio galaxies (Sambruna et al. 1999). Thus, the hard band spectrum is naturally interpreted as an emission from the active nucleus of 4C 73.08 which is thought to be heavily obscured by the molecular torus from our line of sight, like in the case of NGC 612.

We, next, evaluated the soft component, by introducing another PL model or an RS model with 0.4 solar abundance for heavy elements, with the hard-component parameters fixed. We also fixed the column density of the additional soft component at the Galactic value, considering the poor statistics in the soft energy band. Both models are almost acceptable and derived parameters are summarized in Table 5.5 (Double PL 2 and RS+PL). The best-fit RS+PL model is shown in the right panel of Figure 5.10 with histograms.

In the case of the RS plus PL model, the best-fit temperature becomes again very high, $kT \sim 8$ keV. Moreover, the absorption-corrected 0.5 – 10 luminosity of the soft component, $L_{\text{X}} \sim 2 \times 10^{42}$ erg s^{-1} , is nearly an order of magnitude higher than those of

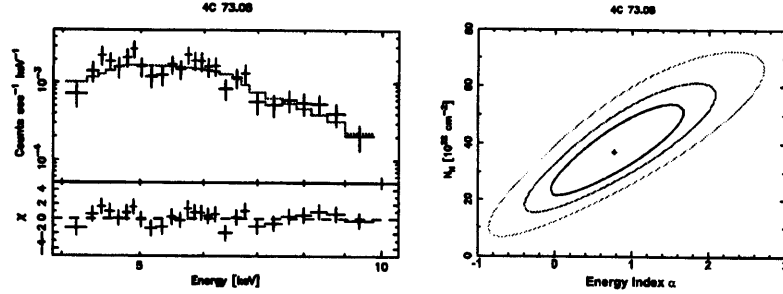


Figure 5.11: (*left*) The X-ray spectrum around the host galaxy of 4C 73.08 above 4 keV. The histogram shows the best-fit heavily absorbed PL model. (*right*) The confidence contours for the absorption column density and the spectral index.

the ISM in nearby elliptical galaxies (Matsushita et al. 2000). Therefore, we think that the thermal emission from the ISM of the host galaxy of 4C 73.08 does not dominate the soft component. On the other hand, in the double PL model, the index $\alpha \sim 0.6$ is consistent within its error with the SR radio index $\alpha_{\text{SR}} = 0.85$. Then, we ascribe the soft component as the contamination from the IC emission from the lobes, which is also reasonable from Figure 5.8.

Table 5.5: The best-fit parameters for the spectrum around the host galaxy of 4C 73.08

| | Soft Component | | Hard Component | | $\chi^2/d.o.f$ |
|--|---------------------------------------|------------------------|---------------------------------------|----------------------|----------------|
| | N_H (cm ⁻²) | α or kT (keV) | N_H (cm ⁻²) | α | |
| PL* | - | - | $3.7^{+1.8}_{-1.7} \times 10^{23}$ | $0.77^{+1.0}_{-0.9}$ | 24.6/24 |
| Double PL 1 | 0 ($\lesssim 1.3 \times 10^{22}$) | $-0.4^{+1.8}_{-0.6}$ | $5.9^{+6.9}_{-3.1} \times 10^{23}$ | $1.3^{+4.0}_{-1.4}$ | 50.1/46 |
| Double PL 2 | 2.52×10^{20} † | 0.6 ± 0.4 | 3.7×10^{23} ‡ | 0.77 † | 60.4/50 |
| RS+PL | 2.52×10^{20} † | $7.9^{+\infty}_{-3.3}$ | 3.7×10^{23} ‡ | 0.77 † | 59.8/50 |
| F_X (erg cm ⁻² s ⁻¹) [‡] | $3.3^{+1.4}_{-1.1} \times 10^{-13}$ * | | $5.7^{+5.9}_{-2.4} \times 10^{-12}$ ◊ | | |
| L_X (erg s ⁻¹) [‡] | $2.1^{+0.9}_{-0.7} \times 10^{42}$ * | | $3.7^{+3.9}_{-1.5} \times 10^{43}$ ◊ | | |

* determined by the fit above 4 keV.

† fixed at the Galactic value.

‡ fixed at the values determined above 4 keV.

‡ absorption-corrected values.

* evaluated in 0.5 – 10 keV by the best-fit RS+PL model.

◊ evaluated in 2 – 10 keV by the PL model above 4 keV.

Chapter 6

Analysis and Results of *Chandra* Observations

6.1 Data Reduction

6.1.1 Data reduction

The standard processing of the *Chandra* data is performed by the *Chandra* X-ray Observatory Center (CXC) at the Harvard-Smithsonian Center for Astrophysics. In the present analysis, we mainly use the fully processed science products (usually called "level-2" event files), which are provided by the CXC. The level-2 event file contains only the data which are obtained during good time intervals (GTI), when the ACIS normally operates. The gain and bias correction of individual CCD pixels are already applied to all the events in these event files. Events which are detected in pixels flagged as "bad", such as hot pixels and the pixels which is located at the node boundary, are rejected. Only the events corresponding to the *ASCA* grade of 0, 2, 3, 4 and 6 are recorded.

We further reduce the ACIS data, using the software package **CIAO** (the *Chandra* Interactive Analysis of Observation) of version 2.1, which is provided and maintained by the *Chandra* X-ray Center (CXC). We take the calibration informations of the ACIS from the **CALDB** version of 2.3, which is released to public by the CXC at March 06, 2000.

6.1.2 Background rejection

The count rate of the non-X-ray background of the ACIS occasionally increases by a factor of up to ~ 100 . This phenomenon, which is not anticipated prior to launch, is called background "flare". The flares have been observed anywhere in the orbit. They are more prominent in the BI CCDs than in the FI ones. The nature of the flares is under

investigation.

Because the IC X-rays associated with the lobes are diffuse and very faint, the detection of them is severely subject to the background flares. Therefore, according to the calibration team (Markevich 2001), we extracted the background light curves of individual observations, by removing any possible X-ray sources. We rejected the data obtained during the time when the background count rate is more than 20 % higher than the quiescent level.

6.2 3C 452

6.2.1 The X-ray image

We show the 0.3 – 7 keV raw *Chandra* ACIS image in Figure 6.1, binned by 4×4 ACIS pixels. The background events are not subtracted. The nucleus of 3C 452 is clearly detected, together with some contaminating bright point sources. Moreover, a faint diffuse X-ray emission surrounding the nucleus of 3C 452 is visible in the east-west direction.

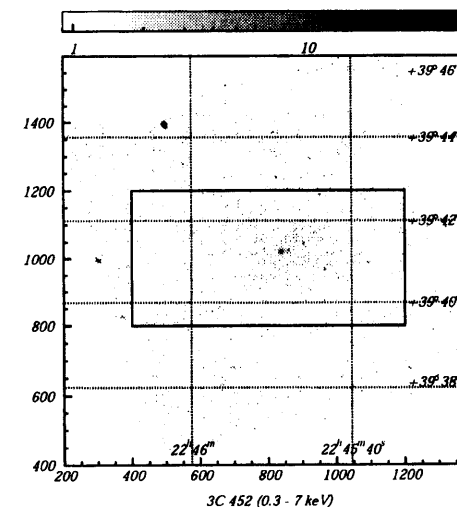


Figure 6.1: The raw 0.3 – 7 keV ACIS image of 3C 452. Only the data obtained with ACIS-S3 are displayed. The image is binned into 4×4 pixels, and hence the angular resolution of the image is 2 arcsec. The rectangular region is expanded to Figure 6.2.

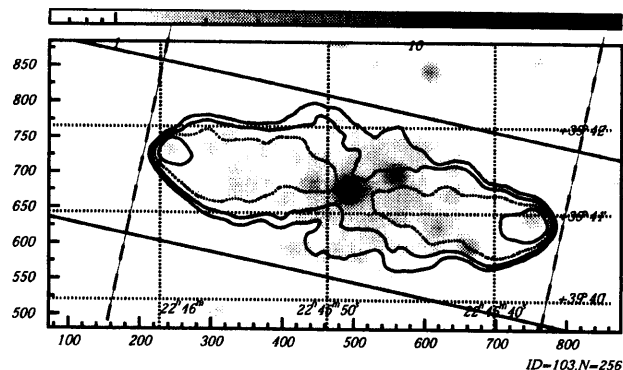


Figure 6.2: The 0.3 – 7 keV image around 3C 452, smoothed with a two dimensional Gaussian kernel of $\sigma = 4$ arcsec (8 ACIS pixels). The 1.4 GHz VLA contours are overlaid (Leahy, Bridle, and Strom 1996). The red cross represents the optical position of the host galaxy of 3C 452. The linear surface brightness profiles are extracted between the two solid lines for the directions parallel to the radio structure and between the two dashed lines for the perpendicular direction.

Figure 6.2 shows the ACIS image around 3C 452 in the same energy band, heavily smoothed with a 2-dimensional Gaussian function of $\sigma = 4$ arcsec. The 1.4 GHz VLA contours are superposed (Leahy, Bridle, and Strom 1996). The brightest X-ray peak coincides with the optical host galaxy of 3C 452, and also with the relatively faint radio nucleus, within the angular resolution of the ACIS. Furthermore, this image more clearly reveals the diffuse X-ray emission which extends up to ~ 2 arcmin (~ 160 kpc) from the nucleus. Some apparent and possible X-ray point sources, none of which have so far been reported in X-rays, are found inside the radio lobes. The diffuse component appears to fill the entire radio lobes with a relatively uniform surface brightness, in a very good positional coincidence. Therefore, its association with the lobes is secure. Because of the superior angular resolution of *Chandra*, it is almost of no doubt that the extended emission is truly of diffuse nature, rather than composed of discrete point sources.

In order to study the spatial distribution of the diffuse X-ray emission in more detail, we have projected the unsmoothed ACIS images in the soft (0.3 – 1.5 keV) and the hard (1.5 – 7 keV) bands, and the radio one, onto two directions; one parallel and the other perpendicular to the the major axis of the radio structure. In order for almost whole the

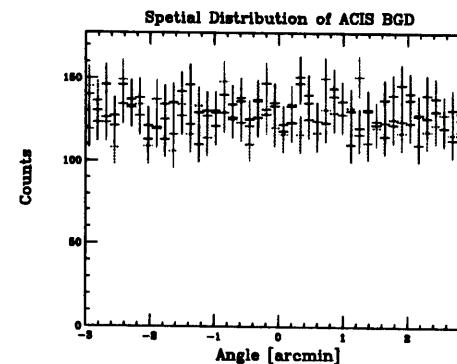


Figure 6.3: The linear profiles of the ACIS background in 0.3 – 7 keV, which are extracted from the point source removed black sky data base (Markevitch 2001). The data shown by black points are integrated over the same detector area as for the profile along the radio axis. The total exposure of this background data is ~ 136 ksec.

lobes to be included, the projection region for the former direction, which is indicated by the two solid lines in Figure 6.2, has an width of 2 arcmin and that for the latter direction, which is indicated by the two dashed lines, has an width of 5 arcmin.

The spatial distribution of the ACIS background is reported to be nonuniform, especially above 5 keV (Markevitch 2001). Then, we extracted the background profiles within some regions near the center of the ACIS-7, which have a width of 2 arcmin, using the point-source removed black sky data base (Markevitch 2001). We show the obtained background profiles in Figure 6.3. We thus confirmed that the spatial variation of the ACIS background in 0.3 – 7 keV is $\sim 7\%$.

The Galactic absorption column density toward 3C 452, $N_H = 1.2 \times 10^{21} \text{ cm}^{-2}$, is significantly higher than those for all observations included in the background data base, $N_H = (1 - 5) \times 10^{20} \text{ cm}^{-2}$. We cannot directly utilize the background profiles shown in Figure 6.3 for 3C 452, because they make us to overestimate the CXB level, and hence to underestimate the signal counts, especially below ~ 1 keV. Then, we assumed that the background is uniform around the lobes of 3C 452, and estimated the background using events in a neighboring source free region. This assumption is almost justified by Figure 6.3.

Figures 6.4 and 6.5 show the background subtracted linear surface brightness profiles around 3C 452. Indeed, the total angular extent of the diffuse X-ray component is quite similar to that of the radio structure, although the detailed structures along the radio

major axis are somewhat different between the X-ray and the radio profiles. Especially, along the major axis, the X-ray profiles reveals a center-filled morphology, while a rim-brightening feature is seen in the radio profile. These properties are also exhibited by the lobes of Fornax A (Tashiro et al. 2001) and Centaurus B (Tashiro et al. 1998), from both of which the CMB-boosted IC X-rays have already been detected. Along the lobe minor axis, the radio and X-ray profiles exhibit a closer resemblance.

Utilizing Figures 6.4 or 6.5, we also calculated the hardness ratio, by dividing the hard band profiles by the soft band ones. Figure 6.6 shows the hardness ratio profiles in the two directions, thus obtained. The hardness ratio remains rather constant (0.5 ~ 0.7) along the both direction. This means that the spectrum of the diffuse X-ray emission is relatively uniform over the lobes of 3C 452, except for the lobe periphery where there is some hint of spectral softening.

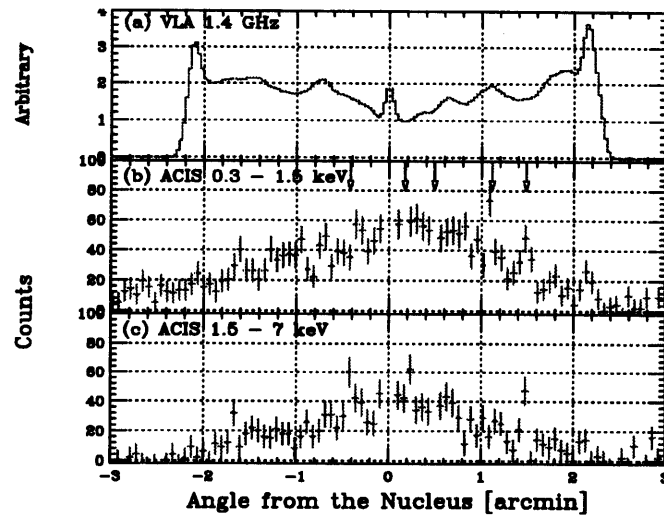


Figure 6.4: The linear profile along the major radio axis of 3C 452, in (a) 1.4 GHz, (b) 0.3 - 1.5 keV, and (c) 1.5 - 7.0 keV. The projected positions of some apparent X-ray point sources are indicated as blue arrows in panel (b). The data points for the nucleus at position 0 are too high to be included in this figure.

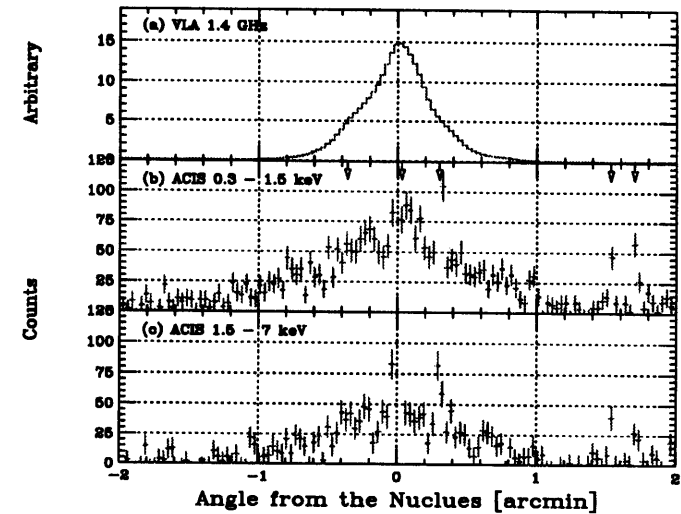


Figure 6.5: The linear profile in the direction perpendicular to the major radio axis of 3C 452, in (a) 1.4 GHz, (b) 0.3 - 1.5 keV, and (c) 1.5 - 7.0 keV. The projected positions of some apparent X-ray point sources are indicated as blue arrows in panel (b).

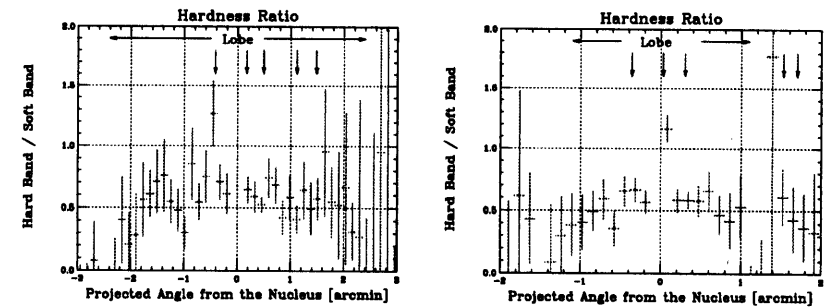


Figure 6.6: The linear profiles of the hardness ratio parallel (left) and perpendicular (right) to the radio structure. Arrows are written in the same way as in Figures 6.4 and 6.5.

6.2.2 The X-ray spectrum of the lobes

In order to examine the mechanism of the diffuse X-ray emission, we extracted the ACIS spectrum of the lobes of 3C 452. Because the hardness ratio of the diffuse X-ray sources appears approximately constant in the lobes, in order to cover the whole lobes, the data spectrum is accumulated over a region which is shown with the red ellipse in Figure 6.7, excluding a circular region with a 6 arcsec radius centered on the host galaxy. The background spectrum is integrated over a surrounding source free region, which is enclosed by the black lines in Figure 6.7. There are some contaminating X-ray point source in both regions. Then, if we found a pixel which contains more than 10 events per one binned pixel of Figure 6.1, we rejected a circular region of a radius 3 arcsec centered on the pixel. These rejected regions are indicated as some small circles in Figure 6.7.

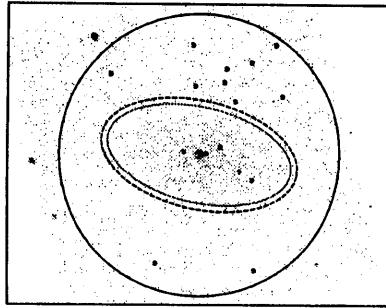


Figure 6.7: The integration region for the data (red) and the background (black) spectra.

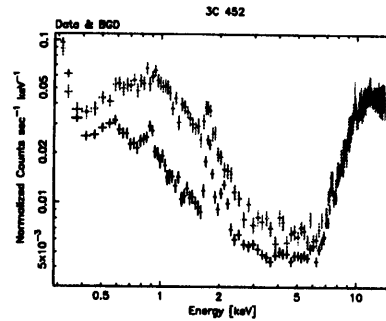


Figure 6.8: A comparison between the raw data (red) and the background (black) spectra, normalized to their integration areas.

Table 6.1: A summary of the data and the background in representative energy bands.

| Band | Data (cts) | BGD (cts) [†] | Excess (cts) | Ratio [‡] |
|--------------|-------------|------------------------|--------------|--------------------|
| 0.3 – 14 keV | 26673 ± 163 | 22474 ± 82 | 4199 ± 182 | 1.19 |
| 0.3 – 10 keV | 13356 ± 116 | 9298 ± 53 | 4058 ± 128 | 1.44 |
| 0.5 – 5 keV | 6675 ± 82 | 3274 ± 31 | 3401 ± 88 | 2.04 |
| 10 – 14 keV | 13207 ± 115 | 13058 ± 63 | 149 ± 131 | 1.01 |

[†] normalized by the integration area.

[‡] Data/BGD.

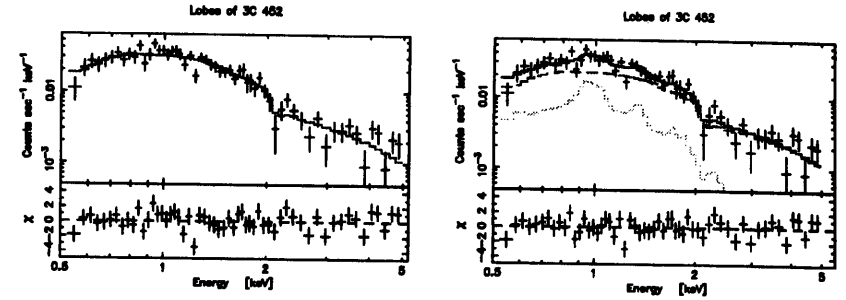


Figure 6.9: The background subtracted ACIS spectrum of the lobes of 3C 452. The histogram in the left panel shows the single PL model and those in the left panel represents the best-fit PL (blue) plus RS (green) model.

Figure 6.8 compares the data and the background ACIS spectra, and Table 6.1 summarize the total counts of the data and the background in representative energy bands. The backgrounds are normalized to the data by the integration area. The data and the background is fairly consistent above 10 keV, where the HRMA is no more efficient and hence the spectrum should be dominated by the NXB. This confirms that we have accurately evaluated the background spectrum. As is clear from the figure, the excess signal X-rays are highly significant, over wide energy range between 0.4 and 7 keV. Below we restrict our spectral analysis to the 0.5 – 5 keV range, where the excess signal is most significant (almost 40σ ; Table 6.1).

In Figure 6.9, we show the background subtracted 0.5 – 5 keV ACIS spectrum of the lobes of 3C 452, without removing the response of the ACIS. The spectrum appears relatively featureless. We tried to reproduce the spectrum with a single PL model, modified by an absorption. However, as is shown in the left panel of Figure 6.9, the data leaves significant residuals ($\chi^2/d.o.f = 1.35$), especially an excess around 1 keV.

In order to describe the excess, we introduced an RS model modified by common absorption as the PL component. A similar soft component is also detected from the lobes of Fornax A (Tashiro et al. 2001). By leaving all the model parameters free the fit has become acceptable. The best-fit model spectrum is shown in the right panel of Figure 6.9 by the histograms, and the obtained spectral parameters are summarized in Table 6.2. The best-fit temperature of the RS model becomes $kT \sim 1.3$ keV, which is roughly the same as those of the soft component of Fornax A.

For the PL plus RS model, the confidence contours of the spectral index α of the PL component and the absorption column density N_H are shown in Figure 6.10. The derived

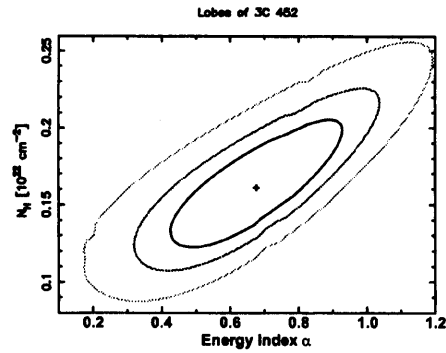


Figure 6.10: The confidence contours of the absorption column density N_{H} and the spectral index α for the PL plus RS model.

Table 6.2: The best-fit spectral parameters of the lobes of 3C 452.

| | Hard Component | | Soft Component | | $\chi^2/d.o.f$ |
|-------------|--------------------------|------------------------|---------------------------|------------------------|----------------|
| | N_{H}^{\dagger} | α or kT (keV) | S_{X}^{\ddagger} | kT (keV) | |
| PL | 2.1 ± 0.5 | $1.02^{+0.21}_{-0.19}$ | 66^{+10}_{-9} | – | 72.8/54 |
| PL + RS | $1.6^{+0.5}_{-0.4}$ | 0.68 ± 0.28 | 41^{+15}_{-14} | $1.36^{+0.47}_{-0.29}$ | 62.0/52 |
| | 1.75 ± 0.15 | 0.78^* | 46^{+6}_{-9} | $1.33^{+0.48}_{-0.28}$ | 62.4/53 |
| Bremss + RS | $1.4^{+0.3}_{-0.4}$ | $6.0^{+13.5}_{-1.7}$ | – | $1.28^{+0.29}_{-0.17}$ | 63.7/52 |

\dagger in 10^{21}cm^{-2}

\ddagger evaluated at 1 keV in nJy

* fixed at the radio SR index

N_{H} is consistent with the Galactic value, $N_{\text{H}} = 1.2 \times 10^{21} \text{cm}^{-2}$. The best-fit spectral index becomes very hard, $\alpha = 0.68 \pm 0.28$, and consistent with the SR radio index, $\alpha_{\text{SR}} = 0.78$, observed from the lobes of 3C 452, within a statistical error.

We also tried to describe the observed spectrum, replacing the PL model with a thermal Bremss model. The model is statistically acceptable with the parameters for the RS component almost unchanged. However, the obtained temperature, $kT \sim 6 \text{keV}$, and the corresponding thermal pressure, $p_e \sim 1 \times 10^{-11} \text{dyne cm}^{-2}$, are both too high. We consider this situation unrealistic, like in the case of the NGC 612 and 4C 73.08.

Based on the clear spatial association and the agreement in the spectral shapes, we conclude that the diffuse X-rays observed with ACIS from the lobes of 3C 452 are of the IC origin. In Chapter 7, we estimate the physical parameters in the lobes, utilizing the multi frequency spectra.

6.2.3 The X-ray spectrum of the nucleus

We have extracted the ACIS spectrum within a circular region of a radius 5 arcsec, centered on the host galaxy of 3C 452. The background spectrum was accumulated over a concentric annulus with an inner and outer radii of 6 arcsec and 9 arcsec, respectively. Figure 6.11 shows the background subtracted ACIS spectrum of the host galaxy of 3C 452 in the 0.5 – 10 keV energy range. The spectrum resembles those of so-called type II AGNs, like the cases of NGC 612 and 4C 73.08. This is quite natural, because 3C 452 is usually classified into narrow line radio galaxies. In the following, we evaluate only the hard component that is dominating above 4 keV, supposing that it originates from the obscured nucleus of 3C 452.

We first tried to describe the spectrum above 4 keV with a single PL model modified by an absorption. However, as shown in the left panel of Figure 6.12, the fit is unacceptable; the data leaves significant residuals around 6 keV, which look like an Fe $K\alpha$ emission line. The Fe $K\alpha$ lines are often observed from AGNs, including radio galaxies (Samburuna et al. 1999). Then, we introduce a Gaussian in order to evaluate this feature. The fit is successful and the best-fit spectral parameters are summarized in Table 6.3. The obtained redshift-corrected center energy for the additional Gaussian coincides well with that of neutral Fe $K\alpha$ lines, and the width, $\sigma \lesssim 0.2 \text{keV}$, and the equivalent width, 0.15 keV, both agree with those from typical radio galaxies.

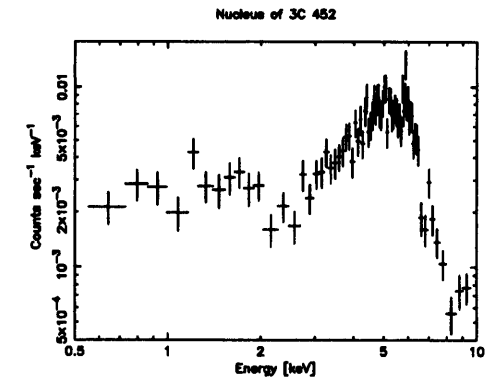


Figure 6.11: The background subtracted ACIS spectrum of the nucleus of 3C 452 in 0.5 – 10 keV energy range.

Figure 6.13 shows the confidence contours of the column density N_H and the spectral index α . The obtained spectral index, $\alpha \sim 0.8$, and the absorption corrected 2–10 keV continuum luminosity, $L_X \sim 8 \times 10^{43} \text{ erg s}^{-1}$, are both quite reasonable for those of the nucleus of radio galaxies (Samburuna et al. 1999). Thus, the hard component is naturally interpreted as an emission from the active nucleus of 3C 452, like in the case of NGC 612 and 4C 73.08.

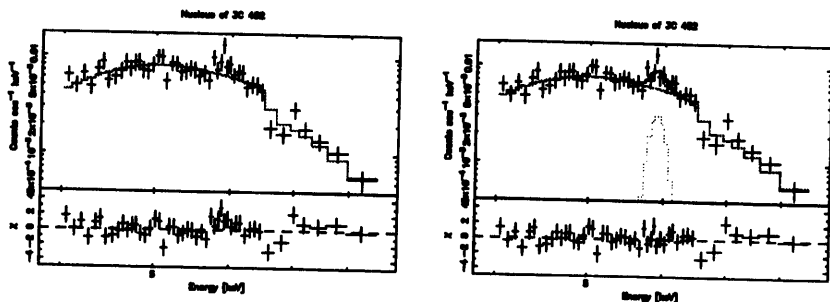


Figure 6.12: The background subtracted ACIS spectrum of the nucleus of 3C 452, above 4 keV. The histogram in the left panel shows a prediction by the single PL model, and that in the right panel a prediction by the best-fit PL plus Gaussian model.

Table 6.3: The best-fit spectral parameters of the nucleus of 3C 452, determined by the spectrum above 4 keV.

| | Continuum | | Line | | | |
|-------------|-------------------------------------|------------------------|---------------|------------------------|--------|----------------|
| | N_H † | α | E ‡ | σ ° | EW * | $\chi^2/d.o.f$ |
| PL | 5.2 ± 1.0 | $1.05^{+0.60}_{-0.57}$ | – | – | – | 62.2/45 |
| PL+Gaussian | $4.5^{+1.1}_{-0.5}$ | $0.77^{+0.64}_{-0.61}$ | 6.4 ± 0.1 | $0.11^{+0.13}_{-0.11}$ | 0.15 | 48.6/42 |
| F_X † | $6.3^{+3.3}_{-1.9} \times 10^{-12}$ | | – | – | – | – |
| L_X * | $8.1^{+4.2}_{-2.4} \times 10^{43}$ | | – | – | – | – |

† in 10^{23} cm^{-2} .

‡ redshift corrected center energy in keV.

° line width in keV.

* line equivalent width in keV.

‡ absorption corrected 2–10 keV continuum flux in $\text{erg cm}^{-2} \text{ s}^{-1}$.

* absorption corrected 2–10 keV continuum luminosity in erg s^{-1} .

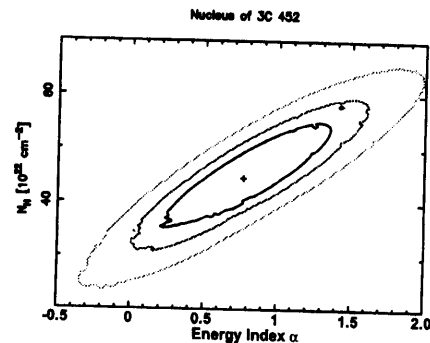


Figure 6.13: The confidence contours of the absorption column density and the spectral index α .

6.3 Pictor A

6.3.1 The X-ray image

We show the 0.3–7 keV raw ACIS image of Pictor A in Figure 6.14, binned by 4×4 ACIS pixels. The data are accumulated only from the observation of ID = 346 (see Table 4.6). The nucleus of Pictor A is clearly detected, although its trailed image is also visible because its flux is very high. The west jet emanating from the nucleus toward nearly due west is also detected, ending at the bright X-ray hot spot, while the east jet and hot spot are both very faint in X-rays. Moreover, a diffuse faint X-ray emission surrounding the nucleus of Pictor A is clearly visible, extending toward the east-west direction, in both ACIS 6 and ACIS 7. Using the same data, Willson et al. (2001) have already reported the X-ray detections of its nucleus, its west jet, and its west hot spot, but they have not yet become aware of this diffuse X-ray source.

Figure 6.15 shows the ACIS image around Pictor A, heavily smoothed with a 2-dimensional Gaussian of $\sigma = 4$ arcsec. As shown in this image, the X-ray positions of the nucleus and the east hot spot clearly coincide with respective radio counterparts. Furthermore, this image more clearly reveals the faint diffuse emission, which extends up to ~ 4 arcmin (~ 150 kpc). Like in the case of 3C 452, the diffuse emission appears to be relatively uniformly distributed over the whole radio lobes, in a fairly good positional coincidence, although the west lobe is intersected by the CCD gaps across which the energy responses are different.

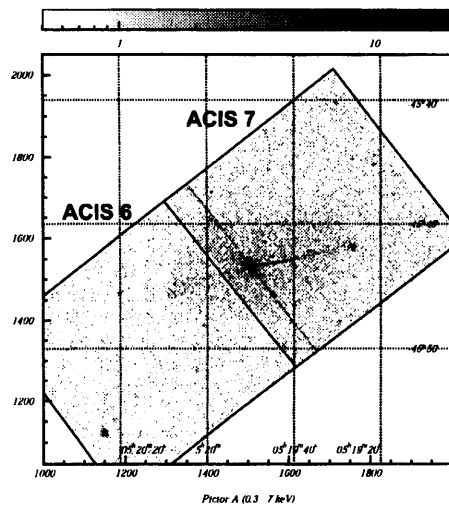


Figure 6.14: The 0.3 – 7 keV raw ACIS image of Pictor A. Only the data obtained with ACIS 6 and 7 in the observation of ID = 346 are displayed. The image is binned into 4 × 4 pixels, and hence the angular resolution of the image is 2 arcsec. The straight line running from north-east to south-west is the trailed image of the nucleus.

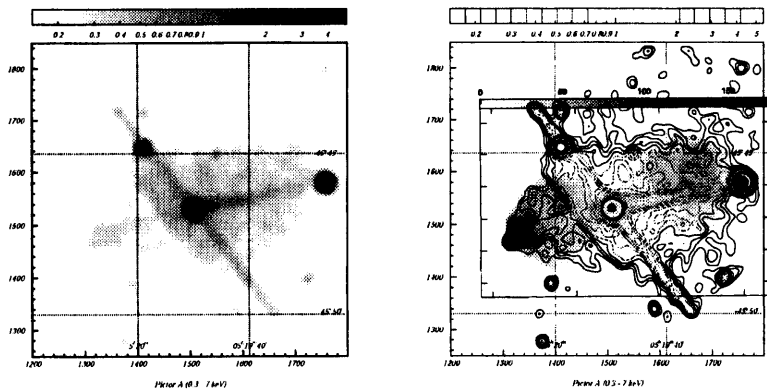


Figure 6.15: The 0.3 – 7 keV ACIS image around Pictor A, smoothed with a 2-dimensional Gaussian function of $\sigma = 4$ arcsec. (left) The X-ray color image. (right) The X-ray contours overlaid on the VLA 1.465 GHz gray scale image (Perlay et al, 1997).

6.3.2 The X-ray spectrum of the west lobe

We examine the X-ray spectrum of the east lobe of Pictor A, which is observed over the entire field of view of ACIS 7. The data spectrum is accumulated over a radius of 2 arcmin, (the red circle in Figure 6.16). We rejected the data within a circle of a radius 20 arcsec centered on the nucleus, within another circle of a radius 15 arcsec centered on the hot spot, and within two elongated rectangles covering the jet and the trailed image. We also excluded some possible point sources by the same criterion adopted for 3C 452. All of the rejected regions are shown with the black dashed lines in Figure 6.16.

As is clear from the X-ray image, a considerable fraction of the ACIS 7 field of view is occupied by various sources, and the remaining source-free regions of ACIS 7 are located mostly at a far side from the aimpoint, where the HRMA effective area decreases even in the soft X-ray energies ($\lesssim 90\%$ of that of the aimpoint; see Figure 3.13). Therefore, instead of using the source-free regions for the background subtraction, we integrated the background spectrum from the point-source removed blank sky data base (Markevitch, 2001), over the same CCD area as for the data one.

As shown in Figure 6.17 and Table 6.4, the excess signal X-rays are highly significant over a wide energy range between 0.3 and almost 6 keV, while the data and the background well agree with each other above ~ 10 keV. This confirms accuracy of the background estimation. In the following, we restrict our spectral analysis to the 0.3 – 5 keV range, where the excess signal is most significant (almost 30σ ; Table 6.4).

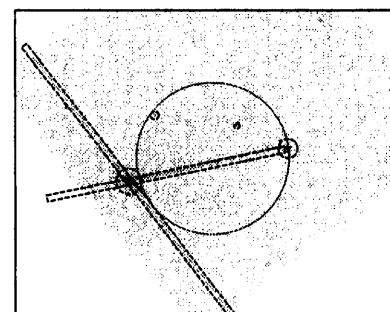


Figure 6.16: The integration region for the spectrum (red circle). The data inside black boxes or circles are rejected.

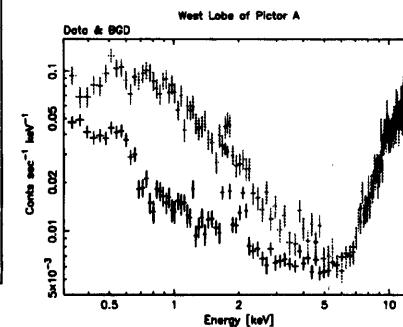


Figure 6.17: A comparison between the raw (red) and the background (black) spectra, normalized to their exposure.

Table 6.4: A summary of the data and background in representative energy bands.

| Band | Signal (cts) | BGD (cts) † | Excess (cts) | Ratio ‡ | |
|--------------|--------------|-------------|--------------|---------|------------------|
| 0.3 – 12 keV | 7464 ± 86 | 5526 ± 33 | 1938 ± 92 | 1.35 | |
| 0.3 – 5 keV | 3186 ± 56 | 1243 ± 16 | 1943 ± 58 | 2.56 | Used for fitting |
| 10 – 12 keV | 2324 ± 48 | 2288 ± 21 | 36 ± 52 | 1.01 | Dominated by NXB |

† normalized by the exposure ‡ Signal/BGD.

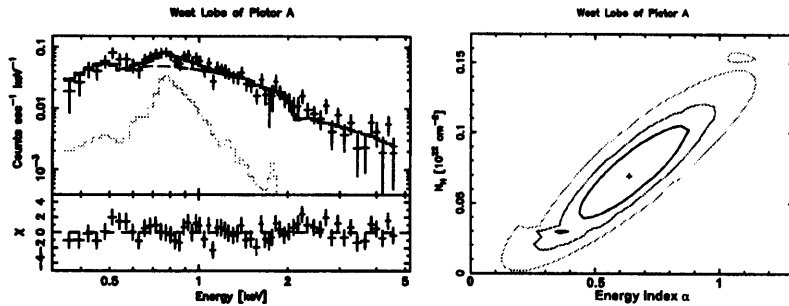
Figure 6.18: The background subtracted ACIS spectrum of the west lobe of Pictor A. The histograms in the left panel show the best-fit PL plus RS model. The right panel shows the confidence contours of the absorption column density N_{H} and the spectral index α .

Table 6.5: The best-fit spectral parameters of the west lobe of Pictor A.

| Model | Hard Component | | Soft Component | | $\chi^2/d.o.f$ |
|-------------|--------------------------|------------------------|---------------------------|------------------------|----------------|
| | N_{H}^{\dagger} | α or kT (keV) | S_{X}^{\ddagger} | kT (keV) | |
| PL + RS | $7.0^{3.0}_{3.1}$ | $0.64^{+0.23}_{-0.30}$ | 56^{+10}_{-14} | $0.76^{+0.20}_{-0.32}$ | 65.6/57 |
| | $8.0^{+1.9}_{-1.7}$ | 0.72* | 59^{+5}_{-9} | $0.66^{+0.19}_{-0.32}$ | 65.8/58 |
| Bremss + RS | $3.6^{+2.5}_{-2.3}$ | $9.5^{+35.1}_{-4.4}$ | – | $0.80^{+0.07}_{-0.41}$ | 66.6/57 |

† in 10^{20}cm^{-2} .

* fixed at the SR index.

‡ evaluated at 1 keV in the unit of nJy.

The left panel of Figure 6.18 shows the background subtracted ACIS spectrum of the west lobe of Pictor A, obtained in this way. We fitted the spectrum with a PL plus RS model modified by a common absorption, like in the case of 3C 452. As shown by the histogram in Figure 6.18, the fit is almost acceptable, and yields the parameters shown in Table 6.5. The temperature of the soft component, $kT \sim 0.8$ keV, becomes nearly the same as those of 3C 452 and Fornax A (Tashiro et al. 2001). As shown in the right panel of Figure 6.18, the derived column density is consistent with the Galactic value, $N_{\text{H}} = 4.2 \times 10^{20} \text{cm}^{-2}$. Moreover, the spectral index turns out to be very hard, $\alpha = 0.64^{+0.23}_{-0.3}$, and agrees with the SR radio index $\alpha_{\text{SR}} = 0.72$, within a statistical error.

We also tried to fit the spectrum replacing the PL model with a Bremss model. Although the fit is statistically acceptable with the parameter for the RS component unchanged, the derived temperature for the Bremss component again becomes unusually high, $kT \sim 10$ keV. Thus, we consider this situation unrealistic, as in the other lobes.

Based on the spatial association and the agreement in the spectral shapes with the radio lobes, we conclude that the diffuse X-rays observed with ACIS from the lobes of Pictor A are of the IC origin, like in the case of the other lobes. This is the second detection of the lobe IC X-rays with the *Chandra* ACIS, subsequent to the lobes of 3C 452. In Chapter 7, we estimate the physical parameters in the lobes, utilizing the multi frequency spectra.

6.3.3 The X-ray spectrum of the nucleus

We also examine the X-ray activity of the nucleus of Pictor A. However, the sufficiently high X-ray flux of the nucleus is thought to cause sever event pileups in the observation of ID = 346. We, therefore, use the data obtained in the observation of ID = 443, which was performed with a shorter frame time of 0.4 sec, employing a 1/8 subarray (i.e. a narrow field of view). We accumulated the spectrum over a circular region with a radius 12 arcsec, centered on the nucleus, and the background within a concentric annulus with an inner and outer radii of 14 and 24 arcsec, respectively.

Figure 6.19 shows the background subtracted ACIS spectrum of the nucleus of Pictor A. The spectrum is quite featureless and well reproduced by a PL model modified by an absorption, as shown by the histograms in Figure 6.19. The derived parameters are shown in Table 6.6. The best-fit index, $\alpha \sim 0.6$, is slightly harder than $\alpha \sim 0.8$, obtained from the *ASCA* observation performed in 1996, and the obtained absorption-corrected 2 – 10 keV luminosity becomes $L_{\text{X}} \sim 1 \times 10^{43} \text{erg s}^{-1}$, which is almost one third that measured with the *ASCA* (Eracleous and Halpern 1998; Sambruna et al. 1999).

Table 6.6: The best-fit spectral parameters of the nucleus of Pictor A.

| | N_{H}^{\dagger} | α | F_{X}^{\ddagger} | L_{X}^* | $\chi^2/d.o.f$ |
|----|--------------------------|------------------------|---------------------------|------------------------|----------------|
| PL | 7.9 ± 1.2 | $0.60^{+0.07}_{-0.06}$ | $5.3^{+0.4}_{-0.3}$ | $1.25^{+0.09}_{-0.07}$ | 110.3/114 |

\dagger in 10^{20}cm^{-2} .

\ddagger absorption corrected 2 – 10 keV flux in $10^{-12} \text{erg cm}^{-2} \text{s}^{-1}$.

* absorption corrected 2 – 10 keV luminosity in $10^{43} \text{erg s}^{-1}$.

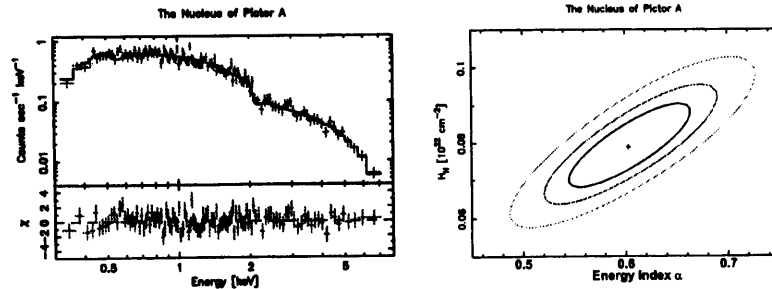


Figure 6.19: (left) The background subtracted ACIS spectrum of the nucleus of Pictor A. The histogram shows the best-fit PL model. (right) The confidence contours of the absorption column density and the spectral index α .

6.4 Hot Spots

Radio hot spots of radio galaxies are thought to be a shock front at the jet terminal. In order to understand the jet phenomena, we think that it is important to examine the energetics in the hot spots. Here, we analyze the X-ray spectra of four bright radio hot spots detected with the ACIS.

6.4.1 The west hot spot of Pictor A

We have extracted the ACIS spectra of the west hot spot of Pictor A, within circular regions of a radius 6 arcsec centered on the hot spot. We accumulated the background spectra over a concentric annulus with an inner and outer radii of 7.5 arcsec and 12 arcsec, respectively.

Figure 6.20 shows the background subtracted ACIS spectrum of the west hot spot. The spectrum is rather featureless and well reproduced by a PL model or a Brems model. Table 6.7 summarizes the best-fit spectral parameters, which are consistent with those of Wilson et al. (2001).

The derived temperature for the Brems model becomes a moderately high, $kT \sim 3$ keV. Then, we think that a non-thermal process is more favorable as the origin of the X-rays from the hot spot. However, the obtained spectral index, $\alpha \sim 1$, is slightly softer than the SR radio index, $\alpha_{\text{SR}} = 0.74$ (Meisenheimer et al. 1997).

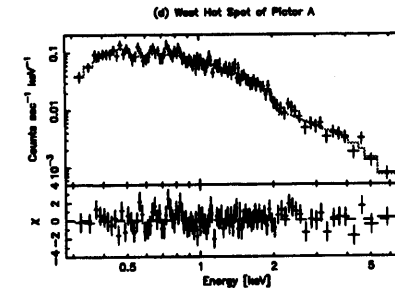


Figure 6.20: The background subtracted ACIS spectrum of the west hot spot of Pictor A. The histogram shows the best-fit PL model.

6.4.2 Cygnus A

We show the raw 0.3 – 7 keV ACIS image of Cygnus A in Figure 6.21. As already reported by Wilson et al. (2000), the nucleus of Cygnus A and two bright radio hot spots, usually

called A and D, are clearly detected in this image, together with a diffuse cluster emission surrounding them. The X-ray position of the nucleus coincides with that of the optical galaxy, and the X-ray positions of the two hot spots are both coincident with those of the radio counterparts, within the angular resolution of the ACIS.

We have extracted the ACIS spectra of the hot spots A and D, within circular regions of a radius 2.5 arcsec centered on them, and background spectra over concentric annuli with an inner and outer radii of 3 arcsec and 5 arcsec, respectively. Figure 6.22 shows the background subtracted ACIS spectra of these two hot spots.

The derived spectra are quite featureless. We have successfully described them, with a single PL model or a Brems model. The best-fit spectral parameters are shown in Table 6.7. These parameters are almost consistent with the results of Wilson et al. (2000).

The obtained absorption column densities for individual hot spots are consistent with the Galactic value, $N_H = 3.6 \times 10^{21} \text{ cm}^{-2}$, in both models. The best-fit temperatures of the Brems model become $kT \gtrsim 5 \text{ keV}$ for hot spot A and $kT \gtrsim 3 \text{ keV}$ for the hot spot D. We consider these high temperatures unrealistic. On the other hand, the derived spectral indices, $\alpha \sim 0.7$ and ~ 0.8 for hot spots A and D, respectively, almost agree with the SR indices $\alpha_{SR} = 0.87$ and 0.80 for hot spots A and D, respectively. We therefore ascribe the X-rays from these two hot spots to be IC origin, as already concluded by Wilson et al. (2000).

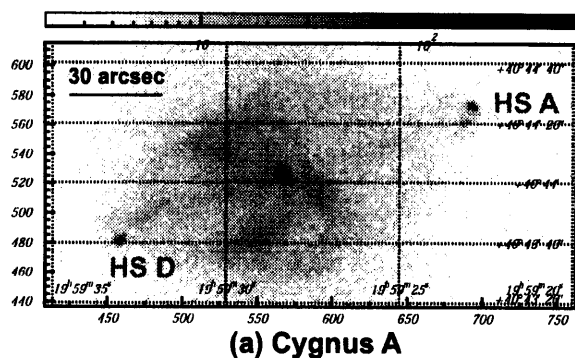


Figure 6.21: The 0.3 – 7 keV raw ACIS image of Cygnus A, binned by 2×2 ACIS pixels. Only the data obtained in the observation of ID = 360 are displayed.

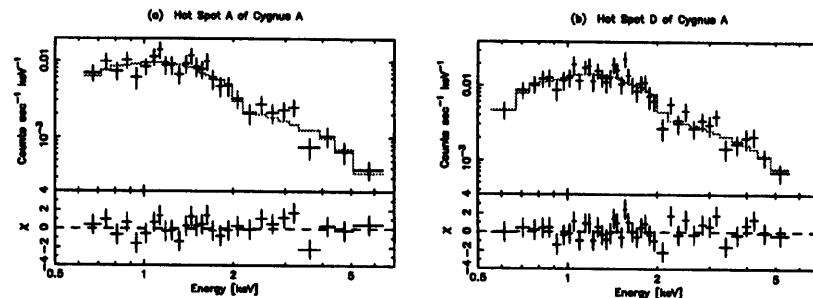


Figure 6.22: The background subtracted ACIS spectra of the hot spots A (*left*) and D (*right*). The histograms in both panels show the best-fit PL model to the individual spectra.

6.4.3 3C 123

We show the raw 0.3 – 7 keV ACIS image of 3C 123 in Figure 6.23. As already reported by Hardcastle et al. (2001), the nucleus and the east radio bright hot spot are clearly detected, together with a diffuse cluster emission surrounding them, while the west one which is faint in radio is also faint in X-rays. The X-ray position of the nucleus coincides with that of the optical galaxy, and the X-ray positions of the east hot spot with the radio position, within the angular resolution of the ACIS.

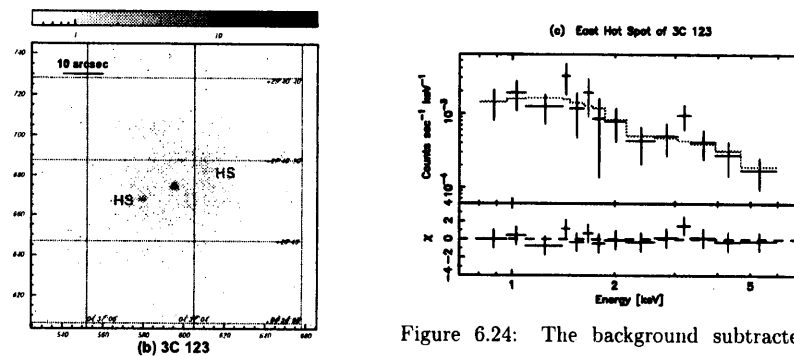


Figure 6.23: The 0.3 – 7 keV raw ACIS image of 3C 123.

Figure 6.24: The background subtracted ACIS spectrum of the east hot spot of 3C 123. The histogram shows the best-fit PL model.

We have extracted the ACIS spectrum of the east hot spot of 3C 123, in the same way as for the two hot spots of Cygnus A. Figure 6.24 shows the background subtracted ACIS spectrum of the hot spot. We have reproduced the spectrum with a single PL model or a Brems model. The spectrum is rather hard and the obtained temperature for the Brems model becomes unrealistically high, $kT \gg 10$ keV. On the other hand, as show in Table 6.7, the best-fit spectral index, $\alpha = -0.6 \sim 0.8$, is consistent with the SR index $\alpha_{\text{SR}} \sim 0.76$, though with large errors. We therefore think that the X-rays from the hot spot of 3C 123 arise via the IC scattering by the SR electrons in the hot spot as already concluded by Hardcastle et al. (2001).

Table 6.7: A summary of the spectral parameters of the hot spots.

| Hot Spot | Model | N_{H}^{\dagger} | α or kT (keV) | S_{X}^{\ddagger} | $\chi^2/d.o.f$ |
|----------|---------|--------------------------|------------------------|---------------------------|----------------|
| Pictor A | West PL | 7.2 ± 1.4 | $1.04_{-0.09}^{+0.1}$ | 90 ± 6 | 86.6/102 |
| | Bremss | $2.5_{-0.8}^{+0.9}$ | $3.1_{-0.4}^{+0.5}$ | - | 96.9/102 |
| Cygnus A | A PL | $2.5_{-1.1}^{+1.2}$ | $0.66_{-0.26}^{+0.29}$ | 18_{-5}^{+7} | 25.0/26 |
| | Bremss | $1.9_{-0.9}^{+1.1}$ | $8.6_{-4.0}^{+16}$ | - | 25.06/26 |
| | D PL | 3.6 ± 0.9 | $0.77_{-0.22}^{+0.24}$ | 33_{-6}^{+9} | 39.1/39 |
| | Bremss | 2.9 ± 0.6 | $6.5_{-2.2}^{+4.5}$ | - | 39.4/39 |
| 3C 123 | East PL | $1.8 (\lesssim 7.1)$ | $0_{-0.6}^{+0.8}$ | $2.5_{-1.3}^{+3.8}$ | 10.8/12 |

† in 10^{20} cm^{-2} .

‡ evaluated at 1 keV in nJy.

Chapter 7

Discussion

7.1 Energetics in Radio Lobes

7.1.1 Multi frequency spectra

Through the analyses presented in Chapter 5 and Chapter 6, using the *ASCA* GIS and the *Chandra* ACIS, we have detected the diffuse faint X-ray sources associated with the lobes of four radio galaxies, NGC 612, 4C 73.08, 3C 452, and Pictor A. The spectrum of the diffuse X-ray emission from each radio lobe is well described by a hard PL model, and the derived spectral index is consistent with the SR radio index, α_{SR} . The latter property is visualized in Figure 7.1, which gives the multi-frequency spectra of these radio lobes. Because of this agreement in the spectral shapes with the SR spectrum, and their spatial association to the radio lobes, we conclude that these diffuse X-rays arise via the IC scattering of some seed photons by the SR electrons in radio lobes. Table 7.1 summarizes the spectral parameters of the IC X-ray emission, which are measured from our analysis, and those of the SR radio emission. The X-ray flux density of the west lobe of 4C 73.08 is evaluated from that of its east lobe, using the surface brightness profile in the soft energy band, shown in Figure 5.8, although we have not performed a detailed spectral fitting to the X-ray spectrum of this lobe.

In the following, we calculate the energy densities of the electrons and the magnetic fields in these radio lobes, u_e and u_m , respectively, by comparing the SR radio flux densities, S_{SR} , and those IC X-rays, S_{IC} .

7.1.2 Candidates for seed photons

As already mentioned in §2.3.3, several different radiation sources can provide the seed photons for the IC scattering in radio lobes; these include the CMB, the IR radiation

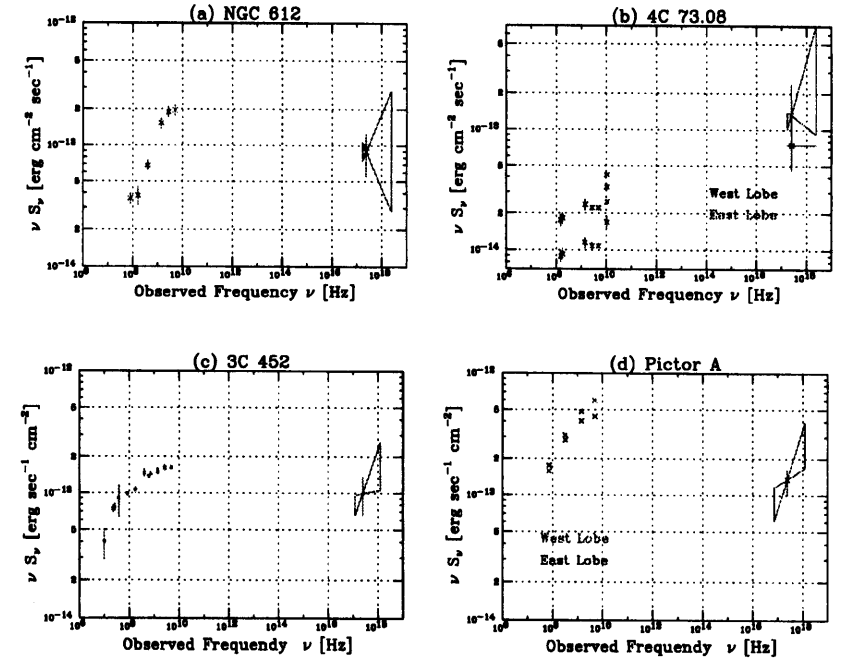


Figure 7.1: The spectral energy distributions of radio lobes. (a) NGC 612. The radio data are taken from Ekers et al. (1978). (b) 4C 73.08. The radio data are from Mayer (1979), Kuhr et al. (1979), and Saripalli et al. (1996). (c) 3C 452. The radio data are from Laing and Peacock (1980), Kuhr et al. (1979), and Jägers (1987). (d) Pictor A. The radio data are from Perley et al. (1997). As the IC X-ray spectra of the lobes of 3C 452 and Pictor A, only their PL components are shown.

Table 7.1: A summary of spectral parameters of the SR radio emission and the IC X-rays from individual lobes.

| Lobe | | SR Radio | | IC X-ray | |
|----------|------|----------------|------------------|------------------------|--------------------|
| | | α_{SR} | S_{SR}^\dagger | α_{IC} | S_{IC}^\ddagger |
| NGC 612 | Both | 0.6 ± 0.08 | 10.9 ± 1.1 | 1.0 ± 0.5 | 37^{+14}_{-12} |
| 4C 73.08 | East | 0.85 | 0.81 ± 0.08 | $0.65^{+0.51}_{-0.38}$ | 54^{+45}_{-21} |
| | West | 0.85 | 1.66 ± 0.08 | — | $31^{+25}_{-12}^*$ |
| 3C 452 | Both | 0.78 | 10.9 | 0.68 ± 0.28 | 41^{+15}_{-14} |
| Pictor A | West | 0.72 | 32.9 | $0.64^{+0.23}_{-0.30}$ | 56^{+10}_{-14} |
| | East | 0.79 | 27.9 | — | — |

† flux density at 1.4 GHz in the unit of Jy.

‡ flux density at 1 keV in the unit of nJy.

* scaled value from the X-ray flux density of its east lobe.

from their nucleus, and the SR photons in the radio lobes themselves. We here evaluate their energy densities, in order to identify the dominant seed photon population in the radio lobes.

We calculate the energy densities of the CMB, u_{CMB} , using equation (2.34). The energy density of the IR photons is written as $u_{IR} = L_{IR}/4\pi r^2$, where L_{IR} is the IR luminosity of the nucleus, and r is the distance from the nucleus. We assume $L_{IR} \sim 10L_X$, where L_X is the observed 2 – 10 keV X-ray luminosity, considering the typical spectrum of quasars (Sanders et al. 1994), and average u_{IR} over the whole radio lobes. We estimate the energy densities of the SR photons, u_{SR} , by averaging the observed SR flux over the radio lobes. Table 7.2 summarizes the energy densities of these possible seed photons, thus obtained. Clearly, u_{CMB} dominates u_{IR} and u_{SR} by more than an order of magnitude, at least in these lobes.

If u_{IR} dominated u_{CMB} and u_{SR} , the IC X-rays would become brighter toward the nucleus, and moreover, the far-side lobe should appear brighter than the near-side one, as reviewed in §2.3.3. Alternatively, if SR photons dominantly provided seed photons, the X-ray surface brightness profile would become similar to those of the SR radio profile. In disagreement with these expectations, the observed IC X-ray are relatively uniformly distributed over the whole lobes in each radio galaxy. We hence conclude that the dominant seed photons are provided by the CMB, of which the spatial distribution is highly uniform all over the universe.

Table 7.2: A comparison of energy densities of possible seed photon sources in radio lobes.

| Lobes | | u_{CMB}^* | u_{IR}^\dagger | u_{SR}^\ddagger |
|----------|------|-----------------------|--------------------------|--------------------------|
| NGC 612 | Both | 4.6×10^{-13} | $\sim 3 \times 10^{-15}$ | $\sim 5 \times 10^{-18}$ |
| 4C 73.08 | East | 5.1×10^{-13} | $\sim 1 \times 10^{-15}$ | $\sim 1 \times 10^{-17}$ |
| | West | 5.1×10^{-13} | $\sim 4 \times 10^{-15}$ | $\sim 2 \times 10^{-17}$ |
| 3C 452 | Both | 5.6×10^{-13} | $\sim 3 \times 10^{-14}$ | $\sim 6 \times 10^{-17}$ |
| Pictor A | West | 4.7×10^{-13} | $\sim 7 \times 10^{-15}$ | $\sim 5 \times 10^{-17}$ |

all values are shown in the unit of erg cm^{-3} .

* calculated from equation (2.34).

† averaged over the individual lobes, assuming $L_{IR} \sim 10L_X$ for the nucleus.

‡ evaluated from the observed SR spectrum, averaged over the individual lobes.

7.1.3 Energy densities of electrons and magnetic fields

Now that we have confirmed that the CMB dominates the seed photons, we next calculate the physical parameters in the radio lobes. We simply assume that the electron spectrum in each lobe is a single power law and that its spectral index is $p = 2\alpha_{SR} + 1$, because the errors in α_{SR} are typically smaller than those in the IC X-ray index, α_{IC} . We also assume that the upper and lower limits of the electron Lorentz factor are $\gamma_1 = 10^3$ and $\gamma_2 = 10^5$, respectively. We choose this range in order to cover almost all of the observable SR and IC frequencies; γ_1 corresponds to that of the electrons from which the IC X-ray photons of 1 keV are produced [see equation (2.36)], and γ_2 corresponds to the electrons which radiate the SR photons of 10 ~ 50 GHz, assuming B_{mc} in the radio lobes [see equation (2.4)]. Then, we can directly measure B , and hence u_m , using equation (2.39).

As is apparent from equation (2.40), we have to precisely estimate their volumes, V , in order to calculate u_e in these lobes. We here assume that the SR radio and the IC X-ray emission arise from the same spatial region, which we in turn identify with those regions where the radio surface brightness is higher than the noise level. This is because the angular resolutions of the VLA radio images are typically better than those of X-ray ones. We further assume that three dimensional shapes of the lobes are symmetric about the radio axis of the lobes. This is schematically explained in Figure 7.2. These assumption allow us to calculate V , with a typical accuracy of $\sim 50\%$.

By substituting S_{SR} , S_{IC} and α_{SR} listed in Table 7.1 and V estimated as shown in Figure 7.2 for equations (2.39) and (2.40), we obtain the physical parameters averaged over the individual radio lobes. These parameters are summarized in Table 7.3, together with the assumed V . We typically find $u_e = 10^{-13} \sim 10^{-12} \text{ erg cm}^{-3}$ and $u_m = 5 \times 10^{-15} \sim$

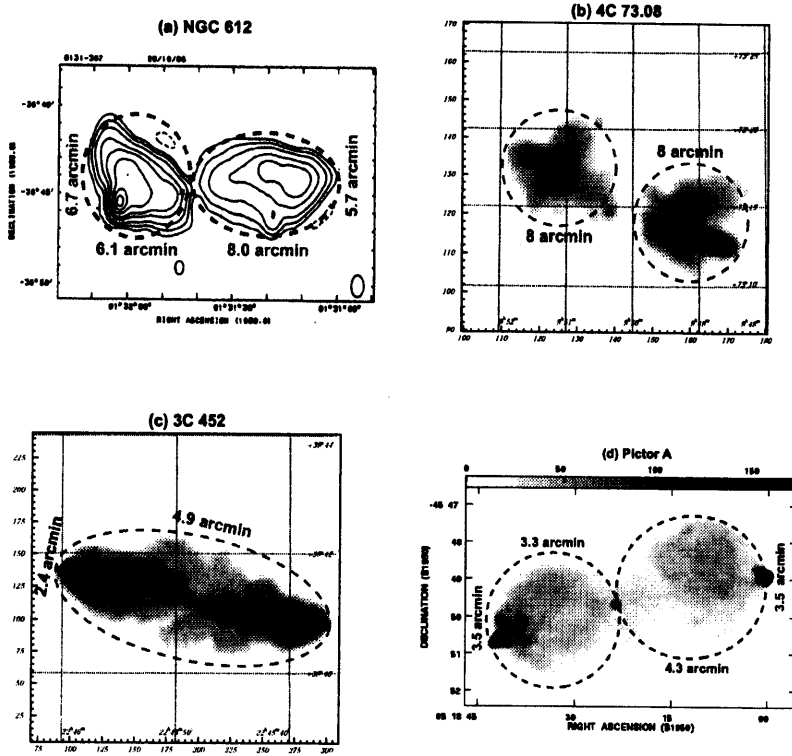


Figure 7.2: Schematic drawings which show how to estimate the volume of the lobes.

$5 \times 10^{-13} \text{ erg cm}^{-3}$; the latter corresponds to $B = 0.3 \sim 3 \mu\text{G}$.

Figure 7.3 shows the relation between u_e and u_m . This figure suggests two important implications. One is that the equipartition between u_e and u_m is no more achieved in these lobes, and that u_e tends to dominate u_m by nearly an order of magnitude. The other is that u_m tends to be smaller than u_{CMB} . This means that in the lobes relativistic electrons are mainly "cooled" by the IC energy losses.

While u_e can be subject to the systematic errors in the estimation V , the total electron energy, is free from this uncertainty, because it is the quality that can be deduced directly from the spatially-integrated IC flux. Accordingly, let us compare the spatially-integrated total energies in the particles and fields, $u_e V$ and $u_e V$, respectively. For 4C 73.08, we

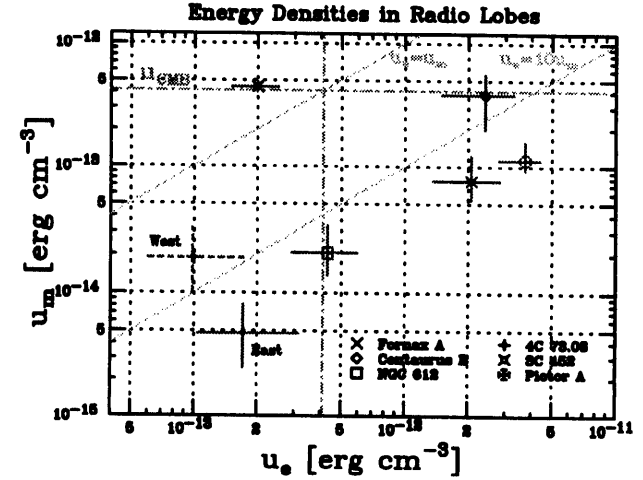


Figure 7.3: The relation between u_e and u_m in each lobe. The data for the lobes of Fornax A and Centaurus B are from Tashiro et al. (2001) and Tashiro et al. (1998), respectively. Two green dashed lines show u_{CMB} , neglecting the redshift dependence.

add energies in the east and west lobes. For Fornax A and Pictor A, our measurements of u_e and u_m have been limited to their single lobes. We found no apparent difference in u_e and u_m between a pair of lobes of the other targets, excluding 4C 73.08. We therefore evaluate the total energies in the lobes of Fornax A and Pictor A, by multiplying the energy densities in their single lobes by their total volume. Table 7.4 summarizes the obtained total electron and magnetic field energies in the lobes.

Figure 7.4 shows the relation between $u_e V$ and $u_m V$. We thus find that $u_e V$ is scattered in a relatively wide range of $10^{58} \sim 10^{60}$ erg, while $u_m V$ is distributed in a rather narrow range around $\sim 10^{58}$ erg, although $u_m V$ now become subject to the volume uncertainty. Moreover, we reconfirm the particle dominance in these lobes.

Table 7.3: A summary of the physical parameters, spatially averaged over each lobe.

| Lobe | V * | B † | u_m ‡ | u_e ‡ | u_e/u_m |
|------------------|------|------------------------|-------------------------------------|-------------------------------------|----------------------|
| Fornax A West | 3.0 | 3.3 ± 0.2 | $(4.4 \pm 0.4) \times 10^{-13}$ | $(2.0 \pm 0.5) \times 10^{-13}$ | 0.45 ± 0.12 |
| Centaurus B Both | 2.9 | $3.1^{+0.7}_{-0.9}$ | $(3.8 \pm 1.8) \times 10^{-13}$ | $(2.4 \pm 0.9) \times 10^{-12}$ | 6.3 ± 3.8 |
| NGC 612 Both | 28.7 | $0.72^{+0.20}_{-0.13}$ | $2.1^{+1.3}_{-0.7} \times 10^{-14}$ | $4.3^{+1.6}_{-1.4} \times 10^{-13}$ | 21^{+22}_{-12} |
| 4C 73.08 East | 180 | 0.35 ± 0.10 | $4.8^{+3.3}_{-2.3} \times 10^{-15}$ | $1.7^{+1.4}_{-0.7} \times 10^{-13}$ | 36^{+91}_{-23} |
| West | 180 | $0.69^{+0.21}_{-0.19}$ | $1.9^{+1.3}_{-0.9} \times 10^{-14}$ | $9.8^{+8.0}_{-3.8} \times 10^{-14}$ | $5.2^{+12.6}_{-3.3}$ |
| 3C 452 Both | 25.6 | $1.39^{+0.36}_{-0.23}$ | $7.7^{+4.5}_{-2.3} \times 10^{-14}$ | $(2.1 \pm 0.7) \times 10^{-12}$ | 27^{+25}_{-16} |
| Pictor A West | 4.60 | $1.69^{+0.31}_{-0.16}$ | $1.1^{+0.5}_{-0.2} \times 10^{-12}$ | $3.7^{+0.7}_{-0.9} \times 10^{-12}$ | 33^{+14}_{-15} |
| East | 3.33 | - | - | - | - |

Parameters for Fornax A and Centaurus B are Thashiro et al. (2001) and Tashiro et al. (1998), respectively

* volume of the lobes in 10^{70} cm^3 , evaluated from the VLA image.

† integrated over $\gamma = 10^3 \sim 10^5$, assuming the electron index is $p = 2\alpha_{\text{SR}} + 1$.

‡ in μG .

‡ in erg cm^{-3} .

Table 7.4: Total electron and magnetic field energy in the lobes.

| | $u_m V$ † | $u_e V$ ‡ |
|-------------|------------------------------------|------------------------------------|
| Fornax A | $(2.1 \pm 0.2) \times 10^{58}$ | $(9.5 \pm 2.4) \times 10^{57}$ |
| Centaurus B | $(1.1 \pm 0.5) \times 10^{58}$ | $(6.9 \pm 2.8) \times 10^{58}$ |
| NGC 612 | $5.9^{+3.7}_{-2.0} \times 10^{57}$ | $1.2^{+0.5}_{-0.4} \times 10^{59}$ |
| 4C 73.08 | $4.3^{+3.0}_{-2.0} \times 10^{58}$ | $4.9^{+4.0}_{-1.9} \times 10^{59}$ |
| 3C 452 | $2.0^{+1.1}_{-0.6} \times 10^{58}$ | $(5.3 \pm 1.9) \times 10^{59}$ |
| Pictor A | $9.0^{+3.6}_{-1.6} \times 10^{57}$ | $3.0^{+0.5}_{-0.8} \times 10^{59}$ |

† total magnetic energy in erg.

‡ total electron energy in erg.

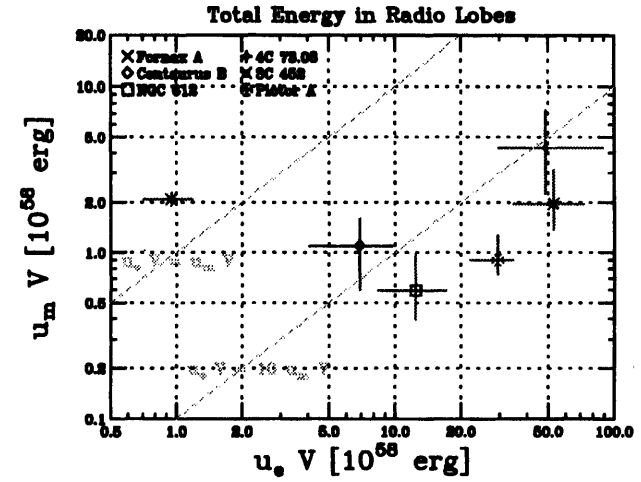


Figure 7.4: The relation between $u_e V$ and $u_m V$ in each lobe.

7.1.4 Uncertainties in the calculation

In the previous section, we have calculated u_e and u_m , and found the electron dominance ($u_e/u_m \sim 10$) in the lobes. However, the calculation is based on a few simplifying assumptions, which are not necessarily warranted. Here, we examine the validity of these assumptions and discuss what happens if they do not hold.

Electron spectrum

We have assumed that the electron power-law spectrum is valid in the range between $\gamma_1 = 10^3$ and $\gamma_1 = 10^5$. Because $\gamma_1 = 10^3$ corresponds to the electrons which emit the IC X-ray photons of 1 keV, a larger value for γ_1 is unpreferable. The possibility of a sufficiently smaller value for γ_1 is not yet rejected, since the SR and IC emissions from such electrons are both difficult to observe. If we assume $\gamma_1 = 500$, u_e becomes larger typically by $\sim 50\%$. On the other hand, even if we substitute 10^6 for γ_2 , u_e increase by only $\sim 5\%$, and our results remain basically unchanged. As is easily recognized from equation (2.39), u_m is independent of both γ_1 and γ_2 . In this way, if we adopt different values of γ_1 and γ_2 , the particle dominance in the lobes becomes even stronger.

Volume

When we calculated u_e using equation (2.40), we have estimated V from the radio images, as shown in Figure 7.2. Since u_e is inversely proportional to V , while u_m is independent of V , an under estimation on V would cause an over estimation on the u_e/u_m ratio by some factor. However, we think that the typical uncertainty in our estimation of V is at most $\sim 50\%$, which is too small to affect our conclusion on the particle dominance.

Isotropy

We have assumed that the magnetic field is randomly oriented and the electron velocity distribution is isotropic all over the lobes. If the orientation of the magnetic fields was systematically aligned with our line of sight, the SR emission would be radiated predominantly away from us, thus causing an underestimation of u_m . However, we think that this is unrealistic, because the lobe is thought to be basically symmetric about the jet axis, which is roughly parallel to the sly plane in our targets. Moreover, as shown in Figure 7.5 which visualizes the polarization structures of the SR radio emission in the lobes of Pictor A and 3C 452, the magnetic field takes random orientation, or tends to be aligned with the lobe periphery. The latter case is likely to cause an over estimation, rather than under estimation, on u_m .

Even if the magnetic fields are randomly oriented, the pitch angle, ϕ , between the magnetic field and the electron velocity could have an anisotropic distribution, because the SR power is proportional to $\sin^2 \phi$ [see equation(2.5)], and hence the electrons moving orthogonal to the magnetic fields will be cooled more rapidly than those moving parallel to the fields. If the pitch angle was concentrated on $\phi \lesssim 20^\circ$, we might have misinterpreted an equipartition actually achieved in the lobe as $u_e/u_m \gtrsim 10$. However, electrons in the lobes are cooled by both the SR and IC emission, and the cooling time by the SR plus IC emission of the electrons moving orthogonal to the fields is by only a factor of 2 shorter than that of electrons moving parallel to the fields. Therefore, we think that such an unisotropic pitch-angle distribution is difficult to produce.

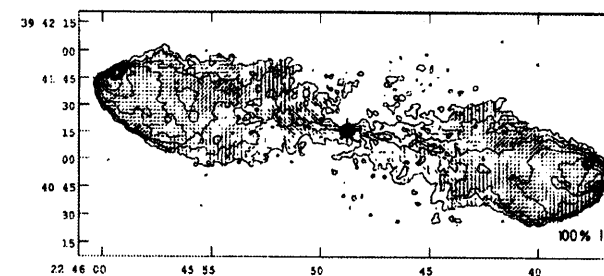
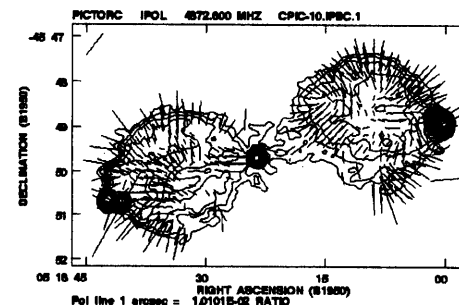


Figure 7.5: The polarization structure of Pictor A at 4.9 GHz (Perley et al. 1997) and 3C 452 (Black et al. 1992) as representatives of our targets. The directions of lines show those of the observed electric field vector, and their length are proportional to the degree of polarization. The projected directions of the magnetic fields are normal to the lines.

Uniformity

We also assumed that the electrons and magnetic fields are uniformly distributed there. We presume that the electron distribution is actually relatively uniform over the lobe, because of the relatively uniform IC X-ray brightness profiles (e.g. Figure 6.4). However, magnetic fields can have significant local inhomogeneities, and may form stings and loops, as is actually observed in the solar corona. Although the high resolution radio images give some clue to this issue, a superposition of numerous loops would be difficult to resolve. Here, we examine the effect of such local inhomogeneities in the magnetic fields in the lobes, employing.

As shown in Figure 7.6, we simply model the lobe as consisting of two regions which cannot be resolved with current telescopes; Region 1 and Region 2. In Region 1, the electrons and the magnetic fields are assumed to be uniformly distributed with the energy densities of u_{e1} and u_{m1} , respectively. In Region 2, the magnetic field is supposed to be rather weak ($u_{m2} \sim 0$) and the electron energy density to be u_{e2} . We let a volume filling factor of Region 1 (i.e. the filling factor of the magnetic fields) to be f ($0 \leq f \leq 1$). The energy densities of electrons and magnetic fields in these two regions are related to the observed volume-integrated IC and SR intensities, as

$$S_{SR} \propto u_{e1} u_{m1} f + u_{e2} u_{m2} (1 - f) = u_e u_m \quad (7.1)$$

$$S_{IC} \propto u_{e1} f + u_{e2} (1 - f) = u_e \quad (7.2)$$

Here u_e and u_m indicate the energy densities which we have so far derived from S_{SR} and S_{IC} , assuming homogeneous distributions of fields and particles. We further assume that a pressure balance is achieved between these two region, as

$$u_{e1} + u_{m1} = u_{e2} \quad (7.3)$$

As is easily recognized by multiplying equation (7.2) by V , the "true" volume-integrated electron energy in the lobe, $(u_e V)_{true} = u_{e1} fV + u_{e2} (1 - f)V$, is equal to the observed volume-integrated energy, $u_e V$, independently of f . On the other hand, using equations (7.2), (7.3), and (7.4), the "true" volume-integrated magnetic energy becomes

$$\begin{aligned} (u_m V)_{true} &= u_{m1} fV \\ &= (u_e V)_{true} \frac{f - \sqrt{f^2 - 4f(1-f)} (u_m/u_e)}{2f(1-f)} \end{aligned} \quad (7.4)$$

In Figure 7.7, we plot $(u_e V)_{true}/(u_m V)_{true}$ calculated from equation (7.4) as a function of the filling factor f , employing two representative value of observed u_e/u_m . Even if f was

107

significantly smaller than 1, $(u_e V)_{true}/(u_m V)_{true}$ would become smaller than u_e/u_m only by $\sim 50\%$.

In practice, it is difficult to actually estimate the filling factor of magnetic field in the lobes, f , from the data presented in this thesis. However, we have confirmed that the estimate on $u_e V$ and $u_m V$ are affected by uncertainties in f , by no more than a factor of two or so. Therefore, our important result presented in the previous section remains basically unchanged regardless of f .

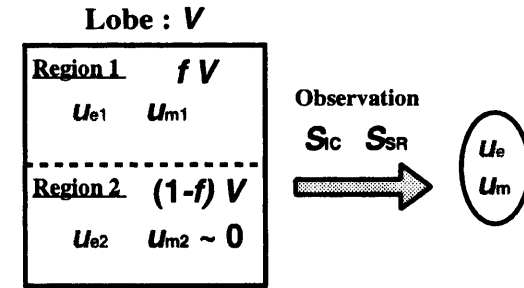


Figure 7.6: A simple modeling of a magnetic field localization in the lobes.

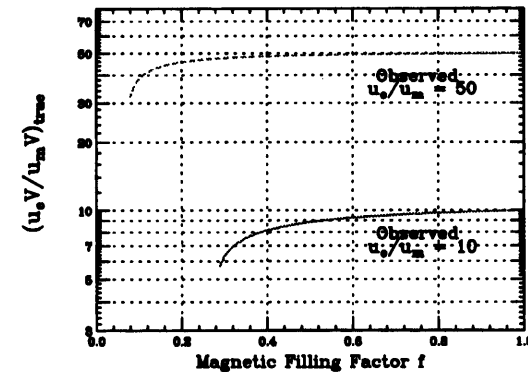


Figure 7.7: The ratio $(u_e V)_{true}/(u_m V)_{true}$ in the lobes as a function of the volume filling factor, f , of magnetic fields. The two curves specify two representative values for the observed electron-to-field energy density ratio, u_e/u_m .

7.2 Kinetic Power of the Jets

7.2.1 Relation between the lobe energetics and the activities of the nuclei

The electrons and magnetic fields in the radio lobes are originally supplied by the jets from the nucleus. As a result, the energetics in the lobes are thought to reflect the properties of the jets. We here examine relations between the energetics in the lobes and the X-ray activities of their nuclei.

Figure 7.8 shows u_e and u_m in the radio lobes as a function of the 2 – 10 keV X-ray luminosity, L_X , of their nucleus. L_X of NGC 612, 4C 73.08, 3C 452 and Pictor A are based on our measurements, and that of Centaurus B is taken from Tashiro et al. (1998). Because the nucleus of Fornax A is thought to have become dormant (Iyomoyo et al. 1998), we calculate an upper limit on its luminosity, using the relation between the radio luminosities of radio galaxies and their nuclear X-ray luminosities, reported by Sambruna et al. (1999). Neither u_e nor u_m exhibits clear correlation with L_X .

We next plot $u_e V$ and $u_m V$ against L_X in Figure 7.9. Apparently, the electron energy in the lobes increases nearly in proportion to L_X , while the magnetic field energy stays relatively constant.

7.2.2 Kinetic power of the jets

As already mentioned in §7.1.3, the relativistic electrons in the lobes, from which we have detected the CMB-boosted X-rays, are mainly cooled by the IC radiation. The electrons in these lobes lose half of their individual energies in a characteristic time T_{IC} [equation (2.24)]. Therefore, in order to maintain the total electron energy in the lobes, their jets have to continuously provide the lobes with their kinetic energies through jet terminal shocks (i.e. hot spots) at a rate described as

$$L_{kin} \simeq \frac{u_e V}{T_{IC}} (1 + \kappa), \quad (7.5)$$

where κ is the energy which is provided to the protons by shock accelerations, normalized to that provided to the electrons. The emission from protons is thought to be now still unobservable in any wavelength, and hence, it is difficult to directly determine the precise value of κ . Because theoretical treatments on the shock acceleration for relativistic particles do not draw any distinctions between relativistic electrons and protons, $\kappa \sim 1$ is usually assumed. However, κ would be as large as ~ 2000 if protons and electrons

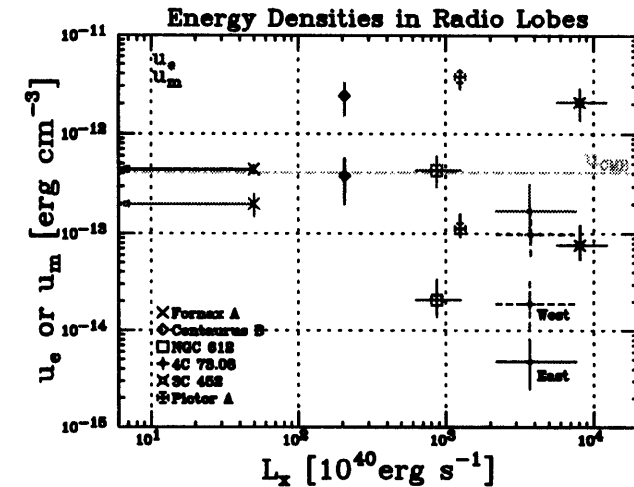


Figure 7.8: The relation between u_e (red) or u_m (blue) in the radio lobes and the X-ray luminosities, L_X , of their nuclei. The green dashed line shows u_{CMB} , neglecting the redshift dependence.

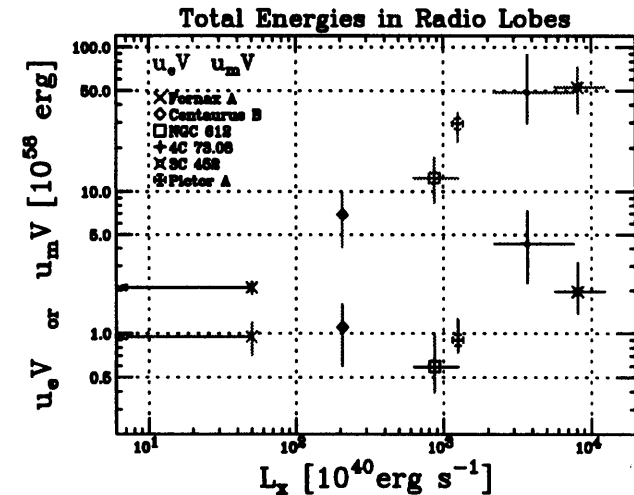


Figure 7.9: The total energy of electrons (red) and magnetic fields (blue) in the lobes, plotted as a functions of their nuclear X-ray luminosities.

are shock accelerated to similar Lorentz factors and κ would become 0, if the jets were composed mainly of electron and positron plasma.

In Table 7.5, we summarize the kinetic power of the jets calculated from equation 7.5. We assume that the typical Lorentz factor of electrons is $\gamma = 10^4$ as a logarithmic mean between 10^3 and 10^5 , over which we have integrated the electron spectrum in order to obtain u_e . The jet is required to supply the kinetic power of $L_{\text{kin}} = 10^{42\sim 44} (1 + \kappa)$ erg s^{-1} with the lobes, for sustaining the energy in these lobes.

Figure 7.10 shows L_{kin} as a function of the nuclear luminosity L_X . Thus, we observe a very tight correlation, even a direct proportionality, between L_{kin} and L_X ; the ratio L_{kin}/L_X stays in a narrow range of $1.2 \sim 5$, even though the luminosities themselves scatter by more than two orders of magnitude. This beautiful result has not been obtained before our work, since we have for the first time succeeded in accurately estimating the lobe energies based on the measurements of the IC emission. The result has three-fold meanings.

- It gives a direct observational confirmation to the very natural belief that the AGN jets are powered by mass accretion onto their central massive black holes.
- Any theoretical model should be able to explain that L_{kin} is several times L_X over a wide luminosity range.
- The proportionality allows us to estimate the kinetic power of the jets in many radio galaxies from their nuclear X-ray luminosities alone.

Table 7.5: Kinetic power of the jets, required to maintain the energies in the lobes.

| | T_{IC}^\dagger | L_{kin}^\ddagger |
|-------------|-------------------------|------------------------------------|
| Fornax A | 7.3 | $(1.3 \pm 0.3) \times 10^{42}$ |
| Centaurus B | 7.2 | $(9.6 \pm 3.9) \times 10^{42}$ |
| NGC 612 | 6.7 | $1.9^{+0.7}_{-0.6} \times 10^{43}$ |
| 4C 73.08 | 6.0 | $8.1^{+6.7}_{-3.1} \times 10^{43}$ |
| 3C 452 | 5.5 | $(9.6 \pm 3.5) \times 10^{43}$ |
| Pictor A | 6.6 | $4.5^{+0.8}_{-1.1} \times 10^{43}$ |

† calculated for electrons of $\gamma = 10^4$ in 10^{15} s.

‡ in $(1 + \kappa)$ erg s^{-1} .

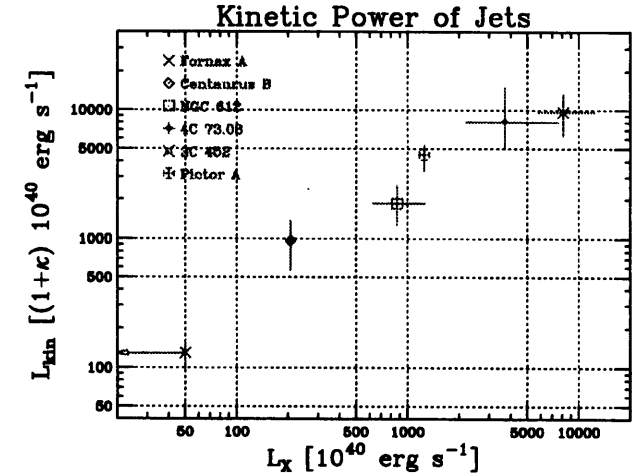


Figure 7.10: Kinetic powers of the jets, L_{kin} , as a function of the X-ray luminosity of the nucleus, L_X .

7.2.3 Comparison with the blazar jets

Through the analysis of the IC X-rays from the lobes of radio galaxies, we have estimated the total kinetic power, L_{kin} , which is continuously supplied to the lobes by the jets. We think that it is very important to compare L_{kin} with the kinetic power which is actually carried by the jets, L_{jet} . Blazars provide one of the ideal laboratories for this purpose, because their emission regions are thought to be located relatively near the base of the jets (e.g. Kataoka 2000), which point almost into our line of sight. In the unified pictures of AGNs, the difference between blazars and radio galaxies is thought to be caused basically by their different viewing angles (see Figure 2.2). Recently, the IC X-rays and γ -rays are observed from a number of blazars, and comparisons between their IC spectra and SR ones allow us to evaluate their L_{jet} (e.g. Kubo 1997, Ghisellini et al. 1998). Therefore, we here compare L_{kin} which we have estimated from the lobes with L_{jet} of blazars.

The electrons in the blazar jets have sufficient amount of kinetic energies in their random motions, even when measured in the frame co-moving with the jets, and consequently, strong SR and IC emissions are observed from them. The random energy is thought to be almost entirely lost by the SR and IC losses in the jets, by the time when they reach their terminal shocks, because the time scales of SR and IC losses are much shorter than the traveling time of the jet. Therefore, only the bulk kinetic energy of the

Table 7.6: Kinetic power of jets of representative blazars.

| Blazar | r † | n_e ‡ | L_{jet} * |
|--------------|-------|-------------------|----------------------|
| Mkn 421 | 1.2 | 1.0×10^3 | 2.3×10^{42} |
| Mkn 501 | 2.5 | 1.6×10^3 | 1.5×10^{43} |
| PKS 2155-304 | 1.2 | 1.6×10^3 | 3.7×10^{42} |
| AO 0235+164 | 4.0 | 1.6×10^4 | 3.9×10^{44} |
| S5 0716+714 | 4.0 | 3.1×10^3 | 7.9×10^{43} |
| PKS 0735 | 1.9 | 2.5×10^4 | 1.3×10^{44} |
| PKS 0208-512 | 9.0 | 2.5×10^3 | 3.1×10^{44} |
| PKS 0528+134 | 1.5 | 7.9×10^4 | 2.9×10^{44} |
| 3C 273 | 2.2 | 7.9×10^4 | 5.7×10^{44} |
| 3C 279 | 3.4 | 1.6×10^4 | 2.8×10^{44} |
| 4C 38.41 | 1.9 | 6.3×10^4 | 3.3×10^{44} |
| CTA 102 | 2.5 | 1.6×10^4 | 1.5×10^{44} |

† in 10^{16} cm. ‡ in cm^{-3} . * in $(1 + \eta)$ erg s^{-1} .
parameters are from Kubo (1997)

jet is thought to be supplied to the lobes. The kinetic power corresponding to the bulk motion of a pair of the blazar jet is calculated as

$$L_{\text{jet}} = 2 \times \pi r^2 mc^2 n_e c \Gamma^2 (1 + \eta), \quad (7.6)$$

where r is a radius of the emission region of the blazar, n_e is the electron number density in the jet, Γ is a bulk Lorentz factor of the jet, and η is a parameter describing the contribution from protons. For jets consisting of electron-proton plasma, η is $m_p/m \sim 2000$, where m_p is the proton mass, while for electron-positron jets, η becomes 0.

Here, we evaluate L_{jet} , using the parameters of blazars taken from Kubo (1997). He has analyzed the multi-frequency spectra of blazars, which are observed by *ASCA*, in the SSC frame work, and has accurately determined the physical parameters in their jets. We assume $\Gamma = 10$, according to him. Table 7.6 summarizes L_{jet} of blazars, which we derived from the parameters of Kubo (1997). We find $L_{\text{jet}} = 10^{42} \sim 10^{44} (1 + \eta)$ erg s^{-1} , on an average.

If the jets were composed of electron-proton plasma ($\eta \sim 2000$), what would happen? We here consider two extreme cases. If the bulk kinetic power of the jet was equally divided to electrons and protons through the jet terminal shock ($\kappa \sim 1$ as usually assumed), the

electrons would gain a kinetic power of $10^{45} \sim 10^{47}$ erg s^{-1} . When this energy input into electrons were accumulated over T_{IC} , the total electron energy in the lobes would amount to $10^{61} \sim 10^{63}$ ergs, which exceed the observed electron energy, $u_e V$, by more than at least an order of magnitude. Therefore, such a case is thought to be unlikely. Alternatively, if the electrons and protons were both accelerated to a similar Lorentz factor at the jet terminal shock, κ would become $m_p/m \sim 2000$ and L_{jet} would be consistent with L_{kin} . However, because the IC cooling time, T_{IC} , is proportional to m^3 , the total energy of invisible protons in the lobes would become $\sim 2000^4$ times higher than that of the observed electrons, $u_e V$. This seems quite unrealistic, because it would be impossible to confine these protons by reasonable external pressures, and hence, the lobes would not be constructed. In this way, we encounter severe difficulties if jets contain protons, regardless of the value of κ .

If instead the jets contain almost no protons ($\eta \sim 0$ and $\kappa \sim 0$), L_{kin} of radio galaxies is inferred to be distributed over the nearly the same range, 10^{42-44} erg s^{-1} , as L_{jet} of blazars. Therefore, all the information becomes self-consistent.

The above discussion on energetics suggests that AGN jets are composed of electron-positron plasma, rather than electron-proton one, if the lobes are common features of radio galaxies, blazars, and besides AGNs which have the jets.

7.2.4 Electron dominance in the lobes

The relation between the nuclear X-ray luminosity, L_X and the total energies of the electrons and the magnetic fields in the lobes, shown in Figure 7.9, implies that the particle dominance in the lobes becomes stronger, as the nucleus is more active. Figure 7.11 shows the ratio u_e/u_m , which quantifies particle dominance in the lobes, as a function of the X-ray luminosity of the nucleus, L_X . Clearly, u_e/u_m increases as $\sim L_X$.

This interesting correlation between u_e/u_m and L_X is a simple result from two underlying fact carried by Figure 7.9. One is that $u_e V$ is nearly proportional to L_X , which can be identified with the proportionality between L_X and L_{kin} (Figure 7.10), because T_{IC} is relatively constant in equation (7.5). The other is that the total magnetic energy, $u_m V$, is quite constant at $\sim 10^{58}$ ergs, without depending on L_X .

Then, how $u_m V$ is kept nearly independent of L_X ? We naturally think that the magnetic flux supplied by the jet per unit time is proportional to L_X . If we assume that the magnetic flux is dissipated in a characteristic time scale of T_B by, e.g., magnetic reconnection, the total magnetic flux in the lobe becomes proportional to $L_X T_B$. Then, an "effective" magnetic field and its energy in the lobe becomes $B_{\text{eff}} \propto L_X T_B V^{-2/3}$, and $(u_m V)_{\text{eff}} \propto L_X T_B V^{-1/3}$, respectively. Because the magnetic energies in the lobes is almost

independent of their nuclear activities as shown in Figure 7.9, T_B has to proportionate to $V^{1/6} L_X^{-1}$. Figure 7.9 suggests that $u_e V$ is also proportional to L_X , and hence, T_B has to be written as $\propto V^{-5/6} u_e^{-1}$.

The inverse proportionality of T_B on u_e can be explained if magnetic reconnection is induced by motions of electrons in the lobes. However, its dependence on V is difficult to explain.

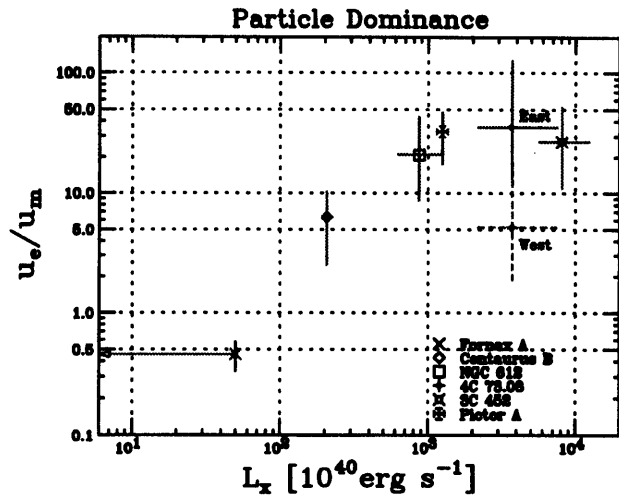


Figure 7.11: The ratio u_e/u_m as a function of the X-ray luminosity of the nucleus.

7.3 Spatial Distributions of Electrons and Magnetic Fields

Because the spatial distribution of the CMB is highly uniform, we can directly evaluate the spatial distribution of electrons in the lobes, by examining the surface brightness profiles of the IC X-rays. We can also measure the magnetic field distribution in the lobes from the ratio of the SR radio brightness to the IC X-ray brightness. In the following, we study the spatial distributions of electrons and magnetic field in the lobes of 3C 452,

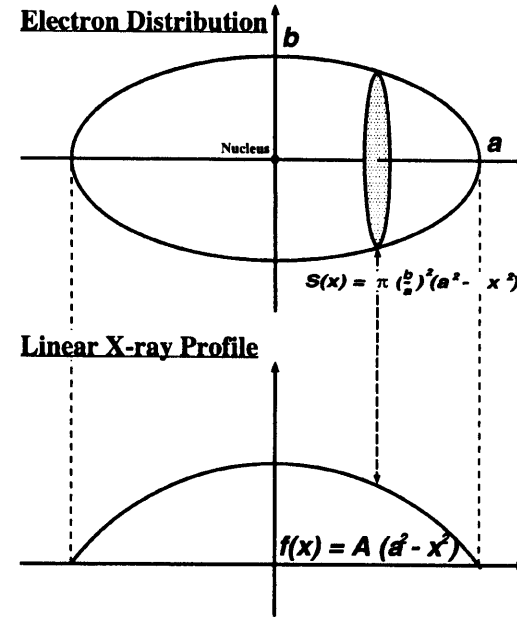


Figure 7.12: A simple modeling of a homogeneous distribution of electrons in an ellipsoid, and the corresponding IC X-ray profile projected onto the major axis.

using the linear brightness profiles shown in Figure 6.4, because the quality of the IC X-ray data from its lobes are the best among our sample.

The spatial distribution of the IC X-rays in the lobes of 3C452 appear relatively uniform (Figure 6.2), which implies that the electrons are rather homogeneously distributed there. Then, we qualitatively examine this possibility, using the observed X-ray profile in Figure 6.4. Considering the X-ray morphology of the lobes, we simply approximate the three-dimensional shape of the whole lobes by an ellipsoid centered on its nucleus, with the length of major and minor axes of a and b , respectively. Assuming that the electrons uniformly fill the ellipsoid, the X-ray profile projected on the major axis becomes $f(x) = A \times (a^2 - x^2)$, where x is a projected distance from the nucleus (i.e., the horizontal axis in Figure 6.4), and A is a parameter proportional to the product between b^2 and the electron number density. This is schematically explained in Figure 7.12.

We fitted $f(x)$ to the observed X-ray profile of the lobes of 3C 452, with A and a left

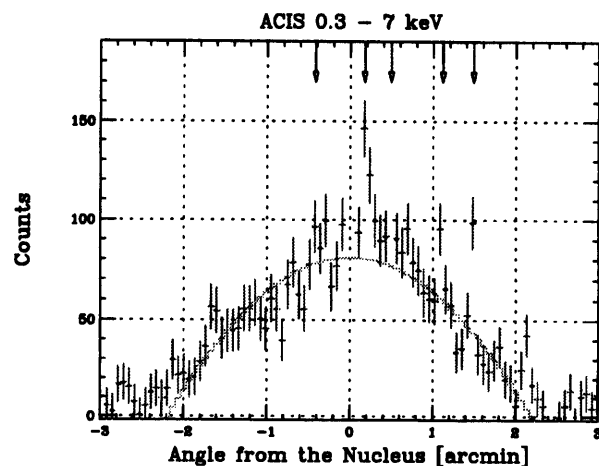


Figure 7.13: The IC X-ray brightness profile of the lobes of 3C 452 in 0.3 – 7 keV, projected on the major axis. The data are the same as Figure 6.4. The histograms represent the model prediction. The blue arrows show the projected positions of the X-ray point sources.

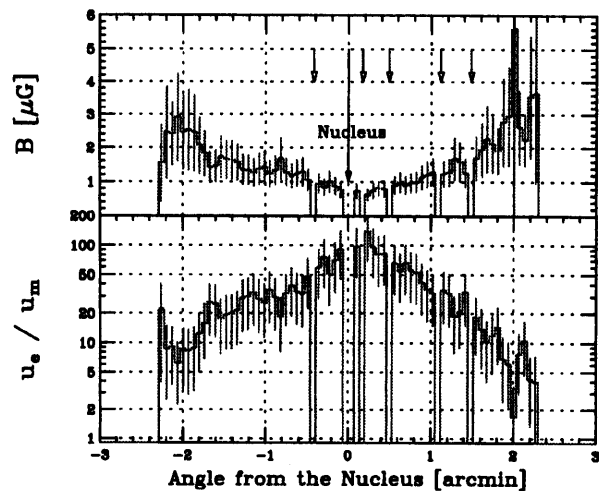


Figure 7.14: A rough estimation of the magnetic field distribution in 3C 452 along its radio axis. The blue arrows show the projected positions of the X-ray point sources.

free. We rejected the data corresponding to the projected position of the nucleus and those of contaminating point sources (blue arrows in Figure 7.13). Because of statistics, we restricted the data from -2 arcmin to 2 arcmin. The fit is acceptable ($\chi^2/d.o.f. = 55.3/52$). The X-ray profile predicted by the model is shown in Figure 7.13 by green histograms. The length of major axis, $a = 2.2 \pm 0.1$ arcmin, becomes consistent with that of the radio profile. Therefore, we think that our modeling using an ellipsoid is appropriate.

We next estimated the magnetic field distribution along the major axis in 3C 452, by dividing the projected profile of SR radio brightness by that of the IC X-ray brightness, both of which are shown in Figure 6.4. We masked the projected position of the nucleus and those of X-ray point sources. We also rejected the data outside the lobes ($|x| \gtrsim 2.2$ arcmin). Figure 7.14 shows the magnetic field strength in 3C 452 as a function of the projected angle from its nucleus along its major axis. Thus, the distribution of the magnetic field is relatively symmetric about its nucleus. The results also indicate that the magnetic field is $B \lesssim 1 \mu\text{G}$ near the center of the lobes (i.e., around the nucleus), while B increase outward, reaching $\sim 3 \mu\text{G}$ at a distance of ~ 2 arcmin (~ 160 kpc) from the nucleus.

We show in the lower panel of Figure 7.14 the distribution of the ratio u_e/u_m in the lobes of 3C 452, which is roughly estimated from the electron and magnetic field distributions. Near the center of its lobes, u_e highly dominate u_m by nearly two order of magnitude, while u_e/u_m decreases toward the lobe edges, and becomes $2 \sim 5$ at a distance of ~ 2 arcmin from its nucleus.

Similarly, a relatively uniform distribution of electrons and an increase of the magnetic field toward the lobe periphery are reported in the west lobe of Fornax A (Tashiro et al. 2001), and in the lobes of Centaurus B (Tashiro et al. 1998), using the *ASCA* GIS. We have confirmed these properties to hold also in the lobes of 3C 452, using the *Chandra* ACIS with a higher spatial resolution.

7.4 Energetics in Radio Hot Spots

7.4.1 Multi frequency spectra

Using the *Chandra* ACIS, we have detected non-thermal X-ray sources associated with bright radio hot spots in three radio galaxies, Cygnus A, 3C 123, and Pictor A. Their X-ray spectra are well reproduced by a hard PL model. Because the measured X-ray spectral indices of the hot spots A and D of Cygnus A, and the east one of 3C 123, are

consistent with their SR radio indices, S_{SR} , we have concluded that the X-rays from these hot spot are of IC origin. However, the X-ray spectral slope of the west hot spot of Pictor A is sufficiently softer than α_{SR} . These properties are visualized in Figure 7.15, which shows the multi-frequency spectra of these hot spots. Table 7.7 summarizes the spectral parameters of the radio and X-ray emissions from these hot spots. The radio parameters are determined through the PL fitting to the radio data over the 1 – 100 GHz range, as are shown in Figure 7.15.

Table 7.7: A summary of radio and X-ray spectral parameters of individual hot spots.

| Hot Spot | Radio | | X-ray | |
|---------------|-----------------|------------|--|-------------------------------------|
| | α_{SR} † | S_{SR} ‡ | α_{IC} | S_{IC} * |
| Cygnus A A | 0.88 | 110 | 0.66 ^{+0.29} _{-0.26} | 18 ⁺⁷ ₋₅ |
| | 0.79 | 118 | 0.77 ^{+0.24} _{-0.22} | 33 ⁺⁹ ₋₆ |
| 3C 123 East | 0.75 | 16.9 | 0.0 ^{+0.8} _{-0.6} | 2.5 ^{+3.8} _{-1.3} |
| Pictor A West | 0.74 | 5.5 | 1.04 ^{+0.1} _{-0.09} | 90 ± 6 |

† evaluated over the 1 – 100 GHz range.

‡ flux density at 1.4 GHz in the unit of Jy.

* flux density at 1 keV in the unit of μ Jy.

7.4.2 Energy densities of electrons and magnetic fields

It is of no doubt that the seed photons for the IC scattering are dominated by the SR photons themselves in the hot spots, because the hot spots are very bright SR sources in spite of their compact volumes. That is, the X-ray emission from the hot spots arises via the SSC process. With this in mind, we quantify their SR and SSC spectra and determine their physical parameters, using the numerical code which is kindly provided by Dr. Kataoka (1999).

As already reviewed in §2.3.3, the estimation of physical properties of hot spots based on their SR and SSC spectra are strongly dependent on their physical sizes. Therefore, we evaluated the hot spot radii R using the high resolution VLA images from Calliri & Barthel (1996) for the both hot spots of Cygnus A, from Hardcastle et al. (1997) and Looney & Hardcastle (2000) for the east hot spot of 3C 123, and from Perley et al. (1997) for the west hot spot of Pictor A. We assumed that the electron index in these hot spots is $p = 2\alpha_{SR} + 1$, because the errors in α_{IC} are too large. We evaluated the minimum and

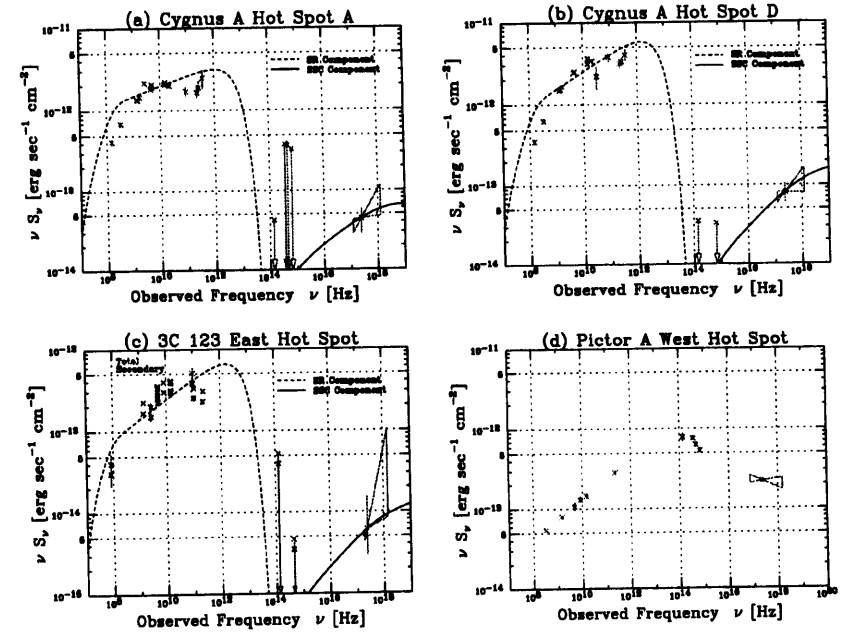


Figure 7.15: The spectral energy distribution of hot spots. (a) The hot spot A of Cygnus A. (b) The hot spot D of Cygnus A. (c) The east hot spot of 3C 123. The red points represent the data of the whole hot spot, and the blue ones represent the data of its secondary component. (d) The west hot spot of Pictor A. The radio data for the two hot spots of Cygnus A are from Carilli et al. (1991), Meisenheimer et al. (1997), and Alexander, Brown & Scott (1984). Those for the east hot spot of 3C 123 are from Looney & Hardcastle (2000), Okayasu et al. (1992), Riley & Pooley (1978), Readhead & Hewish (1974), and Meisenheimer et al. (1997). Those for the west hot spot of Pictor A are from Meisenheimer et al. (1997). The dashed and solid lines in panel (a), (b), and (c) represent the model predictions for the SR and SSC components, respectively, calculated by the numerical code of Kataoka et al. (1999).

maximum Lorentz factors of electrons, γ_1 and γ_2 respectively, in order for the calculated spectra to well cover the observed frequencies.

Among these hot spots, the east one of 3C 123 is resolved into double spatial structures in the high resolution VLA images (Hardcastle et al. 1997 and Looney & Hardcastle 2000); a fainter and smaller component usually called "primary" hot spot, and a brighter and larger component called "secondary" one. The X-ray position is rather coincident with the secondary component, though the separation between the two components ($\gtrsim 1$ arcsec) is near the ACIS angular resolution. The radio flux densities of the secondary component, shown in blue, are about $\sim 75\%$ of the total ones over a sufficiently wide frequency range (Looney and Harcastle 2000). Accordingly, we consider that the X-rays are mainly emitted from the secondary hot spot, and adopt its radius for R .

The obtained physical parameters of the hot spots of Cygnus A and 3C 123 are summarized in Table 7.8, together with R , γ_1 and γ_2 which we have adopted. The dashed and solid lines in Figure 7.7 represent the predicted SR and SSC spectra, respectively. If we adopt a radius larger by 10%, the derived magnetic field B and the electron energy density u_e both decrease by 10% typically. The measured magnetic fields become $B = 100 \sim 300 \mu\text{G}$, and u_e slightly dominates u_m in these hot spots. These values are consistent with the result of Wilson et al. (2000) for Cygnus A and Hardcastle et al. (2001) for 3C 123, although they have not evaluated u_e .

Because the X-ray spectral index of Pictor A is inconsistent with α_{SR} , its X-ray spectrum cannot be easily explained by the IC X-rays from the SR electrons themselves. Moreover, if we try to explain simultaneously the observed SR radio spectra and the X-ray flux density at 1 keV, the magnetic field would become $B \sim 6 \mu\text{G}$ and u_e would dominates u_m by nearly 5 orders of magnitude. We consider this situation unrealistic. Thus, the X-ray emission mechanism of this hot spot remains unclear, but further examination of the issue is beyond the scope of the present thesis.

Table 7.8: A summary of the physical parameters in hot spots

| Hot Spot | Adopted | | | Derived Parameters | | | | |
|----------|---------|------------------|-------------------|--------------------|-------------------|---------------------|---------------------|-----------------|
| | R | γ_e | | B^\dagger | u_m^* | u_e^* | u_e/u_m | |
| Cygnus A | A | 1.5 [†] | 1.48 [‡] | $350 \sim 10^5$ | 160 ± 30 | $1.0^{+0.4}_{-0.3}$ | $2.4^{+0.8}_{-0.7}$ | $1.2 \sim 4.4$ |
| | D | 1.5 [†] | 1.48 [‡] | $350 \sim 10^5$ | 150 ± 15 | 0.9 ± 0.2 | $2.8^{+0.7}_{-0.5}$ | $2.1 \sim 4.8$ |
| 3C 123 | East | 1.1 [†] | 3.28 [‡] | $250 \sim 10^5$ | 180^{+85}_{-65} | $1.3^{+1.5}_{-0.8}$ | $2.3^{+2.2}_{-1.2}$ | $0.4 \sim 10.4$ |

[†] in arcsec [‡] in kpc [‡] in μG * in $10^{-9} \text{ erg cm}^{-3}$

7.4.3 Comparison with the blazar jets

We examine the relation between the magnetic field of hot spots and that of blazar jets. Table 7.9 summarizes typical parameters of the hot spots and blazars.

We assume that the magnetic flux is conserved along the jet; i.e., $B r_{\text{eff}}^2$ is constant in the jet, where r_{eff} is an "effective" radius of the jet. In order for this relation to hold all the way along the jet, hot spots are inferred to have $r_{\text{eff}} = 0.1 \sim 1$ pc, by scaling the radius of the blazar jet by B . Although the actually observed hot spot sizes, $1 \sim 3$ kpc, are much larger than the estimated r_{eff} , what we observe as a hot spot is a post-shock emission region where the collimated flow of the jet partially randomized. We hence consider r_{eff} as the width of the jet terminal. This means that the jet is still highly collimated at its terminal point.

We next examine the dependence of r_{eff} on the distance, d , from the nucleus (i.e., the base of the jet). Assuming a scaling of the form $r_{\text{eff}} \propto d^\beta$, and using the typical values of d and r_{eff} for the blazar jets and hot spots, we have obtained $\beta \sim 0.3$. These are schematically shown in Figure 7.16.

Interestingly, a similar relation is suggested by Yamashita et al.(1994), to explain a multi-frequency spectrum of the blazar H 0323+022. They observed the object with ASCA in 1994 to complete a radio to X-ray spectrum. They also showed that the multi frequency spectra showing a broken power-law like shape is well explained with a simple inhomogeneous jet model proposed by Ghisellini et al. (1985) in the case of $r_{\text{eff}} = d^{1/3}$.

Table 7.9: Typical parameters in the hot spots and blazars.

| | Hot Spot | Blazar * |
|------------------------|----------------------------|------------------------|
| B | $100 \sim 300 \mu\text{G}$ | $0.1 \sim 1 \text{ G}$ |
| d^\ddagger | $\sim 100 \text{ kpc}$ | 0.1 pc |
| r_{eff}° | $0.1 \sim 1 \text{ pc}$ | 10^{-2} pc |
| r^\dagger | $1 \sim 3 \text{ kpc}$ | – |

* evaluated from Kubo (1997) and Kataoka (2000).

[‡] the distance from the base of the jet.

[†] the radius of the emission region.

[◊] the effective radius.

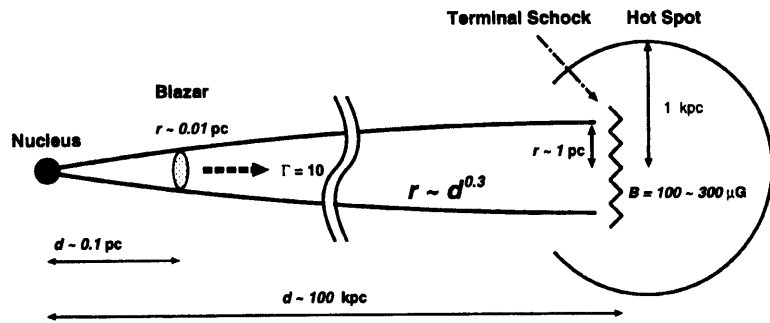


Figure 7.16: A simple picture of the jet and the hot spot.

Chapter 8

Conclusion

Through the detection of the IC X-rays from the lobes and hot spots of a number of radio galaxies, we have arrived at the following conclusions.

- Comparing the SR and IC flux densities, the energy densities of electrons and magnetic field in the lobes are precisely determined to be $u_e \sim 10^{-13}$ – 10^{-12} erg cm⁻³ and $u_m \sim 10^{-15}$ – 10^{-13} erg cm⁻³, respectively. It is found that an equipartition between u_e and u_m is not achieved in these lobes; u_e tends to dominate u_m nearly by an order of magnitude. It is also found that u_m is typically smaller than u_{CMB} , and hence, the electrons in the lobes are inferred to lose their kinetic energies mainly through the IC radiation.
- Using the IC cooling timescale, the kinetic power of the jet, which is required to maintain the total electron energy in the lobes, is estimated to be $L_{\text{kin}} = 10^{42-44}$ erg s⁻¹. A clear correlation was found between L_{kin} and the nuclear X-ray luminosity. This gives an observational confirmation to the belief that the AGN jet is powered by mass accretion onto the central black holes. A detailed comparison of L_{kin} with the bulk kinetic power which is observed from blazar jets implies that the jet is mainly composed of electron-positron plasmas.
- The particle dominance in the lobes becomes more prominent, particularly when their nuclei become more active.
- Using the SR radio and IC X-ray brightness distributions, the spatial distributions of electrons and magnetic fields in the lobes of 3C 452 are examined. The electrons are rather uniformly distributed there, while the magnetic fields are strengthened toward the lobe periphery.

- The magnetic field in radio hot spots are derived to be $B = 100 - 300 \mu\text{G}$, using their SR and IC spectra together with the SSC model prediction. It is found that u_e slightly dominates u_m there. Comparison between the typical parameters of hot spots and those of the blazar jets imply that the width of the jet r depends on the distance, d , from the nucleus as $r \propto d^{0.3}$.

Bibliography

- [1] Alexander, P., Brown, M.T., and Scott, P.F. 1984, MNRAS 209, 851
- [2] Antonucci, R., and Miler, J.S., 1985, ApJ 297, 621
- [3] Antonucci, R., 1993, ARA&A 31, 473
- [4] Awaki, H., Mushotzky, R., Tsuru, T., Fabian, A. C., Fukazawa, Y., Loewenstein, M., Makishima, K., Matsumoto, H., et al., 1994, PASJ 46, L65
- [5] Band, D.L., and Grindlay J.E., 1985, ApJ 289, 128
- [6] Begelman, M.C., McKee, C.F. and Shields, G.A., 1983, ApJ 271, 70
- [7] Black, A.S.R., Baum, S.A., Leahy, J.P., Perley, R.A., Riley, J.M., and Scheuer, P.A.G., 1992, MNRAS 256, 186
- [8] Blandford, R.D., 1976, MNRAS 176, 465
- [9] Blandford, R.D., and Königl, A., 1979, ApJ 232, 34
- [10] Blumenthal G.R., and Gould R.J., 1970, Rev. Mod. Phys. 42, 237
- [11] Bridle, A.H., and Perler R.A., 1984, ARA&A 22, 319
- [12] Brunetti, G., Setti, G., and Comastri, A., 1997, A&A 325, 898
- [13] Brunetti, G., Comastri, A., Setei, G., and Feretti, L. 1999, A&A 342, 68
- [14] Brunetti, G., 2000, APh 13, 107
- [15] Brunetti, G., Cappi, M., Setti, G., Feretti, L., and Harris, D. E., 2001, A&A 372, 775
- [16] Burke, B.E., Mountain, R.W., Harrison, D.C., Bautz, M.W., Doty, J.P., Ricker, G.R. and Daniels P.J., 1991, IEEE Trans. ED-38, 1096
- [17] Carilli, C. L., Perley, R. A., Dreher W., and Leahy J. P., 1991, ApJ 383, 554
- [18] Cameron, M.J. 1971, MNRAS 152, 439
- [19] Celotti, A and Fabian, A. C., 1993, MNRAS 264, 228
- [20] Chartas, G., Worrall, D. M., Birkinshaw, M. Cresitello-Dittmar, M., Cui, W., Ghosh K. K., Harris D. E., Hooper E. J., et al., 2000, ApJ 542, 655
- [21] Christensen, W.N., Frater, R.H., Watkinson, A., O'Sullivan, J.D., Lockhart, I., A., and Goss, W.M., 1977, MNRAS 181, 183
- [22] Cox, C.I., Gull, S.F., and Scheuer, P.A.G., 1991, MNRAS 252, 558
- [23] Dermer, C.D., and Schlickeiser, R., 1994, ApJS 90, 945
- [24] Eales, S.A., Alexander, P., and Duncan, W., D., 1989, MNRAS 240, 817
- [25] Ekers, E.D., Goss, W.M., Kotanyi, C.G., and Skellern, D.J., 1978, A&A 69, L21
- [26] Ekers, R.D., Goss, W.M., Wellington, K.J., Bosma, A., Smith, R.M., and Schwaizer, F., 1983, A&A 127, 361
- [27] Fabbiano, G., Trinchieri, G., Elvis, M., Miller, L., and Longair, M., 1984, ApJ 277, 115
- [28] Fanaroff, B.L., and Riley J.M., 1974, MNRAS 167, 31
- [29] Feigelson, E.D., Laurent-Muehleisen, S.A., and Kollgaard R.I., 1995, ApJ 453, L13
- [30] Fukue, J. 1993, Parity 8, 50
- [31] Ghisellini, G., Maraschi, L., and Treves, A, 1985, A&A 146, 204
- [32] Hardcastle, M.J., Alexander, P., Pooley, G.G., and Riley, J.M., 1997, MNRAS 288, 859
- [33] Hardcastle, M.J., and Worrall, D.M., 1999, MNRAS 309, 969
- [34] Hardcastle, M.J., Birkinshaw, M., and Worrall, D.M. 2001, MNRAS 323, L17
- [35] Hardcastle, M.J., Birkinshaw, M., and Worrall D.M., 2001, MNRAS 326, 1499
- [36] Harris D.E. & Romanishin R., 1974 ApJ, 188, 209
- [37] Harris D.E. & Grindlay J.E., 1979 MNRAS, 188, 25
- [38] Harris, D.E., Carilli, C.L., and Perler, R.A., 1994, Nature 367, 718

- [39] Harris, D.E., Leighly, K.M., and Leahy, J.P., 1998, *ApJ* 449, L149
- [40] Harris, D.E., Nulsen, P.E. J., Ponman, T.J., Bautz, M., Cameron, R.A., David, L.P., Donnelly, R.H. Froman, W.R., et al., 2000, *ApJ* 530, L81
- [41] Herbig, T., and Readhead, C.S., 1992, *ApJS* 81, 83
- [42] Icke, V., 1980, *AJ* 85, 163
- [43] Inoue, S., and Takahara, F., 1996, *ApJ* 463, 555
- [44] Isobe, N., Makishima, K., Tashiro, M., Kaneda, H., and Iyomoto, N. 2001, "New Century of X-ray Astronomy" edited by Inoue, H., and Kunieda, H.
- [45] Iyomoto, N., Makishima, K., Tashiro, M., Inoue, S., Kaneda, H., Matsumoto, Y, and Mizuno, T. 1995, *ApJ* 503, L31
- [46] Iwasawa, K., Fabian, A. C., Ueno, S., Awaki, H., Fukazawa, Y., Matsushita, K., and Makishima, K., 1997, *MNRAS* 285, 683
- [47] Jones, P.A, and McAdam, W.B., 1992, *ApJS* 80, 137
- [48] Jögers, W. J., 1987, *A&AS* 67, 395
- [49] Kaneda, H., Tahiro, M., Ikebe, Y., Ishisaki, Y., Kubo, H., Makishima, K., Ohashi, T., Saito, Y., Tabara, H., and Takahashi, T., 1995, *ApJ* 453, L13
- [50] Kataoka, J., Mattox, J.R., Quinn, J., Kubo, H., Makino, F., Takahashi, T., Inoue, S., Hartman, R.C., Madejski, G.M., Sreekumar, P., and Wagner, S.J., 1999, *ApJ* 514, 138
- [51] Klein, U., Mack, K.-H., Strom, R., Wielebinski, R., and Achatz, U., 1994, *A&A* 283, 729
- [52] Koyama, K. Ikegami, T., Inoue, H., Kawai, N., Makishima, K., Matsuoka, M., Mitsuda, K., Murakami, T., et al. 1984, *PASJ* 36, 659
- [53] Kraft, R.P., Forman, W., Jones, C., Kenter, A.T., Murray, S.S., Aldcroft, T.L., Elvis, M.S., Evans, I.N., et al., 2001, *ApJ* 531, L9
- [54] Kubo, H., Takahashi, T., Madefski, G., Tashiro, M., Makino, F., Inoue, S., and Takahara, F., 1998, *ApJ* 504, 694
- [55] Kudoh, T., Matsumoto, R., Shibata, K., 1998, *ApJ* 508, 186

- [56] Klein, U., Mack, K.-H., Strom, R., Wielebinski, R., and Achatz, U., 1994, *A&A* 283, 729
- [57] Kuhr, H., Nauber, U., Pauling-Toth, I.I.K., and Witzel, A., 1979. A catalogue of radio sources. MPIfR Preprint.
- [58] Laing, R.A., and Peacock, J.A., 1980. *MNRAS* 190, 903
- [59] Leahy, J.P., and Perley R.A., 1991, *AJ* 102, 537
- [60] Leahy, J.P., Bridle, A.H., and Strom, R.G., 1996 "An Atlas of DRAGNs", at <http://www.jb.man.ac.uk/atlas/>
- [61] Leahy, J.P., Black, A.S.R., Dennett-Thorpe, J., Hardcastle M.J., Komissarov, S., Perley, R.A., Riley, J.M., and Scheuer, P.A.G., 1997, *MNRAS* 291, 20
- [62] Looney, L.W., and Hardcastle, M., 2000, *ApJ* 534, 172
- [63] Makishima, K., Fujimoto, R., Ishisaki, Y. Kii, T., Loewenstein, M., Mushotzky, R., Serlemitsos, P., Sonobe, T., et al., 1994, *PASJ* 46, L77
- [64] Makishima, K., Tashiro, M., Ebisawa, K., Ezawa, H., Fukazawa, Y., Gunji, S., Hirayama, M., Idesawa, E., et al., 1996, *PASJ*, 48, 171
- [65] Marchvitch, M., 2001 "ACIS background" at <http://cxc.harvard.edu/cal/Links/Acis/acia/Cal.prods/bkgnd/current>
- [66] Marshall, H.L., Harris, D.E., Grimes, J.P., Drake, J.J., Fruscione A., Juda, M., Kraft R.P., Mathur S., et al., 2001, *ApJ* 549, L167
- [67] Marshall, H.L., Miller, B.P., Davis, D.S., Perlman, E.S., Wise, M., Canizares, C.R., Harris, D.E., 2001 *ApJ* in press (astro-ph/0109160)
- [68] Matsushita, K., 1997 Ph. D. Thesis, Department of Astronomy, University of Tokyo
- [69] Matsushita, K., Ohashi, T., and Makishima, K., 2000, *PASJ* 52, 685
- [70] Matsumoto, Y., Fukazawa, Y., Nakazawa, K., Iyomoto, N., and Makishima, K. 2001, *PASJ* 53, 475
- [71] Mayer, C.J., 1979, *MNRAS* 186, 99
- [72] McAdam, W.B., 1991, *Proc. Astron. Soc. Australia*, 9, 255

- [73] Meisenheimer, K., Röser, H. -J., Hiltner, P.R., Yate, M.G., Longair, M.S., Chini, R., and Perley R.A., 1989, *A&A* 219, 63
- [74] Meisenheimer, K., Yates, M.G., and Röser, H.-J., 1997, *A&A* 352, 57
- [75] Miley G., 1980, *ARA&A* 18, 165
- [76] Nefs, S.G., Roberts, L., and Hutchings, J.B., 1995, *ApJS* 99, 349
- [77] Ohashi, T., Ebisawa, K., Fukazawa, Y., Hiyoshi, K., Horii, M., Ikebe, Y., Ikeda, H., Inoue, H., et al., 1996, *PASJ*, 48, 157
- [78] Okayasu, R., Ishiguro, M., and Tabara, H., 1992, *PASJ* 44, 335
- [79] Pacholczyk, A.G, 1970 "Radio Astrophysics" Chap. 7 (San Francisco; Freeman)
- [80] Perlay, R.A., Dreher, J.W., Cowan, J.J., 1984, *ApJ* 285, 35
- [81] Perley, R.A., Röser, H.-J., and Meisenheimer, K., 1997, *A&A* 328, 12
- [82] Pesce, J.E., Sambruna, R.M., Tavecchio F., Maraschi, L., Cheung, C.C., Urry, C.M., and Scarpa R., 2001, *ApJ* 556, L70
- [83] Prieto, M.A., 1997, *MNRAS* 284, 627
- [84] Riley, J.M., and Pooley, G.G., 1978, *MNRAS* 183, 245
- [85] Rybicki, G.B., and Lightman, A.P., "Radiative Processes in Astrophysics" (New York; Wiley)
- [86] Salter, C.J., Chini, R., Haslam, C.G.T, Junor, W., Kreysa, E., Mezger, R.E., Spencer R.E., Wink, J.E., and Zylka, R., 1989, *A&A* 220, 42
- [87] Sambruna, R.M., Eracleous, M., and Mushotzky, R.F., 1999, *ApJ* 526, 60
- [88] Sambruna, R.M., Urry, C.M., Tavecchio, F., Maraschi, L., Scappa, R., Chartas, G., and Muxlow, T. 2001, *ApJ* 549, L161
- [89] Sanders, D.B., Phinney, E.S., Neugebauer, G., Soifer, B.T., and Matthews, K., 1989, *ApJ* 347, 29
- [90] Saripalli, L., Mack, K.-H., Klein, U., Strom, R., and Singal, A. K., 1996, *A&A* 306, 708

- [91] Schwartz, D.A., Marshall, H.L., Lovell, J.E.J., Piner B.G., Tingay, S.J., Birkinshaw, M., Chartas G., Elvis E., et al., 2000, *ApJ* 540, 69
- [92] Serlemitsos, P.J., Jalota, L., Soong, Y., Kunieda, H., Tawara, Y., Tsusaka, Y., Suzuki, H., Sakima, Y., et al., 1995, *PASJ* 47, 105
- [93] Shimmins, A.J., 1971, *Australian J. Phys. Astrophys. Suppl.*, 21, 1
- [94] Spinrad, H., Djorgovski, S., Marr, J., and Aguilar, L., 1985, *PASP* 97, 932
- [95] Tajima, Y., and Fukue, J., 1996, *PASJ* 48, 529
- [96] Takahara, F., Rosner, R., and Kusunose, M., 1989, *ApJ* 346, 122
- [97] Tanaka, Y., Inoue, H., and Holt, S.S., 1994, *PASJ* 46, L37
- [98] Tashiro, M., Kaneda, H., Makishima, K., Idesawa, E., Ishisaki, Y., Kotani, T., Takahashi, T., and Yamashita, A., 1998, *ApJ* 449, 713
- [99] Tashiro, M., Iyomoto, N., Kaneda, H., Makishima, K., and Isobe, N., 1999, *Astron. Nachr.* 320, 217
- [100] Tashiro, M., Makishima, K., Iyomoto, N., Isobe, N., and Kaneda H., 2001, *ApJ* 546, L19
- [101] Tavecchio, F., Maraschi, L., Sambruna, R.M., and Urry, C.M., 2000, *ApJ* 544, L23
- [102] Taylor, G.B., Perlay, R.A., Inoue, M. Kato, T., Tabara, H. and Aizu, K., 1990, *ApJ* 360, 41
- [103] Tsusaka, Y., Suzuki, H., Yamashita, K., Kunieda, H., Tawara, Y., Ogasaka, Y., Uchibori, Y., Honda, H., et al., 1995 *Appl. Opt.*, 34, 4848
- [104] Uchida, Y. and Shibata, K 1985, *PASJ* 37, 515
- [105] Urry, C. M., and Padovani P. 1995, *PASP* 107, 517
- [106] Wilson, A.S., Young, A.J., and Shopbell, P.L., 2000, *ApJ* 544, L27
- [107] Wilson, A. S., Young, A. S., and Shopbell, P. L., 2001, *ApJ* 547, 740
- [108] Wright, M., and Brinkshaw, M. 1984, *ApJ* 281, 135
- [109] Yamashita, A., et al. 1997, *IEEE Trans. Nucl. Sci.*, 44, 847
- [110] Yamashita, A. et al. 1994, The annual meeting of the Astronomical Society of Japan.

[111] Zensus, J., A., Marchall, H. C., and Unwin, S., C., 1995, ApJ 443, 35

Acknowledgments

長いようであつという間だった、5年間の牧島研究室での生活も間もなく終りを向かえます。私も、何とかこうして博士論文を仕上げることができました。この5年間とおして、牧島先生に御指導を頂いたこと、大変あり難く思います。先生の御意見は常に新鮮かつ力強く、私は大量の“power”をいただき、恐ろしいほどの速度で博士論文完成に向け突き進むことができました。エネルギーを持ってよからぬ方向へと暴走してしまいそうな私ですが、牧島先生には、目的にまっすぐ向かうよういつも“collimate”していただきました。また、博士論文という学生生活の“terminal shock”を通過して、広大な“lobe”へと飛び出していくために必要な多くのことを先生から学んだような気がします。

また、田代先生には電波ロープの逆コンプトン散乱X線の大先輩として、解析の方法やパラメタの計算方法など、いろいろと御指導いただきました。先生との数々の議論はとても貴重で、博士論文の柱となったことは間違いありません。金田さん、伊予本さん電波銀河解析の先輩としていろいろな御意見ありがとうございました。深沢先生、中沢さん、広がった天体の解析は大変ですねえ... 鈴木君、村島さん解析のあとつぎ募集中しています。

同期として牧島研の仲間入りをした寺田君、松本さん5年間ありがとうございました。何度も喧嘩したり、徹夜で語り明かしたり、その他いろいろなことがありますが、すべて忘れません。

このほか、当然ながら牧島研究室の皆さんには本当にお世話になりました。

「あすか」衛星の開発、運用などを行なってきたチームの皆様、本当にありがとうございました。私がこのような博士論文を作成できたのも、まさに「あすか」あってこそです。まことに残念ながら、「あすか」はすでにその貴重な一生を終えてしまいましたが、その重要な成果はこれからも生き続けることでしょう。私もその1ページに記録を残せたこと、ひじょうに光栄でなりません。

Chandra X-ray Observatory Center の Contact Scientist である S. Virani さん、観測計画についていろいろと御迷惑をおかけ致しました。お蔭様で、*Chandra* による電波銀河 3C 452 の観測は予想以上の大成功をおさめることができました。これが私の博士論文の大きな力となったことは、言うまでもありません。

最後に、わたくしの感謝の気持ちを正直に伝えるため、あえて日本語で記したことをお許し下さい。

2001年 吉日

4.2. Nakazawa, Kazuhiro: Ph. D. thesis

121

4.2 Nakazawa, Kazuhiro: Ph. D. thesis

Hard X-ray Emission from Groups of Galaxies Detected with ASCA

Kazuhiro NAKAZAWA

Department of Physics, Faculty of Science, University of Tokyo

kazu@amalthea.phys.s.u-tokyo.ac.jp

December 20, 2000

abstract

Clusters and groups of galaxies are one of the most energetic objects in the universe. We analyzed the ASCA data of near-by 18 groups of galaxies, and found that about half the sample show evidence for an excess hard emission, in addition to the ~ 1 keV thermal emission from the hot intra-group matter (IGM). We present the detailed analysis of HCG 62, which shows the most significant hard excess, as well as the results from the systematical analyses of other 17 groups. With these results, we for the first time study statistical properties of the hard excess X-rays in galaxy groups.

The hard component in HCG 62 is clearly extended; its radial profile is similar to or rather wider than that of the IGM. Its spectra are well fitted by a power-law with photon index ~ 2 or a thermal emission with temperature > 5.7 keV. The $2-10$ keV luminosity of the hard component is derived as $4.2 \times 10^{41} h_{75}^{-2}$ erg s^{-1} , which is $\sim 20\%$ of the IGM luminosity in the $0.5-10$ keV band. For the other groups, 9 out of 17 sample show evidence of a hard component, with the luminosity in the range $1 \sim 18 \times 10^{41} h_{75}^{-2}$ erg s^{-1} , which is $10 \sim 40\%$ of that of the IGM. On the other hand, the remaining 8 groups do not exhibit statistically significant hard emission, with an upper limit of $\sim 5\%$ of the IGM.

The hard X-rays suggest the existence of high energy particles widely distributed in the inter-galactic space. We searched many parameters for correlation with the strength of the hard X-rays, and found that most of the groups with significant hard excess emission host a few bright galaxies in their central regions, while those without hard emission predominantly host a single dominant galaxy. Using all these results, we derive constraints on the emission mechanisms proposed for the hard X-rays, and discuss possible acceleration mechanisms of the high energy particles.

Contents

| | |
|--|----------|
| 1 INTRODUCTION | 1 |
| 2 REVIEW | 3 |
| 2.1 Clusters and Groups of Galaxies | 3 |
| 2.1.1 What are clusters and groups of galaxies? | 3 |
| 2.1.2 Optical observations | 4 |
| 2.1.3 X-ray observations | 5 |
| 2.2 X-ray Properties of Clusters and Groups of Galaxies | 7 |
| 2.2.1 X-ray morphology and system mass determination | 7 |
| 2.2.2 X-ray spectra from the ICM | 11 |
| 2.2.3 Correlations between the observed parameters | 14 |
| 2.2.4 X-ray emission from discrete sources | 15 |
| 2.3 Theoretical Backgrounds of High Energy Electrons in Diffuse Plasma | 19 |
| 2.3.1 Power law population of high energy electrons | 19 |
| 2.3.2 Synchrotron emission | 19 |
| 2.3.3 Inverse Compton (IC) emission | 20 |
| 2.3.4 Non-thermal bremsstrahlung emission | 21 |
| 2.3.5 Cooling times | 22 |
| 2.4 Non-thermal Electrons in Clusters of Galaxies | 22 |
| 2.4.1 Cluster radio halos | 23 |
| 2.4.2 Hard X-ray emission | 25 |
| 2.5 Hard X-ray Emission from Other Diffuse Plasma Sources | 28 |
| 2.5.1 Supernova remnant: SN 1006 | 28 |
| 2.5.2 Galactic ridge X-ray emission | 29 |
| 2.5.3 Inverse Compton (IC) emission from the radio lobe | 30 |

| | |
|---|-----------|
| 3 THE ASCA SATELLITE | 33 |
| 3.1 Spacecraft | 33 |
| 3.2 X-Ray Telescope (XRT) | 35 |
| 3.2.1 Design and structure | 35 |
| 3.2.2 Effective area and point spread function (PSF) | 36 |
| 3.3 Gas Imaging Spectrometer (GIS) | 40 |
| 3.3.1 Design and structure | 40 |
| 3.3.2 Data processing | 43 |
| 3.3.3 Background estimation of the GIS | 49 |
| 3.3.4 Subtraction of non X-ray background (NXB) | 50 |
| 3.3.5 Derivation of the cosmic X-ray background (CXB) | 55 |
| 3.3.6 A finer adjustment of the NXB level | 57 |
| 3.4 Solid-state Imaging Spectrometer (SIS) | 61 |
| 3.4.1 Design and structure | 61 |
| 3.4.2 Data processing | 63 |
| 3.4.3 SIS background | 65 |
| 3.4.4 Degradation of the SIS performance | 65 |
| 3.5 Comparison of the GIS and the SIS | 66 |
| 4 THE HCG 62 GROUP | 68 |
| 4.1 Overview | 68 |
| 4.1.1 The HCG 62 Group | 68 |
| 4.1.2 Previous X-ray observations | 70 |
| 4.2 ASCA Observations and Images | 72 |
| 4.3 Spectral Analysis | 76 |
| 4.3.1 Derivation of the spectra | 76 |
| 4.3.2 Single component fits | 77 |
| 4.3.3 Two component fits | 80 |
| 4.3.4 Improved modeling of the IGM emission | 81 |
| 4.3.5 Possible origins of the hard excess emission | 83 |
| 4.4 Spatial Distribution of the Hard X-ray Emission | 86 |
| 4.4.1 Radial dependence of the spectra | 86 |
| 4.4.2 Radial surface brightness profiles | 88 |
| 4.5 Significance of the Hard X-ray Emission | 90 |
| 4.5.1 Photon counts of the hard X-ray emission | 90 |

| | | |
|-------|--|-----|
| 4.5.2 | Justification of the NXB estimation | 91 |
| 4.5.3 | Effects of the XRT+GIS point spread function (PSF) | 94 |
| 4.5.4 | Problems with the IGM modeling | 96 |
| 4.5.5 | Fluctuation of the CXB | 97 |
| 4.5.6 | Effect of the fainter contaminating sources | 99 |
| 4.5.7 | Overall errors | 100 |
| 4.6 | Summary of the Analysis | 101 |

5 DATA ANALYSIS AND RESULTS OF OTHER GROUPS 103

| | | |
|-------|---|-----|
| 5.1 | Observations and Targets | 103 |
| 5.2 | Spectral Analysis | 104 |
| 5.2.1 | Single component fits | 104 |
| 5.2.2 | Two component fits | 109 |
| 5.2.3 | Comments on individual objects | 114 |
| 5.3 | General Properties of the Sample Groups | 117 |
| 5.3.1 | Comparison with the IGM properties | 117 |
| 5.3.2 | The CXB fluctuation and the LMXB contribution | 119 |
| 5.4 | Averaged Properties of HCG 97, RGH 80 and S49-147 | 120 |
| 5.5 | Brief Summary of the Analysis of 17 Groups | 122 |

6 Discussion 124

| | | |
|-------|--|-----|
| 6.1 | Observed Properties of the Hard X-ray Emission | 124 |
| 6.2 | Comparison with Cluster Hard X-ray Emission | 124 |
| 6.3 | Inverse Compton Scattering | 126 |
| 6.3.1 | Derived parameters | 126 |
| 6.3.2 | Comparison with radio observations | 127 |
| 6.3.3 | Total energies and energy densities | 128 |
| 6.3.4 | Examination of the model | 131 |
| 6.4 | Non Thermal Bremsstrahlung | 133 |
| 6.5 | Thermal Interpretation | 134 |
| 6.6 | Candidates for Acceleration and Heating Mechanisms | 136 |
| 6.6.1 | Super novae | 136 |
| 6.6.2 | Active galactic nucleus | 137 |
| 6.6.3 | Galaxy motion | 138 |
| 6.6.4 | Group merger | 141 |

ERROR: syntaxerror
OFFENDING COMMAND:

STACK:

/BT
/GlyphProcs
-savelevel-

Hard X-ray Emission from Groups of Galaxies Detected with ASCA

Kazuhiro NAKAZAWA

Department of Physics, Faculty of Science, University of Tokyo

kazu@amalthea.phys.s.u-tokyo.ac.jp

December 20, 2000

abstract

Clusters and groups of galaxies are one of the most energetic objects in the universe. We analyzed the ASCA data of near-by 18 groups of galaxies, and found that about half the sample show evidence for an excess hard emission, in addition to the ~ 1 keV thermal emission from the hot intra-group matter (IGM). We present the detailed analysis of HCG 62, which shows the most significant hard excess, as well as the results from the systematical analyses of other 17 groups. With these results, we for the first time study statistical properties of the hard excess X-rays in galaxy groups.

The hard component in HCG 62 is clearly extended; its radial profile is similar to or rather wider than that of the IGM. Its spectra are well fitted by a power-law with photon index ~ 2 or a thermal emission with temperature > 5.7 keV. The 2–10 keV luminosity of the hard component is derived as $4.2 \times 10^{41} h_{75}^{-2}$ erg s^{-1} , which is $\sim 20\%$ of the IGM luminosity in the 0.5–10 keV band. For the other groups, 9 out of 17 sample show evidence of a hard component, with the luminosity in the range $1 \sim 18 \times 10^{41} h_{75}^{-2}$ erg s^{-1} , which is 10 \sim 40% of that of the IGM. On the other hand, the remaining 8 groups do not exhibit statistically significant hard emission, with an upper limit of $\sim 5\%$ of the IGM.

The hard X-rays suggest the existence of high energy particles widely distributed in the inter-galactic space. We searched many parameters for correlation with the strength of the hard X-rays, and found that most of the groups with significant hard excess emission host a few bright galaxies in their central regions, while those without hard emission predominantly host a single dominant galaxy. Using all these results, we derive constraints on the emission mechanisms proposed for the hard X-rays, and discuss possible acceleration mechanisms of the high energy particles.

Contents

| | |
|--|----------|
| 1 INTRODUCTION | 1 |
| 2 REVIEW | 3 |
| 2.1 Clusters and Groups of Galaxies | 3 |
| 2.1.1 What are clusters and groups of galaxies ? | 3 |
| 2.1.2 Optical observations | 4 |
| 2.1.3 X-ray observations | 5 |
| 2.2 X-ray Properties of Clusters and Groups of Galaxies | 7 |
| 2.2.1 X-ray morphology and system mass determination | 7 |
| 2.2.2 X-ray spectra from the ICM | 11 |
| 2.2.3 Correlations between the observed parameters | 14 |
| 2.2.4 X-ray emission from discrete sources | 15 |
| 2.3 Theoretical Backgrounds of High Energy Electrons in Diffuse Plasma | 19 |
| 2.3.1 Power law population of high energy electrons | 19 |
| 2.3.2 Synchrotron emission | 19 |
| 2.3.3 Inverse Compton (IC) emission | 20 |
| 2.3.4 Non-thermal bremsstrahlung emission | 21 |
| 2.3.5 Cooling times | 22 |
| 2.4 Non-thermal Electrons in Clusters of Galaxies | 22 |
| 2.4.1 Cluster radio halos | 23 |
| 2.4.2 Hard X-ray emission | 25 |
| 2.5 Hard X-ray Emission from Other Diffuse Plasma Sources | 28 |
| 2.5.1 Supernova remnant: SN 1006 | 28 |
| 2.5.2 Galactic ridge X-ray emission | 29 |
| 2.5.3 Inverse Compton (IC) emission from the radio lobe | 30 |

| | |
|---|-----------|
| 3 THE ASCA SATELLITE | 33 |
| 3.1 Spacecraft | 33 |
| 3.2 X-Ray Telescope (XRT) | 35 |
| 3.2.1 Design and structure | 35 |
| 3.2.2 Effective area and point spread function (PSF) | 36 |
| 3.3 Gas Imaging Spectrometer (GIS) | 40 |
| 3.3.1 Design and structure | 40 |
| 3.3.2 Data processing | 43 |
| 3.3.3 Background estimation of the GIS | 49 |
| 3.3.4 Subtraction of non X-ray background (NXB) | 50 |
| 3.3.5 Derivation of the cosmic X-ray background (CXB) | 55 |
| 3.3.6 A finer adjustment of the NXB level | 57 |
| 3.4 Solid-state Imaging Spectrometer (SIS) | 61 |
| 3.4.1 Design and structure | 61 |
| 3.4.2 Data processing | 63 |
| 3.4.3 SIS background | 65 |
| 3.4.4 Degradation of the SIS performance | 65 |
| 3.5 Comparison of the GIS and the SIS | 66 |
| 4 THE HCG 62 GROUP | 68 |
| 4.1 Overview | 68 |
| 4.1.1 The HCG 62 Group | 68 |
| 4.1.2 Previous X-ray observations | 70 |
| 4.2 ASCA Observations and Images | 72 |
| 4.3 Spectral Analysis | 76 |
| 4.3.1 Derivation of the spectra | 76 |
| 4.3.2 Single component fits | 77 |
| 4.3.3 Two component fits | 80 |
| 4.3.4 Improved modeling of the IGM emission | 81 |
| 4.3.5 Possible origins of the hard excess emission | 83 |
| 4.4 Spatial Distribution of the Hard X-ray Emission | 86 |
| 4.4.1 Radial dependence of the spectra | 86 |
| 4.4.2 Radial surface brightness profiles | 88 |
| 4.5 Significance of the Hard X-ray Emission | 90 |
| 4.5.1 Photon counts of the hard X-ray emission | 90 |

| | | |
|----------|--|------------|
| 4.5.2 | Justification of the NXB estimation | 91 |
| 4.5.3 | Effects of the XRT+GIS point spread function (PSF) | 94 |
| 4.5.4 | Problems with the IGM modeling | 96 |
| 4.5.5 | Fluctuation of the CXB | 97 |
| 4.5.6 | Effect of the fainter contaminating sources | 99 |
| 4.5.7 | Overall errors | 100 |
| 4.6 | Summary of the Analysis | 101 |
| 5 | DATA ANALYSIS AND RESULTS OF OTHER GROUPS | 103 |
| 5.1 | Observations and Targets | 103 |
| 5.2 | Spectral Analysis | 104 |
| 5.2.1 | Single component fits | 104 |
| 5.2.2 | Two component fits | 109 |
| 5.2.3 | Comments on individual objects | 114 |
| 5.3 | General Properties of the Sample Groups | 117 |
| 5.3.1 | Comparison with the IGM properties | 117 |
| 5.3.2 | The CXB fluctuation and the LMXB contribution | 119 |
| 5.4 | Averaged Properties of HCG 97, RGH 80 and S49-147 | 120 |
| 5.5 | Brief Summary of the Analysis of 17 Groups | 122 |
| 6 | Discussion | 124 |
| 6.1 | Observed Properties of the Hard X-ray Emission | 124 |
| 6.2 | Comparison with Cluster Hard X-ray Emission | 124 |
| 6.3 | Inverse Compton Scattering | 126 |
| 6.3.1 | Derived parameters | 126 |
| 6.3.2 | Comparison with radio observations | 127 |
| 6.3.3 | Total energies and energy densities | 128 |
| 6.3.4 | Examination of the model | 131 |
| 6.4 | Non Thermal Bremsstrahlung | 133 |
| 6.5 | Thermal Interpretation | 134 |
| 6.6 | Candidates for Acceleration and Heating Mechanisms | 136 |
| 6.6.1 | Super novae | 136 |
| 6.6.2 | Active galactic nucleus | 137 |
| 6.6.3 | Galaxy motion | 138 |
| 6.6.4 | Group merger | 141 |

| | | |
|----------|--|------------|
| 7 | Conclusion | 142 |
| A | Individual Properties of the Five Observations of HCG 62 | 144 |
| A.1 | Ratio of the spectra | 144 |
| A.2 | Radial Profiles | 145 |
| B | Detailed Analysis of the 4.0–8.0 keV Band Image of HCG 62 | 146 |
| B.1 | Image clumpiness | 146 |
| B.2 | Correlation with the galaxies | 146 |
| B.3 | Azimuthal dependence | 147 |
| C | Calculation of the CXB Fluctuation | 149 |
| C.1 | Formulation of the CXB fluctuation | 149 |
| C.2 | Effective beam size for the XRT+GIS | 150 |
| D | Analysis Results of All Groups | 153 |
| D.1 | Images and integration regions | 153 |
| D.2 | Spectra | 159 |
| D.2.1 | Single component fits | 159 |
| D.2.2 | Two component fits | 161 |
| D.3 | Optical images of central 300 h_{75}^{-1} kpc. | 163 |

List of Tables

| | | |
|-----|---|----|
| 2.1 | Definitions of the solar abundances by number, employed in the present thesis | 14 |
| 2.2 | Observed properties of cluster radio halos (Feretti and Giovannini 1996, Liang 1999). | 24 |
| 2.3 | Observed properties of cluster radio relics (Feretti and Giovannini 1996). Columns are similar to those of Table 2.2. | 24 |
| 2.4 | Observed properties of cluster hard X-ray emission. | 28 |
| 3.1 | Design parameters and performance of the ASCA XRT. | 39 |
| 3.2 | Design parameters and performance of the GIS | 40 |
| 3.3 | The "flare cut" screening criteria for the GIS. Time region satisfying this criteria are excluded from the analysis. | 54 |
| 3.4 | Design parameters and performance of the SIS | 62 |
| 3.5 | The major contents of "rev.2 standard" data screening criteria for the SIS (from <i>The ASCA Data Reduction Guide</i>). | 65 |
| 4.1 | Optical properties of the central four galaxies of HCG 62 | 69 |
| 4.2 | Log of ASCA Observations of the HCG 62 group. | 73 |
| 4.3 | Best fit parameters from the joint fit to the GIS and SIS spectra obtain from the circular region of $r < 15'$ | 79 |
| 4.4 | Results of the joint fit to the GIS and SIS spectra with two component models. | 81 |
| 4.5 | Results of the joint fit to the GIS and SIS spectra with multi component models involving a vMEKAL component. | 83 |
| 4.6 | Possible origins of the hard excess emission. | 85 |
| 4.7 | Best fit parameters to the radially sorted GIS and SIS spectra, fitted with a sum of a single temperature vMEKAL component and a power law component with $\Gamma = 2.0$ (vMEKAL+PL model). | 86 |

| | | |
|------|--|-----|
| 4.8 | Best fit parameters of the $0' < r < 3'$ GIS and SIS spectra, fitted with a sum of double vMEKAL components and a power law component with $\Gamma = 2.0$ (2-vMEKAL+PL model). | 88 |
| 4.9 | Photon counts in the 4.0-8.0 keV band detected in each pointing within the $0' < r < 15'$ region of HCG 62. Errors are 1σ | 90 |
| 4.10 | Sum of photon counts derived from Table 4.9, with the estimated IGM contribution. | 91 |
| 4.11 | Determination of the NXB correction factor f_{cor} . ⁽¹⁾ | 92 |
| 4.12 | CXB fluctuation in the 2.0-10.0 keV band, derived from past studies. | 97 |
| 4.13 | Summary of the excess hard photons in the $r < 15'$ region. Contributions from all examined components are listed, with the estimated errors. | 101 |
| 4.14 | Luminosities of the soft and hard components of HCG 62. | 101 |
| 5.1 | The sample objects selected for the present study. | 105 |
| 5.2 | Observation log of the targets. | 106 |
| 5.3 | Results of the joint fit to the GIS and SIS spectra with a single component vMEKAL model. | 108 |
| 5.4 | Results of the joint fit to the GIS and SIS spectra with the two component model. | 111 |
| 5.5 | Results of the joint fit to the GIS and SIS spectra averaged over HCG 97, RGH 80 and S49-147, with vMEKAL+PL model. | 121 |
| 6.1 | Radio observations of the HCG 62 sky field. | 127 |
| 6.2 | The energy density of the thermal and non-thermal components in HCG 62, derived from the IC model. | 129 |
| 6.3 | The total energy of the thermal and non-thermal components in HCG 62 and the three clusters, derived from the IC model. | 130 |
| 6.4 | Criteria for dividing the group sample into three sub-categories. | 139 |
| 6.5 | Galaxy number counts within $50h_{75}^{-1}$ kpc of the group center. | 139 |

List of Figures

2.1 (a) Optical image of the Coma cluster (1.5×1.5 Mpc scale), which is a rich, non-cD cluster. (b) The NGC 5044 group (0.5×0.5 Mpc scale), which is a poor, cD group. 5

2.2 The X-ray gray scale image of (a) the Coma cluster and (b) the NGC 5044 group. The images observed with the ROSAT PSPC (Position Sensitive Proportional Counter) are shown in the same scale as those in Fig.2.1. The image level is logarithmically spaced, by factors of 1.33. 6

2.3 Integrated mass profile of total gravitating mass (solid lines), dark matter (dashed lines), X-ray emitting plasma (dot-dashed lines) and stellar component (dotted line). Three curves for the former three components show the little difference depending on the plasma modeling (see Ikebe et al 1996). 8

2.4 Radial X-ray surface brightness profile of (a) the Abell 262 cluster and (b) the Abell 401 cluster. The former is fitted with a single β -model, while the latter is fitted by adding another β -model ($2\text{-}\beta$ -model) to compensate for the central excess (Mohr et al. 1999). In the image, contour appears at factors of 2.5 in surface brightness, and the heavy contour corresponds to 4×10^{-14} erg s $^{-1}$ cm $^{-2}$ arcmin $^{-2}$ 10

2.5 Optically thin thermal emission model from hot plasma with metal abundances of one solar value (Mewe et al. 1985, 1986; Kaastra et al. 1992, Liedahl et al. 1995; black lines), at a temperature of (a) 1 keV and (b) 4 keV. In panel (a), we also plot the model spectrum from other emission code (Raymond and Smith 1977), which has the same parameters, except the normalization, to show the difference among the models. 12

2.6 X-ray spectra from (a) the NGC 5044 group (this thesis) and (b) the Abell 2199 cluster (Fukazawa 1996), observed with ASCA. Data from the GIS and SIS detectors are presented with crosses. Solid histograms are the best fit single temperature thermal emission models, with (a) $kT = 1.02$ keV and (b) 4.1 keV. Both spectra include the instrumental responses. 13

2.7 The Fe abundance of the ICM of various clusters and groups, plotted as a function of the ICM temperature. The data are derived from the spectra obtained with ASCA. X-ray emission from the cluster central regions are excluded (Fukazawa 1997). 13

2.8 $kT - L_X$ relation of cluster of galaxies obtained with ASCA. The X-ray luminosity is measured in 0.5-10 keV (Fukazawa 1996). 15

2.9 $kT - \sigma$ relation of clusters and groups of galaxies (Xue and Wu 2000). Data from 66 groups and 274 clusters drawn from the literature are shown. Solid line indicates the relation, $\mu n_p \sigma_{V_r}^2 = kT_{\text{gas}}$ 16

2.10 The X-ray luminosity of several AGN as compared with the radio luminosity of core region (Matsumoto et al. 2001). 16

2.11 X-ray luminosity of the galaxy as compared with the optical B-band luminosity. (a) Einstein results by Canizares et al. (1987). X-ray luminosity is in the 0.5-4.5 keV band. Long-dashed line represents the LMXB component estimated from the early-type spiral galaxies and their bulge emission. (b) ASCA results by Matsushita (1998). X-ray luminosity is in the 0.5-10 keV band. Solid line is the same as the long-dashed line in panel (a), converted for the energy band. Filled circles are the luminosity of the hard component in the X-ray spectra of elliptical galaxies, while the open circles are those of the ICM component. Double circles indicate the galaxies possibly hosting an AGN. 17

2.12 The energy loss function in condition of (a) $n_e = 1 \times 10^{-3}$ cm $^{-3}$ and $B = 1\mu\text{G}$, and (b) $n_e = 0.1 \times 10^{-3}$ cm $^{-3}$ and $B = 0.1\mu\text{G}$. Dotted lines indicate the cooling time of 10^8 yr and 10^9 yr, respectively. 22

| | | |
|------|---|----|
| 2.13 | (a) A contour image of the radio halo, Coma-C, at 1.4 GHz. The width of the image corresponds to $\sim 3.2h_{75}^{-1}$ Mpc. Point sources are subtracted. In the bottom right, there is a relic (1253 + 275), and another relic (Coma Bridge) is also visible between Coma-C and 1253 + 275 (Deiss et al. 1997). Contours are 10 mJy beam ⁻¹ apart, where the dashed one represents the zero level. (b) A gray scale image of relics in A3667 at 843 MHz, superposed on the X-ray contour image from ROSAT (Röttgering et al. 1997). The width of the image corresponds to $\sim 2.8h_{75}^{-1}$ Mpc. X-ray contours are set at 2,8,18,32,50,72,98,128,162,200 and 242 times the background noise. | 25 |
| 2.14 | Radio properties of Coma-C (Deiss et al. 1997). (a) Azimuthally averaged surface brightness profile from Fig.2.13a (solid curve). Dotted line represents the surface brightness of the X-ray emission. (b) Integrated flux density spectrum. | 26 |
| 2.15 | X-ray spectra of the Coma cluster observed with BeppoSAX (Fusco-Femiano et al. 1999). Combined spectra from the HPGSPC (High Pressure Gas Scintillator Proportional Counter) and PDS (Phoswich Detection System) detectors are fitted with a sum of a 8.5 keV thermal emission and a power law with a photon index of $\Gamma = 1.57$ | 26 |
| 2.16 | (a) X-ray image of SN 1006. (b) X-ray spectra, obtained from the rim region and interior region. | 29 |
| 2.17 | X-ray image and spectra of GRXE. (a) The 2-6 keV band image from EXOSAT (Warwik et al. 1985). (b) ASCA spectra obtained from galactic latitudes of 0°, 0.5°, 1.1° and 1.7° (Kaneda et al. 1997). (c) Ginga X-ray and other γ -ray spectra (Yamasaki et al. 1997). | 31 |
| 2.18 | X-ray gray scale image from ASCA, overlaid on the 1.4 GHz radio contour map of Fornax-A. The solid circle represents the ASCA GIS field of view of $\sim 22'$ radius. In the X-ray image, contribution from a central source have been subtracted. Contours are at 125,187.5,250,375,1125 and 1375 mJy beam ⁻² | 32 |
| 3.1 | In orbit configuration of ASCA. | 34 |
| 3.2 | Configuration of the onboard instruments. | 34 |
| 3.3 | Walter type I optics. | 36 |
| 3.4 | The schematic view of the ASCA XRT. A top view of a quadrant (left) and a cross section of one telescope (right). | 37 |

| | | |
|------|---|----|
| 3.5 | (a) Effective area of the four X-ray telescopes on boresight position. (b) The incident angle (θ) dependence of the effective area (vignetting). | 37 |
| 3.6 | (a) X-ray contour image of a point source observed with GIS2. The actual images of Cyg X-1 obtained from three different observations are plotted together. (b) Radial profile of the XRT+GIS PSF at 1'.8 offset (position 1 in panel a). (c) Radial profile of the PSF at 8' offset (position 3 in panel a). | 38 |
| 3.7 | Cross section view of the GIS detector. | 41 |
| 3.8 | Schematic view of the GIS sensor system. | 42 |
| 3.9 | (a) Quantum efficiency of the GIS detector. Energy dependence of the thermal shield transmission (thin solid line), 10.5 μ m thick Be window transmission (dashed line), and total GIS quantum efficiency including thermal shield, plasma shield, Be window, and meshes (thick solid line). (b) Energy dependence of the energy resolution (FWHM) of the GIS. | 44 |
| 3.10 | Rise time discrimination. (a) An example of <i>RAWX-RAWY</i> image of a celestial X-ray point source, obtained with GIS2 in a very early observation. No background rejection was applied, except the pulse-height UD. (b) The X-ray events contained in the image of panel (a), displayed on the plane of <i>PH</i> vs. <i>RT</i> . Two horizontal lines represent the standard onboard <i>RT</i> window. Panel (c) and (d) are the same as (a) and (b), respectively, but after the strict <i>RT</i> mask is applied. | 45 |
| 3.11 | A scatter plot of events from a blank sky displayed on the plane of squared radial distance from the center in <i>RAWX-RAWY</i> image vs. <i>SP</i> . A nearly horizontal branch is formed by signal X-rays of the CXB, while a nearly vertical branch, which means a large scatter in the spread of UV light, originates from background near the detector wall. Two slant lines indicate the standard <i>SPD</i> window. | 46 |
| 3.12 | Schematic view of the 6 monitor data in the <i>PH</i> vs <i>RT</i> plane. | 46 |
| 3.13 | The gain maps in (<i>RAWX,RAWY</i>) coordinates for GIS2 (left panel) and GIS3 (right panel). Contour levels are every 10 step from 350. | 47 |
| 3.14 | (a) Peak <i>PH</i> channels of the ⁵⁵ Fe calibration isotope, plotted against the detector temperature measured in orbit on the side wall of IPMT. (b) Long-term gain history since the launch till July 2000, expressed in terms of the temperature-corrected ⁵⁵ Fe <i>PH</i> . In both plots, upper and lower panels are for GIS2 and GIS3, respectively. | 48 |

3.15 The spectra of the Crab Nebula obtained with (a) the GIS2 and (b) GIS 3. Both spectra are fitted by a power law model with $\Gamma = 2.09$, which is consistent with previously observed results of $\Gamma = 2.08 \sim 2.11$ (Toor and Seward 1974). In the lower panels, the data to model ratios are plotted, which demonstrate the accuracy of the current understanding of the instrumental responses. 49

3.16 (a) Long-exposure GIS2+GIS3 spectra accumulated over the whole field of view, from day-earth pointings (smooth line; representing the NXB plus scattered solar X-rays), night-earth pointings (filled circles; the NXB only), and blank skies observations (crosses; the NXB plus the CXB). The exposure time is given in parentheses. Identifications of the atomic lines, either celestial or instrumental, are also given in the figure together with their energies in keV. The flare-cut (Table 3.3) is NOT applied. (b) Projected count-rate profiles of the blank-sky and night-earth data in a strip of $-5 \text{ mm} \leq XRTY \leq +5 \text{ mm}$ for GIS2. Here "cm²" is defined on the actual detector dimension of the GIS, and is not the effective area of the XRT. Upper panel shows a profile in the 1-2 keV energy band, and lower panel 4-8 keV. The origin of the coordinates for *XRTX-XRTY* is the optical axis defined on the *DETX-DETY* plane. Filled circles, crosses, and diamonds represents the raw CXB including NXB, the NXB, and the CXB after subtracting the NXB, respectively. The flare-cut (Table 3.3) is applied for both the CXB and the residual night-earth data. 51

3.17 Correlation between *COR* and *H02* counts during the night-earth observations. *H02* is integrated for every 32 s. A dashed line means a function $f(x) = (109.3 - 17.05x + 1.127x^2 - 0.02627x^3)/32$ derived from fitting. Two solid lines below and above show $f(x)$ scaled by a factor of 0.9 and 1.5, respectively. A vertical branch observed around $COR \sim 12 \text{ GeV c}^{-1}$ is caused by some flares. The flare-cut (Table 3.3) is NOT applied. 52

3.18 Distribution map for flares on the Earth surface. The symbols "•" and "+" represent positions of the detected flares. The symbol "." represents positions where the *COR*-map is suspected to be inaccurate. Two regions surrounded by solid lines define the dangerous areas where flare events can frequently take place. 53

3.19 (a) The 0.6-7.0 keV radial profiles (upper panel) and spectra (lower panel) of the NXB templates, produced from the GIS data during the night-earth observations. The five *H02* intervals are indicated by '+' (50-80 c/s), 'o' (40-45 c/s), '•' (30-35 c/s), and 'x' (20-25 c/s). The *H02* counts are integrated for every 16 s. The flare-cut (table 3.3) is applied. (b) Long-term histories of the actual 0.7-7.0 keV night-earth counts, normalized to the *H02*-method prediction before correction for secular changes. Each data point represents an exposure of 40 ks. The solid line shows the best fit 4-th order polynomial, of which the coefficients are given in the figure inset. Lower panel shows the residual after subtracting the polynomial fit. 56

3.20 An example of blank-sky GIS image. (a) A 0.5-10 keV GIS2 image of NEP field observed in July 1993, smoothed by convolution with the XRT PSF model. The contours are linearly spaced by $4 \times 10^{-4} \text{ cts s}^{-1} \text{ arcmin}^{-2}$. (b) The associated mask image to eliminate faint discrete sources. 58

3.21 Example of the determination of the NXB correction factor f_{cor} , in terms of the pulse-height spectrum. Abscissa is Pulse Invariant (PI), and ordinate is the number of events. Open boxes represent the on-source spectrum ($Data_{out}(E)$), crosses are the CXB spectrum ($CXB_{out}(E)$) and filled boxes are the NXB template spectrum derived with the *H02* method ($NXB_{out}^{H02}(E)$). 59

3.22 Cross section view of the SIS camera. 61

3.23 (a) Detection efficiency of the SIS as a function of incoming X-ray energy. K-edges of O (0.53keV), Al (1.56keV), and Si (1.84keV) are clearly seen in the figure. This efficiency does not include optical blocking filter. (b) Energy resolutions of the SIS as a function of incoming X-ray energy for the single event. Energy resolutions with different read-out noise N are plotted ($N \sim 5$ for the SIS). The read-out noise levels are given as the equivalent number of electrons. 63

3.24 The SIS background spectra of 4 CCD mode, integrated over all the chips. 66

3.25 Comparison of the GIS (black) and SIS (gray); (a) the effective area, and (b) the background spectra. The latter is normalized by a solid angle of arcmin^2 67

- 4.1 Optical image of the central $6' \times 6'$ region of the HCG 62 group. The four central galaxies are visible. A bright source with a ring and a cross near the center is a foreground star. 69
- 4.2 The 0.5-2.3 keV PSPC X-ray image of HCG 62, smoothed with a Gaussian filter of $\sigma = 0'.25$. The contours are logarithmically spaced, by factors of 1.34, where the lowest one corresponds to 7.2×10^{-4} counts sec^{-1} arcmin^{-2} . The dotted circle indicates the region $15'$ around the group center, and solid circles shows the detected contaminating sources. 70
- 4.3 Temperature of the IGM obtained with Raymond-Smith model fits to the ring sorted PSPC spectra. Errors are in 1σ (Zabludoff and Mulchaey 1998). 71
- 4.4 Radial count-rate profile of the 0.6-2.3 keV PSPC image, fitted with a double-beta model (Zabludoff and Mulchaey 1998). 71
- 4.5 (a) The GIS 0.5-10.0 keV X-ray mosaic image synthesized from five pointings, plotted with their observing positions (indicated by numbers). North is top, and east is to the left. Contours are logarithmically spaced, by factors of 1.7 starting from 1.9×10^{-5} cts s^{-1} arcmin^{-2} . The image is presented after background subtraction, correction for exposure (but not for the vignetting), and smoothing with a Gaussian function with $\sigma = 0'.5$. Solid circle represents the region $15'$ from the group center. (b) The same GIS contour image, overlaid on an optical gray scale image from Digitized Sky Survey. 74
- 4.6 The same as Fig.4.5 but in 0.5-2.0 keV (left) and 2.0-10 keV (right). The contours are logarithmically spaced, by factors of 1.7 starting from 1.6 and 1.3×10^{-5} cts s^{-1} arcmin^{-2} for the left and right panels, respectively. Small and large circles centered on the X-ray peak represent $3'$ and $15'$ from NGC 4761, respectively. Other circles indicate regions eliminated to exclude the five point sources detected with the ROSAT PSPC. 75
- 4.7 The SIS image in 0.5-2.0 keV (left) and 2.0-7.5 keV (right) obtained by combining the five pointings. Both images are smoothed with a $\sigma = 0'.3$ Gaussian kernel. Background is inclusive and exposure is corrected. The contours are logarithmically spaced, by factors of 1.7 starting from 8.1 and 6.5×10^{-5} cts s^{-1} arcmin^{-2} for the left and right panels, respectively. Circles are the same as those of Fig.4.6. Boxes show the region observed with the first pointing, part of which is used for the spectral study. 75

- 4.8 The raw GIS spectra of the HCG 62 group obtained in the five observations. The on-source spectra and the estimated background are shown. The numbers plotted indicates the observation ID. 76
- 4.9 Raw spectra of the HCG 62 group. (a) The raw GIS spectrum extracted from a circular region of radius $15'$ centered on the X-ray centroid, co-adding the five spectra shown in Fig.4.8. Shown for comparison is the background spectrum. (b) The raw SIS spectrum extracted from the same circular region, compared with that of background derived from blank-sky observations. Note that the SIS does not cover the whole region within $15'$. 78
- 4.10 The background-subtracted GIS (black) and SIS (gray) spectra of HCG 62, accumulated within $15'$ from the group center. The histogram in the upper panels show the best fit hot gas model (MEKAL model), and the lower panels present the residual spectra. The joint GIS and SIS fit is performed over the full energy range (left), and in the range above 2.5 keV (right). 79
- 4.11 Two component joint fits to the GIS and SIS spectra as in Fig.4.10. (a) A sum of a MEKAL and a power law model with photon index fixed at $\Gamma = 2.0$. (b) The same as (a), but the photon index is set free. (c) A sum of two MEKAL components. 82
- 4.12 Joint fits to the same GIS and SIS spectra as in Fig.4.10 with a multi component models. In all cases, the photon index of the power law component is fixed at $\Gamma = 2.0$. (a) A sum of a vMEKAL and a power law. (b) A sum of two MEKAL components and a power law. (c) A sum of two vMEKAL components and a power law. 84
- 4.13 Ring sorted spectra of HCG 62, fitted with vMEKAL+PL model, shown for (a) $0' < r < 3'$, (b) $3' < r < 7'.5$, (c) $7'.5 < r < 15'$ and (d) $3' < r < 15'$. (a') is the same as panel (a), but fitted with 2-vMEKAL+PL model. Γ is fixed at 2.0 in all cases. 87

4.14 (a) The 4.0-8.0 keV GIS gray scale image for the central $35' \times 35'$ of HCG 62, corrected for the exposure after subtracting the background. The image was smoothed with a $\sigma = 1'$ Gaussian function. The contour is linearly spaced with separations of 0.5×10^{-5} cts s^{-1} arcmin $^{-2}$, which roughly corresponds to the 1σ level of the CXB fluctuation. The thick line shows the extraction region of the spectra. Crosses represent the position of the galaxies (Zabludoff and Mulchaey 1998). (b) Similar to panel (a), but for the 0.5-4.0 keV band. The contour is scaled by the central brightness to that of panel (a), linearly spaced with separations of 1.2×10^{-4} cts s^{-1} arcmin $^{-2}$. A supplemental contour of 0.6×10^{-4} cts s^{-1} arcmin $^{-2}$ is also plotted in dotted lines. (c) Radial profiles of the X-ray emission, in 4.0-8.0 keV (filled boxes) and 0.5-4.0 keV (open circles with histograms). Thick solid histograms indicate the XRT+GIS PSF in the 4.0-8.0 keV band. X-axis is shown in arcmin, while Y-axis is in cts s^{-1} arcmin $^{-2}$. The later two profiles are rescaled to match the former at the center. 89

4.15 The GIS radial count-rate profile from the group center in the (a) 5.9-10.6 keV band and (b) 4.0-8.0 keV band. The on-source data are shown with black crosses and the background with gray crosses. X-axis is shown in arcmin, while Y-axis is in cts s^{-1} arcmin $^{-2}$ 93

4.16 The 0.5-4.0 keV azimuthally averaged surface brightness profile of the first observation (plotted with crosses), compared with the simulation (histograms), in cts s^{-1} arcmin $^{-2}$. The "central" and the "extended" components of the simulated profile are shown together with their sum. X-axis is shown in arcmin. 95

4.17 The 4.0-8.0 keV counts in the $0' < r < 15'$ region of the five observations (points with error bars) compared with the simulated counts (dashed line). X-axis is shown in channel. 96

4.18 Distribution of the 4.0-8.0 keV CXB counts summed over the five on-source masks, among the 20 blank sky observations. Also plotted is a Gaussian function with $\sigma = 180$ counts, which is the quadrature sum of the typical Poisson error of ~ 100 counts and predicted CXB fluctuation of ~ 150 counts. 99

4.19 Positions of the discrete sources plotted on the (a) 0.4-2.4 PSPC image, and (b) 2-10 keV GIS image. The images are smoothed with a Gaussian filter of $\sigma = 0'.25$ and $0'.5$ for the left and right panels, respectively. The scale levels are shown in the right side of each panel, in units of cts s^{-1} arcmin $^{-2}$. Thick dashed line indicates $3'$ and $15'$ from the group center and thick solid circles represent the five sources already eliminated. Boxes represent the six sources with PSPC count-rate in the range of $2.0 \sim 4.0 \times 10^{-3}$ counts s^{-1} 100

5.1 The 0.5-10.0 keV band X-ray contour images of the GIS and the SIS, for (a) the NGC 1399 group, and (b) the RGH 80 group. They are the same as Figs.4.6(GIS) and 4.7(SIS), except for the energy band. The contours are logarithmically spaced by factors of 1.7, starting from 5×10^{-5} cts s^{-1} arcmin $^{-2}$ for the GIS image of NGC 1399, and from 2.9×10^{-5} cts s^{-1} arcmin $^{-2}$ for that of RGH 80. For the SIS images, the first contour shows 1×10^{-4} cts s^{-1} arcmin $^{-2}$. The smaller dashed circles represent $3'$ from the group center, and the larger ones the integration region for spectral analysis, $20'$ for NGC 1399 and $10'$ for RGH 80. Open squares indicate the positions of the point sources detected with the PSPC, around $3'$ of which are excluded from the analysis. See Fig.D.1 for the remaining groups. . . . 107

5.2 The GIS and SIS spectra of representative object in our sample, jointly fitted with a vMEKAL component. All spectra are plotted to the same scale. The last panel shows the spectra of the elliptical galaxy, NGC 4636. See Fig.D.2 for the remaining targets. 110

5.3 The best fit temperature from the hard-band fitting, compared to that from the full-band fitting. A diamond represents HCG 62, circles the two ellipticals, and squares the other 17 groups. Solid line indicates equal temperature, dotted line 10% higher and dashed line twice of that of the full-band fitting. 112

5.4 The same spectra as shown in Fig.5.2, fitted with a sum of a vMEKAL and a power law components. See Fig.D.3 for the remaining targets. 113

| | | |
|------|---|-----|
| 5.5 | (a) The hard component flux plotted against that of the IGM component. Dashed line represents the ratio of 10%, and dotted line 20%. (b) The luminosity ratio of the hard component to the IGM emission, plotted against the IGM temperature. In both panels, symbols are the same as those in Fig.5.3. | 117 |
| 5.6 | Spectra of the groups divided with those of the NGC 5044. (a) HCG 62, (b) RGH 80, (c) NGC 4325, and (d) NGC 1550. Black crosses represents the GIS, and gray crosses the SIS. | 118 |
| 5.7 | (a) The hard component luminosity (L_{hard}) plotted against that of the IGM (L_{IGM}). Dashed line represents the ratio of 10%, and dotted line 20%. (b) The hard component luminosity (L_{hard}) plotted against the IGM temperature. In both panels, symbols are the same as those in Fig.5.3. | 119 |
| 5.8 | (a) The hard vs IGM luminosity ratio plotted against the full-band flux. Dashed line represents the typical fluctuation of the CXB flux, for an integration region with $r = 10'$. (b) The hard component luminosity (L_{hard}) plotted against the optical B -band luminosity. Dashed line represents the estimated contribution from LMXBs, calculated from equation 2.16. For both panels, symbols are the same as those in Fig.5.3. | 120 |
| 5.9 | The averaged spectra summed over HCG 97, RGH 80 and S49-147, fitted with the vMEKAL+PL model. | 121 |
| 5.10 | The azimuthally averaged radial surface brightness profile, similar to Fig.4.14b of HCG 62. The data from HCG 97, RGH 80 and S49-147 are averaged. The profiles in 4.0-8.0 keV (filled boxes), 0.5-4.0 keV (open circles with histograms), and the PSF of XRT+GIS in the 4.0-8.0 keV band (thick solid histograms) are plotted. | 122 |
| 6.1 | The hard component luminosity plotted against the (a) luminosity and (b) temperature of the hot gas component. Those plots are the same as Fig.5.7, but includes the three clusters (large circles) with significant excess hard X-ray emission. | 125 |
| 6.2 | The 1.4 GHz radio image of HCG 62 from NVSS, The scale levels are shown in the right side, in units of mJy arcmin ⁻² . Solid circle represents $r = 15'$ from the group center. | 128 |
| 6.3 | The total non-thermal energy plotted against that of the thermal component. Dotted line represents a ratio of $1(\frac{1000}{\tau_{\text{min}}})\%$ | 130 |

| | | |
|-----|--|-----|
| 6.4 | The ratio of the observed 4-8 keV radial profile and that of the simulation. See text for details. | 132 |
| 6.5 | Histogram of the groups sorted with the galaxy count within $50h_{75}$ kpc of the group center. Open squares represent the "hard groups", open triangle the "possible hard group". and filled circles the "no hard groups". | 140 |
| A.1 | The raw GIS spectra from the five pointings obtained within 15' from the group center (Fig.4.8), divided by the averaged spectra (Fig.4.9) after the correction for the difference in the detector effective area. | 144 |
| A.2 | The same as Fig.4.15a, but for each observation. | 145 |
| B.1 | The 4.0-8.0 keV GIS gray scale image of the SA-57 region, which is similar to Fig.4.14a for the HCG 62 group. The contour is linearly spaced with distances of 0.5×10^{-5} cts s ⁻¹ arcmin ⁻² . A supplemental contour of -0.5×10^{-4} cts s ⁻¹ arcmin ⁻² is also plotted (dotted lines). | 147 |
| B.2 | Averaged 4-8 keV radial profile centered on 9 galaxies in the HCG 62 field (black crosses), and that of the background (gray crosses), in cts s ⁻¹ arcmin ⁻² . Error bars are in 1σ , which are averaged over the 9 galaxies. The background error includes the CXB fluctuation. Thin histograms show what is expected if the hard component is entirely emitted from these 9 galaxies. | 148 |
| B.3 | Azimuthal profile of the 4-8 keV image of HCG 62, in cts s ⁻¹ arcmin ⁻² . The angle is defined clockwise, the north being the origin. Thin line represents the 1σ level of the estimated CXB fluctuation. Errors are 1σ statistical. | 148 |
| C.1 | (a) The observed Crab counting rate in the 0.7-10 keV energy band plotted against the offset angle from the XRT optical axis. Filled circles represent GIS2 and open circles GIS3. (b) Same as panel (a) but for the larger θ . Solid line represents equation (C.10). | 151 |
| C.2 | Calculation of Ω_e for the XRT+GIS. | 152 |

D.1 The full band X-ray contour images of the GIS and the SIS, similar to Fig.5.1, but for the other groups. In most of the GIS images and all the SIS images, background is not subtracted. The contours are logarithmically spaced by factors of 1.7, starting from 5×10^{-5} cts s^{-1} arcmin $^{-2}$ for the GIS (2.9×10^{-5} cts s^{-1} arcmin $^{-2}$ for NGC 507), and 1×10^{-4} cts s^{-1} arcmin $^{-2}$ for the SIS. Spectral intergration region and positions of the point sources are shown only in the GIS image. 153

D.2 The same as Fig.5.2, plotted for the remaining targets. 159

D.3 The same as Fig.5.4, plotted for the remaining targets. 161

D.4 Optical images of the central $300h_75^{-1}$ kpc region of the groups. "H" indicates the "hard groups", "P" the "possible hard groups", and "N" the "no hard groups" (see Table 6.5). 163

Chapter 1

INTRODUCTION

Clusters of galaxies are known as the largest gravitationally bound system in the universe. A cluster contains thousands of galaxies. It also contains thermal hot plasma (intra-cluster matter, ICM), which is observed as an extended X-ray source, as well as dark matter, which dominates the gravity source. They hold a large amount of gravitational energy, as much as 10^{64} erg, and are one of the most energetic objects among the universe.

Recently, non-thermal hard X-ray emission has been discovered from the Coma cluster by Beppo-SAX and RXTE satellites (Fusco-Femiano et al. 1999, Rephaeli et al. 1999). The emission is observed as a hard excess above the thermal ICM emission, appearing in energies above ~ 30 keV. Together with the diffuse radio halo detected in this cluster, the hard X-rays strongly suggest the existence of high energy particles widely distributed in the inter-galactic space.

The detection of the cluster hard X-rays has a great impact in two aspects. First, the acceleration mechanism itself has a potential to be the long sought origin of the "highest energy cosmic rays", the extremely energetic particles with energy $\sim 10^{20}$ eV arriving at the top of the earth's atmosphere. This is because galaxy clusters are the largest plasma source among the universe with a scale of $\sim 10^{24}$ cm, so that the high energy particles cannot escape from the region for a long time, and it has a relatively low density ($\sim 10^{-11}$ erg cm^{-3}), so that the energy dissipations of the particles are limited. Another issue is the non-thermal pressure associated with the high energy particles and magnetic fields. Because the cluster total mass estimates do not take these effects into account, the amount of the dark matter associated with clusters may increase if these non-thermal pressure components are properly considered. This has a great impact upon the current model of cosmology.

In clusters, the hard excess emission is detectable only above ~ 30 keV, below which

the strong ICM emission with a temperature of $kT = 5 \sim 10$ keV dominates the X-ray spectra. As the sensitivity of the hard X-ray detectors operating above ~ 20 keV is quite limited, currently the non-thermal X-rays are detected from only three clusters, including the Coma cluster (Fusco-Femiano et al. 1999, Rephaeli et al. 1999), the Abell 2256 cluster (Fusco-Femiano et al. 2000) and the Abell 2199 cluster (Kaastra et al. 1999).

Groups of galaxies have many properties similar to those of the clusters. In fact, the major difference between the two types of objects are only in their scale. A group of galaxies also contains a large amount of gravitational energy, as much as 10^{62} erg. On the other hand, the temperature of the hot plasma in a group is fairly low, typically ~ 1 keV. Thus, if a group hosts a non-thermal emission, it may be visible as a hard tail above ~ 4 keV. This is detectable with the current X-ray imaging instruments, such as those onboard the ASCA satellite. ASCA is equipped with X-ray mirror optics covering the energy range up to ~ 10 keV, and provides a high sensitivity and a good imaging capability that is currently unavailable above 10 keV. The GIS experiment onboard ASCA is characterized by its very low and stable background, and we believe that it currently provides the best tool for this study.

In this thesis, we present the observational evidence of excess hard X-ray emission from groups of galaxies obtained with ASCA. We have detected a significant hard excess emission from the HCG 62 group, as is already reported in a brief letter (Fukazawa Y., Nakazawa K. et al. 2001). Here, we perform detailed investigation of the significance and properties of the hard X-rays from HCG 62. In addition, we systematically analyze the ASCA data of other near-by 17 groups. We found about half of them host a significant hard X-rays, while the other half show little evidence for such emission. Utilizing these results, we study statistical properties of the group hard X-rays.

Throughout this thesis, we assume the Hubble constant to be $H_0 = 75h_{75} \frac{\text{Mpc}}{\text{km s}^{-1}}$. All the errors are listed in 90 % confidence level, unless otherwise noted.

Chapter 2

REVIEW

2.1 Clusters and Groups of Galaxies

2.1.1 What are clusters and groups of galaxies ?

Clusters of galaxies have a scale of $L \sim 1$ Mpc (3×10^{24} cm), each consisting of 50–1000 member galaxies (Fig.2.1a). A galaxy itself has a scale of ~ 30 kpc and contains $\sim 10^{10-11}$ stars. Clusters of galaxies are identified mainly on optical plates. They are called rich when they contain many (up to thousand) galaxies and called poor when they contain fewer (down to tens of) galaxies. Sometimes, an extremely luminous elliptical galaxy sits in the cluster center. They are called cD galaxy, and the cluster hosting it is called a cD cluster.

Abell and his colleges cataloged about 5000 rich clusters (Abell 1958, Abell et al. 1989). These clusters are named as, e.g. Abell 1656 (A1656) and Abell S373 (AS373). Zwicky catalog (Zwicky et al. 1961-68) is also well known. For poor clusters, there are several catalogs, including the MKW catalog (Morgan et al. 1975) and AWM catalog (Albert et al. 1977).

Groups of galaxies consist of about ten galaxies, and have a scale of $L = 250 \sim 500$ kpc (Fig.2.1b). They are also mainly identified on optical plates. Hickson (1982) cataloged about 100 compact groups (Hickson's Compact Groups; HCG), which form one of the best studied catalog of groups of galaxies. Another compact group catalog by Shakhbazyan and his colleges (Shakhbazyan's Compact Groups of Galaxies; SCGG or SHK; Shakhbazyan 1973; Shakhbazyan, Petrosyan 1974; Baier et al. 1974; Petrosyan 1974, 1978; Baier and Tiersch 1975, 1976ab, 1978, 1979), as well as a group catalogue by Ramella and his colleges (RGH; 1995a,b), are also known. Groups are also named after its central brightest galaxy,

such as the NGC 5044 group, as well as the constellation name, such as the Pavo group. A group is called "compact" when there are several galaxies within a limited radius (see, e.g. Hickson 1982), and called "loose" when there are not.

2.1.2 Optical observations

The spatial distribution of galaxies in a cluster is empirically known to follow so called King model (King 1962),

$$N(R) = N_0 \left[1 + (R/R_{\text{core}})^2 \right]^{-3/2}. \quad (2.1)$$

Here, R_{core} is the core radius of the cluster which is typically ~ 250 kpc, and N_0 is the central galaxy number density. Throughout this thesis, we denote the three dimensional radius R , and the projected radius r . The King model is an analytic approximation to the equation describing particle distribution in a self-gravitating hydrostatic isothermal system, although it is not valid for $R \gg R_{\text{core}}$ (see also § 2.2.1).

By measuring the redshifts of the member galaxies, we can derive the line-of-sight velocity dispersion, σ_v of the cluster or group, which reflects the depth of the gravitational potential of the system. For rich clusters, this value ranges from 500 km s⁻¹ up to 1300 km s⁻¹. Combining σ_v with the system size L , we can estimate the total gravitating mass of the cluster M_{tot} as

$$M_{\text{tot}} \sim 3\sigma_v^2 \frac{L}{G}, \quad (2.2)$$

where G is the gravitational constant. For example, the Coma cluster, a rich cluster with a velocity dispersion of ~ 1000 km s⁻¹, is shown by this method to have $M_{\text{tot}} \sim 1 \times 10^{15} M_{\odot}$ within 1 Mpc (e.g. Geller et al. 1999). Here, $M_{\odot} = 2 \times 10^{33}$ g is the solar mass. The value is more than an order of magnitude larger than that of the "visible mass", i.e., the mass of the stellar components in galaxies estimated from their optical luminosities. This is so-called "missing mass" problem, which is now regarded as due to the existence of huge amount of dark matter as a major constituent of M_{tot} . The total kinetic energy of a cluster thus derived becomes $\frac{3}{2} M_{\text{total}} \times \sigma_v^2 \sim 10^{64}$ erg, which makes the cluster one of the most energetic objects in the universe.

In groups of galaxies, the velocity dispersion ranges from 100 km⁻¹ to 400 km⁻¹. They have $M_{\text{tot}} \sim$ several times $10^{13} M_{\odot}$ within ~ 250 kpc (e.g., Mulchaey et al. 1996), which is again dominated by the dark matter. Thus, the groups and clusters are similar in their physical states, and differs only in their scales. In other words, group of galaxies is a mini-sized cluster of galaxies. The kinetic energy of a group becomes $\sim 10^{61-62}$ erg, so that the groups are still among the most energetic objects in the universe.

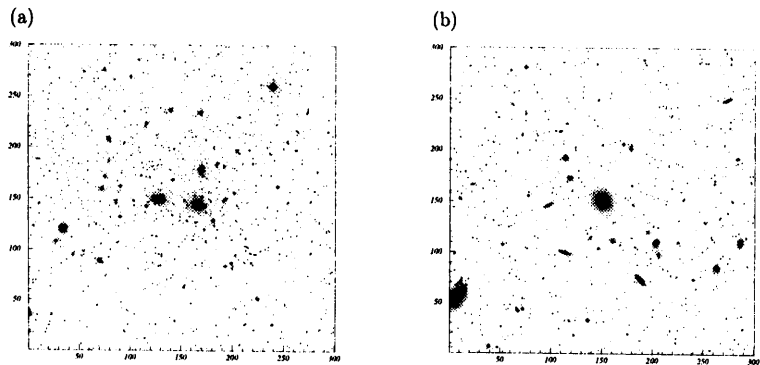


Figure 2.1: (a) Optical image of the Coma cluster (1.5×1.5 Mpc scale), which is a rich, non-cD cluster. (b) The NGC 5044 group (0.5×0.5 Mpc scale), which is a poor, cD group.

2.1.3 X-ray observations

From the days of Uhuru, the first cosmic X-ray satellite launched in 1970, clusters of galaxy have been known as a strong X-ray emitters, with an X-ray luminosity of $L_X \sim 10^{44-45}$ erg s^{-1} . The X-ray emission is extended (Fig.2.2), so that there were two alternative explanations for its emission mechanism; inverse Compton (IC) of cosmic microwave background (CMB) photons by relativistic electrons (see § 2.3.3), and thermal bremsstrahlung from optically thin hot plasma (see § 2.2.2). Later, the detection of He-like Fe-K line emission (Mitchel et al. 1976) showed that the thermal explanation is correct; in fact the X-ray spectra of several brightest clusters were well fitted by a hot plasma emission model with a temperature of $3 \sim 10$ keV (Serlemitsos et al. 1977). These results indicate that clusters are filled with hot plasma, which is called intra-cluster medium (ICM). This has given a big surprise, because the presence of such a large amount of hot plasma had never been anticipated before. The ICM is considered to be confined by the gravitational potential of the cluster. This was justified by the fact that the galaxy velocity dispersion is generally consistent with the potential required to confine the ICM.

The X-ray study of clusters of galaxies has made a big progress with the Einstein observatory, the world's first imaging X-ray mission launched in 1978. In addition to its high sensitivity, the observatory for the first time resolved the spatial distribution of the ICM of many clusters, and derived the total mass distribution in the cluster (e.g.,

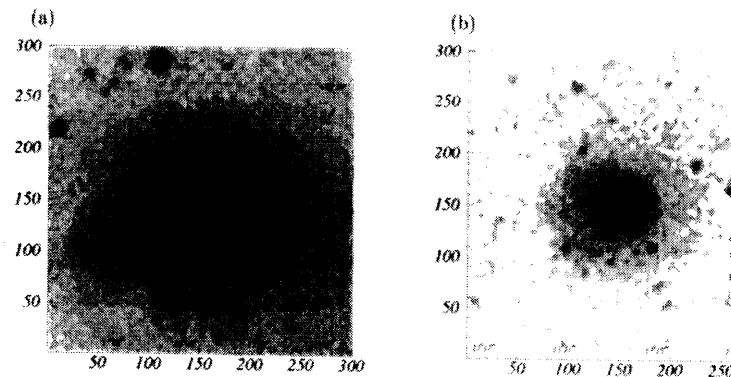


Figure 2.2: The X-ray gray scale image of (a) the Coma cluster and (b) the NGC 5044 group. The images observed with the ROSAT PSPC (Position Sensitive Proportional Counter) are shown in the same scale as those in Fig.2.1. The image level is logarithmically spaced, by factors of 1.33.

Jones and Formann 1984). It was found that the ICM mass often exceeds that of the stellar component, while the total mass is about an order of magnitude larger than the sum of these two. The subsequent ROSAT mission, launched in 1990, with a better angular resolution and a higher sensitivity, has further advanced the X-ray imaging study of clusters. Furthermore, it has initiated the X-ray observation of groups of galaxies (e.g., Mulchaey et al. 1996), which had not been considered generally as X-ray emitters before. With ROSAT, it has become clear that groups host its own hot gas halo, called the intra-group medium (IGM), which is similar to the ICM of the cluster except its lower temperature, around 1 keV. The imaging instruments onboard the two satellites, however, are limited in the soft energy band, 0.2-4.5 keV for the former and 0.1-2.4 keV for the latter, and their spectroscopic resolving power was poor.

Spectroscopic studies of the cluster X-ray emission have been developed by satellites including OSO-8, HEAO-1, Tenma, EXOSAT, and Ginga. Although they lacked imaging capability, they had a wide energy pass-band, ranging from ~ 1 keV up to as high as ~ 30 keV, as well as moderate spectral resolution. From a number of clusters, they measured the spatially-integrated X-ray properties of ICM, such as the temperature and abundance of heavy elements, the latter determined mainly utilizing Fe-K line emission around ~ 6.7 keV.

The ASCA satellite, launched in 1993, is the first observatory to possess both the moderate imaging capability and the high spectroscopic resolving power over a wide energy band, ranging from 0.5 keV up to 10 keV. With ASCA, we have for the first time become able to measure accurately the spatial properties of the ICM temperature and metal abundances (e.g., Fukazawa et al. 2000, Markevitch 1998).

2.2 X-ray Properties of Clusters and Groups of Galaxies

In this section, we outline the basic physics underlying X-ray production in clusters and groups of galaxies, together with their observational results. We briefly summarize the general method of mass determination of the system using the X-ray data, and explain the mechanism of thermal emission from an optically thin hot gas. See Sarazin (1988) for details.

2.2.1 X-ray morphology and system mass determination

Hydrostatic equation of ICM hot gas

The typical value of the density, temperature and extent of the cluster ICM (as well as group IGM and elliptical galaxy ISM) are $n_{\text{gas}} = 10^{-4} - 10^{-2} \text{ cm}^{-3}$, $T = 10^7 - 10^8 \text{ K}$ and $L = 0.3 - 3 \text{ Mpc}$, respectively, while the age of a cluster is thought to be comparable to the Hubble time, $\sim 10^{10} \text{ yr}$. From these parameters, the mean free path of Coulomb collisions between ions and electron is given as $23 \left(\frac{T}{10^8 \text{ K}}\right)^2 \left(\frac{n_{\text{gas}}}{10^{-4} \text{ cm}^{-3}}\right) \text{ kpc}$, which is much shorter than the cluster extent. Similarly the sound crossing time across the cluster is given as $6.6 \times 10^8 \left(\frac{T}{10^8 \text{ K}}\right)^{-1/2} \left(\frac{R}{\text{Mpc}}\right) \text{ yr}$ which is also much shorter than the cluster age. Therefore, the ICM is thought to be under hydrostatic equilibrium, satisfying the equation

$$\nabla P_{\text{gas}} = -\mu m_p n_{\text{gas}} \nabla \phi \quad (2.3)$$

Here P_{gas} is the ICM pressure, ϕ is the gravitational potential, and $\mu \sim 0.6$ is the mean molecular weight of the ICM relative to the proton mass m_p .

Although there are some clusters and groups showing irregular shape in their X-ray image, most of them have generally circular profiles (see Fig.2.1). Assuming a spherical symmetry, and substituting the ICM pressure by $P_{\text{gas}} = n_{\text{gas}} kT$, where k is the Boltzmann

constant, equation 2.3 is re-written as

$$\frac{kT(R)}{\mu m_p} \frac{d \ln [T(R) n_{\text{gas}}(R)]}{dR} = -\frac{d\phi(R)}{dR} \quad (2.4)$$

Then, the total mass within a radius R is derived as

$$M_{\text{tot}}(R) = -\frac{kT}{\mu m_p G} R \left(\frac{d \ln T}{d \ln R} + \frac{d \ln n_{\text{gas}}}{d \ln R} \right) \quad (2.5)$$

Therefore, once the density distribution $n_{\text{gas}}(R)$ and the temperature distribution $T(R)$ of the ICM are known through X-ray observations, we can derive the total mass $M_{\text{tot}}(R)$ of the system. Because we can also derive the ICM mass from $n_{\text{gas}}(R)$, and the stellar mass from the optical luminosity of the member galaxies, we are able to construct the mass profiles of a cluster. In Fig.2.3, we show the mass profiles of the Fornax cluster, derived from the ASCA observations (Ikebe et al. 1996).

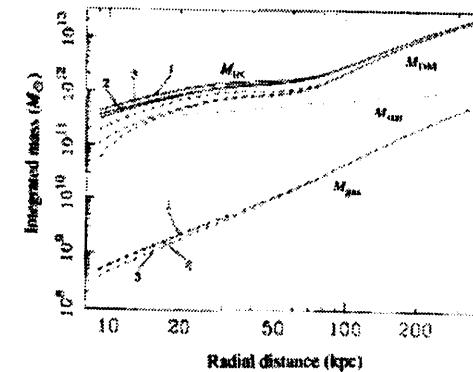


Figure 2.3: Integrated mass profile of total gravitating mass (solid lines), dark matter (dashed lines), X-ray emitting plasma (dot-dashed lines) and stellar component (dotted line). Three curves for the former three components show the little difference depending on the plasma modeling (see Ikebe et al 1996).

Mass profiles

As we have already mentioned in § 2.1.3, there are three mass components consisting a cluster; stars (= galaxies), ICM, and the dark matter. A contemporary consensus is that they have roughly a ratio of $\sim 5:10:90$ (e.g., Rousseld et al. 2000; see also Fig.2.3). Thus,

the majority of the mass is the dark matter, which may be considered as collision-less particles. For a self gravitating system consisting of such particles, hydrostatic equation under spherical symmetry can be written as

$$\sigma_v(R)^2 \frac{d \ln \rho(R)}{dR} = - \frac{d\phi(R)}{dR} \quad (2.6)$$

Here σ_v and ρ are the velocity dispersion and density of the particles, respectively. Combining this equation with the Poisson equation, $\nabla^2 \phi = 4\pi G\rho$, King (1962) derived an analytic approximate solution, as already shown in equation 2.1.

By comparing equations 2.4 and 2.6 we obtain $n_{\text{gas}} \propto \rho^\beta$, where β is the specific energy ratio between the gas and dark matter, given as

$$\beta \equiv \frac{\mu n_p \sigma_v^2}{kT} = 0.726 \left(\frac{\sigma}{10^3 \text{ km s}^{-1}} \right)^2 \left(\frac{T}{10^8 \text{ K}} \right)^{-1} \quad (2.7)$$

When the ICM is isothermal, its density profile in a King potential is given as

$$n_{\text{gas}}(R) = n_0 \left[1 + (R/R_{\text{core}})^2 \right]^{-\frac{3}{2}\beta} \quad (2.8)$$

Thus, the parameter β also represents the steepness of the ICM distribution. This is known as a β -model (Cavaliere and Fusco-Femiano 1976).

The X-ray emissivity is expressed by $n_{\text{gas}}^2 \Lambda(T, Z)$, where Λ is a function of temperature and metal abundance (see § 2.2.2). Therefore, assuming a uniform temperature and abundance we can calculate the surface brightness of the cluster X-ray emission by integrating this emissivity along the line-of-sight as

$$S_B(r) = \int_{-\infty}^{+\infty} n_{\text{gas}}^2 \Lambda dl = S_0 \left[1 + \left(\frac{r}{R_{\text{core}}} \right)^2 \right]^{-3\beta + \frac{1}{2}} \quad (2.9)$$

Here, r is the projected 2-dimensional radius. This formula is known to well reproduce the observed cluster surface brightness, except in the very central regions of some clusters (e.g., Jones and Forman 1984, Mohr et al. 1999; Fig.2.4). Therefore, the β -model is generally used to parameterize the cluster mass distribution.

The central excess emission is generally associated with a cD galaxy (Jones and Forman 1984). In the excess region, there are frequently X-ray spectral evidence for cooler components. Together with short ($\sim 10^8$ yr) cooling time (see next subsection) inferred in such a region, it has been interpreted as a signature of the cooling flow, i.e., ICM inflow driven by its radiative cooling (e.g. Fabian 1994). Alternative explanation for the phenomenon is that the central excess emission is simply due to the particular shape of the gravitational potential associated with the cD galaxy, and the cool component is the

interstellar medium (ISM) of the cD galaxy (e.g., Ikebe 1996, Matsushita et al. 1996, Makishima et al. 2001). In groups of galaxies, the excess emission coincident in position with the central bright elliptical galaxy is common (e.g. Mulchacy and Zabludoff 1998), which is also true of the X-ray brightest elliptical galaxies (e.g. Matsushita 1996).

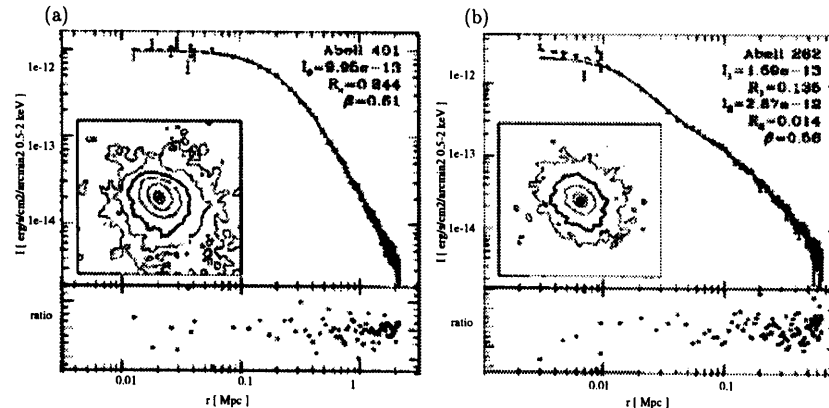


Figure 2.4: Radial X-ray surface brightness profile of (a) the Abell 262 cluster and (b) the Abell 401 cluster. The former is fitted with a single β -model, while the latter is fitted by adding another β -model (2- β -model) to compensate for the central excess (Mohr et al. 1999). In the image, contour appears at factors of 2.5 in surface brightness, and the heavy contour corresponds to 4×10^{-14} erg s $^{-1}$ cm $^{-2}$ arcmin $^{-2}$.

Recent N -body simulation on the formation of clusters in a cold dark matter (CDM) universe has shown that, instead of a King-like profile with a central core, a profile with central cusp is formed (Navarro et al. 1996, 1997; Fukushige et al. 1997; Moore et al. 1998: hereafter NFW profile); it is represented as

$$\rho(R) = \frac{\rho_0}{(R/R_s)(1 + R/R_s)^2} \quad (2.10)$$

where ρ_0 is a normalization parameter, and r_s is a scale parameter. However, there are some observational results which cannot be explained by the NFW potential (e.g. Ikebe et al. 1996). Thus, the actual profile of the dark matter density is still under discussion. The gas density profile in the NFW potential calculated by Makino et al. (1998) was shown to be very similar to the β -model profile. Thus, the β -model still works as a reasonable description of a gas density profile.

All the above calculations assume that the gas pressure is the only force sustaining the hot gas against the gravitational potential. However, there may exist non-thermal pressures, originating from the magnetic field, and/or a population of high energy particles distributed in the ICM. Generally, their contributions are assumed to be small compared to the gas pressure, though we must carefully examine its possibility, which is one of the aim of this thesis.

Recent observations with ROSAT and ASCA have shown the existence of temperature and morphology sub-structures in some clusters. This is thought as an evidence of on-going merger process. Because a galaxy group falling into a cluster has a kinematic energy of $\sim 10^{62-63}$ erg, the merger process is important in the ICM heating and, possibly, particle acceleration.

2.2.2 X-ray spectra from the ICM

The ICM (including the IGM and ISM) is an optically thin hot plasma, and its main radiation mechanism is thermal bremsstrahlung (free-free emission). The emissivity is given as

$$\epsilon^{ff}(\nu) = 6.8 \times 10^{-38} Z^2 n_e n_i T^{-1/2} e^{-h\nu/kT} \bar{g}_{ff} \quad [\text{ergs}^{-1} \text{cm}^{-3} \text{Hz}^{-1}] \quad , \quad (2.11)$$

where ν is the frequency of the photons emitted, n_e and n_i are the densities of electron and ion, respectively, Z is the effective charge number of the ion, and T is the temperature of the plasma. The velocity averaged Gaunt factor \bar{g}_{ff} has a value of ~ 1 , and weakly dependent on ν and T (Rybicki and Lightman 1979).

In addition to the free-free continuum, heavy elements in the ICM produce line emissions. When the ICM temperature is lower than ~ 2 keV, these lines carry as high luminosity as the thermal bremsstrahlung continuum. The emission line spectra from a hot plasma in an ionization equilibrium have been calculated by various authors, e.g. Raymond and Smith (1977), Masai (1984), Kaastra and Mewe (1993) and so on. Their predictions are consistent to one another, as well as the observed spectra, as least as to K-shell emission lines, such as those at 6.6–6.9 keV from Fe, and 1.8–2.0 keV from Si. However, the ionization and recombination rates of L-shell electrons are not easily calculated, and the results differ considerably among the authors (e.g. Masai 1997). In practice, this problem is most prominent for the Fe-L line complex observed in the 0.7–1.5 keV region (Arimoto et al. 1997, see Fig.2.5a). We have to be careful about this problem when fitting the observed spectra with these models. Examples of the calculated

model spectra are shown in Fig.2.5, and those from actual clusters and groups observed by ASCA are shown in Fig.2.6, together with the best fit thermal model.

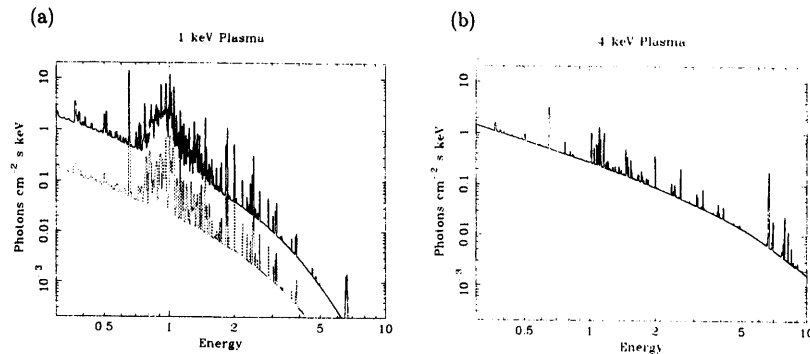


Figure 2.5: Optically thin thermal emission model from hot plasma with metal abundances of one solar value (Mewe et al. 1985, 1986; Kaastra et al. 1992; Liedahl et al. 1995; black lines), at a temperature of (a) 1 keV and (b) 4 keV. In panel (a), we also plot the model spectrum from other emission code (Raymond and Smith 1977), which has the same parameters, except the normalization, to show the difference among the models.

The total volume emissivity of a plasma, including continuum and line emissions and integrated over whole frequency, is expressed as

$$\epsilon = n_{\text{gas}}^2 \Lambda(T, Z) \quad [\text{erg s}^{-1} \text{cm}^{-3}] \quad . \quad (2.12)$$

Here $\Lambda(T, Z)$ is called the cooling function and Z represents the heavy element abundances. From this equation, the cooling time of a plasma is derived as $t_{\text{cool}} = n_{\text{gas}} kT / n_{\text{gas}}^2 \Lambda(T, Z)$. When we consider only the thermal bremsstrahlung continuum, it becomes

$$t_{\text{cool}} = 8.5 \times 10^{10} \left(\frac{n_{\text{gas}}}{10^{-3} \text{cm}^{-3}} \right) \left(\frac{T}{10^8 \text{K}} \right) \quad [\text{yr}] \quad , \quad (2.13)$$

which is longer than the cluster age for most cases.

Before detected by the X-ray detectors in orbit, photons emitted from a cluster travel along the vast universe. Thus, it is red-shifted by the Hubble's law, and suffers absorption from materials along its journey. The latter is mainly due to the gas and dust of our Galaxy, which can be estimated from radio observations (e.g. Dicky and Lockmann 1990).

In calculating the emission models, the abundances of heavy elements (Z) must be specified. They are usually defined as a ratio to so-called solar abundances (Z_{\odot}). In this

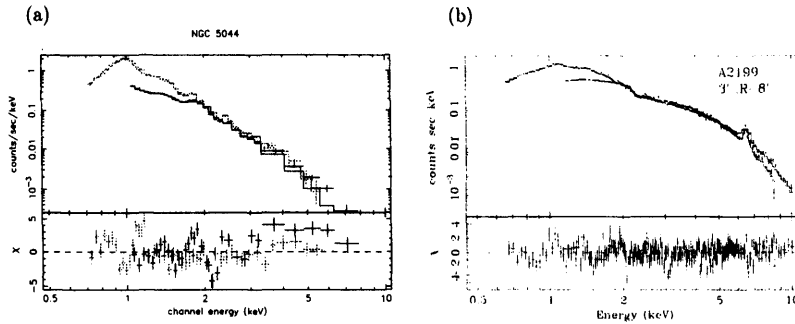


Figure 2.6: X-ray spectra from (a) the NGC 5044 group (this thesis) and (b) the Abell 2199 cluster (Fukazawa 1996), observed with ASCA. Data from the GIS and SIS detectors are presented with crosses. Solid histograms are the best fit single temperature thermal emission models, with (a) $kT = 1.02$ keV and (b) 4.1 keV. Both spectra include the instrumental responses.

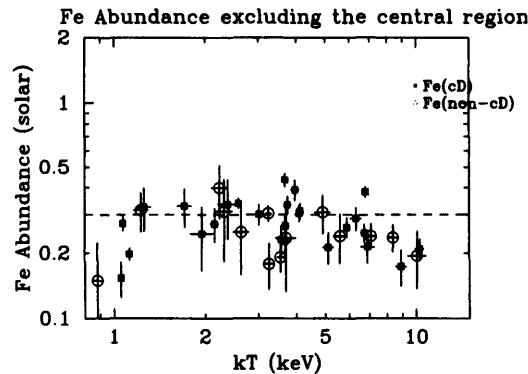


Figure 2.7: The Fe abundance of the ICM of various clusters and groups, plotted as a function of the ICM temperature. The data are derived from the spectra obtained with ASCA. X-ray emission from the cluster central regions are excluded (Fukazawa 1997).

thesis, we use the solar abundances given by Anders and Grevesse (1989), listed in Table 2.1. The metal abundances of ICM and IGM, derived from the spectral fitting, generally range $Z = 0.1 \sim 0.5 Z_{\odot}$, which are typically $\sim 0.3 Z_{\odot}$ (e.g. Fukazawa 1997; Fig.2.7).

Table 2.1: Definitions of the solar abundances by number, employed in the present thesis

| element | number | element | number | element | number |
|---------|---------|---------|---------|---------|---------|
| H | 1.00e+0 | Na | 2.14e-6 | Ar | 3.63e-6 |
| He | 9.77e-2 | Mg | 3.80e-5 | Ca | 2.29e-6 |
| C | 3.63e-4 | Al | 2.95e-6 | Cr | 4.84e-7 |
| N | 1.12e-4 | Si | 3.55e-5 | Fe | 4.68e-5 |
| O | 8.51e-4 | S | 1.62e-5 | Co | 8.60e-8 |
| Ne | 1.23e-4 | Cl | 1.88e-7 | Ni | 1.78e-6 |

2.2.3 Correlations between the observed parameters

There are several correlations in the X-ray, optical and radio properties of clusters, groups and elliptical galaxies. Some are theoretically predicted, while others are empirical (e.g. Sarazin 1988). Among them, we here review a few of the highest importance.

$kT - L_X$ relation

As exemplified by Fig.2.8, a clear correlation has been observed between the temperature of the ICM and the X-ray luminosity (e.g., Mushotzky 1984; David et al 1993; Markevitch 1998; Fukazawa 1997). This can be expressed as

$$L_X = (kT)^\alpha, \quad (2.14)$$

with $\alpha \sim 3$. The intrinsic scatter in luminosity is very large, factor of ~ 10 for the same temperature. This is partly due to the central excess emission, and the scatter decreases by eliminating the contribution from this region (Markevitch 1998). By introducing another parameter, the central gas density derived after excluding the central excess component, Fujita and Takahara (1999) found that clusters of galaxy do form a two parameter family, which is called the X-ray fundamental plane of clusters. They showed that the $kT - L_X$ plane is slightly offset from the plane, which causes the scatter. From the $kT - L_X$ relation, $L_X \sim 10^{41-42} \text{ erg s}^{-1}$ is expected for a galaxy group with $kT = 1$ keV.

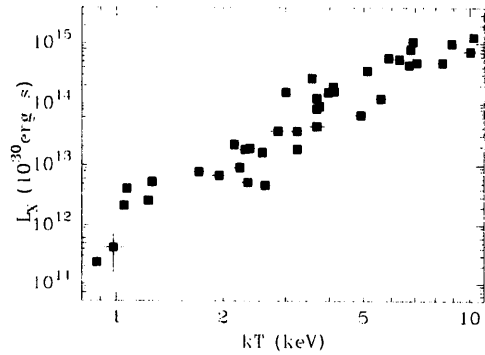


Figure 2.8: $kT - L_X$ relation of cluster of galaxies obtained with ASCA. The X-ray luminosity is measured in 0.5-10 keV (Fukazawa 1996).

$kT - \sigma$ relation

Galaxies in a cluster can be treated as collision-less particles. Therefore, the velocity dispersion (σ_v) of the member galaxies of a cluster should be the same as that of the dark matter. As a result, equation 2.7 predicts a strong correlation between the galaxy velocity dispersion σ_v and the ICM temperature, so that the ratio

$$\beta_{\text{spec}} = \frac{\mu m_p \sigma_v^2}{kT_{\text{gas}}} \quad (2.15)$$

becomes close to unity. As shown in Fig.2.9, this relation is observationally confirmed. For a galaxy group with $kT = 1$ keV, $\sigma_v = 400$ km s⁻¹ is predicted.

2.2.4 X-ray emission from discrete sources

Apart from the diffuse ICM emission, there are X-rays from discrete sources contained in the cluster. One of them is the emission from active galactic nuclei (AGNs) of the individual member galaxies of the cluster. The other is compact stellar-mass discrete sources, accreting mass from their companions. Among them, the most abundant and luminous population is so called low mass X-ray binaries (LMXBs), consisting of low-mass stars and weakly-magnetized neutron stars. When these X-ray sources are not negligible compared with the ICM, we must be careful in fitting the spectra.

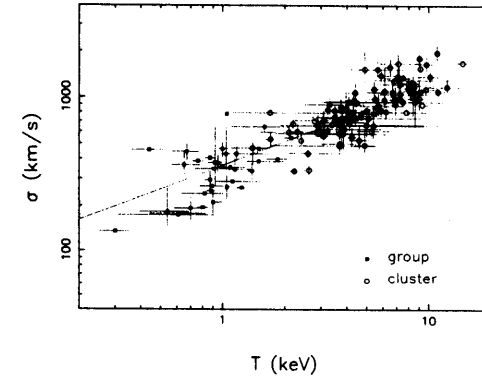


Figure 2.9: $kT - \sigma$ relation of clusters and groups of galaxies (Xue and Wu 2000). Data from 66 groups and 274 clusters drawn from the literature are shown. Solid line indicates the relation, $\mu m_p \sigma_v^2 = kT_{\text{gas}}$.

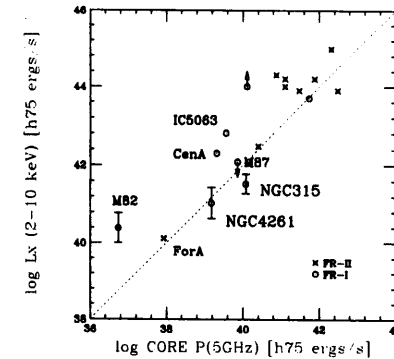


Figure 2.10: The X-ray luminosity of several AGN as compared with the radio luminosity of core region (Matsumoto et al. 2001).

An AGN is considered to be a huge black-hole with a mass of $\sim 10^6\text{--}8M_\odot$, sitting in the center of some, if not all, galaxies. Matters falling into the black-hole emit significant fraction of their gravitational energy in various wave-bands, from radio to γ -rays. We plot the X-ray luminosity plotted with the radio luminosity of the core region of the AGN in Fig.2.10. They are one of the brightest X-ray sources in the sky, sometimes up to a luminosity of $\sim 10^{45}$ erg s $^{-1}$. Their spectra are rather hard, and can be generally represented with a power law model with $\Gamma = 1 \sim 2$. Because an AGN is associated with a galaxy, most of the X-ray bright AGNs can be identified as point-like X-ray sources, coincident in position with galaxies in the optical image. AGNs are also identified by radio observations and optical spectroscopy, which are generally cataloged.

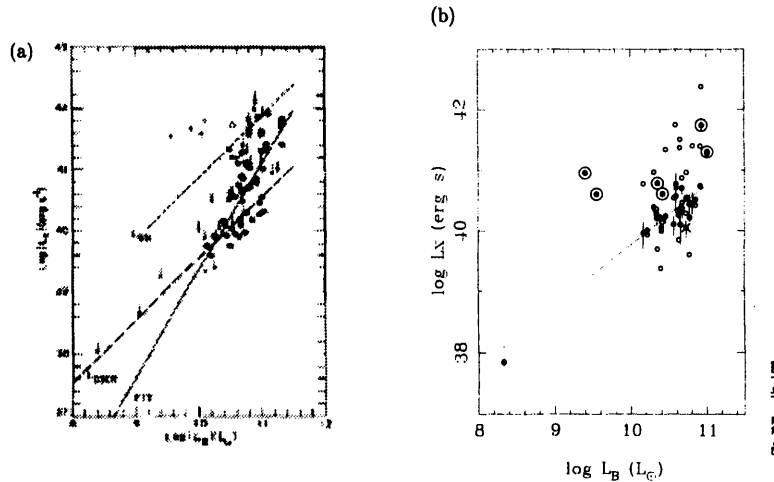


Figure 2.11: X-ray luminosity of the galaxy as compared with the optical B-band luminosity. (a) Einstein results by Canizares et al. (1987). X-ray luminosity is in the 0.5–4.5 keV band. Long-dashed line represents the LMXB component estimated from the early-type spiral galaxies and their bulge emission. (b) ASCA results by Matsushita (1998). X-ray luminosity is in the 0.5–10 keV band. Solid line is the same as the long-dashed line in panel (a), converted for the energy band. Filled circles are the luminosity of the hard component in the X-ray spectra of elliptical galaxies, while the open circles are those of the ICM component. Double circles indicate the galaxies possibly hosting an AGN.

The X-ray spectra of LMXB are known to be approximated by a ~ 10 keV thermal

bremstrahlung emission model (e.g. Makishima et al. 1989, Matsushita et al. 1994, Matsumoto et al. 1997). Although the X-ray luminosity of the individual LMXBs are fairly low ($\sim 10^{36\text{--}37}$ erg s $^{-1}$), their integrated luminosity within a galaxy is as much as $\sim 10^{40}$ erg s $^{-1}$. The latter luminosity is considered to be proportional to its optical luminosity, since the number of X-ray binaries in a galaxy should be roughly proportional to its total stellar content. By analyzing the X-ray luminosity of early-type spirals observed with Einstein, Canizares et al. (1987) found a linear relation of $L_X = 10^{-3.82}L_B$, between the optical B-band luminosity and the X-ray luminosity. Here, we converted the latter value from the original 0.5–4.5 keV band to the 0.5–10 keV band, assuming a 10 keV bremsstrahlung emission model. Later, Matsushita (1998) analyzed 27 elliptical galaxies observed with ASCA, and found that there is a hard emission distinct from the ISM emission, which can be attributed to LMXBs. By fitting the former component with a $kT = 10$ keV bremsstrahlung model, they confirmed a similar relation of $L_X = 10^{-3.81}L_B$. This can be converted to the 2–10 keV luminosity as,

$$L_X(2 - 10 \text{ keV}) = 4.1 \times 10^{39} (L_B/10^{10} L_\odot) \text{ [erg s}^{-1}\text{]} \quad (2.16)$$

2.3 Theoretical Backgrounds of High Energy Electrons in Diffuse Plasma

2.3.1 Power law population of high energy electrons

As we show in § 2.4 and 2.5, there are observational pieces of evidence for high energy electrons in celestial diffuse plasma sources. They show non-thermal emission through various processes, such as synchrotron, inverse Compton and bremsstrahlung mechanisms. In this section, we briefly review theories of these emissions and estimate life times of high energy particles, (in practice, electrons).

High energy particles are considered to be produced via shock acceleration. One possible scenario is the 1st order Fermi acceleration in various shocks in cosmic plasma. Another is the 2nd order Fermi acceleration by randomly moving scatterers, such as magneto-hydro-dynamical turbulence. There are various energy sources powering these process, including supernova (SN), active galactic nuclei (AGN), galaxy motion through the plasma, merging events between galaxies, and those between groups and clusters.

Relativistic particles thus generated exhibit a power-law like energy distribution, in the form of

$$N(\gamma) = N_0 \gamma^{-\mu} \quad (2.17)$$

Here, γ is the Lorents factor of the electrons, so that their energy is $\gamma m_e c^2$, $N(\gamma)$ is a number of electrons within energy range of $\gamma \sim \gamma + d\gamma$, and μ is the power-law index. Power-law energy distribution of high energy particles are observed in the cosmic rays reaching at the top of earth's atmosphere, and also at the geomagnetic shock-front of the solar wind.

2.3.2 Synchrotron emission

The relativistic electrons interact with magnetic field and produces a synchrotron emission. When an electron with energy $\gamma m_e c^2$ moves across a magnetic field B , it emits a synchrotron photon with a frequency of

$$\nu_{\text{sync}} = 4.2 \left(\frac{B}{\mu\text{G}} \right) \gamma^2 \text{ [Hz]} \quad (2.18)$$

The energy loss function due to this emission is then

$$b_{\text{sync}} = \frac{4}{3} \frac{\sigma_T}{m_e c} \gamma^2 U_B \text{ [s}^{-1}\text{]} \quad (2.19)$$

Here, $\sigma_T = 6.65 \times 10^{-25} \text{ cm}^{-2}$ is the Thomson cross section, $m_e = 9.1 \times 10^{-28} \text{ g}$ is the electron mass, $c = 3 \times 10^{10} \text{ cm s}^{-1}$ is the light speed, and $U_B = \frac{1}{8\pi} B^2 \text{ erg cm}^{-3}$ is the energy density of the magnetic field (Sarazin 1999).

Assuming a power-law distribution of electrons given by equation 2.17, the spectrum of the synchrotron emission becomes also a power-law, with energy index of $\alpha = (\mu - 1)/2$. It is represented as

$$\frac{dL_{\text{sync}}}{d\nu} = \frac{\sqrt{3} e^3 B N_0 \Gamma(\frac{3\mu+19}{12}) \Gamma(\frac{3\mu-1}{12})}{m_e c^2 (\mu+1)} \left(\frac{3eB}{2\pi m_e c \nu_{\text{sync}}} \right)^\alpha, \quad (2.20)$$

where $e = 4.8 \times 10^{-10}$ is the electron charge in cgs (gauss) unit, and Γ is the gamma function (Rybicki and Lightnman 1979).

2.3.3 Inverse Compton (IC) emission

The relativistic electrons also scatters off low energy photons via inverse-compton (IC) scattering. The mechanism is similar to the synchrotron process, and the formulae describing the IC process also resemble those of it. When an electron with energy $\gamma m_e c^2$ scatters off a photon with energy $h\nu_{\text{seed}}$, the frequency of the resulting IC photon is given as

$$\nu_{\text{IC}} = \frac{4}{3} \gamma^2 \nu_{\text{seed}} \text{ [Hz]} \quad (2.21)$$

for the energy region of $h\nu_{\text{IC}} \ll \gamma m_e c^2$. Here, h is the Planck constant. The energy loss function due to this emission is given as

$$b_{\text{IC}} = \frac{4}{3} \frac{\sigma_T}{m_e c} \gamma^2 U_{\text{seed}} \text{ [s}^{-1}\text{]} \quad (2.22)$$

where U_{seed} is the energy density of the seed photons.

The low energy photons that is present everywhere and dominates the overall photon density in the universe is the cosmic microwave background radiation (CMB), a black body radiation with $T_{\text{CMB}} = 2.73 \text{ K}$. We therefore take it as the seed photons. By equation 2.17, the spectrum of the IC emission again becomes a power-law, with energy index of $\alpha = (\mu - 1)/2$, the same as that of the synchrotron emission. The spectrum is represented as

$$\frac{dL_{\text{IC}}}{d\nu} = \frac{3\pi\sigma_{\text{rmT}}}{h^2 c^2} b(\mu) N_0 (kT_{\text{CMB}})^3 \left(\frac{kT_{\text{CMB}}}{h\nu_{\text{IC}}} \right)^\alpha, \quad (2.23)$$

where $b(\mu) = \frac{2^{\mu+3}(\mu^2+4\mu+11)\Gamma(\frac{\mu+3}{2})\zeta(\frac{\mu+3}{2})}{(\mu+3)^2(\mu+1)(\mu+5)}$, and ζ is the Riemann zeta function (Sarazin 1999).

From above equations, the total luminosity ratio of the synchrotron and IC emissions is simply given as

$$\frac{L_{\text{IC}}}{L_{\text{sync}}} = \frac{U_{\text{CMB}}}{U_B} \quad (2.24)$$

Because the CMB energy density (U_{CMB}) is known, we can obtain U_B , and hence the cluster averaged magnetic field strength using only the observables.

2.3.4 Non-thermal bremsstrahlung emission

The above two emissions are from the relativistic electrons. An alternative mechanism for the production of non-thermal X-rays is the bremsstrahlung from suprathermal population of electrons, colliding with low energy (mostly thermal) plasma (e.g. Ensslin et al. 1998, Sarazin and Kempner 2000). Following Sarazin and Kempner (2000), we introduce a power-law momentum distribution for these electrons. We define $N(p)dp$ to be the number of electrons with momenta in the range P to $P + dP$ as,

$$N(p) = N_0 p^{-\mu} \quad (2.25)$$

Here, $p \equiv P/m_e c$ is the normalized momentum and μ is the power-law index which becomes the same as that used in equation 2.17 at the relativistic limit.

In the non-relativistic limit, the Bethe-Heitler bremsstrahlung cross section (Heitler 1954) is

$$\frac{d\sigma(p, \epsilon, Z)}{d\epsilon} = \frac{32\pi}{3} \frac{e^6}{m_e^2 c^4 h p_i^2 \epsilon} \ln \left(\frac{p_i + p_f}{p_i - p_f} \right), \quad (2.26)$$

where p_i and p_f is the initial and final values of the normalized electron momentum, Z is the atomic number of ions, and ϵ is the produced photon energy in erg.

From equation 2.26, the non-thermal bremsstrahlung emission from electrons with a power-law momentum distribution (equation 2.25) is calculated as

$$\frac{dL_\epsilon}{d\epsilon} = \frac{32\pi^{3/2}}{3} \frac{e^6}{m_e c^4 h} \left[\frac{\Gamma(\frac{\mu}{2})}{\mu \Gamma(\frac{\mu+1}{2})} \right] \times \left(\sum n_x Z^2 \right) N_0 \left(\frac{m_e c}{2\epsilon} \right)^{\mu/2} \quad (2.27)$$

By comparing the prediction from this formula with a spectrum calculated by fully including the trans-relativistic and relativistic effects, Sarazin et al. (2000) found that the formula is in good agreement when $\mu \sim 4$, and shows a short-fall of about a factor of 2 for $2 < \mu < 3$. Thus, equation 2.27 provides a good approximation for the non-thermal bremsstrahlung emission.

In the relativistic region, the energy loss function of an electron with energy $\gamma m_e c^2$ due to the bremsstrahlung process is approximately given as (e.g. Blumenthal and Gould 1970)

$$b_{\text{brems}}(\gamma) \sim 1.51 \times 10^{-16} n_e \gamma [\ln(\gamma) + 0.36] \quad [\text{s}^{-1}], \quad (2.28)$$

including the electron-ion and electron-electron bremsstrahlung (Sarazin 1999).

2.3.5 Cooling times

High energy electrons lose their energies by interactions with fields and matters in the plasma, including the three channels listed above. Here we again focus on the relativistic case, and present the cooling time defined from these interactions.

One of the other major cooling mechanisms is the Coulomb losses due to collisions with thermal electrons, which is approximately given as (e.g. Rephaeli 1979)

$$b_{\text{Coulomb}}(\gamma) \sim 1.2 \times 10^{-12} n_e \left[1.0 + \frac{\ln(\gamma/n_e)}{75} \right] \quad [\text{s}^{-1}], \quad (2.29)$$

Combining equations 2.19, 2.22, 2.29 and 2.28, we obtain the cumulative energy loss function as

$$b(\gamma) = b_{\text{sync}} + b_{\text{IC}} + b_{\text{Coulomb}} + b_{\text{brems}} \quad [\text{s}^{-1}] \quad (2.30)$$

In Fig.2.12 we plot the individual components of this equation. The cooling time is then given as $\tau_{\text{cool}} = \gamma/b(\gamma)$, which is also shown in the figure. Thus, the electrons with $\gamma = 100 \sim 300$ have the longest life time of $\sim 10^9$ yr.

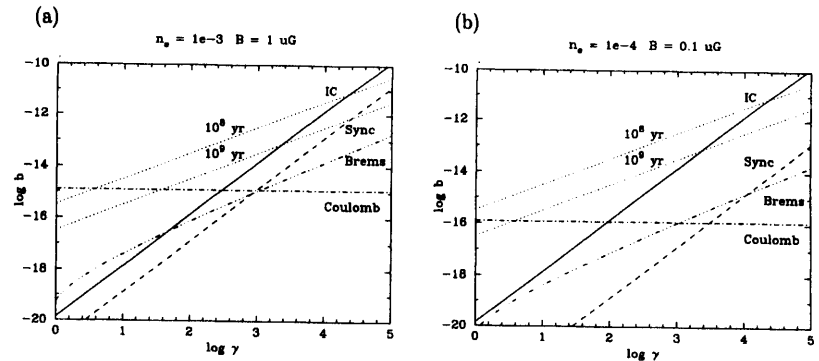


Figure 2.12: The energy loss function in condition of (a) $n_e = 1 \times 10^{-3} \text{ cm}^{-3}$ and $B = 1 \mu\text{G}$, and (b) $n_e = 0.1 \times 10^{-3} \text{ cm}^{-3}$ and $B = 0.1 \mu\text{G}$. Dotted lines indicate the cooling time of 10^8 yr and 10^9 yr, respectively.

2.4 Non-thermal Electrons in Clusters of Galaxies

So far, we have briefly reviewed the X-ray properties of clusters and groups of galaxies, the latter being the "theater" of this thesis (§ 2.2). From now on, we present observational

evidence for the high energy particles distributed in diffuse plasma, which is the “target” of this thesis. We deal with clusters of galaxies in this section, and other objects, such as supernova remnants (SNR), in the next section.

2.4.1 Cluster radio halos

From the radio observations, diffuse emission associated with some clusters has been detected; so-called radio halos and relics. The source is called a halo when it is located at the cluster center, and called a relic when located at the cluster peripheries. They have a power-law like spectra with steep energy index ($\alpha \sim 1$). This suggests that they are a synchrotron emission by relativistic electrons with a power law energy distribution, interacting with intra-cluster magnetic field of $\sim \mu\text{G}$. Thus, the radio halo and relic provide direct evidence for the existence of such population of electrons, as well as a magnetic field, distributed cluster-wide in the ICM.

Radio halos and relics have been thought to be a rare phenomenon. Their low surface brightness makes their detection difficult, and there had been only about ten objects known (Feretti and Giovannini 1996). Recently, their number is increasing (as much as ~ 40), due to improvements in the instrumental capability (e.g. Sarazin 2000), although it is not yet a popular phenomenon among clusters.

The most famous radio halo is Coma-C, associated with the Coma cluster. As shown in Fig.2.13 and 2.14, the halo shows a regular shape with a scale of ~ 1 Mpc, as extended as the X-ray emission (e.g. Deiss et al. 1997). It has a flux of ~ 600 Jy at 1.4 GHz, and is detected in the wave-band ranging from 30.9 MHz to 2.7 GHz. Here, $1 \text{ Jy} = 1 \times 10^{-23} \text{ erg s}^{-1} \text{ cm}^{-2} \text{ Hz}^{-1}$. It has a power-law like spectra with a steep energy index of $\alpha \sim 1.3$, and the total luminosity in 10 MHz to 10 GHz is $6.1 \times 10^{40} \text{ erg s}^{-1}$ (Feretti and Giovannini 1996).

Currently, about ten clusters are known to host a halo, including Coma, A2256, and A2319. We list them in Table 2.2. All of them are massive rich clusters with a high temperature ($kT > 7 \text{ keV}$), and a high X-ray luminosity ($L_X > 5 \times 10^{44} \text{ erg s}^{-1}$). There energy index of the radio spectra is $1 \sim 2$. In the lower frequency ($\sim 100 \text{ MHz}$), some halos show evidence of spectral hardening, such that α reaches ~ 1 . This phenomena may suggesting the aging effect of the electrons with higher energies. No polarized flux has been detected so far in radio halos, with an upper limit of $\sim 10\%$.

Apart from its location, relics has properties generally similar to those of halos; a steep spectra, a large scale order on $\sim 100 \text{ kpc}$, and low surface brightness. In addition,

Table 2.2: Observed properties of cluster radio halos (Feretti and Giovannini 1996, Liang 1999).

| cluster | Size (kpc) | $P_{1.4}^{(1)}$ (erg Hz ⁻¹) | $P_{\text{tot}}^{(2)}$ (erg s ⁻¹) | $\alpha^{(4)}$ |
|---------|---------------|--|--|----------------|
| Coma | 550 | 3.2×10^{30} | 6.1×10^{40} | 1.34 |
| A2163 | - | 1.8×10^{32} | 3×10^{41} | |
| A2218 | 250 | 7.9×10^{29} | 9.0×10^{39} | 1.1 |
| A2255 | 725 | 2.5×10^{30} | 1.6×10^{41} | > 1.5 |
| A2256 | 700 | 1.2×10^{30} | 1.6×10^{41} | 1.9 |
| A2319 | 660 | 5.1×10^{30} | 9.2×10^{40} | 1.3 |

(1) Radio flux in 1.4 GHz.

(2) Radio luminosity in the range of 10 MHz - 10 GHz.

(3) Energy index of radio spectra.

Table 2.3: Observed properties of cluster radio relics (Feretti and Giovannini 1996). Columns are similar to those of Table 2.2.

| name | cluster | Size (kpc) | $P_{1.4}$ (erg Hz ⁻¹) | P_{tot} (erg s ⁻¹) | α |
|-------------|---------|---------------|--------------------------------------|--|----------|
| 0038 - 096 | A85 | 200 | 5.1×10^{30} | 1.6×10^{41} | > 1.5 |
| 0917 + 75 | A786 | 780 | 2.0×10^{31} | 1.7×10^{41} | 1.34 |
| 1253 + 275 | Coma | 580 | 1.7×10^{30} | 2.0×10^{40} | 1.1 |
| Coma Bridge | Coma | 970 | 4.9×10^{29} | 1.6×10^{40} | 1.5 |
| 1401 - 33 | AS753 | 220 | 1.0×10^{30} | 2.5×10^{40} | 1.4 |
| 2006 - 56 | A3667 | 870 | 2.6×10^{31} | 3.7×10^{41} | 1.2 |

relics are sometimes highly polarized, up to $\sim 30\%$. They are also detected in about ten clusters (Table 2.3), including A85, A1656 and A3667, which generally show evidence for on-going merger event. There are also several clusters hosting both a halo and relic(s), such as the Coma cluster (e.g. Deiss 1999).

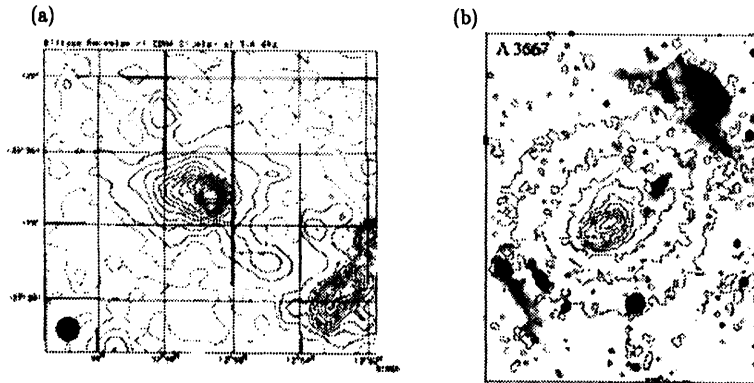


Figure 2.13: (a) A contour image of the radio halo, Coma-C, at 1.4 GHz. The width of the image corresponds to $\sim 3.2h_{75}^{-1}$ Mpc. Point sources are subtracted. In the bottom right, there is a relic (1253 + 275), and another relic (Coma Bridge) is also visible between Coma-C and 1253 + 275 (Deiss et al. 1997). Contours are 10 mJy beam^{-1} apart, where the dashed one represents the zero level. (b) A gray scale image of relics in A3667 at 843 MHz, superposed on the X-ray contour image from ROSAT (Röttgering et al. 1997). The width of the image corresponds to $\sim 2.8h_{75}^{-1}$ Mpc. X-ray contours are set at 2, 8, 18, 32, 50, 72, 98, 128, 162, 200 and 242 times the background noise.

2.4.2 Hard X-ray emission

The relativistic electrons, inferred from the radio halo and relics, are expected to produce IC emission with a power-law spectra, scattering off the CMB photons (§ 2.3.3). Because the ICM thermal emission rapidly decreases above its temperature, the IC emission would be observed as a hard excess emission in X-ray spectra. Accordingly, extensive searches for the expected hard excess emission were conducted with HEAO-A1 (Rephaeli et al. 1987), OSSE (Rephaeli et al. 1994) and so on, all yielding only upper limits.

Recently the BeppoSAX and RXTE satellites with their superior sensitivity in the hard X-ray band above $\sim 10 \text{ keV}$, have detected the excess hard emission from the Coma

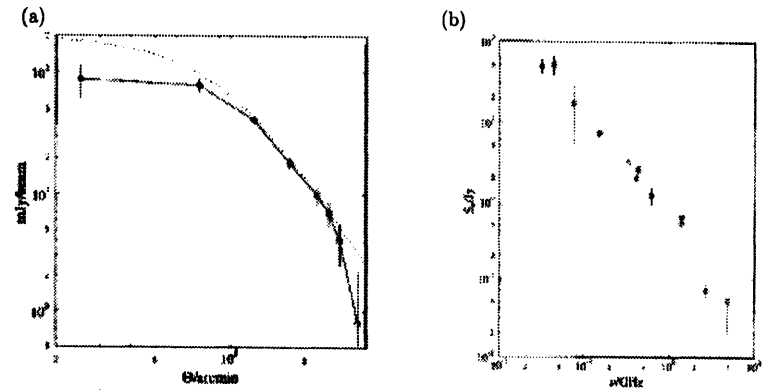


Figure 2.14: Radio properties of Coma-C (Deiss et al. 1997). (a) Azimuthally averaged surface brightness profile from Fig.2.13a (solid curve). Dotted line represents the surface brightness of the X-ray emission. (b) Integrated flux density spectrum.

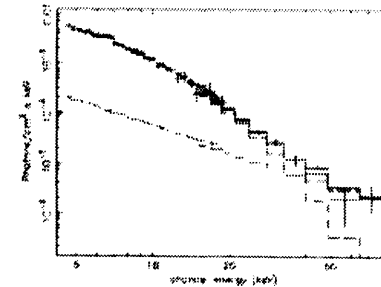


Figure 2.15: X-ray spectra of the Coma cluster observed with BeppoSAX (Fusco-Femiano et al. 1999). Combined spectra from the HPGSPC (High Pressure Gas Scintillator Proportional Counter) and PDS (Phoswich Detection System) detectors are fitted with a sum of a 8.5 keV thermal emission and a power law with a photon index of $\Gamma = 1.57$.

cluster (Fusco-Femiano et al. 1999, Rephaeli et al. 1999). The spectrum observed with SAX is shown in Fig.2.15. It clearly requires an excess hard component, and fitted well by a sum of a 8.5 keV thermal component and a power law with a photon index of $\Gamma = 1.6 \pm 0.9$ (energy index $\alpha = \Gamma - 1 = 0.6 \pm 0.9$), which is consistent with the radio observations (see Table 2.2). When the latter component is replaced with a thermal emission, a temperature higher than 40 keV is required. The 20–80 keV luminosity of the excess hard component is $5 \times 10^{43} h_{75}^{-2} \text{ erg s}^{-1}$, which is $\sim 10\%$ of the 2–10 keV luminosity of the ICM component.

If the observed hard X-ray emission is indeed the long-sought IC emission, we can obtain a cluster averaged magnetic field strength of $\sim 0.14 \mu\text{G}$, by combining equations 2.20 and 2.23. This value, however, seems to contradict with those derived from Faraday rotation measurements in radio band, which suggest $B = 1 \sim 10 \mu\text{G}$ (e.g. Kim 1990). Fusco-Femiano et al. (1999) suggest that this problem may be solved considering the positional difference in the magnetic field, in such a way that regions threaded by strong magnetic flux tubes are devoid of relativistic electrons.

If the IC interpretation works, the non-thermal energy density of the relativistic electrons and the cluster magnetic field are estimated as $\sim 7 \times 10^{-14} \text{ erg cm}^{-3}$ and $\sim 8 \times 10^{-16} \text{ erg cm}^{-3}$, respectively; they are small compared to the ICM energy density of $2 \times 10^{-11} \left(\frac{n_{\text{rel}}}{10^{-3} \text{ cm}^{-3}}\right) \text{ erg cm}^{-3}$ (Fusco-Femiano 1999).

There also are different interpretations of the observed hard X-rays, including in particular the non-thermal bremsstrahlung emission from suprathermal electrons in the ICM (see § 2.3.4). As the populations of the electrons emitting the hard X-ray emission and radio synchrotron emission are different in this model, the derived magnetic field value can be regarded as a lower limit; we can thus avoid the discrepancy with the radio measurement.

Currently, there are only 3 detections of non-thermal emission; the Coma cluster, A2256 cluster and A2199 cluster. Parameters of their non-thermal components are listed in Table 2.4. The BeppoSAX spectra of A2256 show a clear excess hard emission in the PDS spectra above $\sim 20 \text{ keV}$. The joint MECS (medium energy counter system) and PDS (phoswich detector system) spectra are fitted with a sum of a thermal component with $kT = 6.9_{-0.35}^{+0.45}$ and a power-law with $\Gamma = 1.3 \sim 2.7$ (Fusco-Femiano et al. 2000). In the A2199 cluster, however, the hard excess is not positively detected in the PDS energy band ($> 20 \text{ keV}$). Kaastra et al. (1999) carefully fitted a thermal emission model to the broad band extreme ultra violet (EUV) and X-ray spectra of A2199, obtained from EUVE, ROSAT and SAX, ranging from $\sim 0.1 \text{ keV}$ up to $\sim 50 \text{ keV}$. They found soft and hard

excess from the cluster outer regions, which is interpreted as a power-law with $\Gamma \sim 1.8$.

Together with the radio halo observations, these results are strong evidence that there is a population of high energy electrons in the ICM. However, as we have mentioned in § 1, the limited number of clusters with detected hard excess and lack of imaging capabilities in these hard X-ray experiments make it difficult to understand the nature of these non-thermal emissions.

Table 2.4: Observed properties of cluster hard X-ray emission.

| cluster | redshift | $kT^{(2)}$ | Hard ⁽²⁾ | Hard ⁽³⁾ | ICM ⁽⁴⁾ |
|---------|----------|-----------------|---------------------------------|--------------------------------|----------------------|
| | | | Flux | Luminosity | Luminosity |
| Coma | 0.0232 | 8.38 ± 0.34 | $(2.2 \pm 0.2) \times 10^{11}$ | $(2.4 \pm 0.2) \times 10^{43}$ | 3.6×10^{44} |
| A2256 | 0.0581 | 7.08 ± 0.23 | $(1.2 \pm 0.2) \times 10^{11}$ | $(7.7 \pm 1.2) \times 10^{43}$ | 3.4×10^{44} |
| A2199 | 0.0303 | 4.10 ± 0.08 | $(1.0 \pm 0.25) \times 10^{11}$ | $(1.8 \pm 0.4) \times 10^{43}$ | 1.3×10^{44} |

(1) ICM temperature in keV, from Fukazawa 1997.

(2) The 20–80 keV flux of the hard component in $\text{erg s}^{-1} \text{ cm}^{-2}$. For A2256, the error of 15% are derived from the PDS count rate error (1σ) presented in Fusco-Femiano et al. (2000), and do not include any fitting errors. For the Coma cluster, we assumed $\sim 10\%$ error in flux by scaling the error of A2256 with their flux ratio. i.e. $1/\sqrt{2}$. For A2199, the original paper presents the flux in 0.1–100 keV range. This is converted to 20–80 keV band by assuming $\alpha = 1.8$.

(3) The 20–80 keV luminosity of the hard component in erg s^{-1} . Distances of $92.0 h_{75}^{-1} \text{ Mpc}$, $232.7 h_{75}^{-1} \text{ Mpc}$ and $120.6 h_{75}^{-1} \text{ Mpc}$ are assumed for Coma, A2256 and A2199, respectively.

(4) The 2–10 keV ICM luminosity in erg s^{-1} .

2.5 Hard X-ray Emission from Other Diffuse Plasma Sources

2.5.1 Supernova remnant: SN 1006

From ASCA observations of galactic supernova remnant (SNR) SN 1006, Koyama et al. (1995) found that the edges of the remnant shell is dominated by a power-law X-ray emission with $\alpha \sim 1.95$ within 0.5–10 keV (Fig.2.16). It was interpreted as a synchrotron emission from electrons accelerated up to $\sim 100 \text{ TeV}$ in the shock front, interacting with $\sim \text{mG}$ magnetic field. This was further supported by the detection of TeV γ -ray from the north rim of the SNR, with the CANGAROO imaging air Cerenkov telescope (Tanimori et al. 1998). The γ -rays are attributed to be the IC scattering off the CMB photons. Because

the IC photon cannot exceed the incident electron energy, this is the direct evidence that the electrons are accelerated to at least several times 10 TeV in the region.

The SN 1006 is thought to be a type-Ia super nova remnant, with typical shell-type structure and no central engine for high energy particles, such as a neutron star or a black-hole. Therefore, this is the first direct evidence of a particle acceleration to such a high energy in the shock region around SNR.

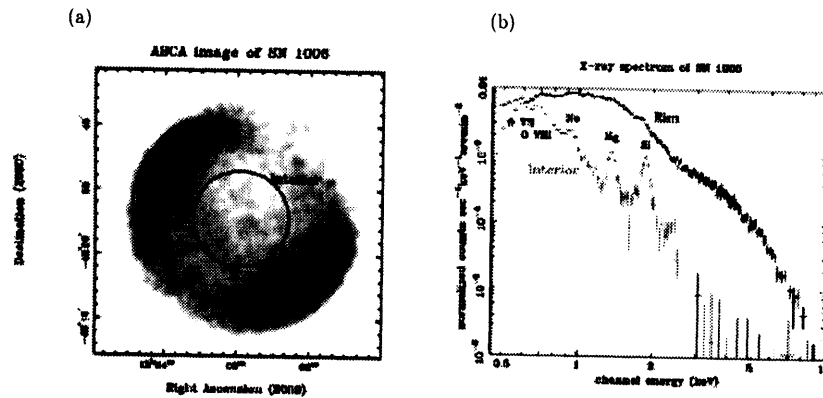


Figure 2.16: (a) X-ray image of SN 1006. (b) X-ray spectra, obtained from the rim region and interior region.

2.5.2 Galactic ridge X-ray emission

HEAO-1 satellite has discovered a diffusely distributed emission along the disk of Milky Way (Worrall et al. 1982). This phenomenon is generally called "galactic ridge X-ray emission" (GRXE). The X-ray image taken with EXOSAT is shown in Fig.2.17a. GRXE is considered to have a disk-like shape, with a radius of ~ 10 kpc and thickness of ~ 200 pc. Its total luminosity is estimated to be $(1 \sim 2) \times 10^{36}$ erg s^{-1} in the energy band of 2–10 keV (e.g. Yamauchi and Koyama 1993). Although many studies are carried out to, the origin of GRXE is not yet clear.

Detection of Fe-K line emission with Tenma satellite (Koyama et al. 1986) revealed that a major component of GRXE is due to thermal emission from optically thin hot plasma. Using ASCA, Kaneda et al. (1997) found that GRXE consists of at least two thermal components in non-equilibrium ionization state; a soft component with $kT \sim 0.8$

keV and a hard component with $kT \sim 7$ keV. They also suggest that the equivalent width of the Fe-K line decreases with increasing galactic latitude, and the hard component gradually becomes power-law like (Fig.2.17b). By using Ginga and a balloon experiment Welcome-1, Yamasaki et al. (1997) found a hard tail, which cannot be explained by $kT \sim 7$ keV hot component. The combined spectra seems to continue up to the γ -ray region with a power-law spectra (Fig.2.17c). Vallinot and Marchall (1998) found similar results using the RXTE data.

From these observational results, it has become clear that GRXE consists of at least three components; soft and hard thermal components, and a non-thermal component. Among them, the soft component can be well explained by a sum of SNRs (Kaneda et al. 1997). On the other hand, origin of the later two components is not yet clear, which may be implying the existence of new type of heating and accelerating sources in the vast inter-stellar space of our galaxy (e.g. Kaneda et al. 1997).

2.5.3 Inverse Compton (IC) emission from the radio lobe

ASCA (Kaneda et al. 1995) and ROSAT (Feigelson et al. 1995) has discovered an X-ray emission from the radio lobe of Fornax-A, the forth strongest extra-galactic radio source in the GHz region. It has a prototypical double lobe morphology in radio band, with continuous spectra detected in the range of 408 MHz to 4.8 GHz. We show the X-ray image obtained with ASCA overlayed on the radio image in Fig.2.17. The source is located at a distance of 17 Mpc, and the size of each lobe is ~ 200 kpc in diameter.

The radio emission is considered to be a synchrotron emission from a population of high energy electrons, and the X-ray emission is interpreted as IC scattering off the CMB photons. The same as the case of the Coma cluster, we can obtain the lobe averaged magnetic field strength by combining equations 2.20 and 2.23. The value becomes $2 \sim 4 \mu G$. This was the first case that the magnetic field strength of an extragalactic diffuse plasma with such a large scale is directly determined only from observables. From equation 2.18, the magnetic field of $\sim 3 \mu G$ implies that the relativistic electrons should reach the energy of ~ 10 GeV to produce the 4.8 GHz radio emission. The energy density of the relativistic electrons and the magnetic field are calculated to be $\sim 3 \times 10^{-13}$ erg cm^{-3} and 3.6×10^{-13} erg cm^{-3} , respectively. Their total energies are derived to be 4×10^{58} erg and 6×10^{58} erg, respectively, assuming a lobe volume of 1.3×10^{71} cm^3 .

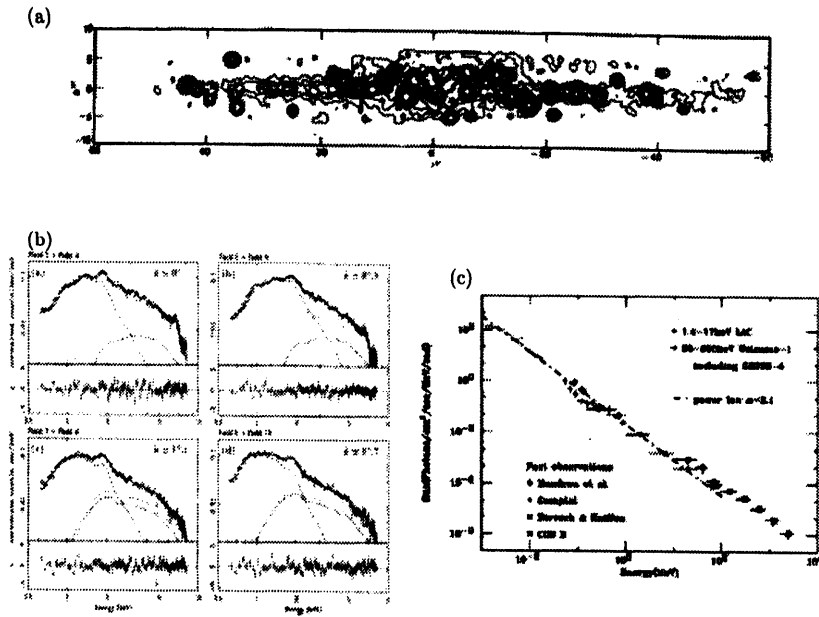


Figure 2.17: X-ray image and spectra of GRXE. (a) The 2–6 keV band image from EXOSAT (Warwick et al. 1985). (b) ASCA spectra obtained from galactic latitudes of 0° , 0.5° , 1.1° and 1.7° (Kaneda et al. 1997). (c) Ginga X-ray and other γ -ray spectra (Yamasaki et al. 1997).

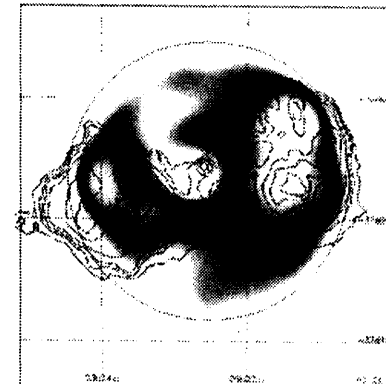


Figure 2.18: X-ray gray scale image from ASCA, overlaid on the 1.4 GHz radio contour map of Fornax-A. The solid circle represents the ASCA GIS field of view of $\sim 22'$ radius. In the X-ray image, contribution from a central source have been subtracted. Contours are at 125, 187.5, 250, 375, 1125 and 1375 mJy beam^{-2} .

Chapter 3

THE ASCA SATELLITE

3.1 Spacecraft

The ASCA (Advanced Satellite for Cosmologies and Astrophysics; Tanaka et al. 1994) is the Japanese fourth satellite devoted to cosmic X-ray researches, developed under US-Japan collaboration managed by ISAS (Institute for Space and Astronautical Science). The satellite was launched on 20 February 1993 at 11 a.m. JST, from Kagoshima Space Center (KSC) of ISAS at Uchinoura, Kagoshima, with the M-3S-II-7 three stage rocket. ASCA has achieved a near-circular orbit with perigee of 520 km, apogee of 620 km, an inclination of 31° and a period of 96 min.

In Fig. 3.1, we show the in-orbit configuration of ASCA. The satellite has a length of 4.7 m and weighs 420 kg, and is operated from the power supply from its solar panel, which looks like a wing. A schematic view of the scientific instruments onboard ASCA is shown in figure 3.2. The satellite is equipped with four identical X-ray telescopes (XRT; § 3.2) with a focal length of 3.5 m. At the four foci, two gas scintillation imaging proportional counters (GIS; § 3.3) and two X-ray CCD camera (SIS; § 3.4) are located. ASCA is the first satellite that simultaneously performs imaging and spectroscopy in the wide energy band of 0.5–10.0 keV. The previous imaging missions such as Einstein and ROSAT were limited to energies below ~ 3 and 2.4 keV, respectively. The superior energy resolution of the SIS, high through-put of the GIS and low background levels of both instrument, particularly the latter, also characterize the satellite.

The satellite attitude is measured by gyros, geomagnetic sensors and star sensors. In reference to these real-time measurements, the satellite is controlled using four bias momentum reaction wheels and three-axis magnetic torquers. The absolute pointing accuracy is typically 1', and we can reconstruct the resulting pointing position with a

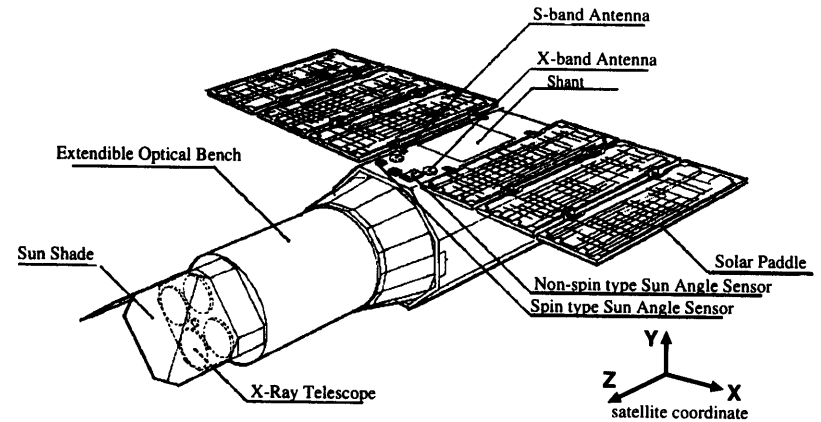


Figure 3.1: In orbit configuration of ASCA.

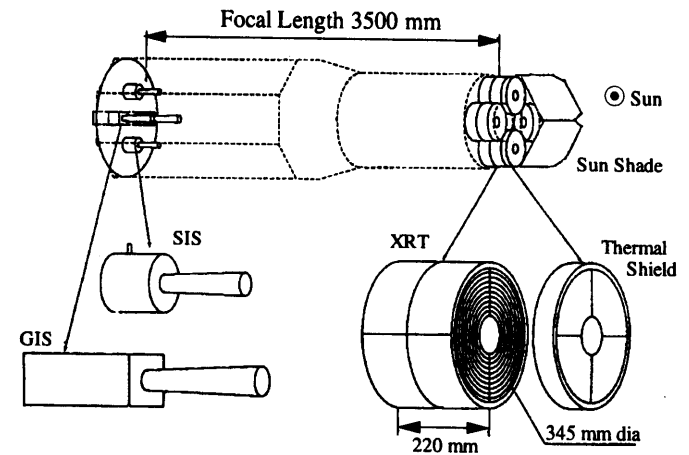


Figure 3.2: Configuration of the onboard instruments.

~ 0.5 accuracy from the telemetry data.

ASCA flies over KSC five times a day, each lasting ~ 10 minutes. All the necessary commanding and maintenance are done during these short contact intervals. The CPU-based onboard commanding unit keeps control of the satellite all the time, by handling the commanding time table uploaded from KSC. The observed data (~ 75 % scientific and ~ 25 % housekeeping) are stored in the onboard data recorder with a 128 Mbits capacity. The data acquisition rate is commandable at either 32 (high bit-rate), 4 (medium bit-rate) or 1 (low bit-rate) kbit/s. The stored data are transmitted to ground via down-link telemetry at KSC, as well as the US NASA's Deep Space Network stations. The data amounts to ~ 1 Gbits a day.

3.2 X-Ray Telescope (XRT)

3.2.1 Design and structure

The X-ray telescope (XRT) onboard ASCA has for the first time enabled the cosmic X-ray imaging up to 10 keV (Serlemitsos et al. 1995). Soft X-rays are totally reflected off a smooth surface, when their incident angle is less than a certain critical value. This phenomenon is known as a grazing incident reflection. The critical angle of order ~ 1° is inversely proportional to the X-ray energy, and proportional to the electron density of the reflecting material.

The XRT is design to form a Wolter type I optics, consisting of two mirrors with paraboloid and hyperboloid sections (Fig.3.3). This optics are used in many cosmic X-ray satellites, including Einstein (1978-81), EXOSAT (1983-86), ROSAT (1991-1999) and Yohkoh (1991-). All these missions use a polished glass or glass ceramic with heavy metal, such as gold, evaporated as a reflecting material. The effective area is usually increased by having multiple nested set of mirrors with a common focus. For example, both Einstein and ROSAT telescopes use four nesting.

To reflect higher energy X-rays, the incident angle must be very small; hence the projected area also becomes very small. To overcome this dilemma, the ASCA XRT adopted "multiple thin foil" optics. This design makes each shell extremely thin, by using metal foils instead of polished glass, and drastically increases the number of nesting. Because it is very difficult to shape a thin foil into a paraboloid or a hyperboloid, a conical surface is used as an approximation. A prototype multiple thin-foil mirrors were successfully used in the BBXRT experiment onboard Space Shuttle in December 1990.

The reflector shells are all made of 127 μm thick aluminium foils. The foils are ~ 10 μm lacquer-coated to improve the surface smoothness, and then ~ 50 nm gold-evaporated to increase the reflectivity. The 120 of these foils are closely packed together in an onion-ring configuration with a typical space of 1 mm. The foils are packed and manufactured in four quadrants, and aligned by 13 alignment bars into 14 sectors. Four quadrants make up the first mirror section of 100 mm long, and another set make up the second mirror. One mirror assembly weighs 9.8 kg. In table 3.1, we summarize the design parameters and performance of the ASCA XRT. Because the focal length is 3500 mm, a 1' distance in the sky corresponds to 1 mm distance on the focal plane.

Although the imaging resolution is moderate (~ 3'), the weight of the telescope is significantly saved. For example, the X-ray telescope onboard the Chandra satellite, which is characterized by its high imaging quality with resolution better than 1", has a weight of 1.5 tones. This is about 150 times that of an ASCA XRT, and even larger by a factor of 4 than the whole ASCA satellite weight. In spite of the huge weight difference, the effective area of the ASCA XRTs is comparable to that of the Chandra mirror. Thus, the ASCA XRT is optimized to achieve a large effective area.

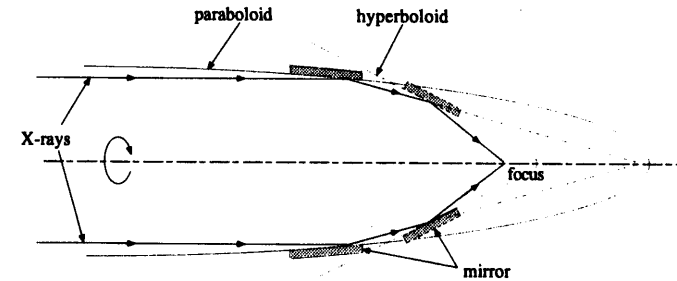


Figure 3.3: Wolter type I optics.

3.2.2 Effective area and point spread function (PSF)

The effective area of the ASCA XRT compared with the earlier missions are shown in Fig.3.5a. It shows an M-edge structure of gold around 2.2 keV, and gradually decreases with increasing photon energies. This is because the critical angle of higher energy X-rays is smaller, so that the outer shell of the XRT gradually becomes ineffective toward higher energies.

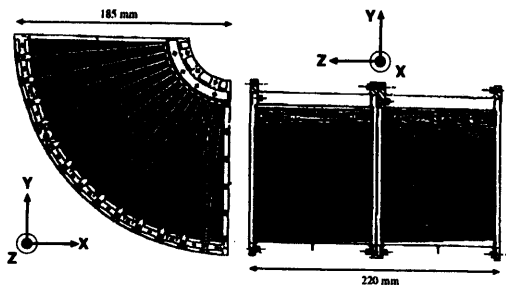


Figure 3.4: The schematic view of the ASCA XRT. A top view of a quadrant (left) and a cross section of one telescope (right).

For the same reason, the ineffective region increases as the off-axis angle gets larger. It also suffers shadowing effects between the foil shells. Therefore, the effective area depends on both the incident angle (θ) and the energy of the X-rays. This is called the vignetting effect. In addition, because of the quadrant structure of the XRT, it also depends on the roll angle (ϕ). In Fig.3.5b, we present the $\theta - \phi$ dependence of the effective area. The actual effective area, including its position dependences, is calibrated in-flight using the Crab nebula, which is a standard candle in X-ray astronomy.

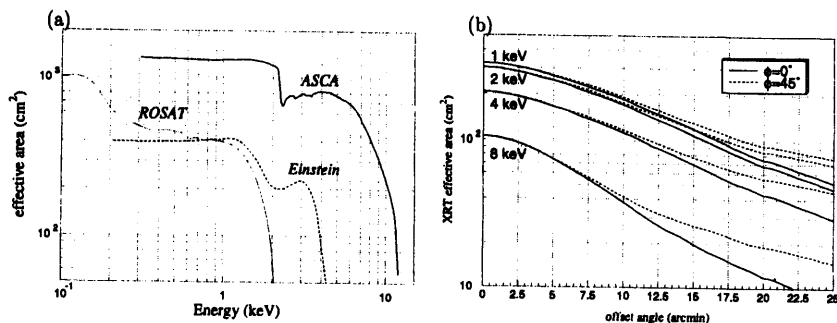


Figure 3.5: (a) Effective area of the four X-ray telescopes on boresight position. (b) The incident angle (θ) dependence of the effective area (vignetting).

Due to the waviness of the aluminum foils as well as the conical approximation of paraboloid and hyperboloid, the angular resolution of the XRT is limited to $\sim 3'$. Furthermore, the point spread function (PSF), i.e., the image of the point source is the

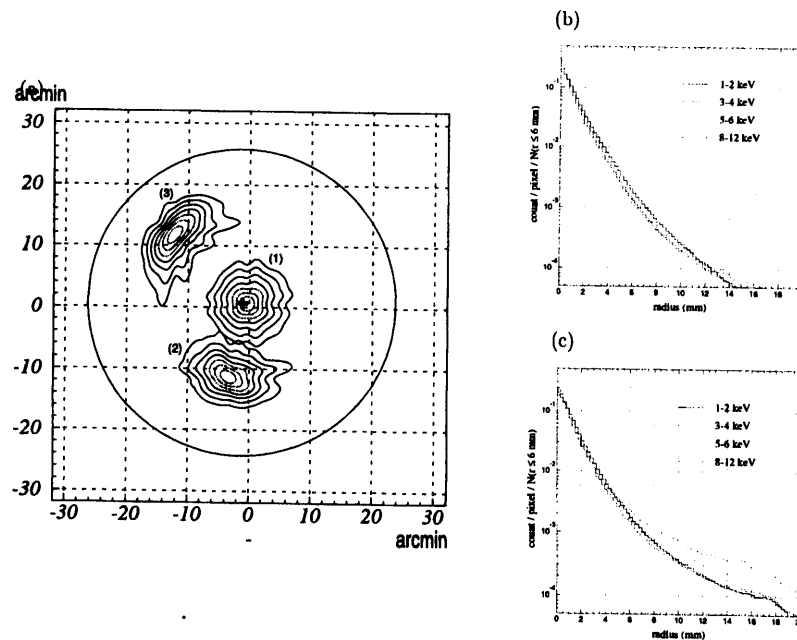


Figure 3.6: (a) X-ray contour image of a point source observed with GIS2. The actual images of Cyg X-1 obtained from three different observations are plotted together. (b) Radial profile of the XRT+GIS PSF at $1'.8$ offset (position 1 in panel a). (c) Radial profile of the PSF at $8'$ offset (position 3 in panel a).

Table 3.1: Design parameters and performance of the ASCA XRT.

| | |
|------------------------------|--|
| Mirror substrate | Aluminum foil (127 μm) |
| Mirror surface | Acrylic lacquer (10 μm) + Au (50 nm) |
| Mirror length | 100 mm |
| Number of foils per quadrant | 120 foils |
| Inner / outer diameter | 120 mm / 345 mm |
| Focal length | 3500 mm |
| Incident angle | 0.24° 0.7° |
| Total weight of four XRTs | ~ 40 kg |
| Geometrical area | 558 cm^2 / telescope |
| Field of view | ~ 24' (FWHM at 1 keV) / ~ 16' (FWHM at 7 keV) |
| Energy range | \lesssim 10 keV |
| Effective area of four XRTs | ~ 1300 cm^2 (1 keV) / ~ 600 cm^2 (7 keV) |
| Half power diameter | ~ 3 arcmin |

energy- and position-dependent. In Fig.3.6a, we plot the actual images of Cyg X-1, which can be regarded as a point source at infinity observed with the GIS detector. The radial brightness profile in different energy bands for two source positions are shown in Fig.3.6b and c. The PSF has a sharply peaked core, although it is somewhat broadened in the image by the finite position resolution of the GIS. For the on-axis image, half the detected counts are contained within a diameter of 3'.2 on the focal plane. This diameter, called half-power diameter, gives a rough measure of the combined XRT+GIS angular resolution. The PSF has a rather wide tail outside the core, which depends on the source position as well as the X-ray energy (Fig.3.6b and c). There is an additional cross shaped component in the tail due to the quadrant structure of the XRT (Fig.3.6a). These structures depend not only on the position, but also on the X-ray energy. The PSF is calibrated with a pre-launch beam line data, and a set of actual images of Cyg X-1 (Takahashi et al. 1995 ASCA News Letters No.3, 25).

3.3 Gas Imaging Spectrometer (GIS)

The Gas Imaging Spectrometer (GIS) has been developed mainly by the University of Tokyo, ISAS, Tokyo Metropolitan University, Meisei Electric Co.Ltd. and Japan Radio Corporation Co.Ltd., with collaborators at Institute of Physical and Chemical Researches (RIKEN), Kyoto University (Department of Physics), NASA/Goddard Space Flight Center (GSFC), and so on (Ohashi et al. 1996; Makishima et al. 1996). The GIS design is mainly based on the GSPC experiment (Koyama et al. 1984) onboard Tenma (Tanaka et al. 1984) which was operating for 1983-1984.

3.3.1 Design and structure

The GIS is a general-purpose X-ray imaging spectroscopy system. It consists of the two detector assemblies (GIS-S), namely GIS2 and GIS3 serving as X-ray detectors, and the main electronics called GIS-E. GIS2 and GIS3 are almost identical except that there is a Radiation Belt Monitor (RBM), a small PIN-diode particle monitor, attached to the bottom of GIS2. GIS2 and GIS3 are coupled to two of the four XRTs, and measure pulse-heights and positions of X-rays reflected by the XRTs, photon-by-photon basis. Design parameters and performance of the GIS are summarized in Table 3.2.

Table 3.2: Design parameters and performance of the GIS

| | |
|-----------------------|--|
| Energy Band | 0.7-15 keV |
| Energy Resolution | 8% at 5.9 keV (FWHM) |
| Effective Area | 50 mm diameter |
| Entrance Window | 10 μm beryllium |
| Absorption Material | Xe (96%) + He (4%), 10 mm depth, 1.2 atm at 0 °C |
| Positional Resolution | 0.5 mm (FWHM) |
| Time Resolution | ~ 61 μsec (Minimum in PH Mode) 1.95 msec (Minimum in MPC Mode) |
| Weight | 4.30 kg (GIS2), 4.16 kg (GIS3) |

The structure of GIS2 sensor is shown in Fig.3.7. Each sensor consists of a detector assembly and a high-voltage supply unit. Each detector assembly in turn consists of a gas cell, an imaging photo-multiplier tube (IPMT) and front-end electronics, all of which are placed in a housing made of magnesium-alloy. The top section forms a hood, which limits the field of view of the GIS into the XRT direction. In order to prevent ionospheric

plated with copper, and a stainless steel mesh coated with tin is placed between the grid and the beryllium foil to provide a fine support. To stand against several atmospheric pressure, the molybdenum grid has a height of 3.5 mm and a thickness of 0.1 mm and runs at 5 mm pitch. The shadow of the grid onto the X-ray image is not a major problem since the wall thickness is smaller than the point spread function (~ 3 mm) of the XRT. The fine-supporting mesh has 1.2 mm pitch and 84% transmission with a wire thickness of about $80 \mu\text{m}$. The exit window is made of 2.5 mm thick quartz plate with a diameter of 72 mm. Quartz has short-wavelength cutoff of ~ 150 nm and a relatively high transmission for the UV lights ($\lambda \sim 170$ nm).

The IPMT is positioned beneath the exit window. We employ Hamamatsu Photonics type R4268 IPMT, which is equipped with a quartz window and 10-stage dynodes. The anode has a cross-wire configuration with 16 wires running in each X and Y direction at an interval of 3.75 mm. From the anode signals, the onboard CPU calculates the width (spread: *SP*) of the distribution together with the position (*RAWX*, *RAWY*) of the event. A pencil-beam light input to the IPMT shows a distribution of the output charge of about 7 ± 1 mm FWHM and the intrinsic position resolution of the phototube to be about 0.1 mm FWHM. From the last dynode, we derive the pulse-height (*PH*) and the rise-time (*RT*) information.

Figure 3.9 illustrates the resulting quantum efficiency and energy resolution of the GIS as a function of incoming X-ray energy. Thus the GIS sensitivity covers approximately 0.7-10 keV, with a spectral resolving power of $\sim 8\%$.

3.3.2 Data processing

One of the major design goals of the GIS is to achieve a very low level of non X-ray background (NXB). For this purpose, the GIS employs both hard-wired and software-based rejection.

One of the selection processes is the *RT* discrimination (RTD). All the X-ray events properly absorbed in the drift region should exhibit a *RT* of $3 \mu\text{sec}$, which corresponds to the drift time of electrons in the scintillation region. On the other hand, particle events creating a long electron track in the drift region exhibit longer *RT*. By controlling the levels of upper (RTUD) and lower discriminators (RTL D) for the rise time, we can efficiently remove NXB by hard-wire electronics. However, the *RT* distribution broadens significantly toward lower values of *PH*, because the signal to noise ratio gets worse. Therefore we set the *RT* window rather loose in orbit. We can further reduce NXB by

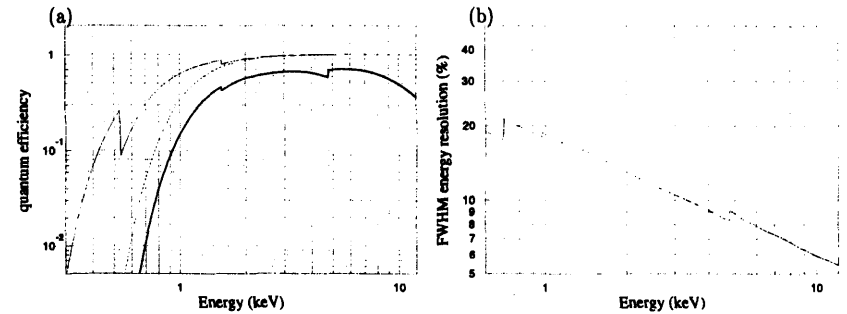


Figure 3.9: (a) Quantum efficiency of the GIS detector. Energy dependence of the thermal shield transmission (thin solid line), 10.5 μm thick Be window transmission (dashed line), and total GIS quantum efficiency including thermal shield, plasma shield, Be window, and meshes (thick solid line). (b) Energy dependence of the energy resolution (FWHM) of the GIS.

applying a *PH* dependent *RT* mask on ground processing. Here, the position dependent *RT* is converted to a position independent value *RTI* (rise-time invariant). Figs.3.10 demonstrates the background rejection with the strict *RT* mask on ground.

Besides the *RT* discrimination, we utilize another background rejection logic called *SP* discrimination (SPD). SPD is sensitive to the direction of a charge track perpendicular to the electric field. If an ionizing particle runs in parallel to the window plane, RTD does not work efficiently. By SPD, we can reject these events, which have much larger *SP* than those for the X-ray events. As shown in figure 3.11, *SP* is usually plotted against the squared radius from the detector center. Figure 3.11 also indicates the thresholds of SPD employed in orbit. SPD was enabled on 28 May 1993.

Apart from the position, pulse-height and the rise-time information of each event, the GIS provides scaler data using the combined signals from upper (UD) and lower discriminators (LD) of the signal pulse height, and upper (RTUD) and lower discriminators (RTL D) for the rise time. In Fig.3.12, we plot a schematic of the 6 monitoring scaler counts, *L0*, 1, 2 and *H0*, 1, 2, in the *PH-RT* space. These values are used to estimate the residual non X-ray background (§ 3.3.4).

The raw GIS outputs for an event, *PH*, *RT*, and calculated position (*RAWX*, *RAWY*), are subject to various non-ideal instrumental properties of the GIS. Therefore, we convert them into linearized quantities: *PI*, *RTI*, and (*DETX*, *DETY*), respec-

tively on ground. In these linearized values, *RTI* is utilized to apply the strict *RT* mask described above. We finally use *PI* and (*DETX*, *DETY*) for scientific analyses.

The position linearization are performed with the calibration table obtained from pre-launch scanning measurements with collimated X-ray beams. The tables have been confirmed in orbit in reference to the shadows caused by the window support girds and various observations.

When accumulating X-ray photons into an X-ray spectrum, we usually convert *PH* (pulse-height) of each detected event into *PI* (pulse-invariant) so that X-rays of the same energy give the same *PI* value (except the finite energy resolution) independently of the position, the temperature of phototube or the observation period. The conversion factor from *PH* to *PI* is called gain. The gain depends on three factors: (1) detected position of the incoming X-rays, (2) the temperature of the GIS, and (3) the long-term gain drift.

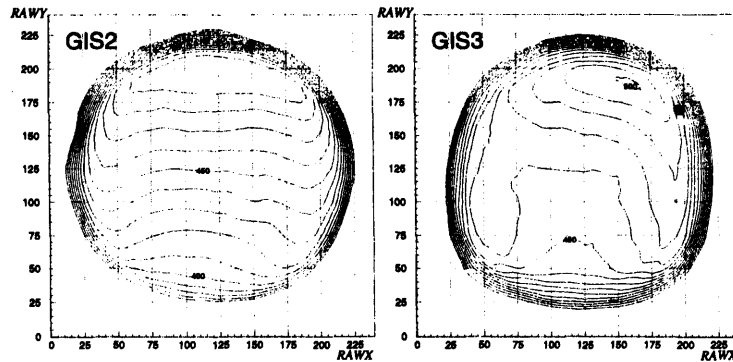


Figure 3.13: The gain maps in (*RAWX*, *RAWY*) coordinates for GIS2 (left panel) and GIS3 (right panel). Contour levels are every 10 step from 350.

The GIS gain is position dependent by $\sim \pm 10\%$ peak-to-peak due to non-uniformity in the IPMT gain. Calibration of this effect involves a look-up table called "gain map", which summarizes relative gains of each detector as a function of the position of event occurrence. The gain map is based on the pre-launch scanning measurements and also on the in-orbit data using the instrumental Cu-K line seen in the NXB spectrum (§ 3.3.4) after a long data integration. The gain maps are found to change gradually, especially for the GIS3 (Idesawa et al. 1997 ASCA News Letters No.5). The change of gain maps is

approximately represented as a function of radii from the detector center. This additional correction is $\sim 0.5\%$ and $\sim 3\%$ for GIS2 and 3, respectively. The reliability of the gain map is within $\pm 1\%$ and $\pm 2\%$ for the regions of radius < 15 mm and 15-20 mm, respectively, for both detectors.

The GIS gain depends significantly on the temperature, because of the temperature dependence in the IPMT and gas cell. The GIS gain is monitored continuously in orbit in reference to the built-in ^{55}Fe isotope, and so is the IPMT temperature. In Fig.3.14a, we show the gain vs. temperature relation thus calibrated in orbit. This relation is frequently updated taking into account the long-term gain change (see next paragraph), and is used to correct the GIS gain for the temperature variance. This relation between the temperature and the GIS gain, including the long-term gain change, is called "gain history". The temperatures of the two GIS detectors vary by $\sim 10^\circ\text{C}$ in orbit, mainly in response to satellite attitude changes.

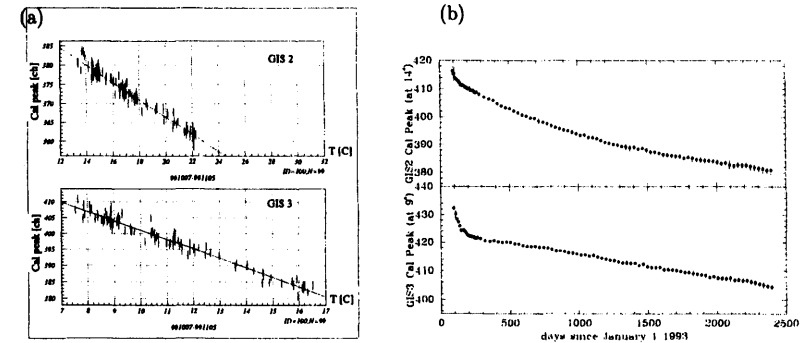


Figure 3.14: (a) Peak *PH* channels of the ^{55}Fe calibration isotope, plotted against the detector temperature measured in orbit on the side wall of IPMT. (b) Long-term gain history since the launch till July 2000, expressed in terms of the temperature-corrected ^{55}Fe *PH*. In both plots, upper and lower panels are for GIS2 and GIS3, respectively.

Figure 3.14b shows the long-term GIS gain history in reference to the ^{55}Fe isotope, after correction for the temperature variation. Thus, the gain of both detectors are gradually decreasing. This gradual gain decrease is unlikely to be caused by out-gassing in the detector, since the *RT* characteristics have remained constant. Therefore, the phenomenon is possibly due to a slow degradation in the UV transmission of quartz windows of the gas cell and the IPMT, or changes in the IPMT performance. In any way,

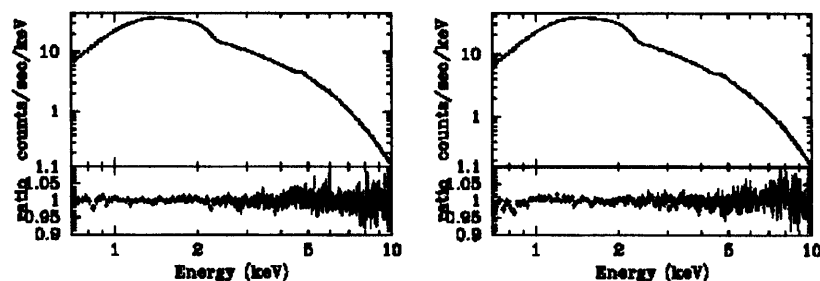


Figure 3.15: The spectra of the Crab Nebula obtained with (a) the GIS2 and (b) GIS 3. Both spectra are fitted by a power law model with $\Gamma = 2.09$, which is consistent with previously observed results of $\Gamma = 2.08 \sim 2.11$ (Toor and Seward 1974). In the lower panels, the data to model ratios are plotted, which demonstrate the accuracy of the current understanding of the instrumental responses.

the secular gain decrease is so slow that it does not affect scientific objectives at all.

All these gain correction process are confirmed using the instrumental Cu-K line seen in the NXB spectrum and other stellar sources such as SNR and clusters of galaxies. In addition, the X-rays from the Crab nebula, which is the standard candle of the X-ray sky, are used; this is also useful for the effective area calibration. In Fig.3.15, we plot the Crab Nebula spectra obtained with the GIS, fitted by the generally accepted power law emission model. From the residual plot, we can see that the calculated model well reproduces the data by an accuracy of $\sim 1\%$. Together with many other calibration results, we believe that the absolute GIS response thus established is accurate to $\sim 1.2\%$.

3.3.3 Background estimation of the GIS

Even though the *RT* and *SP* discriminations (see § 3.3.2) very efficiently reject particle- or gamma-ray induced GIS events, the NXB left over after these discriminations ("residual NXB") still dominates over faint signal X-rays. In addition, the sky itself emits X-rays, which is called the Cosmic X-ray Background (CXB). This emission is considered to originate from numerous faint X-ray sources distributed in the universe, and is observationally shown to be almost isotropic in the sky. We must carefully estimate these two background components, and subtract them from the on-source images and spectra. This

process is technically of crucial importance to the subject of the present thesis.

Figure 3.16a gives three typical GIS background spectra, accumulated over the entire detector area for sufficiently long times while the XRT is pointing onto night earth, sunlit earth, and blank skies. The night-earth spectrum represents the residual NXB itself (see § 3.3.2). The day-earth spectrum in addition contains bright solar X-rays scattered by the earth's atmosphere. The blank-sky spectrum consists of the Cosmic X-ray Background (CXB; § 3.3.5), as well as the residual NXB. Thus, the difference between the blank-sky spectrum and the NXB spectrum shows the pure CXB component. The NXB exceeds the CXB above ~ 5 keV. In Fig.3.16b, we show projected profiles of the CXB and NXB components of GIS2, in the 1–2 keV and 4–8 keV bands. The CXB is brightest at the XRT optical axis because of the vignetting effect of the XRT, while the NXB brightness is virtually flat across the detector area.

We used the blank-sky data to obtain the averaged CXB (§3.3.5), and used the night earth data as a template for the NXB. In the latter case, we scale the night earth spectra or image by *reffrig* to the event rate rejected through the on-board processing in the on-source observation (§3.3.6), and further trim it by *reffrig* to the image brightness in the outer region of the detector during the observation (§3.3.4).

3.3.4 Subtraction of non X-ray background (NXB)

To estimate the NXB, we need in turn to know its basic properties, including its time variation in particular. The NXB properties have been studied extensively by many authors, including Ishisaki (1995) in particular. He showed that its time variation is predominantly correlated with geomagnetic cut-off rigidity (COR) for cosmic rays along the satellite orbit: COR is the minimum momentum of charged particles that can penetrate the terrestrial magnetism. However, the COR is merely one of the many factors that affect NXB, and several features cannot be explained by COR alone. Ishisaki (1995) searched the GIS monitor data for a more direct indicator of NXB. By analyzing the night-earth data, he has found that "H02 counts", defined as a sum of two monitor counts, H0 and H2 (see § 3.3.2), are tightly correlated with the residual NXB counts. The H02 counts are believed to express the count rate of the particle induced events, rejected in the on-board processing, and is almost free from signal X-rays even during the observations of bright X-ray sources. Therefore, it can be used as a good indicator of the residual NXB contained in the on-source data.

Figure 3.17 shows the H02 count against the COR during the night-earth observations.

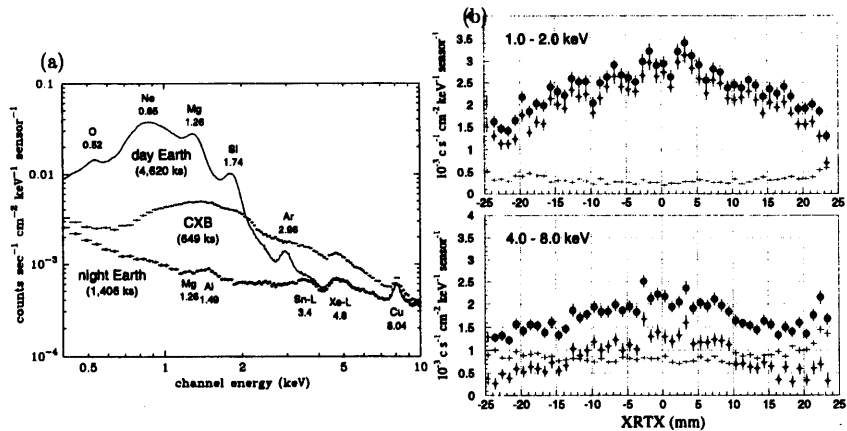


Figure 3.16: (a) Long-exposure GIS2+GIS3 spectra accumulated over the whole field of view, from day-earth pointings (smooth line; representing the NXB plus scattered solar X-rays), night-earth pointings (filled circles; the NXB only), and blank skies observations (crosses; the NXB plus the CXB). The exposure time is given in parentheses. Identifications of the atomic lines, either celestial or instrumental, are also given in the figure together with their energies in keV. The flare-cut (Table 3.3) is NOT applied. (b) Projected count-rate profiles of the blank-sky and night-earth data in a strip of $-5 \text{ mm} \leq XRTY \leq +5 \text{ mm}$ for GIS2. Here "cm²" is defined on the actual detector dimension of the GIS, and is not the effective area of the XRT. Filled circles, crosses, and diamonds represents the raw CXB including NXB, the NXB, and the CXB after subtracting the NXB, respectively. The flare-cut (Table 3.3) is applied for both the CXB and the residual night-earth data.

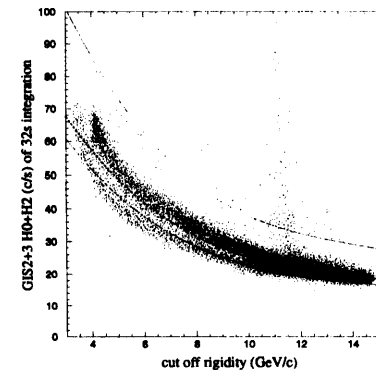


Figure 3.17: Correlation between *COR* and *H02* counts during the night-earth observations. *H02* is integrated for every 32 s. A dashed line means a function $f(x) = (109.3 - 17.05x + 1.127x^2 - 0.02627x^3)/32$ derived from fitting. Two solid lines below and above show $f(x)$ scaled by a factor of 0.9 and 1.5, respectively. A vertical branch observed around $COR \sim 12 \text{ GeV c}^{-1}$ is caused by some flares. The flare-cut (Table 3.3) is NOT applied.

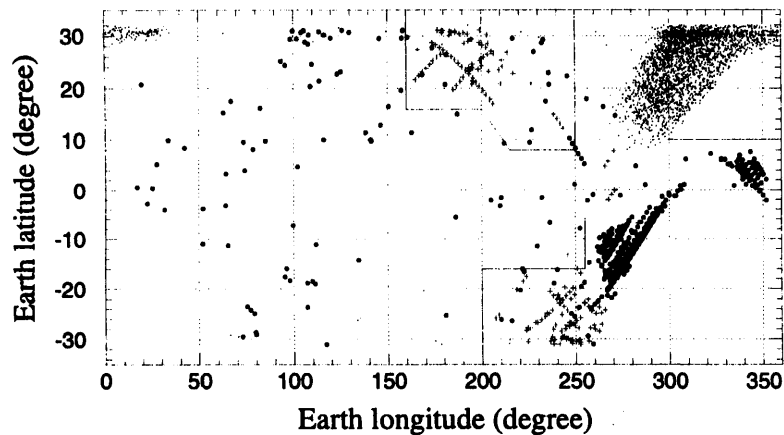


Figure 3.18: Distribution map for flares on the Earth surface. The symbols “•” and “+” represent positions of the detected flares. The symbol “•” represents positions where the COR-map is suspected to be inaccurate. Two regions surrounded by solid lines define the dangerous areas where flare events can frequently take place.

A clear correlation is found between the two quantities. Nevertheless, the H02 count exhibits a considerable scatter for a given COR, partly due to suspected inaccuracy of the COR map (in particular, over north Atlantic regions; Fig.3.18). This makes the H02 count a better NXB indicator than the COR. In addition, a sudden increase in the GIS background rate, called a flare event, sometimes happens, producing an upward branch in Fig.3.17. Ishisaki (1995) clarified that these flares tend to occur in two particular regions (“dangerous regions”) around south Atlantic and north Pacific (Fig.3.18). Taking these pieces of information into account, Ishisaki (1995) finally developed criteria, called “*flare cut*”, used to exclude the data portion contaminated by these flare events. As listed in Table 3.3, the criteria are based on a combined use of the H02 rate, the satellite position, and the RBM count rate. We apply the *flare cut* processing to both the on-source data and the background data (see below).

Table 3.3: The “*flare cut*” screening criteria for the GIS. Time region satisfying this criteria are excluded from the analysis.

| Condition | Reason |
|--|-------------------|
| $15 \text{ c/s} \leq \text{H02} \leq 45 \text{ c/s}$ | to avoid high NXB |
| $\text{H02} \leq 1.5 \times f(\text{COR})^\dagger \text{ c/s}$ | for flares |
| $\text{RBM} \leq 300 \text{ c/16 s} = 18.75 \text{ c/s everywhere}$ | for flares |
| $\text{RBM} \leq 100 \text{ c/16 s} = 6.25 \text{ c/s in the dangerous areas (figure 3.18)}$ | for flares |

$$^\dagger f(x) = 0.5(109.3 - 17.05x + 1.127x^2 - 0.02627x^3) \text{ c/16 s.}$$

Our basic strategy of constructing the NXB data, to be subtracted from the on-source images or spectra, is to utilize the night-earth GIS pointing data accumulated over very long periods (up to the entire mission lifetime of ASCA). We process all these background data in the same manner as the on-source data, by applying the *RT*, *SP*, and flare cuts. We then sort all these background events according to appropriate intervals of the H02 counts, in every 5 c/s step, as 15–20 c/s, 20–25 c/s, 25–30 c/s, etc. This yields a large number of NXB events for each H02 interval. We call this datasets “NXB templates”. In Fig.3.19, we plot the spectra and radial profiles of these NXB templates for five H02 intervals. As H02 increases, the spectrum gets softer and the slope of the radial profile gets steeper towards the detector rim.

Now that the NXB templates have been prepared, we can estimate the NXB spectrum

H contained in a particular on-source datasets as

$$H(PI) = \sum_i H_i^{NTE}(PI) \frac{T_i^{OBS}}{T_i^{NTE}} \quad (3.1)$$

Here i is the sorting interval of the H02 counts, H_i^{NTE} is the night-earth spectrum of the i -th interval, T_i^{OBS} is the total exposure of the on-source data in that H02 interval, and T_i^{NTE} is that of the NXB template. We call this method "H02 method". In order to examine the validity of this method, in Fig.3.19b we calculated the residual NXB counts for individual night-earth observations comprising the NXB template, and compared them with the H02-method prediction. Clearly, the actual NXB exhibits a secular change. It is thought to reflect a combination of various effects, such as changes in the solar activity, a gradual decrease in the satellite orbit altitude, build-up of the radio-active material in the detector and spacecraft, and so on. Accordingly, we have modified the above equation as

$$H(PI) = F(t) \times \sum_i H_i^{NTE}(PI) \frac{T_i^{OBS}}{T_i^{NTE}} \quad (3.2)$$

where $F(t)$ is an empirical factor describing the secular change. It has been determined as shown in the top panel of Fig.3.19b, in terms of a polynomial function. After subtracting $F(t)$ (which is equivalent to using equation 3.2 instead of 3.1), the NXB count-rate history becomes as shown in the lower panel of Fig.3.19b. Thus, the systematic error included in the NXB subtraction is typically 5 ~ 6% for a 40 ks observation.

3.3.5 Derivation of the cosmic X-ray background (CXB)

In the study of faint diffuse emission, we must accurately subtract not only the NXB but also the CXB that inevitably contributes to the on-source data. We may reproduce and subtract the CXB in two alternative ways. One is to use the actual CXB data acquired from blank sky fields; by subtracting the NXB contribution in them (using the same procedure as described above), we can obtain the pure CXB data, or "CXB template". The other is to start from the CXB model spectrum with a given constant brightness, and convert them through instrumental responses into predicted GIS data. This method is feasible because the CXB surface brightness is quite uniform, and its spectral shape is known to a reasonable accuracy. Among the two methods, the former allows a more reliable CXB subtraction, because it is free from any systematic error involved in the instrumental response. Accordingly, we here employ the former method. Specifically, we use "Master Background Database" prepared by Ikebe (1994) which consists of 20

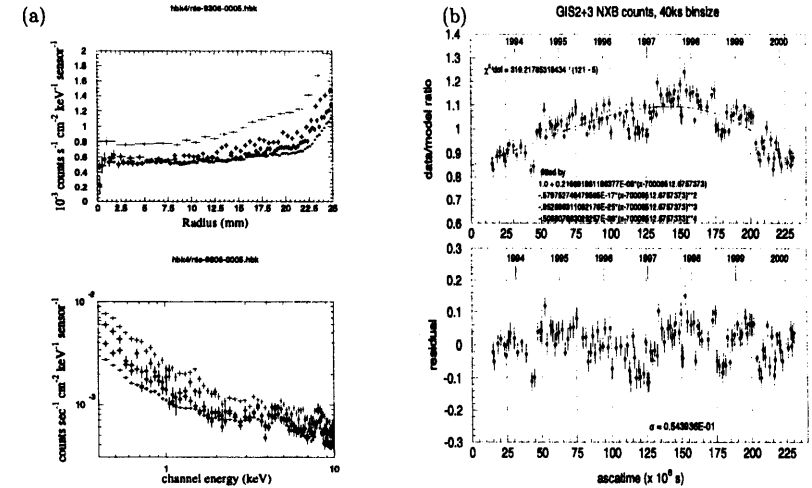


Figure 3.19: (a) The 0.6–7.0 keV radial profiles (upper panel) and spectra (lower panel) of the NXB templates, produced from the GIS data during the night-earth observations. The five H02 intervals are indicated by '+' (50–80 c/s), 'o' (40–45 c/s), '•' (30–35 c/s), and 'x' (20–25 c/s). The H02 counts are integrated for every 16 s. The flare-cut (table 3.3) is applied. (b) Long-term histories of the actual 0.7–7.0 keV night-earth counts, normalized to the H02-method prediction before correction for secular changes. Each data point represents an exposure of 40 ks. The solid line shows the best fit 4-th order polynomial, of which the coefficients are given in the figure inset. Lower panel shows the residual after subtracting the polynomial fit.

observations of 4 different blank sky fields: "Draco", "NEP", "QSF3" and "SA57". All these fields are in high Galactic latitudes with $|b| > 29^\circ$ (Ishisaki 1995).

This method of CXB subtraction, however, has one drawback, that there is no "blank sky" in its strict sense. Every sky field contains a number of faint X-ray sources that ultimately compose the CXB, and sometimes relatively bright discrete sources appear above the detection limit due to statistical fluctuations. We must remove such contaminating discrete sources from the blank-sky data. To do this, Ikebe (1994) discarded the regions in his Master Background Database where the photon counts exceed that in the surrounding region by more than 2.5σ . This process eliminates all the sources resolvable with the GIS, at a threshold of $\sim 1 \times 10^{-13} \text{ erg s}^{-1} \text{ cm}^{-2}$ in the 2-10 keV band for a typical observation parameters. Figure 3.20 exemplifies a GIS image of a blank sky, and the associated mask image utilized to eliminate faint discrete sources found in it.

We reprocessed each blank sky datum with *flare cut* condition, as the original database was not processed in that way. The CXB data were then generated by summing the 20 observations, filtered with corresponding masks. The NXB contribution was subtracted via the H02 method. Thus, the total exposure map is a mosaic of 20 masks weighted by corresponding exposures. The resulting CXB data have a total exposure of 645 ksec, and an average exposure of 623 ksec when considering the mask. When subtracting the CXB spectrum or image from particular on-source data, we produce a "CXB template" from the above-mentioned CXB data. Namely, we extract the CXB events in the CXB template falling onto the same integration region as is used for the on-source data, and correct the former data for exposure using the mosaic exposure map. Then, the CXB template (either a spectrum or an image) is subtracted from the on-source data.

3.3.6 A finer adjustment of the NXB level

Although the H02 method (§ 3.3.4) allows us to subtract the NXB contribution from the on-source data, its reproducibility is limited to a level of $\sim 6\%$. Presumably, this is because there are still unknown factors affecting the NXB variation. We need to overcome this limit and improve the accuracy as much as possible, because this will ultimately limit our study of faint, diffuse, hard emission. For this purpose, we may recollect that, even in the on-source data, hard-band events detected in the outer regions of the GIS field-of-view are dominated by the NXB (see Fig.3.16a,b). Then, we can apply a fine adjustment to the NXB template to be subtracted, so that the on-source data and the NXB template agree with each other in a hard energy band and over the detector periphery (e.g., Fukazawa

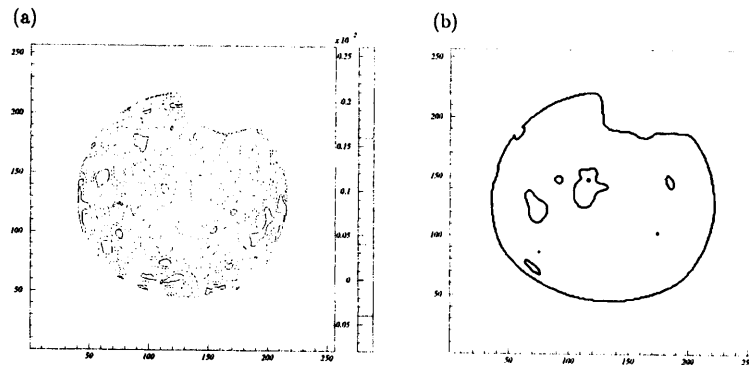


Figure 3.20: An example of blank-sky GIS image. (a) A 0.5-10 keV GIS2 image of NEP field observed in July 1993, smoothed by convolution with the XRT PSF model. The contours are linearly spaced by $4 \times 10^{-4} \text{ cts s}^{-1} \text{ arcmin}^{-2}$. (b) The associated mask image to eliminate faint discrete sources.

et al. 2001).

To conduct the above idea, we utilize an energy region of 5.9-10.6 keV, and a detector region of $r > 15'$ from the detector center. The upper-limit of the energy range is set by the calibration uncertainty, and the lower-limit is near the crossing point of the NXB and CXB. About 80% of the events thus obtained are NXB events. We then determine "NXB correction factor" f_{cor} through error minimization of the equation as

$$\text{Data}_{out}(E) = \text{CXB}_{out}(E) + f_{cor} \times \text{NXB}_{out}^{H02}(E) \quad (3.3)$$

Here, Data_{out} is the hard-band spectrum obtained from the on-source data in the specified outer region, CXB_{out} is that of the template CXB, and NXB_{out}^{H02} is that of NXB estimated by the H02 method. Evidently, f_{cor} is expected to take a value close to 1.0. We plot an example of these spectra in Fig.3.21.

Once f_{cor} is determined for a particular on-source data set, we can define the background BGD_{in} (either spectrum or image) in an inner region used for the actual data analysis, as

$$\text{BGD}_{in} = \text{CXB}_{in} + f_{cor} \times \text{NXB}_{in}^{H02} \quad (3.4)$$

Here, CXB_{in} and NXB_{in}^{H02} are the CXB and NXB templates for the same region, respectively. In this case, various systematic errors originally associated with the NXB

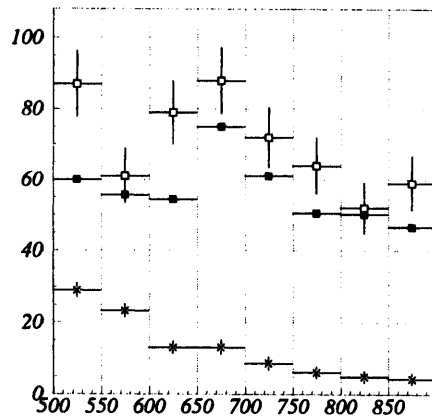


Figure 3.21: Example of the determination of the NXB correction factor f_{cor} , in terms of the pulse-height spectrum. Abscissa is Pulse Invariant (PI), and ordinate is the number of events. Open boxes represent the on-source spectrum ($Data_{out}(E)$), crosses are the CXB spectrum ($CXB_{out}(E)$) and filled boxes are the NXB template spectrum derived with the H02 method ($NXB_{out}^{H02}(E)$).

estimation are absorbed into the statistical error of the f_{cor} determination. To confirm it, we divided the night earth data into ~ 60 subsets, each with ~ 100 msec exposure and an integration time of a month, and applied this method to them. The estimated background was consistent with the actual data within the statistical error.

Then, how high is the statistical accuracy of the f_{cor} determination? For example, a 80 ks exposure will provide ~ 2000 counts in the 5.9-10.6 keV band of the outer region. This allows us to estimate f_{cor} with an accuracy of $\sim 1/\sqrt{2000} = 2.2\%$, which is better than the 6% error of the H02 method. Even when the observation was split into several pointings, we can use the quadrature sum of the errors of the individual pointings for the averaged data, because the NXB estimation errors derived by this correction method are based on the actual data of each pointing and independent to one another. This is not true of the original H02 method.

Strictly speaking, the improved background estimation described above is still subject to fluctuations in the CXB counts, mostly due to the presence of discrete sources. Such a contribution has already removed from the CXB template (first term on the right-hand side of equation 3.3), but that in the on-source data (left-hand side) has not. Accordingly, when we utilize equation 3.3, we exclude, in advance, sources visible in the on-source data. The detection threshold for this process is set again at 1×10^{-13} erg s^{-1} cm^{-2} in the 2-10 keV band; a source with the 2-10 keV flux four times higher than this threshold, located 18' from the optical axis, will contribute $\sim 2\%$ of the overall event counts in the outer region. When the emission from the target source is greatly extended, which is often the case with the clusters and groups of galaxies, we cannot use the same source-finding procedure as used for the CXB template (§ 3.3.5). In such a case, we utilize the images from other instruments, particularly the ROSAT image if available, to find these sources.

3.4 Solid-state Imaging Spectrometer (SIS)

The Solid State Spectrometer (SIS) experiment is the first X-ray detector in orbit that utilizes CCDs (charge coupled devices) in the photon counting mode. It was jointly developed by Massachusetts institute of Technology (MIT), Pennsylvania State University, ISAS, and Osaka University (Burke et al. 1991).

3.4.1 Design and structure

The SIS experiment consists of two detectors (SIS camera; SIS0 and SIS1), an analog electronics unit (SIS-AE), and a digital processing unit (SIS-DE) which is combined with the satellite data processor (DP). Figure 3.22 shows a cross section view of the SIS camera.

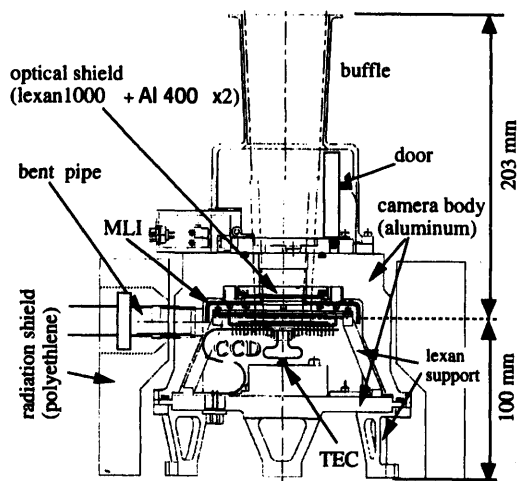


Figure 3.22: Cross section view of the SIS camera.

Each SIS detector is made up of four CCD chips of 11 mm square each developed in the MIT Lincoln laboratory, to achieve a 22 mm × 22 mm square area for X-ray detection. Each chip has 4096 by 4096 pixels of 27 μm square each, and a depletion layer of about 40 μm thick which ensures an improved efficiency for harder X-rays than conventional CCDs. Design parameters and performance of the SIS are summarized in table 3.4.

Table 3.4: Design parameters and performance of the SIS

| | |
|----------------------------------|--|
| Irradiation Method | Front irradiation |
| Charge Transfer Method | Frame Transfer |
| Clock | 3-phase drive |
| Number of pixels in Image Region | 420 pixels × 422 lines per chip |
| Pixel Size | 27 μm |
| Area | 11×11 mm square per chip 22×22 mm square per detector |
| Field of View | 11×11 arcmin square per chip 22×22 arcmin square per detector |
| Thickness of Depletion Layer | ~ 40 μm |
| Optical Blocking Filter | 100 nm Lexan film coated with 40 nm aluminum |
| Operating temperature | ~ -62 °C |
| Energy Band | 0.4-12 keV |
| Quantum Efficiency | ~ 80% at 5.9 keV |
| Energy Resolution | 2% at 5.9 keV (FWHM) |

The CCD chip used for the SIS is a frame transfer type CCD and has the same structure as an optical CCD of the same type. Its detection part is made of an Si semiconductor of p-type and n-type connected each other through p-n junction. An insulator layer made of SiO₂ are attached on the front surface of the n-type Si, and electrodes are built on it. By supplying specific patterns of voltages on the electrodes charges in a pixel are transferred from a pixel to a next pixel. An electrode is also attached on the back. A depletion layer is developed in the device by supplying a bias voltage between the electrodes on the front and on the back.

Electric signals from the SIS camera are fed into SIS-AE and their pulse height are converted into digital signals with analog-to-digital converters. SIS-AE also generates driving clocks for the CCD chips, and monitors and controls temperature of the CCD chips. SIS-DE picks up X-ray events in the digital signals from SIS-AE with two digital signal processor (DSP) and sends them to the satellite data processor (DP), which commonly processes data from the SIS and the GIS and edits them into a telemetry format.

Figure 3.23a illustrates the quantum efficiency of the SIS as a function of incoming X-ray energy. Thus the SIS sensitivity covers approximately 0.4-10 keV. The CCD chips

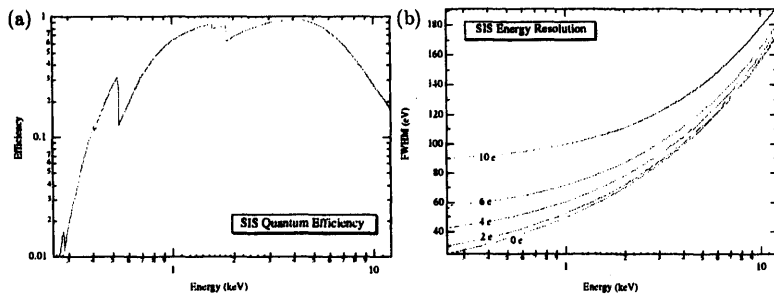


Figure 3.23: (a) Detection efficiency of the SIS as a function of incoming X-ray energy. K-edges of O (0.53keV), Al (1.56keV), and Si (1.84keV) are clearly seen in the figure. This efficiency does not include optical blocking filter. (b) Energy resolutions of the SIS as a function of incoming X-ray energy for the single event. Energy resolutions with different read-out noise N are plotted ($N \sim 5$ for the SIS). The read-out noise levels are given as the equivalent number of electrons.

and preamplifiers are cooled down to -60 °C with a thermo-electric cooler (TEC) from the backside of the chips in order to reduce thermal noise down to $N \sim 5$ electrons level. Thus the SIS achieves an energy resolution of about 150 eV FWHM over the whole energy range (Fig.3.23b); this is the best energy resolution ever achieved by non-dispersive X-ray spectrometers so far put into orbit.

3.4.2 Data processing

In order to perform proper photon-counting spectroscopy, the CCD frame must be scanned and read out fast enough so that event pile up (i.e. one pixel receiving more than one X-rays) is virtually negligible. Since the read out cycle is usually limited by the telemetry capacity, the SIS performs an extensive onboard CPU processing to compress the information. Instead of sending data from all the pixels to ground, the SIS basically picks up only those pixels in which the charge exceeds a certain threshold, and sends out their positions and pulse-heights. Moreover, to handle targets with different X-ray intensities and angular sizes under different telemetry rates, the SIS uses three different clocking modes: 1CCD, 2CCD and 4CCD modes. In the n CCD mode ($n = 1, 2, 4$), data from n chips for each detector are read out. Because the time required to read a chip is fixed, this means that the integration time per chip per read out sequence is proportional to n . In the 1CCD mode, e.g., the usable field of view becomes limited to a quarter of the detector,

but the event pile up becomes least severe so that we can observe brighter sources than in other clocking modes. In view of background events and hot pixels (see below), this also means that the telemetry limit is relaxed.

The electrons produced in the depletion layer by an X-ray photon may be split into several adjacent pixels. The pattern of charge splitting over 3×3 pixels is called "event grade". Because the splitting pattern of the particle induced events are generally different from that of the X-ray events, we can reduce the background by selecting the correct grades. When the charge is spread over more than 3×3 pixels, the event is rejected by the onboard CPU as a background event. In order to cope with the splitting of normal X-ray events, the SIS incorporates several data selection modes. For example, in so called "faint mode", pulse-height of a certain pixel with event detection is always accompanied with pulse-heights of the eight surrounding pixels. We can then examine the event grade on ground, and restore the total pulse-height if necessary. In so called "bright mode", the onboard CPU recognizes the charge splitting pattern, and sends only the total pulse-height for events with specified grades. The faint mode requires a larger telemetry capacity, but provides more information than the bright mode. Actually we can convert the faint mode data into the bright mode data on ground, but the reverse is impossible.

After the launch, several additional complications have been recognized with the SIS. One is so called "hot pixels", i.e. particular pixels (though not necessarily fixed ones) which report false event detections too frequently. We must carefully remove these hot pixels in data analysis. When the hot pixels become too many, the SIS data suffer from significant telemetry deadtime. The hot pixels are increasing, and it has become almost impossible to utilize 4CCD mode with the faint mode before the end of 1994. Another problem is the light leakage, particularly in chip 2 and chip 3 of SIS0 (S0C2 and S0C3, respectively), presumably caused by a damage in the optical blocking filter. This makes the observation with S0C2 and S0C3 almost impossible when the day Earth is within $\sim 25^\circ$ from the target. It also affects the dark current of the whole CCDs in the daytime, and causes a subtle change in the energy to pulse-height relation.

In addition to the hot pixel rejection, the data filtering processing includes grade selections, and good time selection such as to avoid the influence of the day Earth. The major contents of the standard screening criteria (called *rev. 2 standard* criteria) are listed in Table 3.5. See *The ASCA Data Reduction Guide* for details. Such as the case with the GIS, the *PH* information of the raw data is corrected for gain difference depending on the detector position. This is calibrated using the line features in the intrinsic background and the observed data of SNRs, particularly that of Cas-A. The position information is also

corrected. Thus, the raw data are converted to a set of event lists with PI , $DETX/Y$, and some other quantities. We use these filtered and corrected event lists in our analysis.

Table 3.5: The major contents of "rev.2 standard" data screening criteria for the SIS (from *The ASCA Data Reduction Guide*).

| Condition | meaning | Reason |
|---------------|------------------------------------|------------------------------------|
| GRADE=0,2,3,4 | reject particle events | to reduce the background |
| SAA=0 | not in the south atlantic region | to avoid high background region |
| COR>6 | | to avoid high background region |
| BR_EARTH>20 | target is far from day Earth rim | to avoid the day Earth effects |
| ELV>10 | target is far from night Earth rim | to avoid obscuration by atmosphere |

3.4.3 SIS background

The background of the SIS is described in Gendreau (1994 ASCA News Letters No.2, p5) in detail. Here we describe it briefly. Like in the case with the GIS, the SIS background consists of the CXB and the internal background (NXB). The NXB of the SIS is sub-divided into two components: that accumulated on the imaging region, and that accumulated on the frame store region. The first component is proportional to the sky exposure time, while the second is proportional to the number of readouts and thus dependent on the SIS mode. Due to this second component, the count rate ratio of the internal background between 1 CCD mode and 4 CCD mode is ~ 1.2 . In Fig.3.24, the internal background and the total background including CXB for 4 CCD mode are shown. The internal background consists of a flat continuum, as well as several fluorescence lines due to Fe-K (6.4, 7.0 keV), Ni-K (7.5, 8.3 keV), Au-L (9.7 keV), and Al-K (1.5 keV). The count rate of the internal background is reported to be constant for 2 years after launch, except in the soft band of 4 CCD mode (Ueda et al. 1996 ASCA News Letters No.4, p28 ; Ueda 1996).

3.4.4 Degradation of the SIS performance

The SIS energy resolution have been decreasing with time. The value at 6.7 keV was ~ 168 eV just after the launch, ~ 180 eV in 1996, and getting worse afterwards. Furthermore, the quantum efficiency of the detector is decreasing with time, which is significant in the lower end of the spectra below ~ 1 keV. This phenomena is known to have been growing since 1994, possibly from immediately after the launch.

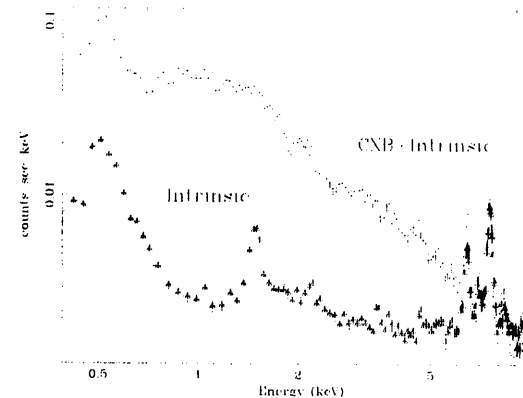


Figure 3.24: The SIS background spectra of 4 CCD mode, integrated over all the chips.

The loss of quantum efficiency in the lower energy band is observed as an artificial excess absorption in the spectral fitting. This value was equivalent to the column density of $\leq 1 \times 10^{20} \text{ cm}^{-2}$ in 1994, $2 \sim 7 \times 10^{20} \text{ cm}^{-2}$ in 1996, and $7 \sim 10 \times 10^{20} \text{ cm}^{-2}$ in 2000. Because the column density at high galactic latitude is typically several times 10^{20} cm^{-2} , this can affect low-energy part of the SIS spectra taken after ~ 1997 , although the data statistics often make it insignificant. A work is currently undergoing to understand the nature of this phenomenon and solve it, but there is no established correction method at this time. The "excess absorption" interpretation is solely empirical.

3.5 Comparison of the GIS and the SIS

As presented in the preceding sections, the two detectors have slightly different and complementary characteristics. In Fig.3.25a, we plot the effective area of the two detectors, which shows that the GIS has a larger effective area above ~ 5 keV, while that of the SIS is larger below ~ 2 keV. In Fig.3.25b, we plot the normalized background spectra of the two detectors. In general, both detectors have very low and stable background compared to other X-ray instruments. What is more, the GIS background can be estimated very well, up to an accuracy of $\sim 2\%$, and shape of the GIS background is nearly constant in

energies above ~ 4 keV, even though the background normalization varies (§3.3.6). For the SIS, the accuracy is $\sim 10\%$ (Ueda 1995).

The higher energy resolving power and efficiency for the soft X-rays make the SIS a better tool to study the hot gas component in groups of galaxies. In contrast, the accurate background estimation and the higher efficiency for the hard X-rays make the GIS more suited to the search for diffuse hard X-rays. This combination makes ASCA the best satellite for studying the hard X-rays from groups of galaxies.

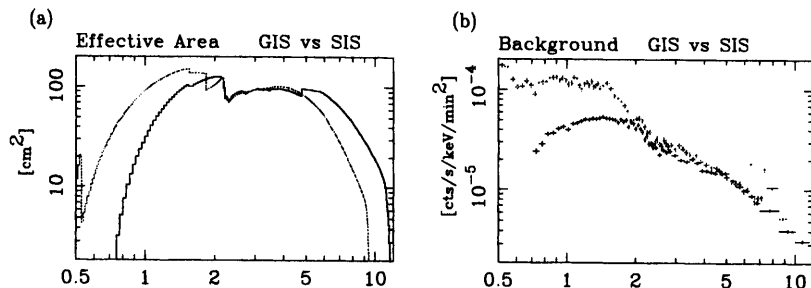


Figure 3.25: Comparison of the GIS (black) and SIS (gray); (a) the effective area, and (b) the background spectra. The latter is normalized by a solid angle of arcmin².

Chapter 4

THE HCG 62 GROUP

In this chapter, we analyze the ASCA data of the HCG 62 group, which is a near-by, X-ray bright group with the strongest evidence for a diffuse hard X-ray emission.

4.1 Overview

4.1.1 The HCG 62 Group

The HCG 62 group is one of the compact groups identified from the optical plates by Hickson and his colleagues (e.g. Hickson 1982). It originally consists of four galaxies, NGC 4761, NGC 4759, NGC 4764 and HCG 062d. NGC 4761, the brightest among the four, is optically identified as a low luminosity AGN (LLAGN) by Coziol et al. (1998). None of them is a bright infrared source (e.g. Verdes-Montenegro et al. 1998).

Zabludoff and Mulchaey (1998a) extensively surveyed a $1^\circ.5 \times 1^\circ.5$ region around the group and measured the redshifts of 106 galaxies. They identified 45 of them as members of the group, and derived the mean recession velocity of 4385 ± 59 km s⁻¹, which indicates a redshift of 0.0146 and a distance of $58.5 h_{75}^{-1}$ Mpc. Here $H_0 = 75 h_{75}$ km s⁻¹ Mpc⁻¹ is the Hubble constant. The velocity dispersion was measured to be 376_{-46}^{+52} km s⁻¹, which is a typical value for galaxy groups.

The central four galaxies are located extremely close to one another, within $3'.7$ on the sky (Fig 4.1). In fact, NGC 4761 and NGC 4759 are separated by only $0'.4$. Here, $1'$ corresponds to $17 h_{75}^{-1}$ kpc. Such a high galaxy density and a fairly low velocity dispersion are thought to lead to galaxy merger. From comparison with N -body simulations, these four galaxies are suspected to merge into a large elliptical galaxy in ~ 1 Gyr (Ponman and Bertram 1993).

Table 4.1: Optical properties of the central four galaxies of HCG 62

| name | HCG name | Pos ⁽¹⁾ | type ⁽²⁾ | m_B ⁽³⁾ | V ⁽⁴⁾ |
|----------|----------|-----------------------|---------------------|----------------------|--------------------|
| NGC 4761 | HCG 62a | (193.274, -9.20444) | E3 | 13.30 | 4259 ± 10 |
| NGC 4759 | HCG 62b | (193.269, -9.20056) | S0 | 13.91 | 3561 ± 18 |
| NGC 4764 | HCG 62c | (193.291, -9.19861) | S0 | 14.97 | 4432 ± 17 |
| HCG 62d | HCG 62d | (193.278, -9.25833) | E2 | 15.92 | 4174 ± 33 |

- (1) Position in J2000 (NASA Extragalactic Database).
 (2) Morphological type (Hickson et al. 1989).
 (3) Blue magnitude (Carvalho et al. 1997).
 (4) Recession velocity and error, in km/s (Carvalho et al. 1997).

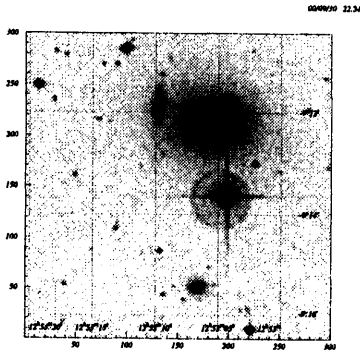


Figure 4.1: Optical image of the central $6' \times 6'$ region of the HCG 62 group. The four central galaxies are visible. A bright source with a ring and a cross near the center is a foreground star.

4.1.2 Previous X-ray observations

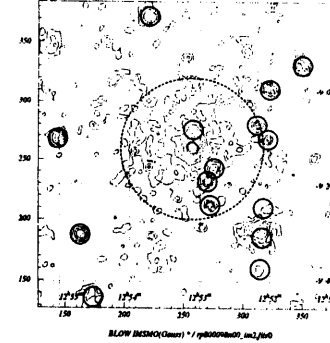


Figure 4.2: The 0.5–2.3 keV PSPC X-ray image of HCG 62, smoothed with a Gaussian filter of $\sigma = 0'.25$. The contours are logarithmically spaced, by factors of 1.34, where the lowest one corresponds to 7.2×10^{-4} counts $\text{sec}^{-1} \text{arcmin}^{-2}$. The dotted circle indicates the region $15'$ around the group center, and solid circles shows the detected contaminating sources.

The HCG 62 group is known as the first compact group in which the X-ray emission from the extended hot gas, namely IGM (intra-group medium; § 2.1.3) has been confirmed (Ponman and Bertram 1993). Many authors have subsequently published results of their analysis of the ROSAT data of this group (e.g. Pildis et al. 1995; Saracco et al. 1995; Mulchaey et al. 1996; Ponman et al. 1996; Mulchaey and Zabludoff 1998; Davis 2000; Finoguenov et al 1999; Boute 2000; Nevalainen et al. 2000; Helsdon et al. 2000; Lloyd-Davies et al. 2000). They found a bright emission centered on the NGC 4761 galaxy, extending up to, at least, $15'$ from the center (Fig.4.2). The emission is elongated a little toward the north east direction. The overall 0.5–2.3 keV spectrum was well fitted by a hot plasma model of temperature $kT \sim 1$ keV and metal abundance of $Z \sim 0.2Z_{\odot}$, with a mild temperature gradient as shown in Fig.4.3. The bolometric luminosity of the IGM component within a projected radius $r < 22'.4$ is $L_{\text{bol}} = 3.9 \times 10^{42} h_{75}^{-2}$ erg s^{-1} (Mulchaey and Zabludoff 1998).

The azimuthally averaged radial X-ray surface brightness profile shows a clear central peak compared with the canonical beta-model profile, requiring a narrower second

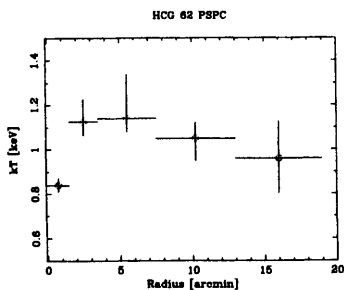


Figure 4.3: Temperature of the IGM obtained with Raymond-Smith model fits to the ring sorted PSPC spectra. Errors are in 1σ (Zabludoff and Mulchaey 1998).

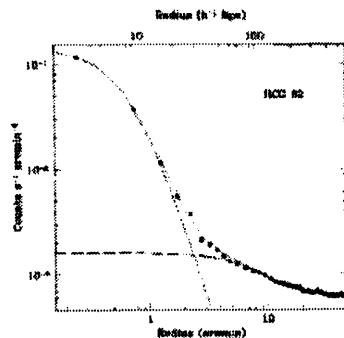


Figure 4.4: Radial count-rate profile of the 0.6–2.3 keV PSPC image, fitted with a double-beta model (Zabludoff and Mulchaey 1998).

beta-model component (Fig.4.4). The component larger in scale is called “extended” component and the smaller one “central” component. The best fit parameters of the double beta-model, however, differs significantly among the authors. This is possibly due to a little difference in the background modeling of the PSPC detector, which will affect the “extended” component parameters and then those of the “central” component through parameter coupling between the two model components.

Using the parameters by Ponman and Bertran (1993), the gas mass within a three dimensional radius of $R = 340h_{75}^{-1}$ kpc ($20'$) from the group center is calculated as $M_{\text{gas}} = 9.0 \times 10^{11} h_{75}^{-2.5} M_{\odot}$, and the total gravitating mass as $M_{\text{total}} = 1.7 \times 10^{13} h_{75}^{-1} M_{\odot}$. These values are thought to be typical of X-ray luminous groups. Using results of other authors change these values by a factor of up to ~ 3 .

In the $r < 15'$ region of the PSPC image (Fig.4.2), there are 5 point sources clearly visible. We mask out the regions within $r < 3'$ from these sources, when we analyze the spectra of the data in the following sections.

4.2 ASCA Observations and Images

We observed the HCG 62 group five times with ASCA, covering a $\sim 1^{\circ} \times 1^{\circ}$ region with the GIS. These consist of a pointing at the group center performed in the AO-1 phase (1994 January), and additional four surrounding pointings performed in the AO-6 phase (1998 January). These pointing positions are shown in Fig.4.5a. In all observations, the GIS was operated in PH-mode with nominal bit assignment, and the SIS was operated in 2 CCD clocking mode. The SIS data-format of the first observation was faint-mode throughout the observation, while that of the latter four observations was faint-mode for high bit-rate data and bright-mode for medium bit-rate data.

All the data are processed through the standard analysis procedure as described in Chapter 3. For the GIS, we selected the time interval when the source elevation angle from the earth rim is greater than 5° , and the data satisfy the “flare cut” condition listed in Table 3.3. For the SIS, we used the “rev.2 standard” screening criteria listed in Table 3.5.

Each observation yielded a good exposure of 21 \sim 29 ksec for the GIS, and the obtained net exposure sums up to be 121 ksec. For the GIS, we use the data from all observations in both image and spectral analysis. The SIS exposure was 17 ksec for the first observation, and 21 \sim 23 ksec for the latter four. For analysis of the SIS spectra, we however use only the data from the first observation, because the strong performance degradation in

late years made it difficult to use the last four SIS data in combination with the first observation (see § 3.4.4 for detail).

Table 4.2: Log of ASCA Observations of the HCG 62 group.

| Obs. ID | date | sequence ID ⁽¹⁾ | GIS-2 center position (Ra, Dec, Roll ⁽²⁾) _(deg) | GIS exposure (sec) | SIS mode ⁽³⁾ |
|---------|-------------|----------------------------|--|--------------------|-------------------------|
| 1 | 14 Jan 1994 | 81012000 | (193.34, -9.10, 269.24) | 29293 | 2 CCD F/F |
| 2 | 13 Jan 1998 | 86008000 | (193.26, -9.06, 238.73) | 21467 | 2 CCD F/B |
| 3 | 14 Jan 1998 | 86008010 | (193.49, -9.00, 238.73) | 23290 | 2 CCD F/B |
| 4 | 15 Jan 1998 | 86008020 | (193.54, -9.23, 238.73) | 25466 | 2 CCD F/B |
| 5 | 16 Jan 1998 | 86008030 | (193.30, -9.29, 238.73) | 21962 | 2 CCD F/B |

(1) PI of the first observation is Yasuhiro Sakima, and that of the latter four observations is Yasushi Fukazawa.

(2) Roll of the satellite is defined as the angle from the north to the satellite Y-axis, measured clockwise; 270° means that the satellite Y-axis is pointing to the east.

(3) SIS clocking-mode and data-mode. See text for detail.

In Fig. 4.5b, we show the obtained 0.5–10 keV GIS image of the HCG 62 group, overlaid on an optical image. We have subtracted the background in a standard manner (§ 3.3) and combined the data from the two GIS sensors. Then we combined images from the five observing positions and corrected the result for exposure difference among them. We also corrected the satellite attitude for thermal distortion of the star sensor axis, using a software 'offsetcoord'.

Figure 4.5 clearly reveals diffuse X-ray emission, which extends up to $\sim 15'$ from the group center, in agreement with the PSPC image (Fig. 4.2). X-ray centroid of the GIS image is within $\sim 0'.2$ from NGC 4761, which is well within the astrometric accuracy of ASCA ($\sim 0'.5$).

In Figs. 4.6 and 4.7, we show two-band X-ray images, obtained with the GIS and the SIS, respectively. The largely extended emission is dominant in the soft-band image, below 2.0 keV, because of the low temperature of the IGM. The extended emission is also observable in the hard-band image. In these GIS/SIS images, the five ROSAT point sources (Fig. 4.2) are generally recognized. We must hence remove them in the following data analysis. Precisely speaking, some sources clearly visible in the PSPC image are not so clear in, for example, the GIS hard band image. This is naturally explained by the difference of the spectra among these sources and the band pass among three detectors (PSPC, GIS and SIS).

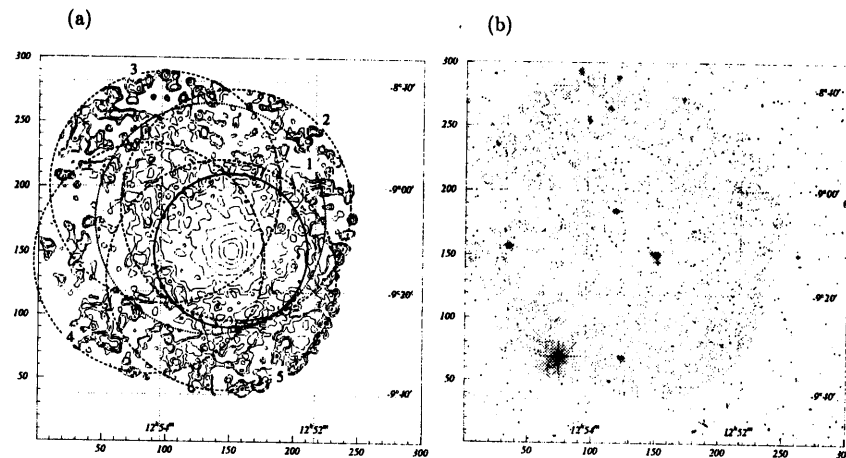


Figure 4.5: (a) The GIS 0.5–10.0 keV X-ray mosaic image synthesized from five pointings, plotted with their observing positions (indicated by numbers). North is top, and east is to the left. Contours are logarithmically spaced, by factors of 1.7 starting from 1.9×10^{-5} cts s^{-1} arcmin $^{-2}$. The image is presented after background subtraction, correction for exposure (but not for the vignetting), and smoothing with a Gaussian function with $\sigma = 0'.5$. Solid circle represents the region 15' from the group center. (b) The same GIS contour image, overlaid on an optical gray scale image from Digitized Sky Survey.

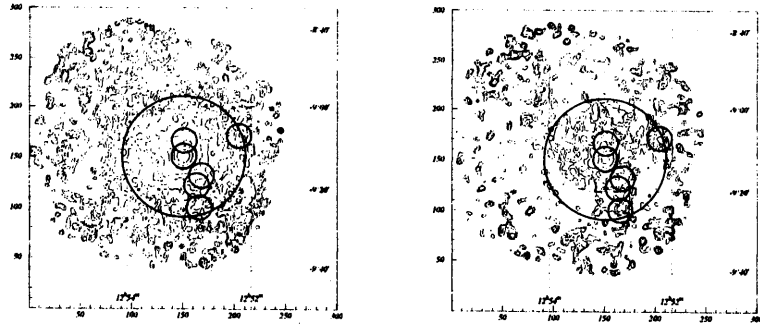


Figure 4.6: The same as Fig.4.5 but in 0.5-2.0 keV (left) and 2.0-10 keV (right). The contours are logarithmically spaced, by factors of 1.7 starting from 1.6 and 1.3×10^{-5} $\text{cts s}^{-1} \text{arcmin}^{-2}$ for the left and right panels, respectively. Small and large circles centered on the X-ray peak represent $3'$ and $15'$ from NGC 4761, respectively. Other circles indicate regions eliminated to exclude the five point sources detected with the ROSAT PSPC.

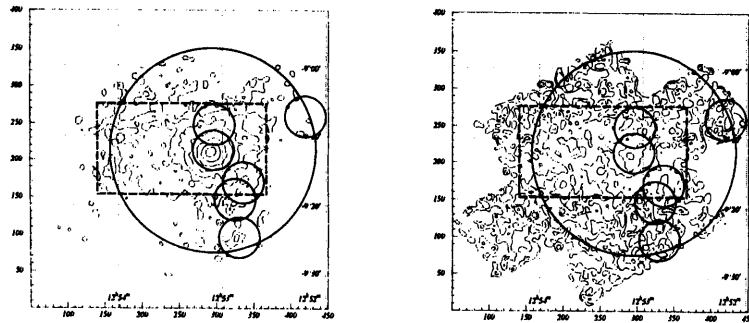


Figure 4.7: The SIS image in 0.5-2.0 keV (left) and 2.0-7.5 keV (right) obtained by combining the five pointings. Both images are smoothed with a $\sigma = 0'.3$ Gaussian kernel. Background is inclusive and exposure is corrected. The contours are logarithmically spaced, by factors of 1.7 starting from 8.1 and 6.5×10^{-5} $\text{cts s}^{-1} \text{arcmin}^{-2}$ for the left and right panels, respectively. Circles are the same as those of Fig.4.6. Boxes show the region observed with the first pointing, part of which is used for the spectral study.

4.3 Spectral Analysis

4.3.1 Derivation of the spectra

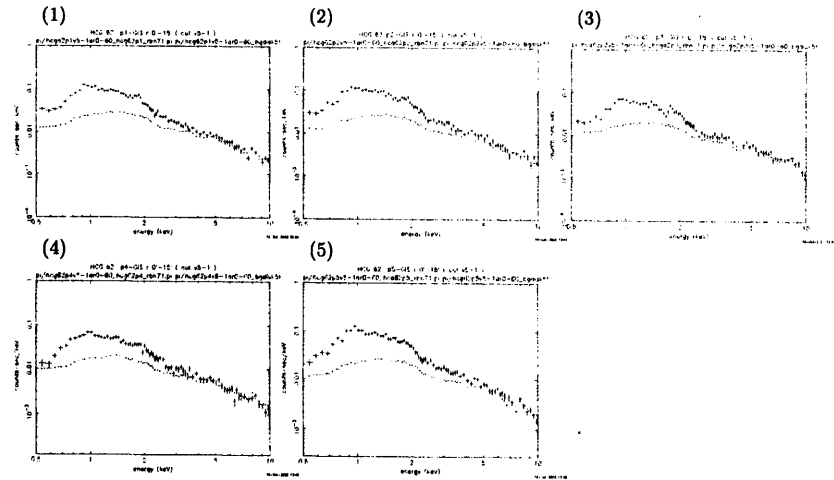


Figure 4.8: The raw GIS spectra of the HCG 62 group obtained in the five observations. The on-source spectra and the estimated background are shown. The numbers plotted indicates the observation ID.

We extracted the spectra from a circular region of radius $15'$ centered on the X-ray centroid, where the regions $3'$ around the five point sources were masked out (see Figs. 4.5 and 4.7). For the GIS, we first collected the spectra of each observation separately. Note that the spectral accumulation region is only partially covered by most of the latter four pointings. We next added spectra from the two GIS detectors (GIS2 and GIS 3) into a single GIS spectrum, after appropriate corrections for their gain differences. In Fig.4.8, we show the obtained spectra together with the background (CXB+NXB; § 3.3.5 and 3.3.4), which were obtained from blank-sky observations and corrected for the NXB variation. The background estimation error for each observation ranges from 3.7 to 4.7%, and we added these values as a systematic error in the background spectra in Fig.4.8 (see § 4.5.2).

Then, we added the five spectra to obtain an average GIS spectrum, which is shown in Fig.4.9a. We divided the spectrum of each observation with the averaged spectrum,

after correcting it for the difference of the XRT effective area. The ratio spectra become almost flat, and fittings with a constant value were acceptable for all observations. This indicates that the five spectra have generally similar shapes. The derived relative spectral normalization ranges from 0.8 to 1.1; this is not surprising because the region $r < 15'$ is not completely covered by some observations. In the following analysis, we therefore mainly use the averaged spectrum which has the best photon statistics. The background estimation error involved in this averaged spectrum reduced to 1.9%, which is considered as a systematic error in the spectral evaluation. The background subtraction procedure is evaluated in further detail later in § 4.5.2.

For the SIS, we added data from the two SIS detectors (SIS0 and SIS1) of the first observation into a single SIS spectrum. Again, regions around the five point sources were masked out. The background spectrum was obtained from blank-sky observations. We show this spectrum in Fig.4.9b. As noted before, we did not analyze the SIS spectra of the other four pointings.

In the GIS spectra (Fig 4.9a), the majority of signal photons are in low energies (< 2 keV), but the signal is detectable up to ~ 8 keV. Above ~ 8 keV, the on-source spectrum agrees very well with the background spectrum, indicating that our background estimation is accurate. In the SIS spectra (Fig 4.9b), the signal photons are detected up to ~ 4 keV. Clear peaks at 6.4 keV and 7.5 keV, both observable in the on-source and background spectra, are instrumental Fe-K and Ni-K lines, respectively.

Both the GIS and SIS spectra show bumpy structures around 1 keV, 1.4 keV and 1.8 keV. They are line emissions from Fe-L shell, Mg-K and Si-K shell, respectively, which are characteristic of emission from optically thin hot plasma with $kT \sim 1$ keV.

4.3.2 Single component fits

By using the background and on-source spectra in Fig.4.9, we have obtained background-subtracted GIS and SIS spectra, as shown together in Fig.4.10. We jointly fitted them with an optically thin thermal plasma emission model, which is based on the emissivity calculations of Mewe and Kaastra (Mewe et al. 1985, 1986; Kaastra et al. 1992), with Fe-L calculations by Liedahl et al. (1995). Hereafter, we call this model MEKAL model. We also tried a model by Raymond and Smith (hereafter Raymond-Smith model; Raymond and Smith 1977). The mutual abundance ratios of the metals were constrained to be the same as the solar ratios (see § 2.2.2), while the overall metal normalization was set free. We fixed the redshift to 0.0146, and the hydrogen column density to the Galactic value

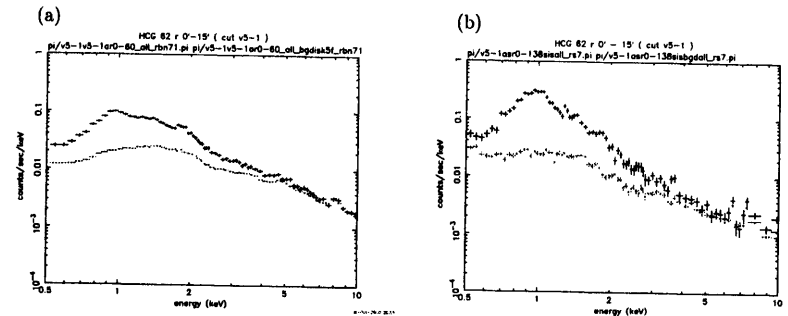


Figure 4.9: Raw spectra of the HCG 62 group. (a) The raw GIS spectrum extracted from a circular region of radius $15'$ centered on the X-ray centroid, co-adding the five spectra shown in Fig.4.8. Shown for comparison is the background spectrum. (b) The raw SIS spectrum extracted from the same circular region, compared with that of background derived from blank-sky observations. Note that the SIS does not cover the whole region within $15'$.

($N_H = 3.01 \times 10^{20} \text{ cm}^{-2}$), derived from HI radio emission map by Dickey and Lockmann (1990). We used XSPEC v10.0 (Arnaud 1996) package throughout the spectrum fitting. To compensate the difference in the integration region between the GIS and SIS, we allowed the model normalization to change separately between the two types of detectors.

Compared to the GIS, the SIS has a better energy resolution together with a larger effective area around ~ 1 keV. Because the X-ray emission from hot plasma with $kT \sim 1$ keV is characterized by strong line emissions around ~ 1 keV, the SIS mainly determines the parameters of the IGM component. On the other hand, the GIS has a larger effective area above ~ 2 keV with a well calibrated and even lower detector background, which dominates the spectra in the hard band. Therefore, the GIS is sensitive to any excess hard X-ray emission above the IGM component, though it can also determine the IGM component to a modest extent. In the spectral fitting, we accordingly use the 0.9–9.0 keV energy band for the GIS and the 0.7–4.0 keV energy band for the SIS.

The results of the single component fits are summarized in Fig.4.10 and Table 4.3. When we fitted spectra jointly over the full energy band, we obtained a temperature of ~ 1 keV with either plasma model, in agreement with the ROSAT results. The fit, however, is very poor with reduced χ^2 of ~ 3 . The data clearly shows a strong hard X-ray excess above the model prediction. In contrast, when we fitted the spectra in the hard

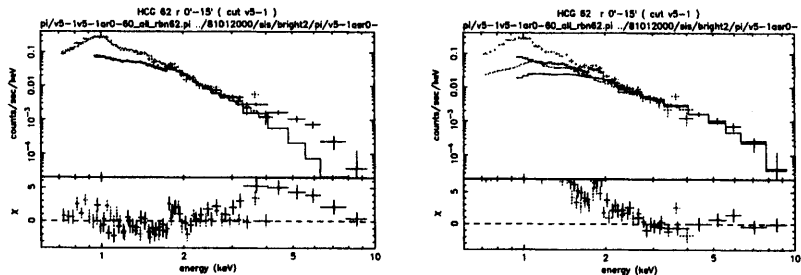


Figure 4.10: The background-subtracted GIS (black) and SIS (gray) spectra of HCG 62, accumulated within 15' from the group center. The histogram in the upper panels show the best fit hot gas model (MEKAL model), and the lower panels present the residual spectra. The joint GIS and SIS fit is performed over the full energy range (left), and in the range above 2.5 keV (right).

Table 4.3: Best fit parameters from the joint fit to the GIS and SIS spectra obtain from the circular region of $r < 15'$.

| MEKAL model fit | | | Raymond-Smith model fit | | |
|------------------------|------------------------|----------------|-------------------------|------------------------|----------------|
| kT (keV) | Abun. (Z_{\odot}) | $\chi^2/d.o.f$ | kT (keV) | Abun. (Z_{\odot}) | $\chi^2/d.o.f$ |
| $1.03^{+0.03}_{-0.02}$ | $0.13^{+0.02}_{-0.01}$ | 241.2/74 | $1.01^{+0.02}_{-0.02}$ | $0.18^{+0.02}_{-0.03}$ | 247.0/74 |

energy band above 2.5 keV with the same spectral model, we obtained $kT = 2.35^{+0.66}_{-0.42}$ keV. This is inconsistent with the temperature derived from the full-band fitting, and the structure around ~ 1 keV in the data remain unexplained (Fig.4.10 right panel).

In general, there is a relation between the galaxy velocity dispersion and the IGM temperature as $\beta_{\text{spec}} = \frac{\mu m_p \sigma_v^2}{kT_{\text{gas}}} \sim 1.0$ (kT - σ relation; equation 2.15). Using the fitted temperature and the measured velocity dispersion of the HCG 62 group (376^{+52}_{-46} km s $^{-1}$), the ratio becomes $\beta_{\text{spec}} = 0.86^{+0.27}_{-0.22}$ for the full-band fitting and $\beta_{\text{spec}} = 0.38^{+0.21}_{-0.15}$ for the hard-band fitting. The later value largely deviates from the general value of 1.0, suggesting strongly that the $kT \sim 1$ keV component is the “real” IGM of the group, and there is some additional hard X-ray emission from this sky region.

4.3.3 Two component fits

Now that the spectra of HCG 62 cannot be fitted with a single temperature plasma model, we attempt two-component fits. We first fitted the spectra with a sum of a single temperature MEKAL and a power law model (hereafter, MEKAL+PL model). Because our aim here is to quantify the amount of the “excess hard X-ray emission”, we fixed the photon index Γ to 2.0, which is a representative value for various non-thermal emission from energetic particles. Then, as shown in Table 4.4 and Fig.4.11a, the fit has been dramatically improved and become acceptable, at 99% confidence level. The hard component dominates the spectra above ~ 4 keV, and the 2-10 keV flux of the hard component is $\sim 20\%$ of the 0.5-10 keV flux of the IGM component.

We also examined the fit with Γ set free. As shown in Table 4.4 and Fig.4.11b, the index becomes $\Gamma = 2.63^{+0.09}_{-0.38}$, and the power law component dominates the spectra, above 1.5 keV as well as bellow 0.8 keV. The flux of the hard component increased by 15% compared to the case of $\Gamma = 2.0$. Although the χ^2 value decreases by ~ 3 , we may not use this result since it implies too large a contribution from the hard component, and hence unrealistic.

We also tried a second MEKAL component with a higher temperature (hereafter, 2-MEKAL model), in place of the power law component. In the fitting, the metal abundances for the two MEKAL components were constrained to be the same, because we cannot constrain them separately. As shown in Table 4.4 and Fig.4.11c, this gave a hot component temperature of $kT_{\text{hot}} > 4.4$ keV. The goodness of the fit is very similar to that from the MEKAL+PL model fit, and the fluxes of the hard component are also similar. With this high temperature, the hot component is very similar in shape to the power law

component with $\Gamma = 2.0$.

Table 4.4: Results of the joint fit to the GIS and SIS spectra with two component models.

| model ID | kT (keV) | Abun. (Z_{\odot}) | Γ or kT_{hot} | Soft Flux ⁽¹⁾ ($\text{erg s}^{-1} \text{cm}^{-2}$) | Hard Flux ⁽²⁾ ($\text{erg s}^{-1} \text{cm}^{-2}$) | $\chi^2/d.o.f$ |
|----------|------------------------|--------------------------|----------------------------------|--|--|----------------|
| MEKAL+PL | $0.98^{+0.04}_{-0.04}$ | $0.59^{+2.5}_{-0.4}$ | $2.63^{+0.09}_{-0.38}$ | 3.16×10^{-12} | 1.34×10^{-12} | 98.5/72 |
| | $0.95^{+0.05}_{-0.04}$ | $0.21^{+0.04}_{-0.04}$ | 2.0 (fixed) | 4.84×10^{-12} | $1.16^{+0.16}_{-0.17} \times 10^{-12}$ | 101.6/73 |
| 2-MEKAL | $0.96^{+0.03}_{-0.04}$ | $0.17^{+0.03}_{-0.03}$ | $11.8^{+90}_{-7.4}$ | 5.37×10^{-12} | $1.10^{+0.17}_{-0.17} \times 10^{-12}$ | 102.3/72 |

(1) The 0.5–10 keV flux of the (cooler) MEKAL component.

(2) The 2–10 keV flux of the power-law or hotter MEKAL component.

4.3.4 Improved modeling of the IGM emission

Although the spectral fit has been improved considerably by introducing the two component models, the χ^2 values of both MEKAL+PL model and 2-MEKAL model are still unacceptable at 90% confidence level. This is mainly due to two peaks visible in the residual spectra, around 1.1 keV and 1.8 keV. The former is in the Fe-L line region, and the latter is in the Si-K line region, suggesting that the modeling of these lines needs improvements. This may occur when the abundance ratio between the Si and Fe is different from the solar ratio and/or the IGM involves multiple temperature as suggested by the PSPC results (Fig.4.3).

We set the abundance ratios free, by introducing a variable-abundance MEKAL model (vMEKAL model), where the abundance of each heavy element can be changed separately. For simplicity, we group major heavy elements into two groups in view of their origin, following Matsushita (1996); O, Ne, Na, Mg, Al, Si, S, Ar and Ca; and Fe and Ni. Majority of the first group is the “ α -elements”, which are mainly produced through α -process in type-II supernova (e.g. Nomoto et al. 1984). The second group is mainly synthesized in type-Ia supernova. Abundances of the other elements (He, C and N) are fixed at the solar value. Hereafter, we denote the abundance of the first group Z_{α} , and that of the second group Z_{Fe} . We jointly fitted the GIS and SIS spectra with a sum of a vMEKAL and a power law model (vMEKAL+PL model). As shown in Fig.4.12a and Table 4.5, the χ^2 value decreased and the obtained two abundances are reasonable in comparison with previous ASCA works (e.g. Matsuhita 1997), but the fit is not yet acceptable: the residual around 1.8 keV has decreased but that around 1.1 keV has not.

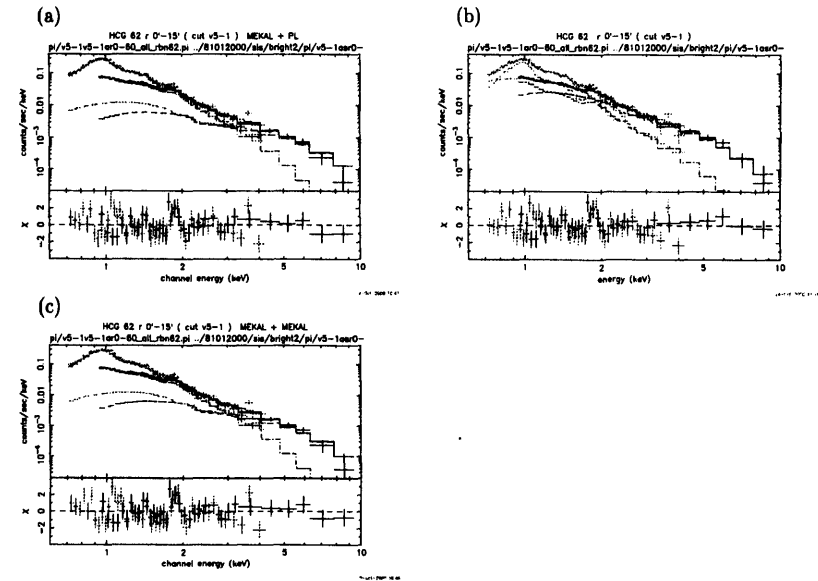


Figure 4.11: Two component joint fits to the GIS and SIS spectra as in Fig.4.10. (a) A sum of a MEKAL and a power law model with photon index fixed at $\Gamma = 2.0$. (b) The same as (a), but the photon index is set free. (c) A sum of two MEKAL components.

We accordingly fixed again the abundance ratio back to the solar ratios, and tried a model with two MEKAL components and a power law (2-MEKAL+PL model), to represent non-isothermality of the IGM. The metal abundances of the two MEKAL component are constrained to be the same. As shown in Fig.4.12b and Table 4.5, the fit has further been improved, but still unacceptable. In this case, the residual feature around 1.1 keV has decreased but that around 1.8 keV remained. Thus, we need to consider both the non-isothermal effect and non-solar abundance ratios of the IGM.

Then we fitted the spectra with a sum of two vMEKAL components and a power law component (2-vMEKAL+PL model). Both Z_{α} and Z_{Fe} are constrained to be the same between the two vMEKAL components. The results are shown in Fig.4.12c and Table 4.5. The fit has finally attained an acceptable level at 90%. The derived temperatures of 0.73 keV and 1.14 keV are consistent with the PSPC result in general. The 0.5–10 keV flux of the IGM components is $5.05_{-0.32}^{+0.36} \times 10^{-12} \text{ erg s}^{-1} \text{ cm}^{-2}$, and the 2–10 keV flux of the hard component is $1.08_{-0.22}^{+0.18} \times 10^{-12} \text{ erg s}^{-1} \text{ cm}^{-2}$, the latter being similar to that derived from the MEKAL+PL model fit in the last subsection.

We also tried a fit where we set Γ free, and obtained $\Gamma = 1.55_{-0.89}^{+1.21}$ with $\chi^2 = 81.5$ for 69 dof. If we put another (i.e., a third) vMEKAL component in place of the power law component, the resulting temperature is $kT = 32.0_{-28.3}^{+58.0} \text{ keV}$ with $\chi^2 = 81.6$ for 69 dof. Again these results are similar to the MEKAL+PL model fit in the last subsection. In summary, we regard the 2-vMEKAL+PL model as our best favorite spectral model for the X-ray emission from HCG 62.

Table 4.5: Results of the joint fit to the GIS and SIS spectra with multi component models involving a vMEKAL component.

| model ID | kT_1 (keV) | kT_2 (keV) | Z_{α} (Z_{\odot}) | Z_{Fe} (Z_{\odot}) | Γ | $\chi^2/d.o.f$ |
|-------------|------------------------|------------------------|---------------------------------|------------------------------------|-------------|----------------|
| vMEKAL+PL | $0.94_{-0.07}^{+0.04}$ | | $0.33_{-0.10}^{+0.13}$ | $0.23_{-0.04}^{+0.06}$ | 2.0 (fixed) | 97.3/72 |
| 2-MEKAL+PL | $0.71_{-0.18}^{+0.14}$ | $1.09_{-0.33}^{+0.38}$ | | $0.26_{-0.05}^{+0.10}$ | 2.0 (fixed) | 91.1/71 |
| 2-vMEKAL+PL | $0.73_{-0.23}^{+0.10}$ | $1.14_{-0.64}^{+0.18}$ | $0.53_{-0.18}^{+0.27}$ | $0.34_{-0.08}^{+0.12}$ | 2.0 (fixed) | 82.3/70 |

4.3.5 Possible origins of the hard excess emission

As shown in the preceding subsections, the spectra of the $0' < r < 15'$ region of HCG 62 have been found to exhibit a strong hard excess component. There are several possible

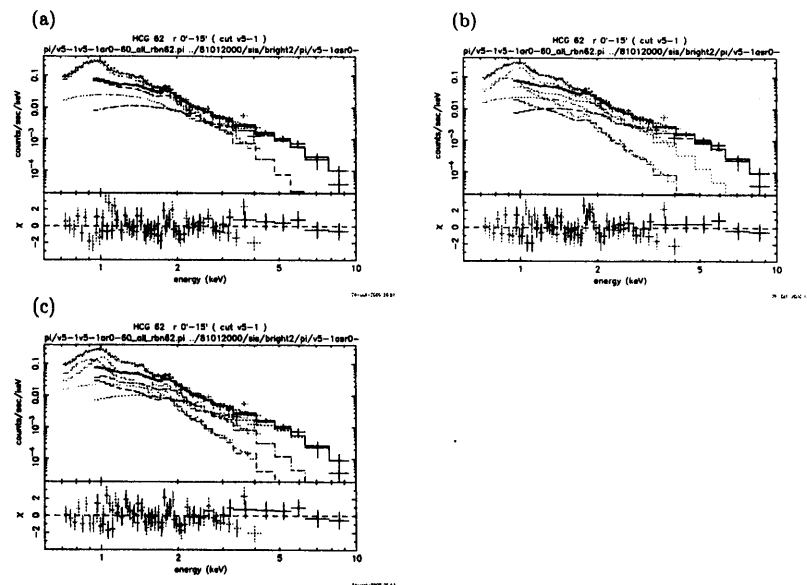


Figure 4.12: Joint fits to the same GIS and SIS spectra as in Fig.4.10 with a multi component models. In all cases, the photon index of the power law component is fixed at $\Gamma = 2.0$. (a) A sum of a vMEKAL and a power law. (b) A sum of two MEKAL components and a power law. (c) A sum of two vMEKAL components and a power law.

Table 4.6: Possible origins of the hard excess emission.

| type | item | | |
|-----------------------|--------------|--|----------------|
| Artifacts | background | NXB | § 4.5.2 |
| | estimation | CXB ⁽¹⁾ | § 4.5.5, 4.5.6 |
| | XRT response | PSF and effective area | § 4.5.3 |
| | IGM modeling | | § 4.5.4 |
| Celestial | point-like | central AGN | § 4.4.1 |
| | extended | LMXBs in the member galaxies | § 4.6 |
| | | AGNs in the member galaxies | § 4.4.2 |
| | | AGNs in the background sky (\sim CXB) | § 4.5.5, 4.5.6 |
| | | diffuse (thermal) | § 4.6 |
| diffuse (non-thermal) | § 4.6 | | |

(1) Also treated as a celestial origin.

candidates for the origin of this component, celestial and artificial, as listed in Table 4.6.

First of all, we must examine whether the hard X-ray emission is artificial or not. Apart from its statistical significance, we have to consider all systematic origins. We must critically examine the background estimation, which is crucial to this study. There are two components, the NXB (§ 3.3.4) and the CXB (§ 3.3.5). The former is completely instrumental, while the CXB, considered to be a sum of discrete sources among the sky, is partially celestial. Other possibilities include the effect of the complicated point spread function (PSF) of the XRT+GIS and wrong modeling of the IGM emission.

If the hard X-ray emission truly has a celestial origin, it may be a discrete source, a sum of many discrete sources, or a diffuse source. Candidates for the discrete sources are, AGN(s) and LMXBs of the member galaxies of the group, and also AGN(s) in the background sky. As a diffuse source, it may be either of a thermal origin, with high temperature such as ~ 10 keV, or of a non-thermal origin, such as the relativistic electrons distributed in the vicinity of the group.

In the following sections, we examine all these possibilities one by one. No matter whether the origin is instrumental or celestial, the spatial distribution of the detected hard excess gives us a strong clue to the nature of the hard excess. In the next section, we therefore start with analyzing the spatial extent of the emission.

4.4 Spatial Distribution of the Hard X-ray Emission

4.4.1 Radial dependence of the spectra

To see the spatial distribution of the excess hard X-ray emission, we divided the spectral integration region into three annular regions; $r < 3'$, $3' < r < 7'.5$ and $7'.5 < r < 15'$, with r denoting the projected radius from the X-ray centroid. We also examined the added spectra of the latter two regions ($3' < r < 15'$). The obtained spectra are shown in Fig.4.13, and the fit results are listed in Tables 4.7 and 4.8. All of them show similar shape to the spectra of the $0' < r < 15'$ region (see Fig.4.10): majority of signal photons are in low energies (< 2 keV), while the signal is detectable up to ~ 8 keV with the GIS. When we fit them with a single temperature vMEKAL model, they show clear hard tails which make the fits unacceptable, with reduced χ^2 ranging from 1.5 to 2.2. By adding a power law component with $\Gamma = 2.0$ (vMEKAL+PL model), the fits became acceptable except that of the central region, which in turn became acceptable by adding another vMEKAL component (2-vMEKAL+PL model). This is reasonable, because the IGM temperature gradient is strongest within the central $1'.5$ (Fig.4.3).

Thus, the excess hard X-ray emission is visible in all the four spectra. Furthermore, the hard component appears to become progressively prominent, relative to the IGM component, toward the outer regions. Because $\sim 80\%$ of the photons from a point source falls within $3'$ of the image centroid, the hard component may not be attributed to any point-like source located around the group center. Thus, we have ruled out one particular candidate in Table 4.6 (i.e., "central AGN").

Table 4.7: Best fit parameters to the radially sorted GIS and SIS spectra, fitted with a sum of a single temperature vMEKAL component and a power law component with $\Gamma = 2.0$ (vMEKAL+PL model).

| data ID | kT (keV) | Z_α (Z_\odot) | Z_{Fe} (Z_\odot) | Flux _(0.5-10 keV) ^{MEKAL} (erg/s/cm ²) | Flux _(2-10 keV) ^{PL} (erg/s/cm ²) | $\chi^2/d.o.f$ |
|------------------|------------------------|-----------------------------|----------------------------------|---|--|----------------|
| $0' < r < 3'$ | $0.88^{+0.09}_{-0.03}$ | $0.63^{+0.41}_{-0.25}$ | $0.34^{+0.16}_{-0.08}$ | $1.38^{+0.06}_{-0.04} \times 10^{-12}$ | $2.56^{+0.29}_{-0.49} \times 10^{-13}$ | 88.3/72 |
| $3' < r < 7'.5$ | $0.99^{+0.06}_{-0.07}$ | $0.39^{+0.27}_{-0.17}$ | $0.21^{+0.10}_{-0.06}$ | $1.40^{+0.08}_{-0.08} \times 10^{-12}$ | $2.99^{+0.79}_{-0.80} \times 10^{-13}$ | 71.9/72 |
| $7'.5 < r < 15'$ | $0.85^{+0.12}_{-0.08}$ | $0.11^{+0.21}_{-0.11}$ | $0.15^{+0.08}_{-0.05}$ | $2.12^{+0.14}_{-0.16} \times 10^{-12}$ | $6.68^{+1.53}_{-1.55} \times 10^{-13}$ | 59.3/60 |
| $3' < r < 15'$ | $0.96^{+0.06}_{-0.08}$ | $0.21^{+0.15}_{-0.11}$ | $0.19^{+0.06}_{-0.05}$ | $3.43^{+0.23}_{-0.13} \times 10^{-12}$ | $9.17^{+1.85}_{-1.90} \times 10^{-13}$ | 81.9/72 |

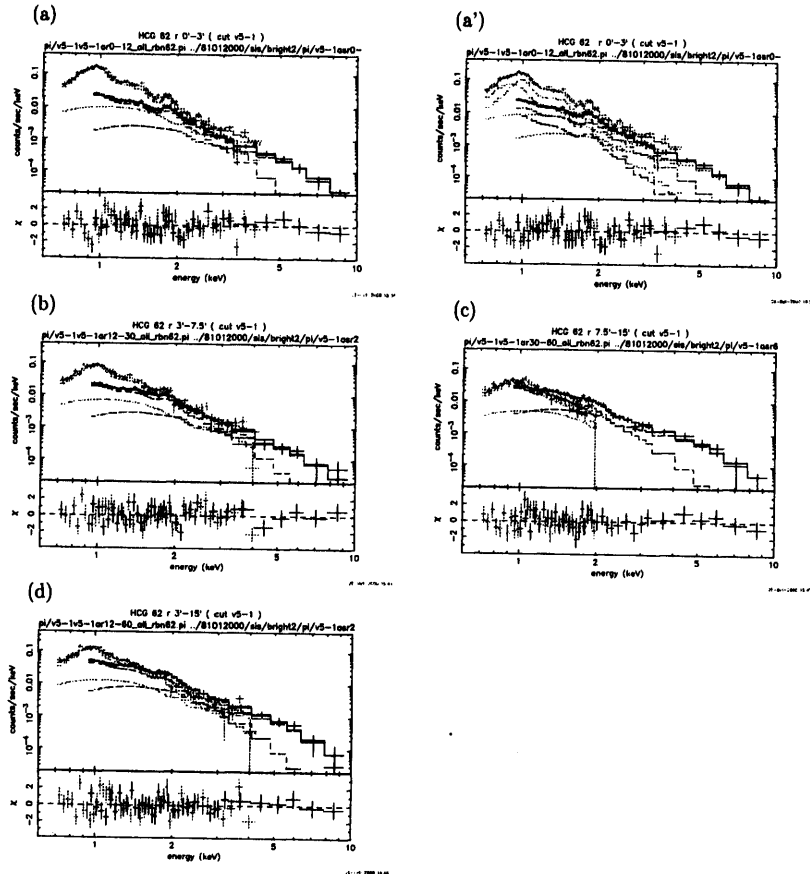


Figure 4.13: Ring sorted spectra of HCG 62, fitted with vMEKAL+PL model, shown for (a) $0' < r < 3'$, (b) $3' < r < 7'.5$, (c) $7'.5 < r < 15'$ and (d) $3' < r < 15'$. (a') is the same as panel (a), but fitted with 2-vMEKAL+PL model. Γ is fixed at 2.0 in all cases.

Table 4.8: Best fit parameters of the $0' < r < 3'$ GIS and SIS spectra, fitted with a sum of double vMEKAL components and a power law component with $\Gamma = 2.0$ (2-vMEKAL+PL model).

| kT_1 (keV) | kT_2 (keV) | Z_α (Z_\odot) | Z_{Fe} (Z_\odot) | Flux _(0.5-10 keV) ^{MEKAL} (erg/s/cm ²) | Flux _(2-10 keV) ^{PL} (erg/s/cm ²) | $\chi^2/d.o.f$ |
|------------------------|------------------------|-----------------------------|---------------------------|---|--|----------------|
| $0.69^{+0.12}_{-0.20}$ | $1.12^{+0.22}_{-0.14}$ | $1.17^{+1.09}_{-0.52}$ | $0.66^{+0.35}_{-0.25}$ | $1.36^{+0.04}_{-0.03} \times 10^{-12}$ | $2.19^{+0.44}_{-0.50} \times 10^{-13}$ | 74.0/70 |

4.4.2 Radial surface brightness profiles

In order to complement the analyses of the last subsection, we have directly analyzed the spatial extent of the hard component utilizing the GIS images. From the spectral fittings shown in Fig.4.13, the hard component is dominant above ~ 4 keV. We therefore made an X-ray image in the highest 4.0–8.0 keV range. The result is shown in Fig.4.14a, where the positions of the galaxies around HCG 62 are also plotted. We also plot the 0.5–4.0 keV band image in Fig.4.14b, which represents the distribution of the hot gas component. The X-ray image of the hard component is rather clumpy and occasionally becomes even negative. This is due to the poor photon statistics (~ 700 cts in the encircled region; see § 4.5.1) and the clumpy nature of the CXB. Here, the CXB fluctuation level is estimated to be $\sim 0.5 \times 10^{-5}$ cts s^{-1} arcmin $^{-2}$ at 1σ level, which can naturally explain the image clumpiness (see also Appendix B.1). Two out of the five ROSAT point sources are detectable in both images, especially in the hard band. However, there is no correlation between the galaxies and hard X-ray distribution, implying that the galaxies contribute little in the 4.0–8.0 keV band image (see Appendix B.2). We have hence excluded another candidate origin, i.e., “AGNs in the member galaxies” in Table 4.6. We also searched the 4.0–8.0 keV band image for any azimuthal anisotropy of the hard component, and found no statistically significant evidence for it, when we take the CXB fluctuation into account (see Appendix B.3).

We then made an azimuthally-averaged radial profile of both images, excluding the region around the five point sources as before. The results, given in Fig.4.14c, show that the 4.0–8.0 keV emission is detectable up to $\sim 15'$, and is nearly as extended as the soft X-ray emission, which is significantly more extended than the instrumental PSF. Since the 4.0–8.0 keV emission is dominated by the hard component, the hard component itself is inferred to be significantly extended, at least to the level of the IGM emission.

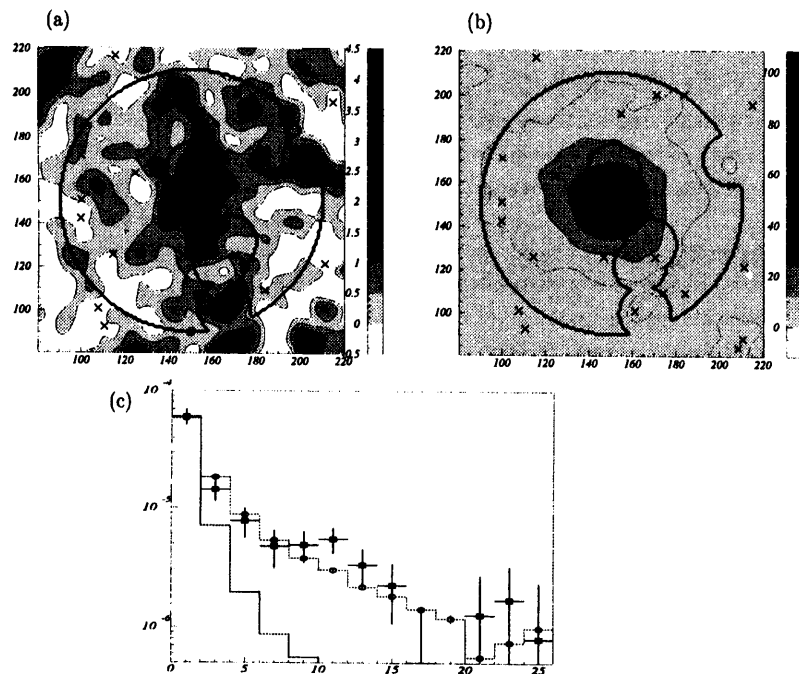


Figure 4.14: (a) The 4.0-8.0 keV GIS gray scale image for the central $35' \times 35'$ of HCG 62, corrected for the exposure after subtracting the background. The image was smoothed with a $\sigma = 1'$ Gaussian function. The contour is linearly spaced with separations of $0.5 \times 10^{-5} \text{ cts s}^{-1} \text{ arcmin}^{-2}$, which roughly corresponds to the 1σ level of the CXB fluctuation. The thick line shows the extraction region of the spectra. Crosses represents the position of the galaxies (Zabludoff and Mulchaey 1998). (b) Similar to panel (a), but for the 0.5-4.0 keV band. The contour is scaled by the central brightness to that of panel (a), linearly spaced with separations of $1.2 \times 10^{-4} \text{ cts s}^{-1} \text{ arcmin}^{-2}$. A supplemental contour of $0.6 \times 10^{-4} \text{ cts s}^{-1} \text{ arcmin}^{-2}$ is also plotted in dotted lines. (c) Radial profiles of the X-ray emission, in 4.0-8.0 keV (filled boxes) and 0.5-4.0 keV (open circles with histograms). Thick solid histograms indicate the XRT+GIS PSF in the 4.0-8.0 keV band. X-axis is shown in arcmin, while Y-axis is in $\text{cts s}^{-1} \text{ arcmin}^{-2}$. The later two profiles are rescaled to match the former at the center.

From these spatial analyses, we confirm that the excess hard X-ray emission is widely distributed in the vicinity of the group, rather than localized to particular regions, such as the group center or the member galaxies. However, the emission is far less extended than could be explained by wrong background subtraction, since the NXB and CXB have very flat distributions across the field of view; a more detailed examination is carried out in § 4.5.

4.5 Significance of the Hard X-ray Emission

The analyses in § 4.3 and 4.4 have revealed a strong evidence of an extended hard X-ray emission from HCG 62. However, we have not yet taken into account all the systematic errors and artifacts pointed out in § 4.3.5. In this section, we examine these effects in detail.

4.5.1 Photon counts of the hard X-ray emission

Table 4.9: Photon counts in the 4.0-8.0 keV band detected in each pointing within the $0' < r < 15'$ region of HCG 62. Errors are 1σ .

| Obs. ID | Data counts (N_{arc}) | BGD counts ⁽¹⁾ (N_{bgd}) | $(N_{\text{cxb}}/N_{\text{nxb}})^{(2)}$ | Signal counts ⁽¹⁾ (N_{sig}) |
|---------|-------------------------------------|---|---|--|
| Obs. 1 | 1416 ± 37.6 | $1237.3 \pm 7.7 \pm 48.2$ | 618.4/618.4 | $178.7 \pm 38.4 \pm 48.2$ |
| Obs. 2 | 1107 ± 33.3 | $865.4 \pm 5.4 \pm 31.6$ | 427.2/438.1 | $241.6 \pm 33.7 \pm 31.6$ |
| Obs. 3 | 799 ± 28.3 | $717.8 \pm 5.2 \pm 32.4$ | 298.9/418.9 | $81.2 \pm 28.8 \pm 32.4$ |
| Obs. 4 | 800 ± 28.3 | $750.7 \pm 5.6 \pm 34.8$ | 321.6/429.1 | $49.3 \pm 28.8 \pm 34.8$ |
| Obs. 5 | 1059 ± 32.5 | $879.1 \pm 5.6 \pm 35.6$ | 425.8/453.3 | $170.9 \pm 33.0 \pm 35.6$ |
| Sum | 5181 ± 72.0 | $4450.3 \pm 13.3 \pm 82.8$ | 2092.4/2357.8 | $730.7 \pm 73.2 \pm 82.8$ |

(1) The first errors represent the photon statistics and the seconds are the systematic errors in the NXB estimation (see § 4.5.2).

(2) Estimated CXB and NXB counts in the total background counts.

In Table 4.9, we have evaluated photon counts in the 4.0-8.0 keV band detected within the $0' < r < 15'$ region of HCG 62, where the five point sources were masked-out as before. By subtracting the background counts (N_{bgd}) from the on-source data counts (N_{arc}), we have obtained the signal counts of $N_{\text{sig}} = N_{\text{arc}} - N_{\text{bgd}} = 50 \sim 240$. The errors (a quadrature sum of those in N_{arc} and N_{bgd}) are typically ~ 45 counts, which is sometimes comparable to N_{sig} . The values of N_{sig} differ significantly among pointings, because the

Table 4.10: Sum of photon counts derived from Table 4.9, with the estimated IGM contribution.

| IGM model ⁽¹⁾ | Signal counts (N_{sig}) | IGM counts (N_{IGM}) | excess counts (N_{excess}) |
|--------------------------|--------------------------------|-----------------------------|-----------------------------------|
| best | $730.7 \pm 73.2 \pm 82.8$ | 111.5 | $619.2 \pm 73.2 \pm 82.8$ |
| high | | 97.9 | $632.8 \pm 73.2 \pm 82.8$ |
| low | | 192.3 | $538.4 \pm 73.2 \pm 82.8$ |

(1) Calculated from the 2-vMEKAL+PL model in § 4.3.4. The best fit model is labeled "best", and the 90% upper and lower-limit values, "high" and "low", respectively. It corresponds to a 1σ error of $(192.3 - 97.9)/1.65/2 = 28.6$ cts.

data accumulation regions, though identical in the sky plane, were different in the GIS field of view. Further examination follows in § 4.5.3.

Because the spectra of the five observations have already been shown to be consistent with one another (see § 4.3.1), we added all on-source data from the five observations to obtain the counts with the best statistics. The summed results are listed in Table 4.10, together with the estimated contribution from the IGM emission, N_{IGM} , using the spectral fitting performed in § 4.3.4. We quoted three alternatives for N_{IGM} , representing the best fit, 90% upper and lower-limit values. Thus, the excess signal counts in the 4.0–8.0 keV band have become

$$N_{excess} = 619.2 \pm 73.2 \pm 87.6 \quad (4.1)$$

where the first error is the statistical 1σ error, and the second one is systematic. This reconfirms the statistical significance of the hard X-ray emission, in a more straightforward manner than in previous sections.

4.5.2 Justification of the NXB estimation

In § 4.3, § 4.4, and § 4.5.1, we have subtracted the NXB from the on-source data employing the procedure described in § 3.3.6. Judging from the radial profile of the signal hard photons (Fig.4.14), we are already confident of the reliability of our NXB subtraction. Nevertheless, the issue has such a high technical importance, that we wish to describe below in some detail what we have actually done in estimating and subtracting the NXB from the five on-source datasets.

Our NXB estimation is based primarily on the "H02 sorting method" using the 5.2 Msec night earth data as an NXB template (§ 3.3.4). Because this method involves a systematic error of about 6% for a typical observation, we apply a finer adjustment to

the NXB level of each on-source dataset, by comparing it with the blank-sky data over a source-free outer region and in a sufficiently hard energy band, in which the NXB is dominant (§ 3.3.6). In the present case, we carried out this comparison using the 5.9–10.6 keV range, and over a region $> 15'$ from the detector center. Because all the pointing positions are offset from HCG 62, the on-source data accumulation circle ($< 15'$ from the HCG 62 centroid) partially falls on this "NXB adjustment region"; we masked out such overlapping regions in order for the IGM emission not to affect the background determination. We also excluded regions around bright discrete sources detected in the PSPC and the GIS images (see § 3.3.6).

For each of the five pointings, we obtained the the 5.9–10.6 keV spectrum in the NXB adjustment region defined in the above manner. The resulting event counts are given in the first column of Table 4.11. By comparing this value with those predicted from the background templates (2nd and 3rd column of the same Table), we have estimated the NXB correction factor f_{cor} , according to equation 3.3. The values of f_{cor} thus derived, given in the last column of Table 4.11, range from 0.848 to 1.026 with a typical uncertainty of ~ 0.075 . Because f_{cor} is the ratio between the real data and the "H02 method" prediction, they must obey the $\sim 6\%$ systematic scatter of the "H02 method" (§ 3.3.4). Actually, all the values of f_{cor} are acceptable in this respect, except for the second pointing. Although the probability of obtaining a value of $f_{cor} = 0.848$ is 5%, there is a 22% probability to obtain such a value from one out of five independent trials. We therefore conclude that the derived NXB correction factors behave well.

Table 4.11: Determination of the NXB correction factor f_{cor} .⁽¹⁾

| Obs. ID | Data _{out} | CXB _{out} ⁽²⁾ | NXB _{out} ^{H02 (3)} | f_{cor} |
|---------|---------------------|-----------------------------------|---------------------------------------|-------------------------|
| Obs. 1 | 564 | 102.0 | 454.5 | 1.026 ± 0.078 |
| Obs. 2 | 413 | 71.8 | 400.5 | 0.848 ± 0.072 |
| Obs. 3 | 503 | 78.8 | 428.4 | 0.992 ± 0.077 |
| Obs. 4 | 465 | 70.4 | 392.4 | 0.994 ± 0.081 |
| Obs. 5 | 443 | 76.3 | 398.2 | 0.913 ± 0.079 |
| sum | 2388 | 399.3 | 2074.0 | $0.959 \pm 0.035^{(4)}$ |

(1) The 5.9–10.6 keV spectra detected in the NXB adjustment regions of the five pointings are compared with the estimated CXB and NXB spectra in the same region through equation 3.3.

(2) Event counts of the blank sky observations after subtracting their own NXB contribution estimated with "H02 sorting method".

(3) NXB counts of the data estimated with "H02 sorting method".

(4) Average weighted by the photon counts.

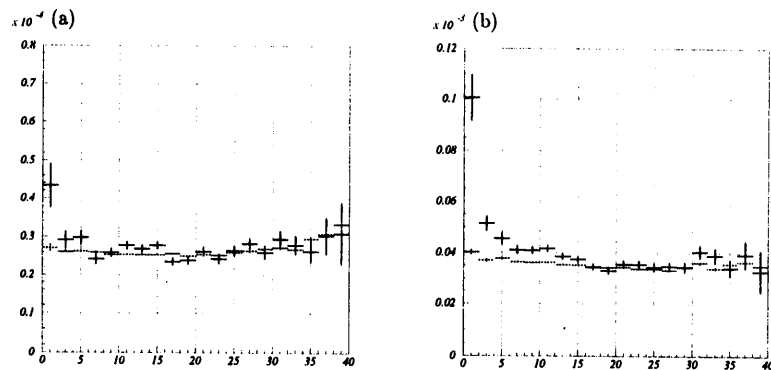


Figure 4.15: The GIS radial count-rate profile from the group center in the (a) 5.9–10.6 keV band and (b) 4.0–8.0 keV band. The on-source data are shown with black crosses and the background with gray crosses. X-axis is shown in arcmin, while Y-axis is in $\text{cts s}^{-1} \text{ arcmin}^{-2}$.

In order to visualize that f_{cor} has been determined correctly, in Fig. 4.15a we plot the 5.9–10.6 keV radial count-rate profiles of the on-source and background data, averaged over all five observations. Except at the very center of the group, which was excluded when we calculated f_{cor} , the data profile thus matches very well with that of the adjusted background. Examination of the profiles of individual pointings leads to the same conclusion (see Appendix A.2). Figure 4.15b performs the same comparison in the 4.0–8.0 keV band; their difference yields the hard-band radial profile in Fig. 4.14b. Again, the data and background agree well in the region $r > 15'$, even though we clearly see the excess signal inside $\sim 15'$. From these results, we conclude that the NXB estimation has been performed correctly.

Thus, we have determined the correction factor f_{cor} with a typical accuracy of $\sim 7.5\%$ for each pointing (Table 4.11). Because f_{cor} has been determined by the individual on-source dataset, the uncertainties associated with the five values are independent of one another. This allows us to average them to obtain $f_{\text{cor}}^{\text{ave}} = 0.959 \pm 0.035$. We regard this final error, 3.5%, as the systematic uncertainty associated with the NXB estimation. This value translates into 1.9% ($= 82.8$ counts) of the overall 4.0–8.0 keV background (CXB+NXB). We therefore quote 1.9% as the systematic uncertainty in the background subtraction. This value has already been included in Tables 4.9 and 4.10.

4.5.3 Effects of the XRT+GIS point spread function (PSF)

Another possible instrumental origin for the hard component is artifacts of the point spread function (PSF) of the XRT+GIS, which depends in a complex way on the detector position and the photon energy (§ 3.2.2). In particular, harder photons are more heavily scattered outside the PSF core into its outskirts, making the PSF wider for higher energies. As a result, peripheral regions of a soft X-ray source, such as a group of galaxies, artificially exhibit harder spectra than they are. Therefore, the observed excess hard X-rays could be the scattered IGM emission, artificially hardened by the above mechanism.

Of course, the spectral response files, used in fitting the ASCA spectra, properly takes these effects into account, as long as the source is pointlike. However, for the spectral analysis of an extended source, such as was performed in § 4.3 and 4.4, the spectral response is averaged over the detector surface weighted by the event count distribution. This process makes the response file less accurate, because what we ought to use in the averaging process is the true surface distribution of the source on the sky, rather than the observed distorted image on the detector plane. Consequently, an artificial “hard X-ray halo” could arise around a soft IGM emission.

To evaluate the suspected PSF artifacts, we use the instrument simulator “*SimASCA*” (e.g. Ikebe 1996). This is a Monte-Carlo simulation tool, and works completely in the “forward” manner, incorporating all the known instrumental responses. That is, we start from a numerically modeled X-ray source, and generate Monte-Carlo photons by specifying their spectral and spatial probability distributions on the sky coordinate. The Monte-Carlo photons are subjected to the XRT and GIS simulators, to become a set of simulated GIS events. We then analyze these events exactly in the same way as the real events, and produce fake spectra as well as fake X-ray images. By quantitatively comparing these fake results against the actual spectra and images, we can judge whether the assumed source model is appropriate or not.

We have actually used this simulator to examine whether the simulated IGM emission of HCG62 bears an artificial “hard X-ray halo” around it. Specifically, after Mulchaey and Zabludoff (1998), we modeled the IGM surface brightness distribution with a double-beta model, using $(R_{\text{core}}, \beta) = (0'.56, 0.79)$ for the “central” β component and $(10'.5, 0.67)$ for the “extended” β component (§ 4.1.2). The spectrum for the model IGM emission was approximated by a single component Raymond-Smith model with $kT = 1.2$ keV and $Z = 0.3Z_{\odot}$, which exhibits a little harder spectrum compared to the best-fit two-temperature vMEKAL model found in § 4.3.4.

Using the simulated IGM model, we have generated $\sim 3 \times 10^8$ fake GIS photons, separately for each of the five observations. In Fig.4.16, we compare the soft-band (0.5–4.0 keV) radial count-rate profiles of the fake and actual data sets. The good agreement between the two datasets confirms that the surface brightness distribution assumed for the model source is correct.

We finally accumulated the Monte-Carlo GIS events over the $0' < r < 15'$ regions of the five fake images, into a single fake GIS spectrum. Then, employing the same response files as used for the actual spectrum in § 4.3, we fitted the fake spectrum with the Raymond-Smith spectral model, of which the parameters except for normalization were fixed to the simulation input values. We have found that the 4.0–8.0 keV photon counts contained in the simulated data are larger by 8.4% than the prediction of the fitted spectral model. This excess is thought to represent the suspected PSF artifact. As the IGM contribution to the 4.0–8.0 keV counts is estimated to be $92 \sim 178$ counts (§ 4.5.1), the PSF effect will increase this number by $8 \sim 15$ counts. This is only $1 \sim 3\%$ of the actually observed excess counts, and negligible compared to the statistical error of 73.2 counts. We therefore conclude that the PSF artifacts contribute little to the observed excess hard X-ray emission.

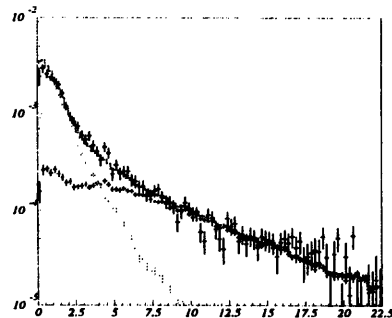


Figure 4.16: The 0.5–4.0 keV azimuthally averaged surface brightness profile of the first observation (plotted with crosses), compared with the simulation (histograms), in $\text{cts s}^{-1} \text{arcmin}^{-2}$. The “central” and the “extended” components of the simulated profile are shown together with their sum. X-axis is shown in arcmin.

Using the simulator, we also examined whether the hard signal counts, N_{sig} in Table 4.10, are consistent among the five observations. Here, the hard X-ray emission was

assumed to be spherically symmetric, and follow the radial distribution similar to the double-beta IGM profile employed above. As the spectral model, we used a thermal bremsstrahlung emission with $kT = 10.0$ keV. The simulated counts for the five pointings are shown in Fig.4.17, normalized to fit the actual signal counts, N_{sig} in Table 4.10. The simulation compares with the actual measurements with $\chi^2 = 4.65$ for 4 dof. Therefore, the hard signal counts, N_{sig} , detected in the five pointings are confirmed to be consistent to one another.

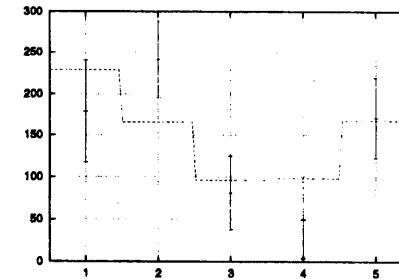


Figure 4.17: The 4.0–8.0 keV counts in the $0' < r < 15'$ region of the five observations (points with error bars) compared with the simulated counts (dashed line). X-axis is shown in channel.

4.5.4 Problems with the IGM modeling

Another systematic error is the theoretical uncertainty of the IGM spectral calculation. As we have estimated the contribution from the IGM emission, N_{IGM} (Table 4.10), by fitting these models to the actual spectra, there is a possibility that we under-estimate the value.

As reviewed in § 2.2.2, there are several plasma emission codes, such as the Raymond-Smith model and the MEKAL model. They differ mainly in the treatment of the Fe-L atomic physics (e.g. Masai 1997), and they produce considerably different emission spectra in the Fe-L line region (~ 0.8 – 1.6 keV) when the plasma temperature is $kT \sim 1$ keV.

As already described in § 4.3.2, the two plasma codes were not much different (both unacceptable) in terms of the single-temperature fit. Then, what happens if we replace the vMEKAL code in our improved fitting model (vMEKAL+PL model in Table 4.5) by a variable-abundance Raymond-Smith (vRS) component? Actually, a sum of a vRS

component and a power law with $\Gamma = 2.0$ (vRS+PL model) gives a somewhat better fit with $\chi^2 = 86.5$ for 72 dof than the vMEKAL+PL model. The derived IGM parameters are $kT = 0.92^{+0.04}_{-0.03}$ keV, $Z_{\alpha} = 0.37^{+0.14}_{-0.12}$ and $Z_{Fe} = 0.29^{+0.08}_{-0.06}$, which are generally similar to those obtained from the vMEKAL+PL model fitting (see Table 4.5). The fit does not improve by adding another vRS component (2-vRS+PL model), which is different from the vMEKAL case where a significant improvement has been shown between the vMEKAL+PL model and the 2-vMEKAL+PL model.

The IGM counts in the 4.0–8.0 keV band, N_{IGM} , has slightly decreased from 111.5 to 74.8. Therefore, in view of the difference in the plasma model, our nominal value of 111.5 (Table 4.10) may not be underestimated. Furthermore, the spectra from some other groups, such as the NGC 5044 group and the NGC 4325 group, are generally fitted well with the IGM model with parameters similar to those of HCG 62, with requiring almost no hard component (see Chapter 5). Therefore, the theoretical error in the IGM modeling is thought to be rather small. For simplicity, we quote the difference derived above, $\Delta N_{IGM} = 37$ counts, as the typical error in the IGM spectral calculation.

4.5.5 Fluctuation of the CXB

Table 4.12: CXB fluctuation in the 2.0–10.0 keV band, derived from past studies.

| Instrument | HEAO-1 A2 ⁽¹⁾ | Ginga LAC ⁽²⁾ | ASCA XRT+GIS ⁽³⁾ |
|---|--------------------------|--------------------------|---|
| Data | 698 sample | 151 sample | 10 sample |
| Effective Area | 530 cm ² | 4,000 cm ² | 200 cm ² |
| Energy Band | 2.5–46 keV | 2–10 keV | 0.6–10.0 keV |
| FOV | 3° × 3° | 1° × 2° | $r = 20'$ with $\sim 3'$ imaging |
| $\Omega_e^{(4)}$ | 15.8 deg ² | 1.3deg ² | ~ 0.5 deg ² /sample (0.14deg ² /pointing) |
| $S_c^{(5)}$ (erg s ⁻¹ cm ⁻²) | 8×10^{-11} | 6×10^{-12} | 2×10^{-12} |
| $\sigma_{CXB}/I_{CXB}^{(6)}$ | 2.8% | $\sim 6\%$ | $\leq 3.4\%$ |

(1) From Shafer (1998) (2) From Hayashida (1990) (3) From Ishisaki (1996)

(4) Effective solid angle of the observations (see appendix C).

(5) Upper cut-off of the 2–10 keV flux from discrete sources in the FOV.

(6) Observed fractional rms CXB fluctuation, i.e., excess variance after subtracting statistical errors and NXB estimation errors.

Since all the instrumental artifacts have so far been shown to be small compared to the detected excess hard counts, the phenomenon must be of celestial origin. One of such candidates is the fluctuation of the CXB. The CXB is considered to be a sum of numerous

discrete sources distributed in the sky, most of which are thought to be AGNs. Therefore, the CXB surface brightness I_{CXB} fluctuates due to the statistical fluctuation of the source number counts in the detector field of view (FOV).

In Table 4.12, we list the value of the fractional CXB fluctuation, σ_{CXB}/I_{CXB} , in the 2.0–10.0 keV band derived from the past studies. As shown in Appendix C, it is described as

$$\sigma_{CXB}/I_{CXB} \propto \Omega_e^{-0.5} S_c^{0.25}, \quad (4.2)$$

where Ω_e represents the effective solid angle of the observation and S_c represents the upper cut-off flux of the detectable (hence removable) discrete sources in the detector FOV. This equation assumes the Euclidean log N -log S relation, represented as $N(> S) \propto S^{-1.5}$. Results from the three experiments given in Table 4.12 satisfy this scaling relation.

The integration area we used, $r < 15'$, or 0.196 deg², yields $\Omega_e = 0.1$ deg², when weighted with the detector angular transmission (see Appendix C). When the value is scaled with the integration area of 0.164 deg² after masking out the five sources, the effective solid angle reduces to $\Omega_e = 0.084$ deg². As the upper cut-off flux in 2–10 keV is typically $S_c = 1 \times 10^{-13}$ erg s⁻¹ cm⁻² in our analysis (see § 4.5.6), the fractional CXB fluctuation is estimated as $\sigma_{CXB}/I_{CXB} = 2.8 \times (15.8/0.084)^{0.5} \times (8 \times 10^{-11}/1 \times 10^{-13})^{-0.25} = 7.2\%$, by scaling the HEAO-1 A2 results with equation 4.2. By multiplying this value to the estimated CXB count of $N_{CXB} = 2092.3$ in the 4.0–8.0 keV band (Table 4.9), we estimate the CXB fluctuation counts in our integration region as 150.6 counts.

We cross check the above estimate experimentally with the 20 blank-sky observations that we used to construct the CXB template (§ 3.3.5). From each of them, we collected photon counts using the same detector regions we used for the five on-source observations, after adjusting the NXB variance using the counts from its outer region. Hence, we obtained 100 samples. As a blank-sky observation itself has regions masked out to avoid contributions from the contaminating sources (§ 3.3.5), we corrected the obtained photon counts for the difference in the integration area. The results are shown in Fig.4.18. To improve the statistics, each data point is given as a sum of five on-source masks. The obtained CXB counts, N_{CXB} , ranges from 1801 to 2370 with a typical statistic error of ~ 100 counts. Their rms scatter is 167.4 counts, which gives an intrinsic scatter of 127.9 after subtracting the Poisson errors. This result is consistent with the value, 150.6, obtained above.

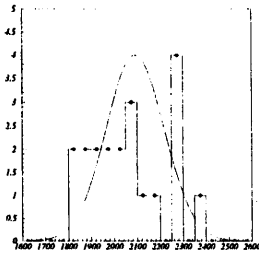


Figure 4.18: Distribution of the 4.0-8.0 keV CXB counts summed over the five on-source masks, among the 20 blank sky observations. Also plotted is a Gaussian function with $\sigma = 180$ counts, which is the quadrature sum of the typical Poisson error of ~ 100 counts and predicted CXB fluctuation of ~ 150 counts.

4.5.6 Effect of the fainter contaminating sources

In the last subsection, we found that the expected CXB fluctuation falls short of the detected excess hard photon counts. Hence, the hard X-ray emission cannot be explained by the contribution from the background AGNs behind HCG 62, provided they belong to the ordinary population. Furthermore, we have already eliminated five point sources (Fig.4.2) at the earliest stage of our data analysis. Nevertheless, we cannot rule out the possibility that there is peculiar over-density of fainter point sources in the present field, and their sum produces the observed excess hard X-rays. In this subsection, we search for such point source candidates in the $0' < r < 15'$ region of HCG 62.

Because the IGM emission fills up the analysis field, it is difficult to find sources only from the GIS image. Therefore, as we have done in § 4.5.2, we used the ROSAT PSPC, which has a higher sensitivity to the point sources. From the PSPC point source catalog (2RXP catalog ; <http://wave.xray.mpe.mpg.de/rosat/rra/rospspc>) supplied by the German ROSAT team, there are five sources with count-rate exceeding 4×10^{-3} counts s^{-1} , and additional six sources exceeding 2×10^{-3} counts s^{-1} . We plot their positions in Fig.4.19. The former are the very sources that we have eliminated in § 4.3 and afterwards, so our results are not affected by them. The latter six sources may also be negligible, by the following reasons. Their number count is consistent with the ordinary CXB population (e.g. Hasinger 1998), and their 2-10 keV flux is $\sim 0.5 \times 10^{-13}$ erg s^{-1} cm^{-2} , about half the typical cut-off flux in our analysis. Here we assumed a power law emission with $\Gamma = 1.7$.

These two characteristics mean that they belong to ordinary population, and hence their contribution has already been included in the CXB fluctuation estimates. This conclusion is supported by the general absence of emission associated with these sources in the GIS 2-10 keV image (Fig.4.19b). In summary, we found no peculiar over-density of faint point sources in the analysis region, at least down to the 2-10 keV flux limit of $\sim 0.5 \times 10^{-13}$ erg s^{-1} cm^{-2} .

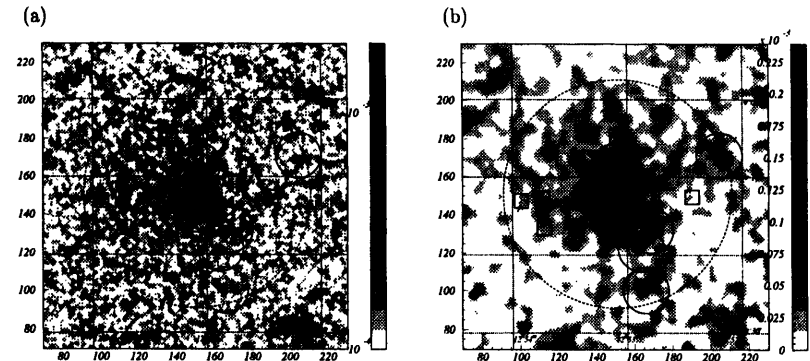


Figure 4.19: Positions of the discrete sources plotted on the (a) 0.4-2.4 keV PSPC image, and (b) 2-10 keV GIS image. The images are smoothed with a Gaussian filter of $\sigma = 0'.25$ and $0'.5$ for the left and right panels, respectively. The scale levels are shown in the right side of each panel, in units of $cts s^{-1} arcmin^{-2}$. Thick dashed line indicates $3'$ and $15'$ from the group center and thick solid circles represent the five sources already eliminated. Boxes represent the six sources with PSPC count-rate in the range of $2.0 \sim 4.0 \times 10^{-3}$ counts s^{-1} .

4.5.7 Overall errors

By considering the analyses made in § 4.5.1 through § 4.5.6, we summarize in Table 4.13 all the conceivable errors, statistical and systematic, that can affect the excess hard X-ray emission from HCG 62. From this table, we finally quote

$$N_{\text{excess}} = 609.8 \pm 73.2 \pm 178.5 \quad (4.3)$$

for the excess hard X-ray counts over the $r < 15'$ region in the 4.0-8.0 keV band. Here, the first and second errors represent statistical and systematic errors, respectively. The

difference in N_{excess} between equations 4.1 and 4.3 is due to the subtraction of the PSF effect. We thus conclude that the phenomenon is significant at about 3.2 sigma level.

Table 4.13: Summary of the excess hard photons in the $r < 15'$ region. Contributions from all examined components are listed, with the estimated errors.

| | item | error estimation | counts | error |
|-------------------|----------------------|-----------------------|-----------------------------|----------------------|
| Poisson errors | data | $\sqrt{5181}$ | $N_{\text{Data}} = 5181$ | ± 72.0 |
| | NXB ⁽¹⁾ | | $N_{\text{NXB}} = -2357.8$ | ± 1.9 |
| | CXB ⁽²⁾ | | $N_{\text{CXB}} = -2092.4$ | ± 13.3 |
| sum | | excess counts = | 730.7 | ± 73.2 |
| systematic errors | NXB estimation error | 2357.8×0.035 | | ± 82.8 |
| | CXB fluctuation | 2092.3×0.072 | | ± 150.6 |
| | IGM contribution | | $N_{\text{IGM}} = -111.5$ | $+13.6 / - 80.8$ |
| | XRT PSF effect | | -9.4 | $+1.1 / - 6.8$ |
| | IGM modeling error | | | ± 37 |
| sum | | excess counts = | 609.8 | $\pm 178.5^{(3)}$ |
| sum of all errors | | excess counts = | $N_{\text{excess}} = 609.8$ | $\pm 73.2 \pm 178.5$ |

(1) Statistical error of the NXB template (§ 3.3.4).

(2) From the sum of background (CXB+NXB) count.

(3) Quadrature sum of the systematic errors. "IGM contribution" error, including the PSF effect, was converted to $\sim 1\sigma$ error from $N(90\%pk - pk) = 101.5$ to $101.5/1.65/2.0 = 30.7$ counts.

4.6 Summary of the Analysis

Table 4.14: Luminosities of the soft and hard components of HCG 62.

| Component | Energy Range (keV) | luminosity (h_{75}^{-2} erg s ⁻¹) |
|-------------|--------------------|--|
| IGM | 0.5-10 | $1.95_{-0.12}^{+0.14} \times 10^{42}$ |
| hard X-rays | 2-10 | $4.18_{-0.85}^{+0.70} \times 10^{41}$ |
| LMXB | 2-10 | 0.35×10^{41} |

We have analyzed extensively the five ASCA observations of HCG 62. In addition to the $kT \sim 1$ keV IGM component extending at least up to $r = 15'$ from the group center, we have found a clear hard excess emission. We obtained a successful fit by

modeling the spectra with two IGM components of $kT_1 = 0.73$ keV and $kT_2 = 1.14$ keV with $Z_{\alpha} = 0.53Z_{\odot}$ and $Z_{Fe} = 0.34Z_{\odot}$, and a power law component with photon index Γ fixed to 2.0 (§ 4.3.4). The Γ is poorly constrained if we set it free, and it can be also replaced by a thermal component with $kT > 5.7$ keV. In Table 4.14, we summarize the luminosities of the IGM component and the hard X-ray emission, derived from the spectral fitting in § 4.3.4. The former is in good agreement with the previous PSPC result of $2.16 \times 10^{42} h_{75}^{-2}$ erg s⁻¹, where no hard component is included in the fitting. The PSPC value was scaled from the original result by Mulchaey and Zabludoff (1998), for the difference of the integration region, the energy range and the Hubble constant. The hard component luminosity is $\sim 20\%$ of the IGM.

We have examined the excess hard X-ray emission against various experimental artifacts; wrong NXB estimation (§ 4.5.2), PSF effects (§ 4.5.3), and IGM modeling error (§ 4.5.4). All of them have fallen short of the observed hard excess. Hence, we confirmed that the phenomenon is celestial.

Among the celestial candidates (Table 4.6), we have already excluded the "central AGN" in § 4.4.1, and the "AGNs in the member galaxies" in § 4.4.2. Furthermore, our investigation in § 4.5.5 and 4.5.6 have also ruled out the CXB fluctuation scenario and the contribution from the contaminating sources, respectively.

Then, how about the LMXB component? From the optical B-band magnitude of the 13 member galaxies of HCG 62 (Carvalho et al. 1997), the sum of their luminosity is $L_B = 6.0 \times 10^{10} h_{75}^{-2} L_{\odot}$. Using equation 2.16, the 2-10 keV flux from LMXBs in these galaxies is estimated as $2.5 \times 10^{40} h_{75}^{-2}$ erg s⁻¹, which is more than an order of magnitude small compared to the observed hard X-ray flux.

Thus, the only possibility left is that the excess hard X-ray emission comes from a diffuse source associated with HCG 62 itself. Its surface brightness profile is similar to, or somewhat more extended than, that of the IGM emission. From the current data alone, however, we cannot tell whether the emission is of thermal or non-thermal origin (§ 4.3.4). We further discuss the origin of the hard excess emission in Chapter 6.

Chapter 5

DATA ANALYSIS AND RESULTS OF OTHER GROUPS

In the last Chapter, we have shown that the HCG 62 group exhibits strong evidence of a diffuse hard X-ray emission. Then, the next question is whether the phenomenon is observed in other groups or not, and how common it is among them. In this Chapter, we accordingly analyze the ASCA data of 17 other galaxy groups in the same way as HCG 62.

5.1 Observations and Targets

To search for the hard X-ray emission, we have surveyed all the groups of galaxies available in the ASCA archival data. In practice, we checked every target which were observed as a group, and also as an elliptical galaxy, because some groups are known to be formed around such galaxies. As we have to separate the hard X-rays from the IGM emission, we need sufficient photon statistics. Therefore, the source must be bright with the 0.5–10 keV flux higher than $\sim 1 \times 10^{-12}$ erg s $^{-1}$ cm $^{-2}$. For the same reason, it should not contain any bright AGN, and the IGM emission itself must be “soft”, i.e., with a temperature lower than ~ 1.7 keV. We also exclude the sources with luminosity less than 5×10^{41} erg s $^{-1}$, most of which are elliptical galaxies and not groups. The sample thus selected consists of 18 groups, including HCG 62. Among them, data for two targets are not yet archived, but the data right belongs to the present author (five offset pointings of NGC 1399 group, performed in 1999) or his supervisor (the NGC 1550 group). We list them in Table 5.1 with their optical properties. Although it is far from being complete, it includes three Hickson’s compact groups, another three (NGC 1132, NGC 1550 and NGC

6521) X-ray selected groups, and 11 relatively loose groups, with their velocity dispersion ranging from $\sigma = 169$ to 474 km s $^{-1}$. In addition, we analyze two X-ray bright elliptical galaxies (NGC 4472 and NGC 4636) for comparison, mainly to determine the level of hard X-ray emission from the underlying LMXBs. Because the sample is large, we sometimes show results only on several representative groups in this Chapter, leaving those of the remaining objects to Appendix D.

In Table 5.2, we summarize observational log of the objects in our sample. For the 17 groups, there are 34 observations in total, of which about one third are offset pointings. We obtained the data from both the GIS and the SIS, following the analysis procedure established for the HCG 62 group (see § 4). For the GIS, we used all the data available. For the SIS, we used the data from the earliest observation of the relevant group, unless otherwise noted, to avoid problems due to the variation of the SIS response (§ 3.4.4).

In Fig.5.1, we present the full band GIS and SIS images for three representative targets, the NGC 1399 group ($z = 0.0048$) and the RGH 80 group ($z = 0.0370$). The former is the nearest target in the sample, and the latter is the farthest. From every group, a diffuse emission with roughly circular profile was detected up to a radius of $r = 10' \sim 25'$, and the X-ray centroid was generally coincident in position with a bright elliptical galaxy. We defined the spectral integration region to be fully contained within the detected diffuse emission, as listed in Table 5.2 and illustrated in Fig.5.1. We also eliminated regions around bright contaminating sources, such as the NGC 1404 galaxy aside NGC 1399, and $3'$ around bright point sources detected with the PSPC. For example, the PSPC sources eliminated in the NGC 1399 group will contribute additional $\sim 0.4 \times 10^{-12}$ erg s $^{-1}$ cm $^{-2}$, or $\sim 2\%$ increase in the 2–10 keV band flux. The region thus defined is completely covered by the GIS, but only partially by the SIS.

5.2 Spectral Analysis

5.2.1 Single component fits

We extracted spectra from both the GIS and the SIS within the integration regions as defined above. For the SIS, we used the bright-mode data for all the following analysis, while the faint-mode data were converted to bright-mode. The background was estimated with the same method as for HCG 62 (see § 4.3.1), and the NXB estimation errors are already included as a systematic error in the background data. Representative spectra obtained in this way are presented in Fig.5.2. All targets show soft spectra, peaking near

Table 5.1: The sample objects selected for the present study.

| target | position ⁽¹⁾ (Ra, Dec) | | $D^{(2)}$ | $z^{(3)}$ | $\sigma_v^{(4)}$ | $L_B^{(6)}$ | $N_{\text{H gal}}^{(6)}$ | note |
|----------|--|---------|-----------|-----------|-----------------------------------|-------------|--------------------------|---------------------|
| HCG 51 | 170.614, | 24.294 | 103 | 0.0258 | 240 ^h | 1.05 | 1.27 | |
| HCG 97 | 356.844, | -2.303 | 87.2 | 0.0218 | 372 ^h | 0.62 | 3.65 | |
| NGC 1132 | 43.223, | -1.275 | 92.8 | 0.0232 | - | 0.47 | 5.17 | |
| NGC 1399 | 54.622, | -35.450 | 19.0 | 0.0048 | 325 ^f | 0.45 | 1.34 | Fornax cluster |
| NGC 1550 | 64.908, | 2.410 | 49.6 | 0.0123 | - | 0.21 | 11.5 | RX J0419.6+0225 |
| NGC 2563 | 125.149, | 21.068 | 59.8 | 0.0149 | 336 ⁺⁴⁴ ₋₄₀ | 0.55 | 4.23 | |
| NGC 4325 | 185.796, | 10.606 | 102 | 0.0257 | 265 ⁺⁵⁰ ₋₄₄ | 0.48 | 2.22 | |
| NGC 5044 | 198.859, | -16.398 | 36.1 | 0.0090 | 474 ^f | 0.73 | 4.93 | WP 23 |
| NGC 507 | 20.901, | 33.257 | 65.8 | 0.0165 | 595 ^w | 1.73 | 2.26 | |
| NGC 533 | 21.397, | 1.772 | 73.7 | 0.0184 | 464 ⁺⁵⁸ ₋₅₂ | 0.86 | 3.10 | |
| NGC 5846 | 226.622, | 1.606 | 24.3 | 0.0061 | 368 ⁺⁷² ₋₆₁ | 0.57 | 4.26 | |
| NGC 6329 | 258.562, | 43.684 | 110 | 0.0276 | - | 1.03 | 2.12 | |
| NGC 6521 | 268.942, | 62.604 | 111 | 0.0266 | 387 ^z | 0.67 | 3.39 | RX J1755.8+6236 |
| NGC 7619 | 350.060, | 8.206 | 50.1 | 0.0125 | 780 ^f | 1.08 | 0.50 | Pegasus group |
| Pavo | 304.628, | -70.859 | 56.0 | 0.0137 | 169 ^{rc} | 1.71 | 7.00 | |
| RGH 80 | 200.058, | 33.146 | 148 | 0.0370 | 467 ^r | 0.32 | 1.05 | |
| S49-147 | 5.375, | 22.402 | 76.0 | 0.0190 | 464 ⁺⁵⁹ ₋₂₁ | 1.13 | 4.06 | |
| HCG 62 | 193.277, | -9.209 | 58.4 | 0.0146 | 376 ⁺⁵² ₋₄₆ | 0.6 | 3.01 | see Chapter 4 |
| NGC 4472 | 187.445, | 8.000 | 11.6 | 0.0029 | - | 0.38 | 1.66 | Elliptical in Virgo |
| NGC 4636 | 190.708, | 2.688 | 14.6 | 0.0037 | - | 0.21 | 1.81 | Elliptical in Virgo |

(1) Position of the X-ray centroid, from this analysis.

(2) Distance to the group in Mpc, converted from the recession velocity listed in NED database, assuming a Hubble constant of $H_0 = 75 \text{ km s}^{-1} \text{ Mpc}^{-1}$.

(3) Redshift, from NED database.

(4) Radial velocity dispersion. Groups without index are from Zabludoff and Mulchaey (1998a), "h" from Hickson et al. (1982), "fs" from Ferguson and Sandage (1990), "w" from Wegner (1993), "f" from Fadda et al. (1996), "rc" from RC3 catalog, "r" from Ramella (1995), and "l" from Ledlow et al. (1996).

(5) Optical B-band luminosity of the member galaxies of the group, in $10^{11} L_{\odot}$. Obtained from RC3 catalog (de Vaucouleurs et al. 1991)

(6) Galactic absorption column density derived from HI radio emission map by Dickey and Lockmann (1990).

Table 5.2: Observation log of the targets.

| target | r ⁽¹⁾ | date ⁽²⁾ | sequence ID | exposure | | SIS mode ⁽⁴⁾ | note |
|----------|------------------|---------------------|-------------------------|---------------------------|---------------------------|-------------------------|--------|
| | | | | GIS (ksec) ⁽³⁾ | SIS (ksec) ⁽³⁾ | | |
| HCG 51 | 10' | 94/06/03 | 82028000 | 62 | 72 | 1 CCD F/F | |
| HCG 97 | 10' | 96/06/18 | 84006000 | 79 | 81 | 1 CCD F | |
| NGC 1132 | 10' | 97/08/16 | 65021000 | 27 | 20 | 1 CCD F/B | |
| NGC 1550 | 15' | 99/08/28 | 87005000 ⁽⁵⁾ | 70 | 23 | 1 CCD F | |
| NGC 1399 | 20' | 93/07/15 | 80038000 | 19 | 17 | 4 CCD F | |
| | | 93/07/15 | 80039000 | 17 | (15) | 4 CCD F | |
| | | 94/01/25 | 81021000 | 27 | (16) | 4 CCD F | offset |
| | | 99/08/10 | 87006000 ⁽⁶⁾ | 12 | (17) | c4 CCD F/B | offset |
| | | 99/08/10 | 87006010 ⁽⁶⁾ | 16 | (10) | c4 CCD F/B | offset |
| | | 99/08/19 | 87006020 ⁽⁶⁾ | 21 | (14) | c4 CCD F/B | offset |
| | | 99/08/20 | 87006030 ⁽⁶⁾ | 11 | (9) | c4 CCD F/B | offset |
| | | 99/08/20 | 87006040 ⁽⁶⁾ | 22 | (18) | c4 CCD F/B | |
| NGC 2563 | 12' | 95/10/26 | 63008000 | 46 | 52 | 1 CCD F | |
| NGC 4325 | 10' | 97/01/05 | 85066000 | 27 | 25 | 2 CCD B | |
| NGC 5044 | 15' | 93/06/20 | 80026000-10 | 25 | 19 | 4 CCD B | |
| | | 99/01/14 | 87002000 | 22 | (15) | 1 CCD F/F | offset |
| | | 99/01/14 | 87002010 | 21 | (22) | 1 CCD F/F | offset |
| | | 99/01/15 | 87002020 | 21 | (22) | 1 CCD F/F | offset |
| | | 99/01/16 | 87002030 | 22 | (21) | 1 CCD F/F | offset |
| NGC 507 | 15' | 94/01/23 | 61007000 | 36 | 25 ⁽⁷⁾ | 2 CCD F | |
| | | 95/01/29 | 61007010 | 7 | (6) | 2 CCD | |
| | | 95/01/28 | 63026000 | 37 | (35) | 2 CCD | NGC 45 |
| NGC 533 | 10' | 94/08/05 | 62009000 | 18 | (14) | 4 CCD F | |
| | | 96/01/06 | 62009010 | 17 | 18 ⁽⁸⁾ | 2 CCD B | |
| NGC 5846 | 15' | 94/02/07 | 61012000 | 36 | 28 | 4 CCD B | |
| NGC 6329 | 12' | 96/04/21 | 84047000 | 37 | 34 | 2 CCD B | |
| NGC 6521 | 10' | 97/11/29 | 85034000 | 36 | 19 | 1 CCD F | |
| NGC 7619 | 12' | 95/06/28 | 63017000 | 56 | 59 | 2 CCD B | |
| Pavo | 10' | 94/04/28 | 81020000 | 29 | 26 | 4 CCD B | |
| RGH 80 | 10' | 95/06/23 | 83012000 | 41 | 42 | 2 CCD B | |
| | | 95/06/19 | 93007040 | 9 | (9) | 4 CCD B | offset |
| | | 95/07/01 | 93007080 | 9 | (8) | 4 CCD B | offset |
| | | 95/07/01 | 93007070 | 8 | (9) | 4 CCD B | offset |
| S49-147 | 15' | 93/12/12 | 81001000 | 32 | 29 | 2 CCD F | |
| NGC 4472 | 8' | 93/07/04 | 60029000 | 19 | 18 | 4 CCD B | |
| | | 93/06/30 | 60030000 | (22) | (18) | 4 CCD F/B | offset |
| NGC 4636 | 8' | 93/06/23 | 60032000 | (35) | 34 | 4 CCD F | |
| | | 95/12/28 | 64008000 | 175 | (244) | 1 CCD F | |

(1) Radius of the spectral integration region. (2) Observation start date.

(3) The data with the exposure listed with parenthesis are not used in the spectral analysis.

(4) SIS clocking-mode and data-mode.

(5) Non-archival data. PI, K. Makishima. (6) Non-archival data. PI, K. Nakazawa.

(7) The data only from the SIS-0 is used. See § 5.2.3.

(8) The SIS data from the first observation is not used. See § 5.2.3.

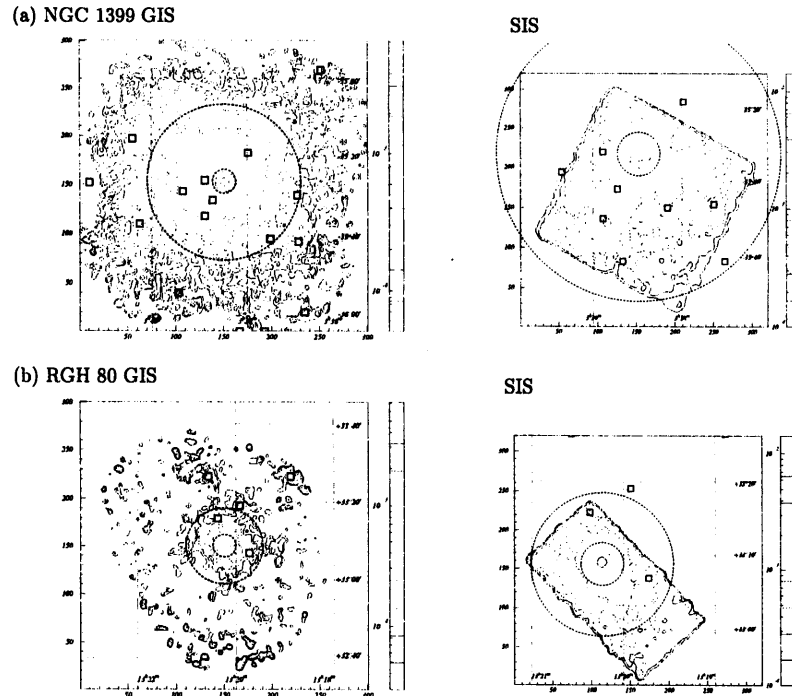


Figure 5.1: The 0.5–10.0 keV band X-ray contour images of the GIS and the SIS, for (a) the NGC 1399 group, and (b) the RGH 80 group. They are the same as Figs.4.6 (GIS) and 4.7 (SIS), except for the energy band. The contours are logarithmically spaced by factors of 1.7, starting from 5×10^{-5} cts s^{-1} arcmin $^{-2}$ for the GIS image of NGC 1399, and from 2.9×10^{-5} cts s^{-1} arcmin $^{-2}$ for that of RGH 80. For the SIS images, the first contour shows 1×10^{-4} cts s^{-1} arcmin $^{-2}$. The smaller dashed circles represent 3' from the group center, and the larger ones the integration region for spectral analysis, 20' for NGC 1399 and 10' for RGH 80. Open squares indicate the positions of the point sources detected with the PSPC, around 3' of which are excluded from the analysis. See Fig.D.1 for the remaining groups.

~ 1 keV, with clear Fe-L lines that characterize hot plasma with $kT = 0.5 \sim 2$ keV. Some groups, such as the NGC 4325 group and the NGC 5044 group, show a spectral peak below 1 keV and their spectral continua are very soft, while others, such as the NGC 2563 group, show a peak above 1 keV and exhibit relatively hard continua. In addition, several groups, such as RGH 80 and S49-147, simultaneously exhibits the Fe-L peak below 1 keV and hard continua. Their spectra resemble those of HCG 62 (e.g., Fig.4.10).

Table 5.3: Results of the joint fit to the GIS and SIS spectra with a single component vMEKAL model.

| target | $kT^{(1)}$ | Abundance ⁽²⁾ | | $\chi^2/d.o.f$ | $kT_H^{(3)}$ |
|----------|------------------------|--------------------------|------------------------|----------------|------------------------|
| | (keV) | $Z_\alpha(Z_\odot)$ | $Z_{Fe}(Z_\odot)$ | | |
| HCG 51 | $1.38^{+0.03}_{-0.03}$ | $0.44^{+0.15}_{-0.13}$ | $0.38^{+0.06}_{-0.05}$ | 97.35/71 | $0.97^{+0.44}_{-0.26}$ |
| HCG 97 | $1.04^{+0.03}_{-0.04}$ | $0.30^{+0.15}_{-0.12}$ | $0.18^{+0.04}_{-0.03}$ | 81.48/71 | $1.83^{+1.60}_{-0.77}$ |
| NGC 1132 | $1.09^{+0.02}_{-0.03}$ | $0.32^{+0.15}_{-0.12}$ | $0.27^{+0.05}_{-0.04}$ | 69.41/71 | $1.14^{+0.46}_{-0.38}$ |
| NGC 1399 | $1.38^{+0.01}_{-0.01}$ | $0.46^{+0.05}_{-0.05}$ | $0.36^{+0.03}_{-0.02}$ | 374.65/69 | $1.84^{+0.09}_{-0.12}$ |
| NGC 1550 | $1.42^{+0.02}_{-0.02}$ | $0.53^{+0.07}_{-0.06}$ | $0.40^{+0.03}_{-0.03}$ | 164.80/57 | $1.86^{+0.68}_{-0.46}$ |
| NGC 2563 | $1.36^{+0.04}_{-0.05}$ | $0.63^{+0.27}_{-0.21}$ | $0.33^{+0.09}_{-0.07}$ | 63.52/71 | $1.63^{+0.86}_{-0.52}$ |
| NGC 4325 | $1.04^{+0.02}_{-0.02}$ | $0.42^{+0.15}_{-0.12}$ | $0.34^{+0.06}_{-0.05}$ | 79.48/67 | $1.22^{+0.65}_{-0.41}$ |
| NGC 5044 | $1.02^{+0.01}_{-0.01}$ | $0.38^{+0.04}_{-0.04}$ | $0.27^{+0.02}_{-0.02}$ | 312.98/74 | $1.34^{+0.11}_{-0.09}$ |
| NGC 507 | $1.39^{+0.02}_{-0.02}$ | $0.68^{+0.13}_{-0.11}$ | $0.43^{+0.05}_{-0.05}$ | 192.75/73 | $1.89^{+0.21}_{-0.19}$ |
| NGC 533 | $1.27^{+0.06}_{-0.06}$ | $0.49^{+0.25}_{-0.18}$ | $0.33^{+0.11}_{-0.10}$ | 92.61/69 | $1.25^{+0.63}_{-0.40}$ |
| NGC 5846 | $0.75^{+0.02}_{-0.02}$ | $0.28^{+0.12}_{-0.09}$ | $0.20^{+0.04}_{-0.03}$ | 150.70/67 | $2.63^{+3.77}_{-1.18}$ |
| NGC 6329 | $1.39^{+0.07}_{-0.07}$ | $0.27^{+0.18}_{-0.15}$ | $0.18^{+0.06}_{-0.05}$ | 89.76/71 | $2.44^{+1.73}_{-0.87}$ |
| NGC 6521 | $1.77^{+0.31}_{-0.12}$ | $0.66^{+0.44}_{-0.32}$ | $0.39^{+0.28}_{-0.13}$ | 57.21/67 | $1.86^{+0.68}_{-0.46}$ |
| NGC 7619 | $0.97^{+0.03}_{-0.03}$ | $0.38^{+0.14}_{-0.11}$ | $0.24^{+0.05}_{-0.04}$ | 73.35/71 | $1.33^{+0.80}_{-0.51}$ |
| Pavo | $0.59^{+0.04}_{-0.07}$ | $0.10^{+0.12}_{-0.08}$ | $0.08^{+0.03}_{-0.02}$ | 104.47/71 | $0.76^{+1.09}_{-0.40}$ |
| RGH 80 | $1.25^{+0.05}_{-0.05}$ | $0.40^{+0.16}_{-0.13}$ | $0.21^{+0.05}_{-0.04}$ | 130.45/73 | $2.66^{+1.07}_{-0.66}$ |
| S49-147 | $1.04^{+0.05}_{-0.05}$ | $0.12^{+0.08}_{-0.07}$ | $0.07^{+0.02}_{-0.02}$ | 108.31/71 | $2.23^{+1.73}_{-0.82}$ |
| NGC 4472 | $1.08^{+0.01}_{-0.01}$ | $0.43^{+0.06}_{-0.06}$ | $0.28^{+0.02}_{-0.02}$ | 381.76/71 | $2.41^{+0.42}_{-0.37}$ |
| NGC 4636 | $0.70^{+0.01}_{-0.01}$ | $0.45^{+0.07}_{-0.06}$ | $0.25^{+0.02}_{-0.02}$ | 619.20/74 | $2.48^{+0.40}_{-0.35}$ |

(1) Best fit temperature in the full-band. (2) Best fit metal abundances in the full-band.

(3) Best fit temperature from the hard-band fitting, i.e., above 2.5 keV.

We jointly fitted the GIS and SIS spectra with a vMEKAL model, in which the metal abundances are splitted into the two groups as before, Z_α and Z_{Fe} (see § 4.3.4). The fitting results are listed in Table 5.3, and the best fit model predictions are superposed

on the spectra in Fig.5.2. In the fitting, the redshift and the absorption column are fixed at the values listed in Table 5.2. We examined the SIS data taken after 1997, against the effect of the decreasing quantum efficiency in low-energies (§ 3.4.4), and found it to be generally insignificant, due to the limited photon statistics of the data. Only those of the NGC 1550 group, the second brightest group among the sky, require excess absorption, and we set the value free for its SIS spectra.

The best fit temperature ranges from 0.6 to 1.8 keV. The fits are acceptable for only 6 and 9 groups, in 90% and 99% confidence level, respectively. Some groups show excess hard tails, while the brightest groups show large residuals around the Fe-L line region. The former objects possibly exhibit the excess hard X-ray emission, like HCG 62. To further investigate this possibility, we then fitted the hard-band spectra, above 2.5 keV, using the same model with a fixed metal abundance of $Z_{\alpha} = Z_{\text{Fe}} = 0.3$. The obtained temperatures are also listed in Table 5.3, and are compared with the full-band temperatures in Fig.5.3. Although the error-bars are rather large, the hard-band temperature is significantly higher than the full-band temperature in about half the objects. It sometimes reaches twice the latter value, the ratio similar to that of HCG 62. This may be taken as a possible evidence for the excess hard X-ray emission in at least some targets in our sample.

5.2.2 Two component fits

To quantify the amount of the suggested hard excess above the IGM emission, we accordingly added a power law component, with Γ fixed at 2.0, to the vMEKAL component (vMEKAL+PL model; see § 4.3.4). The fitting results with this model are summarized in Fig.5.4 and Table 5.4. The best fit temperatures range from 0.4 keV to 1.6 keV, and the fits become acceptable for 9 (additional 3) and 13 (4) groups, in 90% and 99% confidence level, respectively. The χ^2 values of 7 out of 17 groups have decreased by more than 10%; they are generally those groups which exhibit large differences between the hard and full-band temperatures in Fig.5.3. On the other hand, 6 groups require no hard component, and the remaining 4 groups show moderate improvements in χ^2 . Here, a reduction in χ^2 by $\Delta\chi^2 \sim 7$ with the introduction of the power law component (1 extra fit parameters) is significant in terms of F -test at 99% confidence, for a fit with ~ 70 dof and reduced- $\chi^2 \sim 1$. Thus, about a half of the groups show evidence of hard component.

Even employing the vMEKAL+PL model, the five brightest groups, with the 0.5–10 keV fluxes exceeding $\sim 1 \times 10^{-11}$ erg s^{-1} cm^{-2} , exhibit a rather high value of reduced- χ^2 , larger than 2.2. It is due to residuals around 0.8–2.0 keV, which is the energy range of the

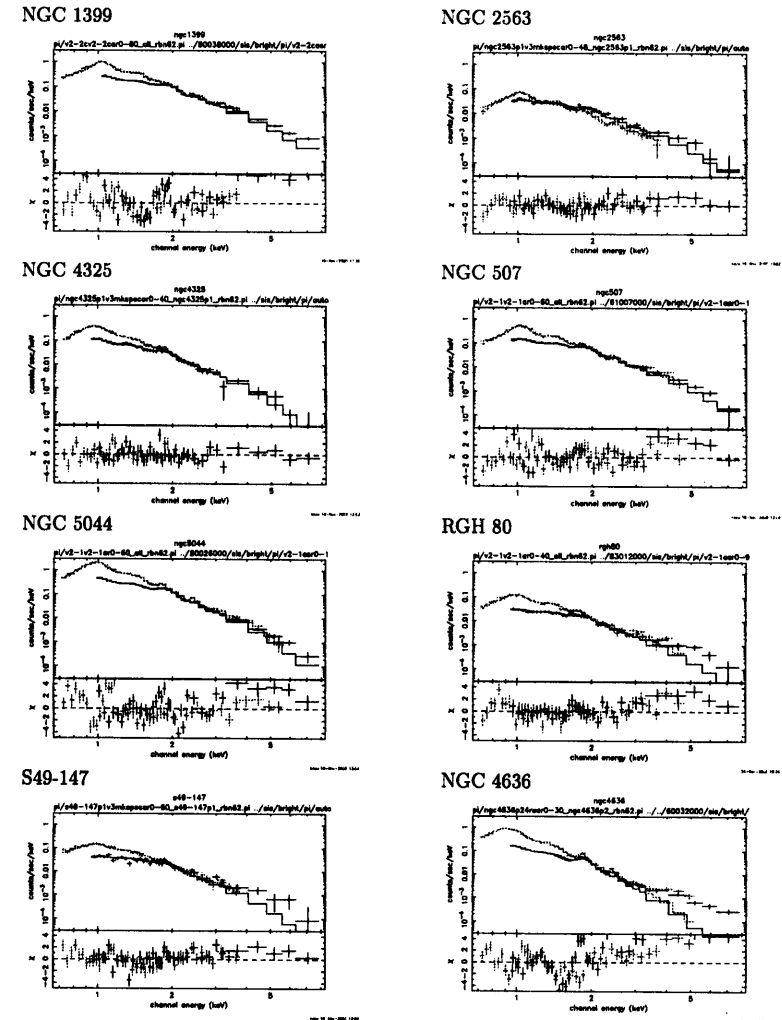


Figure 5.2: The GIS and SIS spectra of representative object in our sample, jointly fitted with a vMEKAL component. All spectra are plotted to the same scale. The last panel shows the spectra of the elliptical galaxy, NGC 4636. See Fig.D.2 for the remaining targets.

Table 5.4: Results of the joint fit to the GIS and SIS spectra with the two component model.

| target | $kT^{(1)}$ | Abundance ⁽²⁾ | | Soft | Hard | $\chi^2/d.o.f$ | $\Delta\chi^2$ ⁽⁵⁾ |
|----------|------------------------|--------------------------|----------------------------|---------------------|------------------------|----------------|-------------------------------|
| | (keV) | $Z_{\alpha}(Z_{\odot})$ | $Z_{\text{Fe}}(Z_{\odot})$ | Flux ⁽³⁾ | Flux ⁽⁴⁾ | | |
| HCG 51 | $1.38^{+0.03}_{-0.03}$ | $0.44^{+0.15}_{-0.13}$ | $0.38^{+0.06}_{-0.05}$ | 2.64 | $0.00^{+0.05}_{-0.00}$ | 97.3/70 | 0.00 |
| HCG 97 | $1.02^{+0.03}_{-0.04}$ | $0.36^{+0.27}_{-0.17}$ | $0.27^{+0.13}_{-0.07}$ | 1.10 | $0.23^{+0.11}_{-0.11}$ | 68.62/70 | -12.86 |
| NGC 1132 | $1.09^{+0.02}_{-0.03}$ | $0.32^{+0.15}_{-0.12}$ | $0.27^{+0.06}_{-0.04}$ | 3.46 | $0.00^{+0.13}_{-0.00}$ | 69.41/70 | 0.00 |
| NGC 1399 | $1.33^{+0.02}_{-0.02}$ | $0.56^{+0.07}_{-0.07}$ | $0.42^{+0.04}_{-0.04}$ | 19.4 | $1.99^{+0.28}_{-0.29}$ | 245.78/68 | -128.87 |
| NGC 1550 | $1.41^{+0.02}_{-0.02}$ | $0.54^{+0.07}_{-0.06}$ | $0.41^{+0.04}_{-0.03}$ | 25.7 | $0.42^{+0.46}_{-0.42}$ | 162.61/56 | -2.18 |
| NGC 2563 | $1.33^{+0.05}_{-0.06}$ | $0.79^{+0.53}_{-0.30}$ | $0.44^{+0.24}_{-0.13}$ | 2.32 | $0.41^{+0.27}_{-0.27}$ | 57.54/70 | -5.98 |
| NGC 4325 | $1.04^{+0.02}_{-0.02}$ | $0.42^{+0.15}_{-0.12}$ | $0.34^{+0.07}_{-0.07}$ | 5.84 | $0.00^{+0.15}_{-0.00}$ | 79.48/66 | 0.00 |
| NGC 5044 | $1.00^{+0.01}_{-0.01}$ | $0.42^{+0.05}_{-0.04}$ | $0.30^{+0.02}_{-0.02}$ | 29.1 | $0.99^{+0.23}_{-0.23}$ | 262.76/73 | -50.22 |
| NGC 507 | $1.35^{+0.03}_{-0.03}$ | $0.83^{+0.19}_{-0.13}$ | $0.52^{+0.09}_{-0.07}$ | 10.6 | $0.97^{+0.29}_{-0.29}$ | 163.30/72 | -29.44 |
| NGC 533 | $1.27^{+0.06}_{-0.06}$ | $0.49^{+0.25}_{-0.18}$ | $0.33^{+0.11}_{-0.08}$ | 3.60 | $0.00^{+0.20}_{-0.00}$ | 92.61/68 | 0.0 |
| NGC 5846 | $0.74^{+0.02}_{-0.02}$ | $0.30^{+0.14}_{-0.10}$ | $0.22^{+0.06}_{-0.04}$ | 8.61 | $0.34^{+0.25}_{-0.25}$ | 145.67/66 | -5.02 |
| NGC 6329 | $1.33^{+0.08}_{-0.11}$ | $0.30^{+0.27}_{-0.19}$ | $0.23^{+0.12}_{-0.08}$ | 2.38 | $0.53^{+0.28}_{-0.29}$ | 80.86/70 | -8.90 |
| NGC 6521 | $1.64^{+0.17}_{-0.22}$ | $0.94^{+1.19}_{-0.50}$ | $0.52^{+0.52}_{-0.21}$ | 2.33 | $0.66^{+0.47}_{-0.48}$ | 51.88/66 | -5.01 |
| NGC 7619 | $0.97^{+0.03}_{-0.03}$ | $0.40^{+0.17}_{-0.12}$ | $0.26^{+0.07}_{-0.05}$ | 3.32 | $0.13^{+0.16}_{-0.13}$ | 71.49/70 | -1.86 |
| Pavo | $0.44^{+0.06}_{-0.04}$ | $0.19^{+0.23}_{-0.11}$ | $0.07^{+0.06}_{-0.03}$ | 2.64 | $0.42^{+0.10}_{-0.13}$ | 77.89/70 | -26.57 |
| RGH 80 | $1.09^{+0.03}_{-0.04}$ | $0.74^{+0.51}_{-0.29}$ | $0.36^{+0.18}_{-0.10}$ | 1.71 | $0.64^{+0.12}_{-0.12}$ | 67.95/72 | -62.50 |
| S49-147 | $0.97^{+0.06}_{-0.13}$ | $0.12^{+0.11}_{-0.09}$ | $0.09^{+0.04}_{-0.03}$ | 2.89 | $0.75^{+0.28}_{-0.28}$ | 90.11/70 | -18.20 |
| NGC 4472 | $1.06^{+0.01}_{-0.01}$ | $0.63^{+0.17}_{-0.13}$ | $0.46^{+0.08}_{-0.05}$ | 9.35 | $1.77^{+0.24}_{-0.24}$ | 239.87/70 | -141.89 |
| NGC 4636 | $0.68^{+0.01}_{-0.01}$ | $0.73^{+0.17}_{-0.13}$ | $0.42^{+0.07}_{-0.05}$ | 9.58 | $0.73^{+0.06}_{-0.06}$ | 259.94/73 | -359.26 |

- (1) Best fit temperature from the full-band fitting with a vMEKAL+PL model.
- (2) Best fit metal abundances from the full-band fitting with a vMEKAL+PL model.
- (3) The 0.5-10 keV flux of the vMEKAL component, in 10^{-12} erg s^{-1} cm^{-2} .
- (4) The 2-10 keV flux of the power-law component, in 10^{-12} erg s^{-1} cm^{-2} .
- (5) The improvement of the χ^2 value by adding a power law component.

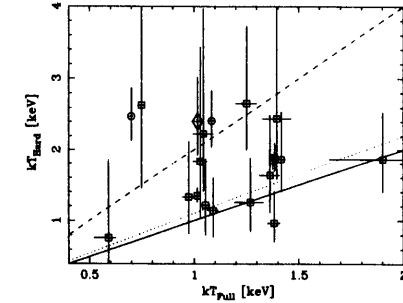


Figure 5.3: The best fit temperature from the hard-band fitting, compared to that from the full-band fitting. A diamond represents HCG 62, circles the two ellipticals, and squares the other 17 groups. Solid line indicates equal temperature, dotted line 10% higher and dashed line twice of that of the full-band fitting.

Fe-L line emission. If we introduce another vMEKAL component with a lower temperature (2-vMEKAL+PL model; see § 4.3.4), the χ^2 values further decreases significantly for most of these targets. By doing so, the normalization of the power law component in NGC 1399 and NGC 5044 decreases by 20 ~ 30%, while in NGC 507, the hotter component temperature become as high as 6 keV and simply replaces the power law component. In case of NGC 1550 and NGC 5846, the hard fluxes are already insignificant, and the second vMEKAL component just make it even less significant. Thus, the introduction is a second vMEKAL component does not drastically influence our results, and the fit residuals remain significant over the 0.8-2.0 keV regions in some objects. This is supposed to be due to errors in the theoretical calculation of the Fe-L line emission (e.g., Matsushita 1996). Because the precise modeling of the line emission is beyond the scope of this thesis, we do not make further effort to obtain an acceptable fit for these handful of brightest groups. In general, we assume that the model well represents the IGM emission in its averaged feature, which is supported by the existence of five groups requiring no hard component, with their IGM temperature widely distributed from 0.97 keV to 1.41 keV (see § 5.3).

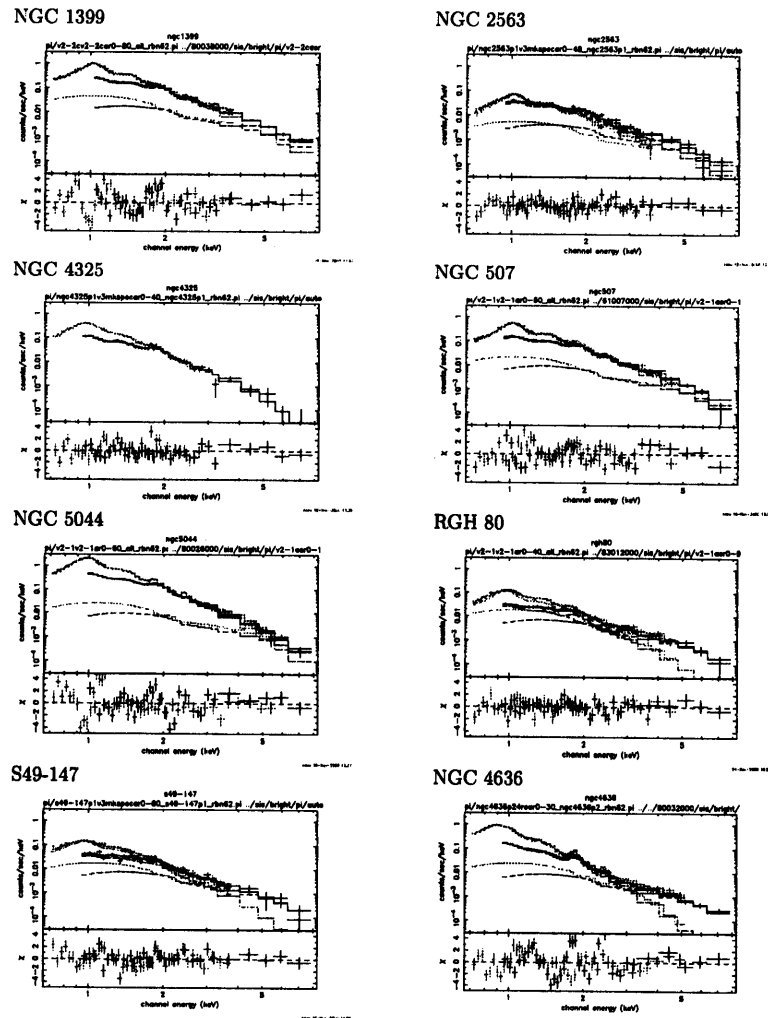


Figure 5.4: The same spectra as shown in Fig.5.2, fitted with a sum of a vMEKAL and a power law components. See Fig.D.3 for the remaining targets.

5.2.3 Comments on individual objects

NGC 1399 group

This object is alternatively called the Fornax cluster, one of the poorest and nearest clusters. This is also one of the X-ray brightest targets in our sample, and a vMEKAL model fit was not acceptable with reduced- $\chi^2 = 375/69$ (shown as χ^2/dof , hereafter χ_r^2 ; see Table 5.3), with prominent hard excess above ~ 4 keV and the residuals around Fe-L line region (Fig.5.2). By adding a power law component (vMEKAL+PL model), the χ_r^2 greatly decreased to 246/68 (Table 5.4), while the residuals around Fe-L line region remained unchanged (Fig.5.4). When we employ a 2-vMEKAL model instead of the vMEKAL+PL model, the latter residual decreased and the fit also greatly improved with a $\chi_r^2 = 240/68$, while the hard excess is still visible. The derived temperatures are $kT_{\text{cool}} = 0.88^{+0.14}_{-0.04}$ keV and $kT_{\text{hot}} = 1.65^{+0.04}_{-0.04}$ keV, the latter being a little lower than the value of the hard-band fitting, $kT = 1.84^{+0.09}_{-0.12}$ keV (Table 5.3), which should be regarded as a lower limit considering the contribution from the cooler component. Restoring a power law component with $\Gamma = 2.0$ (2-vMEKAL+PL model), the χ_r^2 further decreased to 215/67. The derived temperatures are then $kT_{\text{cool}} = 0.84^{+0.16}_{-0.10}$ keV and $kT_{\text{hot}} = 1.45^{+0.04}_{-0.04}$ keV, and the 2–10 keV hard component flux of $1.59^{+0.32}_{-0.54} \times 10^{-12}$ erg s $^{-1}$ cm $^{-2}$. Although this flux is by $\sim 20\%$ lower than derived with the vMEKAL+PL model, it still exceeds both the estimated LMXB component ($\sim 0.4 \times 10^{-12}$ erg s $^{-1}$ cm $^{-2}$) and the CXB fluctuation ($\sim 0.3 \times 10^{-12}$ erg s $^{-1}$ cm $^{-2}$). All the above results are little affected by setting the column density free, except the parameters for the cooler IGM component. Thus, we conclude that there exists a hard component in NGC 1399, which is either a non-thermal emission or a thermal emission with a temperature higher than ~ 2 keV.

Our results are generally consistent with the previous study by Ikebe (1995) and Ikebe et al. (1996), who fitted the GIS spectra using a vRS model for the IGM emission, and obtained a lower temperature and a more prominent excess hard component (see § 4.5.4). By fitting jointly the GIS and SIS spectra, Boute et al. (1998) and Allen et al. (2000) obtained results similar to ours, although they only used the data from the central $\sim 4'$ region. The former authors tried only 2-MEKAL model, while the latter authors argued for the existence of additional power law component and attributed it to the possible AGN in the NGC 1399 galaxy. To examine this possibility, we also extracted spectra from the region excluding $3'$ around NGC 1399. Though less significant, we obtained generally similar results as shown above, where the χ_r^2 of 2-vMEKAL and 2-vMEKAL+PL fit being 184.61/68 and 173.01/67, respectively. These results are also consistent with the ROSAT

PSPC results showing a temperature decrease in the group central region, though the detector has almost no sensitivity to the hard component (e.g., Jones et al. 1997). The AGN interpretation of the excess hard X-ray emission (Allen et al. 2000) was ruled out by the latest Chandra observation.

NGC 5044 group

This is one of the X-ray brightest groups among the sky, and the vMEKAL model fit is not acceptable with $\chi_r^2 = 313/74$ (Table 5.3). With 2-vMEKAL model, we obtain $kT_{\text{cool}} = 0.79^{+0.04}_{-0.05}$ keV and $kT_{\text{hot}} = 1.23^{+0.05}_{-0.04}$ keV, with $\chi_r^2 = 210/72$. These are consistent with the central temperature decrease shown by Fukazawa et al. (1996) using the same ASCA data, and also the previous ROSAT results (e.g., David et al. 1994). Because the residual spectra exhibit some hard excess, we employed the 2-vMEKAL+PL model, and obtained $\chi_r^2 = 180.90/71$. However, the hard component luminosity is lower than 4% of the IGM luminosity in both vMEKAL+PL and 2-vMEKAL+PL fitting, making one of the tightest upper limits in our sample. We think this level is too small to distinguish the hard component from the possible IGM modeling error. We therefore regard the derived hard component luminosity as an upper limit.

NGC 507 group

The spectrum obtained from the SIS1 is flattened around 1 keV, which is inconsistent with the SIS1 data from a short supplemental observation performed later (sequence ID = 61007010). Therefore, we used only the data from the SIS 0 in our analyses. The group is bright in X-rays, and vMEKAL model fit is not acceptable with $\chi_r^2 = 193/73$ (Table 5.3). With the 2-vMEKAL model, we obtain $\chi_r^2 = 164/71$; the temperature of the hotter component became higher than 6.0 keV, while that of the cooler component was $kT_{\text{cool}} = 1.35^{+0.03}_{-0.08}$ keV. The obtained χ^2 and kT_{cool} are very similar to those from the vMEKAL+PL fitting (Table 5.4), indicating that the hot component simply replaced the power law component. The fit does not improve any more by adding a power law component (2-vMEKAL+PL model). Thus, similar to NGC 1399, the data suggest a hard component, either thermal or non-thermal.

NGC 533 group

The temperature of the SIS detectors was rather high, $T > -60$ C° and > -59.5 C° for SIS 0 and 1, respectively, in both of the two observations. This increased the dark current and

the number of the hot and flickering pixels of the detectors, which affected the data taken with long frame interval. Hence, the spectra of the first observation taken with 4 CCD mode, which has the longest frame interval (§ 3.4.2), show strong soft excess below ~ 0.8 keV, while that of the second observation taken with 2 CCD mode do not. Therefore, we used only data from the second observation, which also has a longer exposure, but a smaller FOV. The fit with the vMEKAL model is almost acceptable (Table 5.3), and there is no evidence for any hard component.

NGC 6521 group

The vMEKAL fit is acceptable, while the additional hard component is marginally significant in terms of F -test. This is due to the rather high IGM temperature, ~ 1.64 keV, which make it difficult to separate the hard component, if any, from the IGM emission.

Pavo group

The IGM temperature derived with the vMEKAL+PL model, $kT = 0.44$ keV, may be somewhat too low for the ASCA bandpass to yield an accurate determination. Therefore, the hard component thus obtained is also less reliable. When fitted with a Raymond-Smith model, the best fit temperature is $kT = 0.77$ keV, and the hard component becomes less significant with the best fit flux being $\sim 40\%$ of that of the vMEKAL+PL model.

RGH 80

One of the groups with significant hard X-ray emission. It is also the farthest group in our sample and among the most luminous. If we set the photon index of the power law component free in the vMEKAL+PL fitting, it becomes $\Gamma = 1.61^{+0.74}_{-0.86}$ with $\chi_r^2 = 68.03/71$; this is similar to the case with fixed Γ . When fitted with a 2-vMEKAL model, the temperature of the hotter component becomes $kT_{\text{hot}} = 23.9^{+20.3}_{-20.3}$ keV, and $\chi_r^2 = 68.2/71$. Boute (2000) analyzed the ASCA spectra obtained from the central $\sim 3.6'$, and reported a rather lower temperature for the hot component, $kT_{\text{hot}} = 1.64^{+0.21}_{-0.17}$ keV. We confirmed this result by extracting the spectra from a similar region. Therefore, the hard component is inferred to be stronger in the $3' < r < 10'$ region.

5.3 General Properties of the Sample Groups

In the last section, evidence for excess hard emission was detected from about half objects in our sample. In this section, we examine their properties as a whole. We compare the significance of the hard component against various parameters, such as the IGM temperature, the observed fluxes, and the X-ray and optical luminosities. Then we examine whether the hard component is extended, by averaging three groups with nearly the same spectra. We compare the results with those from HCG 62.

5.3.1 Comparison with the IGM properties

In Fig.5.5a, the 2-10 keV hard component flux (taken from Table 5.4) derived from the vMEKAL+PL fits is plotted against the 0.5-10 keV flux of the IGM component. There is no correlation visible in the plot, which means that the hard component flux derived is independent of the flux of the IGM component. Thus, it eliminates the possibility that the hard tail is originating from slight errors in the modeling of the hard-band continuum of IGM emission.

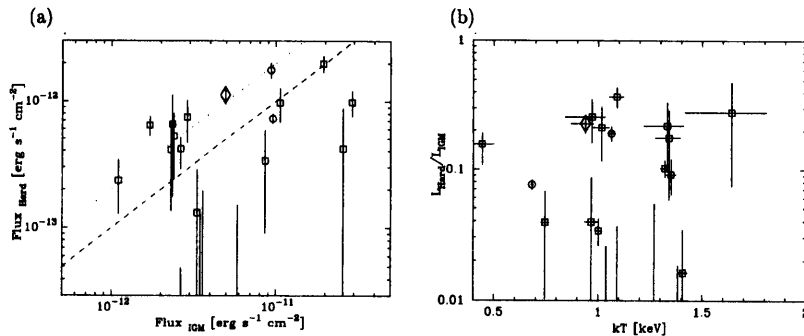


Figure 5.5: (a) The hard component flux plotted against that of the IGM component. Dashed line represents the ratio of 10%, and dotted line 20%. (b) The luminosity ratio of the hard component to the IGM emission, plotted against the IGM temperature. In both panels, symbols are the same as those in Fig.5.3.

In Fig.5.5b, we plot the hard component luminosity L_{hard} (derived from Tables 5.4 and 5.1) divided by the IGM luminosity L_{IGM} (hereafter, the hard-IGM luminosity ratio) against the fitted IGM temperature. The ratio ranges from $< 1\%$ to as high as 40%, and is higher than $\sim 10\%$ in about half the sample groups. Furthermore, groups with

and without the hard excess coexist at any IGM temperature, and there is no correlation between the two quantities. The lack of correlation in this plot is another evidence that the excess hard X-ray emission from some groups is not an artifact caused by the wrong modeling of the IGM emission, which is mainly defined by its temperature.

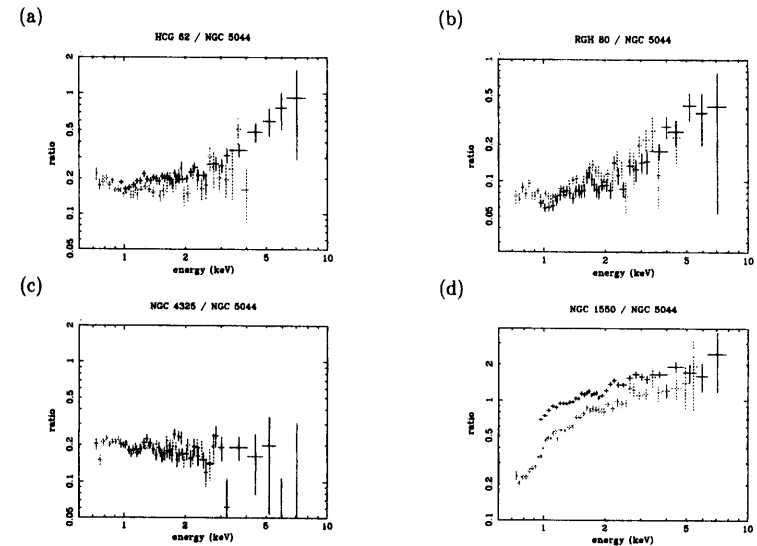


Figure 5.6: Spectra of the groups divided with those of the NGC 5044. (a) HCG 62, (b) RGH 80, (c) NGC 4325, and (d) NGC 1550. Black crosses represents the GIS, and gray crosses the SIS.

In Fig.5.5, there are three targets, HCG 97, RGH 80 and S49-147, sharing almost the same position as HCG 62, with the IGM temperature of $kT \sim 1$ keV and the luminosity ratio around 20 ~ 40%. In addition, there are another three targets, the NGC 1132, NGC 4325 and NGC 5044 groups, sharing similar temperature but with very low luminosity ratio, below $\sim 5\%$. Because the NGC 5044 group has the best statistics in our sample objects, we divided the spectra of these targets with that of the NGC 5044 group. The derived spectral ratios are presented in Fig.5.6. For the former three targets, the ratio spectra are flat around 1 keV, and rapidly increase in the hard band. On the contrary, those of the NGC 4325 group are almost constant throughout the full energy band. Those of the NGC 1550 group, which has the IGM temperature $\sim 40\%$ higher than that of NGC 5044, show a constant increase; this behavior is different from the steep rising of the

spectra seen in HCG 62. Therefore, the hard component required in the former three targets is confirmed to be distinct from the hardening due to the high IGM temperature.

In Fig.5.7a, we plot L_{hard} against L_{IGM} . Unlike the case of the hard component flux (Fig.5.5a), a clear correlation is visible in this plot; targets with luminous hard component also are luminous in the IGM emission. There also exist targets which are luminous in the IGM emission, but not in the hard component. Thus, all the data points are distributed below the line defining the luminosity ratio of $\sim 30\%$. In Fig.5.7b, we plot L_{hard} against the IGM temperature. In contrast to Fig.5.7a, almost no correlation is visible. Therefore, a necessary condition for a group to have a high hard component luminosity is to have a high IGM luminosity, while the IGM temperature is irrelevant.

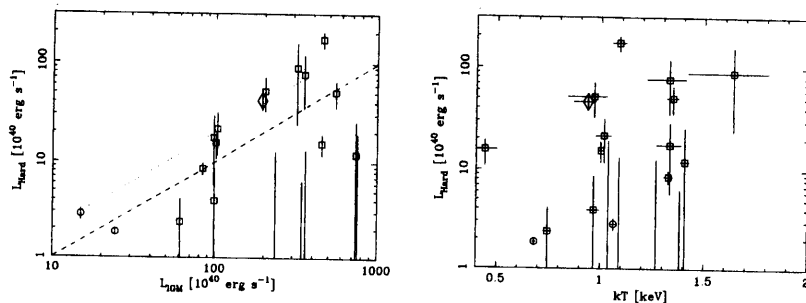


Figure 5.7: (a) The hard component luminosity (L_{hard}) plotted against that of the IGM (L_{IGM}). Dashed line represents the ratio of 10%, and dotted line 20%. (b) The hard component luminosity (L_{hard}) plotted against the IGM temperature. In both panels, symbols are the same as those in Fig.5.3.

5.3.2 The CXB fluctuation and the LMXB contribution

The fluctuation of the CXB surface brightness may contribute some amount to the hard X-ray component (see § 4.5.5). In Fig.5.8a, we plot the hard-IGM luminosity ratio against the group overall flux observed within the integration region. The CXB fluctuation calculated from equation 4.2 and converted into 2–10 keV flux is $1.7 \sim 3.3 \times 10^{-13} \text{ erg s}^{-1} \text{ cm}^{-2}$ for an integration region with $r = 10' \sim 20'$. Although the error bars get larger with decreasing overall flux, the hard excess emission significantly exceeds the CXB fluctuation level for most of the objects in our sample. Furthermore, there is no particular correlation between the two quantities. Thus, our result is little affected by the CXB fluctuation.

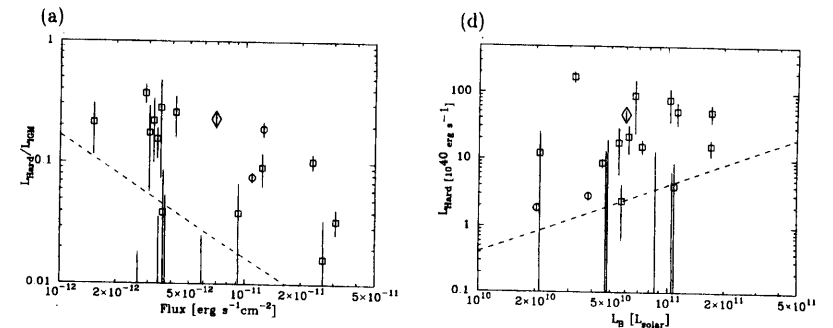


Figure 5.8: (a) The hard vs IGM luminosity ratio plotted against the full-band flux. Dashed line represents the typical fluctuation of the CXB flux, for an integration region with $r = 10'$. (b) The hard component luminosity (L_{hard}) plotted against the optical B -band luminosity. Dashed line represents the estimated contribution from LMXBs, calculated from equation 2.16. For both panels, symbols are the same as those in Fig.5.3.

In Fig.5.8b, we plot L_{hard} against the optical B -band luminosity of the group member galaxies listed in Table 5.1. We also display there the contribution from LMXBs in the member galaxies estimated using equation 2.16 (see § 2.2.4). Thus, the luminosity of the hard excess emission is about an order of magnitude higher than the LMXB component for most of the groups in our sample, although it is explained by the LMXB contribution in case of the elliptical galaxies and several groups (see also Fig.2.11).

5.4 Averaged Properties of HCG 97, RGH 80 and S49-147

Because the objects in our sample generally have poorer data statistics as compared to HCG 62, it is difficult to analyze their properties in further details individually. However, we may sum up data from several objects to improve the data quality. For this purpose, we selected three groups, HCG 97, RGH 80 and S49-147, which have properties similar to those of HCG 62 (see Fig.5.5). These objects have significant hard excess, which is generally well separated from the IGM emission, because of their relatively low temperature.

The summed spectra, with a cumulative exposure of 180 ksec, are presented in Fig.5.9. The fit with a single temperature vMEKAL model is unacceptable with reduced- $\chi^2 =$

164.47/68, which drastically decreases to 91.38/67 by introducing an additional power law component (vMEKAL+PL model). The latter fit results are listed in Table 5.5, and the best fit model is superposed on the spectra in Fig.5.9. Strictly speaking, the fit is not acceptable at 90% confidence, which may be due to the difference of the IGM parameters and redshifts among the three groups. When we set Γ free, its acceptance range is less constrained for the same reason, compared to the fit using the RGH 80 data alone (see § 5.2.3). However, in view of $\Delta\chi^2$, the hard component becomes more significant than in the fits to the individual spectra (Table 5.4), and the 2-10 keV hard component flux is determined with a better accuracy, as $31^{+5}_{-3}\%$ of the IGM flux. The hard component is dominant above 4 keV, and the photon counts in the 4-8 keV band is as much as 513.2 ± 99.6 ; this is twice the value from RGH 80 alone, and almost comparable to that of the HCG 62 listed in the last row of Table 4.9.

Table 5.5: Results of the joint fit to the GIS and SIS spectra averaged over HCG 97, RGH 80 and S49-147, with vMEKAL+PL model.

| kT (keV) | Abundance $Z_{\alpha}(Z_{\odot})$ | $Z_{\text{Fe}}(Z_{\odot})$ | $N_{\text{H}}^{(1)}$ | $z^{(2)}$ | Soft Flux | Hard Flux | $\chi^2/d.o.f$ | $\Delta\chi^2$ |
|------------------------|--------------------------------------|----------------------------|----------------------|-------------------------|--------------|------------------------|----------------|----------------|
| $1.03^{+0.03}_{-0.04}$ | $0.37^{+0.09}_{-0.07}$ | $0.20^{+0.03}_{-0.01}$ | $0.0^{+2.4}_{-0.0}$ | $0.019^{+0.01}_{-0.01}$ | 1.61 | $0.50^{+0.08}_{-0.05}$ | 91.38/67 | -73.09 |

(1) Fitted column density, in 10^{20} cm^{-2} . (2) Fitted redshift.

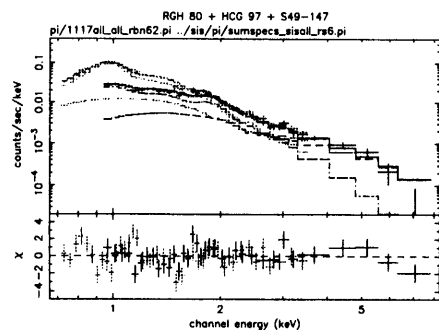


Figure 5.9: The averaged spectra summed over HCG 97, RGH 80 and S49-147, fitted with the vMEKAL+PL model.

Similarly, we have examined the radial profile, summed over the three objects, for

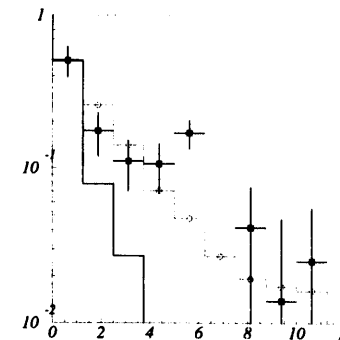


Figure 5.10: The azimuthally averaged radial surface brightness profile, similar to Fig.4.14b of HCG 62. The data from HCG 97, RGH 80 and S49-147 are averaged. The profiles in 4.0-8.0 keV (filled boxes), 0.5-4.0 keV (open circles with histograms), and the PSF of XRT+GIS in the 4.0-8.0 keV band (thick solid histograms) are plotted.

angular extent. The extent of the IGM emission of HCG 97 and RGH 80 is roughly similar, with FWHM of $\sim 4'$ on the GIS image, while that of S49-147 has a FWHM of $\sim 12'$. We therefore scaled the latter image by a factor of 1/3, generated radial profiles for all three groups, and then added them. The result is plotted in Fig.5.10. The 4-8 keV band profile is significantly more extended than the PSF of XRT+GIS, and resembles that of the IGM emission. These properties are similar to the results from HCG 62 (see § 4.4.2), supporting that the hard excess emission in these three groups is the same phenomenon as that in HCG 62.

5.5 Brief Summary of the Analysis of 17 Groups

Following the results from HCG 62, we have analyzed additional 17 groups selected from the ASCA data available. About half the selected groups have been shown to host significant hard emission (§ 5.2.2), which cannot be explained by either the LMXB contribution from the group member galaxies or the fluctuation of the CXB surface brightness (§ 5.3.2). It shows little correlation with the IGM temperature or flux, eliminating the possible systematics due to the IGM modeling error. The hard component luminosity (L_{hard}) shows

clear upper-limit defined as $\sim 30\%$ of the IGM luminosity (§ 5.3.1).

We also analyzed the averaged data of the three groups (HCG 97, RGH 80 and S49-147) with spectral properties similar to HCG 62, and showed that the hard component is distinct from the IGM component. Furthermore, we confirmed that the radial extent of the hard component is significantly extended than the XRT+GIS PSF, as much as the IGM emission (§ 5.4). The average properties of these three groups generally resemble those of HCG 62.

Chapter 6

Discussion

6.1 Observed Properties of the Hard X-ray Emission

We detected excess hard X-rays from about half of the 18 selected groups observed with ASCA. Among them, the HCG 62 group exhibits the most statistically significant hard excess emission, which is clearly extended with its radial profile similar to or rather wider than that of the IGM brightness (§ 4.4.2). Assuming a distance of $58.4h_{75}^{-1}$ Mpc, the 2-10 keV luminosity of the hard emission is $4.18_{-0.85}^{+0.70} \times 10^{41} h_{75}^{-2}$ erg s^{-1} , which is $21.4_{-4.1}^{+3.8}\%$ of the IGM luminosity in the 0.5-10 keV band (§ 4.3.4). When fitted with a power-law spectra, the photon index Γ is not well constrained, $\Gamma = 1.55_{-0.89}^{+1.21}$ (§ 4.3.4). If we adopt a thermal interpretation, the inferred temperature becomes $kT = 32.0_{-26.3}^{+\infty}$ keV, implying a lower limit of 5.7 keV.

Other ~ 9 groups also exhibit evidence for a hard emission, with the 2-10 keV luminosity of the hard X-rays being $1 \sim 18 \times 10^{41} h_{75}^{-2}$ erg s^{-1} , which is $10 \sim 40\%$ of the IGM luminosity. On the other hand, the remaining 8 groups exhibit little evidence for excess hard emission, with typical upper limit luminosity of $\sim 5\%$ of the IGM component (§ 5.3.1).

6.2 Comparison with Cluster Hard X-ray Emission

In this section, we compare our results with those of the three clusters, Coma, A2256 and A2199, which are reported to host a non-thermal emission (see § 2.4.2).

The spectral shape, i.e., the photon index, of the non-thermal component detected in the three clusters are as poorly constrained as the hard X-ray emission from our group sample, and are generally consistent with $\Gamma = 2.0$, adopted for our analysis. To compare

the luminosities, we must convert the cluster quantities to those in more appropriate energy bands. For the hard component with $\Gamma = 2.0$, the 20–80 keV luminosity is nearly equivalent to that in the 2–10 keV band. For the hot gas component (ICM or IGM), the 0.5–10 keV range adopted for groups is equivalent to an energy range of $(0.5–10)kT$, since $kT \sim 1$ keV for most of our sample. We hence adopted this kT -dependent energy ranges in calculating the cluster ICM luminosities, and found them similar to the 2–10 keV values for the particular three clusters. We thus simply use the raw values listed in Table 2.4.

In Fig.6.1a, we plot the luminosities of the hard component against those of the hot gas component, including all groups in our sample and the three clusters. The hard-ICM luminosity ratio of the three clusters ranges from 7% to 23%, similar to the values of the groups with hard X-ray emission. In Fig.6.1b, we plot the luminosity of the hard component against the IGM (or ICM) temperature. There, we can see a general correlation between the two quantities, roughly as $L_{\text{hard}} \propto (kT)^3$, which was not obvious without including the clusters. This relation reflects the $kT - L_X$ relation generally found in clusters and groups (§ 2.2.3), combined with the result from Fig.6.1a. From these results, the group hard excess emission and that of the three clusters are considered to be generally similar in view of their luminosity ratio against that of the hot gas component.

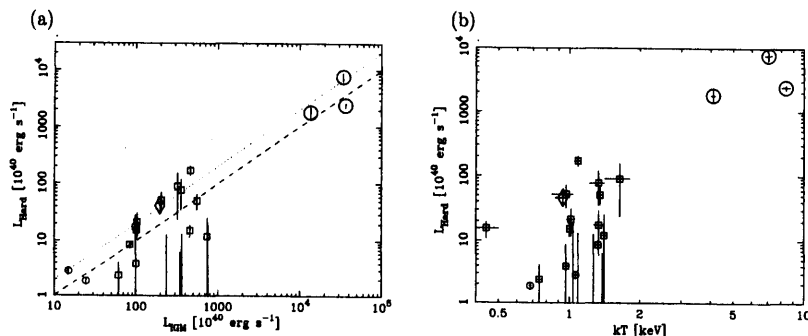


Figure 6.1: The hard component luminosity plotted against the (a) luminosity and (b) temperature of the hot gas component. Those plots are the same as Fig.5.7, but includes the three clusters (large circles) with significant excess hard X-ray emission.

In the following sections, we examine several possible mechanisms for the hard X-ray production in groups of galaxies, sometimes in comparison with those from the three clusters. We constrain relevant physical quantities involved in each mechanism, based on

the observed properties of our sample groups, in particular, HCG 62.

6.3 Inverse Compton Scattering

6.3.1 Derived parameters

One possible interpretation of the hard X-rays is to assume that relativistic electrons are scattering off some soft seed photons via IC process and boost them into hard X-rays (see § 2.3.3). The seed photons are considered to be supplied by the CMB, because the energy density of the CMB photons, $U_{\text{CMB}} = 4.2 \times 10^{-13}(1+z)^4$ erg cm $^{-3}$, is more than an order of magnitude higher than that of the star-light, except at the very center ($R \sim 10$ kpc) of HCG 62. Because the representative CMB photon energy is $\sim 7 \times 10^{-4}$ eV, the Lorentz factor of the electrons required to generate 10 keV IC photons is $\gamma \sim 3.4 \times 10^3$ from equation 2.21. This implies a cooling time of $\tau_{\text{cool}} \sim 7 \times 10^8$ yr, considering only the energy loss due to the IC scattering.

The hard component in HCG 62 and other groups is well fitted by a power law with a photon index of $\Gamma = 2.0$, or an energy index of $\alpha = \Gamma - 1 = 1.0$. This value is generally consistent with the radio halo spectra (§ 2.4.1). The implied electron number index (equation 2.17) of $\mu = 2\alpha + 1 = 3.0$ (see § 2.3.3), is comparable to the cosmic ray electron spectrum at the top of the earth's atmosphere. For these reasons, we adopt $\alpha = 1.0$ and $\mu = 3.0$ for the moment.

Then, equation 2.23 is re-written as

$$\frac{dL_{\text{IC}}}{d\nu} = 5.55 \times 10^{-27} \frac{N_0}{\nu} \text{ [erg s}^{-1} \text{ Hz}^{-1}] \quad (6.1)$$

As the hard component luminosity in the 2–10 keV band is 4.2×10^{41} erg s $^{-1}$ for HCG 62, we obtain $N_0 = 4.72 \times 10^{67}$ in number.

The relativistic electrons produce at the same time synchrotron emission by interacting with a magnetic field (§ 2.3.2). From equation 2.18, the Lorentz factor of the electron required to generate 1.4 GHz radio emission is $\gamma = 1.8 \times 10^4 \left(\frac{B}{\mu\text{G}}\right)^{-1/2}$. This in turn implies a cooling time of $\tau_{\text{cool}} \sim 1 \times 10^8 \left(\frac{B}{\mu\text{G}}\right)^{1/2}$ yr, which is also defined mainly by the IC scattering process (see Fig.2.12).

From $\mu = 3.0$, $\nu = 1.4$ GHz and $N_0 = 4.72 \times 10^{67}$, the synchrotron luminosity is derived as $2.65 \times 10^{31} \left(\frac{B}{\mu\text{G}}\right)^2$ erg s $^{-1}$, using equation 2.20. At the distance of $58.4 h_{75}^{-1}$ Mpc, its flux at 1.4 GHz is thus estimated as

$$f(1.4 \text{ GHz}) = 6.85 \left(\frac{B}{\mu\text{G}}\right)^2 \text{ [Jy]} \quad (6.2)$$

Here, $1 \text{ Jy} = 1 \times 10^{-23} \text{ erg s}^{-1} \text{ cm}^{-2} \text{ Hz}^{-1}$.

6.3.2 Comparison with radio observations

The synchrotron flux predicted by equation 6.2 is rather high (see Table 2.2): the most crucial test of the IC scenario is whether this prediction is consistent with radio observations. We accordingly examined the radio all sky maps and catalogs for the possible radio halo around HCG 62.

We first used the NRAO VLA Sky Survey (NVSS), which presents the sky image in 1.4 GHz radio band, and a catalog of sources brighter than $\sim 2.5 \text{ mJy}$ detected in the image (Condon et al. 1998, <http://www.nrao.edu>). As the synchrotron emission should be as extended as the hard X-rays, it will have a size of $\sim 15'$. We present the NVSS image of HCG 62 in Fig.6.2. There are 10 sources within $15'$ from HCG 62 in the NVSS catalog, all of which are discrete sources. The integrated flux within $r = 15'$ is $\sim 83.5 \text{ mJy}$, while the sum of fluxes of the 10 sources are 118 mJy . Therefore, no diffuse emission is detected by NVSS.

Table 6.1: Radio observations of the HCG 62 sky field.

| name | $\nu^{(1)}$ | beam size | halo flux ⁽²⁾ | halo flux in 1.4 GHz ⁽³⁾ |
|-------|-------------|--------------|--------------------------|--|
| NVSS | 1.4 GHz | 45" | ~ 0 (no detection) | ~ 0 |
| PMN | 4.85 GHz | 4'.2 | < 40 (no detection) | < 138 |
| Texas | 365 MHz | 4' \sim 7' | < 250 (no detection) | < 66 |

(1) Observation frequency.

(2) Observed (upper limit) flux at the observation frequency in mJy.

(3) Observed (upper limit) flux converted to 1.4 GHz assuming $\alpha = 1.0$, in mJy.

NVSS is not sensitive to sources extended more than a few times the $\theta = 45''$ (FWHM) beam-width (Condon et al. 1998). For example, Coma-C is not visible in the NVSS image. Therefore, we searched two other catalogs, the Parkes-MIT-NRAO (PMN) Surveys at 4.85 GHz (e.g., Griffith and Wright 1993), and the Texas Survey at 365 MHz (Douglas et al. 1996), for emission from HCG 62. The former has a beam size of 4'.2 (FWHM) and a flux limit of $\sim 40 \text{ mJy}$, which corresponds to $\sim 138 \text{ mJy}$ at 1.4 GHz assuming $\alpha = 1.0$. The latter has a beam size of 4' \sim 7' and a flux limit of $\sim 250 \text{ mJy}$, which corresponds to $\sim 66 \text{ mJy}$ at 1.4 GHz. Parameters of these catalogs are summarized in Table 6.1. We found no counterpart of HCG 62 in either catalog.

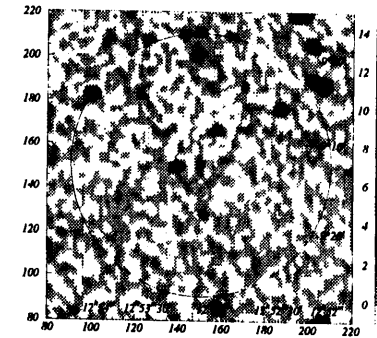


Figure 6.2: The 1.4 GHz radio image of HCG 62 from NVSS. The scale levels are shown in the right side, in units of mJy arcmin^{-2} . Solid circle represents $r = 15'$ from the group center.

As these two surveys have a relatively wide beam-size, in contrast to the NVSS, a halo with $r \sim 15'$ should have been detected, if its flux level exceeds the survey limits. The latter survey with lower frequency provides the most strict constraints. Thus, we found no signature of a synchrotron halo in HCG 62, and quote here a conservative upper-limit of 100 mJy at 1.4 GHz. From equation 6.2, the upper limit of the group averaged magnetic field is derived to be

$$B < 0.12 \text{ } [\mu\text{G}] \text{ ,} \quad (6.3)$$

assuming that the IC interpretation is correct.

6.3.3 Total energies and energy densities

As we have derived the number density of relativistic electrons (§ 6.3.1) and the upper-limit of the magnetic field (§ 6.3.2), we can estimate the total energy of these non-thermal components, and compare them with that of the thermal component.

The total energy of the thermal component can be estimated from the mass and temperature of the IGM. From the IGM surface brightness profile of HCG 62, the total number of thermal proton is derived to be $N_{\text{tot}}^{\text{th}} = 5.9 \times 10^{68}$ within $R = 250 \text{ kpc}$. Here, 250 kpc corresponds to $15'$ for HCG 62. This gives the average proton density of 3.0×10^{-4}

cm⁻³. The total thermal energy of the hot plasma is then

$$E_{\text{tot}}^{\text{th}} \sim \frac{3}{2} (2 \times N_{\text{tot}}^{\text{th}} \times kT) = 2.8 \times 10^{60} \text{ [erg]} \quad (6.4)$$

Assuming a sphere of radius $R = 250$ kpc, the average thermal energy density becomes $U^{\text{th}} = 1.4 \times 10^{-12}$ erg cm⁻³.

The total energy of the relativistic electron can be derived by integrating equation 2.17 multiplied by $\gamma m_e c^2$, as

$$E_{\text{tot}}^{\text{CR}} = \int_{\gamma_{\text{min}}}^{\infty} N_0 \frac{\gamma m_e c^2}{\gamma^3} d\gamma = 3.86 \times 10^{58} \left(\frac{1000}{\gamma_{\text{min}}} \right) \text{ [erg]} \quad (6.5)$$

Assuming the same sphere, the average relativistic electron energy density becomes $U^{\text{CR}} = 2.0 \times 10^{-14} \left(\frac{1000}{\gamma_{\text{min}}} \right)$ erg cm⁻³. For the magnetic field, the energy density is derived as

$$U^{\text{B}} = \frac{1}{8\pi} B^2 = 5.7 \times 10^{-16} \left(\frac{B}{0.12 \mu\text{G}} \right)^2 \text{ [erg cm}^{-3}] \quad (6.6)$$

Thus the total magnetic energy in the same sphere is $E_{\text{tot}}^{\text{B}} = 1.1 \times 10^{57} \left(\frac{B}{0.12 \mu\text{G}} \right)$ erg, if the IC interpretation is true. We summarized all these results in Table 6.2.

Table 6.2: The energy density of the thermal and non-thermal components in HCG 62, derived from the IC model.

| | Total energy [erg] | Energy density ⁽¹⁾ [erg cm ⁻³] |
|-----------------------|--|---|
| thermal | 2.8×10^{60} | 1.4×10^{-12} |
| relativistic electron | $3.9 \times 10^{58} \left(\frac{1000}{\gamma_{\text{min}}} \right)$ | $2.0 \times 10^{-14} \left(\frac{1000}{\gamma_{\text{min}}} \right)$ |
| magnetic field | $1.1 \times 10^{57} \left(\frac{B}{0.12 \mu\text{G}} \right)$ | $5.7 \times 10^{-16} \left(\frac{B}{0.12 \mu\text{G}} \right)$ |

(1) Energy density averaged in a sphere of $R = 250$ kpc.

In Table 6.3 and Fig.6.3, we compare energetics of HCG 62 and the three clusters, assuming that the IC interpretation is correct. The non-thermal energy is dominated by the relativistic electrons. The ratio of the non-thermal energy to the thermal one is similar in all four objects, which is $\sim 0.4 \left(\frac{1000}{\gamma_{\text{min}}} \right) \%$. Here, we take $\gamma_{\text{min}} = 1000$, because it is generally used in the cluster analysis (e.g. Fusco-Femiano et al. 2000). However, we notice that the γ_{min} may be smaller. From the average hot gas density of 3.0×10^{-4} cm⁻³, and the magnetic strength of $B < 0.12 \mu\text{G}$, the cooling time of the relativistic electrons in HCG 62 is longest at $\gamma = 100$ (see Fig.2.12b). Therefore, γ_{min} may well be as low as ~ 100 , and consequently, the non-thermal energy may be an order of magnitude higher.

Table 6.3: The total energy of the thermal and non-thermal components in HCG 62 and the three clusters, derived from the IC model.

| name | integration ⁽¹⁾ radius [Mpc] | $E_{\text{tot}}^{\text{th}}$ ⁽²⁾ [erg] | $E_{\text{tot}}^{\text{CR}}$ ⁽³⁾ $\left(\frac{1000}{\gamma_{\text{min}}} \right) \times$ [erg] | $E_{\text{tot}}^{\text{B}}$ ⁽⁴⁾ [erg] |
|-------------|--|--|---|---|
| Coma | 2.1 | 9.4×10^{63} | 5.8×10^{60} | $8.4 \times 10^{59} \left(\frac{B}{0.14 \mu\text{G}} \right)^2$ |
| A2256 | 2.1 | 9.4×10^{63} | 1.9×10^{61} | $3.7 \times 10^{59} \left(\frac{B}{0.05 \mu\text{G}} \right)^2$ |
| A2199 | 1.5 | 1.7×10^{63} | 4.3×10^{60} | $8.8 \times 10^{58} \left(\frac{B}{0.075 \mu\text{G}} \right)^2$ |
| HCG 62 | 0.50 | 1.1×10^{61} | 3.9×10^{58} | $8.8 \times 10^{57} \left(\frac{B}{0.12 \mu\text{G}} \right)^2$ |
| ($r=15'$) | 0.25 | 2.8×10^{60} | 3.9×10^{58} | $1.1 \times 10^{57} \left(\frac{B}{0.12 \mu\text{G}} \right)^2$ |

(1) Integration radius defined as $r = 1.58 h_{75}^{-1} \text{ Mpc} \left(\frac{kT}{10 \text{ keV}} \right)^{1/2}$ (Mohr et al. 1999). For HCG 62, the radius of the analysis region ~ 250 kpc is also used.

(2) The total thermal energy within the integration radius, derived by converting the parameters listed in Mohr et al. (1999).

(3) Relativistic electron energy derived from the hard component luminosity (Table 2.4), assuming an electron number index $\mu = 3$.

(4) Magnetic field energy within the integration radius. Field strength derived by comparing the hard X-ray emission and the radio halo, taken from; Fusco-Femiano et al. (1999) for Coma, Fusco-Femiano et al. (2000) for A2256, and Kempner and Sarazin (2000) for A2199.

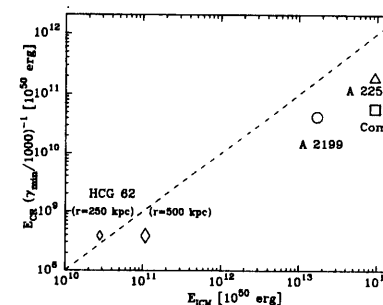


Figure 6.3: The total non-thermal energy plotted against that of the thermal component. Dotted line represents a ratio of $1 \left(\frac{1000}{\gamma_{\text{min}}} \right) \%$.

6.3.4 Examination of the model

The IC interpretation provides a reasonable account of the observed excess hard X-ray emission from groups of galaxies, at least in terms of the implied non-thermal energy content, and various similarities to the hard X-ray emission from the three clusters. However, the scenario involves a serious problem, that the inferred upper limit on the magnetic field, $B = 0.12 \mu\text{G}$ derived in § 6.3.2, clearly contradicts the generally accepted values of the intra-cluster magnetic fields. For example, observations of Faraday rotation of radio sources inside or behind clusters yield the line-averaged intra-cluster magnetic field intensity of

$$B = (1 \sim 10) \times \left(\frac{l}{10 \text{ kpc}} \right)^{-1/2} h_{75}^{1/2} \mu\text{G} ,$$

where $l = 1 \sim 10$ kpc is the field correlation length (e.g. Kim et al. 1991, Clarke et al. 2000). The IC hypothesis of the cluster hard X-rays leads essentially to the same discrepancy (Coma, Fusco-Femiano et al. 1999: A2245, Fusco-Femiano et al. 2000: A2199, Kempner and Sarazin 2000).

Strictly speaking, no Faraday-rotation measurements are yet available for HCG 62. In fact, clusters with the observed Faraday rotation are limited to the brightest ones with the ICM temperature ranging $2.3 \sim 10$ keV (Kim et al. 1991). No correlation between the ICM temperature and the magnetic field strength has so far been reported. Therefore, we do not have any independent information on the magnetic field in HCG 62, and the inferred low values of $B < 0.1 \mu\text{G}$ may not be a problem in itself. Nevertheless, the implied magnetic pressure in HCG 62 falls by more than three orders of magnitude below the IGM gas pressure (Table 6.2). It would be extremely difficult to suppress the magnetic pressure to such an extremely low level, since the member galaxies are moving with trans-sonic speed in the intra-groups space and must be continuously exciting the plasma turbulence (Makishima 2000).

Then, can we somehow avoid this difficulty? If we increased the electron number index μ from 3 to 4, the estimated flux of synchrotron emission would decrease by a factor of ~ 5 at 365 MHz, and the magnetic field upper limit would increase to $0.27 \mu\text{G}$. This is however still insufficient. A more promising way is to give up the homogeneous picture which we have implicitly assumed (e.g. Fusco-Femiano et al. 1999). We may presume that the magnetic field forms a number of compressed thin flux tubes where the field strengths reach micro-Gauss level, while the field may be relatively weak (e.g., sub-micro-Gauss level) outside them. Since the IGM will permeate both inside and outside the flux tubes, a strong Faraday rotation can be produced inside them. If furthermore the relativistic

electrons are somehow kept outside the flux tubes, they will not emit strong synchrotron emission while producing significant IC emission. Such condition may be realized if the electrons are accelerated by magnetic reconnection that takes place near magnetic neutral sheets. Quantitatively, a magnetic-field segregation by a factor of $10 \sim 100$ may be able to solve the problem. This may not be unrealistic, since a similar condition is clearly realized in the solar corona.

We further examined whether the radial profile of the hard component observed with the GIS can constrain the emission mechanisms. If the non-thermal electron has a distribution similar to that of the IGM, the IC emissivity will be proportional to the IGM density itself, because the energy density of the CMB photon is constant. This is in contrast to the IGM emission profile which is proportional to the square of its density. In Fig.6.4, we plot the observed 4-8 keV radial profile of HCG 62 divided by that of the simulated hard component which has the same radial profile as the IGM emission. The dot-dashed line represents the predicted ratio when the emissivity is proportional to the gas density. The prediction is generally consistent with the data profile, except at the innermost region of $r < 2'$. However, it is also consistent with being flat (dashed line). Thus the both possibilities remain.

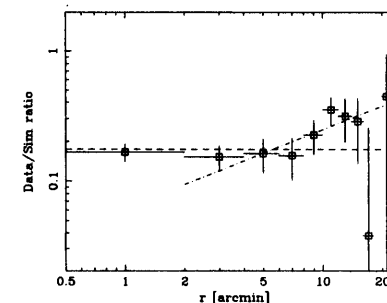


Figure 6.4: The ratio of the observed 4-8 keV radial profile and that of the simulation. See text for details.

In summary, the IC interpretation, otherwise reasonable, requires unrealistically low magnetic fields of $\sim 0.1 \mu\text{G}$. In order for the IC interpretation to be the right answer, a highly inhomogeneous magnetic field may be required. The energy density of the relativistic electrons amount to $0.4 \sim 4\%$ of that of the thermal component, depending on the lower cut off energy of the electrons.

6.4 Non Thermal Bremsstrahlung

An alternative interpretation of the hard X-rays is the non-thermal bremsstrahlung (NTB) emission from suprathermal electrons (see § 2.3.4). In this case, we do not need to worry about the magnetic field, since such electrons do not produce synchrotron radio emission.

Here again we take a model with $\alpha = 1$, which implies the electron number index in momentum of $\mu = 2$ (see equation 2.25). From the average hot gas density of $3.0 \times 10^{-4} \text{ cm}^{-3}$, equation 2.27 gives

$$\frac{dL_c}{d\epsilon} = 1.13 \times 10^{-26} N_0 \left(\frac{1}{\epsilon}\right) \text{ [erg s}^{-1} \text{ cm}^{-2} \text{ erg}^{-1}] \quad (6.7)$$

Then, for the HCG 62 parameters, this gives $N_0 = 2.31 \times 10^{67}$. As we have mentioned in § 2.3.4, this value is an overestimate by a factor of ~ 2 , due to the trans-relativistic effects (Sarazin and Kempner 2000). Thus, the corrected value becomes $N_0 = 1.15 \times 10^{67}$.

Following Sarazin and Kempner (2000), we took the lower cut off energy of the suprathermal electron to be $3kT = 3 \text{ keV}$, which gives $p = \sqrt{(1 + (3kT)/(m_e c^2))^2 - 1} = 0.11$. If we integrate the energy of these electrons up to 100 keV ($p = 0.65$), their total energy is derived to be

$$E_{\text{tot}}^{\text{NTB}} = \int_{0.11}^{0.65} N_0 m_e c^2 \frac{\sqrt{p^2 + 1} - 1}{p^2} dp = 3.2 \times 10^{60} \text{ [erg]} \quad (6.8)$$

This value is comparable to that of the thermal component (see equation 6.4). If we substitute $\mu = 2$ with $\mu = 3$, the total energy becomes $2.6 \times 10^{60} \text{ erg}$, which is almost unchanged. Thus, the non-thermal bremsstrahlung interpretation leads to a rather high non-thermal energy density. The non-thermal pressure will greatly affect the mass estimate relying only on the IGM profile, and the total gravitating mass M_{tot} will increase by a factor of ~ 2 . In this case, the velocity dispersion of the member galaxies (376 km s^{-1} ; see § 4.1.1) is $1/\sqrt{2}$ times short of the required value, which is still within the scatter of the $kT - \sigma$ relation (§ 2.2.3).

The biggest difficulty with the NTB scenario is that the suprathermal electrons suffer a great amount of Coulomb loss due to electron-electron encounter in the thermal plasma (§ 2.3.5). For a 100 keV electron, the Coulomb loss rate is $\sim 10^4$ times higher than the bremsstrahlung loss rate. Accordingly, the cooling time of such an electron becomes as short as $\sim 1 \times 10^8 \text{ yr}$ when we include the Coulomb interactions, while it was $\sim 1 \times 10^{12} \text{ yr}$ when considering the NTB only. In other words, most of the energy input will eventually be used to heat up the IGM, rather than in radiating NTB photons (e.g. Petrosian 2000). Because the radiative cooling time of the IGM is generally longer than $\sim 10^{10} \text{ yr}$,

the IGM temperature will increase by 1 keV within $\sim 10^9 \text{ yr}$. The groups with excess hard emission would then exhibit systematically higher temperature than those without it, leading to a difference in β_{spec} (equation 2.15). However, within the available rather limited information, we find no such a systematic difference between the two types of groups. Even if this theoretical prediction is somehow reconciled with the observation, a still more serious problem is how to supply such a large amount of heating/acceleration energy. Since the NTB loss and the Coulomb loss are both directly proportional to the IGM density, the problem cannot be avoided by changing the IGM density.

In summary, the NTB interpretation requires the total energy of the suprathermal electron to be comparable to the thermal energy, together with relatively short ($\sim 10^8 \text{ yr}$) cooling time. Because most of the electron energy is dissipated by Coulomb collision rather than the bremsstrahlung emission, the IGM must be significantly heated, which is not observed. Furthermore, the energy source would become a serious problem. Therefore, the NTB interpretation seems to be rather implausible, though not completely impossible.

6.5 Thermal Interpretation

Although we have so far considered non-thermal interpretations of the excess hard X-ray emission, its observed properties also allow an interpretation in terms of a thermal emission with high temperature, $kT = 2 \sim 10 \text{ keV}$. The normalization of a thermal emission is given in terms of emission integral (EI), which is expressed as a volume integration of proton density multiplied with that of electron. When we fit the spectra of HCG 62 with a sum of a $kT \sim 1 \text{ keV}$ vMEKAL component and a $kT = 10 \text{ keV}$ bremsstrahlung component, the relative emission integral of the two components is derived to be $EI_{\text{hard}}/EI_{\text{IGM}} = 0.12$. In an isothermal and uniform hot plasma, the emission integral is given by $EI = (N_{\text{proton}} \times N_e)/V$, where N_{proton} and N_e is the total proton and electron number in the volume V , respectively. Assuming a pure hydrogen plasma, the ratio of the emission integral can be re-written as

$$\kappa \equiv \frac{(N_{\text{hard}}^2/V_{\text{hard}})}{(N_{\text{IGM}}^2/V_{\text{IGM}})} = 0.12 \quad (6.9)$$

Here, N_{IGM} and N_{hard} are the total electron (=proton) number of the soft and hard components, respectively, and V_{IGM} and V_{hard} is the volume filled with the corresponding component.

When we assume a pressure balance between the two components, the condition is expressed as $\frac{N_{\text{hard}}}{V_{\text{hard}}} \times T_{\text{hard}} = \frac{N_{\text{IGM}}}{V_{\text{IGM}}} \times T_{\text{IGM}}$. Then, the filling factor of the hot (hard)

component, defined as $\eta = V_{\text{hard}}/V_{\text{IGM}}$, can be described as

$$\eta = \kappa \times \left(\frac{T_{\text{hard}}}{T_{\text{IGM}}} \right)^2 \sim 10 \quad (6.10)$$

This means that the hard component dominates the whole volume. In other words, the plasma emitting the $kT \sim 1$ keV component is not the “real” IGM, and the $kT \sim 10$ keV component instead traces the gravitational potential. However, this clearly contradicts the optical velocity dispersion measurements, as already mentioned in § 4.3.2. Therefore, in case of HCG 62, the thermal interpretation under the pressure balance assumption is not realistic. When T_{hard} is as low as ~ 3 keV, and κ is relatively small, this interpretation may work.

When we alternatively assume that the hard component is confined in some small regions by a magnetic field, what is the required field strength? Here, we take the filling factor η to be 0.1, as a tentative value. Because the total number of the IGM particle is derived as $N_{\text{IGM}} = 5.85 \times 10^{68}$ (§ 6.3.3), equation 6.9 gives $N_{\text{hard}} \sim 6.5 \times 10^{67} (\frac{\eta}{0.1})^{-1/2}$. Then the total energy of the hard component becomes $E_{\text{tot}}^{\text{hard}} = 3.1 \times 10^{60} (\frac{\eta}{0.1})^{-1/2}$ erg, which implies the energy density of $U_{\text{hard}} = 1.6 \times 10^{-11} (\frac{\eta}{0.1})^{-1/2}$ erg cm⁻³. Thus, the required magnetic field strength is about $20 (\frac{\eta}{0.1})^{-1/4}$ μG . This value seems to be rather high, although there are no observational results contradicting it.

In summary, the thermal interpretation does not work under the assumption of pressure balance, at least for the groups of which the hard emission is relatively luminous and requires a high (~ 10 keV) temperature, such as the HCG 62 group. The three clusters are in the same situation. It may work, however, for the groups of which the hard emission is relatively weak and allows a relatively lower (~ 3 keV) temperature, such as the NGC 1399 group. As an alternative to the pressure balance assumption, we may speculate that magnetic fields of 20 μG or higher confine the hard component. This scenario might work, depending on the required filling factor.

6.6 Candidates for Acceleration and Heating Mechanisms

Since every emission mechanism discussed so far requires the presence of either relativistic or semi-relativistic particles, a significant particle acceleration or heating must be in progress in some, if not all, groups of galaxies. Our final task in the present thesis is to discuss possible acceleration/heating mechanisms and the available energy source. For the IC and thermal interpretation, the required energy input rate (luminosity) is comparable to the observed hard X-ray luminosity, although it must actually be $2 \sim 10$ times higher due to the limited energy range (2–10 keV) of our analysis. On the other hand, for the NTB interpretation, the actual energy loss rate must be about four orders of magnitude higher than the observed hard X-ray luminosity, due to the Coulomb loss. Therefore, we need $\sim 10^{42}$ erg s⁻¹ as a minimum energy input rate for the IC and thermal interpretations, whereas $\sim 10^{45-46}$ erg s⁻¹ for the NTB interpretation. Below we briefly review several candidates for the acceleration or heating source, including: the supernova (SN), the active galactic nucleus (AGN), kinetic energy of the group member galaxies, and group merger events. Here again, we mainly take HCG 62 as a template.

6.6.1 Super novae

A supernova (SN) produces an explosion energy of $\sim 10^{51}$ erg, and can accelerate cosmic rays up to ~ 100 TeV, as observed in SN 1006 (§ 2.5.1). Therefore, it may be the origin of the hard component. To account for a luminosity of $\sim 10^{42}$ erg s⁻¹, we need a SN rate of $0.3 (\frac{f_c}{0.1})^{-1}$ SNe yr⁻¹. Here, f_c is the average conversion efficiency of the the SN explosion energy to the particle acceleration, which ranges from a few % up to $\sim 50\%$, depending on the models (e.g., Berezhinsky et al. 1997, Ellison et al. 2000). From the optical luminosity of the member galaxies in HCG 62 ($L_B = 6.0 \times 10^{10} L_\odot$; Carvalho et al. 1997), the SN rate is estimated to be relatively low, 0.06 SNe yr⁻¹ (e.g., van-den-Berg and Tanman 1991), since there is no evidence for ongoing rapid star formation activity in HCG 62 (e.g. Verdes-Montenegro et al. 1998). Therefore, the SN scenario can marginally explain the energy input required by HCG 62, on condition that f_c is relatively high.

The hard component luminosity (L_{hard}) in fact varies among the groups by an order of magnitude, with no correlation to the their optical luminosities (see Fig.5.8b). This leaves a room for the possibility that the phenomenon is transient rather than steady, and we are observing an after effect of a strong star forming activity in the past. In order

for this scenario to be valid, the putative star forming activity should have taken place within $\sim 10^9$ yr, considering the cooling time of $\tau_{\text{cool}} = 7 \times 10^8$ yr estimated for electrons with $\gamma = 3.4 \times 10^3$ (§ 6.3.1). There is yet another possibility that the SN rate significantly differs among the groups.

In short, the SN origin may work for the IC and thermal scenarios. However, for the NTB interpretation, the required SN rate, $300(\frac{L}{L_{6.1}})^{-1} \text{ SNe yr}^{-1}$, is too high to be realistic.

6.6.2 Active galactic nucleus

Another possibility is the active galactic nucleus (AGNs) hosted in the member galaxies (see § 2.2.4). It can produce a radio lobe filled with ~ 10 GeV electrons, as observed in Fornax-A (§2.5.3). When matter accretes onto a massive black hole that is thought to be the nature of the AGN, $\sim 10\%$ of the rest mass energy of the accreting matter will be converted into heating or acceleration of particles (Ensslin et al. 1998). This is sometimes observed as jets and halos of the AGNs. The scenario works even though we do not see obvious AGNs at present in these groups, on condition that the past AGN activity was sufficiently high. Specifically, a black hole with a typical mass of $10^7 M_{\odot}$ can generate a high energy particles with a total energy of $\sim 2 \times 10^{61}$ erg, over its typical formation epoch of $\sim 10^8$ yr (e.g. Valagas and Silk 1999). This value is sufficient for all three emission models discussed in § 6.3~6.5.

While the AGN scenario is thus promising from the energetics viewpoint, problems remain as to the actual energy transfer from the AGNs to the intra-group space. In the case of the Fornax-A radio lobes, the emission mechanism of the hard X-rays is the IC process. From its radio and X-ray luminosity, Kaneda et al. (1995) found that the magnetic field is as strong as $\sim 3\mu\text{G}$, which is an order of magnitude higher than those estimated from HCG 62 and the three clusters (see Table 6.3). This cannot be explained by the decay of the magnetic field, because its life time is sufficiently long (e.g. Tribble 1993). Moreover, the size of a radio lobe is ~ 100 kpc, which is an order of magnitude smaller than the radio halo, such as Coma-C. As the electron dissipation within the ICM is quite limited (e.g. Sarazin 1988), the lobe remnant cannot by itself form a cluster-wide halo. From these reasons, for the AGN to be the origin of the hard component, we need some mechanisms other than those working in the radio lobes.

6.6.3 Galaxy motion

Yet another candidate for the origin of the hard component is the huge kinetic energy contained in the groups and clusters, in the form of random motion of galaxies.

Galaxies with a total luminosity of $L_B = 6 \times 10^{10} L_{\odot}$ have a total stellar component mass of $M_{\text{star}}^{\text{gal}} = 5 \times 10^{11} M_{\odot}$, assuming $M_{\text{star}}/L_{\odot} = 8$ in solar units. When these galaxies are moving in the intra-group space with a line-of sight velocity dispersion of 400 km s^{-1} , they have three dimensional velocity of $v \sim 700 \text{ km s}^{-1}$. Thus, their kinetic energy becomes as much as $\frac{1}{2} M_{\text{star}}^{\text{gal}} \times (700 \text{ km s}^{-1})^2 = 2.5 \times 10^{60}$ erg. This is taken as a typical value for the member galaxies in HCG 62. If $\sim 10\%$ of this energy is converted into particle acceleration, it is sufficient to supply $1 \times 10^{42} \text{ erg s}^{-1}$ for as long as the Hubble time. Therefore, this picture may potentially be successful for the IC and thermal scenarios.

If we include the possible dark-halo component associated with each galaxy, the estimated heating luminosity further increases. However, even this increased kinetic energy must be dissipated within $\sim 10^{7-8}$ yr, in order to sustain the NTB mechanism. This seems to be too short, compared with the crossing time of these galaxies of $\sim 10^9$ yr. Therefore, the NTB scenario is again unlikely.

A practical problem associated with this galaxy-motion picture is how the kinetic energy is efficiently dissipated. A drag force exerted onto a galaxy moving through the ICM can be written as $\frac{dE}{dt} \sim -\pi \rho_{\text{ICM}} \times v^3 \times R_D^2$. Here ρ_{ICM} is the ICM density, v is the galaxy velocity, and R_D is the effective radius of the galaxy (e.g. Sarazin 1988). The force will lead to an acceleration or heating of the hot plasma, while a deceleration of the galaxy motion. For the galaxies shown above, the total drag force is given as $1.7 \times 10^{41} N^{\text{gal}} (\frac{R_D}{10 \text{ kpc}})^2 \text{ erg s}^{-1}$, where N^{gal} is the number of the galaxies and R_D is the average effective radius. Therefore, the energy dissipation rate may be sufficient depending on R_D . Unfortunately, the actual value of R_D is not well understood. It strongly depends on the model of the galaxy: a galaxy with neither the inter-stellar gas nor the magnetic field will be virtually transparent against the ICM. If, on the other hand, the inter-stellar plasma and the inter-stellar magnetic field of each galaxy is fully taken into account, R_D may be as large as 10 kpc as employed in the above estimate (e.g. Makishima 1999). In any way, the conversion mechanism and efficiency of the kinetic energy of a galaxy, through its interaction with the plasma, is an important subject of future study, particularly from the viewpoint of plasma astrophysics.

Then, are there any observational results which favor this model? In view of our group sample, the HCG 62 and RGH 80 groups, which show strong excess hard X-rays,

Table 6.4: Criteria for dividing the group sample into three sub-categories.

| | |
|-----------------|--|
| Hard : | L_{hard} is consistent with being larger than 10% of L_{IGM} , while its 3.3σ error (two times that of the 90% error) does not cross with zero. |
| Possible hard : | similar to the above groups, while its 3.3σ error do cross with zero. |
| No hard : | L_{hard} is well below 10% of that of L_{IGM} . |

Table 6.5: Galaxy number counts within $50h_{75}^{-1}$ kpc of the group center.

| hard | $N_{50 \text{ kpc}}^{\text{gal}}$ | possible hard | $N_{50 \text{ kpc}}^{\text{gal}}$ | no hard | $N_{50 \text{ kpc}}^{\text{gal}}$ |
|----------|-----------------------------------|---------------------|-----------------------------------|----------|-----------------------------------|
| HCG 62 | 4 | NGC 2563 | 1 | HCG 51 | 4 |
| HCG 97 | 2 | NGC 6329 | 1 | NGC 1132 | 1 |
| NGC 1399 | 2 | NGC 6521 | 1 | NGC 1550 | 1 |
| NGC 507 | 2 | Pavo ⁽¹⁾ | 2 | NGC 4325 | 1 |
| RGH 80 | 2 | See § 5.2.3. | | NGC 5044 | 1 |
| S49-147 | 1 | | | NGC 533 | 1 |
| | | | | NGC 5846 | 1 |
| | | | | NGC 7619 | 1 |

host several galaxies in their central regions. In contrast, the NGC 5044 and NGC 4325 groups, which show little evidence for excess hard X-rays, have a single, relatively isolated central galaxy in the center (see Appendix D.3). To quantify this possible difference, we accordingly divide our group sample into 3 sub-categories using the results of spectral analysis listed in Table 5.4: groups with strong hard excess (“hard groups”), those with possible hard excess (“possible hard groups”), and those with little (limited) hard excess (“no hard groups”). The classification criteria are summarized in Table 6.4. We then count the number of bright galaxies within $50h_{75}$ kpc ($N_{50 \text{ kpc}}^{\text{gal}}$) of the X-ray centroid by eye. Here, 50 kpc is taken to be two times the typical galaxy diameter. The results are summarized in Table 6.5 and Fig.6.5. A clear tendency is visible: most of the groups with little signature of hard X-rays have a single isolated galaxy in its center, while those with significant hard X-rays seems to have more than two galaxies. The average galaxy count is 2.2 ± 0.6 , 1.3 ± 0.6 and 1.4 ± 0.4 for the “hard groups”, the “possible hard groups”, and the “no hard groups”, respectively. The errors are poisson error of the total galaxy counts in the sub-categories. Although this result is not statistically significant, and our sample is far from being complete, it fits in the current model: a dominant galaxy sitting at the center of the group potential does not move, hence do not dissipate any kinetic energy into the intra-group space. If, in contrast, multiple galaxies reside in the central group region, they must be continuously moving around one another, possibly leading to an efficient IGM heating.

In summary, the galaxy motion will be a reasonable candidate as an origin for the hard component, though its acceleration (or heating) mechanisms is poorly understood.

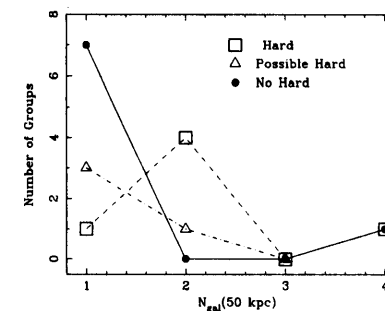


Figure 6.5: Histogram of the groups sorted with the galaxy count within $50h_{75}$ kpc of the group center. Open squares represent the “hard groups”, open triangle the “possible hard group”. and filled circles the “no hard groups”.

6.6.4 Group merger

A galaxy group with a bulk velocity of 1000 km s^{-1} has a kinetic energy of 10^{62} erg, assuming a group mass of $10^{13} M_{\odot}$. Thus, a group merger event can generate sufficient energy for all the three emission models discussed above. Because it is intrinsically a temporal phenomenon, the group merger can explain the variation in the hard component luminosities among the groups, and it is also in principle consistent with the correlation between the central galaxy number and the hard component. However, the merging events are not observationally confirmed to be a common feature among the groups, in contrast to the case of clusters (e.g. Sarazin et al. 1999, Honda et al. 1996, Markevitch et al 1998). Thus we will just refer to it as a candidate of the acceleration source.

Chapter 7

Conclusion

From our study of excess hard X-ray emission from groups of galaxies with ASCA, we have arrived at following conclusions.

- The existence of an excess hard X-ray emission is confirmed in about half of the 18 galaxy groups selected from the ASCA data. The emission cannot be explained by either the point sources (LMXBs or AGNs) in the member galaxies, or the fluctuation in the CXB brightness. In several groups, in particular HCG 62, the hard X-rays are confirmed to be extended, with its radial profile similar to or rather wider than that of the IGM brightness. Therefore the hard component is suggested to be truly of diffuse nature.
- The spectra of the hard component is described by a power law with $\Gamma \sim 2$. It is also consistent with a thermal origin. In the groups with strong hard excess, the inferred temperature becomes as high as ~ 10 keV. When the hard component is weak, rather lower temperature ($2 \sim 3$ keV) is obtained.
- The observed hard component luminosity varies considerably among the group sample. In the most convincing cases, it amounts to $1 \sim 18 \times 10^{41} h_{75}^{-2} \text{ erg s}^{-1}$, or $10 \sim 40\%$ of that of the IGM luminosity. In the least significant cases, the upper-limit becomes $\sim 5\%$ of that of the IGM component.
- The luminosity ratio between the hard component and the IGM, obtained from the groups with significant hard excess, is similar to those obtained from the three clusters from which the hard excess emission are reported.
- As the emission mechanisms of the hard X-rays, the non-thermal bremsstrahlung (NTB) interpretation is unrealistic, due to the huge Coulomb loss. The inverse

Compton (IC) interpretation predicts very low magnetic field strength, of $\sim 0.1\mu\text{G}$, requiring an inhomogeneity of the magnetic field. The thermal interpretation under pressure equilibrium assumption is not applicable to at least several groups and all the clusters, while magnetic confinement picture requires a large field strength of $\sim 20\mu\text{G}$. The non-thermal pressure associated with the hard component remains a few percent of that of the hot gas component for the IC interpretation.

- The acceleration or heating mechanism for the hard component is not well constrained from current data. However, we found that most of the groups with significant hard excess emission host a few bright galaxies in their central regions, while those without predominantly host a single dominant galaxy. We propose that the member galaxies moving in a plasma may be supplying their kinetic energy to the hard component.

Appendix A

Individual Properties of the Five Observations of HCG 62

A.1 Ratio of the spectra

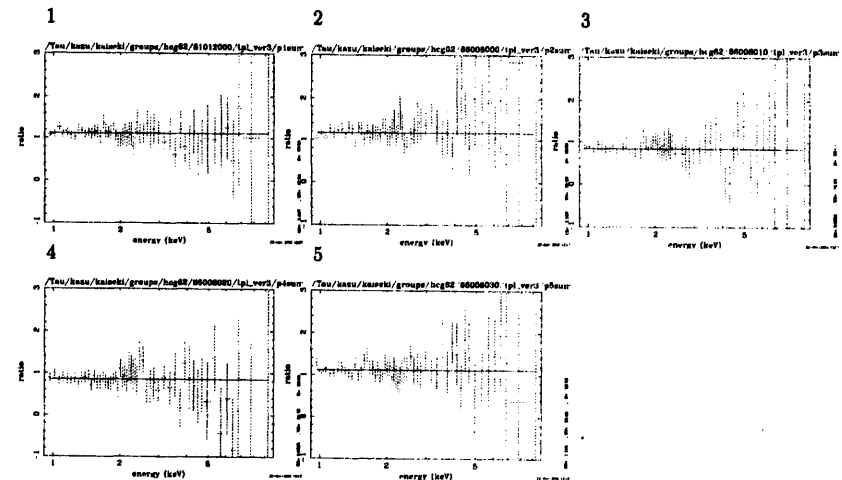


Figure A.1: The raw GIS spectra from the five pointings obtained within $15'$ from the group center (Fig.4.8), divided by the averaged spectra (Fig.4.9) after the correction for the difference in the detector effective area.

A.2 Radial Profiles

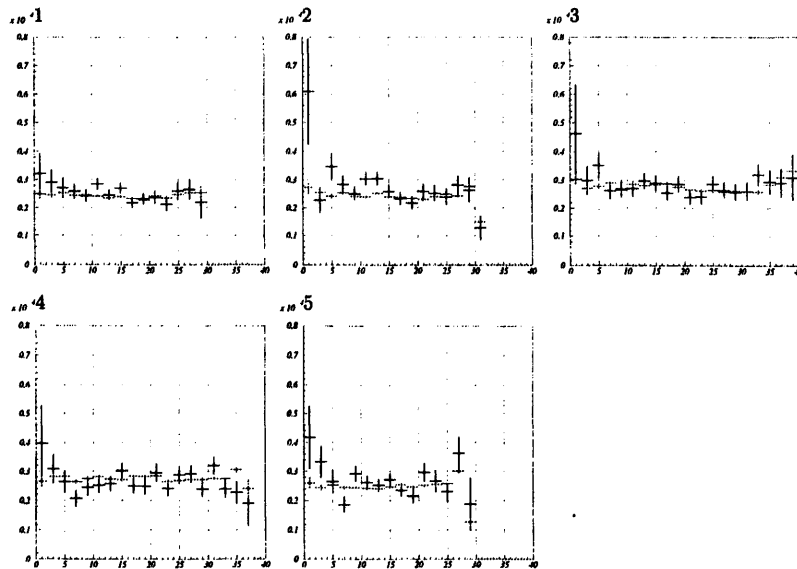


Figure A.2: The same as Fig.4.15a, but for each observation.

Appendix B

Detailed Analysis of the 4.0–8.0 keV Band Image of HCG 62

B.1 Image clumpiness

In §4.4.2, we analytically estimated the CXB fluctuation to be $\sim 0.5 \times 10^{-5}$ cts s^{-1} arcmin $^{-2}$ at 1σ level in the 4.0–8.0 keV band. To verify this estimation by the actual data, we also analyzed blank sky data in the same manner as for HCG 62. In Fig.B.1, we show the resulting 4–8 keV image obtained from the sky region SA-57 (observation ID = 91001040), which is one of the blank sky data sets used in the CXB template (§3.3.5). It has an exposure of 105 ksec, which is comparable to the sum of the five observations of the HCG 62 group. By comparing this image with Fig.4.14a, we can see that the fluctuation level is very similar between the two images.

We also quantified the clumpiness of the 4.0–8.0 keV band image of HCG 62 (Fig.4.14a) and SA-57 (Fig.B.1). The average signal brightness and the 1σ fluctuation in the $4'.5 < r < 15'$ region of HCG 62 are both derived to be 0.44×10^{-5} cts s^{-1} arcmin $^{-2}$. On the other hand, those of SA-57 are 0.0 and 0.42×10^{-5} cts s^{-1} arcmin $^{-2}$. Thus, the fluctuation level is in good agreement with the analytically estimated value for both cases, while HCG 62 shows a systematic excess in this energy band.

B.2 Correlation with the galaxies

If the hard X-rays are emitted from galaxies located within the integration regions, the distribution of the hard X-rays and those of the galaxies will show a correlation. To examine this effect, we made a radial profile in the 4.0–8.0 keV band centered on each

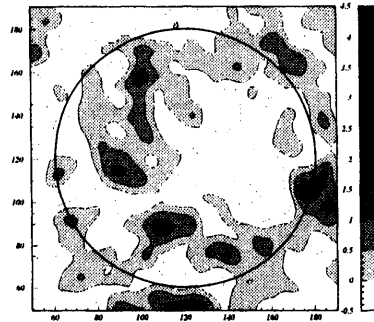


Figure B.1: The 4.0-8.0 keV GIS gray scale image of the SA-57 region, which is similar to Fig.4.14a for the HCG 62 group. The contour is linearly spaced with distances of 0.5×10^{-5} cts s^{-1} arcmin $^{-2}$. A supplemental contour of -0.5×10^{-4} cts s^{-1} arcmin $^{-2}$ is also plotted (dotted lines).

galaxy, and averaged the obtained profiles. For simplicity, we excluded the central $4'.5$ of the group, because the region is very crowded, and used the 9 galaxies within $4'.5 < r < 15'$ of the integration region. The background profiles were made by the same manner using the template CXB and NXB, in which the CXB fluctuation calculated from equation 4.2 was included as a systematic error. The results are plotted in Fig.B.2. We also show the radial profile expected when all the hard X-rays (~ 500 photons) are emitted from these 9 galaxies. The profile shows no enhancement around the galaxies, and clearly differs from the expected profile. Thus, the galaxy contribution to the hard X-rays is concluded to be insignificant.

B.3 Azimuthal dependence

In Fig.4.14a, there is a tendency that the hard emission is brighter in the northern half of HCG 62 than in the southern half. If this tendency is significant, it may contain some information about the origin of the hard X-rays. To examine this possibility, we divided the spectrum integration region into 8 sectors, each having 45° angular scale, where the central $r < 3'$ is excluded. The count rate of these 8 sectors obtained after subtracting the background are plotted in Fig.B.3. Thus, the surface brightness of the southern regions is about half that of the northern regions. However, the CXB fluctuation expected in

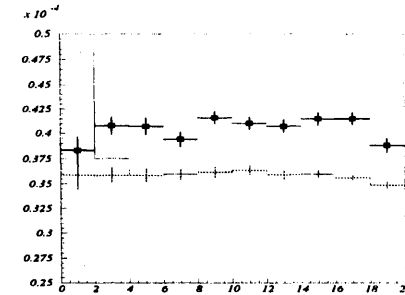


Figure B.2: Averaged 4-8 keV radial profile centered on 9 galaxies in the HCG 62 field (black crosses), and that of the background (gray crosses), in cts s^{-1} arcmin $^{-2}$. Error bars are in 1σ , which are averaged over the 9 galaxies. The background error includes the CXB fluctuation. Thin histograms show what is expected if the hard component is entirely emitted from these 9 galaxies.

these integration regions is $\sim 4 \times 10^{-6}$ cts s^{-1} arcmin $^{-2}$, and the profile is statistically consistent with being flat when we consider this effect. Thus, we found no evidence for azimuthal variation in the hard component distribution.

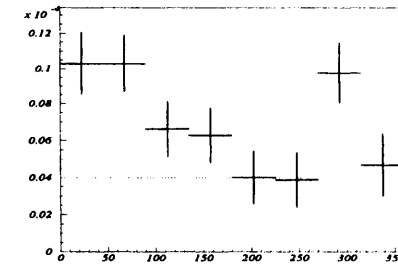


Figure B.3: Azimuthal profile of the 4-8 keV image of HCG 62, in cts s^{-1} arcmin $^{-2}$. The angle is defined clockwise, the north being the origin. Thin line represents the 1σ level of the estimated CXB fluctuation. Errors are 1σ statistical.

Appendix C

Calculation of the CXB Fluctuation

We present here a brief summary of the calculation we used in estimating the CXB fluctuation. See Ishisaki (1996) for detail.

C.1 Formulation of the CXB fluctuation

Condon (1974) estimated the CXB fluctuation level, and we below introduce her results briefly.

Let $n(S)$ denote the differential source number density with the flux S ($\text{erg cm}^{-2} \text{s}^{-1}$). This $n(S)$ represents the log N -log S relation, usually expressed by

$$n(S) = k S^{-\gamma} \quad (\gamma = 2.5 \text{ for the Euclidian universe}). \quad (\text{C.1})$$

We next define the transmission function $f(\theta, \phi)$ for the detector, which relates the observed counting rate x ($\text{c s}^{-1} \text{cm}^{-2}$) for the detector to the flux S from the source locating at $\Omega = (\theta, \phi)$ on the sky as:

$$x = A f(\Omega) S, \quad (\text{C.2})$$

where A is a constant which normalizes $f(\theta, \phi)$ to be 1.0 at the peak, i.e., $f(0, 0) = 1$. Then, the expectation $d\bar{n}(x)$ of the source number with the counting rate in the range $x \sim x + dx$ can be estimated as

$$d\bar{n}(x) d\Omega = n(S) dS d\Omega = n\left(\frac{x}{A f(\Omega)}\right) \frac{dx}{A f(\Omega)} d\Omega, \quad (\text{C.3})$$

since $dx = A f(\Omega) d\Omega$. Assuming equation (C.1), we derive

$$d\bar{n}(x) = k A^{\gamma-1} x^{-\gamma} \Omega_e dx, \quad (\text{C.4})$$

where

$$\Omega_e \equiv \int [f(\Omega)]^{\gamma-1} d\Omega. \quad (\text{C.5})$$

This Ω_e is called "effective beam size" and represents the response of the detector to the source confusion.

Utilizing equation (C.4), we can calculate the expectation \bar{D} of the observed counting rate D ($\text{c s}^{-1} \text{cm}^{-2}$) as:

$$\bar{D} = \int_{D_0}^{\infty} x d\bar{n} = k A^{\gamma-1} \Omega_e \int_{D_0}^{\infty} x^{-\gamma+1} dx = \frac{k A^{\gamma-1} \Omega_e}{2-\gamma} D_0^{2-\gamma}, \quad (\text{C.6})$$

where D_0 is a lower cut-off of x , which is introduced to avoid the divergence of the integral. Physically, this means that the log N -log S relation should flatten below some flux. Since $d\bar{n}$ should be subject to the Poisson distribution, i.e., $\delta(d\bar{n})^2 = d\bar{n}$, we can also calculate the standard deviation σ_D of the observed counting rate D as:

$$\sigma_D^2 = \int_0^{D_c} \frac{[x \delta(d\bar{n})]^2}{dx} dx = \int_0^{D_c} x^2 d\bar{n} = \frac{k A^{\gamma-1} \Omega_e}{3-\gamma} D_c^{3-\gamma}, \quad (\text{C.7})$$

where D_c is an upper cut-off of x , i.e. we discard the data brighter than D_c regarding not a blank sky. Therefore, the fraction of the CXB fluctuation is

$$\sigma_D / \bar{D} = \frac{(k A^{\gamma-1} \Omega_e D_c^{3-\gamma})^{1/2} (2-\gamma)}{(3-\gamma)^{1/2} k A^{\gamma-1} \Omega_e D_0^{2-\gamma}} = \frac{2-\gamma}{\sqrt{(3-\gamma) k \Omega_e}} \left(\frac{D_c}{A}\right)^{(3-\gamma)/2} \left(\frac{D_0}{A}\right)^{\gamma-2}. \quad (\text{C.8})$$

for the Euclidian universe, i.e., $\gamma = 2.5$, this becomes

$$\sigma_D / \bar{D} \propto \Omega_e^{-0.5} S_c^{0.25} \quad (S_c \equiv D_c/A). \quad (\text{C.9})$$

C.2 Effective beam size for the XRT+GIS

Taking into account both vignetting and stray-light effects, we calculate Ω_e for the XRT+GIS when we use inside 20 mm from the optical axis as the data integration region. Fig.C.1 shows the dependence of the Crab counting rate on the offset angle θ from the XRT optical axis. As seen in the figure, we approximate the counting rate as:

$$f(\theta) = \begin{cases} \frac{710}{1 + (x/13)^2} & \dots (\theta < 18') \\ -51.6(\theta - 22) + 20 & \dots (18' \leq \theta < 22') \\ \frac{20}{1 + 0.5 \exp[(\theta - 60)/9]} & \dots (22' \leq \theta) \end{cases} \quad (\text{C.10})$$

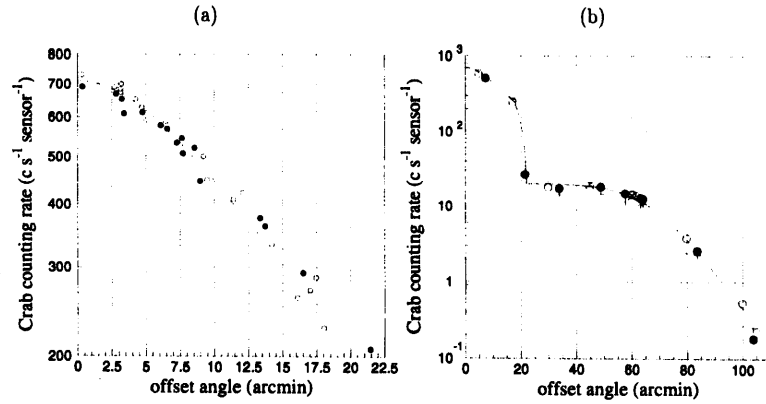


Figure C.1: (a) The observed Crab counting rate in the 0.7-10 keV energy band plotted against the offset angle from the XRT optical axis. Filled circles represent GIS2 and open circles GIS3. (b) Same as panel (a) but for the larger θ . Solid line represents equation (C.10).

If we ignore the azimuth angle dependence, we can calculate Ω_e as:

$$\Omega_e = 2\pi \int_0^\infty [f(\theta)/f(0)]^{\gamma-1} \sin \theta d\theta. \quad (\text{C.11})$$

In figure C.2, we show

$$\Omega_e(\theta_e) = 2\pi \int_0^{\theta_e} [f(\theta)/f(0)]^{1.5} \sin \theta d\theta. \quad (\text{C.12})$$

Therefore, Ω_e for the XRT+GIS is 0.142 deg². Contribution of the stray light to Ω_e is ~ 0.01 deg² and almost negligible.

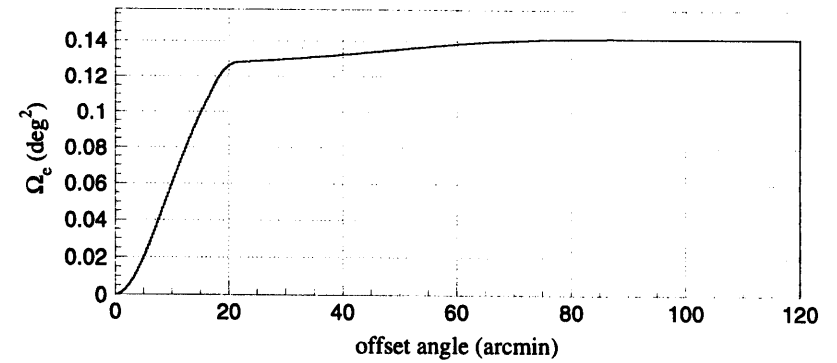


Figure C.2: Calculation of Ω_e for the XRT+GIS.

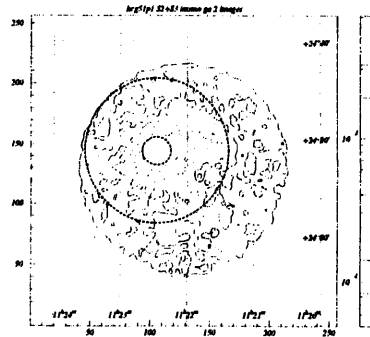
Appendix D

Analysis Results of All Groups

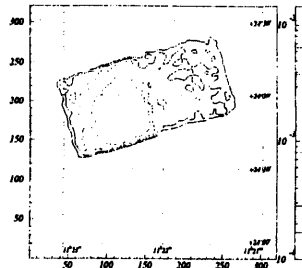
D.1 Images and integration regions

Figure D.1: The full band X-ray contour images of the GIS and the SIS, similar to Fig.5.1, but for the other groups. In most of the GIS images and all the SIS images, background is not subtracted. The contours are logarithmically spaced by factors of 1.7, starting from 5×10^{-5} cts s^{-1} arcmin $^{-2}$ for the GIS (2.9×10^{-5} cts s^{-1} arcmin $^{-2}$ for NGC 507), and 1×10^{-4} cts s^{-1} arcmin $^{-2}$ for the SIS. Spectral intergration region and positions of the point sources are shown only in the GIS image.

(a) HCG 51 GIS (bgd inclusive)

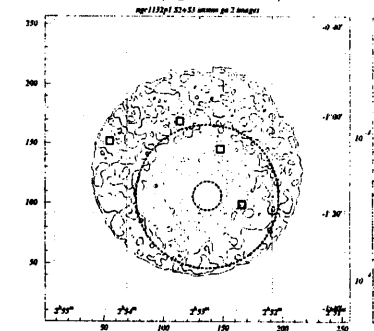


SIS

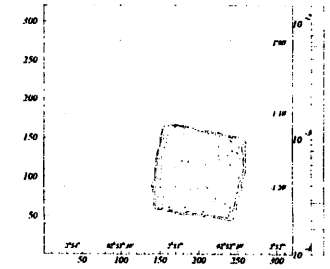


153

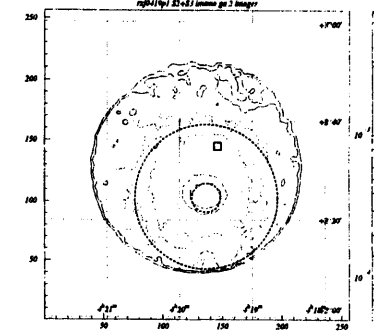
(b) NGC 1132 GIS (bgd inclusive)



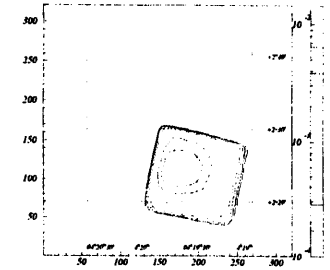
SIS



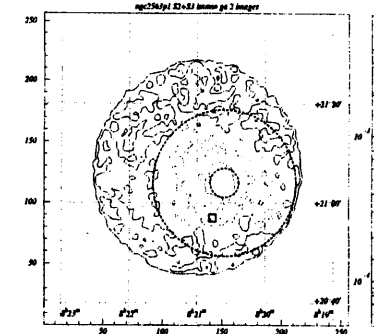
(c) NGC 1550 GIS (bgd inclusive)



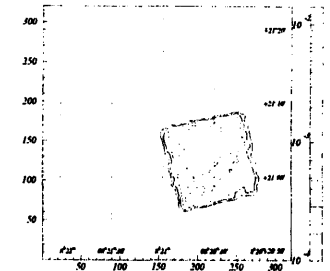
SIS



(d) NGC 2563 GIS (bgd inclusive)

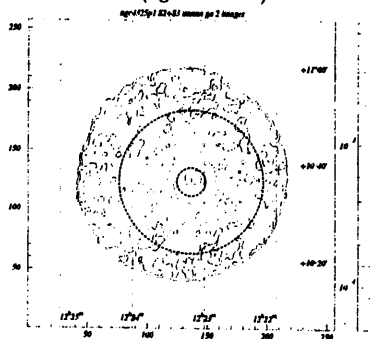


SIS

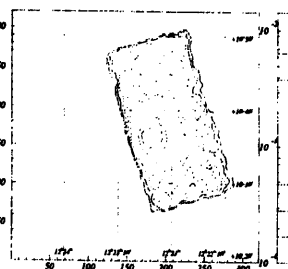


154

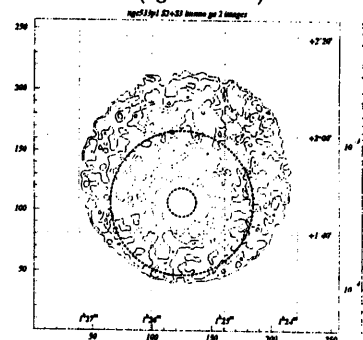
(e) NGC 4325 GIS (bgd inclusive)



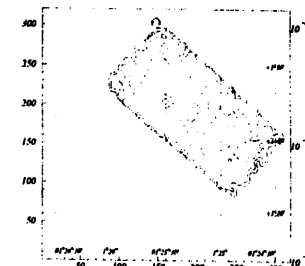
SIS



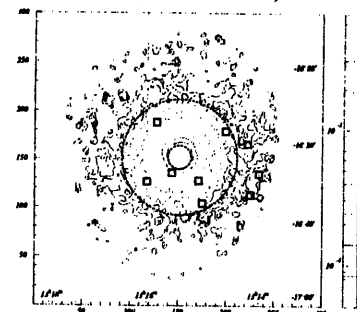
(h) NGC 533 GIS (bgd inclusive)



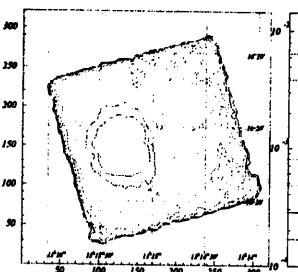
SIS



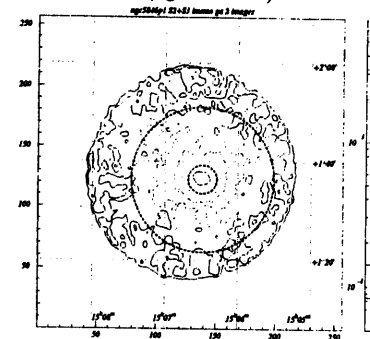
(f) NGC 5044 GIS (bgd subtracted)



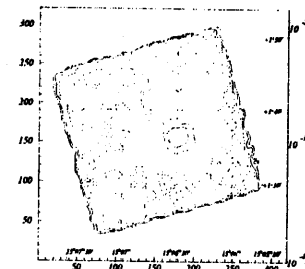
SIS



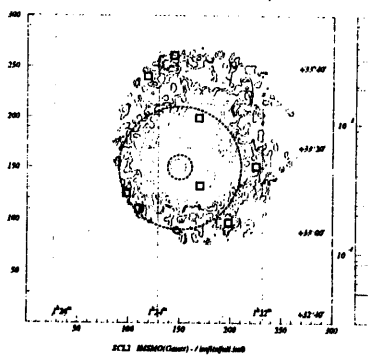
(i) NGC 5846 GIS (bgd inclusive)



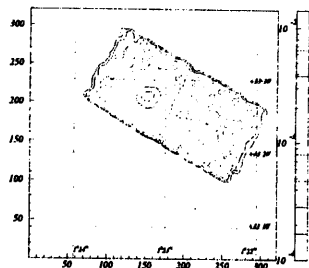
SIS



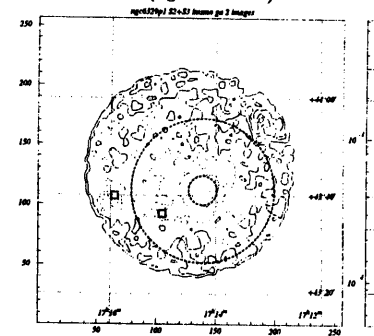
(g) NGC 507 GIS (bgd subtracted)



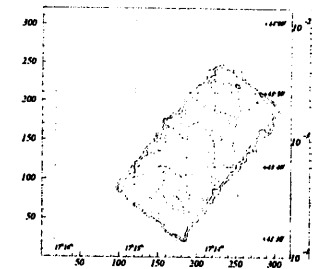
SIS



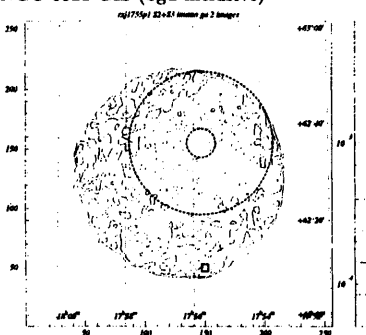
(j) NGC 6329 GIS (bgd inclusive)



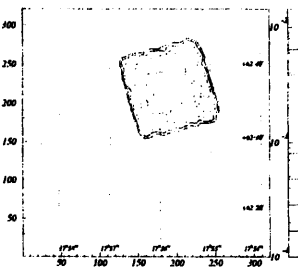
SIS



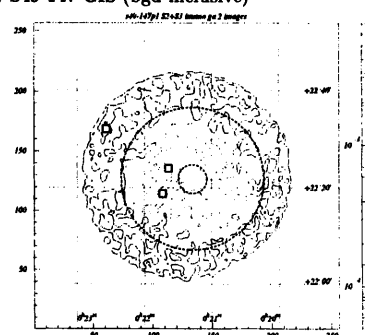
(k) NGC 6521 GIS (bgd inclusive)



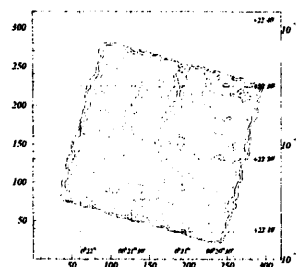
SIS



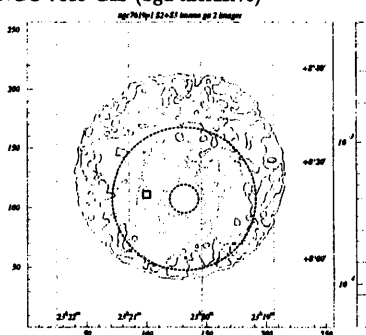
(n) S49-147 GIS (bgd inclusive)



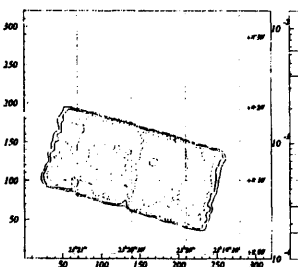
SIS



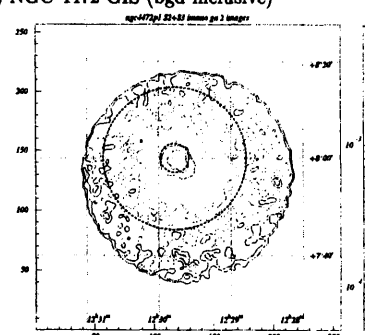
(l) NGC 7619 GIS (bgd inclusive)



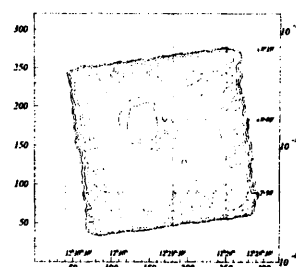
SIS



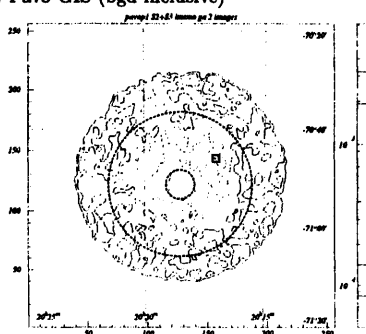
(o) NGC 4472 GIS (bgd inclusive)



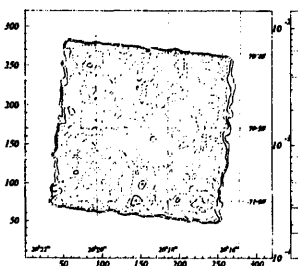
SIS



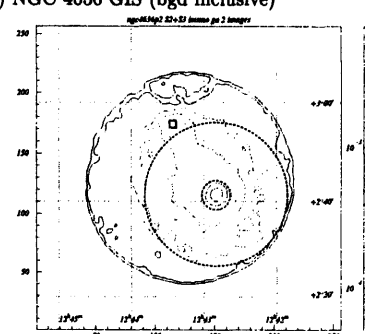
(m) Pavo GIS (bgd inclusive)



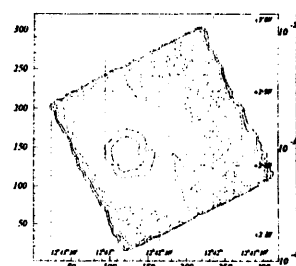
SIS



(p) NGC 4636 GIS (bgd inclusive)



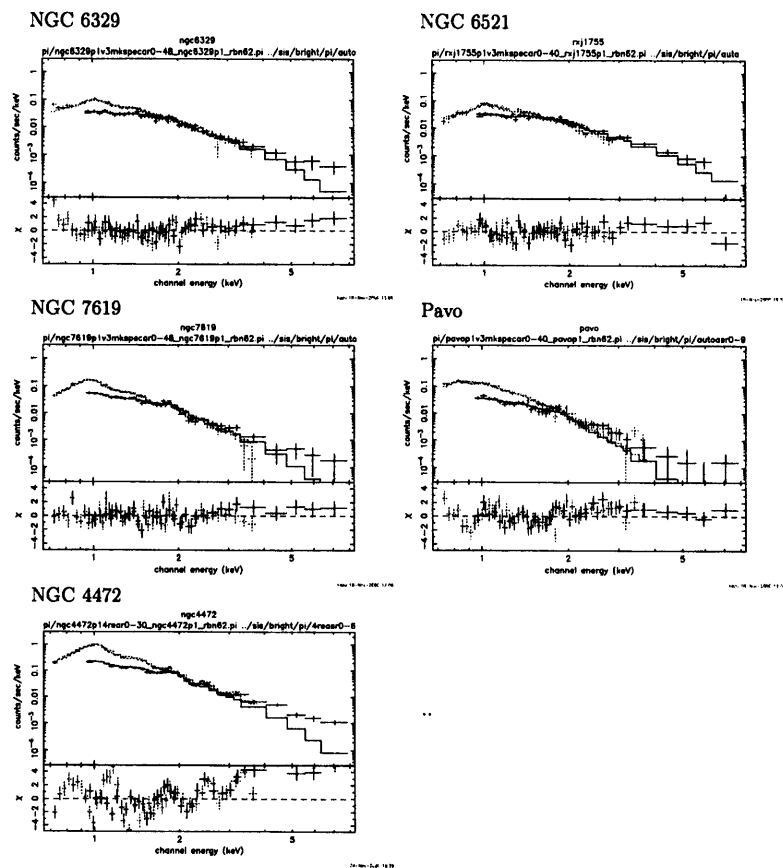
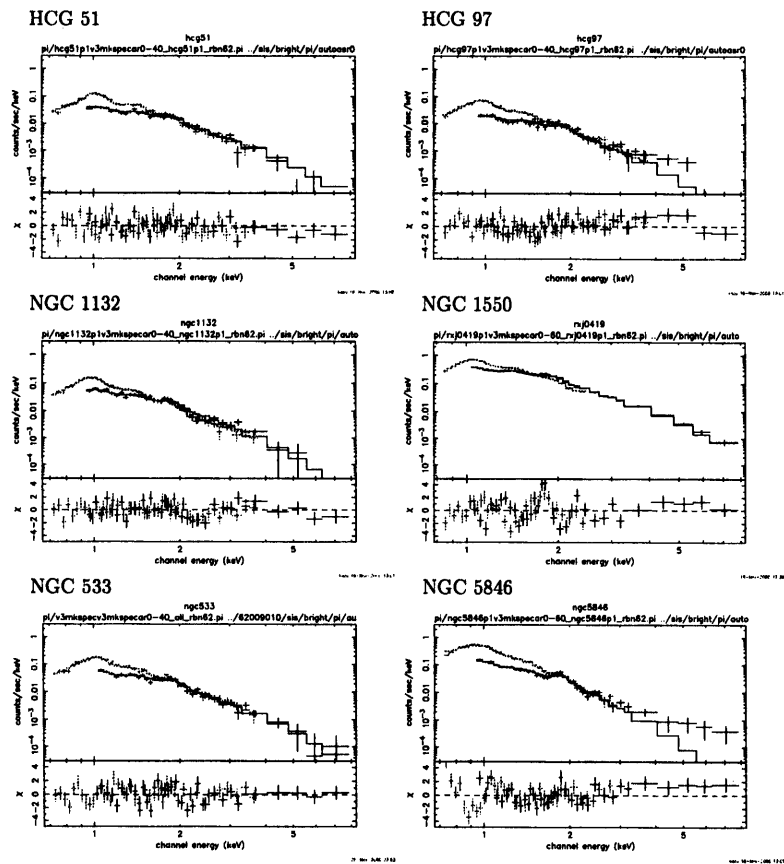
SIS



D.2 Spectra

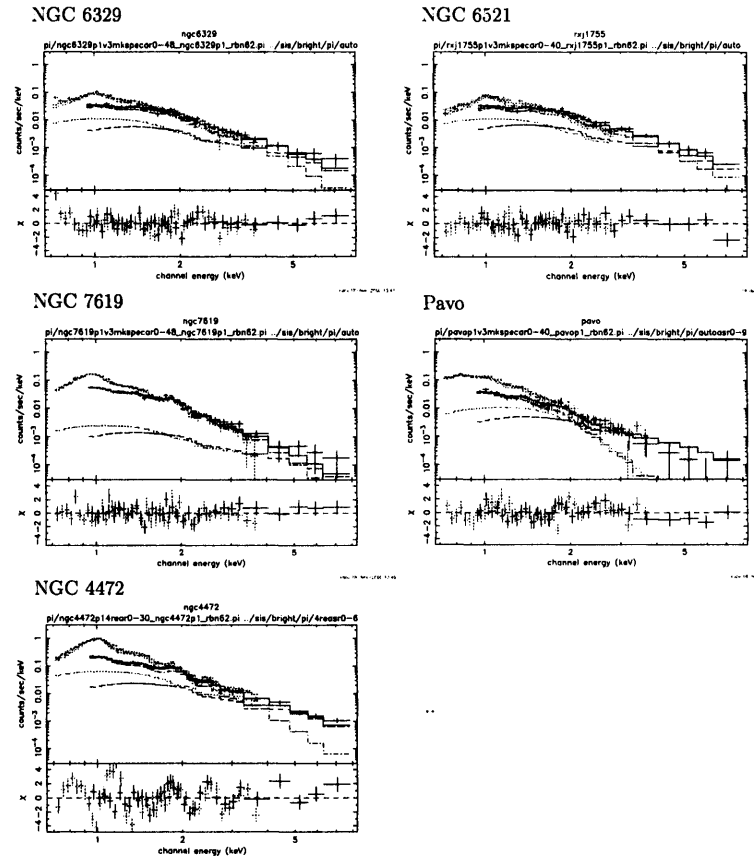
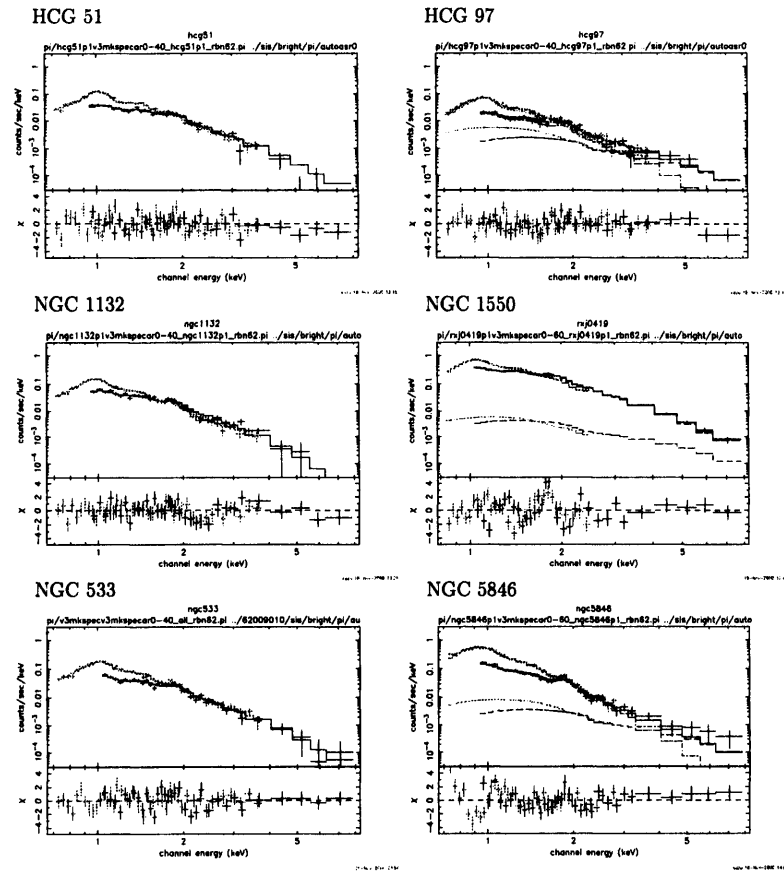
D.2.1 Single component fits

Figure D.2: The same as Fig.5.2, plotted for the remaining targets.



D.2.2 Two component fits

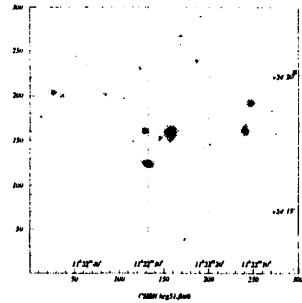
Figure D.3: The same as Fig.5.4, plotted for the remaining targets.



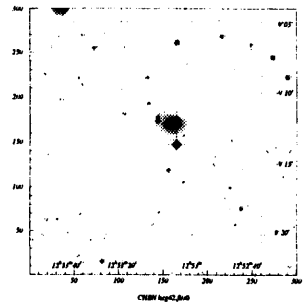
D.3 Optical images of central $300 h_{75}^{-1}$ kpc.

Figure D.4: Optical images of the central $300 h_{75}^{-1}$ kpc region of the groups. "H" indicates the "hard groups", "P" the "possible hard groups", and "N" the "no hard groups" (see Table 6.5).

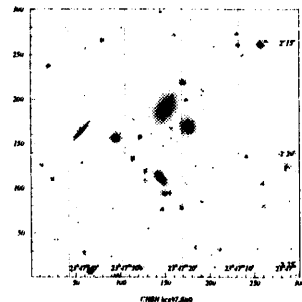
HCG 51 (N)



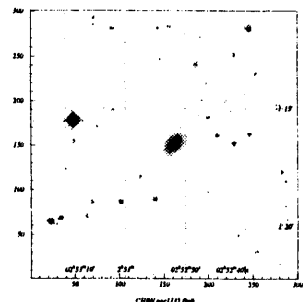
HCG 62 (H)



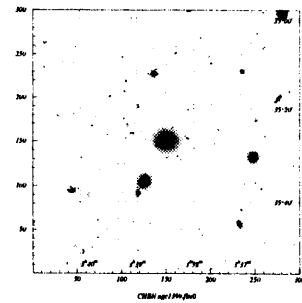
HCG 97 (H)



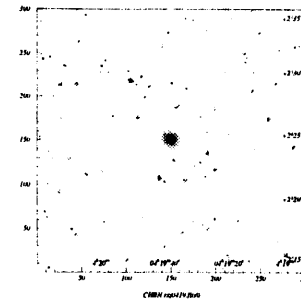
NGC 1132 (N)



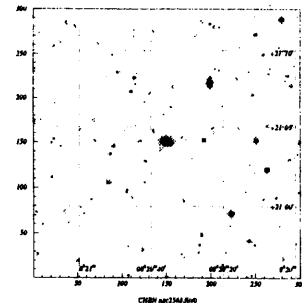
NGC 1399 (H)



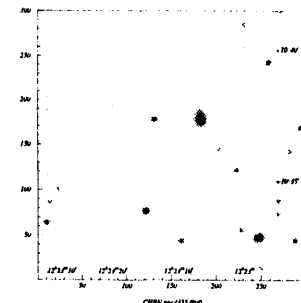
NGC 1550 (N)



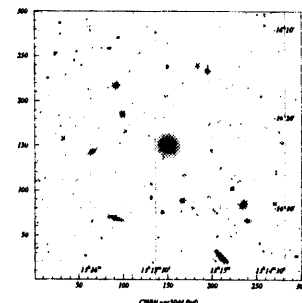
NGC 2563 (P)



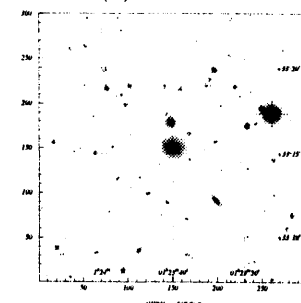
NGC 4325 (N)



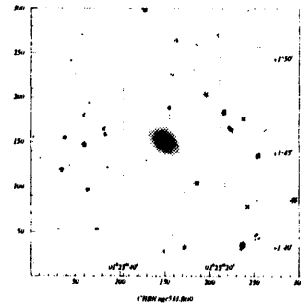
NGC 5044 (N)



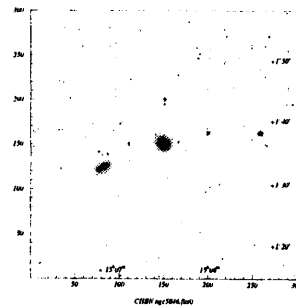
NGC 507 (H)



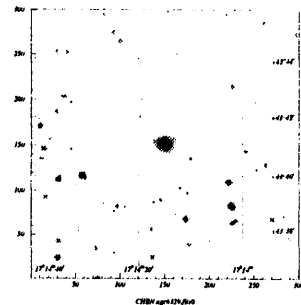
NGC 533 (N)



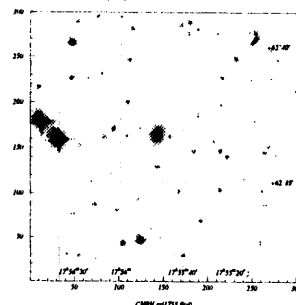
NGC 5846 (N)



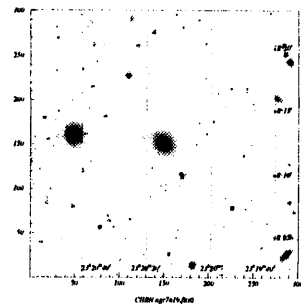
NGC 6329 (P)



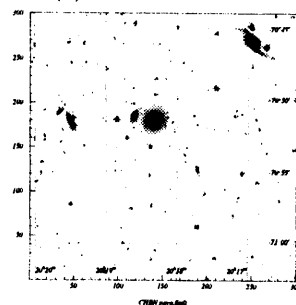
NGC 6521 (P)



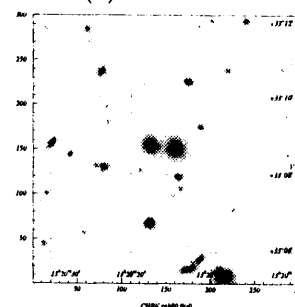
NGC 7619 (N)



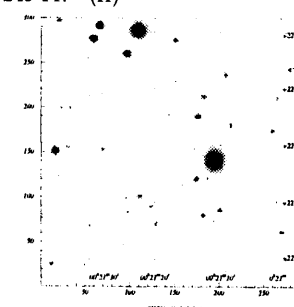
Pavo (P)



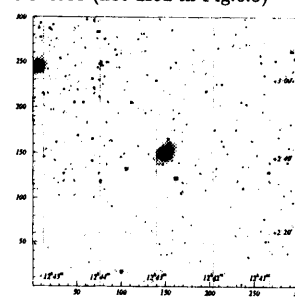
RGH 80 (H)



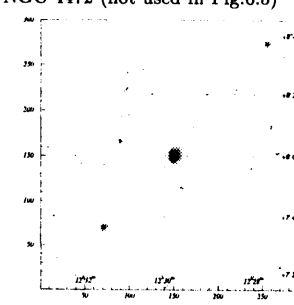
S49-147 (H)



NGC 4636 (not used in Fig.6.5)



NGC 4472 (not used in Fig.6.5)



Abbreviation

GIS: gas imaging spectrometer (onboard ASCA)
SIS: solid-state imaging spectrometer (onboard ASCA)
XRT: X-ray telescope (onboard ASCA)
PSPC: position sensitive proportional counter (onboard ROSAT)
HPGSPC: high pressure gas scintillator proportional counter (onboard Beppo-SAX)
PDS: phoswitch detector system (onboard Beppo-SAX)
MECS: medium energy counter system (onboard Beppo-SAX)
UV: ultra violet
EUV: extream ultra violet
AGN: active galactic nuclei
LLAGN: low luminosity AGN
SN: supernova
SNR: supernova remnant
LMXB: low-mass X-ray binary
HCG: Hickson's compact groups
IC: inverse compton
NTB: non-thermal bremsstrahlung
CMB: cosmic microwave background
CXB: cosmic X-ray background
NXB: non X-ray background
ICM: intra-cluster matter
IGM: intra-group matter
ISM: interstellar matter
CDM: cold dark matter
FWHM: full width half maximum
IPMT: imaging photo-multiplier tube
RT: rise time
RTD: rise time discriminator
PH: pulse hight
COR: cut off rigidity
CCD: charge coupled device
PSF: point spread function
FOV: field of view

PI: principal investigator
EI: emission integral
NGC: new galaxy catalog
KSC: Kagoshima Space Center
ISAS: Institute for Space and Astronautical Science
GSFC: Goddard space flight center

Bibliography

- Abell G.O. 1958, ApJS 3, 211
Allen S.W. et al. 2000, MNRAS 311, 493
Anders E., Grevesse N. 1989, *Goochem. Cosmochim. Acta* 53, 197
Arnaud M. et al. 1991, A&A 243, 56
Berezinsky V.S., Blasi P. and Ptuskin V.S. 1997, ApJ 487, 529
Blumenthal G.R. and Gould R.J. 1970, *Rev.Mod.Phys.* 42, 237
Boute D.A. et al. 1999, MNRAS 310, 483
Burke B.E. et al. 1991, IEEE Trans, ED-38, 1069
Calvalho R.R.de et al. 1997, ApJS 110, 1
Cavaliere A. and Fusco-Femiano R. 1976, A&A 49, 137
Clarke T.E. et al. 2000, astro-ph/0011281
Colles M. and Dunn A.M. 1996, ApJ 458, 435
Condon J.J. et al. 1998 ApJ 115, 1693
Coziol R. et al. 1998, ApJ 493, 563
David L.P. et al. 1993, ApJ 412, 479
Deiss B.M. et al. 1997 A&A 321, 55
de Vaucouleurs G. et al. 1991, (RC3) Springer-Verlag: New York
Dickey and Lockman 1990, ARAA 28, 215
Douglas J.N., Bash F.N., Bozyan F.A., Torrence G.W. and Wolfe C. 1996, AJ 111, 1945
Ekers R.D. et al. 1983, A&A, 127, 361
Ellison D.C. et al. 2000, ApJ 540, 292
Ensslin T.A. et al. 1998, A&A 333, L47
Fabian A.C. et al. 1994, ApJ 436, L63
Fadda D., Girardi M., Giuricin G., Mardirossian F. and Mezzetti M. 1996, ApJ 473, 670
Ferguson H.C. and Sandage A. 1990, AJ 100, 1

- Feigelson E.D. et al. 1995, ApJ 449, L149
Feretti L. and Giovannini G. 1996, IAU *Extragalactic Radio Sources*
Feretti L. and Giovannini G. 1996, *Extragalactic Radio Sources* IAU, 333
Fujita Y. and Takahara F. 1999, ApJ 519, L51
Fukazawa Y. et al. 1996, PASJ 48, 395
Fukazawa Y. et al. 1998, PASJ 50, 187
Fukazawa Y. et al. 2000, MNRAS 313, 21
Fukazawa Y., Nakazawa K., Isobe N., Makishima K., Matsushita K., Ohashi T. and Kamae T. 2001, ApJ Letter, in press.
Fukushige T. and Makini J. 1997, ApJ 477, L9
Fusco-Femiano R. et al. 1999, ApJ 513, L21
Fusco-Femiano R. et al. 2000, ApJ 534, L7
Gendreau K.C. 1994, Doctorial Thesis
Griffith M.R. and Wright A.E. 1993, AJ 105, 1666
Hatsukade I. 1989, Doctorial Thesis, Osaka University
Heitler W. 1954, *The Quantum Theory of Radiation* (Oxford)
Hickson P. 1982, ApJ 255, 382
Hickson P. et al. 1992, ApJ 399, 353
Honda, H. et al. 1996, ApJ 473, L71
Ikebe Y. 1994, Doctorial Thesis, University of Tokyo
Ikebe Y. et al. 1996, Nature 379, 427
Ikebe Y. et al. 1998, Nature 379, 427
Irwin J.A. and Sarazin C.L. 1998, ApJ 499, 650
Ishisaki Y. 1995, Doctorial Thesis, University of Tokyo
Iyomoto N. et al. 1998, ApJ 503, L31
Jones C. and Forman W. 1984, ApJ 276, 38
Jones C. et al. 1997, ApJ 482, 143
Kaastra J.S. et al. 1999, ApJ 519, L119 Kaneda H. 1996, Doctorial Thesis, University of Tokyo
Kaneda H. et al. 1995, ApJ 453, L13
Kaneda H. et al. 1997, ApJ 491, 638
Kempner J.C and Sarazin C.L. 2000, ApJ 530, 282
Kim K.T. et al. 1990, ApJ 355, 29
Kim K.T. et al. 1991, ApJ 379, 80
Koyama K. et al. 1986, PASJ 38, 503

- Koyama K. et al. 1995, *Nature* 378, 255
 Koyama K. et al. 1997, *PASJ* 49, L7
 Koyama K. et al. 1984, *PASJ* 36, 659
 Ledlow M.J., Loken C., Burns J.O., Hill J.M. and White R.A. 1996, *AJ* 112, 388
 Liang H. 1999, MPE Report 271 *Diffuse Thermal and Relativistic Plasma in Galaxy Clusters*, 33
 Lloyd-Davies E.J. et al. 2000, *MNRAS* 315, 689L
 Makino N., Sasaki S. and Suto Y. 1998, *ApJ* 497, 555
 Makishima K. et al. 1996, *PASJ* 41, 697
 Makishima K. et al. 2001, submitted to *ApJ*
 Markevitch M. 1998, *ApJ* 504, 27
 Markevitch M. et al. 1998, *ApJ* 503, 77
 Markevitch M., Forman W.R., Sarazin C.L., Vikhlinin A. 1998, *ApJ* 503, 77
 Matsumoto R. et al. 2000, *Advanced Space Research* 25, 3/4, 499
 Matsumoto Y. et al. 2001, *PASJ*, submitted
 Mitchel R.J. et al. 1976, *MNRAS* 176, 29
 Mohr J.J. et al. 1999, *ApJ* 517, 627
 Moore B. et al. 1998, *ApJ* 499, L5
 Mulchaey J. and Zabludoff A. 1998, *ApJ* 496, 73
 Mulchaey J.S. et al. 1996, *ApJ* 456, 80
 Mushotzky R.F. 1984, *Physica Scripta* (ISSN 0031-8949) vol. T7, 1984, p157
 Navarro J.F., Frenk C.S. and White S.D.M. 1996, *ApJ* 462, 563
 Navarro J.F., Frenk C.S. and White S.D.M. 1997, *ApJ* 490, 493
 Nomoto K. 1984, *ApJ* 277, 791
 Ohashi T. et al. 1996, *PASJ* 48, 157
 Petrosian V. 2000, American Astronomical Society, HEAD meeting #32, #13.07
 Ponmann T. and Bertman D. 1993, *Nature* 363, 51
 Röttgering H.J.A. et al. 1997, *MNRAS* 290, 577
 Ramella M., Geller M.J., Huchra J.P. and Thorstensen J.R. 1995, *AJ* 109, 1458
 Raymond J.C. and Smith B.W. 1977, *ApJS* 35, 419
 Rephaeli Y. 1979, *ApJ* 227, 364
 Rephaeli Y. et al. 1987, *ApJ* 320, 139
 Rephaeli Y. et al. 1994, *ApJ* 429, 554
 Roettiger K. et al. 1999, *ApJ* 518, 594
 Rousseld H. et al. 2000, *A&A* 361, 429

- Rybicki G.B. and Lightman A.P. 1979, *Radiative Processes in Astrophysics*
 Sarazin C.L. 1988, *X-ray emissions from clusters of galaxies* Cambridge press
 Sarazin C.L. 1999, *ApJ* 520, 529
 Sarazin C.L. 2000 *Constructing the Universe with Clusters of Galaxies* Ed. F. Durret and D. Gervais, in press, astro-ph/0009094
 Sarazin C.L. and Kempner J.C. 2000, *ApJ* 533, 73
 Sarazin C.L. and Lieu R. 1998, *ApJ* 494, L177
 Serlemitsos P.J. et al. 1977, *ApJ* 211, L63
 Serlemitsos P.J. et al. 1995, *PASJ* 47, 105
 Snowden S.L., McCammon D., Burrows D.N., Mendenhall J.A. 1994, *ApJ* 424, 714
 Tanaka Y. et al. 1984, *PASJ* 36, 641
 Tanimori T. et al. 1998, *ApJ* 497, L25
 Tibble P.C. 1993, *MNRAS* 263, 31
 Toor, A. and Seward, F.D. 1974, *AJ* 79, 995
 Tusru T.G. 1992, Doctorial Thesis, University of Tokyo
 Ueda Y. 1995, Doctorial Thesis, University of Tokyo
 Ueda et al. 1996
 Valagas P. and Silk J. 1999, *A&A* 350, 725
 Verdes-Montenegro L, et al. 1998, *ApJ* 497, 89
 Wegner G., Haynes M.P. and Giovanelli R, 1993, *AJ* 105, 1251
 Worrall D.M. et al. 1982, *ApJ* 255, 111
 Yamasaki N.Y. et al. 1997, *ApJ* 481, 821
 Yamauchi S. and Koyama K. 1993, *ApJ* 404, 620
 Zabludoff A. I. and Mulchaey J.S. 1998b, *ApJ* 498, L5
 Zabludoff A. and Mulchaey J. 1998a, *ApJ* 496, 39
 van den Berg S. and Tanman G.A. 1991, *ARA&A* 29, 363

Acknowledgement

First of all, I would appreciate very much to Prof. K.Makishima for his continuous guidance for this thesis and hearty support during all the five years of my graduate course. I am deeply indebted to Prof. Y.Fukazawa for his valuable suggestions and encouragement on this thesis, as well as all my research works in these five years. I would also express my thanks to Prof. T.Kamae, Prof. M.Tashiro, Prof. T.Takahashi, Prof. T.Murakami and Dr. K.Matsushita for their suggestions and guidance.

I owe a great deal to all the scientists and engineers who work on ASCA, especially the ASCA-XRT team, the simASCA team, and the GIS team, particularly on the background studies. I am grateful to all the members of Maxima-Kamae group, including Mr. M.Kokubun and Ms. A.Kubota, who shared all the five years, Mr. I.Takahashi and Mr. N.Isobe, who are my colleges on the extended source analysis.

Finally, I would express my thanks to all the people worked on the development of ASTRO-E and the HXD, who shared those hard and sad, but also fruitfull years.